



**HAL**  
open science

# Constraints on the Higgs self-coupling at the LHC with $\sqrt{s} = 13$ TeV and long-lived particles searches with a future lepton collider

Yulei Zhang

► **To cite this version:**

Yulei Zhang. Constraints on the Higgs self-coupling at the LHC with  $\sqrt{s} = 13$  TeV and long-lived particles searches with a future lepton collider. High Energy Physics - Experiment [hep-ex]. Université Paris Cité; Shanghai Jiao Tong University, 2023. English. NNT : 2023UNIP7357 . tel-04874807

**HAL Id: tel-04874807**

**<https://theses.hal.science/tel-04874807v1>**

Submitted on 8 Jan 2025

**HAL** is a multi-disciplinary open access archive for the deposit and dissemination of scientific research documents, whether they are published or not. The documents may come from teaching and research institutions in France or abroad, or from public or private research centers.

L'archive ouverte pluridisciplinaire **HAL**, est destinée au dépôt et à la diffusion de documents scientifiques de niveau recherche, publiés ou non, émanant des établissements d'enseignement et de recherche français ou étrangers, des laboratoires publics ou privés.



上海交通大学  
SHANGHAI JIAO TONG UNIVERSITY



Université Paris Cité

En cotutelle avec Shanghai Jiao Tong University

Laboratoire Astroparticule et Cosmologie (APC-Paris)

École Doctorale des Sciences de la Terre et de l'Environnement  
et Physique de l'Univers de Paris, ED 560

# Constraints on the Higgs Self-coupling at the LHC with $\sqrt{s} = 13$ TeV and Long-lived Particles Searches with a Future Lepton Collider

Par YULEI ZHANG

Thèse de doctorat en PHYSIQUES DE L'UNIVERS  
Dirigée par GREGORIO BERNARDI  
Et par LIANG LI

Présentée et soutenue publiquement le 18 Décembre 2023

Devant un jury composé de:

MME.	SUZANNE SHOTKIN-GASCON	PROFESSEUR	UNIVERSITÉ CLAUDE BERNARD, LYON	RAPPORTEUR
M.	YAQUAN FANG	PROFESSEUR	IHEP, UNIVERSITY OF BEIJING	RAPPORTEUR
MME.	VALENTINA CAIRO	STAFF CERN	CERN	EXAMINATEUR
M.	MATTEO CACCIARI	PROFESSEUR	UNIVERSITÉ PARIS CITÉ	EXAMINATEUR
M.	KUN LIU	ASS. PROFESSEUR	TD LEE INSTITUTE, SHANGHAI	EXAMINATEUR
M.	HAIJUN YANG	PROFESSEUR	SJTU UNIVERSITY OF SHANGHAI	EXAMINATEUR
M.	GREGORIO BERNARDI	DR	APC-PARIS	DIRECTEUR
M.	LIANG LI	PROFESSEUR	SHANGHAI JIAO TONG UNIVERSITY	DIRECTEUR



---

# Résumé

**Titre:** Contraintes sur l’auto-couplage du boson de Higgs au LHC avec  $\sqrt{s} = 13$  TeV et recherches de particules à longue durée de vie avec un futur collisionneur de leptons

**Résumé:** Le Modèle Standard (MS) de la physique des particules fournit un cadre complet qui a été vérifié expérimentalement à un degré impressionnant, avec le boson de Higgs comme élément central. Les investigations sur les interactions di-Higgs offrent des aperçus essentiels sur le comportement d’auto-couplage du boson de Higgs et pourraient potentiellement élucider les mécanismes sous-jacents à la brisure de la symétrie électrofaible. De plus, le boson de Higgs agit comme une voie prospective pour explorer une multitude de théories au-delà du Modèle Standard, avec les Particules à Longue Durée de Vie (LLP) représentant juste un des plusieurs modèles intrigants encore à explorer pleinement.

Dans la première analyse de la thèse, l’attention est centrée sur la production de paires de bosons de Higgs du MS ( $HH$ ) se désintégrant en états finals multileptons, en particulier à 3 leptons. En utilisant  $140 \text{ fb}^{-1}$  de données de collisions proton-proton à  $\sqrt{s} = 13$  TeV provenant du détecteur ATLAS lors du Run 2, l’étude explore principalement la production de  $HH$  par fusion de gluons (ggF), avec une contribution additionnelle par fusion de bosons vectoriels (VBF). Essentiel à ce travail est l’atténuation du bruit de fond principal  $WZ$ , abordée par repondération pour prendre en compte la mauvaise modélisation à de grandes multiplicités de jets, et le bruit de fond de faux leptons, estimé via la méthode "Template Fit". Un arbre de décision boosté par gradient est utilisé pour une discrimination optimale signal-bruit, affinée en outre par une technique d’entraînement triple et un réglage exhaustif des hyperparamètres. De façon remarquable, ce canal à 3 leptons atteint une limite supérieure de 28.1 la section efficace  $HH$  par rapport au MS, constituant une amélioration de 9,4 fois par rapport aux analyses précédentes. Lors de la prise en compte de tous les canaux multileptons, la limite supérieure attendue est de  $9.74_{-7.02}^{+13.91}$ , faisant du résultat du canal à 3 leptons l’une des meilleures limites parmi les canaux de désintégration purement leptoniques.

Le deuxième aspect clé de cette thèse concerne l’analyse  $HH \rightarrow b\bar{b}\tau^+\tau^-$ , s’appuyant sur  $140 \text{ fb}^{-1}$  de données complètes de Run 2 d’ATLAS. Ce travail se distingue par le raffinement ciblé des approches méthodologiques, en particulier en ce qui concerne les modificateurs de couplage  $\kappa_\lambda$  et  $\kappa_{2V}$ . En utilisant des techniques avancées d’analyse multivariée (MVA), l’analyse est optimisée séparément pour les modes de production par fusion de gluons et par Fusion de Bosons Vectoriels. En particulier, la catégorisation des événements est basée sur la masse invariante ( $m_{HH}$ ) de la paire de Higgs dans la région ggF, avec une catégorie VBF supplémentaire introduite pour améliorer la sensibilité à  $\kappa_{2V}$ . L’utilisation des sorties MVA comme ultimes discriminants a engendré des améliorations significatives par rapport aux données précédentes: une amélioration en sensibilité de 17% sur  $\mu_{HH}$ , et des améliorations de 11.9% et 19.8% dans les intervalles de confiance à 95% pour  $\kappa_\lambda$  et  $\kappa_{2V}$ , respectivement.

L’analyse combinée  $HH+H$  conclut les investigations di-Higgs de la thèse. Cette synthèse incorpore les principaux canaux di-Higgs ( $b\bar{b}b\bar{b}$ ,  $b\bar{b}\gamma\gamma$ , et  $b\bar{b}\tau^+\tau^-$ ) avec les observables de Higgs simples pour imposer des contraintes strictes sur les modificateurs de couplage clés, spécifiquement  $\kappa_\lambda$  et  $\kappa_{2V}$ . Dans un ajustement complet, où  $\kappa_t$ ,  $\kappa_b$ ,  $\kappa_\tau$ , et  $\kappa_V$  sont autorisés à varier librement, l’analyse atteint un intervalle de confiance à 95% de  $-1.4 < \kappa_\lambda < 6.1$ , qui se rapproche étroitement de la plage attendue de  $-2.2 < \kappa_\lambda < 7.7$ . La stabilité de ces résultats est corroborée par une sensibilité minimale aux fluctuations de  $\kappa_{2V}$ , affectant les contraintes observées sur  $\kappa_\lambda$  de moins de 5%. Cela confirme la concordance de tous les modificateurs de couplage analysés avec le MS, dans les limites des incertitudes associées.

Dans la dernière partie de la thèse, l'enquête se tourne vers l'examen des modes de désintégration du boson de Higgs dans le domaine de la physique BSM, ciblant spécifiquement les LLP. À cette fin, des algorithmes d'apprentissage automatique de pointe, tels que les réseaux neuronaux convolutionnels (CNN) et les réseaux neuronaux en graphes (GNN), sont déployés pour une analyse directe sur la sortie brute du détecteur, ce qui améliore considérablement l'efficacité de sélection du signal attendu. Par exemple, dans le cas d'une LLP de 50 GeV avec une durée de vie de 1 ns, l'efficacité du signal attendu atteint 99%. Cette recherche atteint une limite supérieure attendue de  $4 \times 10^{-6}$  pour le rapport de branchement du Higgs se désintégrant en LLP sous l'hypothèse de  $10^6$  de Higgs, ce qui dépasse significativement la limite supérieure de  $1 \times 10^{-3}$  actuellement établie par ATLAS et CMS. Pour les LLP avec des durées de vie supérieures à 1 ns, l'analyse produit une limite supérieure attendue qui est un ordre de grandeur meilleur que les résultats attendus du Collisionneur Linéaire International.

Enfin, la section d'annexe de la thèse décrit une étude préliminaire sur les recherches de photons sombres via une expérience cible fixe proposée avec des électrons de 8 GeV reculant à partir d'une cible métallique à grand-Z.

**Mots clefs:** Physique des Hautes Énergies, Collisionneur, di-Higgs, multilepton,  $b\bar{b}\tau^+\tau^-$ , Particules à Longue Durée de Vie, Apprentissage automatique, techniques avancées, Intelligence Artificielle

---

# Résumé étendu

Qu'est ce qui constitue le tissu même de l'univers ? Comment ses plus petits constituants interagissent-ils pour former le monde tel que nous le comprenons ? Ces questions fondamentales sont centrales dans le domaine de la physique des particules, qui étudie les particules élémentaires constituant la matière. Les collisionneurs à haute énergie, machines qui accélèrent les particules à une vitesse proche de celle de la lumière et les font se percuter, offrent des opportunités uniques pour aborder ces questions en permettant aux scientifiques d'étudier les interactions de particules dans des conditions imitant l'univers primordial.

Le Modèle Standard de la physique des particules, une théorie bien établie développée au cours du dernier demi-siècle, explique avec succès ces interactions. Il fournit un cadre pour comprendre comment les particules connues, comme les quarks et les électrons, interagissent à travers des forces fondamentales - à savoir, les forces électromagnétique, faible et forte. La découverte du boson de Higgs en 2012 au Grand Collisionneur de Hadrons (LHC) du CERN, un anneau de 27 kilomètres sous la frontière France-Suisse, a fourni la pierre angulaire de ce modèle. Le boson de Higgs explique pourquoi certaines particules ont une masse, affirmant le succès monumental du Modèle Standard.

Malgré ces succès, il y a des phénomènes qui ne peuvent pas être expliqués par le Modèle Standard, tels que la matière noire, une substance mystérieuse qui constitue environ 27% de l'univers mais n'émet, n'absorbe ni ne reflète aucun rayonnement électromagnétique. Ces lacunes dans la compréhension appellent à l'exploration au-delà de la physique du Modèle Standard (BSM). Une voie intéressante est l'étude des particules à longue durée de vie (LLPs), qui sont des particules hypothétiques qui ne se désintègrent pas aussi rapidement que les autres et pourraient interagir faiblement avec la matière normale.

En réponse aux défis et opportunités posés par ces questions, les scientifiques ont déployé le Grand Collisionneur de Hadrons et planifient de futures machines connues sous le nom de collisionneurs de leptons. Cela inclut des projets tels que le Collisionneur Linéaire International (ILC), le Collisionneur Électron-Positron Circulaire (CEPC) et le Futur Collisionneur Circulaire (FCC-ee). Ces collisionneurs visent à fournir des mesures plus précises du boson de Higgs et à explorer de nouvelles physiques potentielles.

La découverte du boson de Higgs marque un jalon monumental en physique des particules, servant à la fois de confirmation du Modèle Standard et de porte d'entrée vers de nouvelles explorations. Ma recherche contribue à la prochaine phase cruciale de ce domaine en se concentrant sur la recherche di-Higgs, où deux bosons de Higgs sont produits simultanément. C'est un domaine d'étude pivot pour comprendre des aspects uniques du Higgs, en particulier son auto-couplage, qui régit la manière dont le boson de Higgs interagit avec lui-même. Mes analyses se concentrent particulièrement sur les événements avec des états finals multileptons et  $b\bar{b}\tau^+\tau^-$ .

De plus, pour fournir une compréhension plus complète du secteur du Higgs, mon travail intègre une combinaison d'événements de production de Higgs simples et doubles. Cette approche intégrée vise à contraindre l'auto-couplage du boson de Higgs avec une précision accrue, offrant ainsi des aperçus critiques sur la physique du Modèle Standard et au-delà.

Au-delà du champ d'analyse di-Higgs et simple-Higgs, ma recherche s'étend aux phénomènes BSM, en se concentrant particulièrement sur les LLPs. Utilisant des techniques d'apprentissage automatique qui interprètent directement les données brutes du détecteur, j'ai développé une méthodologie novatrice pour distinguer ces particules hypothétiques des particules du Modèle Standard dans des simulations.

Enfin, alors que le corps principal de cette thèse se concentre sur des expériences basées sur des collisionneurs, mes intérêts s'étendent à d'autres formes de recherche en physique des particules. En particulier, j'ai travaillé sur une expérience visant à détecter des photons sombres, particules proposées comme vecteurs de force pour la matière noire, en utilisant une expérience à cible fixe qui utilise des faisceaux d'électrons à haute énergie.

En résumé, cette thèse offre un récit cohérent de mon parcours de recherche en doctorat. Elle couvre de l'investigation de questions fondamentales en physique des particules à des contributions significatives tant dans les études de bosons de Higgs basées sur des collisionneurs que dans les recherches de particules à longue durée de vie BSM, tout en s'aventurant également dans des expériences au-delà des collisionneurs. Chacune de ces entreprises de recherche ajoute une pièce au puzzle complexe de la compréhension de l'univers à son niveau le plus basique. Cette thèse est organisée comme suit :

- **Chapitre 2** : Fournit un aperçu de la physique du Higgs dans le Modèle Standard et au-delà.
- **Chapitre 3** : Discute du Grand Collisionneur de Hadrons et de l'expérience ATLAS.
- **Chapitre 4** : Se concentre sur les techniques de simulation et de reconstruction d'événements dans ATLAS.
- **Chapitre 5** : Présente les recherches di-Higgs SM dans les états finals multileptons.
- **Chapitre 6** : Couvre les recherches di-Higgs SM dans les états finals  $b\bar{b}\tau^+\tau^-$ .
- **Chapitre 7** : Vise à contraindre l'auto-couplage du boson de Higgs en utilisant des données de production de Higgs simples et doubles.
- **Chapitre 8** : Discute des stratégies de recherche pour les particules à longue durée de vie avec les futurs collisionneurs de leptons.
- **Chapitre 9** : Résume les découvertes et discute des perspectives futures.
- **Annexe** : Décrit une expérience à cible fixe pour sonder le photon sombre en utilisant un faisceau d'électrons de 8 GeV.

## Recherche de la production di-Higgs avec des états finals multileptons

Dans cette étude, nous examinons la production de paires de bosons de Higgs ( $HH$ ) via la fusion de gluons, en utilisant les données du détecteur ATLAS basées sur des collisions proton-proton à une énergie au centre de masse de  $\sqrt{s} = 13$  TeV. L'ensemble de données englobe une luminosité totale de  $140 \text{ fb}^{-1}$ , collectée pendant la seconde phase du Grand Collisionneur de Hadrons. En accord avec les analyses existantes des collaborations ATLAS et CMS, cette recherche mène une recherche exhaustive à travers de multiples canaux de désintégration, incluant  $VVVV$ ,  $VV\tau\tau$ ,  $\tau\tau\tau\tau$ ,  $\gamma\gamma VV$ , et  $\gamma\gamma\tau\tau$ , où  $V$  représente les bosons  $W^\pm$  ou  $Z$ . Spécifiquement, l'étude se concentre sur les désintégrations  $HH$  en  $b\bar{b}ZZ$ , avec les bosons  $Z$  se désintégrant en leptons. Étant donné la variété des états finals dans les analyses multileptons, cette thèse restreint son champ d'application au canal à 3 leptons, un choix motivé par la phénoménologie complexe et l'intrication du canal.

Concluant cette étude, l'analyse du canal à 3 leptons basée sur  $140 \text{ fb}^{-1}$  de données de collision proton-proton à  $\sqrt{s} = 13$  TeV collectées par le détecteur ATLAS est présentée. L'accent a été mis sur la production de paires de Higgs SM ( $HH$ ), principalement à travers la fusion de gluons (ggF) avec la fusion de bosons vectoriels (VBF) comme rendement supplémentaire. Le bruit de fond principal,  $WZ$ , a été ajusté pour tenir compte d'une modélisation incorrecte dans les multiplicités de jets élevées à l'aide d'une fonction d'ajustement. Le bruit de fond secondaire, résultant de faux leptons, a été estimé par la méthode d'Ajustement de Modèle, avec des facteurs de normalisation dérivés de multiples régions de contrôle. Une méthode d'Arbres de Décision à Gradient Boosté, améliorée par une stratégie d'entraînement en trois étapes et un réglage détaillé des hyperparamètres, a été employée pour la discrimination signal-bruit. L'étude a atteint une signification

maximale du signal de 0.073 dans le canal à 3 leptons, avec une limite supérieure de la section efficace  $HH \rightarrow 3\ell$  de  $23.13^{+10.21}_{-6.66}$  par rapport au SM, s'améliorant à  $28.09^{+12.81}_{-7.86}$  en incluant toutes les incertitudes. Ceci représente une avancée significative par rapport aux analyses précédentes. Dans les résultats multileptons combinés, la limite supérieure attendue est de  $8.93^{+12.69}_{-6.44}$  statistiquement, et  $9.74^{+13.91}_{-7.02}$  avec toutes les incertitudes systématiques incluses. Le canal à 3 leptons émerge comme l'un des plus robustes dans les canaux purement leptoniques, rivalisant étroitement avec le canal leader  $\gamma\gamma + 1\ell$ .

## Recherche de la production di-Higgs avec des états finals $b\bar{b}\tau^+\tau^-$

Dans l'exploration de la production SM de paires de bosons de Higgs ( $HH$ ), cette étude met l'accent sur le canal de désintégration  $b\bar{b}\tau^+\tau^-$ , notable pour sa signature unique et son utilité analytique. Malgré une fraction de branchement plus faible de 7,3% par rapport aux canaux  $b\bar{b}b\bar{b}$  et  $b\bar{b}WW$ , le canal  $b\bar{b}\tau^+\tau^-$  offre une signature expérimentale plus claire, essentielle pour une détection et une analyse précises. La désintégration des leptons  $\tau$  en électrons ou en muons ( $\tau_{\text{lep}}$ ) ou en hadrons chargés et neutres ( $\tau_{\text{had}}$ ) conduit à la considération de deux sous-canaux spécifiques :  $b\bar{b}\tau_{\text{lep}}\tau_{\text{had}}$  et  $b\bar{b}\tau_{\text{had}}\tau_{\text{had}}$ , les événements  $b\bar{b}\tau_{\text{lep}}\tau_{\text{lep}}$  étant analysés dans un canal distinct  $b\bar{b}l\bar{l}$ .

Cette analyse complète s'appuie sur des études précédentes, qui se concentraient principalement sur le mode de production SM par fusion de gluons (ggF). L'analyse précédente avait fixé une limite supérieure à la section efficace  $HH$  à 130 (110) fb à 95% CL, correspondant à 4,7 (3,9) fois la prédiction du SM. Cette étude, avec ses raffinements méthodologiques et catégorisations supplémentaires, vise à avancer ces résultats, en particulier concernant les modificateurs  $\kappa_\lambda$  et  $\kappa_{2V}$ . Les améliorations significatives de cette analyse incluent :

- Une réoptimisation de  $\kappa_\lambda$  en mettant en œuvre une catégorisation d'événements basée sur la masse invariante du système  $HH$  ( $m_{HH}$ ) dans la région ggF, permettant des mesures et des contraintes plus précises sur ce paramètre.
- L'introduction d'une catégorie dédiée à la fusion de bosons vectoriels (VBF) améliore la sensibilité de l'étude au paramètre  $\kappa_{2V}$ , élargissant la portée de l'analyse.
- L'adoption de techniques avancées d'Analyse Multivariée (MVA) pour maximiser la discrimination signal-bruit. Cette approche a été cruciale pour affiner l'analyse, avec les sorties MVA servant de discriminants finaux dans l'ajustement.

Les résultats de cette analyse démontrent une amélioration marquée par rapport aux études précédentes. Une amélioration de 17% sur la sensibilité de  $\mu_{HH}$  a été atteinte, indiquant une mesure plus robuste et précise du taux de production de paires de bosons de Higgs. De plus, les intervalles de confiance pour  $\kappa_\lambda$  et  $\kappa_{2V}$  ont été resserrés, avec une amélioration de 11,9% de l'intervalle de confiance à 95% pour  $\kappa_\lambda$  et une amélioration encore plus notable de 19,8% pour  $\kappa_{2V}$ . Ces avancées soulignent l'efficacité des améliorations méthodologiques et des catégorisations supplémentaires introduites dans cette étude. L'analyse raffinée fournit non seulement des contraintes plus strictes sur les paramètres clés mais aussi une compréhension plus complète des processus de production et de désintégration  $HH$ , en particulier dans le canal  $b\bar{b}\tau^+\tau^-$ .

## Contraintes sur l'auto-couplage du Higgs avec la production de Higgs simple et double

Suite à la découverte du boson de Higgs par les collaborations ATLAS et CMS, le Grand Collisionneur de Hadrons (LHC) a joué un rôle déterminant dans la mesure méticuleuse des propriétés

du boson de Higgs. Cette entreprise vise à corroborer les prédictions du Modèle Standard (SM) ou à révéler de nouveaux phénomènes physiques. Dans le cadre du SM, le boson de Higgs est central dans la brisure de la symétrie électrofaible, donnant de la masse aux particules élémentaires et assurant l'unitarité perturbative. L'auto-couplage trilineaire du boson de Higgs,  $\lambda_{\text{HHH}}$ , lié à la masse du Higgs  $m_H$  et à la constante de Fermi  $G_F$ , est un point central de cette étude.

Cette analyse consolide les données des trois canaux de désintégration double-Higgs les plus sensibles :  $b\bar{b}\gamma\gamma$ ,  $b\bar{b}\tau^+\tau^-$ , et  $b\bar{b}b\bar{b}$ , en utilisant les données d'ATLAS collectées entre 2015 et 2018. Ces données, correspondant à une luminosité intégrée de 126–139 fb<sup>-1</sup> à  $\sqrt{s} = 13$  TeV, sont employées pour évaluer le modificateur de couplage  $\kappa_\lambda$ , défini comme  $\kappa_\lambda = \lambda_{\text{HHH}}/\lambda_{\text{HHH}}^{\text{SM}}$ . De plus, l'étude incorpore les résultats de la production de Higgs simple, en considérant d'importantes corrections électrofaibles d'ordre suivant (NLO), pour obtenir des contraintes plus complètes sur  $\kappa_\lambda$ .

Des études précédentes d'ATLAS, utilisant des données partielles de Run 2, ont établi une limite supérieure sur la production de  $HH$  SM, et la collaboration CMS a rapporté des résultats similaires. Cependant, cette étude fait progresser ces efforts en intégrant les principales analyses de double-Higgs avec les résultats de Higgs simple, améliorant la précision sur  $\kappa_\lambda$  et  $\kappa_{2V}$ . En employant un ajustement qui permet la variation de multiples modificateurs de couplage, y compris  $\kappa_t$ ,  $\kappa_b$ ,  $\kappa_\tau$ , et  $\kappa_V$ , l'analyse présente un intervalle de confiance à 95% pour  $\kappa_\lambda$  de  $-1.4 < \kappa_\lambda < 6.1$ , un résultat qui reflète étroitement les limites attendues de  $-2.2 < \kappa_\lambda < 7.7$ . Notamment, l'impact des variations de  $\kappa_{2V}$  sur les limites de  $\kappa_\lambda$  est minimal, moins de 5%, renforçant la force et la fiabilité de ces contraintes. Ce résultat est significatif car il confirme la cohérence de tous les autres modificateurs de couplage avec les prédictions du SM dans leurs incertitudes respectives, consolidant ainsi la compréhension fondamentale du boson de Higgs dans le contexte du Modèle Standard.

## Recherche de particules à longue durée de vie avec les futurs collisionneurs de leptons

La physique des particules est apparue comme une discipline distincte avec la découverte du muon en 1936 et du kaon en 1947, leurs durées de vie macroscopiques étant détectables avec la technologie de la chambre à nuages du début du 20e siècle. La progression vers des technologies modernes telles que les traceurs en silicium et les chambres de projection temporelle n'a pas diminué l'importance de la mesure des longueurs de désintégration en physique des particules. Malgré le changement d'orientation vers des énergies et des luminosités plus élevées avec l'avènement de grands accélérateurs de particules, la mesure des durées de vie des particules reste un aspect fondamental du domaine. Ceci est particulièrement évident dans la recherche de particules exotiques à longue durée de vie (LLPs) dans des installations telles que LEP et Tevatron, où les LLPs sont considérées cruciales pour des découvertes potentielles au-delà du Modèle Standard (SM), en particulier dans le domaine de la supersymétrie. Les approches théoriques se sont élargies pour englober une plus large gamme de signatures LLP, soutenues par des avancées dans les algorithmes de déclenchement et de reconstruction et une compréhension plus approfondie du bruit de fond dans les recherches de LLP.

Le lien entre les LLPs et le boson de Higgs est particulièrement intéressant. Le mécanisme de Higgs, central à la brisure de symétrie électrofaible et à l'acquisition de masse pour les bosons  $W$  et  $Z$ , peut également être une porte d'entrée vers de nouveaux secteurs en physique des particules. La nature scalaire et la structure de couplage du boson de Higgs en font un candidat probable pour se désintégrer en états exotiques, produisant potentiellement des LLPs détectables. Ces LLPs induits par le Higgs offrent une perspective unique pour sonder à la fois les propriétés structurelles du secteur Higgs et les nouvelles frontières de la physique. Des paramètres clés tels que le taux de production, la longueur de désintégration et la dilatation du temps sont cruciaux pour évaluer

la détectabilité et l'interprétation de tels événements de désintégration exotiques. S'appuyant sur cette prémisse, l'étude actuelle se penche sur les désintégrations du Higgs en LLPs, en employant un cadre analytique de pointe adapté aux futurs Collisionneurs de Leptons. Tirant parti des réseaux de neurones convolutifs (CNNs) et des réseaux de neurones graphiques (GNNs) appliqués directement aux données brutes du détecteur, cette approche a non seulement rationalisé l'analyse mais a également obtenu des résultats remarquables. L'étude rapporte une limite supérieure attendue d'environ  $4 \times 10^{-6}$  pour les LLPs, une amélioration significative par rapport aux limites de  $1 \times 10^{-3}$  établies par des collisionneurs hadroniques comme ATLAS et CMS. De plus, cette méthode dépasse les capacités des collisionneurs de leptons, telles que démontrées par les expériences auprès du Collisionneur Linéaire International (ILC), d'environ un ordre de grandeur dans les limites d'exclusion attendues pour les LLPs avec des durées de vie supérieures à 1 ns.

## Contribution de l'auteur

Dans l'étude diHiggs vers multileptons, mes rôles clés comprenaient la direction de la stratégie d'analyse à 3 leptons, agissant en tant qu'éditeur de la note interne, et représentant notre groupe lors des réunions du comité éditorial et des discussions d'approbation de demande de dévoilement.

Pour l'analyse  $HH \rightarrow b\bar{b}\tau^+\tau^-$ , je me suis concentré sur l'application et l'optimisation des Arbres de Décision Boostés (BDTs) pour la séparation des régions ggF et VBF, et pour la différenciation signal-bruit. Cela impliquait une étude détaillée et un réglage fin des hyperparamètres et des variables d'entrée des BDT, ayant un impact significatif sur les résultats finaux.

Dans le travail de combinaison HH+H, j'ai joué un rôle crucial dans la consolidation des espaces de travail double-Higgs pour l'intégration dans l'analyse du Higgs simple.

Quant à l'étude des Particules à Longue Durée de Vie (LLPs) avec les futurs collisionneurs de leptons, j'ai servi en tant que premier auteur, dirigeant la recherche et rédigeant l'étude.





上海交通大学博士学位论文

在 **13 TeV** 对撞能量下利用大型强子对撞机对  
希格斯粒子自耦合作用的约束研究以及在未  
来轻子对撞机上寻找长寿命粒子

姓 名: 张 宇 雷

学 号: 019072210002

导 师: 李亮教授, Gregorio Bernardi 教授

院 系: 物理与天文学院

学 科/专 业: 粒子物理

申 请 学 位: 理学博士

2023 年 12 月 18 日



13

**A Dissertation Submitted to**

14

**Shanghai Jiao Tong University for Doctoral Degree**

15

**CONSTRAINTS ON THE HIGGS SELF-COUPLING**

16

**AT THE LHC WITH  $\sqrt{s} = 13$  TEV AND LONG-LIVED**

17

**PARTICLES SEARCHES WITH A FUTURE LEPTON**

18

**COLLIDER**

19

**Author:** Yulei Zhang

20

**Supervisor:** Prof. Liang Li, Prof. Gregorio Bernardi

21

School of Physics and Astronomy

22

Shanghai Jiao Tong University

23

Shanghai, P.R. China

24

December 18<sup>th</sup>, 2023



25

## 上海交通大学

26

### 学位论文原创性声明

27

28

29

30

本人郑重声明：所呈交的学位论文，是本人在导师的指导下，独立进行研究工作所取得的成果。除文中已经注明引用的内容外，本论文不包含任何其他个人或集体已经发表或撰写过的作品成果。对本文的研究做出重要贡献的个人和集体，均已在文中以明确方式标明。本人完全知晓本声明的法律后果由本人承担。

31

学位论文作者签名：

日期： 年 月 日

32

## 上海交通大学

33

### 学位论文使用授权书

34

35

本人同意学校保留并向国家有关部门或机构送交论文的复印件和电子版，允许论文被查阅和借阅。

36

本学位论文属于：

37

公开论文

38

内部论文，保密  1 年 /  2 年 /  3 年，过保密期后适用本授权书。

39

秘密论文，保密 \_\_\_\_ 年（不超过 10 年），过保密期后适用本授权书。

40

机密论文，保密 \_\_\_\_ 年（不超过 20 年），过保密期后适用本授权书。

41

（请在以上方框内选择打“√”）

42

学位论文作者签名：

指导教师签名：

日期： 年 月 日

日期： 年 月 日



## 摘要

43

44 粒子物理中的标准模型提供了一个在实验上已经获得广泛证实的理论框架。在  
45 该框架内，希格斯粒子起到了至关重要的作用，成为了研究标准模型以及寻找该模型  
46 以外新物理现象的关键。对双希格斯产生过程的研究不仅有助于我们深入了解希格  
47 斯粒子的自耦合性质，还有望揭示电弱对称破缺现象背后更深刻的物理机制，科学意  
48 义重大。此外，长寿命粒子作为一种新物理的候选粒子，它们可以由希格斯粒子发生  
49 稀有衰变而产生。一旦在实验上找到长寿命粒子，它们将为超出标准模型的新物理提  
50 供旗帜鲜明的信号，因此长寿命粒子的寻找一直是高能物理领域的重要研究课题之  
51 一。

52 本论文的首个分析研究了标准模型下希格斯粒子对 ( $HH$ ) 衰变到多轻子末态反  
53 应道，尤其三轻子末态的衰变道。该分析使用了 ATLAS 探测器在 2015-2018 年第二  
54 阶段取数期间的  $140 \text{ fb}^{-1}$  的全部质子-质子碰撞数据，主要涵盖了由胶子-胶子融合引  
55 发的希格斯粒子对产生，同时还考虑了矢量玻色子融合作为附加的信号贡献。三轻子  
56 末态的主要背景过程为  $WZ$ ，其在多强子喷注区域的动力学模拟存在一定的偏差，因  
57 此该研究采用了拟合函数并通过真实数据对其进行修正。次要的背景过程为假轻子  
58 背景，通过模版拟合使用了数据驱动方法进行估算。三轻子末态使用梯度提升决策树  
59 作为研究方法区分  $HH$  信号和主要本底，得到了信号和背景的鉴别函数，极大提升  
60 了信噪比 ( $S/B$ )。三轻子末态在 95% 置信度下预期截面上限为  $28.09_{-7.86}^{+12.81}$  倍标准模  
61 型  $HH$  的产生截面，比 2019 年发表的结果好了 9.4 倍。在考虑到所有多轻子末态后，  
62 预计的截面上限为  $9.74_{-7.02}^{+13.91}$  倍标准模型产生截面。三轻子末态反应道在多轻子末态  
63 中是测量结果最为灵敏的通道之一。

64 论文的第二部分侧重于分析  $HH \rightarrow b\bar{b}\tau^+\tau^-$  的衰变过程，该分析采用了 ATLAS  
65 探测器在 2015-2018 年第二阶段取数期间收集的  $140 \text{ fb}^{-1}$  全部质子-质子碰撞数据。相  
66 较于 2022 年的  $b\bar{b}\tau^+\tau^-$  分析，该分析针对耦合强度因子  $\kappa_\lambda$  和  $\kappa_{2V}$  等相关参数进行了  
67 特别的优化。通过应用多变量分析的方法，对胶子-胶子融合和矢量玻色子融合这两  
68 种主要的希格斯粒子对产生的途径进行了定向优化。希格斯粒子对在胶子-胶子融合  
69 模式下的不变质量 ( $m_{HH}$ ) 作为判别变量对事件进行了分类，同时为了提高对  $\kappa_{2V}$  的  
70 灵敏度，额外引入了一个矢量玻色子融合的分类。通过使用多变量分析的输出作为判  
71 别因子，相较于 2022 年的分析结果，信号强度 ( $\mu_{HH}$ ) 提高了 17%。同时， $\kappa_\lambda$  和  $\kappa_{2V}$   
72 在 95% 置信区间内的灵敏度分别提升了 11.9% 和 19.8%。

73 作为一项关于标准模型双希格斯的综合研究，本论文的第三部份焦点在希格斯  
74 粒子的对产生与单希格斯粒子产生的联合分析上。这一综合研究整合了主要的双希  
75 格斯衰变末态，包括  $b\bar{b}b\bar{b}$ ， $b\bar{b}\gamma\gamma$  和  $b\bar{b}\tau^+\tau^-$ ，以及所有的单希格斯粒子产生道。其  
76 主要目的是对希格斯耦合强度因子，尤其是  $\kappa_\lambda$  和  $\kappa_{2V}$ ，施加严格的约束。该研究采用  
77 了多种情况下的拟合，允许各个耦合强度因子在不同假设下变化。在对  $\kappa_t$ ， $\kappa_b$ ， $\kappa_\tau$  和  
78  $\kappa_V$  不施加任何假设的情况下， $\kappa_\lambda$  观测到的 95% 置信区间为  $-1.4 < \kappa_\lambda < 6.1$ ，与预期  
79 的范围  $-2.2 < \kappa_\lambda < 7.7$  非常接近。同时，在只允许  $\kappa_{2V}$  自由变化和假设为标准模型  
80 的情况对比中， $\kappa_\lambda$  的观察拟合结果的波动不超过 5%。目前观察到的所有耦合强度因  
81 子都在误差范围内与标准模型一致。

82 在超标准模型中，希格斯粒子的稀有衰变产物中包含长寿命粒子。论文的较后部  
83 分针对此类长寿命粒子进行了寻找。该研究采用了先进的机器学习技术，包括卷积  
84 神经网络和图神经网络，直接利用了探测器的原始信息展开了分析研究，在最大限度  
85 排除背景事例的前提下，和传统方法相比大大提高了信号的预期选择效率，例如在  
86 长寿命粒子质量 50 GeV 和寿命 1 纳秒的情况下，信号预期效率达到了 99%。该研究  
87 在  $10^6$  希格斯粒子的统计量下对  $H \rightarrow \text{LLPs}$  的衰变分支比给出了最低  $4 \times 10^{-6}$  的预期  
88 排除上限，这显著优于 ATLAS 和 CMS 目前设定的  $1 \times 10^{-3}$  的上限。在粒子寿命大于  
89 1 纳秒的情形下，该分析给出的预期排除上限比国际直线对撞机的相关研究结果好了  
90 一个数量级。

91 最后，本论文的附录部分描述了一项利用固定靶实验寻找暗光子的预先研究。该  
92 实验利用 8 GeV 的高能电子轰击重金属靶并寻找在电子散射过程中可能产生的暗光  
93 子。

94

95 **关键词：**高能物理，对撞机，双希格斯粒子，多轻子末态， $b\bar{b}\tau^+\tau^-$ ，长寿命粒子，机  
96 器学习

## ABSTRACT

97

98 The Standard Model (SM) of particle physics provides a comprehensive framework that  
99 has been experimentally verified to an impressive degree, with the Higgs boson as a pivotal el-  
100 ement. Investigations into di-Higgs interactions offer vital insights into the self-coupling be-  
101 havior of the Higgs boson and potentially elucidate the mechanisms underlying electroweak  
102 symmetry breaking. Moreover, the Higgs boson acts as a prospective avenue for explor-  
103 ing a multitude of theories beyond the Standard Model, with Long-Lived Particles (LLPs)  
104 representing just one of several intriguing models yet to be fully explored.

105 In the dissertation's first analysis, attention is centered on the production of SM Higgs  
106 boson pairs ( $HH$ ) decaying to multilepton final states, especially 3-lepton. Utilizing  $140 \text{ fb}^{-1}$   
107 of proton-proton collision data at  $\sqrt{s} = 13 \text{ TeV}$  from the ATLAS detector's Run 2, the study  
108 predominantly explores  $HH$  production via gluon-gluon fusion, with Vector Boson Fusion  
109 contributing additional signal yield. Critical to this work is the mitigation of the primary  $WZ$   
110 background, addressed through reweighting to account for mismodeling at high jet multiplic-  
111 ities, and the secondary fake-lepton background, estimated via the Template Fit method. A  
112 Gradient Boosted Decision Tree is employed for optimal signal-background discrimination,  
113 further refined through a 3-fold training technique and exhaustive hyperparameter tuning.  
114 Remarkably, this 3-lepton channel achieves an upper limit of  $28.09_{-7.86}^{+12.81}$  on the  $HH$  cross-  
115 section over SM, constituting a 9.4-fold enhancement over previous analyses. When con-  
116 sidering all multilepton channels, the expected upper limit stands at  $9.74_{-7.02}^{+13.91}$ , making the  
117 3-lepton channel result as one of the best limits among pure leptonic decay channels.

118 The second key facet of this dissertation revolves around the  $HH \rightarrow b\bar{b}\tau^+\tau^-$  analysis,  
119 building on  $140 \text{ fb}^{-1}$  of Full Run 2 ATLAS data. This work distinguishes itself by the targeted  
120 refinement of methodological approaches, particularly concerning the  $\kappa_\lambda$  and  $\kappa_{2V}$  coupling  
121 modifiers. Employing advanced Multivariate Analysis (MVA) techniques, the analysis opti-  
122 mizes for both gluon-gluon fusion and Vector Boson Fusion production modes. Specifically,  
123 event categorization is influenced by the invariant mass ( $m_{HH}$ ) of the Higgs pair in the ggF  
124 region, with an additional VBF category introduced to enhance sensitivity to  $\kappa_{2V}$ . Utilizing  
125 MVA outputs as the ultimate discriminants has engendered significant improvements over  
126 legacy data: a 17% boost in the systematic-adjusted baseline for  $\mu_{HH}$ , and 11.9% and 19.8%

127 enhancements in the 95% confidence intervals for  $\kappa_\lambda$  and  $\kappa_{2V}$ , respectively.

128 The HH+H combination analysis concludes the dissertation's SM di-Higgs investiga-  
129 tions. This synthesis incorporates the primary di-Higgs channels ( $b\bar{b}b\bar{b}$ ,  $b\bar{b}\gamma\gamma$ , and  $b\bar{b}\tau^+\tau^-$ )  
130 with single-Higgs observables to impose stringent constraints on key coupling modifiers,  
131 specifically  $\kappa_\lambda$  and  $\kappa_{2V}$ . In a comprehensive fit, where  $\kappa_t$ ,  $\kappa_b$ ,  $\kappa_\tau$ , and  $\kappa_V$  are allowed to vary  
132 freely, the analysis attains a 95% confidence interval of  $-1.4 < \kappa_\lambda < 6.1$ , which closely  
133 approximates the expected range of  $-2.2 < \kappa_\lambda < 7.7$ . The stability of these results is cor-  
134 roborated by a minimal sensitivity to  $\kappa_{2V}$  fluctuations, affecting the observed  $\kappa_\lambda$  constraints  
135 by less than 5%. This substantiates the concordance of all analyzed coupling modifiers with  
136 the SM, within the limits of the associated uncertainties.

137 In the later part of the dissertation, the investigation transitions to scrutinizing decay  
138 modes of the Higgs boson in the realm of BSM physics, specifically targeting LLPs. To this  
139 end, state-of-the-art machine learning algorithms, such as Convolutional Neural Networks  
140 (CNNs) and Graph Neural Networks (GNNs), are deployed for direct analysis on raw detector  
141 output, which significantly enhances the expected signal selection efficiency. For example, in  
142 the case of a 50 GeV LLP with a lifetime of 1 ns, the expected signal efficiency reaches 99%.  
143 This research achieves an expected upper limit of  $4 \times 10^{-6}$  for the branching ratio of Higgs  
144 decaying to LLPs under the assumption of  $10^6$  Higgs, which significantly outperforms the  
145 upper limit of  $1 \times 10^{-3}$  currently established by ATLAS and CMS, For LLPs with lifetimes  
146 greater than 1 ns, the analysis yields an expected upper limit that is one order of magnitude  
147 better than the expected results from the International Linear Collider.

148 Last but not least, the appendix section of the dissertation describes a preliminary study  
149 on dark photon searches via a proposed fixed target experiment with 8 GeV electrons recoiling  
150 from a High-Z metal target.

151  
152 **Key words:** High Energy Physics, Collider, di-Higgs, multilepton,  $b\bar{b}\tau^+\tau^-$ , LLP, Machine  
153 learning

154

## Contents

155	<b>Chapter 1 Introduction</b> .....	<b>1</b>
156	<b>Chapter 2 Higgs Physics in Standard Model and Beyond</b> .....	<b>5</b>
157	2.1 Introduction to the Standard Model .....	7
158	2.1.1 Fermions and Bosons .....	7
159	2.1.2 The Quantum Field Theory and the Lagrangian of the Standard Model	8
160	2.2 Electroweak Symmetry Breaking and the Brout-Englert-Higgs Mechanism ...	10
161	2.2.1 Electroweak unification .....	10
162	2.2.2 The role of the Higgs field in symmetry breaking .....	12
163	2.3 Higgs Physics at the LHC .....	14
164	2.3.1 Higgs boson production.....	14
165	2.3.2 Di-Higgs production .....	17
166	2.4 Long-Lived Particles (LLPs) and Beyond Standard Model Search.....	19
167	<b>Chapter 3 The Large Hadron Collider and ATLAS Experiment</b> .....	<b>21</b>
168	3.1 Introduction to the Large Hadron Collider (LHC) .....	22
169	3.1.1 Accelerator design and parameters .....	22
170	3.1.2 Operation status .....	26
171	3.2 The ATLAS Experiment.....	29
172	3.2.1 Overview and scientific goals .....	29
173	3.2.2 Detector subsystems and components.....	33
174	<b>Chapter 4 Event Simulation and Reconstruction in ATLAS</b> .....	<b>47</b>
175	4.1 Event Simulation.....	47
176	4.1.1 Simulation Overview and Large-Scale Production System .....	47
177	4.1.2 Event generation .....	49
178	4.1.3 Detector simulation and response .....	53
179	4.2 Object Reconstruction .....	55
180	4.2.1 Tracks.....	55

181	4.2.2	Electrons .....	58
182	4.2.3	Photons .....	68
183	4.2.4	Muons .....	78
184	4.2.5	Hadronically decaying taus .....	83
185	4.2.6	Jets and b-jets .....	84
186	4.2.7	Missing Transverse Energy .....	87
187	<b>Chapter 5 SM Di-Higgs Searches in Multi-Lepton Final States .....</b>		<b>89</b>
188	5.1	Introduction .....	89
189	5.2	Data and Monte Carlo samples .....	90
190	5.2.1	Data Preparation and Analytical Framework .....	90
191	5.2.2	Data Collection and Quality .....	91
192	5.2.3	Monte Carlo Simulations .....	91
193	5.3	Analysis Strategy .....	93
194	5.3.1	Object definitions .....	94
195	5.3.2	Jet and b-jet .....	97
196	5.3.3	Overlap Removal .....	98
197	5.3.4	Event Selection .....	99
198	5.3.5	Background Modelling .....	100
199	5.3.6	Multivariate Analysis .....	106
200	5.3.7	Validation Plots .....	109
201	5.4	Systematic Uncertainties .....	117
202	5.4.1	Experimental uncertainties .....	117
203	5.4.2	Theory uncertainties .....	118
204	5.4.3	WZ reweighting uncertainties .....	118
205	5.4.4	Uncertainties on data-driven background estimation .....	120
206	5.5	Statistical Interpretation .....	121
207	5.5.1	Statistical model .....	121
208	5.5.2	Statistical analysis and Results .....	123
209	5.6	Combination Results .....	125
210	5.6.1	Overview of other channels .....	125
211	5.6.2	Treatment of the Normalization Factors (NFs) .....	128

212	<b>Chapter 6 SM Di-Higgs Searches in <math>b\bar{b}\tau^+\tau^-</math> Final States</b> .....	<b>131</b>
213	6.1 Introduction .....	131
214	6.2 Data and Monte Carlo samples .....	132
215	6.2.1 Simulation of Signal Datasets .....	133
216	6.2.2 Background Simulation Samples .....	135
217	6.3 Event selection .....	136
218	6.3.1 Object Reconstruction .....	138
219	6.3.2 Trigger Selection .....	143
220	6.3.3 $\tau_{\text{had}}\tau_{\text{had}}$ Event Selection .....	143
221	6.3.4 Event Categorization .....	147
222	6.3.5 Z+HF control region .....	148
223	6.4 Background Modelling .....	151
224	6.4.1 Multijet with fake- $\tau$ backgrounds in the $\tau_{\text{had}}\tau_{\text{had}}$ channel .....	152
225	6.4.2 $t\bar{t}$ with fake- $\tau_{\text{had}}$ in the $\tau_{\text{had}}\tau_{\text{had}}$ channel with scale-factor method .....	153
226	6.5 Multivariate signal extraction .....	154
227	6.5.1 General MVA and optimisation strategy .....	154
228	6.5.2 $\tau_{\text{had}}\tau_{\text{had}}$ MVAs .....	157
229	6.6 Systematic uncertainties .....	174
230	6.7 Statistical interpretation .....	177
231	6.7.1 Fit step .....	177
232	6.7.2 Binning .....	178
233	6.7.3 Blinding strategy .....	178
234	6.8 Results .....	179
235	6.8.1 Fits .....	179
236	6.8.2 Data-driven $t\bar{t}$ Modelling .....	180
237	6.8.3 $\tau_{\text{had}}\tau_{\text{had}}$ Fitting Results .....	181
238	6.8.4 Limits and scans .....	184
239	<b>Chapter 7 Constraining the Higgs boson self-coupling from single- and double-</b>	
240	<b>Higgs production</b> .....	<b>189</b>
241	7.1 Introduction .....	189
242	7.2 Theoretical framework .....	189

243	7.3	Individual channel measurements .....	191
244	7.4	Statistical Methodology and Analysis Combination .....	192
245	7.5	Di-Higgs Combined Results .....	193
246	7.5.1	Global signal strength .....	193
247	7.5.2	Constraints on Higgs self-coupling .....	194
248	7.6	Single- and Di-Higgs Combined Results .....	195
249	<b>Chapter 8 Search for Long-Lived Particle with the Future Lepton Collider .....</b>		<b>199</b>
250	8.1	Introduction .....	199
251	8.1.1	Methods and Subsystems for LLP Detection in Collider Experiments .	199
252	8.1.2	Challenges and Considerations in LLP Detection .....	199
253	8.1.3	Signatures of Neutral Long-Lived Particles .....	200
254	8.2	Event Generation and Simulation at CEPC .....	203
255	8.2.1	Overview of CEPC .....	203
256	8.2.2	Event generation and simulation .....	205
257	8.2.3	LLP Signal Production .....	206
258	8.3	Analysis Strategy .....	207
259	8.3.1	General Training Configuration .....	208
260	8.3.2	Image-based Deep Learning Analysis (CNN) .....	210
261	8.3.3	Graph-based Deep Learning Analysis (GNN) .....	213
262	8.3.4	Event selection with XGBoost .....	216
263	8.3.5	Efficiency comparison between CNN and GNN .....	217
264	8.4	Results .....	218
265	8.5	Discussion and Summary .....	221
266	8.5.1	Comparison with Hadron Colliders: ATLAS and CMS .....	221
267	<b>Chapter 9 Summary and Future prospects .....</b>		<b>225</b>
268	<b>Bibliography .....</b>		<b>231</b>
269	<b>Appendix A DarkSHINE Experiment .....</b>		<b>261</b>
270	A.1	Theory Assumption .....	262
271	A.2	Experimental Setup .....	263

---

272	A.2.1 SHINE Facility .....	263
273	A.2.2 Detector Design .....	264
274	A.3 Simulation .....	267
275	A.3.1 Signal Sample Production .....	268
276	A.3.2 Background Sample Production .....	269
277	A.4 Signal Region Definition .....	271
278	A.5 Background Estimation .....	274
279	A.5.1 Extrapolation from rare processes simulation .....	275
280	A.5.2 Validation from inclusive background simulation .....	278
281	A.5.3 Invisible background estimation .....	280
282	A.5.4 Background Estimation Summary .....	281
283	A.6 Sensitivity study .....	282
284	A.7 Summary .....	284
285	<b>Acknowledgements .....</b>	<b>287</b>
286	<b>List of Research Achievements .....</b>	<b>289</b>



## List of Figures

287

- 288 Figure 2–1 The properties of elementary particles in the Standard Model..... 8
- 289 Figure 2–2 The illustration of Higgs potential  $V(\phi)$ . Point B represents for the non-  
290 zero vacuum expectation value (VEV) of the field. .... 14
- 291 Figure 2–3 A collection of the primary Feynman diagrams at leading order con-  
292 tributing to Higgs boson production. (a) Represents the gluon fusion  
293 process, (b) showcases Vector-boson fusion, (c) displays Higgs-strahlung  
294 or associated production with a gauge boson arising from a quark-quark  
295 interaction at the tree level, (d) outlines associated production with a  
296 gauge boson from a gluon-gluon interaction at the loop level, (e) depicts  
297 the associated production with a pair of top quarks (a similar diagram  
298 would represent the associated production with a pair of bottom quarks),  
299 (e-f) illustrates the process of production in association with a single top  
300 quark. .... 15
- 301 Figure 2–4 (Left) The production cross sections of the SM Higgs boson as a function  
302 of the center of mass energy,  $\sqrt{s}$ , for proton-proton collisions<sup>[21]</sup>. The  
303 VBF process is denoted here as  $qqH$ . (Right) Branching ratios for the  
304 primary decays of the SM Higgs boson near a mass ( $m_H$ ) of 125 GeV<sup>[20]</sup>.  
305 Bands represent theoretical uncertainties. .... 16
- 306 Figure 2–5 The major Feynman diagrams for the production of two Higgs bosons  
307 via gluon fusion. (Left) Triangle diagram sensitive to the self-coupling  
308 vertex  $\kappa_\lambda$ , (Right) Box diagram, which interferes destructively at the self-  
309 coupling vertex  $\kappa_\lambda$ . .... 18
- 310 Figure 2–6 Depiction of Vector Boson Fusion (VBF) processes in Higgs boson pair  
311 production: (a) the VVHH vertex process, (b) the trilinear coupling, and  
312 (c) the VVH production mode. .... 18
- 313 Figure 3–1 Diagram of CERN’s sequential accelerator system<sup>[35]</sup>. .... 24

314	Figure 3–2	Public ATLAS Luminosity Results for Run-2 of the LHC <sup>[36]</sup> . <b>Left: Delivered Luminosity Over Time (2011-2018): The graph depicts the cumulative luminosity delivered to ATLAS as a function of time during stable beams and for high-energy p-p collisions. Right: Interactions per Crossing (2015-2018 at 13 TeV): This illustration showcases the luminosity-weighted distribution of the average interactions per crossing. The data encompasses all records from ATLAS during stable beams between 2015 and 2018. The integrated luminosity and the mean mu value are indicated. The average interactions per crossing align with the Poisson distribution’s mean, ascertained for each bunch.</b> .....	27
315			
316			
317			
318			
319			
320			
321			
322			
323			
324			
325	Figure 3–3	The layout of the whole ATLAS detector <sup>[40]</sup> . .....	32
326	Figure 3–4	Illustration of the global track coordinate with respect to perigee. ....	33
327	Figure 3–5	The layout of the ATLAS Inner Detector <sup>[42]</sup> . Left: Overview of the ID; Right: Cross-sectional view of the Inner Detector, with layers from innermost to outermost being the pixel detector, SCT, and TRT. ....	36
328			
329			
330	Figure 3–6	The layout of the ATLAS calorimeters <sup>[44]</sup> . .....	38
331	Figure 3–7	The layout of the ATLAS muon system <sup>[46]</sup> . .....	41
332	Figure 3–8	The layout of the ATLAS magnet system <sup>[48]</sup> . .....	42
333	Figure 3–9	Left: A schematic view of the ATLAS trigger system <sup>[49]</sup> ; Right: Block scheme of the first level trigger <sup>[49]</sup> . .....	44
334			
335	Figure 3–10	A schematic view of the ATLAS DAQ system <sup>[50]</sup> . .....	45

336	Figure 4–1	Schematic representation of a $pp \rightarrow t\bar{t}$ event as simulated by PYTHIA <sup>[64]</sup> , with certain simplifications for visual clarity. 1) The number of shower branchings and final-state hadrons is reduced compared to an actual PYTHIA simulation; 2) Recoil effects are not depicted to scale; 3) Weak decays of light-flavor hadrons are omitted, implying, for example, a $K_S^0$ meson is shown as stable; 4) Incoming momenta are illustrated as inversed ( $p \rightarrow -p$ ), necessitating that the momentum direction for both beam remnants and ISR branchings should be interpreted as outward-facing to avoid diagrammatic complexity. This convention prevents the need for beam remnants and ISR emissions to intersect in the central region of the figure. ....	51
347	Figure 4–2	Overview of Track Candidate Progression within the Ambiguity Solver <sup>[83]</sup> . ....	58
349	Figure 4–3	A conceptual diagram depicting an electron’s journey through the various components of the detector <sup>[91]</sup> . The solid red line represents the speculated path of an electron as it moves initially through the tracking system, starting with the pixel detectors, followed by the silicon-strip detectors, and finally through the TRT, before entering the electromagnetic calorimeter. The dotted red line illustrates the trajectory of a photon generated due to the electron’s interaction with the tracking system’s material. ....	60
357	Figure 4–4	Algorithm flow diagram for the new electron and photon reconstruction <sup>[88]</sup> . ....	61
359	Figure 4–5	Efficiency plots of electron ID working points <sup>[96]</sup> . ....	65
360	Figure 4–6	Efficiency plots of electron Isolation working points <sup>[88]</sup> . ....	67
361	Figure 4–7	Efficiency measurements for unconverted and converted photons across different $\eta$ bins <sup>[98]</sup> . ....	69
363	Figure 4–8	Flowchart of the ambiguity resolution procedure for electron and photon objects <sup>[97]</sup> . ....	70
365	Figure 4–9	The distribution of reweighting scale factor (signal over background) in each $p_T$ and $\eta$ bin for both unconverted and converted case. ....	73

367	Figure 4–10	The 1D basic kinematic distributions before (top) and after (bottom)	
368		reweighting the basic kinematics of $Z \rightarrow e^+e^-$ to those of $\gamma + \text{jets}$ events.	73
369	Figure 4–11	The ROC performance of rectangular optimization for all $p_T$ and $\eta$ bins.	
370		The grey line is signal efficiency of 80%. . . . .	78
371	Figure 4–12	Comparison of Photon Conversion Efficiency: Rows correspond to 80%,	
372		60%, and 50% efficiency levels. Each row comprises unconverted and	
373		converted $\gamma$ for signal and background. . . . .	79
374	Figure 4–13	Efficiency vs $\eta$ and $p_T$ for different WPs in simulated $t\bar{t}$ events <sup>[107]</sup> . . . . .	81
375	Figure 4–14	Rejection power for different prong configurations of $\tau_{\text{had-vis}}$ candidates,	
376		comparing RNN-based and BDT-based algorithms <sup>[112]</sup> . . . . .	84
377	Figure 4–15	Flow chart depicting the sequential steps of the Particle Flow algorithm	
378		from track selection to energy subtraction in the calorimeter <sup>[115]</sup> . The	
379		end result comprises charged particles, unmodified topo-clusters, and	
380		topo-cluster remnants with partially removed energy. . . . .	85
381	Figure 4–16	Comparison of light-jet (left) and c-jet (right) rejection against b-tagging	
382		efficiency for jets with $p_T > 20 \text{ GeV}$ and $ \eta  < 2.5$ . Statistical errors	
383		are within 3%. MV2c10 serves as a high-level BDT-based benchmark,	
384		incorporating both IP3D and additional vertex metrics from JetFitter and	
385		SV1 <sup>[122]</sup> . . . . .	87
386	Figure 5–1	Overview of the multi-lepton final states considered. . . . .	89
387	Figure 5–2	The pre-fit (let) and post-fit (right) nJets distribution plots of the WZ	
388		control regions, using fitting function of Eq.5–1. Both statistical uncer-	
389		tainties and systematic errors are accounted for. . . . .	103
390	Figure 5–3	From left to right shows the pre-fit (top) and post-fit (bottom) plots of	
391		the HF-E, HF-MU, External Conversion control regions. All entries	
392		represent uncorrected Monte Carlo simulations.Both statistical uncer-	
393		tainties and systematic errors are accounted for.Additionally, the WZ	
394		background is adjusted using a fitted scaling function. . . . .	105
395	Figure 5–4	The correlation matrix of MVA variables for signal and background	
396		(pure MC) training samples. . . . .	108

397	Figure 5–5	Training results of BDTG: Receiver Operating Characteristic (ROC) curve for 3-lepton channel, illustrating the trade-off between signal efficiency (True Positive Rate) and background inefficiency (False Positive Rate). ..	109
398			
399			
400	Figure 5–6	The pre-fit and post-fit distributions of the BDTG score in low BDT VR and WZ-enriched region. Scaling factors for External Conversion, HF(electron), and HF(muon) are applied. Additionally, the WZ background is adjusted using a fitted scaling function.Both statistical uncertainties and systematic errors are accounted for. ....	110
401			
402			
403			
404			
405	Figure 5–7	The post-fit distribution of distance of lepton pairs and jets, where all the events are required to pass the pre-selection and BDTG score $\leq 0.55$ . Scaling factors for External Conversion, HF(electron), and HF(muon) are applied. Additionally, the WZ background is adjusted using a fitted scaling function.Both statistical uncertainties and systematic errors are accounted for. ....	111
406			
407			
408			
409			
410			
411	Figure 5–8	The post-fit distribution of invariant mass of lepton pairs and jets, where all the events are required to pass the pre-selection and BDTG score $\leq 0.55$ . Scaling factors for External Conversion, HF(electron), and HF(muon) are applied. Additionally, the WZ background is adjusted using a fitted scaling function.Both statistical uncertainties and systematic errors are accounted for. ....	112
412			
413			
414			
415			
416			
417	Figure 5–9	The post-fit distribution of the remaining kinematics, where all the events are required to pass the pre-selection and BDTG score $\leq 0.55$ . Scaling factors for External Conversion, HF(electron), and HF(muon) are applied. Additionally, the WZ background is adjusted using a fitted scaling function.Both statistical uncertainties and systematic errors are accounted for. ....	113
418			
419			
420			
421			
422			
423	Figure 5–10	The post-fit distribution of distance of lepton pairs and jets, where all the events are required to pass the pre-selection. Scaling factors for External Conversion, HF(electron), and HF(muon) are applied. Additionally, the WZ background is adjusted using a fitted scaling function.Both statistical uncertainties and systematic errors are accounted for. ....	114
424			
425			
426			
427			

428	Figure 5–11	The post-fit distribution of invariant mass of lepton pairs and jets, where	
429		all the events are required to pass the pre-selection. Scaling factors for	
430		External Conversion, HF(electron), and HF(muon) are applied. Ad-	
431		ditionally, the WZ background is adjusted using a fitted scaling func-	
432		tion. Both statistical uncertainties and systematic errors are accounted	
433		for. ....	115
434	Figure 5–12	The post-fit distribution of the remaining kinematics, where all the events	
435		are required to pass the pre-selection. Scaling factors for External Con-	
436		version, HF(electron), and HF(muon) are applied. Additionally, the WZ	
437		background is adjusted using a fitted scaling function. Both statistical un-	
438		certainties and systematic errors are accounted for. ....	116
439	Figure 5–13	The systematics plots for reweighted WZ samples in WZ enriched re-	
440		gion. ....	120
441	Figure 5–14	Fitting results for $3\ell$ channel, including all systematics and data-driven	
442		nuisance parameters. ....	123
443	Figure 5–15	The correlation matrix in $3\ell$ channel. All systematics and data driven	
444		nuisance parameters included. ....	124
445	Figure 5–16	Correlation scheme of the systematic uncertainties in the analysis. ....	129
446	Figure 5–17	Expected individual and combined upper limits in channels, with full	
447		systematic uncertainties (left) and statistics only (right). ....	130
448	Figure 6–1	Invariant mass ( $m_{HH}$ ) distribution at the parton level for the ggF $HH$	
449		signal in the $\tau_{had}\tau_{had}$ channel, with overlaid $\kappa_\lambda$ values of 1.0 and 10.0. ....	134
450	Figure 6–2	Inclusive distributions of VBF $HH$ samples for varying $\kappa_{2V}$ at parton-	
451		level, presented for the $\tau_{had}\tau_{had}$ and $\tau_{lep}\tau_{had}$ channels. Couplings are ad-	
452		justed as outlined in Table 6–2. ....	135
453	Figure 6–3	Schematic representation of the analysis strategy. ....	137
454	Figure 6–4	Sub-leading $b$ -jet DL1r quantiles. Figure (a) shows the SM ggF, ggF	
455		( $\kappa_\lambda = 10.0$ ) and SM VBF signals, along with the sum of the back-	
456		grounds. Figure (b) shows the same variable for each background com-	
457		ponent. ....	142

458	Figure 6–5	Event categorisation into low- $m_{\text{HH}}$ ggF, high- $m_{\text{HH}}$ ggF, and VBF signal regions. ....	147
459			
460	Figure 6–6	Data/MC comparison in the prior $Z + HF$ control region. ....	149
461	Figure 6–7	Comparison of $V p_{\text{T}}$ shapes between the SRs and the $Z$ CR.....	149
462	Figure 6–8	(a) Quantification of the $V p_{\text{T}}$ shape uncertainty, representing the full discrepancy between data and nominal MC forecast in the $Z$ CR. (b)	
463		The subsequent discrete parameterization of the shape uncertainty. ....	151
464			
465	Figure 6–9	Schematic illustration of the application of the fake-factor method for estimating multi-jet backgrounds featuring fake- $\tau_{\text{had-vis}}$ in the $\tau_{\text{had}}\tau_{\text{had}}$ channel. In all control regions, non-multi-jet backgrounds are simulated and subsequently deducted from the observed data, as denoted by 'Subtracted Non-Multi-Jet Backgrounds' in the legend. ....	152
466			
467			
468			
469			
470	Figure 6–10	Fake factors for 1-prong DTT (top), 3-prong DTT (middle), and STT (bottom) for the data-taking periods 15-16 (left), 17 (centre), and 18 (right) for the di-Higgs $\tau_{\text{had}}\tau_{\text{had}}$ channel. ....	153
471			
472			
473	Figure 6–11	Illustrative summary of the data-corrected scale-factor technique employed for evaluating $t\bar{t}$ background containing fake- $\tau_{\text{had-vis}}$ in the $\tau_{\text{had}}\tau_{\text{had}}$ channel.....	154
474			
475			
476	Figure 6–12	Performance progression of the ggF/VBF classification BDT as supplementary variables are incrementally appended to the baseline variables, which consist of $m_{\text{jj}}$ and $\Delta\eta_{\text{jj}}$ . ....	158
477			
478			
479	Figure 6–13	Histograms of input variables for the ggF/VBF BDT in the $\tau_{\text{had}}\tau_{\text{had}}$ channel, illustrating the distinction between ggF HH events (signal in blue) and VBF HH events (background in red). ....	159
480			
481			
482	Figure 6–14	Variation of binned significance, as assessed on the validation partitions, with respect to the ensemble's tree count (NTrees) and each tree's maximum depth (MaxDepth). ....	160
483			
484			
485	Figure 6–15	Dependence of HH signal strengths on the ggF vs VBF BDT cut value for the refined set of variables (left). The right figure shows the aggregate signal-to-background ratio also as a function of the cut value. A vertical dashed line marks the chosen cut value of 0.1. ....	160
486			
487			
488			

489	Figure 6–16	Distribution of ggF/VBF BDT scores for various VBF processes under	
490		signal region preselection conditions. ....	161
491	Figure 6–17	Impact of the NTrees and MaxDepth hyperparameters on the validation	
492		significance for the respective BDT training sets in the $\tau_{\text{had}}\tau_{\text{had}}$ channel. ..	162
493	Figure 6–18	Trajectory of the validation significance as additional predictor variables	
494		are incorporated. The baseline set consists of $m_{jj}$ , $m_{bb}$ , $m_{\tau\tau}^{\text{MMC}}$ , $\Delta R_{bb}$ ,	
495		and $\Delta R_{\tau\tau}$ . Red curves (trafo60_5_total_sig_val) represent binned sig-	
496		nificance with at least 5.0 expected background events per bin, whereas	
497		black curves (trafo60_total_sig_val) require only a minimum of 1.0 ex-	
498		pected background events per bin. ....	164
499	Figure 6–19	Representative set of pre-fit MVA input variable distributions in the	
500		$\tau_{\text{had}}\tau_{\text{had}}$ SRs. ....	167
501	Figure 6–20	Representative set of pre-fit MVA input variable distributions in the	
502		$\tau_{\text{had}}\tau_{\text{had}}$ SRs. ....	168
503	Figure 6–21	Categorisation BDT variable distributions in the $\tau_{\text{had}}\tau_{\text{had}}$ SRs. ....	168
504	Figure 6–22	Pre-fit BDT score distributions in the $\tau_{\text{had}}\tau_{\text{had}}$ signal regions. ....	169
505	Figure 6–23	Prefit yields of the main background components, the total signal, as	
506		well as the total background in the most signal-like BDT bins in the	
507		$\tau_{\text{had}}\tau_{\text{had}}$ SRs. ....	169
508	Figure 6–24	Top row: Sensitivity as a function of the cut on the ggF vs VBF classi-	
509		fication BDT for different variable sets. Bottom row: Inclusive S/B as	
510		a function of the cut on the ggF vs VBF classification BDT for different	
511		variable sets. ....	174
512	Figure 6–25	Post-fit values of the NPs included in the fit of the di-lepton invariant	
513		mass distribution in the CR. ....	180
514	Figure 6–26	Post-fit modelling of the di-lepton invariant mass (left) and $p_T$ (right)	
515		distribution in the CR. In both cases the NP extracted from the fit to $m_{ll}$	
516		are used. ....	181
517	Figure 6–27	<b>a</b> Post-fit modelling of the di-lepton invariant mass distribution in the	
518		CR, when the $t\bar{t}$ contribution is taken from a dedicated $e\mu$ CR. <b>b</b> Post-fit	
519		values of the nuisance parameters included in the fit. ....	181

520	Figure 6–28	Nuisance parameter ranking in the $\tau_{\text{had}}\tau_{\text{had}}$ fit using the Asimov dataset. . .	182
521	Figure 6–29	Correlations among NPs in the $\tau_{\text{had}}\tau_{\text{had}}$ SM fit to the Asimov dataset	
522		(left) and real data (right). MC statistical uncertainties are purposefully	
523		omitted. ....	183
524	Figure 6–30	Post-fit BDT score distributions in the $\tau_{\text{had}}\tau_{\text{had}}$ signal regions. ....	184
525	Figure 6–31	Negative logarithm of the likelihood ratio comparing different $\kappa_\lambda$ (a)	
526		and $\kappa_{2V}$ (b) hypotheses to an Asimov dataset constructed under the SM	
527		hypothesis in the $\tau_{\text{had}}\tau_{\text{had}}$ channel. ....	185
528	Figure 6–32	Negative log-likelihood ratios assessing various $\kappa_\lambda$ and $\kappa_{2V}$ scenarios, in	
529		reference to an Asimov dataset created under the SM framework. Anal-	
530		yses incorporate both individual channels and their amalgamation. Solid	
531		lines intersecting dashed horizontal lines indicate 68% and 95% confi-	
532		dence levels. ....	187
533	Figure 7–1	Illustration of the observed and expected 95% CL upper bounds on the	
534		signal strength $\mu_{\text{HH}}$ for the considered decay channels and their statistical	
535		amalgamation. The SM prediction assumes $m_H = 125.09$ GeV. ....	193
536	Figure 7–2	95% CL constraints on $\kappa_\lambda$ and $\kappa_{2V}$ from the combined analysis. The	
537		red lines indicate the theory constraints, while the solid lines represent	
538		observed limits. ....	194
539	Figure 7–3	Observed (a) and projected (b) test statistics in terms of $\kappa_\lambda$ . ....	195
540	Figure 7–4	Constraints in the $\kappa_\lambda$ - $\kappa_t$ parameter space. ....	196
541	Figure 8–1	The schematic representation of LLPs' decaying process in the detector. .	200
542	Figure 8–2	Feynman diagrams illustrating LLP production via the Higgsstrahlung	
543		process. ....	207
544	Figure 8–3	Illustration of image built from raw detector hits for four different pro-	
545		cesses. ....	211
546	Figure 8–4	Illustration of the architecture of ResNet-18 based neural network. ....	212
547	Figure 8–5	Illustration of the architecture of the GNN-based neural network. ....	215
548	Figure 8–6	The product of signal efficiencies and acceptance for different assump-	
549		tions of LLPs' mass and lifetime obtained with CNN-based (solid) and	
550		GNN-based (dot) approaches. ....	218

- 551 Figure 8–7 The 95% C.L. upper limit on  $\text{BR}(h \rightarrow X_1 X_2)$  for the process  $e^+ e^- \rightarrow$   
 552  $Zh$  with the condition of  $\epsilon_V$  fixed (left) and  $\epsilon_V$  floated (right), where  
 553  $\epsilon_V := \frac{\text{BR}(X \rightarrow \nu \bar{\nu})}{\text{BR}(X \rightarrow q \bar{q})}$ . Different colored lines indicate different LLPs masses.  
 554 Shaded area indicate statistical and systematic uncertainties combined. . . . . 220
- 555 Figure 8–8 The 95% C.L. 2-D upper limit on  $(\mathcal{B}_{2\text{-jet}}, \mathcal{B}_{4\text{-jet}})$  for the process  $e^+ e^- \rightarrow$   
 556  $Zh$  for three LLPs masses 50 GeV (left), 10 GeV (middle), 1 GeV (right).  
 557 Different colored lines indicate different LLPs lifetimes. The uncertain-  
 558 ties on the limits are omitted and a few limits are scaled by a factor for  
 559 better visibility. . . . . 220
- 560 Figure 8–9 The 2D fitting for  $(\mathcal{B}_{2\text{-jet}}, \mathcal{B}_{4\text{-jet}})$ . From top to bottom, the mass is 50, 10,  
 561 1  $\text{GeV}/c^2$ ; From left to right, the lifetime is 0.0001, 0.1, 1.0, 10 ns. . . . . 221

## List of Tables

562

563	Table 2–1	Production cross sections of the Standard Model Higgs boson, with a mass of 125 GeV, in proton-proton collision .....	16
564			
565	Table 3–1	Circumference, curvature radius $\rho$ , and beam momentum upon injection for the primary accelerators in the LHC injection sequence <sup>[32]</sup> . .....	25
566			
567	Table 3–2	Summary of integrated luminosities post standard data-quality checks, alongside uncertainties for the calibration of each yearly data sample from Run 2 pp at $\sqrt{s} = 13$ TeV, including the cumulative sample <sup>[37]</sup> . The table presents the integrated luminosities, total uncertainties, a detailed split of contributions to the vdM calibration’s absolute accuracy, extra uncertainties associated with the physics data sample, and the overall relative uncertainty in percentage. ....	28
568			
569			
570			
571			
572			
573			
574	Table 3–3	Summary of the resolution and $\eta$ coverage for various subdetectors. ECAL and HCAL represent for electromagnet calorimeter and hadronic calorimeter, respectively. The listed resolutions for trackers and the ECAL are parametrized forms dependent on either $p_T$ or $E$ (in GeV), while the Muon Spectrometer provides a specific resolution at a given $p_T$ value. The $\eta$ coverage is further categorized into measurement and trigger regions. ....	34
575			
576			
577			
578			
579			
580			
581	Table 3–4	Inner Detector Parameters and Resolutions <sup>[41]</sup> : The provided resolutions are indicative values (the precise resolution in each detector varies with $ \eta $ ). ....	36
582			
583			
584	Table 3–5	Specifications for the four subsystems of the muon detector <sup>[47]</sup> : The stated spatial resolution (in columns 3 and 4) excludes uncertainties from chamber alignment. The intrinsic time accuracy for each chamber type is detailed in column 5, with additional time required for signal propagation and electronic factors. Numbers in parentheses relate to the full detector setup anticipated for 2009. ....	40
585			
586			
587			
588			
589			

590	Table 4–1	Quantities of materials, solids, logical volumes, physical volumes, and aggregate volumes essential for the assembly of diverse segments of the ATLAS detector are outlined. The term "Inner Detector" encompasses components such as the beampipe, BCM, pixel tracker, SCT, and TRT. ...	54
591			
592			
593			
594	Table 4–2	Summary of Quantities for Electron Identification. ....	64
595	Table 4–3	Description of electron isolation benchmarks and their corresponding performance metrics. For the Gradient strategy, the transverse momentum ( $p_T$ ) is expressed in GeV. A consistent cone dimension of $\Delta R = 0.2$ is employed for both calorimeter and track-based isolation methods, with a maximum cone size of $\Delta R_{\max} = 0.2$ designated for track isolation. ....	67
596			
597			
598			
599			
600	Table 4–4	Definition of the photon isolation working points <sup>[97]</sup> . ....	70
601	Table 4–5	Single Photon signal samples and $Z \rightarrow e^+e^-$ background samples. ....	72
602	Table 4–6	Yields of pre-selected ambiguous events and total pre-selected events before ambiguity requirement for $\gamma + \text{jets}$ and $Z \rightarrow e^+e^-$ . ....	74
603			
604	Table 4–7	Separation power of shower shapes, topo-cluster, and ambiguity variables, which are retrieved from the BDT method from TMVA package, since the kCut method does not provide the variable ranking ....	77
605			
606			
607	Table 4–8	Definitions of the muon isolation WPs. ....	82
608	Table 5–1	Good Run List XML Files by Year. ....	91
609	Table 5–2	Event generation configurations for signal and background processes. ....	92
610	Table 5–3	List of lowest $p_T$ -threshold, un-prescaled single lepton and di-lepton triggers used for 2015-2018 data taking. ....	95
611			
612	Table 5–4	Definitions of Baseline, Loose, and Tight criteria in multilepton channels.	96
613	Table 5–5	Summary of Overlap Removal Criteria in Multilepton Channels. ....	98
614	Table 5–6	The raw yields with pre-selection cut-flow for the $3\ell$ analysis. ....	100
615	Table 5–7	Summary of Monte Carlo (MC) samples with applied normalization factors and re-weighted $WZ$ contributions, alongside data for all control and validation regions in the $3\ell$ channel. Only the principal background processes are enumerated. ....	101
616			
617			
618			
619	Table 5–8	The systematics of three fake sources and the corresponding yields in the signal region, which is estimated by the template fit method. ....	106
620			

621	Table 5–9	Discriminant variables used in BDTG training for $3\ell$ channel.....	107
622	Table 5–10	The background sample normalizations and their uncertainties were used	
623		in the analysis. The uncertainties on the inclusive cross sections are taken	
624		from the ATLAS Physics Modelling Group Twiki. ....	119
625	Table 5–11	Correlation and Covariance Matrix for Parameters A, B, and C.....	120
626	Table 5–12	Eigenvalues and Eigenvectors of the Covariance Matrix for Parameters	
627		A, B, and C .....	120
628	Table 5–13	Expected Upper limits in $3\ell$ channel. First row: Limits with stats only;	
629		Second row: Limits with systematics. ....	125
630	Table 5–14	Selection criteria applied to each of the control and validation regions	
631		defined in each channel. The requirements that guarantees orthogonality	
632		with respect to the corresponding signal region are highlighted in blue.....	126
633	Table 5–15	Selection criteria applied to each channel to form the signal regions.....	127
634	Table 5–16	Summary table of employed normalization factors, detailing individual	
635		and composite fit values. Specific channels without normalization factors	
636		are also indicated. ....	128
637	Table 5–17	Table of 95% C.L. upper limits on signal strength for multi-lepton chan-	
638		nels. Limits are derived using Asimov datasets under varying scenarios	
639		of statistical and systematic uncertainties. ....	130
640	Table 6–1	Summary of MC samples for signal and background processes. ....	132
641	Table 6–2	Considered $\kappa_\lambda$ , $\kappa_{2V}$ , and $\kappa_V$ coupling modifiers for VBF $HH$ simulations. .	134
642	Table 6–3	Coupling modifier values for generating alternative VBF $HH$ samples. ....	135
643	Table 6–4	Summary of the event selections, shown separately for events that are	
644		selected by different triggers. ....	138
645	Table 6–5	Summary of overlap-removal procedures with the standard working point.	142
646	Table 6–6	Data-taking triggers for the $\tau_{\text{had}}\tau_{\text{had}}$ channel. ....	144
647	Table 6–7	SM ggF $HH$ signal cutflow (POWHEG + PYTHIA 8) in the $\tau_{\text{had}}\tau_{\text{had}}$ sub-	
648		channel.....	145
649	Table 6–8	SM VBF $HH$ signal cutflow (POWHEG + PYTHIA 8) in the $\tau_{\text{had}}\tau_{\text{had}}$ sub-	
650		channel.....	146

651	Table 6–9	Demarcation of the simulated event pools used for the learning, fine-tuning, and scrutiny of the BDT algorithms. ....	155
652			
653	Table 6–10	Input variables used for the ggF/VBF BDT training in the $\tau_{\text{had}}\tau_{\text{had}}$ channel.	158
654	Table 6–11	Chosen hyperparameters for the ggF/VBF BDT training in the $\tau_{\text{had}}\tau_{\text{had}}$ channel. ....	159
655			
656	Table 6–12	Training hyperparameters chosen for the BDTs used in the three $\tau_{\text{had}}\tau_{\text{had}}$ analysis categories. ....	163
657			
658	Table 6–13	Input variables used for the low- $m_{\text{HH}}$ ggF BDT training in the $\tau_{\text{had}}\tau_{\text{had}}$ channel. ....	165
659			
660	Table 6–14	Input variables used for the high- $m_{\text{HH}}$ ggF BDT training in the $\tau_{\text{had}}\tau_{\text{had}}$ channel. ....	166
661			
662	Table 6–15	Input variables used for the VBF BDT training in the $\tau_{\text{had}}\tau_{\text{had}}$ channel. ....	166
663	Table 6–16	Pre-fit yields of the individual background components and the total ggF+VBF HH signal (labelled signal) in the four most signal-like BDT bins, shown for the $\tau_{\text{had}}\tau_{\text{had}}$ high- $m_{\text{HH}}$ region. ....	170
664			
665			
666	Table 6–17	Pre-fit yields of the individual background components and the total ggF+VBF HH signal (labelled signal) in the four most signal-like BDT bins, shown for the $\tau_{\text{had}}\tau_{\text{had}}$ low- $m_{\text{HH}}$ region. ....	171
667			
668			
669	Table 6–18	Pre-fit yields of the individual background components and the total ggF+VBF HH signal (labelled signal) in the four most signal-like BDT bins, shown for the $\tau_{\text{had}}\tau_{\text{had}}$ VBF region. ....	172
670			
671			
672	Table 6–19	Comparison of BDT configurations for ggF/VBF in relation to the ultimate fit outcomes. These limits are derived from a fit that incorporates solely floating normalizations and MC statistical uncertainties. A consistent BDT threshold of 0.1 is employed across all scenarios. The percentage enhancement relative to the 15-var BDT outcome is indicated in parentheses. ....	173
673			
674			
675			
676			
677			
678	Table 6–20	Summarized 95% CL expected upper boundaries on $HH$ signal strength and intervals for $\kappa_\lambda$ and $\kappa_{2V}$ , categorized by production mode in the $\tau_{\text{had}}\tau_{\text{had}}$ channel. All estimations with and without systematic uncertainties are included. ....	185
679			
680			
681			

682	Table 6–21	Expected 95% CL limits on $HH$ signal strength and intervals for $\kappa_\lambda$ and	
683		$\kappa_{2V}$ from the combined fit. The statistics are reported both with and with-	
684		out systematic uncertainties.....	186
685	Table 7–1	Summary of datasets for each contributing analysis channel, with their	
686		corresponding integrated luminosities in $\text{fb}^{-1}$ . Detailed descriptions of	
687		each channel can be found in the last column’s references. ....	191
688	Table 7–2	Comprehensive summary of $\kappa_\lambda$ constraints. ....	197
689	Table 8–1	Projected Operational Modes of CEPC and Corresponding Yields of Higgs,	
690		W, and Z Bosons; calculations Based on Two Interaction Points and In-	
691		tegrated Luminosity.....	203
692	Table 8–2	Fundamental Specifications and Efficacy Metrics of the CEPC Detector	
693		System. ....	204
694	Table 8–3	Cross-Section of Higgs and Background Processes at CEPC .....	206
695	Table 8–4	Signal Acceptance for Different Mass and Lifetime Parameters.....	207
696	Table 8–5	Node and edge features defined in the heterogenous graph. ....	214
697	Table 8–6	Signal efficiencies for different assumptions of LLPs’ mass and lifetime	
698		obtained with CNN-based and GNN-based approaches.....	217
699	Table 8–7	The 95% C.L. exclusion limit on $\text{BR}(h \rightarrow X_1 X_2)$ for all signal channels:	
700		fixed and floated $\epsilon_V$ , based on CNN’s efficiency.....	219



## Chapter 1 Introduction

701

702 What makes up the very fabric of the universe? How do its smallest constituents interact  
703 to form the world as we understand it? These overarching questions are central to the field  
704 of particle physics, which investigates the fundamental particles that make up matter. High-  
705 energy colliders, machines that accelerate particles to nearly the speed of light and smash  
706 them together, offer unique opportunities to address these questions by allowing scientists to  
707 study particle interactions in conditions that mimic the early universe.

708 The Standard Model of particle physics, a well-established theory developed over the  
709 past half-century, successfully explains these interactions. It provides a framework for un-  
710 derstanding how known particles, like quarks and electrons, interact through fundamental  
711 forces—namely, the electromagnetic, weak, and strong forces. The discovery of the Higgs  
712 boson in 2012 at CERN’s Large Hadron Collider, a 27-kilometer ring beneath the France-  
713 Switzerland border, provided the capstone to this model. The Higgs boson explains why  
714 some particles have mass, affirming the monumental success of the Standard Model.

715 Despite these successes, there are phenomena that cannot be fully accounted for by the  
716 Standard Model alone, such as dark matter, a mysterious substance that makes up about 27%  
717 of the universe but doesn’t emit, absorb, or reflect any electromagnetic radiation. These gaps  
718 in understanding call for exploration into Beyond the Standard Model (BSM) physics. One  
719 interesting avenue is the study of long-lived particles (LLPs), which are hypothetical particles  
720 that do not decay as rapidly as others and could possibly interact weakly with normal matter.

721 In response to the challenges and opportunities posed by these questions, scientists have  
722 deployed the Large Hadron Collider and are planning future machines known as lepton collid-  
723 ers. These include projects like the International Linear Collider (ILC), the Circular Electron-  
724 Positron Collider (CEPC), and the Future Circular Collider (FCC-ee). These colliders aim to  
725 provide more precise measurements of the Higgs boson and to explore potential new physics.

726 The discovery of the Higgs boson marks a monumental milestone in particle physics,  
727 serving as both a confirmation of the Standard Model and a gateway to further explorations.  
728 My research contributes to the next crucial phase of this field by focusing on di-Higgs search,  
729 where two Higgs bosons are produced simultaneously. This is a pivotal area of study to  
730 understand unique aspects of the Higgs, particularly its self-coupling, which governs how

731 the Higgs boson interacts with itself. My analyses particularly center on events with multi-  
732 lepton and  $b\bar{b}\tau^+\tau^-$  final states.

733 Additionally, to provide a more comprehensive understanding of the Higgs sector, my  
734 work incorporates a combination of both single- and double-Higgs production events. This  
735 integrated approach aims to constrain the Higgs boson self-coupling with increased precision,  
736 thereby offering critical insights into both Standard Model and Beyond the Standard Model  
737 physics.

738 Beyond the scope of di-Higgs and single-Higgs analyses, my research extends to BSM  
739 phenomena, particularly focusing on LLPs. Utilizing machine learning techniques that di-  
740 rectly interpret raw detector data, I've developed a novel methodology for distinguishing  
741 these hypothetical particles from Standard Model particles in simulations.

742 Finally, while the main body of this dissertation focuses on collider-based experiments,  
743 my interests extend to other forms of particle physics research. Specifically, I have worked  
744 on an experiment aiming to detect dark photons, particles that are proposed as force carriers  
745 for dark matter, using a fixed-target experiment that utilizes high-energy electron beams.

746 In sum, this dissertation offers a coherent narrative of my Ph.D. research journey. It spans  
747 from probing fundamental questions in particle physics to making significant contributions  
748 in both collider-based Higgs boson studies and BSM long-lived particle searches, while also  
749 venturing into experiments beyond colliders. Each of these research endeavors adds a piece  
750 to the complex puzzle of understanding the universe at its most basic level. This dissertation  
751 is organized as follows:

- 752 • **Chapter 2:** Provides an overview of Higgs physics within the Standard Model and  
753 beyond.
- 754 • **Chapter 3:** Discusses the Large Hadron Collider and the ATLAS experiment.
- 755 • **Chapter 4:** Focuses on event simulation and reconstruction techniques in ATLAS.
- 756 • **Chapter 5:** Presents SM di-Higgs searches in multi-lepton final states.
- 757 • **Chapter 6:** Covers SM di-Higgs searches in  $bb\tau\tau$  final states.
- 758 • **Chapter 7:** Aims to constrain the Higgs boson self-coupling using data from single-  
759 and double-Higgs production.
- 760 • **Chapter 8:** Discusses search strategies for long-lived particles with future lepton col-  
761 liders.

- 762 • **Chapter 9:** Summarizes the findings and discusses future prospects.
- 763 • **Appendix A:** Describes a fixed-target experiment to probe dark photon using 8 GeV
- 764 electron beam.



## Chapter 2 Higgs Physics in Standard Model and Beyond

The Standard Model (SM) of particle physics is the pinnacle of over a century's worth of scientific research, culminating in our current understanding of the fundamental particles and the forces that govern their interactions. It is one of the most complicated theories, yet elegant in both mathematics and physics that has stood the test of time and experimental scrutiny.

The story of the Standard Model starts in the mid 20<sup>th</sup> century, when quantum electrodynamics (QED) was born. This theory is developed by the great physicist Richard Feynman<sup>[1]</sup>, Julian Schwinger<sup>[2]</sup>, Sin-Itiro Tomonaga, and Freeman Dyson, describing how photons interact with electrons and positrons. The development of QED was a major achievement, as it successfully reconciled quantum mechanics, which governs the small scale, with special relativity, which describes the fast-moving world. It provided a framework that could make incredibly precise predictions, many of which have been confirmed by experiments. QED was the first example of a quantum field theory, which would serve as the template for the rest of the Standard Model.

In the 1960s and 70s, the understanding of the strong nuclear force, one of the four fundamental forces of nature, underwent a significant revolution with the introduction of partons, namely quarks and gluons. This force is responsible for holding together the protons and neutrons inside atomic nuclei, and the particles that mediate this force are called gluons. The theory that describes the strong force is called quantum chromodynamics (QCD), developed by scientists such as Murray Gell-Mann<sup>[3][4]</sup> and Harald Fritzsch<sup>[5]</sup>. The particles involved in this force, quarks and gluons, carry a property called "color charge" (analogous to electric charge in electromagnetism), and the theory gets its name from this color charge. QCD provided a framework for understanding how quarks combine to form protons, neutrons, and other particles.

Meanwhile, scientists were also making progress on understanding the weak nuclear force, which is responsible for radioactive decay and plays a key role in nuclear fusion in stars. The weak force was initially puzzling because it is very different from the other forces, which is much weaker (hence the name), and it only operates at very short distances. In the 1960s, Sheldon Glashow<sup>[6]</sup>, Abdus Salam<sup>[7]</sup>, and Steven Weinberg<sup>[8]</sup> developed a theory that

795 unified the weak force with electromagnetism, resulting in the "electroweak" theory. This  
796 theory predicted the existence of three new particles, the  $W^+$ ,  $W^-$ , and  $Z$ , which mediate the  
797 weak force. These particles were later discovered in experiments at CERN in the 1980s.

798 The final piece of the puzzle was electroweak symmetry breaking, and this happens  
799 through the Brout-Englert-Higgs mechanism. This mechanism necessitates the existence  
800 of a Higgs field, and after EWS breaking, a scalar boson (the Higgs boson) appears. This  
801 particle was predicted in 1964 by several scientists, including Peter Higgs, François Englert,  
802 and Robert Brout. According to the theory, particles, especially for fermions, gain mass by  
803 interacting with this field, which means the more they interact, the more mass they have.  
804 The Higgs boson remained elusive for many years, but it was finally discovered in 2012 at  
805 CERN's Large Hadron Collider<sup>[9]</sup>, in one of the most celebrated scientific achievements of  
806 the 21st century.

807 The discovery of the Higgs boson was indeed a watershed moment in the history of par-  
808 ticle physics, confirming the last missing piece of the Standard Model puzzle. However, it is  
809 important to note that the Higgs boson itself is not the end of the story. Its discovery opened  
810 up new avenues of research, including the study of its properties and the search for possible  
811 new particles and forces associated with it.

812 Moreover, the Standard Model, while extraordinarily successful, does not account for  
813 some observed phenomena, indicating that there is physics beyond it - often referred to as  
814 "Beyond the Standard Model" (BSM) physics. One of the major areas of research in BSM  
815 physics involves long-lived particles (LLPs). These are hypothetical particles that do not  
816 decay immediately after being produced in high-energy collisions, as most known particles  
817 do. Instead, they would travel a significant distance before decaying, potentially leaving a  
818 distinctive signature in detectors at particle accelerators. This unusual behavior could be  
819 linked to the mysteries of dark matter, neutrino masses, or the imbalance between matter and  
820 antimatter in the universe.

821 This chapter delves into the intricacies of the Standard Model and its fundamental compo-  
822 nents, beginning with an overview in Section 2.1. Next, Section 2.2 illuminates the concept of  
823 Electroweak Symmetry Breaking and the Brout-Englert-Higgs Mechanism. The subsequent  
824 focus in Section 2.3 is on the research surrounding the Higgs bosons at the Large Hadron  
825 Collider (LHC). Finally, Section 2.4 delves into the frontier of Long-Lived Particles (LLPs)

826 and their potential to further the understanding of physics beyond the Standard Model.

## 827 **2.1 Introduction to the Standard Model**

### 828 **2.1.1 Fermions and Bosons**

829 The SM theoretical framework categorizes elementary particles into two principal classes,  
830 known as fermions and bosons, each with distinctive characteristics and roles in the cosmos,  
831 as summarized in Figure 2–1.

832 Fermions comprise the building blocks of matter and adhere to the Pauli Exclusion Princi-  
833 ple, implying that they cannot simultaneously occupy identical quantum states. Characterized  
834 by half-integer spins, fermions are sub-categorized into two classes: quarks and leptons.

- 835 • **Quarks:** There exist six flavors of quarks: up, down, charm, strange, top, and bottom.  
836 The up, charm, and top quarks carry a fractional electric charge of  $+2/3$ , while the  
837 down, strange, and bottom quarks carry a fractional charge of  $-1/3$ . Quarks are unique  
838 in that they interact via all three fundamental non-gravitational forces: strong, weak,  
839 and electromagnetic. Additionally, quarks carry an intrinsic property termed 'color  
840 charge', which mediates their interaction via the strong force. There are 3 color charges  
841 (and 3 opposite charges) for each flavor.
- 842 • **Leptons:** Analogous to quarks, leptons are also divided into six types across three  
843 generations: electron, muon, tau particles, and their corresponding neutrinos. The  
844 electron, muon, and tau each carry a unit negative charge and interact via the weak and  
845 electromagnetic forces. Neutrinos, on the other hand, being neutral, solely partake in  
846 weak interactions.

847 Bosons, contrarily, are force mediators and possess integer spins, permitting them to in-  
848 habit the same quantum state. The Standard Model recognizes the following bosons: photon,  
849 W and Z bosons, gluons, and the Higgs boson.

- 850 • **Photon:** The photon is the force carrier for the electromagnetic force, governing inter-  
851 actions between electrically charged particles. It is a massless particle that propagates  
852 at the speed of light.
- 853 • **W and Z bosons:** These are the mediators of the weak nuclear force, which controls  
854 certain types of nuclear decay, such as beta decay. The W bosons carry a unit positive

855 or negative charge, while the Z boson is electrically neutral. Their considerable masses  
 856 lead to the short-range nature of the weak force.

- 857 • **Gluons:** Gluons mediate the strong nuclear force, responsible for binding quarks within  
 858 protons, neutrons, and other hadronic particles. They carry a color charge, allowing  
 859 them to interact among themselves.
- 860 • **Higgs boson:** The Higgs boson is associated with the Higgs field, as proposed by the  
 861 Brout-Englert-Higgs mechanism, which also explains the unique "Yukawa" interac-  
 862 tion<sup>[10]</sup> through which particles acquire mass.

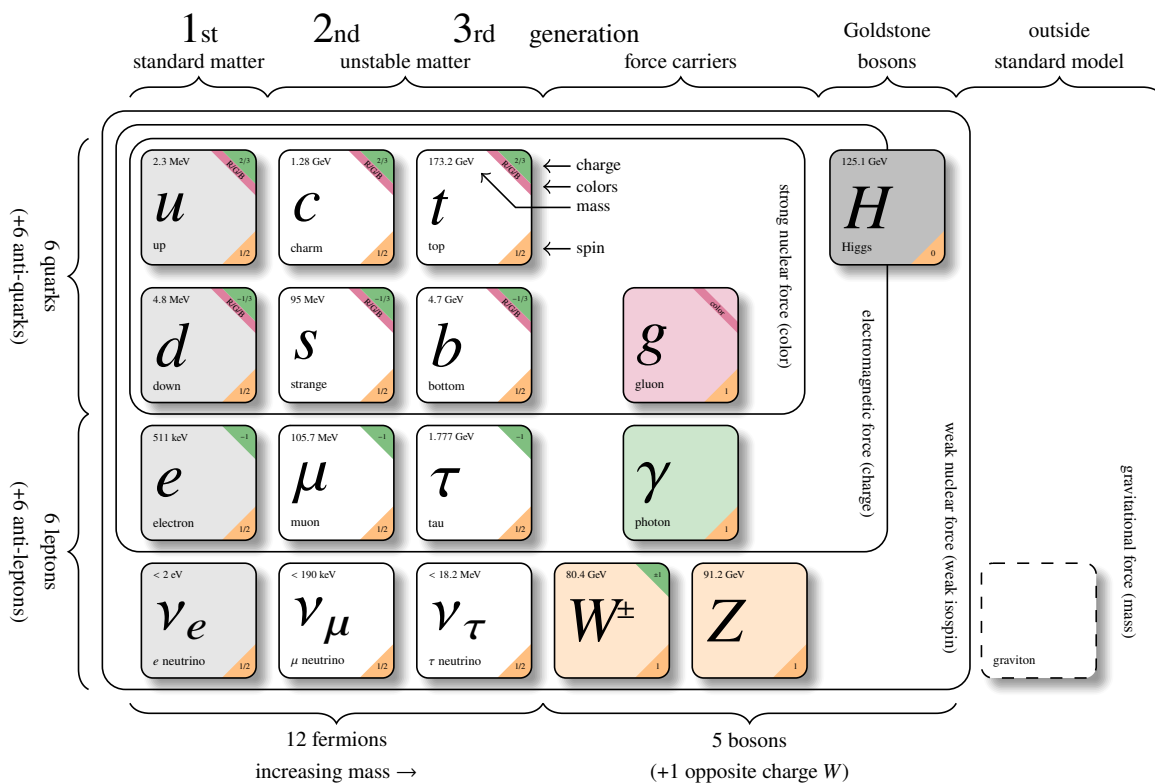


Figure 2-1 The properties of elementary particles in the Standard Model.

863 **2.1.2 The Quantum Field Theory and the Lagrangian of the Standard Model**

864 Quantum Field Theory (QFT) is the theoretical framework that combines classical field  
 865 theory<sup>[11]</sup>, quantum mechanics, and special relativity. QFT treats particles as excited states,  
 866 or quanta, of underlying quantum fields. These fields are mapped across spacetime, and par-  
 867 ticles are represented by field oscillations. The most successful application of QFT is the

868 Standard Model of particle physics. The mathematical structure that describes the dynamics  
 869 and interactions of the quantum fields in the Standard Model is given by the so-called Stan-  
 870 dard Model Lagrangian. This Lagrangian includes terms for each of the particles and their  
 871 interactions in the model.

872 To describe the Standard Model in the language of QFT, the concept of gauge symmetry  
 873 is introduced. This is a fundamental symmetry principle that states that the laws of physics  
 874 should not change under certain transformations, known as gauge transformations. In the  
 875 context of QFT, gauge transformations change the phase of the quantum fields, and different  
 876 types of gauge transformations lead to different types of forces.

877 The Lagrangian of the Standard Model encompasses all known elementary particles and  
 878 their interactions, excluding gravity. The full Lagrangian is the sum of these parts:

$$L = -\frac{1}{4}F_{\mu\nu}F^{\mu\nu} + i\bar{\psi}\not{D}\psi + h.c. + \psi_i y_{ij} \psi_j \phi + h.c. + |D_\mu \phi|^2 + -V(\phi), \quad (2-1)$$

879 which is usually divided into several parts that describe different kinds of interactions<sup>[12]</sup>:

- 880 1.  $-\frac{1}{4}F_{\mu\nu}F^{\mu\nu}$  This term represents the kinetic energy of the matter fields. It describes  
 881 the propagation of matter particles in space and time. This term includes the fields of  
 882 quarks and leptons, which are the building blocks of matter.
- 883 2.  $i\bar{\psi}\not{D}\psi$  This term describes the interactions between matter particles and force parti-  
 884 cles. It includes the electromagnetic interaction, the strong interaction, and the weak  
 885 interaction. The electromagnetic interaction is mediated by the photon, the strong in-  
 886 teraction by the gluon, and the weak interaction by the W and Z bosons. The weak  
 887 interaction is unique in that it can transform one type of matter particle into another.
- 888 3.  $h.c.$  This term represents the 'hermitian conjugate' of term 2. The hermitian conjugate  
 889 is necessary if arithmetic operations on matrices produce complex numbers.
- 890 4.  $\psi_i y_{ij} \psi_j \phi$  This term represents how matter particles couple to the Brout-Englert-Higgs  
 891 (BEH) field  $\phi$  and thereby obtain mass. It includes the coupling of quarks and leptons  
 892 to the Higgs field.
- 893 5.  $h.c.$  This term describes is necessary since this hermitian conjugate of term 4 describes  
 894 the same interaction, but with antimatter particles.
- 895 6.  $|D_\mu \phi|^2$  This term represents how the propagator particles of weak interaction couple  
 896 to the BEH field. It only appies to the W and Z bosons, because photons and gluons  
 897 are massless.

898 7.  $-V(\phi)$  This term describes the Brout-Englert-Higgs field potential and how Higgs  
899 bosons couple to each other.

900 The specific form of each of these terms is dictated by the principles of gauge symmetry,  
901 special relativity, and quantum mechanics. The parameters in the Lagrangian (the particle  
902 masses, the coupling constants, etc.) are determined by experiments. In this framework, par-  
903 ticles interact by exchanging gauge bosons. For instance, two electrons repel each other by  
904 exchanging a photon, the gauge boson of the electromagnetic field. Similarly, quarks interact  
905 by exchanging gluons, the gauge bosons of the strong force. The Higgs field, as introduced  
906 in the Lagrangian, plays a critical role in the Standard Model. When the Higgs field under-  
907 goes spontaneous symmetry breaking, it gives rise to the masses of the other particles. The  
908 interaction of the particles with the Higgs field is proportional to their mass. More details  
909 about the Higgs field are discussed in Section 2.2.

## 910 **2.2 Electroweak Symmetry Breaking and the Brout-Englert-Higgs Mech-** 911 **anism**

### 912 **2.2.1 Electroweak unification**

913 Electroweak unification is a fundamental concept in particle physics that ties together two  
914 of the four known forces of nature, namely the weak nuclear force and electromagnetism.  
915 This unification is a cornerstone of the Standard Model (SM) of particle physics, providing  
916 an elegant theoretical framework to understand the interactions of elementary particles.

917 At the heart of electroweak unification is the realization that at high enough energies,  
918 electromagnetism, mediated by photons ( $\gamma$ ), and the weak nuclear force, mediated by W and  
919 Z bosons ( $W^+$ ,  $W^-$ , and  $Z^0$ ), manifest as facets of the same force: the electroweak force. The  
920 connection between these two fundamental interactions was initially proposed by Sheldon  
921 Glashow, Abdus Salam, and Steven Weinberg, earning them the Nobel Prize in Physics in  
922 1979.

923 The theory begins with an invariant Lagrangian under the  $SU(2)_L \times U(1)_Y$  gauge group,  
924 with  $SU(2)_L$  and  $U(1)_Y$  representing the weak isospin and hypercharge symmetries, respec-  
925 tively. The gauge fields corresponding to these symmetries are  $W_\mu^a$  ( $a = 1, 2, 3$ ) and  $B_\mu$ . The

926 electroweak part of the SM Lagrangian can be written as follows:

$$\mathcal{L}_{EW} = -\frac{1}{4}W_{\mu\nu}^a W^{a\mu\nu} - \frac{1}{4}B_{\mu\nu}B^{\mu\nu} \quad (2-2)$$

927 Here,  $W_{\mu\nu}^a$  and  $B_{\mu\nu}$  are the field strength tensors for the  $SU(2)_L$  and  $U(1)_Y$  gauge fields,  
928 defined as:

$$W_{\mu\nu}^a = \partial_\mu W_\nu^a - \partial_\nu W_\mu^a + g\epsilon^{abc}W_\mu^b W_\nu^c \quad (2-3)$$

929

$$B_{\mu\nu} = \partial_\mu B_\nu - \partial_\nu B_\mu \quad (2-4)$$

930 Here,  $\epsilon^{abc}$  is the totally antisymmetric tensor,  $g$  is the  $SU(2)_L$  gauge coupling constant,  
931 and  $\mu, \nu$  are space-time indices. This Lagrangian describes four massless gauge bosons,  
932 which correspond to the three generators of  $SU(2)_L$  and the generator of  $U(1)_Y$ . However,  
933 empirical evidence contravenes this: the weak force has a short range because its mediators,  
934 the W and Z bosons, are massive, while the photon is massless.

935 To reconcile this discrepancy, the Brout-Englert-Higgs mechanism is invoked, which in-  
936 troduces a complex scalar field, the Higgs field. This field spontaneously breaks the  $SU(2)_L \times$   
937  $U(1)_Y$  symmetry down to  $U(1)_{em}$ , the gauge group of electromagnetism. Consequently, three  
938 of the original massless gauge bosons acquire mass, becoming the W and Z bosons, while  
939 the fourth remains massless, recognized as the photon.

940 It is worth noting that the electroweak symmetry breaking also involves the generation of  
941 fermion masses through their Yukawa couplings to the Higgs field. As we know it, without  
942 this mechanism, the elementary particles would all be massless, zipping through space at the  
943 speed of light, and the universe would not exist.

944 The unification of the electromagnetic and weak forces happens at a sufficiently high  
945 energy scale, known as the electroweak scale, at approximately 100 GeV. At energies below  
946 this scale, the weak and electromagnetic forces appear distinct because of the large masses  
947 of the W and Z bosons. Above the electroweak scale, however, the distinction between these  
948 forces blurs, and they behave as a singular electroweak force.

949 Experimental confirmation of electroweak unification came in the 1980s with the discov-  
950 ery of W and Z bosons at CERN's Super Proton Synchrotron<sup>[13]</sup>. Further, precision measure-  
951 ments at the HERA<sup>[14]</sup> ( $e-p$  collider), the Large Electron-Positron (LEP) collider<sup>[15]</sup> and the  
952 Tevatron<sup>[16]</sup> confirmed the predictions of the electroweak theory, solidifying it as an integral

953 part of the SM. At HERA we could see the unification of charged current (CC) and neutral  
954 current (NC) cross sections at high  $Q^2$  (squared momentum transfer)<sup>[17]</sup>.

## 955 2.2.2 The role of the Higgs field in symmetry breaking

956 The Standard Model of particle physics provides an extraordinarily successful framework  
957 for understanding elementary particles and their interactions. Central to the model is the elec-  
958 troweak theory, which describes electromagnetism and the weak nuclear force as two aspects  
959 of a unified electroweak force. However, in order to reconcile the massless nature required  
960 by gauge invariance with the observed massive particles, we need to introduce the Brout-  
961 Englert-Higgs (BEH) mechanism, which is a process of spontaneous symmetry breaking.

962 The spontaneous symmetry breaking<sup>[18]</sup> occurs in the scalar sector of the electroweak  
963 theory, which contains the Higgs field<sup>[19]</sup>, denoted by  $\Phi$ . The Lagrangian density responsible  
964 for this process is given by:

$$\mathcal{L} = (D^\mu \Phi)^\dagger (D_\mu \Phi) - V(\Phi) \quad (2-5)$$

965 where  $D_\mu$  is the covariant derivative that contains the  $W$  and  $B$  fields, and  $V(\Phi)$  is the Higgs  
966 potential. In the Standard Model,  $\Phi$  is a doublet of complex scalar fields given by:

$$\Phi = \frac{1}{\sqrt{2}} \begin{pmatrix} 0 \\ v + h(x) \end{pmatrix} \quad (2-6)$$

967 where  $v$  is the vacuum expectation value (VEV) of the field and  $h(x)$  signifies the real scalar  
968 field representing fluctuations about the vacuum. The Higgs potential  $V(\Phi)$  is given by:

$$V(\Phi) = \mu^2 \Phi^\dagger \Phi + \lambda (\Phi^\dagger \Phi)^2 \quad (2-7)$$

969 with the parameters satisfying  $\mu^2 < 0$  and  $\lambda > 0$ . The negative  $\mu^2$  term allows for a non-  
970 zero minimum of the potential away from the origin, while the positive  $\lambda$  term ensures that  
971 the potential is bounded from below. This generates a "Mexican hat" shape in the Higgs  
972 potential. Figure 2-2 illustrates the Higgs potential for  $\mu^2 < 0$  and  $\mu^2 > 0$ .

973 This non-zero minimum of the potential, also known as the vacuum expectation value  
974 (VEV), is given by  $v = \sqrt{\frac{-\mu^2}{2\lambda}}$ . It is around this value that the Higgs field oscillates, not  
975 around zero, and thus the electroweak symmetry is spontaneously broken, resulting in the  $W$   
976 and  $Z$  bosons acquiring mass. It's also beneficial to understand that the fluctuations about  
977 this vacuum state, represented by  $h(x)$ , correspond to the physical Higgs boson.

978 Upon expanding the kinetic term  $(D^\mu\Phi)^\dagger(D_\mu\Phi)$  and the potential  $V(\Phi)$  around the vac-  
 979 uum expectation value, we find terms proportional to  $W^\mu W_\mu$ ,  $B^\mu B_\mu$ , and  $h^2$ , which give rise  
 980 to the masses of the W boson, Z boson, and the Higgs boson, respectively. Specifically, the  
 981 Higgs boson mass can be identified as  $m_H = \sqrt{2\lambda}v$ .

982 The mass generation for fermions is also an outcome of the Higgs mechanism, however it  
 983 involves a different process, namely the Yukawa interaction between fermions and the Higgs  
 984 field. After the spontaneous symmetry breaking, the Higgs doublet acquires a vacuum expect-  
 985 ation value  $v$ , and the Yukawa interaction term in the Standard Model Lagrangian becomes:

986

$$\mathcal{L}_{\text{Yukawa}} = -\frac{y_f v}{\sqrt{2}}\bar{\Psi}_f\Psi_f - \frac{y_f h}{\sqrt{2}}\bar{\Psi}_f\Psi_f + \text{h.c.} \quad (2-8)$$

987 The first term now clearly signifies the mass term for the fermions,  $m_f = y_f v/\sqrt{2}$ , which  
 988 is non-zero due to the non-zero vacuum expectation value of the Higgs field. This is how  
 989 fermions acquire their mass in the Higgs mechanism. The second term represents the in-  
 990 teraction of the Higgs boson with the fermions, which is proportional to the mass of the  
 991 fermions. These interactions are crucial for the production and decay of the Higgs boson at  
 992 colliders. In the Standard Model, the Yukawa couplings  $y_f$  are free parameters and must be  
 993 determined by experiment.

994 The Brout-Englert-Higgs (BEH) mechanism and its associated spontaneous symmetry  
 995 breaking are fundamental components of the Standard Model of particle physics. They pro-  
 996 vide a consistent framework that unifies the weak nuclear force and electromagnetism, offer-  
 997 ing a profound explanation for the observed masses of fundamental particles. The mechanism  
 998 relies on the Higgs field, which has a non-zero vacuum expectation value and plays a crucial  
 999 role in this process. Rather than actually "breaking" the symmetry, the mechanism merely  
 1000 conceals it. The underlying theory remains symmetric, but the ground state does not exhibit  
 1001 this symmetry. This distinction is crucial for our modern understanding of particle physics.

1002 It is worth emphasizing that direct mass terms for gauge bosons would violate gauge  
 1003 invariance, which is a foundational symmetry of the Standard Model. The Higgs mechanism  
 1004 becomes indispensable in this regard. Starting from a massless theory that requires gauge  
 1005 invariance, the Higgs field and its corresponding mechanism give rise to effective mass terms  
 1006 for particles after electroweak symmetry breaking (EWSB). This ingenious solution ensures  
 1007 that the theory remains consistent and gauge invariant while also explaining the origin of

1008 mass for particles.

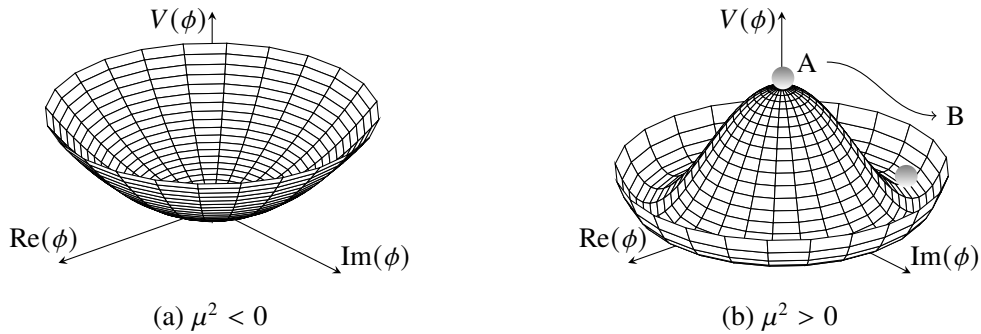


Figure 2–2 The illustration of Higgs potential  $V(\phi)$ . Point B represents for the non-zero vacuum expectation value (VEV) of the field.

## 1009 2.3 Higgs Physics at the LHC

### 1010 2.3.1 Higgs boson production

1011 The key production mechanisms for the Higgs boson at the Large Hadron Collider (LHC)  
 1012 include gluon fusion (ggF), vector-boson fusion (VBF), associated production with a gauge  
 1013 boson (VH), as well as associated production with a pair of top quarks ( $t\bar{t}H$ ) or with a single  
 1014 top quark (tHq). Figure 2–3 illustrates these dominant Higgs boson production processes.  
 1015 In 2–4 (left), the cross sections corresponding to the production of a SM Higgs boson are  
 1016 presented as a function of the center of mass energy,  $\sqrt{s}$ , for proton-proton (pp) collisions.  
 1017 This representation also includes bands to indicate theoretical uncertainties.

1018 A comprehensive discussion on uncertainties in the theoretical calculations, resulting  
 1019 from missing higher-order effects and the experimental uncertainties on the determination of  
 1020 SM parameters used in the calculations, can be found in references<sup>[20]</sup>. These sources also  
 1021 offer advanced discussions on the impact of parton distribution function (PDF) uncertainties,  
 1022 Quantum Chromodynamics (QCD) scale uncertainties, uncertainties stemming from differ-  
 1023 ent procedures for including higher-order corrections matched to parton shower simulations,  
 1024 as well as uncertainties due to hadronisation and parton-shower events.

1025 Table 2–1 tabulates the production cross sections for a SM Higgs boson with a mass of  
 1026 125 GeV in proton-proton collisions. These values are presented as functions of the center-  
 1027 of-mass energy  $\sqrt{s}$ . The projections for the Large Hadron Collider (LHC) energies have been

1028 sourced from reference<sup>[20]</sup>. The estimates for the ggF channel at the LHC are inclusive of the  
 1029 most recent next-to-next-to-next-to leading order (N3LO) results, which have significantly  
 1030 cut down the theoretical uncertainties by approximately a factor of two, in comparison to the  
 1031 next-to-next-to leading order plus next-to leading logarithm (NNLO+NLL) results. It's worth  
 1032 noting that the total uncertainties were calculated under the assumption of no correlations  
 1033 between strong coupling constant ( $\alpha_s$ ) and PDF uncertainties.

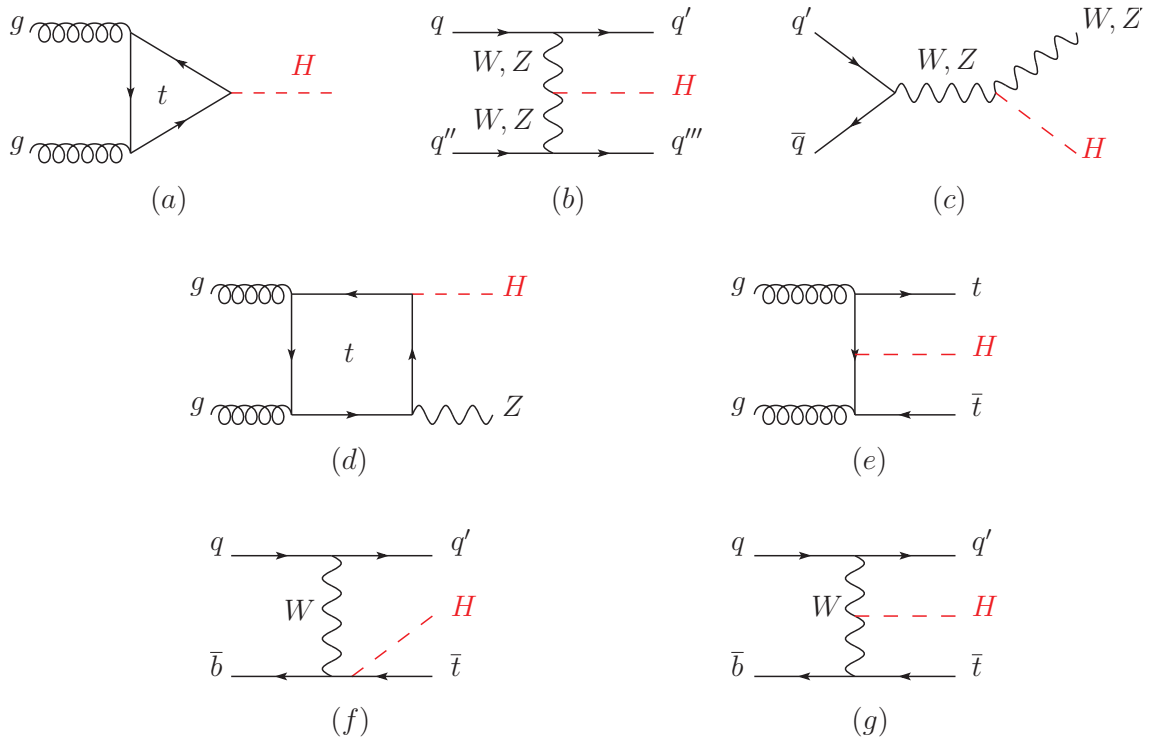


**Figure 2–3** A collection of the primary Feynman diagrams at leading order contributing to Higgs boson production. (a) Represents the gluon fusion process, (b) showcases Vector-boson fusion, (c) displays Higgs-strahlung or associated production with a gauge boson arising from a quark-quark interaction at the tree level, (d) outlines associated production with a gauge boson from a gluon-gluon interaction at the loop level, (e) depicts the associated production with a pair of top quarks (a similar diagram would represent the associated production with a pair of bottom quarks), (e-f) illustrates the process of production in association with a single top quark.

1034 At the LHC, two of the most prominent higgs production modes are the ggF and VBF.  
 1035 The ggF is the dominant production mechanism for Higgs boson at the LHC. This process  
 1036 is a quantum loop process, where two gluons (g) emitted by incoming protons interact to  
 1037 produce a Higgs boson (H), with the help of a top quark loop. Although gluons are massless

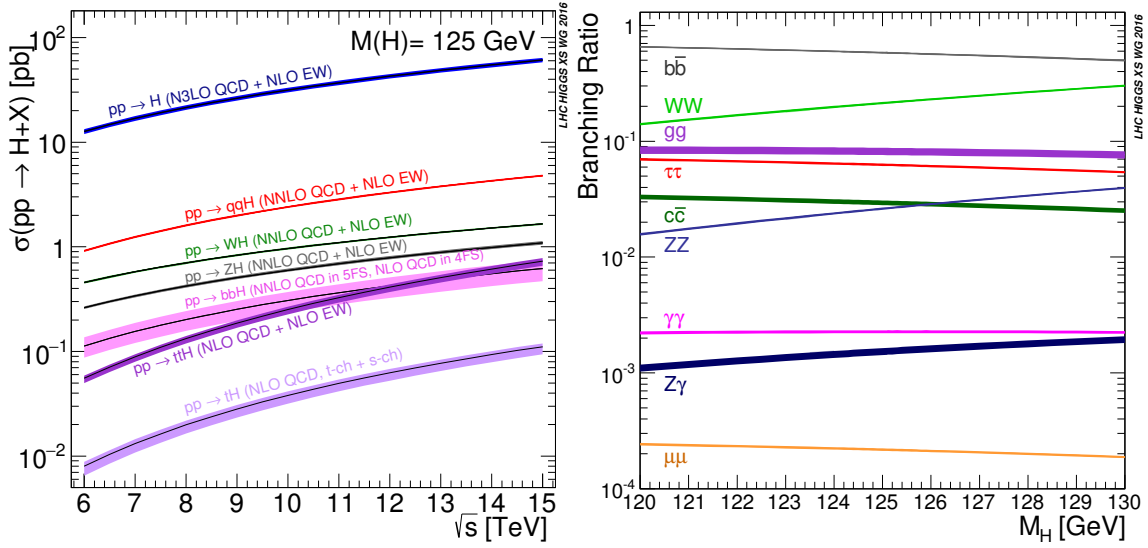


**Figure 2–4 (Left) The production cross sections of the SM Higgs boson as a function of the center of mass energy,  $\sqrt{s}$ , for proton-proton collisions<sup>[21]</sup>. The VBF process is denoted here as  $qqH$ . (Right) Branching ratios for the primary decays of the SM Higgs boson near a mass ( $m_H$ ) of 125 GeV<sup>[20]</sup>. Bands represent theoretical uncertainties.**

$\sqrt{s}$ (TeV)	Production cross section (in pb) for $m_H = 125\text{GeV}$					total
	ggF	VBF	WH	ZH	$t\bar{t}H$	
7	$16.9^{+4.4\%}_{-7.0\%}$	$1.24^{+2.1\%}_{-2.1\%}$	$0.58^{+2.2\%}_{-2.3\%}$	$0.34^{+3.1\%}_{-3.0\%}$	$0.09^{+5.6\%}_{-10.2\%}$	19.1
8	$21.4^{+4.4\%}_{-6.9\%}$	$1.60^{+2.3\%}_{-2.1\%}$	$0.70^{+2.1\%}_{-2.2\%}$	$0.42^{+3.4\%}_{-2.9\%}$	$0.13^{+5.9\%}_{-10.1\%}$	24.2
13	$48.6^{+4.6\%}_{-6.7\%}$	$3.78^{+2.2\%}_{-2.2\%}$	$1.37^{+2.6\%}_{-2.6\%}$	$0.88^{+4.1\%}_{-3.5\%}$	$0.50^{+6.8\%}_{-9.9\%}$	55.1
14	$54.7^{+4.6\%}_{-6.7\%}$	$4.28^{+2.2\%}_{-2.2\%}$	$1.51^{+1.9\%}_{-2.0\%}$	$0.99^{+4.1\%}_{-3.7\%}$	$0.60^{+6.9\%}_{-9.8\%}$	62.1

**Table 2–1 Production cross sections of the Standard Model Higgs boson, with a mass of 125 GeV, in proton-proton collision**

1038 and the Higgs boson couples to particles with mass, the strong coupling between gluons  
 1039 and top quarks allows this process via quantum loops. The process can be represented as  
 1040  $g + g \rightarrow H + X$ . Given the high abundance of gluons in the proton at the LHC energies,  
 1041 this process has a high rate of occurrence, making it the primary channel for Higgs boson  
 1042 production at the LHC.

1043 VBF is the second most common process for producing Higgs bosons at the LHC. In  
 1044 this process, the two protons each emit a W or Z boson, which then interact to produce the  
 1045 Higgs boson. This can be represented as  $q + q \rightarrow q' + q' + H$ , where  $q$  and  $q'$  are quarks.

1046 Unlike ggF, this process is not a loop process but a t-channel process. The scattered quarks  
 1047 usually result in two forward jets in the detector, with the Higgs boson produced centrally.  
 1048 This characteristic jet activity often assists in distinguishing the VBF process from other  
 1049 production mechanisms.

### 1050 2.3.2 Di-Higgs production

1051 The production of two Higgs bosons, a process referred to as double Higgs boson pro-  
 1052 duction, is of significant interest due to the wealth of information it provides about the  
 1053 Higgs potential. Specifically, this process gives insights into the trilinear self-coupling of  
 1054 the Higgs. The primary mechanism for double Higgs production is through gluon fusion  
 1055 ( $gg \rightarrow HH$ ), which accounts for more than 90% of the total cross-section. Figure 2–5 de-  
 1056 picts the major Feynman diagrams for the production of two Higgs bosons via gluon fusion.  
 1057 These two diagrams interfere destructively, leading to a very small  $HH$  cross-section, namely  
 1058  $\sigma_{\text{ggF},HH}^{SM} = 31.05 \pm 3\% \text{ (PDF} + \alpha_s) \begin{smallmatrix} +6\% \\ -23\% \end{smallmatrix} \text{ (Scale} + m_{\text{top}}) \text{ fb}$ , calculated at next-to-next-to-leading-  
 1059 order (NNLO) accuracy in the finite top-quark mass approximation for  $m_H = 125 \text{ GeV}$  and  
 1060  $\sqrt{s} = 13 \text{ TeV}$

1061 Under the conditions at the LHC ( $\sqrt{s} = 14\text{TeV}$ ), the cross-section for the  $bbH$  mode  
 1062 can reach up to 550fb, albeit this is still two orders of magnitude below the cross-section  
 1063 for ggF. It is noteworthy that in alternative models such as the two Higgs doublet model or  
 1064 a SUSY model, the Higgs self-coupling is proportional to the ratio of neutral Higgs boson  
 1065 vacuum expectation values. For large values of this ratio, the coupling undergoes signifi-  
 1066 cant amplification, potentially elevating the  $bbH$  mode to be the dominant mechanism for  
 1067 Higgs boson production, a deviation from the Standard Model predictions. Other sub-leading  
 1068 production mechanisms are also present, including VBF  $HHjj$  ( $\sigma_{\text{VBF},HH}^{SM} = 1.726 \pm 2.1\%$   
 1069  $\text{(PDF} + \alpha_s) \begin{smallmatrix} +0.03\% \\ -0.04\% \end{smallmatrix} \text{(Scale) fb}$  at  $\sqrt{s} = 13\text{TeV}$ ) (Figure 2–6),  $HHW$  (0.50fb),  $HHZ$  (0.36fb), and  
 1070  $ttHH$  (0.8fb). QCD corrections, computed in the infinite top mass limit, significantly influ-  
 1071 ence the cross-section, effectively doubling it from LO to NLO<sup>[22]</sup> and further enhancing it  
 1072 by around 20% from NLO to NNLO<sup>[23]</sup>.

1073 In the recent past, complete NLO corrections incorporating all top quark mass effects<sup>[24]</sup>  
 1074 have been determined numerically. These findings reveal a k-factor less flat than that pre-  
 1075 dicted in large top mass approximations<sup>[24]</sup>. This unexpected dependency of the results on

1076 the renormalisation scheme and scale for the top quark mass raises questions about the as-  
 1077 sessment of scale uncertainty and calls for a more accurate NNLO computation, although  
 1078 such a task is likely to remain challenging for some time.

1079 On the differential level, the destructive interference between the box and triangle contri-  
 1080 butions makes the predictions made in the infinite top mass limit for both the HH invariant  
 1081 mass and the leading Higgs boson pT distributions complex. With an inclusive cross-section  
 1082 of around 35 fb at  $\sqrt{s} = 13$  TeV and challenging signal-background discrimination, the double  
 1083 Higgs boson production remains a difficult channel to probe and is expected to significantly  
 1084 benefit from the high-luminosity run of the LHC<sup>[25]</sup>.

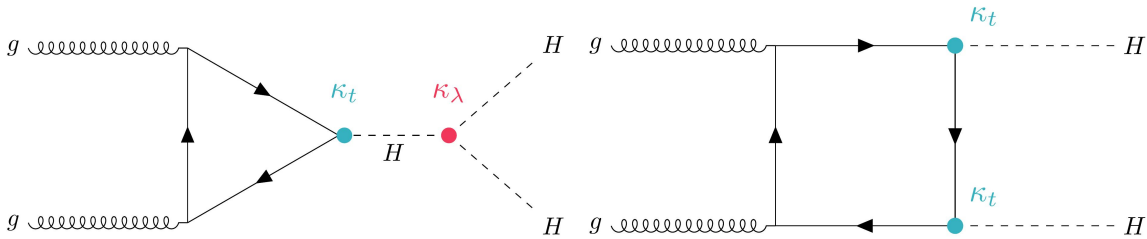


**Figure 2-5** The major Feynman diagrams for the production of two Higgs bosons via gluon fusion. (Left) Triangle diagram sensitive to the self-coupling vertex  $\kappa_\lambda$ , (Right) Box diagram, which interferes destructively at the self-coupling vertex  $\kappa_\lambda$ .

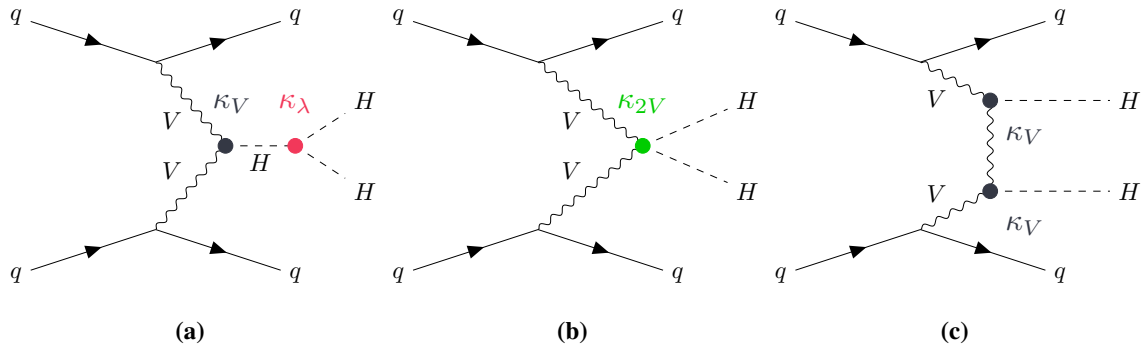


**Figure 2-6** Depiction of Vector Boson Fusion (VBF) processes in Higgs boson pair production: (a) the VVHH vertex process, (b) the trilinear coupling, and (c) the VVH production mode.

1085 Investigations into both resonant and non-resonant Higgs boson pair production can re-  
 1086 veal intriguing insights into various BSM theories. Resonant production involves the creation  
 1087 of unstable, heavier particles that decay into two Higgs bosons, thereby forming a character-  
 1088 istic peak in the energy spectrum. Non-resonant production, however, involves processes

1089 that create two Higgs bosons directly, without the intermediate step of a heavier particle.  
 1090 These mechanisms offer different perspectives and carry distinctive signatures, broadening  
 1091 the scope of the search for new physics. During Run 1 and Run 2, both ATLAS and CMS  
 1092 experiments performed searches for resonant and non-resonant Higgs boson pair production  
 1093 via the following channels:

- 1094 1.  $HH \rightarrow bb\gamma\gamma$ ,
- 1095 2.  $HH \rightarrow bb\tau^+\tau^-$ ,
- 1096 3.  $HH \rightarrow bbbb$ ,
- 1097 4.  $HH \rightarrow bbVV$ ,
- 1098 5.  $HH \rightarrow bll$ ,
- 1099 6. Final states containing multiple leptons (electrons or muons), covering the  $WW^*WW^*$ ,  
 1100  $WW^*ZZ^*$ ,  $ZZ^*ZZ^*$ ,  $ZZ^*\tau^+\tau^-$ ,  $WW^*\tau^+\tau^-$ ,  $ZZ^*bb$ , and  $\tau^+\tau^-\tau^+\tau^-$  channels,

## 1101 2.4 Long-Lived Particles (LLPs) and Beyond Standard Model Search

1102 Particle physics as a distinct field was demarcated by the discoveries of the muon in 1936  
 1103 and the kaon in 1947. These particles exhibited macroscopic lifetimes detectable via early  
 1104 20th-century cloud chamber technology. Transitioning to modern silicon trackers and time  
 1105 projection chambers has preserved the significance of measuring decay lengths. While the  
 1106 advent of large particle accelerators shifted focus to higher energies and luminosities, the  
 1107 measurement of particle lifetimes remains integral. This is evidenced by pivotal searches for  
 1108 exotic long-lived particles (LLPs) at earlier facilities like LEP<sup>[26]</sup> and Tevatron<sup>[27]</sup>.

1109 LLPs have always been considered critical for discoveries beyond the Standard Model,  
 1110 particularly in the context of supersymmetry. The theoretical paradigms have evolved to  
 1111 consider a broader range of LLP signatures, beyond hard signals like high-energy photons  
 1112 or jets<sup>[28]</sup>. This expansion is also aided by a nuanced understanding of modern trigger and  
 1113 reconstruction algorithms, as well as background noise in LLP searches.

1114 The study of LLPs has a rich theoretical and experimental background, with roles both in  
 1115 the discoveries within the Standard Model and in theories that extend it. LLPs are at the fore-  
 1116 front of modern particle physics, offering sophisticated understandings of decay mechanisms  
 1117 and cosmological implications. In the SM, while most particles decay promptly, exceptions  
 1118 such as the neutron can have suppressed decay widths due to phase space suppression<sup>[29-30]</sup>.

1119 In the context of the SM, LLPs can be produced through the decay of a heavier resonance  
1120  $Y$ , which can either be a Standard Model particle like the Higgs boson and the top quark,  
1121 or can represent particles from new physics. These LLPs manifest certain common charac-  
1122 teristics, such as production rate, decay length ( $d$ ), and time dilation ( $\gamma$ ), thereby offering a  
1123 unified framework for analysis.

1124 The connection between LLPs and the Higgs boson is especially compelling. The Higgs  
1125 mechanism, responsible for electroweak symmetry breaking and mass acquisition for  $W$  and  
1126  $Z$  bosons, could also serve as a conduit to new, uncharted sectors in particle physics. Specifi-  
1127 cally, the Higgs boson, given its scalar nature and coupling structure, could decay into exotic  
1128 states, thereby producing LLPs that can be detected.

1129 In summary, Higgs-induced LLPs offer a unique lens through which both the structural  
1130 properties of the Higgs sector and realms of new physics can be investigated. Parameters such  
1131 as production rate, decay length, and time dilation are pivotal in determining the detectability  
1132 and interpretability of such exotic decay events. Consequently, the continued study of LLPs  
1133 produced via Higgs decay is a promising avenue for discovering new physics beyond the  
1134 Standard Model.

## Chapter 3 The Large Hadron Collider and ATLAS Experiment

The Large Hadron Collider (LHC)<sup>[31-32]</sup> and the ATLAS experiment<sup>[33]</sup> are two of the most significant scientific endeavors of the modern era. They represent the culmination of decades of research and development, as well as the collaborative efforts of thousands of scientists from around the world.

The history of the LHC and ATLAS experiment is a testament to humanity's unrelenting quest for knowledge. It all began in the aftermath of the Second World War, when a war-torn Europe sought avenues for unity, collaboration, and rediscovery of its scientific prowess. In 1954, the European Organization for Nuclear Research<sup>[34]</sup>, or CERN, was established, marking a new dawn for European physics. Located near Geneva at the Franco-Swiss border, CERN became a beacon of international collaboration.

The years that followed saw CERN launching multiple accelerators, each more sophisticated than its predecessor. The Proton Synchrotron, completed in 1959, was a marvel of its time, accelerating protons to energies previously unattained. But the scientists at CERN had a grander vision.

By the late 1980s, the Large Electron-Positron Collider<sup>[15]</sup> (LEP) was inaugurated. It was an accelerator designed to collide electrons and positrons at energies that allowed the discovery of the W and Z bosons. These particles, crucial to the electroweak theory, solidified the Standard Model's foundations.

However, while the LEP was a significant achievement, the dream for an even grander machine was taking shape. The field of particle physics was abuzz with questions surrounding the Higgs boson, a particle that had been theorized in the 1960s but had eluded detection. The LHC was envisioned as a solution to this problem.

Conceived in the 1980s and 1990s, the LHC was a monumental undertaking, not only in terms of physics but also engineering. To house such a colossal machine, CERN's underground tunnel, previously used for LEP, was repurposed, marking an evolution from electron-positron collisions to hadron collisions.

But a machine of the LHC's caliber required detectors of exceptional finesse. This need

1164 birthed the ATLAS experiment. Beginning in the early 1990s, ATLAS was an audacious  
1165 plan, with its blueprint promising unparalleled resolution and detection capabilities. The  
1166 experiment was to be a melting pot of international collaboration, with scientists, engineers,  
1167 and students from around the globe contributing to its design, construction, and eventual data  
1168 analysis. The name "ATLAS" was reminiscent of the Titan of Greek mythology, reflecting  
1169 the experiment's grandeur and ambition.

1170 The years of meticulous planning and construction bore fruit in 2008 with the LHC's in-  
1171 auguration. The world watched with bated breath, and in 2012, a groundbreaking announce-  
1172 ment followed: the discovery of the Higgs boson by the ATLAS and CMS experiments.  
1173 This seminal moment was not just a triumph for CERN but also a testament to decades of  
1174 collaborative science, realizing Peter Higgs' and other physicists' 1960s vision.

1175 The LHC and ATLAS are not just about the Higgs boson, however. They represent the  
1176 spirit of scientific inquiry. This chapter provides broad information about the LHC and AT-  
1177 LAS experiments. Section 3.1 discusses the design and general information of the accelera-  
1178 tor, as well as its current operational status. Section 3.2 introduces the ATLAS experiment,  
1179 from the subsystems of the detector to its performance.

## 1180 **3.1 Introduction to the Large Hadron Collider (LHC)**

### 1181 **3.1.1 Accelerator design and parameters**

1182 The complex array of accelerators at CERN has been meticulously constructed to prepare  
1183 and accelerate beams of particles to unprecedented energies, with each accelerator playing a  
1184 distinct role. The pipeline's efficiency ensures that particles, mainly protons, achieve near-  
1185 light speeds, making them fit for the high-energy collisions that the LHC facilitates. Followed  
1186 the details of the accelerator system shown in figure 3-1, the journey of the particles go  
1187 through 5 main stages:

- 1188 • **Linear Accelerators:** Particles begin in the Linac 4, a linear accelerator. Here, pro-  
1189 tons are derived from hydrogen gas by stripping away the electrons from hydrogen  
1190 atoms. These protons are then accelerated to an energy of about 160 MeV using radio-  
1191 frequency quadrupole (RFQ) and drift tube linac (DTL) structures.
- 1192 • **Proton Synchrotron Booster (PSB):** After Linac 4, the protons move to the PSB. This

1193 is where they are grouped into bunches and further accelerated. Using magnetic fields,  
1194 the PSB boosts the protons to energies up to 2 GeV.

- 1195 • **Proton Synchrotron (PS):** The next phase of acceleration occurs in the PS. A cir-  
1196 cular accelerator with a circumference of approximately 628 meters, the PS elevates  
1197 the proton energies to 25 GeV. The PS is also responsible for compressing the proton  
1198 bunches, ensuring they're even tighter and more focused before they're passed onto the  
1199 next stage.
- 1200 • **Super Proton Synchrotron (SPS):** Acting as the final preparatory accelerator before  
1201 the LHC, the Super Proton Synchrotron is a large circular accelerator with a circum-  
1202 ference of 7 kilometers. Here, the proton bunches are further accelerated to energies  
1203 of 450 GeV. Beyond serving the LHC, the SPS has its own experimental halls and has  
1204 been pivotal in numerous significant discoveries in particle physics over the years.
- 1205 • **Large Hadron Collider (LHC):** The culmination of this sequential system is the LHC,  
1206 where the protons, now moving at 99.9999991% of the speed of light, undergo their  
1207 final acceleration. Within the LHC's 27-kilometer ring, the protons reach energies up  
1208 to 6.5 TeV. The LHC's twin beam pipes ensure that proton bunches can be accelerated  
1209 and steered in opposite directions, leading to head-on collisions at four main interaction  
1210 points where the primary experiments are situated.

1211 The complex infrastructure of the LHC's accelerators is characterized by a series of tech-  
1212 nical parameters, fundamental to understanding their capabilities. There's a summary of  
1213 some basic beam parameters of the accelerators in table 3–1.

1214 The starting point, Linac 4, accelerates protons to an energy of 160 MeV. From here, they  
1215 are directed to the Proton Synchrotron Booster (PSB), where their energy is further boosted  
1216 to 2 GeV. The Proton Synchrotron (PS) then takes over, its 628-meter circumference serving  
1217 to escalate the proton energy to 25 GeV. Beyond this, the Super Proton Synchrotron (SPS),  
1218 with its vast 7-kilometer ring, elevates the energy of these protons to 450 GeV. Ultimately,  
1219 the protons find their way to the LHC, where they are accelerated to a staggering 6.5 TeV per  
1220 beam, resulting in a collision energy of 13 TeV.

1221 In the LHC, approximately 2,808 bunches are operated per beam. Intriguingly, each of  
1222 these bunches holds roughly  $1.2 \times 10^{11}$  protons, leading to a dense traffic of particles that  
1223 enhance the collision chances. The measure of this potential for collisions is captured by the

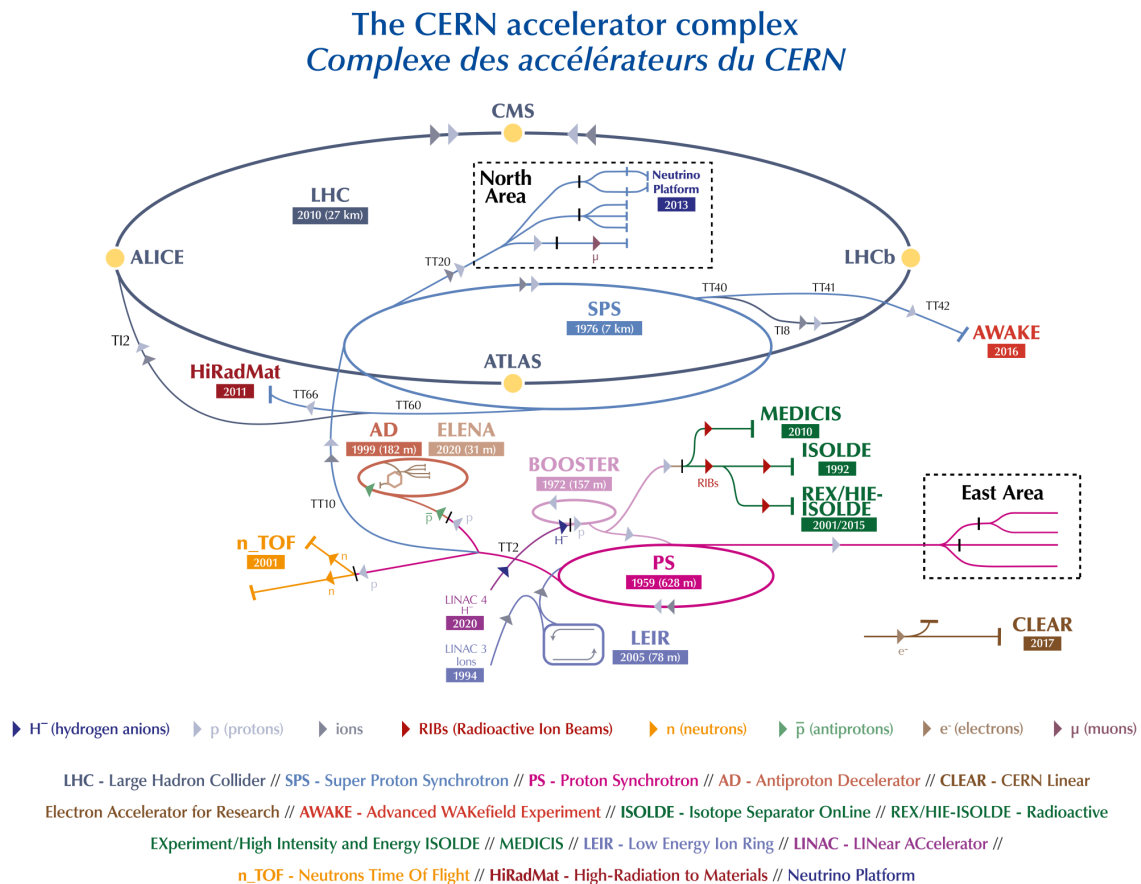


Figure 3–1 Diagram of CERN’s sequential accelerator system<sup>[35]</sup>.

1224 concept of luminosity. For the LHC, its peak luminosity stands around  $1 \times 10^{34} \text{ cm}^{-2} \text{ s}^{-1}$ , a  
1225 figure indicative of the LHC’s exceptional capability to produce particle interactions.

1226 Complementing this data, it’s worth noting the LHC’s revolution frequency, registering  
1227 at about 11.245 kHz. When it comes to beam operations, after being injected into the LHC  
1228 at 450 GeV, the energy of the beam is ramped up to its operational 6.5 TeV in a timespan of  
1229 approximately 20 minutes.

1230 The accelerator works at a chilling 1.9 K. This ultra-cold environment is essential to  
1231 ensure the superconducting state of its magnets, which in turn produce a magnetic field of  
1232 8.33 T, a critical factor in directing the high-energy beams along the 27-km ring.

machine	L[m]	relative	$\rho$ [m]	beam momentum [GeV/c]	bunches
LINAC	30		-	$10^{-4}$	$4 \times 2$
PSB	157		8.3	0.05	$4 \times 2$
PS	628.318	1	70.676	1.4	72
SPS	6911.56	11× PS	741.257	26	$4 \times 72$
LHC	26658.883	27/7× SPS	2803.98	450	$2 \times 2808$

**Table 3–1 Circumference, curvature radius  $\rho$ , and beam momentum upon injection for the primary accelerators in the LHC injection sequence<sup>[32]</sup>.**

1233 The instantaneous luminosity is given by

$$L = \frac{N_1 N_2 n_b f_{\text{rev}}}{\pi \sqrt{(\sigma_{x,1}^2 + \sigma_{x,2}^2)} \sqrt{(\sigma_{y,1}^2 + \sigma_{y,2}^2)}} FH, \quad (3-1)$$

1234 where:

- 1235 •  $f_{\text{rev}}$  is the revolution frequency,
- 1236 •  $n_b$  is the number of bunches colliding at the IP,
- 1237 •  $N_{1,2}$  represent the number of particles in each bunch,
- 1238 •  $\sigma_{x,1,2}$  and  $\sigma_{y,1,2}$  are the horizontal and vertical beam sizes of the colliding bunches  
1239 respectively,
- 1240 •  $F$  signifies the geometric luminosity reduction factor due to transverse offset or cross-  
1241 ing angle collisions at the IP,
- 1242 •  $H$  denotes the reduction factor for the hourglass effect significant when the bunch  
1243 length is similar or larger than the  $\beta$ -functions at the IP.

1244 Assuming round beams at the IP and neglecting any spurious dispersion at the IP one can  
1245 write the instantaneous luminosity in the LHC IPs as:

$$L = \frac{\gamma f_{\text{rev}} n_b N_b^2}{4\pi \epsilon_n \beta^*} F. \quad (3-2)$$

1246 Maximizing the instantaneous luminosity in the LHC therefore implies (in order of priority):

- 1247 • Ensure optimum overlap of the two beams at the IP, which for head-on collisions entails  
1248 matching the optics functions and steering the beam orbits transversely.
- 1249 • Minimize beam size at the IPs. This doesn't necessarily increase total beam power but  
1250 demands adequate aperture.

- 1251 • Increase the number of particles per bunch.
- 1252 • Maximize the number of bunches in the collider. In the LHC, operating with more
- 1253 than 150 bunches necessitates a crossing angle at the IP to prevent undesired parasitic
- 1254 beam interactions.

### 1255 3.1.2 Operation status

1256 In the context of assessing the operational status of the LHC, it is paramount to examine  
1257 the data from its detectors, as the collider itself does not record collision outcomes. Among  
1258 the suite of detectors around the LHC's ring, ATLAS stands as one of the primary general-  
1259 purpose instruments, meticulously capturing a wide range of physics events. Given our affil-  
1260 iation with the ATLAS collaboration, and its comprehensive dataset covering numerous runs  
1261 and periods, we will focus on the data from ATLAS to provide an illustrative example of  
1262 the LHC's operational status over the years. The following figures and tables offer a detailed  
1263 insight into the luminosities achieved and the associated uncertainties throughout different  
1264 operational periods.

1265 The graph on the left of Figure 3–2 details the evolution of luminosity delivered to AT-  
1266 LAS across the years 2011 to 2018. This measurement pertains specifically to stable beams  
1267 and high-energy proton-proton (p-p) collisions. The LHC's primary function is to provide  
1268 high luminosity, ensuring that ATLAS and other experiments have a sufficient number of  
1269 collision events to carry out precision measurements and search for new phenomena. The in-  
1270 crease in luminosity over the years is a testament to the constant enhancements in the LHC's  
1271 machine operation and maintenance. Each point on the curve represents a specific operational  
1272 period, and the rise in luminosity can be attributed to various machine upgrades, operational  
1273 optimizations, and the introduction of more intense beams. The increase in delivered lumi-  
1274 nosity means that a larger number of collisions is available for data analysis, thus enhancing  
1275 the potential for scientific discoveries.

1276 While the right one offers insight into the average interactions per crossing from 2015 to  
1277 2018 at a center-of-mass energy of 13 TeV. During this phase, the LHC resumed operations  
1278 after its initial extended shutdown, operating at an energy level nearly double that of its inau-  
1279 gural run, signaling a significant advancement in its operational capabilities. The displayed  
1280 data encompasses all records from ATLAS during stable beams within this time frame. A

1281 key feature of the graph is the indication of the integrated luminosity and the mean value  
 1282 of  $\mu$  (denoted as the average number of interactions per crossing). This average is aligned  
 1283 with the Poisson distribution's mean, a statistical measure used to predict the probability of  
 1284 events in a fixed interval of time or space. The formula  $\mu = \mathcal{L}_{\text{bunch}} \times \sigma_{\text{inel}}/f$  used in the cap-  
 1285 tion provides a method for calculating this average. Here,  $\mathcal{L}_{\text{bunch}}$  represents the instantaneous  
 1286 luminosity for each bunch. In layman terms, it measures the density of particles in a specific  
 1287 beam bunch. On the other hand,  $\sigma_{\text{inel}}$  denotes the inelastic cross-section, with its value ap-  
 1288 proximated at 80 mb for 13 TeV collisions. It provides a measure of the probability of a  
 1289 particular interaction between particles. Lastly,  $f$  stands for the LHC revolution frequency,  
 1290 indicating how frequently the particles in the beam complete one circuit of the main ring of  
 1291 the accelerator. In collider physics, the number of interactions per crossing determines the  
 1292 event complexity. A higher value means more simultaneous interactions. This increases the  
 1293 chance of significant events, but also requires advanced techniques to isolate desired signals  
 1294 from numerous interactions.

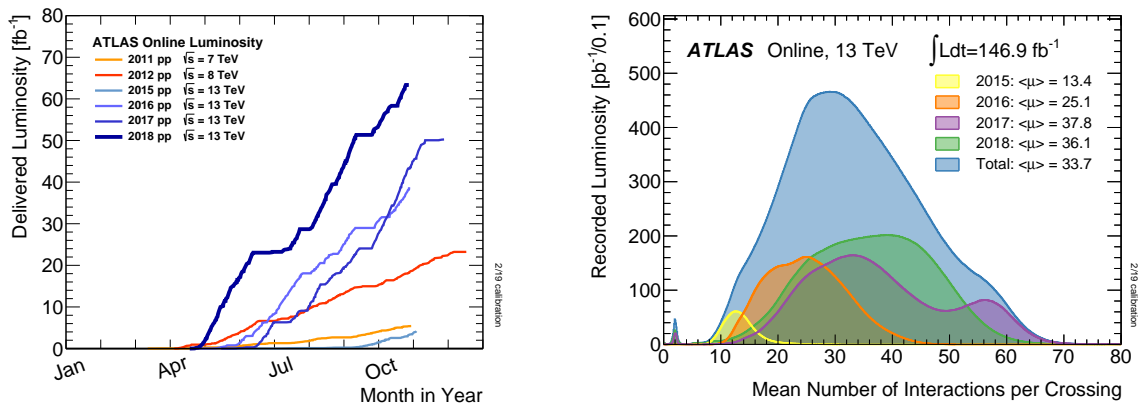


**Figure 3–2 Public ATLAS Luminosity Results for Run-2 of the LHC<sup>[36]</sup>. Left: Delivered Luminosity Over Time (2011-2018):** The graph depicts the cumulative luminosity delivered to ATLAS as a function of time during stable beams and for high-energy p-p collisions. **Right: Interactions per Crossing (2015-2018 at 13 TeV):** This illustration showcases the luminosity-weighted distribution of the average interactions per crossing. The data encompasses all records from ATLAS during stable beams between 2015 and 2018. The integrated luminosity and the mean  $\mu$  value are indicated. The average interactions per crossing align with the Poisson distribution's mean, ascertained for each bunch.

1295 In the ATLAS experiment during the LHC Run 2 at  $\sqrt{s} = 13$  TeV, a comprehensive sum-  
 1296 mary of integrated luminosities, post rigorous data-quality checks, is provided in Table 3–2.

Data sample	2015	2016	2017	2018	Comb
Integrated luminosity [fb <sup>-1</sup> ]	3.24	33.40	44.63	58.79	140.07
Total uncertainty [fb <sup>-1</sup> ]	0.04	0.30	0.50	0.64	1.17
Uncertainty contributions [%]:					
Statistical uncertainty	0.07	0.02	0.02	0.03	0.01
Fit model*	0.14	0.08	0.09	0.17	0.12
Background subtraction*	0.06	0.11	0.19	0.11	0.13
FBCT bunch-by-bunch fractions*	0.07	0.09	0.07	0.07	0.07
Ghost-charge and satellite bunches*	0.04	0.04	0.02	0.09	0.05
DCCT calibration*	0.20	0.20	0.20	0.20	0.20
Orbit-drift correction	0.05	0.02	0.02	0.01	0.01
Beam position jitter	0.20	0.22	0.20	0.23	0.13
Non-factorisation effects*	0.60	0.30	0.10	0.30	0.24
Beam-beam effects*	0.27	0.25	0.26	0.26	0.26
Emittance growth correction*	0.04	0.02	0.09	0.02	0.04
Length scale calibration	0.03	0.06	0.04	0.04	0.03
Inner detector length scale*	0.12	0.12	0.12	0.12	0.12
Magnetic non-linearity	0.37	0.07	0.34	0.60	0.27
Bunch-by-bunch $\sigma_{\text{vis}}$ consistency	0.44	0.28	0.19	0.00	0.09
Scan-to-scan reproducibility	0.09	0.18	0.71	0.30	0.26
Reference specific luminosity	0.13	0.29	0.30	0.31	0.18
Subtotal vdM calibration	0.96	0.70	0.99	0.93	0.65
Calibration transfer*	0.50	0.50	0.50	0.50	0.50
Calibration anchoring	0.22	0.18	0.14	0.26	0.13
Long-term stability	0.23	0.12	0.16	0.12	0.08
Total uncertainty [%]	1.13	0.89	1.13	1.10	0.83

**Table 3–2 Summary of integrated luminosities post standard data-quality checks, alongside uncertainties for the calibration of each yearly data sample from Run 2 pp at  $\sqrt{s} = 13$  TeV, including the cumulative sample<sup>[37]</sup>. The table presents the integrated luminosities, total uncertainties, a detailed split of contributions to the vdM calibration’s absolute accuracy, extra uncertainties associated with the physics data sample, and the overall relative uncertainty in percentage.**

1297 The luminosity data span the years 2015 to 2018, presenting an ascending trend: from 3.24  
1298 fb<sup>-1</sup> in 2015, the values increase progressively to 33.40, 44.63, and 58.79 fb<sup>-1</sup> in 2016, 2017,  
1299 and 2018, respectively. The cumulative sample across these years totals an impressive 140

1300  $\text{fb}^{-1}$ . This table not only enumerates the integrated luminosities for each year but also delves  
1301 into the specific uncertainties associated with the calibration of each yearly data sample. Im-  
1302 portantly, certain contributors to uncertainty, marked with an asterisk (\*), are considered to  
1303 be fully correlated across the years. In contrast, other sources of uncertainty are treated as  
1304 uncorrelated. This meticulous breakdown serves as an essential resource, quantifying both  
1305 the vast amount of collision data ATLAS has accumulated during this period and the preci-  
1306 sion with which the luminosity measurements were made. The various factors influencing  
1307 the absolute accuracy of the vDM calibration and the overall relative uncertainty percentages  
1308 further underscore the diligence and detail invested in these measurements.

## 1309 **3.2 The ATLAS Experiment**

### 1310 **3.2.1 Overview and scientific goals**

1311 Situated at CERN, the European Organization for Nuclear Research, the ATLAS (A  
1312 Toroidal LHC ApparatuS) experiment is one of the largest collaborative efforts in the domain  
1313 of experimental particle physics. It is a general-purpose particle detector with a forward-  
1314 backward symmetric cylindrical geometry and nearly  $4 - \pi$  coverage in solid angle. ATLAS  
1315 is not just an experiment, but a testament to international collaboration, with over 3,000 physi-  
1316 cists from 38 countries and 180 institutions coming together for a common scientific pursuit.  
1317 It stands as tall as a five-story building at about 25 meters and stretching 44 meters in length.  
1318 It weighs approximately 7,000 tons.

1319 ATLAS is a particle detector that has several scientific goals<sup>[38]</sup>. One of its primary goals  
1320 is to search for the Higgs boson, a particle predicted by the Standard Model to explain why  
1321 other particles possess mass. This quest bore fruit in 2012 when the ATLAS and CMS col-  
1322 laborations announced the discovery of the Higgs boson. ATLAS is also constantly searching  
1323 for discrepancies with Standard Model predictions that could be indicative of new physics  
1324 phenomena, including probing supersymmetry, a popular extension to the Standard Model,  
1325 and hunting for dark matter candidates directly or via potential mediators. In addition, by  
1326 analyzing lead-lead ion collisions, ATLAS seeks to understand the state of matter known as  
1327 quark-gluon plasma, which is believed to have been prevalent shortly after the Big Bang. Fi-  
1328 nally, ATLAS aims to provide a deeper understanding of the forces and particles that make up

our universe. It investigates the properties of the top quark, probes the electroweak symmetry breaking mechanism, and studies various aspects of quantum chromodynamics.

The conceptualization of the ATLAS detector was influenced by a range of intricate physics analyses. The fundamental design principles of the detector were shaped around the following core objectives<sup>[38-39]</sup>:

- Achieve superior electromagnetic calorimetry to accurately identify and measure electrons and photons. This should be supplemented by comprehensive hadronic calorimetry to ensure precise measurements of jets and missing transverse energy ( $E_T^{\text{miss}}$ ).
- Ensure high-precision measurements of muon momentum. The design must facilitate accurate measurements even at peak luminosity, relying primarily on the external muon spectrometer.
- Maintain efficient tracking capabilities during high luminosities. This is vital for measurements of high- $p_T$  lepton momentum, identification of electrons, photons,  $\tau$ -leptons, and heavy flavors, as well as enabling a complete event reconstruction during periods of lower luminosity.
- The detector must offer a broad acceptance in pseudorapidity ( $\eta$ ), combined with nearly complete azimuthal angle ( $\phi$ ) coverage. Here,  $\phi$  denotes the angle measured around the beam's axis, while  $\eta$  is associated with the polar angle ( $\theta$ ), where  $\theta$  represents the angle from the z-direction.
- The design should support low- $p_T$  threshold triggers and measurements, ensuring high-efficiency capture of most physics processes that are integral to LHC operations.

The fundamental design principles of the ATLAS detector were meticulously crafted to cater to a spectrum of intricate physics studies. These principles revolve around ensuring precise measurements, large acceptance, and robust performance even under the challenging environment of high luminosities. Each subsystem<sup>[39]</sup> of the detector is designed with specific characteristics that when combined, form the complete and formidable capability of the ATLAS detector.

- **Magnet Configuration:** The detector is equipped with an inner superconducting solenoid, surrounding the inner detector, and large external superconducting toroids having an eight-fold symmetry.
- **Inner Detector (ID):** Situated within a 7 m by 1.15 m cylinder, the ID functions in a

1360 2 T solenoidal magnetic field. The inner part comprises semiconductor pixel and strip  
1361 detectors for accuracy, while the outer portion contains straw-tube trackers ensuring a  
1362 wide tracking range.

- 1363 • **Calorimetry:** Liquid-argon (LAr) electromagnetic calorimetry offers precise energy  
1364 and position measurements up to  $|\eta| < 3.2$ . The end-caps, using LAr technology,  
1365 stretch this to  $|\eta| = 4.9$ . Most hadronic measurements come from the uniquely de-  
1366 signed scintillator-tile calorimeter, segmented into a barrel and two extended barrels.
- 1367 • **Dimensions and Weight:** The LAr calorimetry is contained in a 2.25 m by  $\pm 6.65$  m  
1368 cylinder. Adjacent to it, the tile calorimeter spans an outer radius of 4.25 m and a  
1369 half-length of 6.10 m, together weighing around 4,000 Tons.
- 1370 • **Muon Spectrometer:** Surrounding the calorimeters, the spectrometer features an air-  
1371 core toroid system. It boasts three stations of high-precision tracking chambers, ensur-  
1372 ing stellar muon momentum resolution, supplemented by rapid-response trigger cham-  
1373 bers.
- 1374 • **Overall Dimensions:** The muon spectrometer determines the detector's vast scale.  
1375 Its boundaries, at about 11 m in radius, combined with the 12.5 m barrel toroid coils  
1376 and 23 m distant forward muon chambers, sum up the detector's total weight to an  
1377 impressive 7,000 Tons.

1378 The ATLAS detector is designed with a comprehensive framework consisting of various  
1379 subsystems and components, of which a computer generated image is shown in figure 3–3.  
1380 These elements collectively contribute to its functionality, enabling it to fulfill its scientific  
1381 objectives effectively. In the subsequent sections, we will provide a detailed explanation of  
1382 each subsystem, outlining its design, functionality, and its vital role within the broader goals  
1383 of the ATLAS experiment.

### 1384 3.2.1.1 Detector Coordinate

1385 The LHC beam's direction sets the z-axis, while the x-y plane is perpendicular to this  
1386 beam direction. The positive x-axis extends from the interaction point towards the LHC  
1387 ring's center, and the positive y-axis points upward. The azimuthal angle,  $\phi$ , is determined  
1388 around the beam direction, while  $\theta$  represents the angle from this axis. Pseudorapidity is  
1389 expressed as  $\eta$ , defined as  $\eta \equiv -\ln \tan(\theta/2)$ . Both the transverse momentum  $p_T = \sqrt{p_x^2 + p_y^2}$

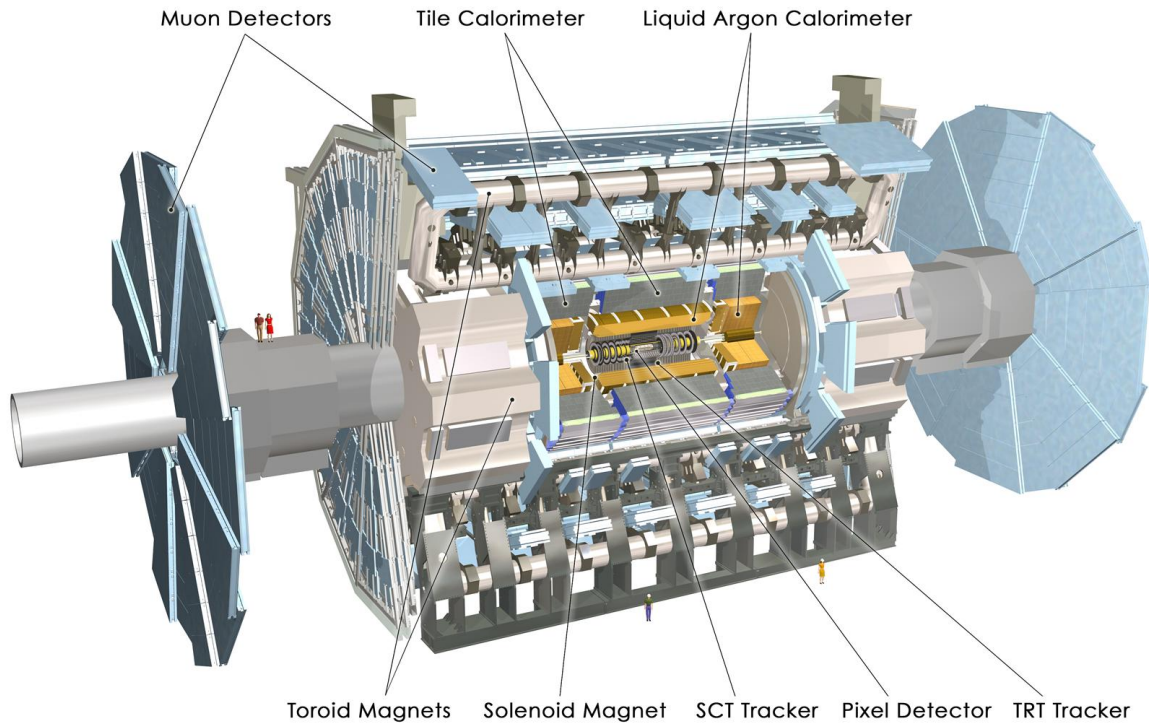


Figure 3–3 The layout of the whole ATLAS detector<sup>[40]</sup>.

1390 and the transverse energy  $E_T = \sqrt{p_T^2 + m^2}$ , as well as the missing transverse energy  $E_T^{\text{miss}}$ ,  
 1391 are generally defined in the x-y plane. The distance  $\Delta R$  in  $\eta - \phi$  space is given by  $\Delta R =$   
 1392  $\sqrt{\Delta^2 \eta + \Delta^2 \phi}$ .

1393 Charged particle trajectories in a consistent magnetic field are characterized using five  
 1394 parameters of a helix. In ATLAS, a specific helix parameterization ( $d_0, z_0, \theta, \phi, q/p$ ) is em-  
 1395 ployed, which is shown in figure 3–4, considering all measurements at the point nearest to  
 1396 the beam line where x and y are zero. Parameters in x – y plane are:

- 1397 •  $d_0$ : The transverse impact parameter, which is the sideways distance from the beam  
 1398 axis at the closest approach point. Its sign is determined by the reconstructed angular  
 1399 momentum of the track around the axis.
- 1400 •  $\phi$ : Azimuthal angle, where  $\tan \phi \equiv p_y/p_x$ , ranged from  $[0, \pi]$ .
- 1401 •  $q/p_T$ : The charge-to-momentum ratio in the transverse plane. "q" is the charge of  
 1402 the particle (either +1 or -1 for singly charged particles) and "p<sub>T</sub>" is the transverse

1403 momentum. It determines the curvature of the trajectory.

1404 Parameters in the  $R - z$  plane are:

- 1405 •  $\theta$ : the polar angle, where  $\cot \theta \equiv p_z/p_T$ .
- 1406 •  $z_0$ : The longitudinal impact parameter, which is the  $z$ -coordinate of the track at the
- 1407 closest approach point.

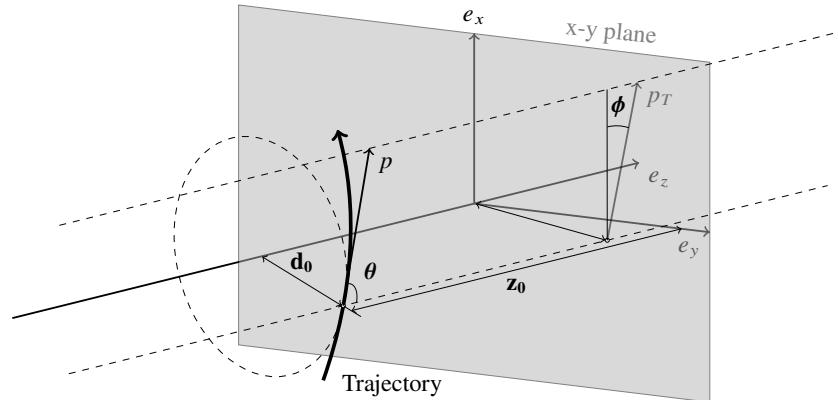


Figure 3-4 Illustration of the global track coordinate with respect to perigee.

### 1408 3.2.2 Detector subsystems and components

1409 In this section, a comprehensive overview of the subsystems that constitute the ATLAS  
 1410 detector is provided, progressing from the innermost components to the outer structures.  
 1411 Each subsystem is pivotal in the detection, tracking, and measurement of particles, con-  
 1412 tributing to the high precision and reliability for which the ATLAS detector is known. The  
 1413 performance characteristics of these integral components are summarized in Table 3-3.

#### 1414 3.2.2.1 Inner tracking system

1415 In every 25 ns proton bunch collision event, approximately 1,000 particles emerge from  
 1416 the collision point, producing extremely dense tracks within the detector region of  $|\eta| \leq$   
 1417 2.5. To achieve the momentum and vertex requirements necessary for measuring critical  
 1418 physical processes, a fine granularity of the detector is essential for precise measurements.  
 1419 The ATLAS Inner tracking system is pivotal in this context and is responsible for detecting  
 1420 and measuring these charged particles. Designed to offer full tracking coverage over  $|\eta| \leq$   
 1421 2.5, it employs high-resolution detectors at inner radii and continuous tracking elements at  
 1422 outer radii. The incorporation of Semiconductor Tracking (SCT) detectors and the TRT

Subdetectors	Resolution	$\eta$ coverage	
		Measurement	Trigger
Trackers	$\sigma_{p_T}/p_T = 0.05\% p_T \oplus 1\%$	$\pm 2.5$	
ECAL	$\sigma_E/E = 10\% \sqrt{E} \oplus 0.7\%$	$\pm 3.2$	$\pm 2.5$
HCAL(jets)			
Barrel & Cap	$\sigma_E/E = 50\% \sqrt{E} \oplus 3\%$	$\pm 3.2$	$\pm 3.2$
Forward	$\sigma_E/E = 100\% \sqrt{E} \oplus 10\%$	$3.1 <  \eta  < 4.9$	$3.1 <  \eta  < 4.9$
Muon Spectrometer	$\sigma_{p_T}/p_T = 10\%$ at $p_T = 1\text{TeV}$	$\pm 2.7$	$\pm 2.4$

**Table 3–3 Summary of the resolution and  $\eta$  coverage for various subdetectors. ECAL and HCAL represent for electromagnet calorimeter and hadronic calorimeter, respectively. The listed resolutions for trackers and the ECAL are parametrized forms dependent on either  $p_T$  or  $E$  (in GeV), while the Muon Spectrometer provides a specific resolution at a given  $p_T$  value. The  $\eta$  coverage is further categorized into measurement and trigger regions.**

1423 (Transition Radiation Tracker) further accentuates the precision of these measurements.

1424 The Inner Detector (ID) is mechanically divided into three units<sup>[41]</sup>:

- 1425 • **Pixel Detector:** The pixel detector, positioned closest to the interaction point in the  
1426 ATLAS Inner Detector, provides three high-precision measurements across its full ac-  
1427 ceptance, aiding in identifying short-lived particles like b-quarks and  $\tau$ -leptons. With  
1428 its 140 million elements, each sized  $50 \mu\text{m}$  in the  $R - \phi$  direction and  $300 \mu\text{m}$  in  $z$ ,  
1429 the pixel detector offers unambiguous two-dimensional space point segmentation. It  
1430 comprises three barrels at average radii of approximately 4 cm, 11 cm, and 14 cm,  
1431 complemented by four disks on each side, spanning radii from 11 to 20 cm. This mod-  
1432 ular system consists of about 1500 identical barrel modules and 1000 disk modules.  
1433 Each barrel module, measuring 62.4 mm by 22.4 mm, is equipped with 61440 pixel  
1434 elements, serviced by 16 readout chips. The design ensures overlapping modules for  
1435 hermetic coverage, and the thickness of each layer in the simulation is less than 1.39%  
1436 of a radiation length.
- 1437 • **Semiconductor Tracker (SCT):** The SCT system, positioned in the intermediate ra-  
1438 dial range of the ATLAS Inner Detector, provides four precision measurements per  
1439 track, contributing to momentum, impact parameter, vertex positioning, and pattern

1440 recognition via its high granularity. The SCT system boasts a significantly larger  
1441 surface area compared to previous silicon microstrip detectors, and it is designed to  
1442 withstand radiation intensities that can modify the inherent characteristics of its sili-  
1443 con wafers. The barrel SCT utilizes four layers of silicon microstrip detectors, each  
1444 measuring  $6.36 \times 6.40 \text{ cm}^2$  with 768 readout strips at an  $80 \mu\text{m}$  pitch. A module en-  
1445 compasses four detectors, and the system's readout comprises a front-end amplifier and  
1446 discriminator connected to a binary pipeline. The detector covers a surface of  $61 \text{ m}^2$ ,  
1447 having 6.2 million readout channels, offering a spatial resolution of  $16 \mu\text{m}$  in  $R-\phi$  and  
1448  $580 \mu\text{m}$  in  $z$ . This structure is further enhanced with specific design elements for cool-  
1449 ing, and thermal stability, using materials with minimal thermal expansion coefficients  
1450 and a unique cooling method employing a methanol-water mixture.

- 1451 • **Transition Radiation Tracker (TRT):** The TRT employs straw detectors, recognized  
1452 for their capability to handle very high rates due to their small diameter and the isola-  
1453 tion of their sense wires. Enhanced by xenon gas, these detectors can identify electrons  
1454 by detecting transition-radiation photons produced in a specific radiator positioned be-  
1455 tween the straws. The design accommodates the LHC's high counting rates and large  
1456 occupancy. Each straw is 4 mm in diameter and can span up to 150 cm in length.  
1457 In total, the system integrates about 420,000 electronic channels which offer a spatial  
1458 resolution of  $170 \mu\text{m}$  per straw. The barrel structure encompasses modules that range  
1459 radially from 56 to 107 cm. In contrast, the two end-caps are structured with 18 wheels,  
1460 covering various radial ranges to maintain consistent straw crossing. The system's de-  
1461 sign priority is to deliver high performance under substantial occupancy and counting  
1462 rates. Even at peak rates, the majority of straws provide accurate drift time measure-  
1463 ments, ensuring a track measurement precision under  $50 \mu\text{m}$ . The TRT enhances the  
1464 momentum measurement precision in the Inner Detector and plays a pivotal role in  
1465 pattern recognition and electron-hadron differentiation.

1466 The fundamental design specifications and space-point measurement resolutions are de-  
1467 tailed in Table 3–4. Additionally, an overview and a cross-sectional view of the Inner Detec-  
1468 tor, showing layers from the innermost to the outermost, is provided in Figure 3–5.

System	Position	Area ( $\text{m}^2$ )	Resolution $\sigma$ ( $\mu\text{m}$ )	Channels ( $10^6$ )	$\eta$ coverage
Pixels	1 removable barrel layer	0.2	$R\phi = 12, z = 66$	16	$\pm 2.5$
	2 barrel layers	1.4	$R\phi = 12, z = 66$	81	$\pm 1.7$
	4 end-cap disks on each side	0.7	$R\phi = 12, R = 77$	43	1.7 – 2.5
Silicon strips	4 barrel layers	34.4	$R\phi = 16, z = 580$	3.2	$\pm 1.4$
	9 end-cap wheels on each side	26.7	$R\phi = 16, R = 580$	3.0	1.4 – 2.5
TRT	Axial barrel straws		170 (per straw)	0.1	$\pm 0.7$
	Radial end-cap straws		170 (per straw)	0.32	0.7 – 2.5

**Table 3–4 Inner Detector Parameters and Resolutions<sup>[41]</sup>: The provided resolutions are indicative values (the precise resolution in each detector varies with  $|\eta|$ ).**

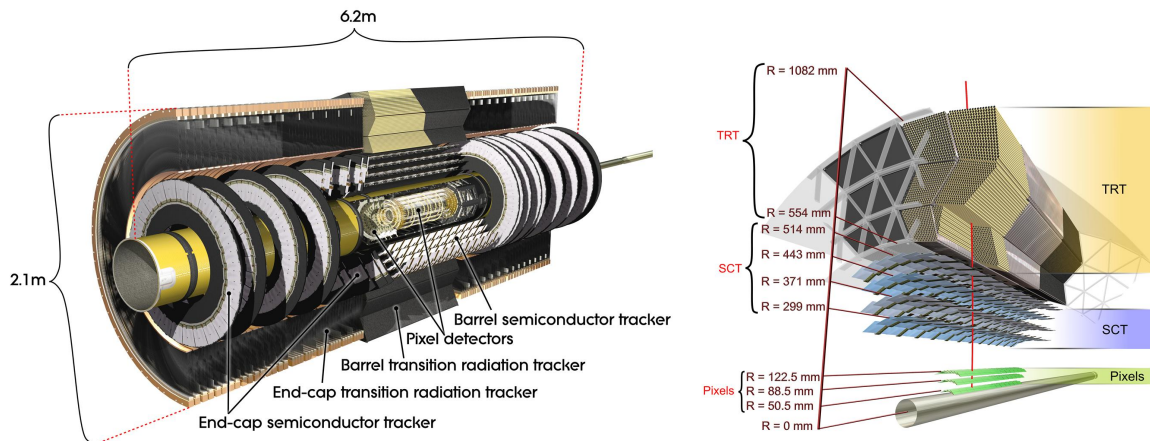


**Figure 3–5 The layout of the ATLAS Inner Detector<sup>[42]</sup>. Left: Overview of the ID; Right: Cross-sectional view of the Inner Detector, with layers from innermost to outermost being the pixel detector, SCT, and TRT.**

### 1469 3.2.2.2 Electromagnetic and hadronic calorimeters

1470 The physics requirements for calorimeters at LHC<sup>[43]</sup>, are of utmost importance. They  
 1471 must accurately measure the energy and position of electrons and photons, the energy and  
 1472 direction of jets, and the missing transverse momentum of events. Particle identification,  
 1473 event selection at the trigger level, and high radiation resistance are also crucial. The LHC's  
 1474 high luminosity and energy range require fast detector response, fine granularity, and rejec-

1475 tion of backgrounds such as jets faking photons. The performance specifications come from  
1476 benchmark channels such as the search for a Higgs boson through the decays  $H \rightarrow \gamma\gamma$  and  
1477  $H \rightarrow 4e$ , and the search for heavy vector bosons ( $W'$ ,  $Z'$ ) with masses up to 5 – 6 TeV  
1478 through the decays  $W' \rightarrow e\nu$  and  $Z' \rightarrow e^+e^-$ . The SM Higgs search imposes specific re-  
1479 quirements on the hadronic calorimetry, such as  $W \rightarrow jj$  mass reconstruction, forward jet  
1480 tagging, and  $H \rightarrow b\bar{b}$  mass reconstruction using jet spectroscopy. These requirements are  
1481 critical for discovering high and low mass Higgs bosons, studying top physics, and detecting  
1482 non-interacting particles in supersymmetric models.

1483 The ATLAS Electromagnetic calorimeter<sup>[43]</sup> (ECAL) has stringent requirements tailored  
1484 to its pivotal role in ATLAS experiments. It boasts a broad rapidity coverage and possesses  
1485 the capability to reconstruct electrons within an energy range spanning from 1 – 2 GeV up to 5  
1486 TeV. In terms of energy resolution, the device excels, demonstrating exceptional performance  
1487 over the energy bracket of 10 – 300 GeV. With a structural robustness, it maintains a total  
1488 thickness of at least 24 radiation lengths at  $\eta = 0$ . Its dynamic range is set between 50 MeV  
1489 and 3 TeV, and it stands out with its energy-scale precision of 0.1%. The linearity of its  
1490 response is noteworthy, surpassing benchmarks by remaining better than 0.5% for energies  
1491 up to 300 GeV. One of its notable features is its ability to measure the shower direction in  $\theta$ ,  
1492 achieving a resolution of approximately 50 mrad per the square root of the energy in GeV.  
1493 As for particle differentiation, the calorimeter has an exceptional capacity for photon/jet,  
1494 electron/jet, and  $\tau$ /jet separations. Furthermore, it is designed to have a rapid response, low  
1495 noise, and offers high granularity. The coherent noise level is maintained below  $E = 3$  MeV  
1496 for each channel, and it is adept at identifying individual bunch crossings.

1497 The EM calorimeter of the LHC is divided into a central barrel ( $|\eta| < 1.475$ ) and two  
1498 end-caps ( $1.375 < |\eta| < 3.2$ ). The barrel consists of two half-barrels, while each end-  
1499 cap is further segmented into outer and inner wheels. Designed as a lead-LAr detector, the  
1500 calorimeter features accordion-shaped Kapton electrodes to ensure complete  $\phi$  symmetry  
1501 without azimuthal gaps. The thickness of the calorimeter varies, exceeding  $24X_0$  in the barrel  
1502 and  $26X_0$  in the end-caps. Within the precision-focused region ( $|\eta| < 2.5$ ), it is divided into  
1503 three longitudinal layers.

1504 • **First Sampling (Preshower Detector):** This layer has a consistent thickness of  $6X_0$   
1505 and is furnished with narrow strips oriented in the  $\eta$  direction. It acts primarily as a

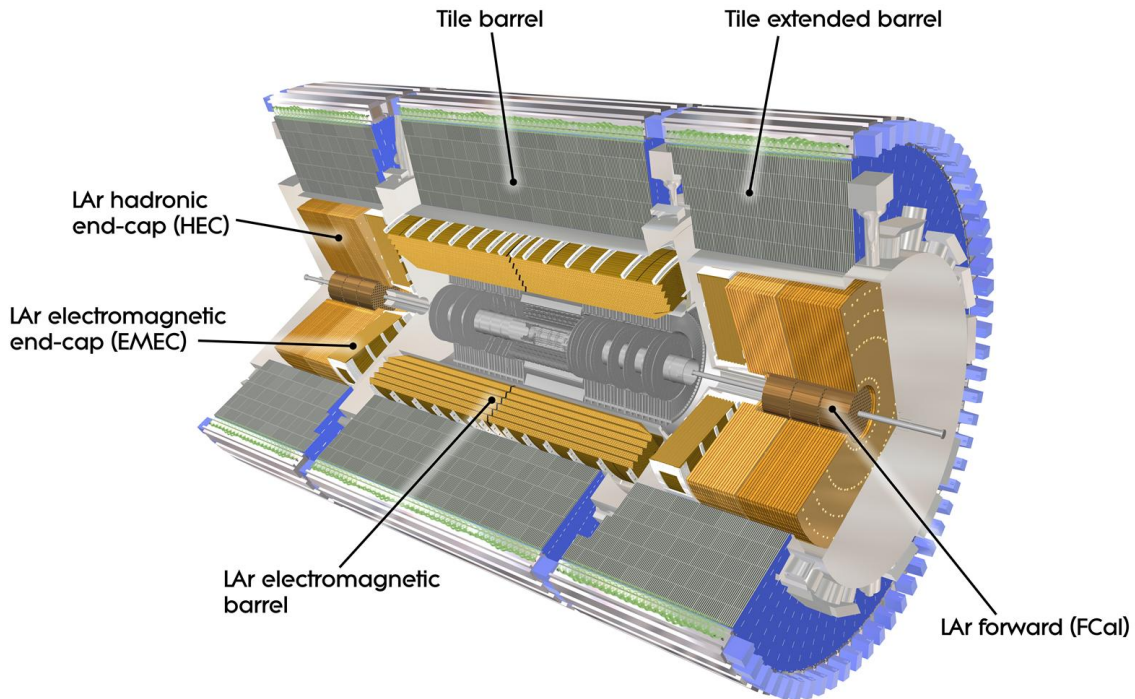


Figure 3-6 The layout of the ATLAS calorimeters<sup>[44]</sup>.

1506 "preshower" detector, aiding in particle identification and precise position measure-  
 1507 ments in the  $\eta$  dimension.

- 1508 • **Second Sampling:** This layer is divided into square towers each spanning  $\Delta\eta \times \Delta\phi =$   
 1509  $0.025 \times 0.025$ . By the end of this second sampling, the total calorimeter thickness  
 1510 reaches around  $24 X_0$ .
- 1511 • **Third Compartment:** This final layer has coarser granularity in the  $\eta$  direction and  
 1512 its thickness varies between  $2X_0$  and  $12X_0$ .

1513 In total, the calorimeter has about 190,000 channels. Materials in front of the calorime-  
 1514 ter, including the inner detector and solenoid coil, sum up to about  $1.8X_0$  at  $\eta = 0$ . Signals  
 1515 from the calorimeter are routed to external preamplifiers, digitized upon trigger events, and  
 1516 forwarded to the Data Acquisition system using a three-gain scale for optimum noise man-  
 1517 agement.

1518 The ATLAS hadronic calorimetry<sup>[43]</sup> (HCAL) covers a pseudo-rapidity range of  $|\eta| < 5$ ,  
 1519 employing various techniques tailored for the radiation environment and diverse require-

1520 ments. The barrel and extended barrel Tile calorimeters, which span up to  $|\eta| < 1.6$ , use  
 1521 iron-scintillating-tiles. The Liquid Argon calorimetry is employed from  $\sim 1.5 < |\eta| < 4.9$ .  
 1522 Total calorimeter thickness at  $\eta = 0$  is 11 interaction lengths, providing sufficient contain-  
 1523 ment for hadronic showers and reducing punch-through for the muon system.

- 1524 • **Tile Calorimeter:** The hadronic barrel calorimeter operates as a sampling device, us-  
 1525 ing iron as the absorber and scintillating tiles as the active medium. Tiles, 3 mm thick,  
 1526 are oriented perpendicular to the colliding beams and staggered in depth with a peri-  
 1527 odic structure along the z-axis. Both tile sides are readout using wavelength shifting  
 1528 fibers, channeling into two separate photomultiplier tubes (PMTs). Comprising one  
 1529 barrel and two extended barrels, the calorimeter spans from an inner radius of 2.28 m  
 1530 to 4.23 m. It features three layers segmented to thicknesses of approximately 1.4, 4.0,  
 1531 and 1.8 interaction lengths at  $\eta = 0$ . The granularity results in a  $\Delta\eta \times \Delta\phi = 0.1 \times 0.1$   
 1532 (or  $0.2 \times 0.1$  in the last layer). The calorimeter is positioned behind the EM calorimeter  
 1533 and the solenoid coil, leading to a total active calorimeter thickness of 9.2 interaction  
 1534 lengths at  $\eta = 0$ . An Intermediate Tile Calorimeter (ITC) enhances the thickness in  
 1535 the gap between the barrel and extended barrels.
- 1536 • **End-cap Liquid Argon calorimetry:** The end-cap Liquid Argon calorimetry, cover-  
 1537 ing  $\sim 1.5 < |\eta| < 3.2$ , features two wheels of equal diameter. The first wheel uses  
 1538 25 mm copper plates, while the second wheel has 50 mm plates. The gap between  
 1539 consecutive plates is 8.5 mm, segmented with 3 electrodes, forming 4 drift spaces of  
 1540 around 1.8 mm each. The first wheel is bifurcated into two longitudinal segments,  
 1541 consisting of 8 and 16 layers, while the second has a single 16-layer segment. The  
 1542 end-cap's active portion has a thickness of around 12 interaction lengths.
- 1543 • **Forward Liquid Argon calorimetry:** Located within the end-cap cryostat, the forward  
 1544 calorimeter covers  $3.2 < |\eta| < 4.9$ . Its close proximity to the interaction point (5  
 1545 meters) exposes it to high radiation levels. Its design ensures uniformity of coverage,  
 1546 minimizing crack and dead space effects around  $\eta = 3.1$ . This calorimeter is high-  
 1547 density, with three longitudinal sections: the first is copper, and the subsequent two  
 1548 are tungsten. Each section features a metal matrix with spaced channels filled with  
 1549 rods, with Liquid Argon serving as the sensitive medium in the gaps. The forward  
 1550 calorimeter's electronic noise for a jet cone of  $\Delta R = 0.5$  is roughly 1 GeV  $E_T$  at  $\eta = 3.2$ ,

1551 decreasing sharply to 0.1 GeV  $E_T$  at  $\eta = 4.6$ .

1552 The overall layout of the ATLAS ECAL and HCAL is shown in Figure 3–6.

### 1553 3.2.2.3 Muon spectrometer

1554 Theoretically, particles that can pass through the entire depth of the calorimeter without  
1555 interacting, or only weakly interacting, include neutrinos and muons which do not deposit  
1556 their full energy. The muon spectrometer is used to identify muons and calculate the energy  
1557 that is not detected.

1558 The ATLAS Muon Spectrometer<sup>[45]</sup>, as shown in Figure 3–7, includes a barrel region  
1559 and three wheel-shaped endcap regions. In the barrel region ( $|\eta| < 1.4$ ), the magnetic field  
1560 is provided by barrel toroidal magnets. In the endcap region ( $1.6 < |\eta| < 2.7$ ), the magnetic  
1561 field is provided by the endcap toroidal magnets in Section 3.2.2.4. In the transition region  
1562 of  $1.4 < |\eta| < 1.6$ , the magnetic field is jointly provided by the endcap and barrel toroidal  
1563 magnets. The muon spectrometer employs four drift chamber technologies: Monitored Drift  
1564 Tubes (MDTs), Cathode Strip Chambers (CSCs), Resistive Plate Chambers (RPCs), and Thin  
1565 Gap Chambers (TGCs). In the barrel region, the drift chambers are arranged in three con-  
1566 centric cylindrical layers along the beam axis. In both endcap regions, the drift chambers are  
1567 also divided into three layers placed on discs perpendicular to the beam direction.

Type	Function	Chamber resolution (RMS) in			Measurements/track		Number of	
		$z/R$	$\phi$	time	barrel	end-cap	chambers	channels
MDT	tracking	35 $\mu\text{m}$ ( $z$ )	-	-	20	20	1088(1150)	339k(354k)
CSC	tracking	40 $\mu\text{m}$ ( $R$ )	5 mm	7 ns	-	4	32	30.7k
RPC	trigger	10 mm( $z$ )	10 mm	1.5 ns	6	-	544(606)	359k(373k)
TGC	trigger	2 – 6 mm( $R$ )	3 – 7 mm	4 ns	-	9	3588	318k

**Table 3–5 Specifications for the four subsystems of the muon detector<sup>[47]</sup>: The stated spatial resolution (in columns 3 and 4) excludes uncertainties from chamber alignment. The intrinsic time accuracy for each chamber type is detailed in column 5, with additional time required for signal propagation and electronic factors. Numbers in parentheses relate to the full detector setup anticipated for 2009.**

1568 The muon spectrometer is divided into two sets of systems: precision chambers and trig-  
1569 ger chambers. High-precision track measurements are based on MDTs in the barrel and  
1570 CSCs in the endcaps, providing 6-8 measurement points. MDTs cover the region  $|\eta| < 2.7$

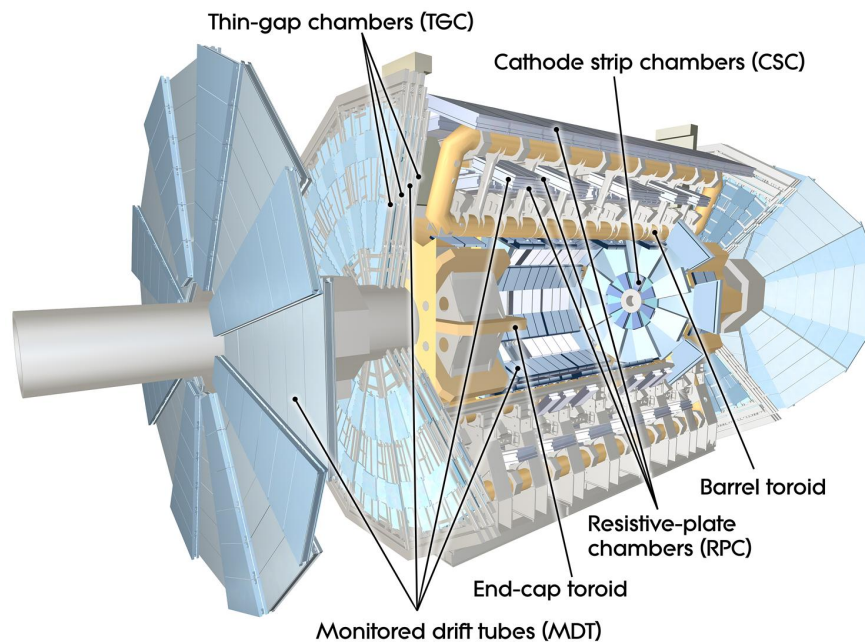


Figure 3–7 The layout of the ATLAS muon system<sup>[46]</sup>.

1571 and consist of drift tubes with a diameter of 3 cm and 50  $\mu\text{m}$  tungsten-rhenium signal wires,  
 1572 filled with a mixture of 93% argon gas and 7% carbon dioxide. They operate under a voltage  
 1573 of 3kV and function similarly to the TRT, working in a drift chamber mode with a maxi-  
 1574 mum drift time of 750 ns. A single drift tube offers a spatial resolution of  $(R - \phi)$  80  $\mu\text{m}$ ,  
 1575 while the average resolution of MDTs can reach 35  $\mu\text{m}$ . In a region of higher pseudorapidity  
 1576 ( $2.0 < |\eta| < 2.7$ ), closer to the interaction point, higher granularity CSCs are used to adapt  
 1577 to higher particle flux and beam background. CSCs are based on Multiwire Proportional  
 1578 Chamber (MRPC) detectors, with a maximum drift time of 40 ns.

1579 Trigger chambers are primarily used for rapid triggering of muon events and are based  
 1580 on RPCs and TGCs. These detectors achieve intrinsic time resolutions of 1.5 ns and 4 ns, re-  
 1581 spectively. Additionally, the trigger chambers provide a second set of position measurements  
 1582 independent of the precision measurements (for  $|\eta| < 2.4$ ), aligned approximately with the  
 1583 magnetic field lines, though with slightly inferior spatial resolution (5-10 mm). RPCs oper-  
 1584 ate as MRPC detectors in saturation mode, filled with a mixture of 55% carbon dioxide and  
 1585 45% n-pentane, covering the barrel region ( $1.05 < |\eta| < 2.4$ ). RPCs function as parallel  
 1586 plate detectors in amplification mode, filled with  $\text{C}_2\text{H}_2\text{F}_4$ , with electrode distances of 2 mm,  
 1587 covering the barrel region ( $|\eta| < 1.05$ ). Detailed parameters are given in Table 3–5.

## 1588 3.2.2.4 Magnet system

1589 The ATLAS experiment is equipped with a distinctive combined system comprising four  
1590 extensive superconducting magnets. Spanning a diameter of 22 m and extending 26 m in  
1591 length, this magnetic setup houses an energy storage capacity of 1.6 GJ. Following roughly a  
1592 decade and a half dedicated to its design, its assembly in industrial settings, and the eventual  
1593 integration at CERN, this system now stands fully operational in its subterranean chamber.  
1594 This section describes the characteristics of these magnets along with their auxiliary services.

1595 Illustrated in Figure 3–8 is the overarching design, spotlighting the four primary layers  
1596 of detectors as well as the quartet of superconducting magnets responsible for generating the  
1597 magnetic field across a vast expanse of about 12000 m<sup>3</sup> (this volume is demarcated by regions  
1598 where the field strength surpasses 50 mT). Central attributes of the ATLAS magnetic system  
1599 encompass:

- 1600 • A central solenoid, strategically positioned along the beam trajectory, furnishing a 2T  
1601 axial magnetic field purposed for the inner detector. This ensures the reduction of  
1602 radiative thickness ahead of the barrel electromagnetic calorimeter.
- 1603 • A cylindrical barrel toroid paired with twin end-cap toroids. Together, they generate a  
1604 toroidal magnetic field, averaging between 0.5T in the core region and amplifying up  
1605 to 1T for the muon detectors located at the end-cap zones.

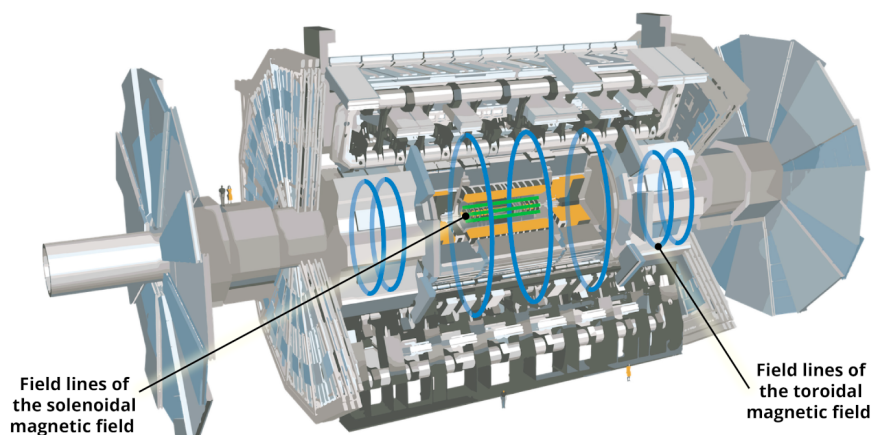


Figure 3–8 The layout of the ATLAS magnet system<sup>[48]</sup>.

### 3.2.2.5 Trigger and data acquisition systems

The ATLAS experiment employs a sophisticated, multi-level event selection mechanism, often referred to as the "trigger system". This system has been designed to sift through the vast number of potential event candidates, selecting only those of highest interest for in-depth analysis.

The trigger system is divided into three hierarchical stages, which is shown in Figure 3–9:

1. **Level-1 (L1) Trigger:** The most immediate and rapid-fire of the selection processes.

Designed with custom electronics, it employs low-resolution data from select detectors, chiefly the Resistive Plate Chambers (RPC) and Thin-Gap Chambers (TGC) for high- $p_T$  muons, along with all calorimeter sub-systems to detect electromagnetic clusters, jets,  $\tau$ -leptons, missing transverse energy  $E_T^{\text{miss}}$ , and overall large transverse energy. This stage primarily searches for signatures from high- $p_T$  muons, electrons/photons, jets, and  $\tau$ -leptons that decay into hadrons. It is tailored to make fast decisions, with a decision window of just  $2.5 \mu\text{s}$  post a bunch-crossing. It operates at an impressive maximum rate of 75 kHz, which holds the potential to be upgraded to 100 kHz.

2. **Level-2 (L2) Trigger (High-Level Trigger - HLT):** Unlike L1, this stage is powered primarily by commercial computing and networking equipment. The L2 trigger operates in a more refined environment, with its activities being directed by the Regions-of-Interest (RoI's) highlighted by the L1 trigger. These RoI's are essentially detector zones where potential event candidates have been spotted. The L2 trigger then utilizes the RoI data to curtail the data volume that needs to be fetched from the detector readout, thereby optimizing the event selection process. At this stage, event rates are scaled down to a manageable 3.5 kHz, while maintaining an average processing time of around 40 ms.

3. **Event Filter:** This serves as the final layer of online event selection. Adopting offline analysis techniques on completely assembled events, it filters the event rate down to approximately 200 Hz. This stage, with an average processing duration of about 4 seconds, ensures only the most pertinent events are stored for further offline scrutiny. The algorithms deployed within the HLT use the full detail of the calorimeter, muon chamber data, and data from the inner detector to perfect their selections. Improved data on energy deposition aids in refining threshold limits, while inner detector track

1637 reconstruction considerably augments particle identification capabilities, such as dif-  
 1638 ferentiating between electrons and photons.

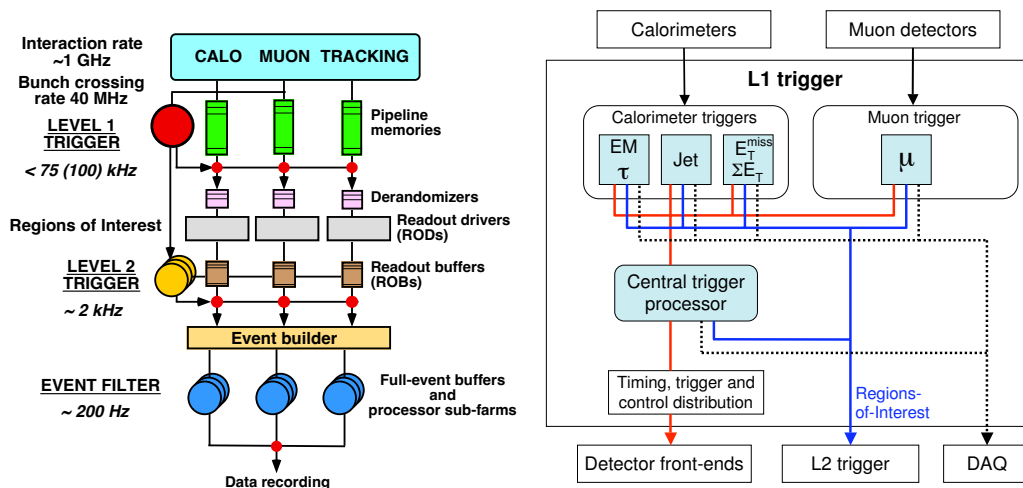


Figure 3–9 Left: A schematic view of the ATLAS trigger system<sup>[49]</sup>; Right: Block scheme of the first level trigger<sup>[49]</sup>.

1639 Alongside the trigger system, the Data Acquisition System (DAQ)<sup>[47,50]</sup> plays a pivotal  
 1640 role, as illustrated in Figure 3–10. It is the backbone that oversees the capture, buffering,  
 1641 and transmission of event data from the specialized readout hardware at the L1 trigger rate.  
 1642 Through dedicated point-to-point Readout Links (ROL's), the DAQ dispatches data requested  
 1643 by the L2 trigger, predominantly related to the RoI's. Upon fulfilling L2 selection criteria,  
 1644 events are compiled and then shuttled by the DAQ to the event filter. Events that pass this  
 1645 stringent filter are then preserved in a permanent storage system.

1646 Additionally, the DAQ is not just a passive data handler. It actively aids in orchestrating  
 1647 the configuration, control, and oversight of the entire ATLAS detector during data collection  
 1648 phases. For hands-on supervision of the myriad elements of the detector infrastructure, like  
 1649 gas systems and power supplies, the Detector Control System (DCS) is brought into play.

1650 In summary, the interplay of the multi-layered trigger system and the DAQ ensures the  
 1651 ATLAS experiment efficiently manages the vast influx of data, making informed selections  
 1652 and effectively archiving events of significance.

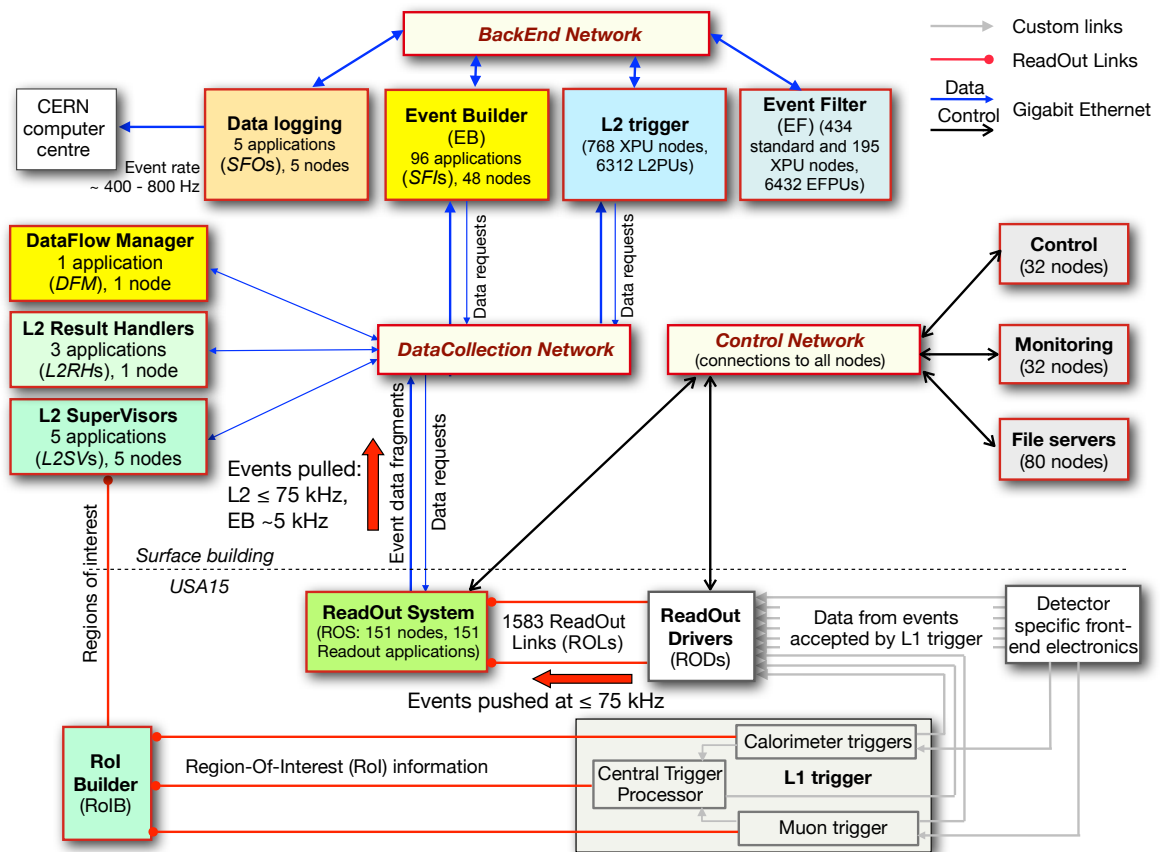


Figure 3-10 A schematic view of the ATLAS DAQ system<sup>[50]</sup>.



## Chapter 4 Event Simulation and Reconstruction in ATLAS

### 4.1 Event Simulation

#### 4.1.1 Simulation Overview and Large-Scale Production System

In the ATLAS experiment, the role of numerical simulation is critical for experimental design and data interpretation. Each aspect of the event process, from initial particle collision to detector response, is replicated within the simulation framework. This approach enables the identification of potential outcomes and limitations, as well as the adjustment of experimental parameters.

Given the data volume generated by the ATLAS detector, which is on the order of petabytes per year, a detailed simulation is essential. It facilitates a robust methodology for the analysis of complex data sets, thereby ensuring that results conform to theoretical expectations within defined statistical limits.

By meticulously mimicking the complete event cycle, the simulation aids in refining analytical methods and optimizing detector settings. Thus, a high level of experimental accuracy is maintained, contributing to a more reliable exploration of particle physics phenomena within the constraints of the Standard Model and beyond.

Central to this simulation is the Athena program<sup>[51]</sup>, integrated into the ATLAS framework and powered by the Geant4 simulation toolkit<sup>[52-53]</sup>. The simulation sequence is typically segmented into the following distinct phases<sup>[54]</sup>:

1. **Event Generation:** In the initial stage of event generation, emphasis is placed on the production and decay of events, which encompasses the calculation of Matrix Elements (ME) and the processes of Parton Shower (PS) or hadronization. Events are generated and filtered in accordance with the HepMC standard format<sup>[55]</sup>, retaining only those that meet specific criteria such as leptonic decay or a predetermined missing energy threshold. Prompt decays, particularly those involving Z or W bosons, are primarily managed at this stage, while particles considered "stable" for detector traversal are retained. Notably, at this phase, consideration is restricted to immediate decays, making the geometric configuration of the detector irrelevant. Within each job, run and event numbers are systematically assigned to simulated data sets.

- 1682     **2. Detector Simulation:** Once events are generated, they're integrated into the simu-  
1683     lation. An exhaustive record of all particles from the generator is preserved, while  
1684     user-defined cuts determine which particles undergo processing. Geant4 controls the  
1685     path of each particle as it moves through the ATLAS detector. Energy deposited in the  
1686     detector's sensitive areas is documented as "hits".
- 1687     **3. Truth Information:** During both the event generation and detector simulation, every  
1688     event is assigned a "truth" record. In the generation phase, this "truth" represents a  
1689     history of particle interactions. In the simulation phase, it focuses on details of indi-  
1690     vidual particle tracks and decays, highlighting events such as photon conversions in  
1691     the inner detector.
- 1692     **4. Digitization:** This phase converts "hit" outputs from the simulation into tangible  
1693     detector signals, such as voltage or time. The pile-up effect is integrated here to en-  
1694     sure computational efficiency. Digitization's output materializes as a Raw Data Object  
1695     (RDO) file, standing out from the detector's "bytestream" format due to the inclusion  
1696     of truth information.
- 1697     **5. High-Level Trigger and Reconstruction:** Both the ATLAS HLT and the subsequent  
1698     reconstruction process are built on the RDO files. The reconstruction remains consis-  
1699     tent for simulated and actual data, with the exception of truth information being ex-  
1700     clusive to the simulation. The HLT, during real data acquisition, leans on bytestream  
1701     files, though a thorough assessment can revert RDOs to this format.

#### 1702 4.1.1.1 Large-Scale Production System

1703     As the ATLAS simulation process is computationally demanding and time-intensive, a  
1704     large-scale production system becomes indispensable for distributing the workload and en-  
1705     suring the timely completion of complex tasks. For this purpose, ATLAS employs the World-  
1706     wide LHC Computing Grid (WLCG)<sup>[56]</sup>, which allows tasks to be divided into multiple jobs  
1707     based on their complexity and computational requirements. Each job is designed to be ex-  
1708     ecuted within a CPU's maximum allowed runtime, typically ranging from 2-3 days. The  
1709     output from these jobs, including log files, is systematically registered with the ATLAS Dis-  
1710     tributed Data Management (DDM) system<sup>[57]</sup> for meticulous bookkeeping and subsequent  
1711     analysis.

1712     To maintain software reliability and uniformity, complete software releases—incorporat-

1713 ing all Athena software, external dependencies like Geant4, and generators—are distributed  
1714 to production sites and end-users at regular intervals. These releases are further updated  
1715 through periodic patches known as 'production caches.' Alongside these software packages,  
1716 a set of data files containing database replicas, external data files, and sample output files are  
1717 included for validation purposes.

1718 Job distribution within the WLCG adheres to a well-structured protocol. Initially, a test  
1719 batch of approximately 10 jobs is run, and the remaining jobs are queued only after the suc-  
1720 cessful completion of this test batch. The process is often hierarchical; each step in a se-  
1721 quence of jobs (generation, simulation, and digitization) remains in the queue until the pre-  
1722 ceding job's data are available. Multiple steps can also be configured to run concurrently for  
1723 efficiency, with about one million events per day being produced using Geant4.

1724 Modifications to each job are permitted but are kept minimal for the sake of consistency.  
1725 These could involve slight adjustments to random number seeds, generator configurations,  
1726 detector geometry, and other job options. Some specialized options are also available for  
1727 unique simulation needs, such as non-standard vertex smearing or simulation of long-lived  
1728 exotic particles.

1729 Through this large-scale production system, ATLAS effectively tackles the computational  
1730 challenges associated with its complex simulation processes, optimizing the use of resources  
1731 for the production of high-quality simulated data.

## 1732 **4.1.2 Event generation**

### 1733 4.1.2.1 General-Purpose Monte Carlo Generators

1734 General-purpose Monte Carlo (GPMC) generators like HERWIG<sup>[58-59]</sup>, PYTHIA<sup>[60-61]</sup>, and  
1735 Sherpa<sup>[62]</sup> are integral in simulating high energy particle collisions. These generators serve  
1736 a dual purpose: first, as theoretical tools for probing Quantum Chromodynamics (QCD)  
1737 beyond fixed-order perturbation, and second, as practical instruments for data analysis and  
1738 experimental planning. They function at different scales, ranging from the perturbative to the  
1739 nonperturbative, capturing the physics from sub-femtometer dimensions to the larger scales  
1740 of hadron formation and decay.

1741 The architecture of GPMC generators is organized into four fundamental components.  
1742 Each component serves a distinct function in simulating high-energy particle interactions,

1743 which are interrelated:

- 1744 • **Short-Distance, Perturbative Phenomena:** At sub-femtometer scales, GPMC gen-  
1745 erators utilize perturbative QCD to model hard scattering and other partonic-level pro-  
1746 cesses<sup>[63]</sup>. Matrix Elements (ME) are employed to provide fixed-order calculations  
1747 for specific scattering processes, and they often serve as the starting point for parton  
1748 shower evolution. The parton shower (PS) technique further refines these calculations  
1749 by capturing the sequential emission of gluons and quarks at lower transverse momenta.  
1750 Additional features like Initial-State Radiation (ISR) and Final-State Radiation (FSR)  
1751 are implemented to account for particle emissions both before and after the core hard-  
1752 scattering event. These mechanisms collectively influence the kinematic attributes of  
1753 the simulated collision. Furthermore, the strong coupling constant, denoted as  $\alpha_s$ ,  
1754 serves as a key parameter in these simulations, dictating the strength of strong force  
1755 interactions and contributing to theoretical uncertainties.
- 1756 • **Nonperturbative Transition:** Beyond the perturbative regime, these generators em-  
1757 ploy phenomenological models like the Lund String or Cluster models to simulate the  
1758 transition from quarks and gluons to observable hadrons.
- 1759 • **Soft Hadron Physics Models:** For larger-scale, nonperturbative interactions, the gen-  
1760 erators incorporate models of the underlying event and minimum-bias interactions,  
1761 along with specialized treatments for Bose-Einstein correlations and color reconnec-  
1762 tion.
- 1763 • **MC Uncertainty Estimates and Tuning:** The generators also provide frameworks  
1764 for uncertainty quantification and parameter tuning, which are crucial for assessing  
1765 the reliability of simulation results.

1766 In elucidating how  $pp$  collision events are simulated by PYTHIA<sup>[64]</sup>, Figure 4–1 offers a  
1767 schematic overview, albeit with certain simplifications for the sake of visual clarity; these  
1768 include a reduced number of shower branchings and final-state hadrons, approximate recoil  
1769 effects, and the exclusion of weak decays in light-flavor hadrons, among other details (see  
1770 caption for a complete list of simplifications).

#### 1771 4.1.2.2 Specialized Generators

1772 Specialized generators serve as auxiliary tools in the high-energy physics ecosystem, de-  
1773 signed to work in conjunction with GPMC generators such as PYTHIA and HERWIG. Unlike

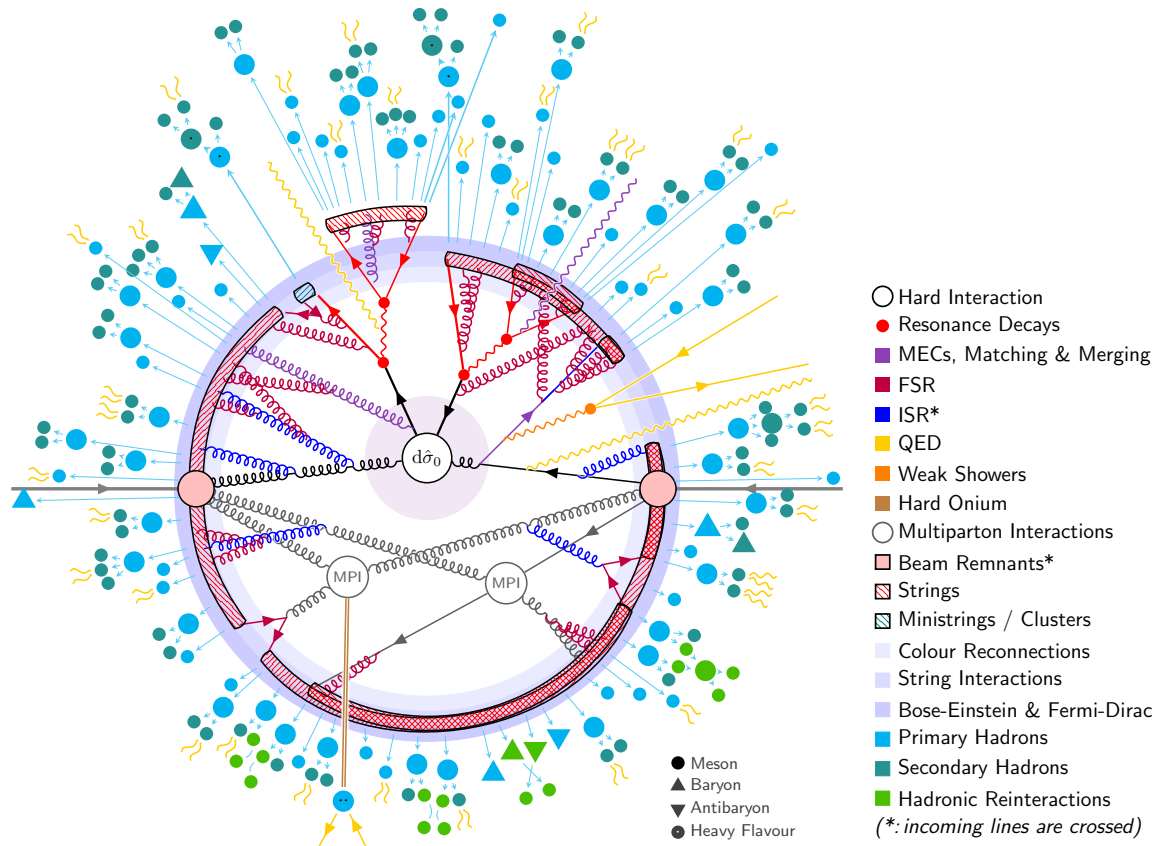


**Figure 4–1 Schematic representation of a  $pp \rightarrow t\bar{t}$  event as simulated by PYTHIA<sup>[64]</sup>, with certain simplifications for visual clarity. 1) The number of shower branchings and final-state hadrons is reduced compared to an actual PYTHIA simulation; 2) Recoil effects are not depicted to scale; 3) Weak decays of light-flavor hadrons are omitted, implying, for example, a  $K_S^0$  meson is shown as stable; 4) Incoming momenta are illustrated as inversed ( $p \rightarrow -p$ ), necessitating that the momentum direction for both beam remnants and ISR branchings should be interpreted as outward-facing to avoid diagrammatic complexity. This convention prevents the need for beam remnants and ISR emissions to intersect in the central region of the figure.**

1774 GPMCs, specialized generators do not produce complete events amenable to direct simula-  
 1775 tion. Instead, their function is to provide a more accurate representation of specific decay  
 1776 processes or specialized final states. These generators often employ advanced theoretical  
 1777 models and methodologies, ranging from next-to-leading order (NLO) perturbative calcula-  
 1778 tions to intricate decay models. By generating partonic four-vectors in compatible formats,  
 1779 they enable seamless integration with GPMC generators, thereby enhancing the overall pre-  
 1780 dictive power and accuracy of event simulations. These specialized generators often produce

1781 outputs in ASCII formats compatible with "Les Houches" standards<sup>[65]</sup>, which are then read  
1782 and processed by GPMC generators via interfaces like Athena.

1783 EvtGen<sup>[66]</sup>, originally conceived by the CLEO collaboration, specializes in providing a  
1784 nuanced description of B meson and hadron decays, thereby enhancing the default capabili-  
1785 ties of general-purpose generators. Recent extensions of EvtGen have incorporated data from  
1786 experiments at the Tevatron, BaBar, and Belle, allowing for more accurate modeling of  $B_s$ ,  
1787 and b-baryon decays. EvtGen is unique in its incorporation of angular correlations, which are  
1788 crucial for calculating the acceptance rates for certain decay modes of B mesons and baryons.  
1789 It has been particularly useful in ATLAS studies that focus on exclusive B decays.

1790 MC@NLO<sup>[67]</sup>, another specialized generator, operates as a standalone "Les Houches"  
1791 type generator. It is notable for its employment of NLO QCD perturbation theory for eval-  
1792 uating hard scattering processes. This makes it especially relevant for generating events in-  
1793 volving top quarks, offering a more precise representation of their transverse momentum  
1794 distributions as compared to general-purpose generators. One of its defining features is the  
1795 inclusion of one-loop corrections, resulting in events with both positive and negative weights  
1796 that must be carefully accounted for in subsequent data analysis.

1797 Parton Distribution Functions (PDFs) serve as essential components to model the inter-  
1798 nal structure of protons. These PDFs are incorporated into all event generators as external  
1799 inputs. Specifically, ATLAS employs the Les Houches Accord PDF Interface (LHAPDF)<sup>[68]</sup>,  
1800 a robust library that has effectively replaced the older PDFLIB<sup>[69]</sup>. This library offers an ex-  
1801 tensive repository of PDFs, with the default being the CTEQ PDFs<sup>[70]</sup>. It is noteworthy that  
1802 MC@NLO employs NLO PDFs, whereas all other generators utilize Leading Order (LO)  
1803 PDFs. The choice of PDFs is intrinsically tied to the tuning parameters associated with initial  
1804 state radiation<sup>[71-72]</sup>. Due to this interconnectedness, altering PDFs independently can result  
1805 in inconsistent outcomes. Hence, whenever a new set of PDFs is adopted, a corresponding  
1806 retuning of the event generator's parameters is performed to ensure result consistency.

1807 Monte Carlo truth is preserved in a HepMC event record, serving as a complete list of par-  
1808 ticles that are directly produced or involved in high-energy interactions. These particles often  
1809 serve as progenitors to a cascade of sub-processes and decays that ultimately interact with  
1810 the detector. The MC truth at the generator level differentiates between particles originat-  
1811 ing from the initial collision and those produced through subsequent interactions or decays,

1812 allowing for a precise understanding of the underlying physical processes. This granularity  
1813 is essential for calibrating the simulation and validating the detector’s response to specific  
1814 types of events.

### 1815 **4.1.3 Detector simulation and response**

#### 1816 4.1.3.1 Detector Simulation

1817 The ATLAS detector’s geometric model is highly detailed, with an extensive list of ma-  
1818 terials and physical volumes. Table 4–1 lists the specific quantities of each, broken down by  
1819 detector component. This level of detail is essential for accurate predictions, particularly in  
1820 variables like missing transverse energy and track reconstruction. To improve computational  
1821 efficiency, the model uses volume parameterization, which allows the reuse of the same log-  
1822 ical volume. Sub-picometer gaps are introduced between volumes to prevent computational  
1823 issues like ‘stuck tracks’.

1824 The system also allows for frequent updates and maintains backward compatibility, en-  
1825 abling older geometries to still function. Users have the option to enable or disable specific  
1826 sections of the detector for resource optimization. The architecture supports the incorpora-  
1827 tion of various detector conditions like misalignments, which can be stored in a database and  
1828 transferred across different data processing stages.

#### 1829 4.1.3.2 Digitization

1830 The digitization stage in the ATLAS software framework translates simulated hits into  
1831 detector readouts, commonly referred to as “digits.” These digits are generated based on  
1832 predefined voltage or current thresholds within specific time windows for individual readout  
1833 channels. The software also accounts for charge collection in each subdetector, including  
1834 cross-talk, electronic noise, and channel-dependent variations.

1835 The digitization software<sup>[73-77]</sup> for each subdetector is orchestrated by a top-level Python  
1836 package, which ensures a unified configuration across all subdetectors. The algorithms’ prop-  
1837 erties are optimized to match the real-world detector response as observed in lab tests, test  
1838 beam data, and cosmic ray measurements. Dead channels and noise rates are incorporated  
1839 from database tables to mirror real experimental conditions.

1840 Raw Data Objects (RDOs) serve as the output of the digitization process. Depending  
1841 on the subdetector, some may require a two-step conversion from hits to digits and then to

Subsystem	Materials	Solids	Logical Vol.	Physical Vol.	Total Vol.
Beampipe	43	195	152	514	514
BCM	40	131	91	453	453
Pixel	121	7,290	8,133	8,825	16,158
SCT	130	1,297	9,403	44,156	52,414
TRT	68	300	357	4,034	1,756,219
LAr Calorimetry	68	674	639	106,519	506,484
Tile Calorimetry	8	51,694	35,227	75,745	1,050,977
Inner Detector	243	12,501	18,440	56,838	1,824,614
Calorimetry	73	52,366	35,864	182,262	1,557,459
Muon System	22	33,594	9,467	76,945	1,424,768
ATLAS TOTAL	327	98,459	63,769	316,043	4,806,839

**Table 4–1 Quantities of materials, solids, logical volumes, physical volumes, and aggregate volumes essential for the assembly of diverse segments of the ATLAS detector are outlined. The term "Inner Detector" encompasses components such as the beampipe, BCM, pixel tracker, SCT, and TRT.**

1842 RDOs, while others bypass the intermediate digit stage and generate RDOs directly from  
 1843 hits. Additionally, Simulated Data Objects (SDOs) may be generated, which offer details on  
 1844 particle interactions and energy contributions. These SDOs are crucial for assessing tracking  
 1845 efficiency and false track rates.

1846 Moreover, the simulation process also accounts for multiple interactions within a single  
 1847 bunch crossing, including both the hard scattering event and any additional inelastic, non-  
 1848 diffractive interactions. These multiple events, often referred to as pile-up, are integrated into  
 1849 the digitization stage to produce a realistic detector response.

1850 Finally, the conversion from bytestream data to RDO format is an essential step before  
 1851 running reconstruction algorithms. While the process from RDO to bytestream involves some  
 1852 data loss due to truncation, the reverse operation is essentially lossless. This bidirectional  
 1853 conversion capability facilitates evaluation of the conversion algorithms themselves.

#### 1854 4.1.3.3 Fast Simulation

1855 In order to meet the demands of complex physics studies without sacrificing computa-  
 1856 tional efficiency, various fast simulation methods have been developed to complement the

1857 standard full simulation in the ATLAS experiment. These fast simulation approaches aim to  
1858 offer a balance between accuracy and speed, targeting specific bottlenecks or computational  
1859 requirements. Here are the key methods:

- 1860 • **Fast G4 Simulation**<sup>[78-79]</sup>: Targets the calorimeter simulations, which consume almost  
1861 80% of full simulation time. By replacing low-energy electromagnetic particles with  
1862 pre-simulated showers, it reduces CPU time by a factor of three in hard scattering  
1863 events such as  $t\bar{t}$  production.
- 1864 • **ATLFAST-I**<sup>[80-81]</sup>: Ideal for studies requiring large statistics but not detailed complex-  
1865 ity. It employs smeared truth objects to mimic physics objects from reconstruction,  
1866 achieving a speed increase of up to 1000 times over full simulation.
- 1867 • **ATLFAST-II**<sup>[82]</sup>: Designed to offer a balance between speed and accuracy. It com-  
1868 prises Fast ATLAS Tracking Simulation (FAtlas) for inner detector and muon simu-  
1869 lations, and Fast Calorimeter Simulation (FastCaloSim) for calorimeter simulations.  
1870 Depending on its configuration, it can achieve a 10-time or 100-time speed improve-  
1871 ment over full simulation.

## 1872 4.2 Object Reconstruction

### 1873 4.2.1 Tracks

1874 In the ATLAS experiment, the accurate reconstruction of charged particle tracks is cru-  
1875 cial for a wide array of physics analyses, from the study of the Higgs boson to the search  
1876 for new phenomena beyond the Standard Model. These tracks provide key insights into the  
1877 underlying collision events and are fundamental for vertex identification, momentum mea-  
1878 surement, and isolation criteria, among other parameters. The structure of the ATLAS Inner  
1879 Detector is introduced in Section 3.2.2.1, and the nomenclature of track coordinate is in Sec-  
1880 tion 3.2.1.1. Accurate track reconstruction<sup>[83-84]</sup> is especially vital for studies involving heavy  
1881 flavor tagging, precision measurements of Standard Model processes, and the identification  
1882 of long-lived particles. The process is complex, involving several steps to convert raw detec-  
1883 tor hits into particle trajectories. Each stage, from clusterization of signals to resolving track  
1884 ambiguities, plays a critical role in ensuring the accuracy of the physics outcomes:

- 1885 1. **The ID Reconstruction Sequences**<sup>[84]</sup>: In contemporary ID track reconstruction, the

1886 boundaries between pattern finding and track fitting have blurred. Many modern pat-  
1887 tern finding strategies go beyond the classical histogram-based methods and include  
1888 both global and local pattern recognition. In this context, track fitting is often incorpo-  
1889 rated into the pattern finding process. Similarly, modern track fitters, like the combi-  
1890 natorial extension of the standard Kalman filter<sup>[85]</sup> or the deterministic annealing filter,  
1891 integrate pattern recognition as part of the fitting process. Therefore, the sequence for  
1892 ID reconstruction in ATLAS combines pattern finding and track fitting into a unified  
1893 chain.

1894 The ID reconstruction adopts two primary sequences: the main inside-out track recon-  
1895 struction and a subsequent outside-in tracking. These sequences are heavily influenced  
1896 by the pre-existing ATLAS ID reconstruction program XKALMAN but have been fur-  
1897 ther enhanced with additional components following the NEWT approach. There's  
1898 also a third sequence for the finding of V0 vertices, kink objects, and their associ-  
1899 ated tracks using common tracking tools and EDM, although this is not specific to the  
1900 NEWT approach.

- 1901 2. **The Inside-Out Sequence**<sup>[84]</sup>: The inside-out tracking sequence begins with seed for-  
1902 mation in the inner silicon tracker and progresses towards the outer regions of the ID.  
1903 This process involves both global and local pattern recognition stages. The global  
1904 stage narrows down the possibilities, and the local stage works on this reduced set of  
1905 candidates. The first phase in the inside-out sequence is the construction of three-  
1906 dimensional representations of the silicon detector measurements. Track seeds are  
1907 formed from these 3D objects. A window search is then performed based on the seed  
1908 direction to build track candidates. Hits from the detector elements that lie within this  
1909 "road window" are collected and evaluated based on a simplified Kalman filtering-  
1910 smoothing approach. These hits are then either added to the track candidates or re-  
1911 jected.
- 1912 3. **Iterative Combinatorial Track Finding**<sup>[83]</sup>: The process starts by forming track seeds  
1913 from sets of three space-points. This is a trade-off to allow a large number of combi-  
1914 nations while still getting a rough initial momentum estimate. The algorithm then  
1915 estimates the impact parameters of these seeds with respect to the interaction region's  
1916 center, assuming a perfect helical trajectory in a uniform magnetic field. Multiple cri-

1917        teria are then applied to these seeds to ensure a high level of purity. These criteria  
1918        include type-dependent momentum and impact parameter requirements, as well as the  
1919        necessity for one additional space-point that is compatible with the estimated particle's  
1920        trajectory. Subsequently, a Combinatorial Kalman filter<sup>[86]</sup> is used to build track can-  
1921        didates by incorporating additional space-points from the remaining layers of the pixel  
1922        and SCT detectors.

1923        4. **Track Candidates and Ambiguity Solving**<sup>[83-84]</sup>: The process begins by assigning a  
1924        score to each track candidate based on a variety of factors that assess the quality of  
1925        the track. This includes the number of clusters the track intersects with and the chi-  
1926        square ( $\chi^2$ ) value of the track fit. After these scores are assigned, the track candidates  
1927        are sorted in descending order. The candidates are processed individually in this order.  
1928        This is under the premise that higher scores likely represent tracks that more accurately  
1929        correspond to the trajectories of primary charged particles.

1930        Once sorted, each track candidate is rigorously evaluated against a set of basic quality  
1931        criteria. These criteria include a transverse momentum ( $p_T$ ) greater than 400 MeV,  
1932        and an absolute value of  $\eta$  that is less than 2.5. Additionally, the candidate must have a  
1933        minimum of seven pixel and SCT clusters; although 12 are typically expected. Limits  
1934        are also imposed on shared clusters: a maximum of one shared pixel cluster or two  
1935        shared SCT clusters on the same layer can be a part of the track. Other parameters  
1936        include not having more than two "holes" in the combined pixel and SCT detectors,  
1937        not having more than one hole in the pixel detector alone, a transverse impact parameter  
1938        ( $|d_0^{BL}|$ ) less than 2.0 mm, and a longitudinal impact parameter ( $|z_0^{BL} \sin \theta|$ ) less than  
1939        3.0 mm.

1940        Following the application of quality criteria, the ambiguity solver moves on to resolve  
1941        any issues with shared clusters. This step is crucial, as clusters can be attributed to more  
1942        than one track. In such cases, preference is given to tracks that were processed earlier.  
1943        Penalties are applied for sharing clusters that haven't been identified as 'merged'. If a  
1944        track candidate doesn't meet any of the quality criteria, it gets rejected. The track is  
1945        then re-scored and placed back into the list of remaining candidates for another round  
1946        of processing. This ensures that only the most promising track candidates make it into  
1947        the final dataset, thus enhancing the reliability and accuracy of particle track recon-

struction. An overview of this ambiguity solving procedures is shown in Figure 4–2.

- 1948
- 1949 **5. Neural-Network Pixel Clustering**<sup>[83]</sup>: An artificial neural network<sup>[87]</sup> is employed to
- 1950 assist in identifying merged clusters, clusters which are created by the charge deposits
- 1951 from multiple particles. This identification is based on the measured charge, relative
- 1952 positions of pixels within a cluster, and additional information about the particle’s in-
- 1953 cident angle. The network has high efficiency in recognizing these merged clusters.
- 1954 However, it doesn’t break down these merged clusters into individual energy deposits.
- 1955 **6. Cluster Identification Logic**: Merged clusters can be identified in two distinct ways.
- 1956 First, they can be flagged by the neural network when they are used in multiple track
- 1957 candidates. Alternatively, clusters can be identified as merged if they appear on two
- 1958 consecutive layers and are used by the same track candidates. Clusters identified as
- 1959 merged are used without penalty, whereas clusters not identified as merged, but which
- 1960 are shared, can still be used but with a penalty as described earlier.

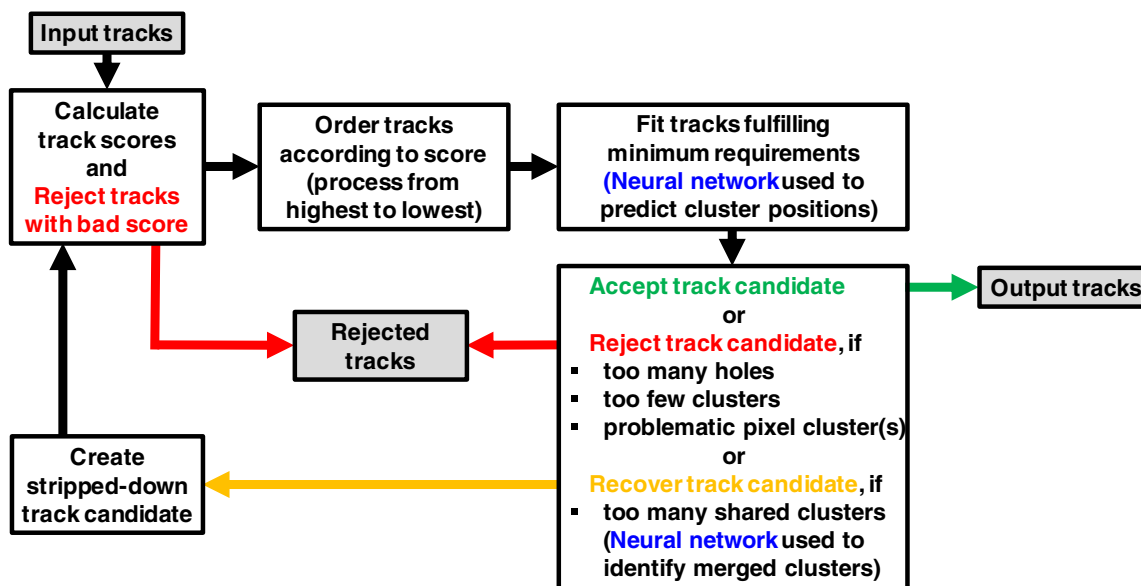


Figure 4–2 Overview of Track Candidate Progression within the Ambiguity Solver<sup>[83]</sup>.

## 1961 4.2.2 Electrons

### 1962 4.2.2.1 Electron Reconstruction

1963 The updated algorithm<sup>[88]</sup> for reconstructing electrons and photons commences by iden-

1964 tifying topo-clusters that are viable candidates for forming these particles. Following this,

1965 the tracks are refitted with an understanding of bremsstrahlung processes and then matched  
 1966 to the previously selected topo-clusters. The refitted tracks also serve as the foundation for  
 1967 constructing conversion vertices, which are then aligned with the selected topo-clusters.

1968 Subsequent to this initial phase of track-cluster association and conversion vertex forma-  
 1969 tion, separate routines for electron and photon superclustering are invoked concurrently. The  
 1970 resulting superclusters undergo preliminary positional adjustments, and are then matched  
 1971 with tracks for electrons and with conversion vertices for photons.

1972 An electron is conventionally described as an entity that pairs a calorimeter-based super-  
 1973 cluster with a compatible track or tracks. Conversely, a converted photon pairs a calorimeter  
 1974 cluster with one or multiple conversion vertices, while an unconverted photon pairs with  
 1975 neither an electron track nor a conversion vertex.

1976 Because a single object can be simultaneously reconstructed as both an electron and a  
 1977 photon, a specialized ambiguity resolution step is employed to minimize such overlaps. How-  
 1978 ever, a certain degree of overlap is deliberately preserved to ensure efficient reconstruction  
 1979 rates for both particle types, enabling subsequent physics analyses to apply more specialized  
 1980 criteria as needed.

1981 The calibrated final forms of the electrons and photons are then produced, paving the way  
 1982 for the computation of various additional metrics that are essential for quality control and  
 1983 further ambiguity resolution. Prior methodologies for electron and photon reconstruction  
 1984 are detailed in References<sup>[89]</sup> and<sup>[90]</sup>. A visual representation summarizing the flow of the  
 1985 revamped algorithm for electron and photon reconstruction can be found in Figure 4–4, and  
 1986 a conceptual diagram depicting an electron’s journey through the various components of the  
 1987 detector is shown in Figure 4–3.

1988 In the formation of topological clusters (topo-clusters) within the ATLAS detector, the  
 1989 concept of cell significance plays a pivotal role. This is represented by the variable  $\zeta_{\text{cell}}^{\text{EM}}$ . The  
 1990 equation for calculating cell significance is given by:

$$\zeta_{\text{cell}}^{\text{EM}} = \frac{|E_{\text{cell}}^{\text{EM}}|}{\sigma_{\text{noise, cell}}^{\text{EM}}} \quad (4-1)$$

1991 Here,  $|E_{\text{cell}}^{\text{EM}}|$  is the absolute energy of the cell at the electromagnetic (EM) scale, and  
 1992  $\sigma_{\text{noise, cell}}^{\text{EM}}$  is the expected noise for that cell. The initial clustering process starts with seed  
 1993 cells having  $\zeta_{\text{cell}}^{\text{EM}} \geq 4$ . These seed cells then collect neighboring cells with  $\zeta_{\text{cell}}^{\text{EM}} \geq 2$ .

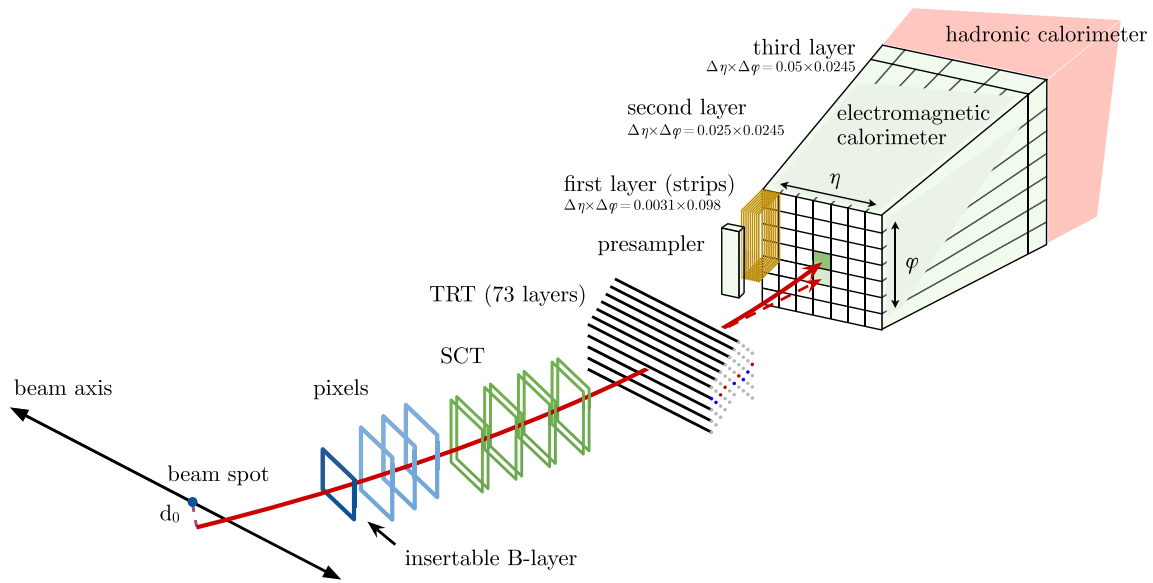


**Figure 4–3** A conceptual diagram depicting an electron’s journey through the various components of the detector<sup>[91]</sup>. The solid red line represents the speculated path of an electron as it moves initially through the tracking system, starting with the pixel detectors, followed by the silicon-strip detectors, and finally through the TRT, before entering the electromagnetic calorimeter. The dotted red line illustrates the trajectory of a photon generated due to the electron’s interaction with the tracking system’s material.

1994 When proto-clusters share a cell and the energy of that cell significantly exceeds the noise  
 1995 threshold, these proto-clusters are merged. After collecting all cells with energies above the  
 1996 noise threshold, an additional set of neighboring cells with  $\zeta_{\text{cell}}^{\text{EM}} \geq 0$  are added to form the  
 1997 cluster. This process is often referred to as the “4-2-0” topo-cluster reconstruction method-  
 1998 ology.

1999 For clusters requiring splitting due to the presence of multiple local energy maxima, frac-  
 2000 tional cell weights are calculated based on cluster energies and distances from the cell to the  
 2001 centers of gravity of the clusters. The formulas for these weights<sup>[92]</sup> are as follows:

$$w_{\text{cell},1} = \frac{E_{\text{clus},1}^{\text{EM}}}{E_{\text{clus},1}^{\text{EM}} + rE_{\text{clus},2}^{\text{EM}}} \quad (4-2)$$

$$w_{\text{cell},2} = 1 - w_{\text{cell},1} = \frac{rE_{\text{clus},2}^{\text{EM}}}{E_{\text{clus},1}^{\text{EM}} + rE_{\text{clus},2}^{\text{EM}}}$$

2002 Here,  $r = \exp(d_1 - d_2)$ , where  $d_1$  and  $d_2$  are the distances of the cell to the centers of gravity  
 2003 of the first and second clusters, respectively.

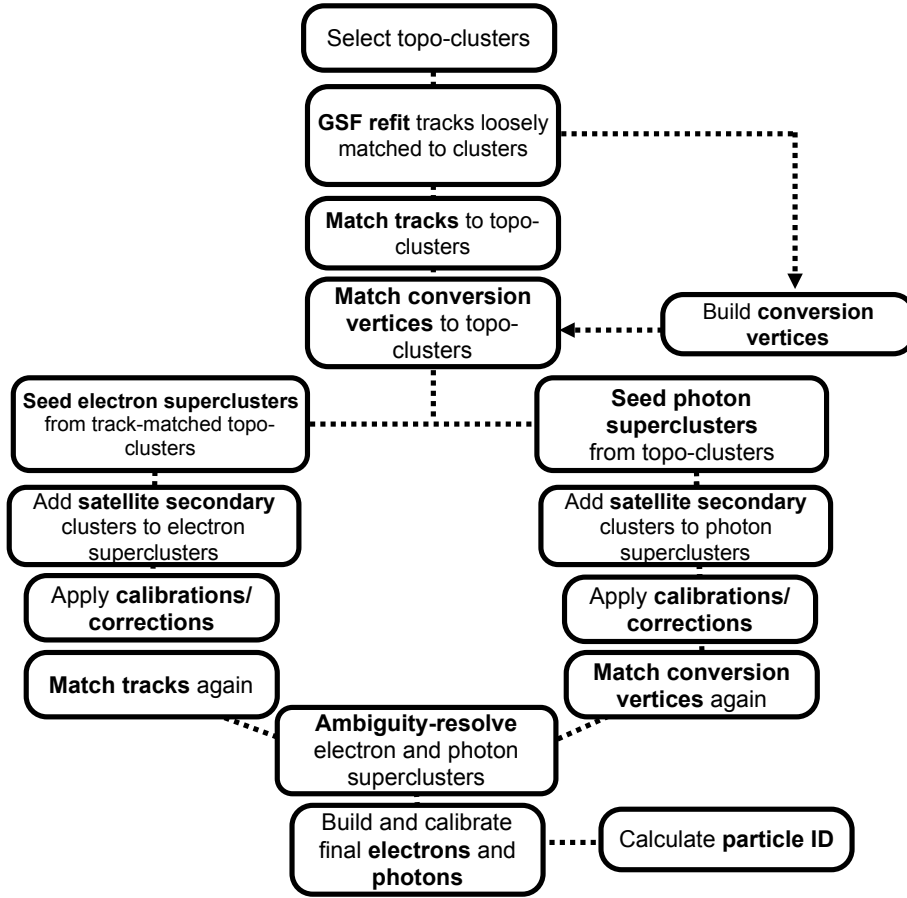


Figure 4–4 Algorithm flow diagram for the new electron and photon reconstruction<sup>[88]</sup>.

2004 Electromagnetic (EM) topological clusters (topo-clusters) are constructed by an algo-  
 2005 rithm that initially uses the universal "4-2-0" rules but later refines these to consider only  
 2006 cells from the EM calorimeter. This procedure serves multiple broader detector goals, in-  
 2007 cluding particle flow reconstruction and future isolation calculation enhancements.

2008 The algorithm starts by duplicating the existing set of 4-2-0 topo-clusters. It then focuses  
 2009 on isolating clusters originating primarily from EM showers by applying an EM fraction  
 2010 ( $f_{EM}$ ) criterion, calculated as follows:

$$f_{EM} = \frac{E_{L1} + E_{L2} + E_{L3} + w \cdot (E_{E4} + E_{PS})}{E_{clus}}, \quad w = \begin{cases} 1, & 1.37 < |\eta| < 1.63 \\ 0, & \text{otherwise} \end{cases} \quad (4-3)$$

2011 Here,  $w$  takes different values based on the  $\eta$  region of the cluster,  $E_{Lx}$  is the energy in

layer  $x$  of the calorimeter, and  $E_{\text{clus}}$  is the total cluster energy. After removing cells from the hadronic calorimeter to reduce noise, the cluster's kinematics are recalculated.

A minimum energy threshold of  $E_T > 400$  MeV is enforced to eliminate noise and irrelevant clusters. Through extensive Monte Carlo simulations, the  $f_{\text{EM}}$  value was optimized, leading to a pre-selection requirement of  $f_{\text{EM}} > 0.5$ . This criterion successfully filters out approximately 60% of pile-up-induced clusters while maintaining efficient electron identification.

In the electron track matching procedure, refitted tracks that are loosely matched initially undergo more stringent selection to be matched to EM clusters. This selection is defined with tighter constraints in  $\eta$  and  $\phi$ . When there are multiple candidate tracks for a single cluster, a hierarchy is applied to determine the track that will define the electron's properties:

1. Tracks with hits in the pixel detector are prioritized.
  2. Next, preference is given to tracks with hits in the SCT, but not in the pixel detector.
- Within each category, tracks are further ranked based on their  $\Delta R$  in  $\eta - \phi$  space. Two types of  $\Delta R$  calculations are performed:

1. The track momentum is rescaled to the cluster energy for the first calculation.
2. The second calculation uses the original, unrescaled track momentum.

The track with the better  $\Delta R$  match is preferred, unless the differences are minimal, in which case the track with more pixel hits is chosen. Special weight is given to a hit in the innermost pixel layer. Momentum rescaling aids in achieving better track-cluster matching, especially when track momentum undergoes significant changes due to bremsstrahlung radiation. Distance-related variables between the track and cluster are also utilized for this matching, as detailed in the referenced studies<sup>[89]</sup>.

The electron supercluster reconstruction<sup>[93]</sup> occurs in two main stages:

1. **Seed Cluster Identification:** EM topoclusters are scrutinized to act as seed cluster candidates. A cluster needs to have a minimum  $E_T$  of 1 GeV and must be associated with a track having at least four hits in the silicon trackers to qualify as a seed.
2. **Satellite Cluster Identification:** EM topoclusters near the seed are identified as potential satellite clusters, which can arise from bremsstrahlung radiation or topo-cluster splitting. If these satellite clusters satisfy specific criteria, they are added to the seed cluster to form the final supercluster.

2043 Spatial criteria for defining a satellite cluster involve two conditions:

- 2044 • A cluster is categorized as a satellite if it lies within a  $\Delta\eta \times \Delta\phi = 0.075 \times 0.125$  window
- 2045 around the seed cluster barycenter.
- 2046 • For electrons, a cluster is also considered a satellite if it is within a  $\Delta\eta \times \Delta\phi = 0.125 \times$
- 2047  $0.300$  window, and its 'best-matched' track is also the best-matched track for the seed
- 2048 cluster.

2049 After superclusters are assembled, initial energy calibration is performed. The superclus-  
 2050 ters, therefore, improve the energy resolution of electron candidates, quantified by the IQE  
 2051 (Interquartile Energy), defined as:

$$\text{IQE} = \frac{Q_3 - Q_1}{1.349} \quad (4-4)$$

2052 Here,  $Q_1$  and  $Q_3$  are the first and third quartiles of the  $E_{\text{calib}}/E_{\text{true}}$  distribution. The normal-  
 2053 ization factor of 1.349 ensures that the IQE for a Gaussian distribution is equivalent to its  
 2054 standard deviation.

#### 2055 4.2.2.2 Electron Identification

2056 One commonly used approach for electron identification<sup>[94]</sup> is the likelihood-based (LH)  
 2057 method, which excels in differentiating prompt electrons from other similar signals, such as  
 2058 jets or non-prompt electrons.

2059 The LH method utilizes a series of measurements obtained from both the tracking and  
 2060 calorimeter systems of the detector. These measurements are modeled using probability den-  
 2061 sity functions (PDFs). Mathematically, the likelihoods for signal  $L_S$  and background  $L_B$  are  
 2062 calculated using the equation

$$L_{S(B)}(x) = \prod_{i=1}^n P_{S(B),i}(x_i). \quad (4-5)$$

2063 To make a decision based on these likelihoods, a discriminant  $d_L$  is formed as  $d_L = \frac{L_S}{L_S + L_B}$ .  
 2064 However,  $d_L$  has a sharp peak, making it difficult to set a threshold for identification. To miti-  
 2065 gate this,  $d_L$  is further transformed using an inverse sigmoid function:  $d'_L = -\tau^{-1} \ln(d_L^{-1} - 1)$ ,  
 2066 where  $\tau$  is a constant set to 15<sup>[95]</sup>. This transformation makes it easier to differentiate between  
 2067 signal and background.

2068 In the Table 4–2 that summarizes quantities for electron identification, various metrics  
 2069 are presented that are instrumental for the identification of prompt electrons. Columns la-

Type	Description	Name	Rejects			Usage
			LF	$\gamma$	HF	
Hadronic leakage	Ratio of $E_T$ in the first layer of the hadronic calorimeter to $E_T$ of the EM cluster (used over the range $\ \eta\  < 0.8$ or $\ \eta\  > 1.37$ )	$R_{had1}$	x	x		LH
	Ratio of $E_T$ in the hadronic calorimeter to $E_T$ of the EM cluster (used over the range $0.8 < \ \eta\  < 1.37$ )	$R_{had}$	x	x		LH
Third layer of EM calorimeter	Ratio of the energy in the third layer to the total energy in the EM calorimeter. This variable is only used for $E_T < 80\text{GeV}$ , due to inefficiencies at high $E_T$ , and is also removed from the LH for $\ \eta\  > 2.37$ , where it is poorly modelled by the simulation.	$f_3$	x			LH
Second layer of EM calorimeter	Lateral shower width, $\sqrt{(\sum E_i \eta_i^2) / (\sum E_i) - ((\sum E_i \eta_i) / (\sum E_i))^2}$ , where $E_i$ is the energy and $\eta_i$ is the pseudorapidity of cell $i$ and the sum is calculated within a window of $3 \times 5$ cells	$w_{\eta 2}$	x	x		LH
	Ratio of the energy in $3 \times 3$ cells over the energy in $3 \times 7$ cells centred at the electron cluster position	$R_\phi$	x	x		LH
	Ratio of the energy in $3 \times 7$ cells over the energy in $7 \times 7$ cells centred at the electron cluster position	$R_\eta$	x	x	x	LH
First layer of EM calorimeter	Shower width, $\sqrt{(\sum E_i (i - i_{max})^2) / (\sum E_i)}$ , where $i$ runs over all strips in a window of $\Delta\eta \times \Delta\phi \approx 0.0625 \times 0.2$ , corresponding typically to 20 strips in $\eta$ , and $i_{max}$ is the index of the highest-energy strip, used for $E_T > 150\text{GeV}$ only	$w_{stot}$	x	x	x	C
	Ratio of the energy difference between the maximum energy deposit and the energy deposit in a secondary maximum in the cluster to the sum of these energies	$E_{ratio}$	x	x		LH
	Ratio of the energy in the first layer to the total energy in the EM calorimeter	$f_1$	x			LH
Track conditions	Number of hits in the innermost pixel layer	$n_{Blayer}$		x		C
	Number of hits in the pixel detector	$n_{Pixel}$		x		C
	Total number of hits in the pixel and SCT detectors	$n_{Si}$		x		C
	Transverse impact parameter relative to the beam-line	$d_0$		x	x	LH
	Significance of transverse impact parameter defined as the ratio of $d_0$ to its uncertainty	$\ d_0/\sigma(d_0)\ $		x	x	LH
	Momentum lost by the track between the perigee and the last measurement point divided by the momentum at perigee	$\Delta p/p$	x			LH
TRT	Likelihood probability based on transition radiation in the TRT	eProbabilityHT	x			LH
Track-cluster matching	$\Delta\eta$ between the cluster position in the first layer and the extrapolated track	$\Delta\eta_1$	x	x		LH
	$\Delta\phi$ between the cluster position in the second layer of the EM calorimeter and the momentum-rescaled track, extrapolated from the perigee, times the charge $q$	$\Delta\phi_{res}$	x	x		LH
	Ratio of the cluster energy to the track momentum, used for $E_T > 150\text{GeV}$ only	$E/p$	x	x		C

Table 4–2 Summary of Quantities for Electron Identification.

2070 beled “Rejects” are provided to indicate the discriminative power of each metric against other  
 2071 signals such as light-flavour (LF) jets, photon conversions ( $\gamma$ ), and non-prompt electrons  
 2072 originating from heavy-flavour (HF) quarks like b- or c-quarks. Another column, labeled  
 2073 “Usage,” is included to specify how each metric is used in the identification process. Metrics  
 2074 marked with “LH” are incorporated into the likelihood functions  $L_S$  and  $L_B$ , as specified in  
 2075 Equation 4–5. Metrics marked with “C” are utilized as direct selection criteria. For metrics  
 2076 that make use of the second layer of the calorimeter, notations like  $3 \times 3$ ,  $3 \times 5$ ,  $3 \times 7$ , and  
 2077  $7 \times 7$  are employed to indicate the specific regions in  $\Delta\eta \times \Delta\phi$  space that are covered, with  
 2078 each unit being  $0.025 \times 0.025$ .

2079 There are two major advantages to using the LH method over traditional cut-based iden-  
 2080 tification techniques. First, it provides a more holistic evaluation of an electron candidate.  
 2081 In cut-based identification, failing to meet even a single condition could result in a false  
 2082 negative. In contrast, the LH method takes into account the collective information from all  
 2083 variables. Second, the LH method can include additional discriminating variables that may  
 2084 not be distinct enough for cut-based methods but still provide valuable information.

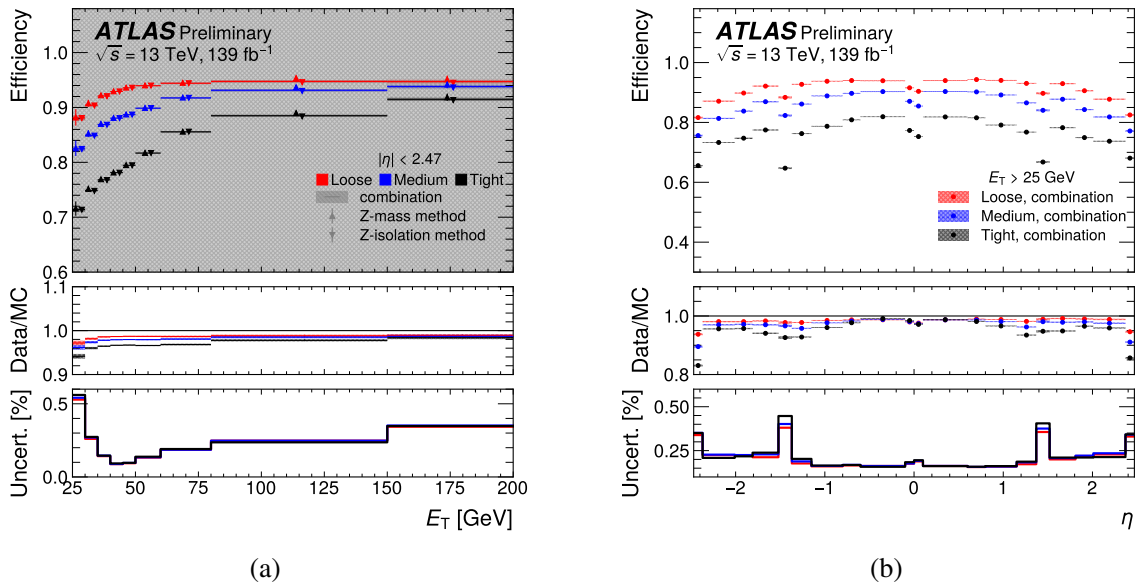


Figure 4–5 Efficiency plots of electron ID working points<sup>[96]</sup>.

2085 Figure 4–5 comprises two plots that present the efficiencies of various electron identifi-  
 2086 cation working points during the 2015-2018 Run 2 data from the LHC in  $Z \rightarrow e^+e^-$  events.  
 2087 Figure 4–5a on the left illustrates these efficiencies as they relate to electron transverse en-

2088 ergy ( $E_T$ ). It not only showcases the aggregate data but also highlights the outcomes of  
 2089 individual efficiency assessment techniques, specifically the Z-mass and Z-isolation meth-  
 2090 ods. These methods and working points can be found in the related study<sup>[97]</sup>. Error indicators  
 2091 on this plot encompass both statistical and systematic uncertainties.

2092 Figure 4–5b on the right focuses on the efficiencies as functions of the electron pseudora-  
 2093 pidity ( $\eta$ ). This plot also provides statistical and systematic uncertainty bands. A noteworthy  
 2094 feature of this plot is the decreased efficiency in the transitional zone between the electro-  
 2095 magnetic calorimeter barrel and endcap, specifically for  $1.37 < |\eta| < 1.52$ , implemented to  
 2096 maintain manageable background levels.

#### 2097 4.2.2.3 Electron Isolation

2098 Isolation for electrons in the study is quantified through two primary methods: calorimeter-  
 2099 based and track-based isolation variables.

2100 In the calorimeter-based approach, the raw transverse energy  $E_{T,\text{raw}}^{\text{isol}}$  is calculated by sum-  
 2101 ming the transverse energies of topological clusters found within a specific cone around the  
 2102 electron or photon cluster center. The EM particle energy  $E_{T,\text{core}}$  is subtracted out from this  
 2103 raw value. Corrections for energy leakage and pile-up are then applied. The final corrected  
 2104 calorimeter isolation variable is given by

$$E_T^{\text{coneXX}} = E_{T,\text{raw}}^{\text{isolXX}} - E_{T,\text{core}} - E_{T,\text{leakage}}(E_T, \eta, \Delta R) - E_{T,\text{pile-up}}(\eta, \Delta R), \quad (4-6)$$

2105 where  $\Delta R = \frac{XX}{100}$ . For electron working points, a cone size of  $\Delta R = 0.2$  is utilized, while for  
 2106 photons, cone sizes of  $\Delta R = 0.2$  and  $\Delta R = 0.4$  are employed.

2107 The track isolation variable  $p_T^{\text{coneXX}}$  considers the transverse momentum of selected tracks  
 2108 within a cone centered around the electron or photon. For electrons, a variable cone size  
 2109  $p_T^{\text{varconeXX}}$  is used, defined as

$$\Delta R = \min\left(\frac{10}{p_T[\text{GeV}]}, \Delta R_{\text{max}}\right) \quad (4-7)$$

2110 with  $\Delta R_{\text{max}}$  typically being 0.2. The tracks in this approach must have  $p_T > 1$  GeV and  
 2111  $|\eta| < 2.5$ , along with certain hit and hole requirements in the silicon detectors.

2112 The electron isolation strategies and their corresponding efficiencies are comprehensively  
 2113 detailed in Table 4–3. Figure 4–6 provides a comparative analysis of electron isolation ef-  
 2114 ficiencies for  $Z \rightarrow e^+e^-$  events collected during the 2018 Run 2 of the LHC. This figure

Working point	Calorimeter isolation	Track isolation
Gradient	$\epsilon = 0.1143 \times p_T + 92.14\%$ ( with $E_T^{\text{cone20}}$ )	$\epsilon = 0.1143 \times p_T + 92.14\%$ (with $p_T^{\text{varcone20}}$ )
HighPtCaloOnly	$E_T^{\text{cone20}} < \max(0.015 \times p_T, 3.5\text{GeV})$	-
Loose	$E_T^{\text{cone20}} / p_T < 0.20$	$p_T^{\text{varcone20}} / p_T < 0.15$
Tight	$E_T^{\text{cone20}} / p_T < 0.06$	$p_T^{\text{varcone20}} / p_T < 0.06$

**Table 4–3 Description of electron isolation benchmarks and their corresponding performance metrics. For the Gradient strategy, the transverse momentum ( $p_T$ ) is expressed in GeV. A consistent cone dimension of  $\Delta R = 0.2$  is employed for both calorimeter and track-based isolation methods, with a maximum cone size of  $\Delta R_{\text{max}} = 0.2$  designated for track isolation.**

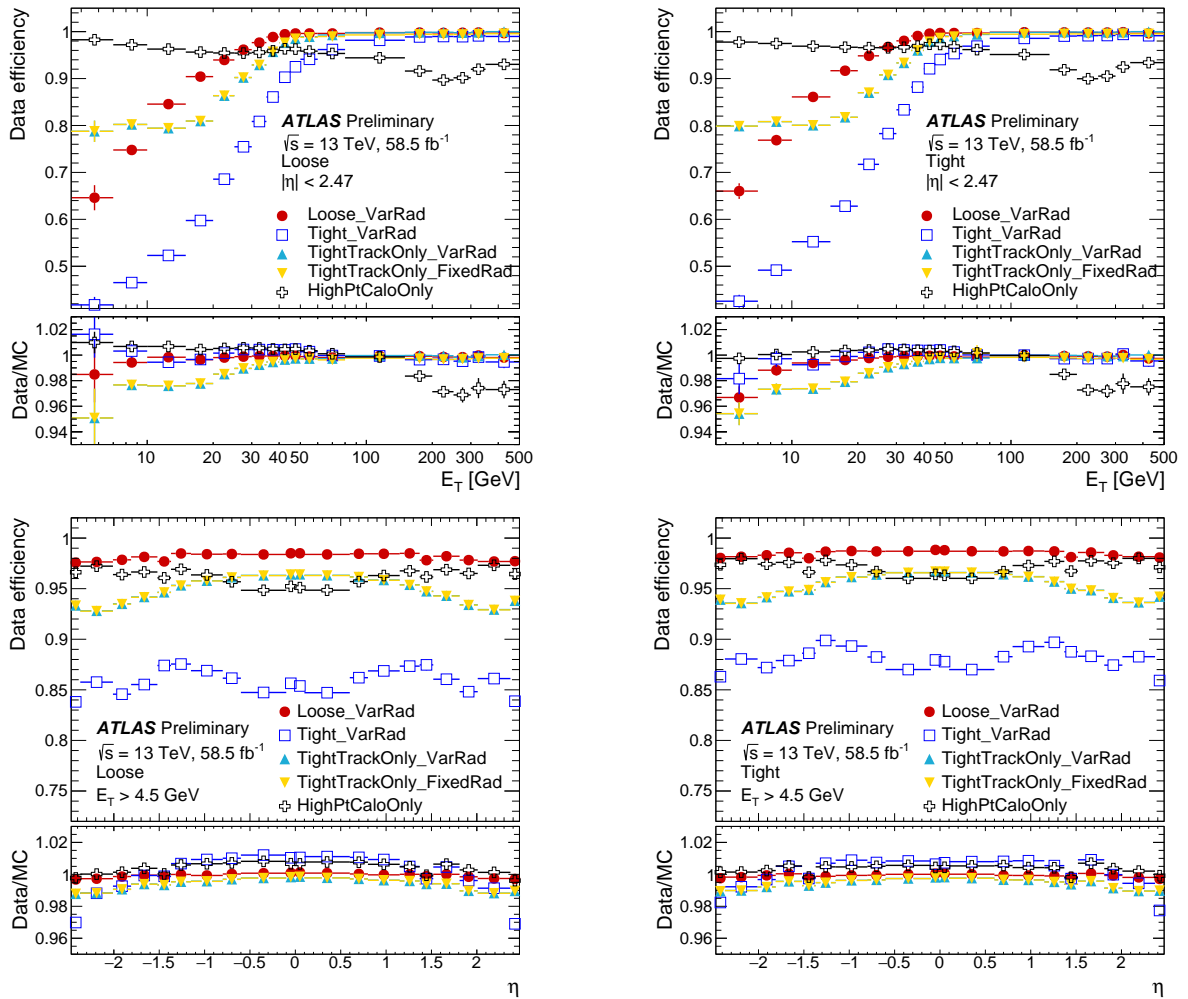


**Figure 4–6 Efficiency plots of electron Isolation working points<sup>[88]</sup>.**

2115 presents data based on two crucial parameters—transverse energy  $E_T$  and pseudorapidity  $\eta$ ,  
 2116 along with two selection criteria: Loose and Tight, which are derived from likelihood-based  
 2117 electron identification methods<sup>[97]</sup>.

### 2118 4.2.3 Photons

2119 In the ATLAS experiment, the techniques used for photon reconstruction closely paral-  
 2120 lel those used for electrons, as described in Section 4.2.2. Given the similarities in how both  
 2121 particles interact within the electromagnetic calorimeter, the foundational reconstruction and  
 2122 identification methodologies are almost identical. As such, this section will not revisit the  
 2123 reconstruction algorithms for photons, but will directly proceed to discuss the specific iden-  
 2124 tification (ID) and isolation procedures tailored for photons.

#### 2125 4.2.3.1 Photon Identification and Isolation

2126 The ATLAS experiment employs a multi-tiered identification system for photons, aimed  
 2127 to effectively segregate prompt, isolated photons from backgrounds predominantly from  
 2128 hadronic jets. This identification is based on a set of one-dimensional selection criteria,  
 2129 commonly referred to as shower shape variables in Table 4–2. The photon identification ef-  
 2130 ficiencies are measured in 68 bins of photon  $E_T$  and  $\eta$  for both converted and unconverted  
 2131 photons. The bin edges are set at

$$E_T = \{10, 15, 20, 25, 30, 35, 40, 45, 50, 60, 80, 100, 125, 150, 175, 250, 350, \infty\} \text{ GeV}$$

2132 and

$$|\eta| = \{0, 0.6, 1.37, 1.52, 1.81, 2.37\}.$$

2133 No measurements are conducted for  $|\eta| = \{1.37, 1.52\}$  due to its overlap with the transition  
 2134 region of the ATLAS calorimeter.

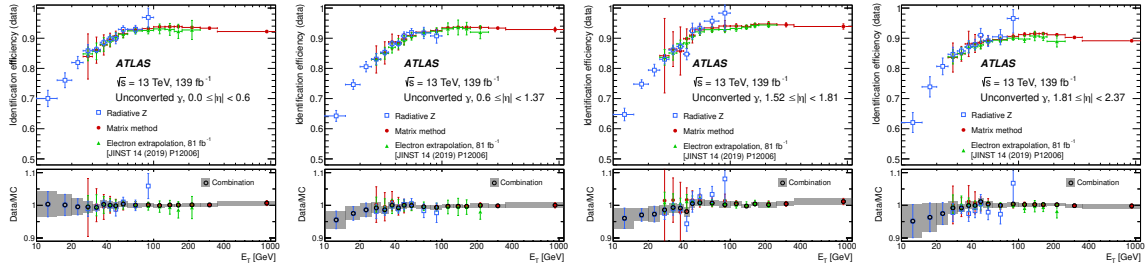
2135 Three distinct methods are employed to measure photon identification efficiencies<sup>[94]</sup>:

- 2136 1. **Radiative Z:** Using probe photons from  $Z \rightarrow \ell\ell\gamma$  decays with specific cuts on the  
 2137 invariant mass of the three-body system. The dominant uncertainty comes from low  
 2138 statistics at high  $E_T$  and MC generator modelling.
- 2139 2. **Matrix Method:** Application of a matrix method on an inclusive photon sample. The  
 2140 efficiency for Loose photon candidates to pass the Tight identification is extracted and

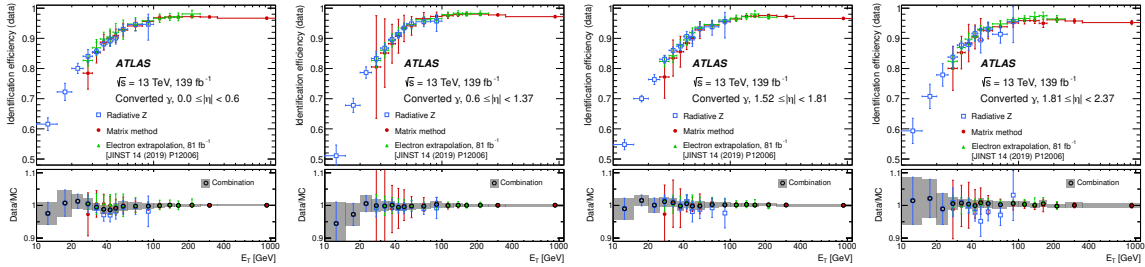
2141 corrected. The dominant systematic uncertainty arises from non-closure related to the  
 2142 assumption that isolation and identification efficiencies are independent.

2143 **3. Electron Extrapolation:** Using electrons from  $Z \rightarrow e^+e^-$  decays to emulate photon  
 2144 behavior. The method closure uncertainty is dominant at low  $E_T$  but decreases with  
 2145 increasing  $E_T$ .

2146 The efficiencies, as shown in Figure 4–7 are first measured in MC simulation, and the  
 2147 photon shower shapes are corrected to better align with the data<sup>[94]</sup>. The data-to-MC simu-  
 2148 lation ratios are then applied to account for residual differences between identification selec-  
 2149 tion efficiencies. These are determined from a weighted average of the three methods in each  
 2150  $E_T - \eta$  bin.



(a) Unconverted photons.



(b) Converted photons.

**Figure 4–7 Efficiency measurements for unconverted and converted photons across different  $\eta$  bins<sup>[98]</sup>.**

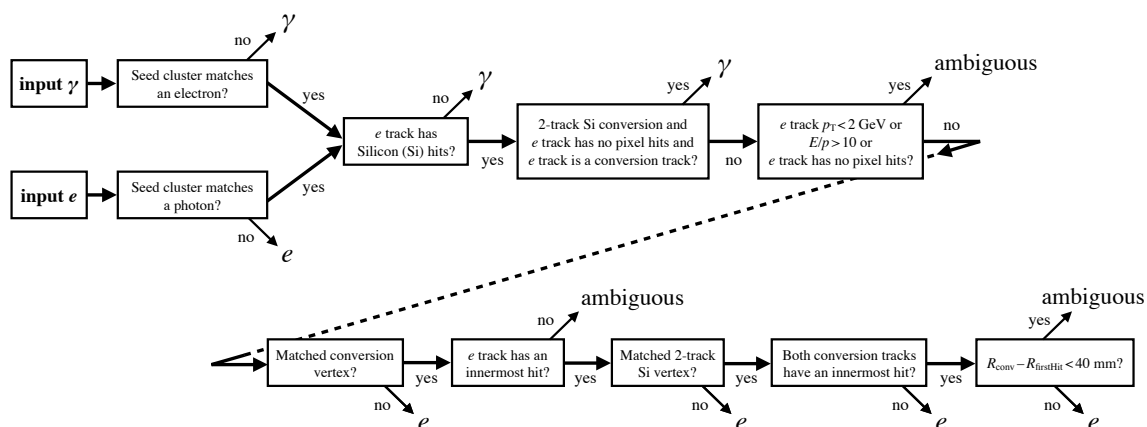
2151 Table 4–4 outlines three distinct operating points for photon isolation, focusing on both  
 2152 calorimeter and track isolation variables. The study<sup>[97]</sup> identifies discrepancies between data  
 2153 and simulations in the calorimeter-based isolation variables, which are then corrected using  
 2154 data-driven shifts. The effectiveness of these corrections is examined across two primary  
 2155 photon signatures: radiative Z decays and inclusive photons.

Working point	Calorimeter isolation	Track isolation
Loose	$E_T^{\text{cone}20} < 0.065 \times E_T$	$p_T^{\text{cone}20} / E_T < 0.05$
Tight	$E_T^{\text{cone}40} < 0.022 \times E_T + 2.45\text{GeV}$	$p_T^{\text{cone}20} / E_T < 0.05$
TightCaloOnly	$E_T^{\text{cone}40} < 0.022 \times E_T + 2.45\text{GeV}$	-

Table 4–4 Definition of the photon isolation working points<sup>[97]</sup>.

## 2156 4.2.3.2 Improvement of photon ID against electron fakes

2157 The ATLAS experiment employs a sophisticated method for resolving ambiguities be-  
 2158 tween electron and photon objects, primarily centered on a data structure known as a su-  
 2159 percluster. These superclusters for electrons and photons are generated independently and  
 2160 are subjected to an initial round of energy calibration and position correction. Following  
 2161 this, tracks are correlated with electron superclusters, and conversion vertices are matched  
 2162 with photon superclusters using the same algorithmic approach that was employed for EM  
 2163 topo-clusters.

Figure 4–8 Flowchart of the ambiguity resolution procedure for electron and photon objects<sup>[97]</sup>.

2164 A key point of differentiation arises here. If a seed cluster gives rise to both an electron  
 2165 and a photon supercluster, a specialized procedure outlined in Figure 4–8 is initiated. The  
 2166 aim is twofold: First, if a given object can be conclusively identified as a photon due to the  
 2167 absence of a 'good' associated track, then only a photon object is generated for downstream  
 2168 analysis. Similarly, if it can only be identified as an electron based on a good track and  
 2169 absence of a suitable photon conversion vertex, only an electron object is created. Second,

2170 if the object is intrinsically ambiguous, both electron and photon objects are generated and  
2171 marked explicitly for future classification depending on the requirements of specific analyses.

2172 After this ambiguity resolution step, another round of energy recalibration is performed,  
2173 given that the initial calibration precedes the final matching of tracks and conversion vertices.  
2174 This recalibration is conducted according to a previously described procedure.

2175 Lastly, discriminative variables such as shower shape are computed for both electrons  
2176 and photons. Interestingly, lateral shower shapes are independent of the clustering algorithm  
2177 used and are based solely on the position of the most energetically active cell. These variables  
2178 are pivotal for the final identification and classification of the electron and photon objects.

2179 With the current ambiguity solver, there is still a comparable amount of objects (electrons  
2180 and photons) which are labelled as “ambiguity” type. With the mixture of pair production and  
2181 photon conversion, separation between electrons and photons becomes challenging. This  
2182 study is considered as the Qualification Task (QT) in the ATLAS experiment<sup>[99]</sup>. In order  
2183 to have better photon identification efficiency and high electron fake rejection efficiency, it  
2184 is worth combining the topo-cluster information<sup>[100]</sup> with the tracks information, which pro-  
2185 vides a set of variables with high separation power and is studied in the ambiguity tool. The  
2186 ambiguity tool is a tool which is used during the EGamma reconstruction of electrons and  
2187 photons. Due to the parallel reconstruction of electrons and photons, it occurs that the same  
2188 constituents, such as topo-clusters and tracks, contribute to the formation of both electrons  
2189 and photons. To avoid to save all the combinations the ambiguity tool removes the easiest  
2190 cases when the reconstructed particles are “for sure not electron” or “for sure not photon”.  
2191 In this cases the particles are saved only under one hypothesis. In the other case the re-  
2192 constructed particles are saved both as electron and as photon and marked as “ambiguous”.  
2193 Using the ambiguity objects is a good starting point to improve the photon identification  
2194 criteria against photons faked by electrons.

2195 The single photon process “ $\gamma$  + jets” is chosen to be the physics sample in order to study  
2196 the variables of truth prompt photon. There are two main mechanisms to produce photon +  
2197 jets with p-p collision:

- 2198 • quark-gluon Compton scattering,  $qg \rightarrow q\gamma$
- 2199 • quark-antiquark annihilation,  $q\bar{q} \rightarrow g\gamma$

2200 In order to study the photon and the electron fakes, two full simulated samples have

2201 been considered, summarized in Table 4–5. The inclusive single photon sample generated  
 2202 with PYTHIA 8<sup>[101]</sup>, including the leading order  $\gamma + \text{jets}$  events are treated as signal. The  
 2203 background samples are generated with POWHEG + PYTHIA 8<sup>[102]</sup>, including the  $Z \rightarrow e^+e^-$   
 2204 process.

Process	Generator	DSID	Tag
$\gamma + \text{jets}$	PYTHIA 8	423101	e3904_s3126_r9364_r9315_p4191
		423102-423106	e3791_s3126_r9364_r9315_p4191
		423107-423112	e4453_s3126_r9364_r9315_p4191
$Z \rightarrow e^+e^-$	PowhegPythia8EvtGen	361106	e3601_e5984_s3126_r10201_r10210_p4323

**Table 4–5 Single Photon signal samples and  $Z \rightarrow e^+e^-$  background samples.**

2205 In the  $Z \rightarrow e^+e^-$  process, what is categorized as a "fake" photon is in fact one of the two  
 2206 electrons misidentified as a photon at the reconstruction level. Compared to a single-photon  
 2207 signal sample ( $\gamma + \text{jets}$ ), these fake photons typically exhibit lower  $p_T$  values, a consequence  
 2208 of originating from the decay of a 90 GeV object. Given these differences in basic kinematic  
 2209 variables ( $p_T$  and  $\eta$ ), it becomes essential to reweight the  $|\eta| - p_T$  distribution of these fake  
 2210 photons in  $Z \rightarrow e^+e^-$  events to align with the photon distribution in  $\gamma + \text{jets}$  signal events.  
 2211 This ensures that the optimization procedures that distinguish true photons from fake ones  
 2212 are not biased by these kinematic discrepancies. Thus, the  $Z \rightarrow e^+e^-$  process serves as  
 2213 an essential background process where one of the decay electrons is misclassified, affecting  
 2214 the overall kinematic distribution. By contrast, in true  $\gamma$  events, the kinematic variables are  
 2215 inherently different, necessitating this reweighting for a more accurate analysis.

2216 A direct 2D ( $p_T$  and  $\eta$ ) reweighting is applied on  $Z \rightarrow e^+e^-$  background samples in  
 2217 order to scale the yields of background samples to signal yields in each  $p_T$  and  $\eta$  bins. The  
 2218 reweighting factor is simply dividing the weighted sum of yields of " $\gamma + \text{jets}$ " samples by the  
 2219 the weighted sum of yields of  $Z \rightarrow e^+e^-$  samples for each  $p_T$  and  $\eta$  bins. In order to have  
 2220 finer reweighting, the kinematics binning strategy has been changed as followed:

- 2221 •  $p_T$  [GeV]: 13 bins
- 2222     – [25, 30), [30, 35), [35, 40), [40, 45), [45, 50), [50, 60), [60, 80), [80, 100)
- 2223     [100, 125), [125, 150), [150, 175), [175, 250), [250, 1500)
- 2224 •  $|\eta|$ : 6 bins

2225

– [0.0, 0.6), [0.6, 0.8), [0.8, 1.37), (1.52, 1.81), [1.81, 2.01), [2.01, 2.37)

2226

The 2D reweighting scale factors can be found in figure 4–9. The 1D basic kinematic

2227

distributions are summarized in figure 4–10.

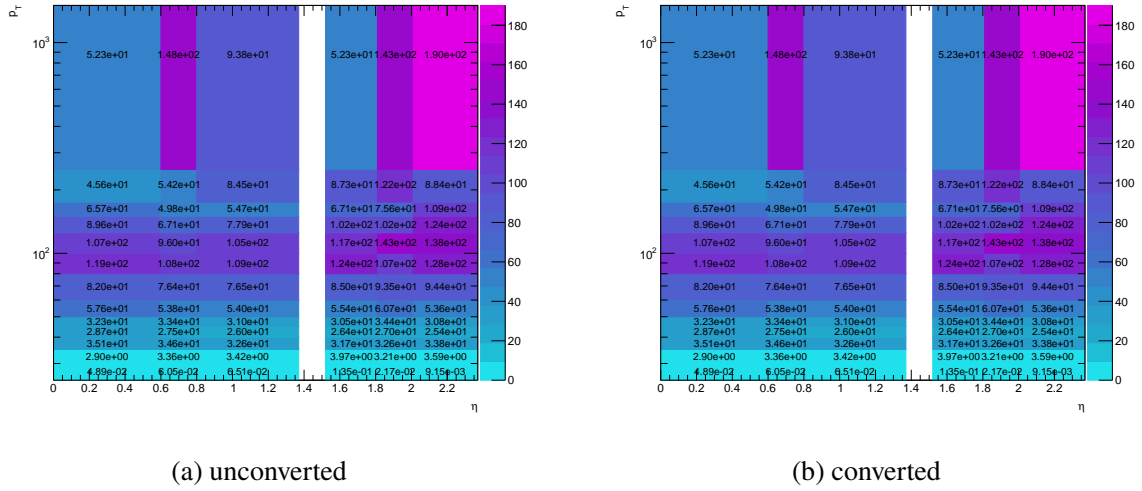


Figure 4–9 The distribution of reweighting scale factor (signal over background) in each  $p_T$  and  $\eta$  bin for both unconverted and converted case.

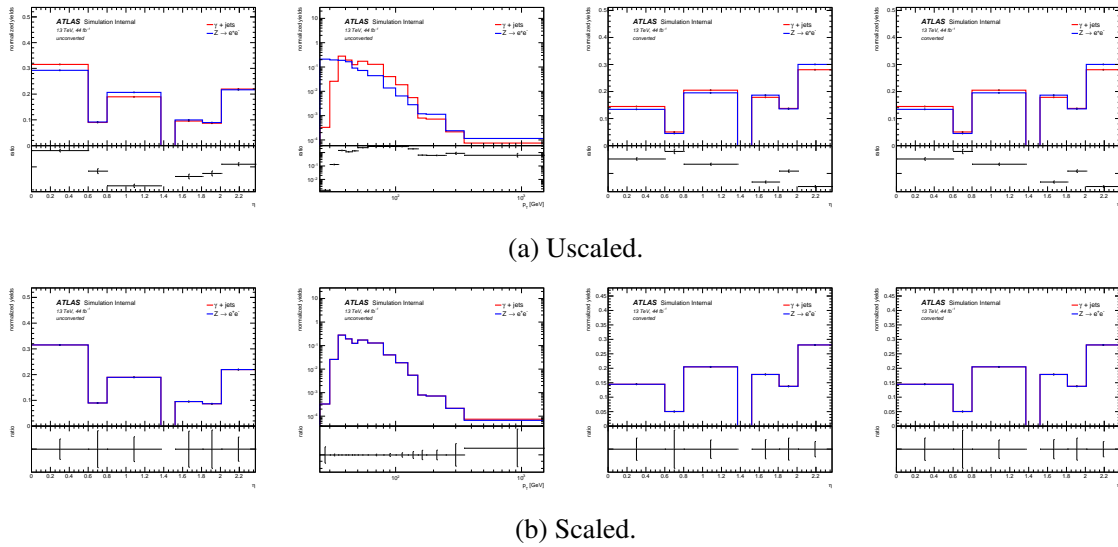


Figure 4–10 The 1D basic kinematic distributions before (top) and after (bottom) reweighting the basic kinematics of  $Z \rightarrow e^+e^-$  to those of  $\gamma + \text{jets}$  events.

2228

In order to achieve good object quality, several basic selections need to be applied:

- 2229 • Event Quality: duplicated events are removed.
- 2230 • Truth matching: signal photons are required to be matched to the truth photon, while
- 2231 background photons should be matched to the truth electron.
- 2232 • Object removal (only signal sample): each signal sample, aims at producing a definite
- 2233 photon  $p_T$  interval. Events out of the  $p_T$  intervals at the truth level are excluded.
- 2234 • Loose photon ID: loose identification working point for photons is the minimal re-
- 2235 quirement for good object quality.
- 2236 • Loose photon Isolation: FixedCutLoose\_proRec<sup>1</sup> working point is used in order to
- 2237 maximize the selection of good photon quality.
- 2238 • Ambiguity type: event is selected if there is at least one ambiguous photon. Yields of
- 2239 ambiguous events and total events are summarized in table 4–6.

		Ambiguous events	Total	Ratio
$\gamma + \text{jets}$	unconverted	679,097	5,368,897	11.3%
	converted	1,352,243	2,540,905	49.8%
$Z \rightarrow e^+e^-$	unconverted	1,564,090	3,125,334	50.7%
	converted	7,077,013	7,701,844	91.9%

**Table 4–6 Yields of pre-selected ambiguous events and total pre-selected events before ambiguity requirement for  $\gamma + \text{jets}$  and  $Z \rightarrow e^+e^-$ .**

2240 In order to improve the identification power to separate true photons from fake photons,  
 2241 this study uses a combination of variables from tracker and calorimeter. Many variables have  
 2242 been studied for distinguishing photon and photons faked by jets. They are the good starting  
 2243 to study photons faked by electrons. This analysis will focus on three sets of variables: shower  
 2244 shapes, Topo-clusters variables and ambiguity (tracker related) variables.

2245 For shower shapes, most of the variables have already been introduced in Table 4–2 and  
 2246  $R_{\text{had}}$  and  $R_{\text{had1}}$  has been combined as one variable with different  $|\eta|$  region. Three new shower  
 2247 shape variables from EM first layer are added to this study:

- 2248 •  $w_{\eta1}$  or  $w_{s3}$ : Lateral shower width calculated from three strips around the strip with the
- 2249 highest energy deposit.
- 2250 •  $F_{\text{side}}$ : Energy fraction outside core of three central cells, within seven cells

<sup>1</sup> isolation defined as  $E_T^{\text{cone20}} < 0.065p_T$  &&  $p_T^{\text{cone20}} < 0.05p_T$

- 2251 •  $\Delta E$ : Difference between the energy of the cell associated with the second maximum,  
 2252 and the energy reconstructed in the cell with the smallest value found between the first  
 2253 and second maxima.

2254 In total five topo-cluster variables are considered in this study (Only variables from the  
 2255 leading topo-cluster are included):

- 2256 •  $E_{\text{topo}}^+$ : total positive energy of the leading topo-cluster.  
 2257 •  $\sqrt{\langle r^2 \rangle}$ : the second moment of the radial (shortest) distance of cell to the shower axis.  
 2258 •  $\sqrt{\langle \lambda^2 \rangle}$ : the second moment of the longitudinal distance of cell from the cluster centre  
 2259 of gravity measured along shower axis.  
 2260 •  $|r|$ : the radial (shortest) distance of cell to the shower axis,  $\sqrt{x^2 + y^2 + z^2}$ .  
 2261 •  $\lambda_{\text{center}}$ : shower depth at its centroid of the topo-cluster.

2262 These variables were studied in detail, and have been proved to be the most discriminating  
 2263 among all moments in the previous analysis<sup>[100]</sup>. Other powerful variables such as signal  
 2264 moments can be studied in the future.

2265 In the current cutflow of the ambiguity tools in figure 4–8, there are 13 variables used to  
 2266 help separating electrons, photons and ambiguity type. In order to optimize the ambiguity  
 2267 efficiency on photon and electron fakes, the following 5 variables are chosen:

- 2268 •  $p_T^{\text{amb}}$ : the transverse momentum of the reconstructed electron which is reconstructed  
 2269 using the same cluster of the reconstructed photon.  
 2270 •  $p_T^{\text{amb,track}}$ : the  $p_T$  measured using the track associated to the reconstructed electron  
 2271 which is using the same cluster of the reconstructed photon.  
 2272 •  $E/P$ : the ratio of energy (measured from the cluster) and momentum (measured from  
 2273 the track) of the ambiguity object. If the track is a random track (for example if the  
 2274 object is a true unconverted photon and it is) this variable is expected to be far from 1.  
 2275 On the contrary if it is a real electron, this variable is expected to be close to 1.  
 2276 • PixelHits: number of pixel hits from the track.  
 2277 • SiliconHits: number of silicon hits from the track.

2278 Due to the detector performance and the reconstruction efficiency, the behaviour of pho-  
 2279 tons will be different in various  $p_T$  and  $\eta$  region. This prompts the kinematics region splitting  
 2280 so that in each region, an individual optimization is studied due to the distinct physics per-  
 2281 formance. The  $p_T$  and  $\eta$  binning is chosen to ensure enough statistics in both low  $p_T$  (large

2282  $Z \rightarrow e^+e^-$  statistics) and high  $p_T$  (large  $\gamma$  + jets statistics) region:

- 2283 •  $p_T$  [GeV]: 4 bins
- 2284     – [25, 40), [40, 55), [55, 80), [80, 1500)
- 2285 •  $|\eta|$ : 5 bins
- 2286     – [0, 0.6), [0.6, 1.37), (1.52, 1.81), [1.81, 2.01), [2.01, 2.37)

2287 Rectangular optimization is considered to be the strategy in this study. In some photon-  
 2288 related analyses such as the  $H \rightarrow \gamma\gamma$  analysis, the selections in the photon identification  
 2289 need to be partially reversed in order to estimate photon fakes. For this specific reason,  
 2290 BDT or deep learning cannot be used in the optimization strategy. There are 19 available  
 2291 discriminating variables, which are unnecessary for rectangular optimization. Rectangular  
 2292 optimization does not heavily rely on the correlation and the underlying effect. So a better  
 2293 way is to shrink the size of available discriminating variables to a relatively small number,  
 2294 reducing the training time. The selection of this number depends on the overall performance  
 2295 of the final results. The cases of 5, 9, 10, and 19 have been tested for the final performance.  
 2296 Results with 9 variables are better than with 5, and give similar performance than when using  
 2297 more variables. It is thus better to use 9 discriminating variables to train for more stable and  
 2298 smooth performance<sup>[99]</sup>. The variable separation ranking from the BDT method<sup>[95]</sup> can be a  
 2299 good guide to select discriminating variables, as listed in table 4–7. There are two strategies  
 2300 for selecting variables:

- 2301 1. Use the variable separation ranking from the inclusive region (not splitting  $p_T$  and  $\eta$   
 2302 into finer bins) and then choose the fixed top 9 variables for all sub-regions.
- 2303 2. Run the variable separation ranking for each  $p_T$  and  $\eta$  region, and then choose the top  
 2304 9 variables for each region.

2305 Both strategies have been studied and the difference in the final signal identification efficiency  
 2306 is small. This study will focus on the first strategy using fixed top 9 variables from the  
 2307 inclusive region. (The performance of these two methods is similar, but for simplicity and  
 2308 stability, method one is preferred.)

2309 Table 4–7 shows that the most discriminating variable for both unconverted and con-  
 2310 verted cases is from the ambiguity variables, which follows the physics intuition that the  
 2311 main difference for photon and electron is if the track is well matching the cluster. For the  
 2312 converted case, the main separating variables are ambiguity variables and Shower shapes.

rank	variable	separation	variable	separation
	unconverted		converted	
1	$E/P$	0.057100	PixelHits	0.071860
2	$p^{\text{amb,track}}$	0.031760	SiliconHits	0.037530
3	$R_\phi$	0.016490	$R_\phi$	0.026240
4	PixelHits	0.016280	$E/P$	0.021060
5	SiliconHits	0.015300	$\Delta E$	0.019500
6	$\sqrt{\langle r^2 \rangle}$	0.008835	$F_1$	0.018310
7	$\Delta E$	0.008517	$E_{\text{ratio}}$	0.016430
8	$E_{\text{ratio}}$	0.006444	$w_{\eta 2}$	0.009212
9	$w_{\eta 2}$	0.004687	$R_\eta$	0.007168
10	$F_1$	0.004124	$p_T^{\text{amb}}$	0.005839
11	$\sqrt{\langle \lambda^2 \rangle}$	0.002756	$\sqrt{\langle r^2 \rangle}$	0.005554
12	$\lambda_{\text{center}}$	0.002653	$\lambda_{\text{center}}$	0.003968
13	$p_T^{\text{amb}}$	0.002644	$E_{\text{topo}}^+$	0.001319
14	$R_{\text{had1}}$	0.002242	$ r $	0.001108
15	$R_\eta$	0.001873	$\sqrt{\langle \lambda^2 \rangle}$	0.000545
16	$w_{\eta 1}$	0.001412	$R_{\text{had1}}$	0.000455
17	$E_{\text{topo}}^+$	0.000907	$w_{\eta 1}$	0.000274
18	$ r $	0.000466	$p^{\text{amb,track}}$	0.000051
19	$w_{\text{tots1}}$	0.000049	$w_{\text{tots1}}$	0.000004

**Table 4–7 Separation power of shower shapes, topo-cluster, and ambiguity variables, which are retrieved from the BDT method from TMVA package, since the kCut method does not provide the variable ranking**

2313 Topo-cluster variables have a relatively low separation power compared with the other two  
 2314 sets of variables. But for the unconverted case, all three sets of variables play an impor-  
 2315 tant role in separation.  $E/P$  and  $R_\phi$  have a high rank for both two cases. So the final top 9  
 2316 discriminating variables are:

- 2317 • **unconverted:**  $E/P$ ,  $p^{\text{amb,track}}$ ,  $\sqrt{\langle r^2 \rangle}$ ,  $R_\phi$ ,  $\Delta E$ ,  $E_{\text{ratio}}$ , PixelHits, SiliconHits and  $w_{\eta 2}$ .
- 2318 • **converted:** PixelHits, SiliconHits,  $E/P$ ,  $E_{\text{ratio}}$ ,  $\Delta E$ ,  $R_\phi$ ,  $F_1$ ,  $w_{\eta 2}$ , and  $R_\eta$ .

2319 The finer rectangular optimization will be based on these 9 variables.

2320 The real application of this rectangular optimization is based on full photon container,  
 2321 which includes both photons identified as photons and photons identified as ambiguous ob-

2322 jects. The performance of this study can be measured using the background efficiency when  
 2323 the signal efficiency is at a certain level (80%, 60%, and 50%). The overall performance  
 2324 for the unconverted case is better than for the converted case. As expected, photons faked  
 2325 by electrons concentrate in the low  $p_T$  and low  $\eta$  regions. The fake photon rate decreases  
 2326 when  $p_T$  and  $\eta$  increase. The corresponding ROC curves are summarized in figure 4–11. Cut  
 2327 efficiencies both for  $\gamma$  + jets and  $Z \rightarrow e^+e^-$  when signal efficiency is 80%, 60% and 50%  
 2328 respectively can be found in Figure 4–12.

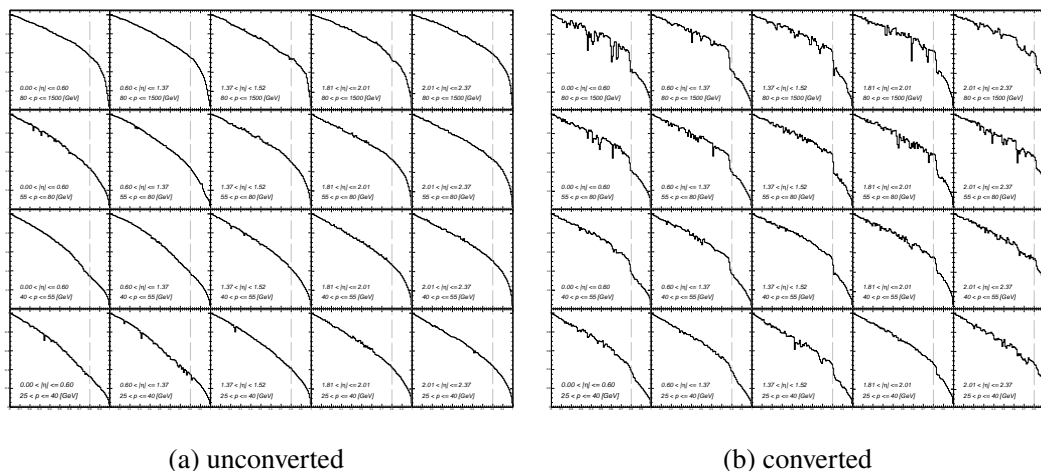


**Figure 4–11 The ROC performance of rectangular optimization for all  $p_T$  and  $\eta$  bins. The grey line is signal efficiency of 80%.**

## 2329 4.2.4 Muons

### 2330 4.2.4.1 Muon reconstruction

2331 Muons in the ATLAS experiment are predominantly identified based on their minimum-  
 2332 ionizing particle signature. This is evident either through a track in the Muon Spectrometer  
 2333 (MS) or unique energy depositions in the calorimeters. The primary sources of information  
 2334 for muon reconstruction<sup>[103-104]</sup> are the Inner Detector (ID) and MS tracking detectors, while  
 2335 calorimeter data is also used for refining track parameters and for MS-independent candidate  
 2336 tagging.

2337 Track reconstruction in the MS initiates with the identification of local, straight-line track  
 2338 segments that are based on hits in individual MS stations. These segments are detected via a  
 2339 Hough transform<sup>[105]</sup>. Preliminary track candidates are then formulated by applying a loose

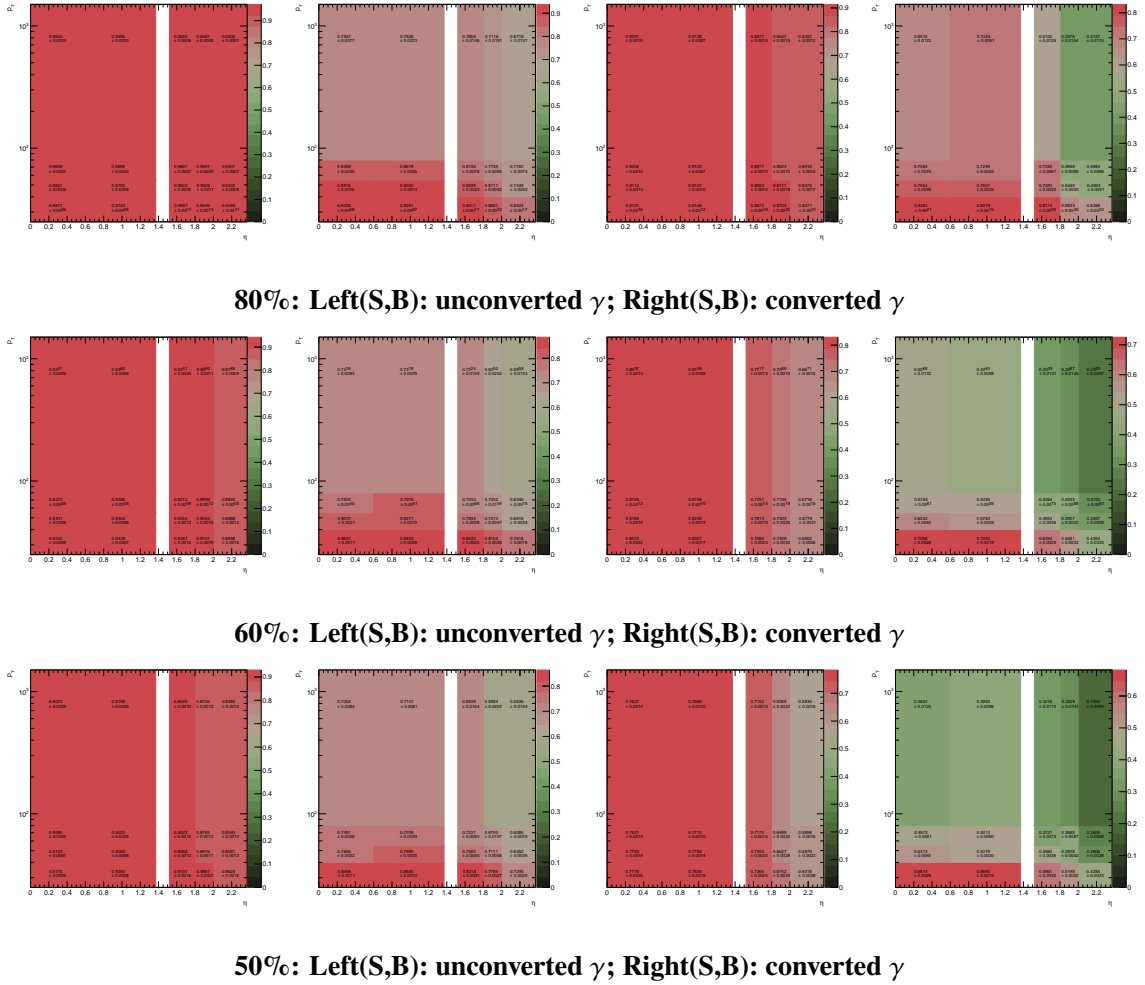


**Figure 4–12 Comparison of Photon Conversion Efficiency: Rows correspond to 80%, 60%, and 50% efficiency levels. Each row comprises unconverted and converted  $\gamma$  for signal and background.**

2340 pointing constraint to the interaction point (IP) via a parabolic trajectory approximation. This  
 2341 accounts for the muon bending in the magnetic field. A global  $\chi^2$  fit is employed to optimize  
 2342 the muon trajectory, taking into account possible interactions in the detector material and  
 2343 potential misalignments between detector chambers.

2344 Global muon reconstruction employs data from both the ID and MS along with calorimeter  
 2345 information. There are five main strategies for muon identification: combined (CB),  
 2346 inside-out combined (IO), muon-spectrometer extrapolated (ME), segment-tagged (ST), and  
 2347 calorimeter-tagged (CT). CB muons are identified by aligning MS and ID tracks followed by  
 2348 a combined track fit, factoring in energy loss in the calorimeters. For regions with  $|\eta| > 2.5$ ,  
 2349 a specific class of muons, known as silicon-associated forward (SiF) muons, is identified.

IO muons are detected by extrapolating ID tracks to the MS and requiring at least three loosely-aligned MS hits. In cases where an MS track cannot be aligned with an ID track, it is extrapolated to the beamline to identify an ME muon, thereby extending the detector's acceptance to  $|\eta| = 2.7$ . ST muons necessitate tight angular matching between an ID track extrapolated to the MS and at least one MS segment. CT muons are identified by examining energy depositions in the calorimeters consistent with a minimum-ionizing particle, applying a  $p_T$  threshold of 5 GeV to mitigate background noise.

Several advancements have been made in muon reconstruction techniques as compared to earlier models<sup>[106]</sup>:

- A parabolic trajectory in pattern recognition enhances segment matching across different stations.
- The introduction of SiF muons optimizes the utility of the ID near its acceptance boundaries.
- Alignment uncertainties are now incorporated into the track fits.
- The calorimeter-tagging algorithm has been fine-tuned for enhanced purity in regions with limited MS coverage.

#### 4.2.4.2 Muon identification

After reconstruction, high-quality muon candidates used for physics analyses are selected based on a set of requirements concerning the number of hits in different ID subdetectors and MS stations, track fit properties, and compatibility tests between the ID and MS measurements. A specific set of requirements for each muon type, as described in Section 4.2.4.1, is called a selection working point (WP). Multiple WPs are defined to cater to a variety of physics analyses involving muons.

Different analyses necessitate varying levels of prompt-muon identification efficiency, momentum measurement resolution, and background rejection capabilities. Special attention is paid to differentiating between muon candidates originating from light hadrons and those from heavy-flavor hadrons. The selection WPs primarily target the rejection of light hadrons which produce lower-quality tracks due to in-flight decays within the detector.

**The Loose, Medium, and Tight selection working points** The selection working points (WPs) are parameterized by several numerical criteria, often dependent on the pseudorapidity

2380  $\eta$  and transverse momentum  $p_T$  of the muon candidate. For the Medium WP, the criteria are:

- 2381 • ID Acceptance:  $|\eta| < 2.5$
- 2382 • Number of Precision Stations:  $\geq 2$  (Exception:  $|\eta| < 0.1$  can have one)
- 2383 •  $q/p$  Compatibility:  $< 7$

2384 For the Loose WP, it includes all muons passing the Medium WP plus additional cases:

- 2385 • For  $|\eta| < 0.1$ : Includes CT and ST muons
- 2386 • For  $p_T < 7$  GeV and  $|\eta| < 1.3$ : Includes IO muons with only one precision station

2387 Efficiency Increase:  $\approx 20\%$  for  $3 \text{ GeV} < p_T < 5 \text{ GeV}$ ;  $\approx 1\% - 2\%$  for  $p_T > 5 \text{ GeV}$ . The Tight  
2388 WP imposes additional constraints:

- 2389 •  $\chi^2/\text{ndf} < 8$  for the combined track fit
- 2390 • Optimized  $q/p$  and  $\rho_0$  based on  $p_T$  and  $|\eta|$

2391 Efficiency Loss:  $\approx 6\%$  for  $6 \text{ GeV} < p_T < 20 \text{ GeV}$ ; Background Reduction:  $> 50\%$  compared  
2392 to Medium WP.

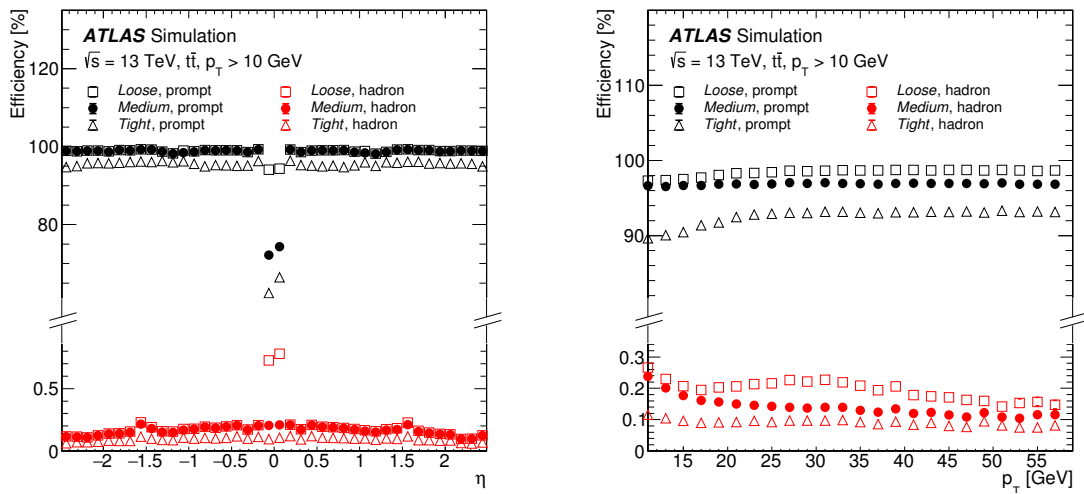


Figure 4–13 Efficiency vs  $\eta$  and  $p_T$  for different WPs in simulated  $t\bar{t}$  events<sup>[107]</sup>.

2393 In Figure 4–13, the efficiencies of various Working Points (WPs) are plotted as functions  
2394 of pseudorapidity ( $\eta$ ) and transverse momentum ( $p_T$ ) under the scope of simulated  $t\bar{t}$  events.  
2395 The figure serves a dual purpose: first, it reveals how the efficiency of each WP correlates  
2396 with  $\eta$  and  $p_T$ ; second, it differentiates between the efficiencies for muons that are promptly  
2397 produced and those that result from hadron decays.

### 4.2.4.3 Muon isolation

Selection requirements are imposed on the impact parameters of the muon track to reject muons originating from hadron decays in-flight and from non-hard-scattering interactions. Two impact parameters are considered: the transverse impact parameter  $|d_0|$  and the longitudinal impact parameter  $z_0$ . The  $|d_0|$  is measured relative to the actual beam position and is defined in terms of its significance,  $|d_0|/\sigma(d_0)$ , which is required to be less than three. The longitudinal distance  $|z_0| \sin \theta$  is used, where  $\theta$  is the polar angle of the muon track. For tracks with  $p_T > 10 \text{ GeV}$ , the impact parameter resolution is approximately  $10 \mu\text{m}$  in the transverse plane and  $50 \mu\text{m}$  in the longitudinal direction.

The isolation variable for track-based isolation is  $p_T^{\text{cone}}$ , defined as the scalar sum of  $p_T$  of ID tracks in an  $\eta - \phi$  cone of size  $\Delta R$  around the muon, excluding the muon itself.  $\Delta R$  varies as either 0.2 or  $\min(10 \text{ GeV}/p_T^\mu, 0.3)$ . Calorimeter-based isolation is denoted as  $E_T^{\text{topocone20}}$ , defined in a cone  $\Delta R = 0.2$  around the muon after correcting for pile-up effects. Particle-flow-based isolation combines track-based and calorimeter-based methods, using a weighting factor  $w = 0.4$  to optimize for heavy-flavour hadron decays.

Several isolation WPs are defined to balance various performance metrics. These are categorized based on track-based isolation variables, possibly with additional criteria for calorimeter-based or particle-flow-based isolation.

Isolation WP	Definition	Track $p_T$ requirement
PflowLoose*	$(p_T^{\text{varcone30}} + 0.4 \cdot E_T^{\text{neflow20}}) < 0.16 \cdot p_T^\mu$	$p_T > 500 \text{ MeV}$
PflowTight*	$(p_T^{\text{varcone30}} + 0.4 \cdot E_T^{\text{neflow20}}) < 0.045 \cdot p_T^\mu$	
Loose*	$p_T^{\text{varcone30}} < 0.15 \cdot p_T^\mu, E_T^{\text{topocone20}} < 0.3 \cdot p_T^\mu$	$p_T > 1 \text{ GeV}$
Tight*	$p_T^{\text{varcone20}} < 0.04 \cdot p_T^\mu, E_T^{\text{topocone20}} < 0.15 \cdot p_T^\mu$	
HighPtTrackOnly	$p_T^{\text{cone20}} < 1.25 \text{ GeV}$	$p_T > 1 \text{ GeV}$
TightTrackOnly*	$p_T^{\text{varcone30}} < 0.06 \cdot p_T^\mu$	
PLBDTLoose ( PLBDTTight )	$p_T^{\text{varcone30}} < \max(1.8 \text{ GeV}, 0.15 \cdot p_T^\mu)$ BDT cut to mimic TightTrackOnly (Tight) efficiency	$p_T > 1 \text{ GeV}$

**Table 4–8 Definitions of the muon isolation WPs.**

The various isolation WPs are summarized in Table 4–8, which also provides the criteria used for each WP in its second column and the minimum track  $p_T$  requirements in the third column. Some WPs are marked with an asterisk (\*) and exist in two variants: one where the cone  $\Delta R$  parameter decreases with  $p_T^\mu$  as  $\min(10 \text{ GeV}/p_T^\mu, 0.3)$ , and the other remaining

2420 constant at  $\Delta R = 0.2$  for  $p_T^\mu > 50$  GeV. A track-only isolation WP is the most robust with  
 2421 respect to pile-up and suffers the lowest drop in efficiency from nearby objects. Two loose  
 2422 isolation WPs are defined using track isolation and either calorimeter or neutral particle-flow  
 2423 isolation, and are optimized for cases where high prompt-muon efficiency is prioritized over  
 2424 rejection of non-prompt muons. Two tight isolation WPs are defined using track isolation  
 2425 and either calorimeter or neutral particle-flow isolation, and are optimized for cases suffering  
 2426 from large backgrounds from non-prompt muons. Moreover, two isolation WPs are defined  
 2427 using the prompt lepton BDT: PLBDTLoose and PLBDTTight. In addition to a loose cut  
 2428 on the track isolation, a  $p_T$ -dependent BDT threshold selection is applied in each of these to  
 2429 achieve the same prompt-muon efficiency as the TIGHTTrackOnly and TIGHT isolation WPs,  
 2430 respectively.

#### 2431 4.2.5 Hadronically decaying taus

2432 The reconstruction of  $\tau_{\text{had-vis}}$  candidates is based on seed jets formed using the anti- $k_r$   
 2433 algorithm with a distance parameter  $R = 0.4$ <sup>[108]</sup>. The seed jets must fulfill  $p_T > 10$  GeV and  
 2434  $|\eta| < 2.5$ . The vertex is determined based on the highest  $p_T$ -weighted fraction of tracks with  
 2435  $p_T > 0.5$  GeV within  $R = 0.2$ <sup>[109]</sup>.

2436 A set of BDTs classify tracks within  $R = 0.4$  into core and isolation tracks. Energy  
 2437 calibration is applied via pile-up subtraction and response correction within  $R = 0.2$ <sup>[106,110]</sup>.

##### 2438 4.2.5.1 RNN Tau Identification

2439 The RNN model uses a combination of low-level and high-level variables<sup>[111]</sup>. Low-level  
 2440 variables include  $p_{\text{track}T}$ ,  $d_{\text{track}0}$ ,  $z_{\text{track}0} \sin \theta$ ,  $\Delta\eta_{\text{track}}$ ,  $\Delta\phi_{\text{track}}$  and the number of hits in differ-  
 2441 ent detector layers. High-level variables comprise  $p_{\text{seed jet}T}$ ,  $f_{\text{cent}}$ ,  $f_{\text{lead track}}^{-1}$ ,  $\Delta R_{\text{max}}$ ,  $|S_{\text{lead track}}|$ ,  
 2442  $S_{\text{flight}T}$ ,  $f_{\text{trackiso}}$ ,  $f_{\text{EMtrack}}$ , and  $m_{\text{EM+track}}$ .

##### 2443 4.2.5.2 Performance Metrics

2444 The rejection power of the RNN-based tau identification is approximately twice as effi-  
 2445 cient as the BDT-based approach for both 1-prong and 3-prong  $\tau_{\text{had-vis}}$  candidates<sup>[109]</sup>. Work-  
 2446 ing points are defined as Very Loose, Loose, Medium, and Tight, with the Tight working  
 2447 point having an RNN score threshold of  $> 0.55$ .

2448 The figure 4–14 accompanying this section illustrates the comparative rejection power of

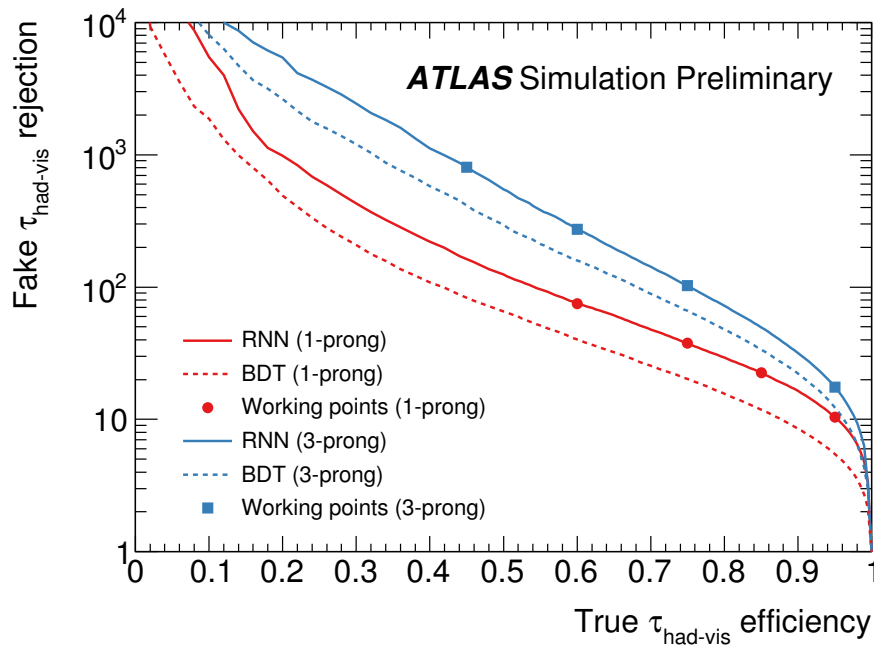


**Figure 4–14 Rejection power for different prong configurations of  $\tau_{\text{had-vis}}$  candidates, comparing RNN-based and BDT-based algorithms<sup>[112]</sup>.**

2449 RNN-based and BDT-based identification algorithms for 1-prong and 3-prong  $\tau_{\text{had-vis}}$  candi-  
 2450 dates. The RNN-based algorithm demonstrates a significantly higher rejection power across  
 2451 both prong configurations.

## 2452 4.2.6 Jets and b-jets

### 2453 4.2.6.1 Jet Reconstruction using PFlow Algorithm

2454 Two principal methodologies are used for jet reconstruction in the ATLAS experiment:  
 2455 calorimeter-based jet reconstruction and particle flow (PFlow) jet reconstruction. The former  
 2456 method utilizes topological clusters of calorimeter cells<sup>[92]</sup> and employs a Jet Energy Scale  
 2457 (JES) correction factor for calibration<sup>[113-114]</sup>. This approach, while widely used, has limita-  
 2458 tions in resolution. The latter, PFlow reconstruction<sup>[115]</sup>, integrates measurements from both  
 2459 the calorimeter and tracking systems to form an ensemble of 'particle flow objects,' aiming  
 2460 for enhanced granularity and resolution. The focus of the subsequent sections will be on  
 2461 the PFlow method, detailing its intricacies, advantages, and potential limitations in the jet  
 2462 reconstruction process.

2463 The PFlow algorithm operates through a systematic, multi-step procedure to optimally

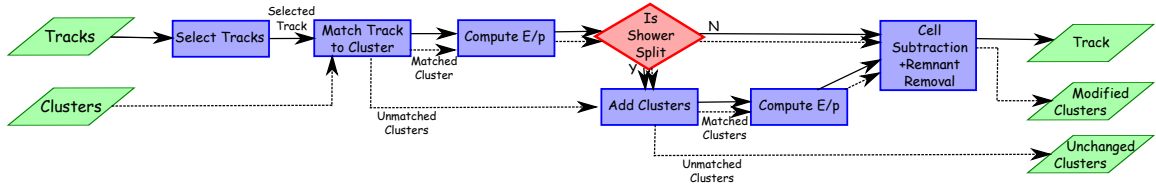


**Figure 4–15** Flow chart depicting the sequential steps of the Particle Flow algorithm from track selection to energy subtraction in the calorimeter<sup>[115]</sup>. The end result comprises charged particles, unmodified topo-clusters, and topo-cluster remnants with partially removed energy.

2464 utilize both tracking and calorimetric information for the reconstruction of hadronic jets and  
 2465 soft activity. The procedure is shown in Figure 4–15. Initially, tracks are sorted in descending  
 2466  $p_T$  order and selected based on stringent criteria. Each of these tracks is then matched to  
 2467 a single topo-cluster in the calorimeter. For each matched track-topo-cluster system, the  
 2468 algorithm calculates the expected energy deposition in the calorimeter based on the topo-  
 2469 cluster position and the track momentum. Given that a single particle may deposit energy in  
 2470 multiple topo-clusters, the algorithm evaluates this possibility and, when required, additional  
 2471 topo-clusters are added to the system to recover the full shower energy. Subsequently, cell-  
 2472 by-cell energy subtraction is performed for the matched topo-clusters. Any remnants that  
 2473 remain are removed if the residual energy aligns with the expected shower fluctuations of a  
 2474 single particle’s signal. This meticulous process is fundamental for the accurate calculation  
 2475 of the missing transverse momentum  $E_{\text{miss}}^T$ , in the event. The algorithm’s validation relies  
 2476 on single-pion and dijet Monte Carlo samples without pile-up, with charged pions typically  
 2477 contributing approximately two-thirds of the visible jet energy.

2478 PFlow jets are reconstructed using the anti- $k_t$  algorithm<sup>[108]</sup> with a radius parameter  $R =$   
 2479 0.4. Topo-clusters and tracks are the primary inputs, selected based on  $|z_0 \sin \theta| < 2$  mm  
 2480 to minimize pile-up contributions. Calorimeter jets employ the same algorithm but use LC-  
 2481 scale topo-clusters. For both jet types, jet ghost-area subtraction<sup>[116-117]</sup> is applied for pile-  
 2482 up correction, while a numerical inversion restores the jet response. The transverse energy  
 2483 density,  $\rho$ , in PFlow jets is computed from both charged and neutral PFlow objects, and is  
 2484 found to have a lower per-event value compared to calorimeter jets due to the exclusion of pile-  
 2485 up tracks. JES corrections account for variables such as charged fraction and energy fractions  
 2486 in different calorimeter layers. Data/MC comparisons<sup>[118]</sup> show a maximum deviation of 2%  
 2487 in jet characteristics, confirming the robustness of the PFlow algorithm for jet reconstruction.

## 2488 4.2.6.2 b-jet Identification using RNN

2489 Jet flavor tagging, particularly the identification of jets originating from bottom quarks  
 2490 (b-jets), plays an indispensable role in the ATLAS experiment. While the baseline high-  
 2491 level b-tagging algorithm termed MV2c10<sup>[119-120]</sup> in ATLAS, utilizes a Boosted Decision  
 2492 Tree (BDT) in combination with kinematic features and algorithms like IP3D, SV1, and Jet-  
 2493 Fitter, the nature of the data prompts an exploration into more advanced machine learning  
 2494 techniques. One key observation is that the transverse impact parameter significances ( $S_{d0}$ )  
 2495 of charged particles emanating from a b-hadron decay are not independently distributed but  
 2496 exhibit intrinsic correlations. MV2c10 and IP3D, which calculate per-flavor conditional like-  
 2497 lihoods in a product space of 29,400 bins—specifically  $35 \times 20 \times 14 \times 3$  for  $S_{d0}$ ,  $S_{z0}$ , and track  
 2498 category—operate under the assumption of feature independence and, thus, do not capture  
 2499 these interdependencies.

2500 These limitations are addressed by employing Recurrent Neural Networks (RNNs)<sup>[121]</sup>,  
 2501 which are capable of processing sequences of arbitrary lengths and capturing time-dependent  
 2502 correlations. Mathematically, given a sequence of tracks  $\{x_1, x_2, \dots, x_T\}$ , an RNN computes  
 2503 its internal state  $h_t$  as follows:

$$h_t = \phi(W_{hh}h_{t-1} + W_{xh}x_t + b_h),$$

2504 where  $\phi$  is an activation function, and  $W_{hh}, W_{xh}$  are the weight matrices. The final state  
 2505  $h_T$  serves as a fixed-dimensional representation of the jet's properties and can be further  
 2506 processed by a fully connected layer to yield a b-tagging discriminant. RNN variants like  
 2507 Long Short-Term Memory (LSTM) and Gated Recurrent Units (GRUs) further extend this  
 2508 capability, enabling the efficient learning of long-term dependencies via specialized gating  
 2509 mechanisms.

2510 In an evaluation of the RNN-based b-tagging algorithm, both the b-tagging efficiency  
 2511 and background rejection were systematically examined across varying jet  $p_T$  values. A  
 2512 discriminant function  $D_{\text{RNN}}$ , defined as

$$D_{\text{RNN}} = \ln \left( \frac{p_b}{f_c \cdot p_c + f_\tau \cdot p_\tau + (1 - f_c - f_\tau) \cdot p_{\text{light}}} \right),$$

2513 was employed, where  $f_c = 0.07$  and  $f_\tau = 0$ . At a preset b-tagging efficiency of 70%, the  
 2514 RNN algorithm surpassed IP3D, the baseline algorithm. Specifically, RNN exhibited a 2.5-  
 2515 fold increase in light-jet rejection and a 1.2-fold increase in c-jet rejection compared to IP3D.

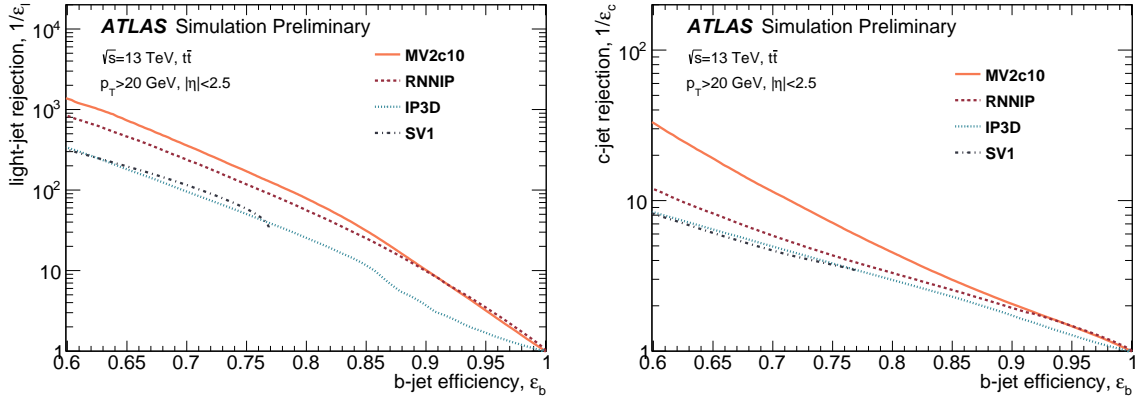


**Figure 4-16 Comparison of light-jet (left) and c-jet (right) rejection against b-tagging efficiency for jets with  $p_T > 20$  GeV and  $|\eta| < 2.5$ . Statistical errors are within 3%. MV2c10 serves as a high-level BDT-based benchmark, incorporating both IP3D and additional vertex metrics from JetFitter and SV1<sup>[122]</sup>.**

2516 The comparative performances of RNN and other algorithms are encapsulated in Figure 4–  
2517 16.

#### 2518 4.2.7 Missing Transverse Energy

2519 The reconstruction of  $E_T^{\text{miss}}$  in ATLAS is categorized into two contributions:

- 2520 • **Hard-Event Signals:** Comprise electrons, photons,  $\tau$ -leptons, muons, and jets.
- 2521 • **Soft-Event Signals:** Consist of charged-particle tracks not associated with hard ob-
- 2522 jects.

2523 The key components are constructed from  $E_{x(y)}^{\text{miss}}$ <sup>[123]</sup>:

$$E_{x(y)}^{\text{miss}} = - \sum_{i \in \text{hard objects}} p_{x(y),i} - \sum_{j \in \text{soft signals}} p_{x(y),j},$$

$$E_T^{\text{miss}} = \sqrt{(E_x^{\text{miss}})^2 + (E_y^{\text{miss}})^2},$$

$$\phi^{\text{miss}} = \tan^{-1} \left( \frac{E_y^{\text{miss}}}{E_x^{\text{miss}}} \right),$$

2524 And the full missing transverse momentum formula is:

$$\begin{aligned} \mathbf{E}_T^{\text{miss}} &= - \sum_{\text{selected electrons}} \mathbf{p}_T^e - \sum_{\text{accepted photons}} \mathbf{p}_T^\gamma - \sum_{\text{accepted } \tau\text{-leptons}} \mathbf{p}_T^{\tau} - \sum_{\text{selected muons}} \mathbf{p}_T^\mu - \sum_{\text{accepted jets}} \mathbf{p}_T^{\text{jet}} - \sum_{\text{unused tracks}} \mathbf{p}_T^{\text{track}} \\ &= \mathbf{E}_T^{\text{miss, e}} + \mathbf{E}_T^{\text{miss, } \gamma} + \mathbf{E}_T^{\text{miss, had}} + \mathbf{E}_T^{\text{miss, } \mu} + \mathbf{E}_T^{\text{miss, jet}} + \mathbf{E}_T^{\text{miss, track}} \end{aligned}$$

2525 In summary, the transverse missing energy does not play an important role in the di-  
 2526 Higgs  $b\bar{b}\tau^+\tau^-$  analysis. And for the multilepton analysis, this variable proves valuable in  
 2527 distinguishing W-related processes from other standard model processes.

## Chapter 5 SM Di-Higgs Searches in Multi-Lepton Final States

### 5.1 Introduction

This study focuses on the production of two Higgs bosons ( $HH$ ) through the mechanism of gluon-gluon fusion. More details for a thorough understanding of  $HH$  physics can be found in Section 2.3.2. The data used in this research comes from the ATLAS detector and is based on proton-proton collisions at a center-of-mass energy of  $\sqrt{s} = 13$  TeV. The dataset covers a total luminosity of  $140 \text{ fb}^{-1}$ , collected during the second run of the Large Hadron Collider.

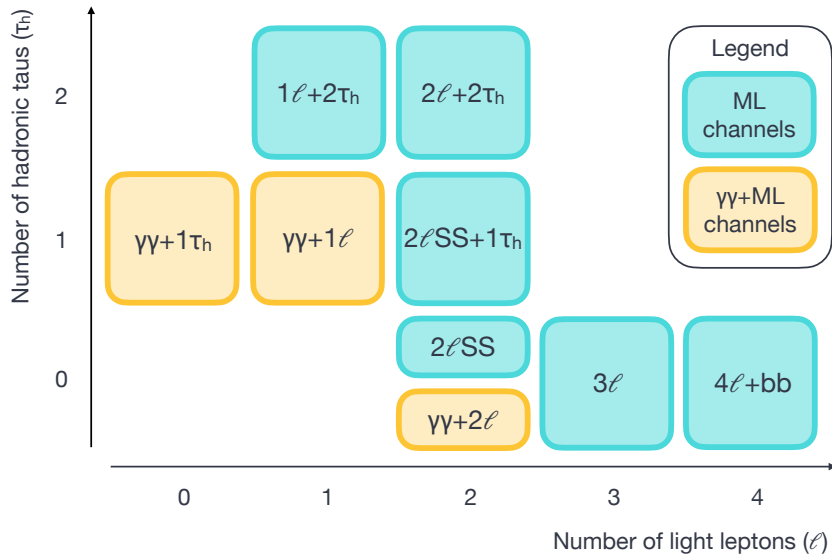


Figure 5-1 Overview of the multi-lepton final states considered.

In alignment with comprehensive analyses already undertaken by the ATLAS and CMS collaborations for this rare process, the present work performs a pioneering comprehensive search in multiple decay channels. These channels span  $VVVV$ ,  $VV\tau\tau$ ,  $\tau\tau\tau\tau$ ,  $\gamma\gamma VV$ , and  $\gamma\gamma\tau\tau$ , where  $V$  can be either a  $W^\pm$  or  $Z$  boson. The study further encompasses  $HH$  decays into  $b\bar{b}ZZ$ , where the  $Z$  bosons subsequently decay into leptons. Figure 5-1 systematically categorizes the explored final states. Channels featuring a combination of diphoton and multiple leptons ( $\gamma\gamma + ML$ ) are highlighted in yellow, while multi-lepton channels that also

involve hadronic taus are outlined in turquoise. Additionally, channels requiring both leptons to have identical electric charges are labeled with the acronym 'SS' (same-sign).

Six primary final states (pure-lepton), differentiated by the flavor and count of leptons, are considered:

- Tri-lepton channel without hadronic  $\tau$  candidates ( $3\ell$ ).
- Quad-lepton final states from  $H \rightarrow ZZ$  and accompanied by two  $b$ -jets ( $b\bar{b} + 4\ell$ ).
- Di-lepton same-sign channel without hadronic  $\tau$  candidates ( $2\ell SS$ ).
- Channel with two same-sign light leptons and a single hadronic  $\tau$  ( $2\ell SS + \tau_{\text{had}}$ ).
- Channel with two light leptons and two hadronic  $\tau$  candidates ( $2\ell + 2\tau_{\text{had}}$ ).
- Single light lepton and two hadronic  $\tau$  candidates ( $\ell + 2\tau_{\text{had}}$ ).

An auxiliary set of final states involves one Higgs decaying to di-photons and the other Higgs decaying to  $WW$ ,  $ZZ$ , or  $\tau\tau$  ( $\gamma\gamma + X$  channels):

- Single light lepton ( $\gamma\gamma + \ell$ ).
- Single hadronic  $\tau$  ( $\gamma\gamma + \tau_{\text{had}}$ ).
- Di-lepton final state, flexible to include either light or hadronic  $\tau$  leptons ( $\gamma\gamma + 2\ell$ ).

Given the multiplicity of final states available in multi-lepton analyses, attention is often concentrated on individual channels to enable a thorough investigation. For the scope of this dissertation, our focus will be explicitly on the 3-lepton channel. The intrinsic complexities and rich phenomenology of this channel warrant a dedicated analysis. Subsequent to this targeted investigation, the results will be aggregated with other channels to provide a more comprehensive picture of the  $HH$  process in the results section.

## 5.2 Data and Monte Carlo samples

### 5.2.1 Data Preparation and Analytical Framework

The analytical process employs data initially structured in the xAOD format, which is subsequently transformed into the DxAOD format via the HIGG8D1 derivation framework. This transition, termed the GN1 framework, has been customized from the ttH multilepton analysis to specifically cater to signal events featuring multilepton final states.

Data size minimization is achieved through slimming (elimination of redundant variables), thinning (removal of entire objects from the event record), and event-level skimming

2572 applied to both the collision data and Monte Carlo samples.

2573 This framework has been particularly optimized for the  $b\bar{b} + 4\ell$  channel, adhering to the  
 2574 lower  $p_T$  lepton thresholds as defined in the *baseline* lepton specification (see Section 5.3.1.3).  
 2575 Contrasting this, other multilepton channels employ more stringent lepton conditions (refer  
 2576 to Table 5–4), especially at the sample production phase (approximating the *Loose* criteria  
 2577 in Table 5–4 but utilizing FCLoose for lepton isolation).

2578 It is noteworthy that channels involving  $\gamma\gamma + X$  utilize a distinct derivation framework,  
 2579 named HIGG1D1, for their DxAOD production. This is complemented by the HGam frame-  
 2580 work, which inherently offers different lepton and  $\tau_{\text{had}}$  definitions when compared to multi-  
 2581 lepton channels.

## 2582 5.2.2 Data Collection and Quality

2583 The current study utilizes a data set comprising  $140 \text{ fb}^{-1}$  of proton-proton collision records  
 2584 acquired by the ATLAS detector in the energy range of  $\sqrt{s} = 13 \text{ TeV}$  spanning the years  
 2585 2015-2018. The data have been collected with a bunch crossing interval of 25 ns, with the  
 2586 IBL (Insertable B-Layer) activated. Data quality verifications<sup>[124]</sup> have been made in accor-  
 2587 dance with the predefined Good Run List (GRL). The GRLs used in this study are listed in  
 2588 Table 5–1.

Year	GRL XML File
2015	data15_13TeV.periodAllYear_DetStatus-v89-pro21-02_Unknown_PHYS_StandardGRL_All_Good_25ns.xml
2016	data16_13TeV.periodAllYear_DetStatus-v89-pro21-01_DQDefects-00-02-04_PHYS_StandardGRL_All_Good_25ns.xml
2017	data17_13TeV.periodAllYear_DetStatus-v99-pro22-01_Unknown_PHYS_StandardGRL_All_Good_25ns_TriggerNo17e33prim.xml
2018	data18_13TeV.periodAllYear_DetStatus-v102-pro22-04_Unknown_PHYS_StandardGRL_All_Good_25ns_TriggerNo17e33prim.xml

**Table 5–1 Good Run List XML Files by Year.**

## 2589 5.2.3 Monte Carlo Simulations

2590 The simulation framework relies on three distinct MC campaigns: mc16a, mc16d, and  
 2591 mc16e. These campaigns are tailored to replicate the conditions of the LHC runs for the  
 2592 years 2015-2016, 2017, and 2018, respectively, with particular emphasis on the interaction  
 2593 multiplicity per bunch crossing. To harmonize the simulated events with the actual collision  
 2594 data, a reweighting strategy is employed via the *PileupReweightingTool*<sup>[125]</sup>. The event sam-  
 2595 ples generated from these simulations are subsequently scaled according to their theoretical

2596 cross-sections.

### 2597 5.2.3.1 Background samples

2598 Monte Carlo simulations for various signal and background processes are based on con-  
 2599 figurations specified in Table 5–2. These configurations are also employed to estimate sys-  
 2600 tematic uncertainties (indicated in parentheses). Electroweak boson production ( $W$  or  $Z/\gamma^*$ )  
 2601 is denoted by  $V$ . Specific parton distribution functions (PDFs) and their roles in matrix el-  
 2602 ement (ME) calculations and parton showers are clarified. The underlying-event tune for  
 2603 the parton shower generator and the software versions used in event generation are outlined.  
 2604 Heavy flavor hadron decays are modeled using EVTGEN 1.2.0, and photon emission is ac-  
 2605 counted for by either the parton shower generator or PHOTOS. The mass settings for the top  
 2606 quark and SM Higgs boson are at 172.5 GeV and 125 GeV, respectively.

Process	Generator	ME order	Parton shower	PDF	Tune
$t\bar{t}W$	SHERPA 2.2.10 (MG5_AMC)	NLO (NLO)	SHERPA (PYTHIA 8)	NNPDF3.0 NNLO (NNPDF3.0 NLO)	SHERPA default (A14)
$t\bar{t}\bar{t}$	MG5_AMC (SHERPA 2.2.10)	NLO (NLO)	PYTHIA 8 (SHERPA)	NNPDF3.1 NLO (NNPDF3.0 NNLO)	A14 (SHERPA default)
$t\bar{t}H$	POWHEG-BOX <sup>powhegft</sup> (Powheg-BOX) (MG5_AMC)	NLO (NLO) (NLO)	PYTHIA 8 (HERWIG7) (PYTHIA 8)	NNPDF3.0 NLO <sup>[126]</sup> (NNPDF3.0 NLO) (NNPDF3.0 NLO)	A14 (H7-UE-MMHT) (A14)
$t\bar{t}(Z/\gamma^* \rightarrow l^+l^-)$	SHERPA 2.2.11 (MG5_AMC)	NLO (NLO)	SHERPA (PYTHIA 8)	NNPDF3.0 NNLO (NNPDF3.0 NLO)	SHERPA default (A14)
$t\bar{t} \rightarrow W^+bW^-\bar{b}l^+l^-$	MG5_AMC	LO	PYTHIA 8	NNPDF3.0 LO	A14
$t(Z/\gamma^*)$	MG5_AMC	NLO	PYTHIA 8	NNPDF2.3 LO	A14
$tW(Z/\gamma^*)$	MG5_AMC	NLO	PYTHIA 8	NNPDF2.3 LO	A14
$t\bar{t}W^+W^-$	MG5_AMC	LO	PYTHIA 8	NNPDF2.3 LO	A14
$t\bar{t}$	POWHEG-BOX (POWHEG-BOX)	NLO (NLO)	PYTHIA 8 (HERWIG7.1.3)	NNPDF3.0 NLO (NNPDF3.0 NLO)	A14 (H7-UE-MMHT)
$t\bar{t}\bar{t}$	MG5_AMC	LO	PYTHIA 8	NNPDF2.3 LO	A14
$s$ -, $t$ -channel, $Wt$ single top	POWHEG-BOX <sup>powhegstp.powhegstp2</sup>	NLO	PYTHIA 8	NNPDF3.0 NLO	A14
$VV$ , $qqVV$ , $lowm_{\ell\ell}$ , $VVV$	SHERPA 2.2.2	NLO	SHERPA	NNPDF3.0 NNLO	SHERPA default
$Z \rightarrow l^+l^-$	SHERPA 2.2.1	NLO	SHERPA	NNPDF3.0 NLO	SHERPA default
$Z \rightarrow l^+l^-$ (matCO)	POWHEG-BOX	NLO	PYTHIA 8	CTEQ6L1 NLO	A14
$Z \rightarrow l^+l^-+(\gamma^*)$	POWHEG-BOX	NLO	PYTHIA 8	CTEQ6L1 NLO	A14
$W$ +jets	SHERPA 2.2.1	NLO	SHERPA	NNPDF3.0 NLO	SHERPA default
$VH$	POWHEG-BOX	NLO	PYTHIA 8	NNPDF3.0 NLO	A14

**Table 5–2 Event generation configurations for signal and background processes.**

2607 Pile-up is modeled through minimum-bias events generated via PYTHIA 8.186<sup>[127]</sup>, using

2608 the NNPDF2.3LO PDFs and the A3 parameter set<sup>[128]</sup>. These are then overlaid onto the pri-  
2609 mary hard-scatter events based on the luminosity profiles of the recorded data. The generated  
2610 events are subjected to a simulation of the ATLAS detector's geometry and response through  
2611 GEANT4<sup>[129]</sup>. The same reconstruction software is applied as in the case of real data. Calibra-  
2612 tions ensure that particle candidate selection efficiencies, energy scales, and resolutions are  
2613 consistent with those determined from control samples in real data. The simulated datasets  
2614 are normalized to their computed cross-sections, evaluated to the highest order available in  
2615 perturbation theory.

### 2616 5.2.3.2 Signal Samples

2617 For ggF mode, events are generated at NLO accuracy using Powheg-Box-V2 for the ma-  
2618 trix element and PYTHIA8 (A14 tune) for parton showering and hadronization. The PDF set  
2619 employed is NNPDF 2.3 LO. Heavy-flavor hadron decays are modeled using EvtGen. Detec-  
2620 tor effects are accounted for by AlfastII (AF2). Lepton filters target multilepton final states,  
2621 focusing on configurations such as  $2\ell 0\tau$ ,  $2\ell 1\tau$ ,  $3\ell 0\tau$ , among others. Lepton kinematics are  
2622 restricted by a MultiLeptonFilter at  $p_T > 7$  GeV and  $|\eta| < 3$ . Alternative ggF samples are pro-  
2623 duced with POWHEGBox-V2 interfaced to HERWIG7, employing the PDF4LHC15 PDF set  
2624 to assess parton shower uncertainties. They adopt the same filtering strategy as the nominal  
2625 samples.

2626 For VBF mode, events are generated at LO with MADGRAPH5\_AMC@NLO. Parton  
2627 shower and hadronization are handled by PYTHIA8 using the A14 tune and the NNPDF 2.3  
2628 LO PDF set. HF hadron decays and detector effects are modeled similarly to the ggF case.  
2629 Lepton filters are applied to target various final states.

## 2630 5.3 Analysis Strategy

2631 The analysis targets a final state characterized by three leptons, a channel that offers a  
2632 relatively clean signal with a low branching ratio. The three-lepton requirement inherently  
2633 acts as an effective filter against multi-jet backgrounds. This is augmented by employing  
2634 advanced lepton identification and isolation working points, specifically the PromptLepton-  
2635 Veto (PLV), thereby further mitigating backgrounds arising from fake leptons, which were  
2636 dominant in prior analyses<sup>[130]</sup>. Before any selection is applied, object definitions are estab-

lished for leptons, jets, and other relevant physics objects, which provide the foundation for the subsequent analysis stages. The major background contamination in this channel originates from the  $WZ \rightarrow 3\ell 0\tau_h$  process. Given that the dominant backgrounds are largely EWK processes, targeted selection cuts are optimized to suppress these while retaining high signal efficiency.

The analysis pipeline comprises the following main stages:

1. **Pre-selection:** A set of baseline criteria applied to all events for initial filtering. Detailed pre-selection criteria are elaborated in Section 5.3.4.2.
2. **Background Modelling:** Four control regions (CRs) are defined to model various background contributions. These CRs are crucial for estimating background rates and for the validation of the analysis methodology. For details, refer to Section 5.3.5.
3. **Signal Region Optimization:** Multi-variate analysis techniques employing Boosted Decision Trees (BDT) are used to finely tune the selection criteria, maximizing signal significance in Section 5.3.6.
4. **Statistical Analysis:** A comprehensive statistical framework is employed for signal extraction, incorporating both statistical and systematic uncertainties, to derive the final results.

### 5.3.1 Object definitions

This section describes the methodologies for defining key objects with respect to multi-lepton channels. Criteria on data corruption or significant calorimeter noise result in event exclusion.

#### 5.3.1.1 Selection of Primary Vertices

For multilepton channels, the primary vertex is designated as the one with the maximal  $\sum p_T^2$  of its constituent tracks, following the criteria outlined in<sup>[131]</sup>.

#### 5.3.1.2 Event Triggering

In multilepton channels, an array of single-lepton and di-lepton triggers, pertinent to the 2015 - 2018 dataset, is listed in Table 5–3. These triggers are exempt from prescaling and are derived from the  $t\bar{t}H$  multilepton  $80 \text{ fb}^{-1}$  analysis<sup>[132]</sup>. An inclusive OR condition is imposed between di-lepton (DL) and single-lepton (SL) triggers when at least two light leptons are

2666 involved. For scenarios involving a single light lepton and two  $\tau_{\text{had}}\tau_{\text{had}}$ , non-prescaled single-  
2667 lepton triggers are required.

Single lepton triggers (2015)	
$\mu$	HLT_mu20_iloose_L1MU15, HLT_mu50
$e$	HLT_e24_lhmedium_L1EM20VH, HLT_e60_lhmedium, HLT_e120_lhloose
Dilepton triggers (2015)	
$\mu\mu$ (asymm.)	HLT_mu18_mu8noL1
$ee$ (symm.)	HLT_2e12_lhloose_L12EM10VH
$e\mu, \mu e$ ( $\sim$ symm.)	HLT_e17_lhloose_mu14
Single lepton triggers (2016)	
$\mu$	HLT_mu26_ivarmedium, HLT_mu50
$e$	HLT_e26_lhtight_nod0_ivarloose, HLT_e60_lhmedium_nod0, HLT_e140_lhloose_nod0
Dilepton triggers (2016)	
$\mu\mu$ (asymm.)	HLT_mu22_mu8noL1
$ee$ (symm.)	HLT_2e17_lhvloose_nod0
$e\mu, \mu e$ ( $\sim$ symm.)	HLT_e17_lhloose_nod0_mu14
Single lepton triggers (2017 / 2018)	
$\mu$	HLT_mu26_ivarmedium, HLT_mu50
$e$	HLT_e26_lhtight_nod0_ivarloose, HLT_e60_lhmedium_nod0, HLT_e140_lhloose_nod0
Dilepton triggers (2017 / 2018)	
$\mu\mu$ (asymm.)	HLT_mu22_mu8noL1
$ee$ (symm.)	HLT_2e24_lhvloose_nod0
$e\mu, \mu e$ ( $\sim$ symm.)	HLT_e17_lhloose_nod0_mu14

**Table 5–3 List of lowest  $p_T$ -threshold, un-prescaled single lepton and di-lepton triggers used for 2015-2018 data taking.**

2668 Trigger corrections for simulation are computed event-wise with the TrigGlobalEfficien-  
2669 cyCorrection package<sup>[133]</sup>. Any relevant scale factors for light lepton identification and iso-  
2670 lation are appropriately integrated into the MC weight.

## 2671 5.3.1.3 Lepton Working Points and Definitions

2672 In signal events, leptons are primarily produced through the leptonic decays of  $WW/ZZ$ ,  
 2673 which are themselves produced by Higgs decays. Harmonized Working Points (WPs) have  
 2674 been developed to optimize performance in both  $2\ell SS$  and  $3\ell$  channels while minimally af-  
 2675 fecting the tau-involved channels.

2676 For multilepton channels, three distinct levels of light lepton selection criteria are imple-  
 2677 mented depending on the final state's object composition. These criteria are referred to as  
 2678 "Baseline" (B), "Loose" (L), and "Tight" (T), as defined in Table 5–4. The Baseline criteria  
 2679 are exclusively used in  $b\bar{b} + 4\ell$  channels to augment the signal sensitivity. For categories  
 2680 other than  $b\bar{b} + 4\ell$ , the *Loose* definition is applied to establish channel orthogonality. Stricter  
 2681 definitions are utilized in channels with up to two light leptons and a single hadronically de-  
 2682 caying tau to maximize signal sensitivity and minimize background interference. Specific  
 2683 lepton criteria for electrons, muons are elaborated in Sections 5.3.1.4, 5.3.1.5, respectively.

	$e$			$\mu$		
	B	L	T	B	L	T
Isolation	None	PLVLoose	PLVTight	None	PLVLoose	PLVTight
Identification	LooseLH		TightLH	Loose		Medium
Charge MisID BDT	No	Yes	Yes	N/A	N/A	N/A
Ambiguity Resolution	No	Yes	Yes	N/A	N/A	N/A
$ d_0 /\sigma_{d_0}$	< 5			< 3		
$ z_0 \sin \theta $	< 0.5 mm					

**Table 5–4 Definitions of Baseline, Loose, and Tight criteria in multilepton channels.**

## 2684 5.3.1.4 Electrons

2685 The selection criteria for electron candidates in different multilepton channels involve  
 2686 several key elements:

- 2687 • Electrons are reconstructed through matching energy deposits in the electromagnetic  
 2688 calorimeter with tracks in the inner detector.
- 2689 • Baseline electrons are required to have  $p_T > 4.5$  GeV and  $|\eta| < 2.5$ . Electrons within  
 2690 the calorimeter transition region  $1.37 < |\eta| < 1.52$  are excluded.
- 2691 • Stringent cuts on  $d_0$  and  $z_0$  ensure that electrons originate from a primary vertex.

- 2692 • Employing a likelihood-based identification, the working points "LooseLH" and "TightLH"
- 2693 are used for Baseline/Loose and Tight electron candidates, respectively.
- 2694 • Loose electrons should pass the *PLVLoose* working point<sup>1</sup> to ensure event isolation<sup>[134]</sup>.
- 2695 • For stricter selection beyond Baseline, additional criteria like charge misidentification
- 2696 BDT and ambiguity selection (details in Section 4.2.3.2) are implemented to reduce
- 2697 background contributions.
- 2698 • For Tight electrons, the *PLVTight* Isolation working point and the *TightLH* ID are
- 2699 mandated.

### 2700 5.3.1.5 Muons

2701 The selection criteria for muon candidates in multilepton channels are outlined below:

- 2702 • Muons are reconstructed using data from both the Muon Spectrometer and the Inner
- 2703 Detector.
- 2704 • Muon candidates must satisfy  $p_T > 3$  GeV and  $|\eta| < 2.5$ .
- 2705 • Two identification working points are used. Baseline muons are required to pass the
- 2706 "Loose" working point, while tighter criteria employ the "Medium" working point.
- 2707 • Similar to electrons, muons must pass *PLVLoose* isolation criteria for baseline selec-
- 2708 tion. Loose muons are required to fulfill *PLVLoose*, while Tight muons are selected
- 2709 from *PLVTight*.
- 2710 • The criteria for both transverse and longitudinal impact parameters are harmonized
- 2711 with electrons. Specifically,  $|d_0|/\sigma_{d_0} < 3$  and  $z_0 < 0.5$  mm.

### 2712 5.3.2 Jet and b-jet

2713 The key elements concerning the selection and definition of jets and b-jets in the analysis  
2714 are itemized below:

- 2715 • The anti- $k_t$  algorithm with a radius parameter  $R = 0.4$  is used, operating on particle-
- 2716 flow (PFlow) objects.
- 2717 • For ML channel, AntiKt4EMPFlowJets\_BTagging201903 is employed.
- 2718 • Events must pass the LooseBad working point as recommended by the Jet- $E_T^{\text{miss}}$  group.
- 2719 A Tight Jet Vertex Tagger (JVT) working point is applied for  $p_T < 60$  GeV and  $|\eta| <$
- 2720 2.4.

---

<sup>1</sup> PromptLeptonVeto

- 2721 • Kinematic Selection:
- 2722 –  $p_T > 25$  GeV
- 2723 –  $|\eta| < 2.5$
- 2724 –  $|y| < 4.4$
- 2725 • Flavour Tagging: Utilizes a deep learning algorithm known as DL1r<sup>[135]</sup>, which has
- 2726 been re-optimized in 2019. The b-tagging working point with a 77% efficiency is
- 2727 selected.

2728 The choices made for the jet and b-jet selections, including specific working points and

2729 efficiencies, are aimed at maximizing orthogonality to other diHiggs analyses. Associated

2730 scale factors for JVT and b-tagging are integrated into the MC event weight calculations.

2731 More details of these selection criteria can be found in the relevant studies<sup>[136-137]</sup>.

### 2732 5.3.3 Overlap Removal

2733 Overlap removal is essential to eliminate double-counting of reconstructed objects, which

2734 may occur due to the parallel use of different algorithms for object reconstruction. The procedure

2735 employed in this analysis is based on the ASG overlap removal tool in AnalysisTop<sup>[138]</sup>.

2736 The criteria for overlap removal are listed in Table 5–5.

Kept Object	Removed Object	Condition
Electron	Calorimeter Muon	Sharing same track
Non-calorimeter Muon	Electron	Sharing same track
Electron	Jet	$\Delta R < 0.2$
Jet	Electron	$\Delta R < 0.4$
Muon	Jet	$n_{\text{track}} < 3$ and $\Delta R < 0.2$
Muon	Jet	$n_{\text{track}} < 3$ and Ghost-associated to muon ID track
Jet	Muon	$\Delta R < 0.4$
Electron	Tau	$\Delta R < 0.2$
Combined-type Muon	Tau	$p_T > 2$ GeV and $\Delta R < 0.2$
Tau	Jet	$\Delta R < 0.2$
Electron/Muon	Photon	$\Delta R < 0.4$
Photon	Jet	$\Delta R < 0.4$

**Table 5–5 Summary of Overlap Removal Criteria in Multilepton Channels.**

### 2737 5.3.4 Event Selection

#### 2738 5.3.4.1 Signal Topology

2739 In the targeted 3-lepton signal, we primarily focus on the di-Higgs decay channels  $WWWW$ ,  
2740  $WWZZ$ , and  $WW\tau\tau$ , which collectively yield the combined final state of  $3\ell 0\tau_h + \text{jets}$ . Among  
2741 these channels,  $WWWW$  is dominant, comprising over 60% of the branching ratios.

2742 The  $3\ell$  channel can be categorized into various sub-channels based on the lepton flavor  
2743 composition:

- 2744 •  $\ell ee$ : Features a same-flavour, same-sign electron pair. Represented as  $\mu^\mp e^\pm e^\pm$  or  
2745  $e^\mp e^\pm e^\pm$ .
- 2746 •  $\ell\mu\mu$ : Features a same-flavour, same-sign muon pair. Represented as  $\mu^\mp e^\pm e^\pm$  or  $e^\mp \mu^\pm \mu^\pm$ .
- 2747 •  $\ell e\mu$ : Contains no same-flavour, same-sign lepton pairs. Represented by four combi-  
2748 nations:  $\mu^\mp e^\pm \mu^\pm$ ,  $\mu^\mp \mu^\pm e^\pm$ ,  $e^\mp \mu^\pm e^\pm$ ,  $e^\mp e^\pm \mu^\pm$ .

2749 Due to statistical limitations in each sub-channel, the analysis treats these sub-channels  
2750 inclusively. Variables that enhance the signal sensitivity are elaborated in Section 5.3.6.  
2751 The analysis employs MVA techniques using BDT. Post-MVA, the background validation  
2752 region and the signal region are defined based on the BDTG score, with  $\text{BDTG} \leq 0.55$  and  
2753  $\text{BDTG} > 0.55$  respectively, according to the maximum of significance.

#### 2754 5.3.4.2 Pre-Selection

2755 Events are required to pass the following common selection, and the corresponding cut-  
2756 flow is summarized in Table 5–6:

- 2757 • **Trigger:**
  - 2758 – Global Trigger Decision required.
  - 2759 – Utilization of either single-lepton or di-lepton triggers.
- 2760 • **Lepton multiplicity:**
  - 2761 – Exactly three leptons with a total electric charge of  $\pm 1$ .
  - 2762 – Events are classified by their lepton flavour/charge composition as  $l_0 l_1 l_2$ , where  
2763 the lepton with opposite charge with respect to the other two is noted as lepton  
2764 index "0". The remaining lepton that is nearest to  $l_0$  in  $\Delta R$  is given the index "1"  
2765 and the final lepton is noted as lepton "2".
  - 2766 –  $p_T^0 > 10 \text{ GeV}$  and  $p_T^{1,2} > 15 \text{ GeV}$ .

- 2767 – Lepton 0 is required to pass the loose selection while lepton 1 and 2 are required  
 2768 to pass the tight selection. The details of the corresponding working points can  
 2769 be found in Section 5.3.1.3.
- 2770 • **Hadronic tau veto:** Events with at least one hadronic tau are vetoed.
  - 2771 • **Jet multiplicity:** Events with at least one jet are selected:  $N_{\text{jet}} \geq 1$ .
  - 2772 • **b-jet veto:** Veto events if they contain any  $b$ -tagged jets.
  - 2773 • **Low mass veto:**
    - 2774 – To remove leptons from quarkonium decays, events with at least one same-flavour  
 2775 opposite-sign (SFOS) lepton pair with an invariant mass less than 12 GeV are  
 2776 vetoed.
  - 2777 • **Z-mass veto:**
    - 2778 – Events with SFOS lepton pair with an invariant mass within a  $\pm 10$  GeV window  
 2779 around  $m_Z$  (91.2 GeV) are vetoed.
    - 2780 – To remove potential backgrounds with Z decays to  $ll\gamma^* \rightarrow ll'l'$  where one lepton  
 2781 has very low momentum and is not reconstructed, invariant mass of the tri-lepton  
 2782 within a  $\pm 10$  GeV window around  $m_Z$  are vetoed:  $|m_{lll} - m_Z| > 10$  GeV

Selection Criteria	SM HH	prompt	fake	total bkg	S/B ( $\times 1000$ )	data
three leptons with a total charge of $\pm 1$	6.32	75116.81	775243.60	850360.41	0.01	1213079
Triggers	5.88	69214.50	653599.08	722813.58	0.01	913339
Hadronic tau veto	5.88	69214.50	653599.08	722813.58	0.01	906509
Electron quality	5.38	63768.03	461547.24	525315.27	0.01	685064
$p_T^{0,1,2} > 10, 15, 15$ GeV	4.14	50731.84	152499.39	203231.22	0.02	251428
$N_{\text{jet}} \geq 1$	3.60	29312.65	94923.35	124236.00	0.03	145937
b-jet veto	3.21	25094.06	53653.52	78747.58	0.04	96919
Low mass veto	3.10	23760.92	51858.30	75619.22	0.04	78347
Z-mass veto	2.26	4169.97	19277.35	23447.32	0.10	25341
Lepton tight quality	1.23	2391.73	357.53	2749.25	0.45	2566

**Table 5–6 The raw yields with pre-selection cut-flow for the  $3\ell$  analysis.**

### 2783 5.3.5 Background Modelling

2784 In this analysis, two primary categories of backgrounds exist: prompt and non-prompt  
 2785 backgrounds. The prompt backgrounds, which consist predominantly of diboson processes,  
 2786 are composed of events that feature three prompt leptons in the final state. On the other hand,

2787 the non-prompt backgrounds, often referred to as 'fakes,' emerge from events where jets or  
2788 photons are misidentified as leptons.

2789 The prompt backgrounds are rigorously modeled using Monte Carlo simulations. These  
2790 include a variety of processes such as  $t\bar{t}V$ ,  $VV$ ,  $tV$ ,  $VH$ ,  $VVV$ , and  $t\bar{t}H$ . Notably,  $WZ$   
2791 processes account for over 85% of all prompt backgrounds. A specialized control region,  
2792 optimized for a  $WZ$ -enriched environment, is introduced to refine this background estima-  
2793 tion. Further details on this control region and its corresponding plots can be found in Sec-  
2794 tions 5.3.5.2 and 5.3.7.3.

2795 The non-prompt backgrounds primarily involve  $t\bar{t}$  and  $Z$  + jets processes. These back-  
2796 grounds are estimated using a template fit method, detailed in Section 5.3.5.2. The non-  
2797 prompt category also encompasses other processes such as  $W$  + jets and  $V\gamma$ , among others.

	HH: ggF	HH: VBF	WZ	ExtConv_e	HF_e	HF_m	Total Bkg	Data	Signal Contamination
ExtConv_e CR	0.00 ± 0.02	0.00 ± 0.00	2.59 ± 0.42	292.97 ± 17.59	0.02 ± 0.00	1.59 ± 0.32	303.64 ± 17.47	303.00	0.000% ± 0.005%
HF_e CR	0.00 ± 0.04	0.00 ± 0.00	1.03 ± 0.15	11.76 ± 2.39	145.97 ± 16.48	0.00 ± 0.00	239.98 ± 15.41	243.00	0.002% ± 0.018%
HF_m CR	0.01 ± 0.07	0.00 ± 0.00	2.32 ± 0.34	0.00 ± 0.00	0.00 ± 0.00	470.00 ± 24.89	566.38 ± 23.74	567.00	0.001% ± 0.013%
Low BDT VR	0.48 ± 5.51	0.03 ± 0.34	1558.72 ± 152.11	79.34 ± 13.74	60.52 ± 10.74	138.51 ± 13.98	2363.74 ± 165.71	2405.00	0.022% ± 0.234%
WZ CR	0.25 ± 2.90	0.01 ± 0.12	7137.60 ± 688.55	8.39 ± 6.18	54.13 ± 15.76	143.45 ± 22.88	8270.25 ± 704.82	8090.00	0.003% ± 0.035%

**Table 5–7 Summary of Monte Carlo (MC) samples with applied normalization factors and re-weighted  $WZ$  contributions, alongside data for all control and validation regions in the  $3\ell$  channel. Only the principal background processes are enumerated.**

2798 A comprehensive summary of all defined control regions and validation regions is pro-  
2799 vided in Table 5–7.

### 2800 5.3.5.1 Estimation of $WZ$ Using fitting function

2801 The  $WZ$  process serves as a crucial contributor to the prompt background within the  $3\ell$   
2802 channel. In order to optimize its simulation, a specialized control region is formulated. This  
2803 region adheres to the general preselection criteria with two specific deviations:

- 2804 • In contrast to the Signal Region, where a veto based on the invariant mass of the SFOS  
2805 lepton pair is applied around  $m_Z$ , the control region is designed to *retain* such events.  
2806 This invariant mass is confined within a  $\pm 10$  GeV window around  $m_Z$ , ensuring or-  
2807 thogonality with respect to the Signal Region.
- 2808 • An additional constraint of  $E_T^{\text{miss}} > 30$  GeV is introduced to further refine the  $WZ$   
2809 control region.

2810 To address the recognized discrepancy in modeling the  $WZ$  background, particularly in

2811 scenarios of high jet multiplicities, a fitting function that has been previously validated<sup>[139]</sup> is  
 2812 applied. The function, given as

$$f(x) = \frac{b \times 2^c - a}{2^c - 1} + \frac{(b - a) \times 2^c}{(2^c - 1)x^c} \quad (5-1)$$

2813 is used to fit the  $WZ$  sample in the dedicated control region. Here,  $x$  corresponds to the  
 2814 number of jets in the event. The fitting is performed using a least-squares method and results  
 2815 in the parameters  $a = -0.706 \pm 0.018$ ,  $b = -0.553 \pm 0.017$ , and  $c = 0.279 \pm 0.026$ . For  
 2816 this fitting procedure, it should be noted that events with a jet count greater than 4 ( $n\text{Jets}$   
 2817  $> 4$ ) are treated as if they have exactly 4 jets ( $n\text{Jets} = 4$ ). This treatment is due to the known  
 2818 limitations in modeling  $WZ$  events with higher jet multiplicities.

2819 The quality of the fit is exemplified by a  $\chi^2/\text{ndof}$  value of 0.84, substantiating the fitting  
 2820 function as a robust modeling correction for  $WZ$  samples across all analytical regions. With  
 2821 this fitting function, it is consequently employed as an additional weighting factor for all  $WZ$   
 2822 samples. This additional weight is used alongside the original sample weights to improve  
 2823 the representation of the  $WZ$  background in this analysis. Importantly, this fitting function  
 2824 is not just used in the control region where it was derived, but is also applied to all other  
 2825 relevant regions in the study. This ensures a consistent and improved modeling of the  $WZ$   
 2826 background throughout the analysis.

2827 Number of jets distributions pre- and post-fitting are visualized in Fig. 5–2, while ad-  
 2828 ditional kinematic distributions subsequent to the fitting are discussed in Sec. 5.3.7.3. The  
 2829 corresponding fitting uncertainties can be found in Section 5.4.3.

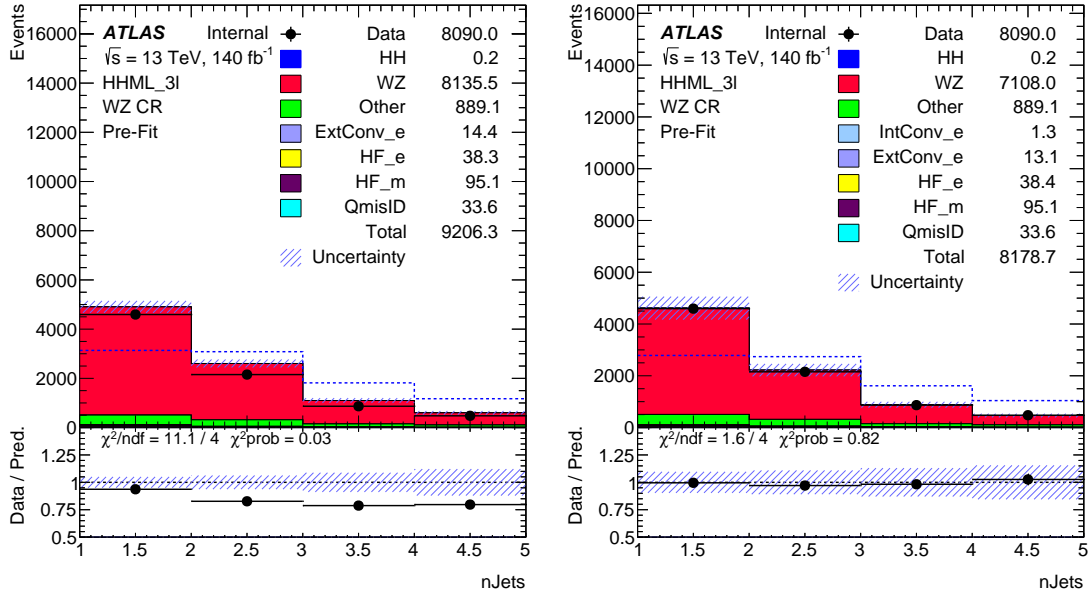


**Figure 5–2** The pre-fit (let) and post-fit (right)  $n$ Jets distribution plots of the WZ control regions, using fitting function of Eq.5–1. Both statistical uncertainties and systematic errors are accounted for.

### 2830 5.3.5.2 Control regions and background estimation using template fit method

2831 Despite strict lepton identification rules, fake leptons remain a significant background in  
 2832 the 3-lepton channel. For the purposes of this analysis, the fake background encompasses  
 2833 both non-prompt and fake leptons. Non-prompt leptons are primarily generated from heavy-  
 2834 flavor hadron decays ( $b$  or  $c$  hadrons), while other contributions may arise from photon con-  
 2835 versions or hadronic jet misidentification. Owing to the intricate nature of fake backgrounds  
 2836 and the imprecision of MC simulations in adequately modeling these processes, a data-driven  
 2837 approach is essential for accurate estimation. The template fit method is employed as a semi-  
 2838 data-driven strategy. It involves a simultaneous fit of all processes contributing to the fake  
 2839 background. All backgrounds, including those arising from charge misidentifications, are  
 2840 extracted from MC simulations. Within this framework, normalization factors for different  
 2841 types of fakes are free parameters in a fit to data. These factors serve to correct MC estimates  
 2842 for fakes and are mainly derived from  $t\bar{t}$  and  $Z$ +jets simulations.

2843 Based on the truth classification of non-prompt lepton events, several key contributions  
 2844 are identified, with free-floating normalization factors (NF) as follows:

- 2845 •  $NF_e^{\text{HF}}$ : For events with a non-prompt electron primarily from b or c decays.
- 2846 •  $NF_\mu^{\text{HF}}$ : For events with a non-prompt muon primarily from b or c decays.
- 2847 •  $NF^{\text{Conv}}$ : For photon conversion events, predominantly from  $V\gamma$  process.

2848 Events are classified into the aforementioned categories based on their truth origin:

- 2849 • Prompt leptons: leptons originating directly from electroweak processes.
- 2850 • Conversion: leptons arising from photon conversions.
- 2851 • B decay and C decay: non-prompt leptons originating from b or c hadron decays.
- 2852 • Other: leptons from light quark decays or other minor sources.

2853 Each CR is defined to be orthogonal to the SR, adhering to the general preselection crite-  
 2854 ria while incorporating several specialized variations. The following outlines the definition  
 2855 criteria for three key CRs:

- 2856 • Electron from Heavy Flavor Decay Control Region (**HF-E CR**):
  - 2857 – No isolation requirements; all set to loose isolation and tight ID.
  - 2858 – Requires a minimum of 2 jets, including 2 or more b-jets to ensure orthogonality
  - 2859 with the SR, which implements a b-jet veto.
  - 2860 – Requires both same-sign leptons to be electrons ( $\ell ee$ ).
- 2861 • Muon from Heavy Flavor Decay Control Region (**HF-MU CR**):
  - 2862 – Adopts identical jet, b-jet, identification and isolation criteria as the HF-E CR for
  - 2863 consistency.
  - 2864 – Requires both same-sign leptons to be muons ( $\ell\mu\mu$ ).
- 2865 • Electron from External Conversion Control Region (**Conv CR**):
  - 2866 – Loose Isolation for  $l_0$  and Tight Isolation for  $l_1/l_2$ , while omitting the standard ID
  - 2867 requirement; all set to loose ID.
  - 2868 – Requires the invariant mass of the three-lepton system to be within 10 GeV of the
  - 2869 Z boson mass, thereby enriching  $V\gamma$  backgrounds.
  - 2870 – Adds a new condition for  $l_1$  or  $l_2$ : a conversion vertex should be present at a
  - 2871 radius greater than 20 mm, and the mass of this vertex should be between 0 and
  - 2872 100 MeV. This condition further assures orthogonality with the SR.

2873 To optimize the discrimination among the various NFs in the simultaneous template fit,  
 2874 specific kinematic distributions in different phase spaces are employed:

- 2875 • For the estimation of the electron heavy flavor normalization factor  $NF_e^{\text{HF}}$ , the angu-

2876 lar separation  $\Delta R_{l_0 l_1}$  in the  $\ell e e$  channel is utilized. This distribution is binned into 3  
 2877 intervals, spanning  $0 \leq \Delta R_{l_0 l_1} \leq 3$ .  
 2878 • Similarly, the muon heavy flavor normalization factor  $NF_{\mu}^{HF}$  is estimated using the  
 2879  $\Delta R_{l_0 l_1}$  distribution in the  $\ell \mu \mu$  channel, also segmented into 3 bins in the range  $0 \leq$   
 2880  $\Delta R_{l_0 l_1} \leq 3$ .  
 2881 • The external conversion electron normalization factor  $NF_e^{Conv}$  is estimated using a single-  
 2882 bin distribution.

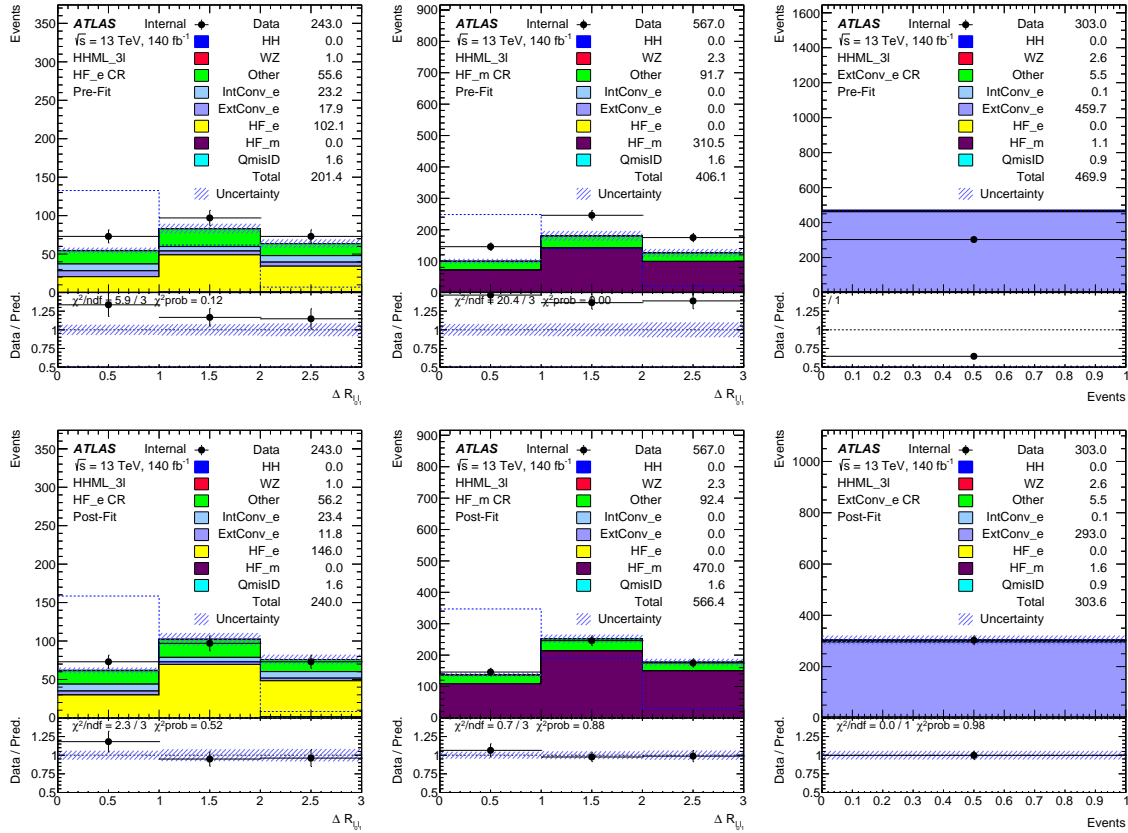


Figure 5–3 From left to right shows the pre-fit (top) and post-fit (bottom) plots of the HF-E, HF-MU, External Conversion control regions. All entries represent uncorrected Monte Carlo simulations. Both statistical uncertainties and systematic errors are accounted for. Additionally, the WZ background is adjusted using a fitted scaling function.

2883 The Template Fit Control Regions are depicted in Figures 5–3, both before and after fit-  
 2884 ting to the data; the derived normalization factors are tabulated in Table 5–8. Due to the  
 2885 limited statistics in each specialized control region, additional sources of fake or non-prompt

leptons, such as internal conversions and light-flavor leptons, are amalgamated in these three CRs. Specifically, the NF for external conversions is also applied to internal conversion samples, and the NFs for heavy-flavor leptons encompass those for light-flavor and other leptonic sources.

Source	Norm Factor	Yields in SR	Uncertainty(%)
External Conversion	$0.66 \pm 0.13$	2.8	13.29
Heavy Flavor (electron)	$1.50 \pm 0.50$	11.3	30.52
Heavy Flavor (muon)	$1.51 \pm 0.23$	29.5	13.12
Prompt Background	-	125.7	-

**Table 5–8 The systematics of three fake sources and the corresponding yields in the signal region, which is estimated by the template fit method.**

### 5.3.6 Multivariate Analysis

The analysis employs a multivariate approach using the Boosted Decision Trees (BDT) method, within the TMVA framework in ROOT 6.18/00<sup>[140]</sup>. An enhanced version, Gradient BDT (BDTG), has also been implemented for this analysis. The training dataset comprises both prompt backgrounds, such as  $t\bar{t}V$ ,  $VV$ ,  $tV$ ,  $VH$ ,  $VVV$ , and  $t\bar{t}H$ , as well as the non-prompt processes, henceforth referred to as "fake background."

#### 5.3.6.1 Input Variable and Correlation

Most of the Higgs bosons in 3-lepton channel are moderately boosted, thereby yielding leptons in the final state that are often spatially close due to the W-boson spin correlations in the Higgs decay processes. Variables coming from the lepton kinematics, such as  $\Delta R_{l_i l_j}$ ,  $m_{l_i l_j}$  are expected to have strong separation power, with W-boson can be partially reconstructed. Other variables like the missing transverse energy ( $\cancel{E}_T$ ), sum of the transverse momentum of all objects ( $HT$ ), and the invariant mass of all three leptons and two leading jets ( $m_{lljj}$ ) are also expected to be useful in separating signal from background. The variables employed in BDTG training are itemized in Table 5–9, selected for their maximal discriminative power; the top 13 variables have been ranked according to their separation efficacy<sup>1</sup>. Observable high correlations exist among certain invariant masses. Specifically, an 82% correlation between

<sup>1</sup> The variables were selected based on their separation power as quantified during BDT training.

2907  $m_{ll}$  and  $m_{l_1l_2}$ , and a 90% correlation between  $m_{ll}$  and  $m_{l_0l_2}$  are in line with expectations.  
 2908 Similarly, an 83% correlation is noted between  $HT$  and  $m_{lljj}$ . The respective correlation  
 2909 matrix is shown in Figures 5–4a and 5–4b.

2910 It is essential to note that despite these substantial correlations, the input variable set has  
 2911 been optimized based on the Area Under the Curve (AUC) metric. Empirical data substanti-  
 2912 ate a marked reduction in performance when the variable set is truncated. Consequently, the  
 2913 presence of high correlations among variables is tolerated in favor of optimized performance.

Variable	Description	Separation
$\Delta R_{l_0l_1}$	Distance in $\eta - \phi$ space between lepton 0 and lepton 1	32.62%
$m_{l_0l_1}$	Invariant mass of lepton 0 and lepton 1	26.90%
min. $m_{ll}^{\text{OS}}$	Minimum invariant mass of opposite-sign lepton pairs	26.23%
$\Delta R_{l_2j}$	Distance in $\eta - \phi$ space between lepton 2 and nearest jet	23.90%
$\Delta R_{l_1l_2}$	Distance in $\eta - \phi$ space between lepton 1 and lepton 2	12.67%
min. $m_{ll}^{\text{OSSF}}$	Minimum invariant mass of opposite-sign same-flavor lepton pairs	11.41%
$m_{ll}^{\text{Z-matched}}$	Invariant mass of lepton pair closest to $Z$ mass	11.38%
$m_{lljj}$	Invariant mass of all three leptons and two leading jets	3.49%
$m_{lll}$	Invariant mass of all three leptons	2.94%
$m_{l_2j}$	Invariant mass of lepton 2 and nearest jet	2.40%
$m_{l_0l_2}$	Invariant mass of lepton 0 and lepton 2	2.11%
$\cancel{E}_T$	Missing transverse energy	1.80%
$\Delta R_{l_0j}$	Distance in $\eta - \phi$ space between lepton 0 and nearest jet	1.20%
FlavorCategory	Categorization of lepton flavors, details in Sec. 5.3.4.1	1.17%
$HT_{\text{lep}}$	Scalar sum of lepton $p_T$ 's and missing transverse momentum	0.96%
$HT$	Scalar sum of jet $p_T$ 's	0.52%
$\Delta R_{l_1j}$	Distance in $\eta - \phi$ space between lepton 1 and nearest jet	0.33%
$\Delta R_{l_0l_2}$	Distance in $\eta - \phi$ space between lepton 0 and lepton 2	0.26%
$m_{l_1j}$	Invariant mass of lepton 1 and nearest jet	0.19%
$HT_{\text{jets}}$	Scalar sum of jet $p_T$ 's	0.05%
$m_{l_0j}$	Invariant mass of lepton 0 and nearest jet	0.01%
$m_{l_1l_2}$	Invariant mass of lepton 1 and lepton 2	0.01%

**Table 5–9 Discriminant variables used in BDTG training for  $3\ell$  channel.**

### 2914 5.3.6.2 3-Fold Cross-Validation

2915 Owing to the statistical constraints of the Monte Carlo training samples, a  $k$ -fold Cross-  
 2916 Validation ( $k$ -CV) strategy is employed, specifically 3-fold cross-validation. This approach



2934 compiled in Figure 5–5.

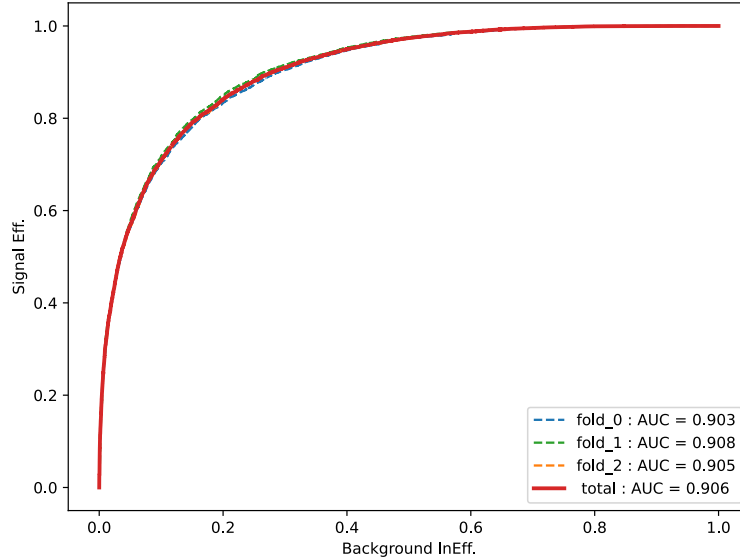


**Figure 5–5 Training results of BDTG: Receiver Operating Characteristic (ROC) curve for 3-lepton channel, illustrating the trade-off between signal efficiency (True Positive Rate) and background inefficiency (False Positive Rate).**

### 2935 5.3.7 Validation Plots

#### 2936 5.3.7.1 BDTG score distribution in validation region

2937 Figure 5–6 depicts the pre-fit and post-fit distributions of the BDTG score in both the low  
 2938 BDT Validation Region and the WZ-enriched region. The left panel showcases the BDTG  
 2939 score distributions before fitting, whereas the right panel reveals the distributions after the  
 2940 fitting process.

#### 2941 5.3.7.2 Control plots in low BDTG region

2942 With satisfying the selections in Section 5.3.4.2, the region with low BDTG score<sup>1</sup> is  
 2943 defined as the validation region, with 0.012% signal contamination in table 5–7 (calculated as  
 2944 the ratio of raw yields between signal and total background). Invariant mass related variables  
 2945 are shown in figure 5–8. Distance related variables and  $HT$  are summarized in figure 5–7.

<sup>1</sup> BDTG score  $\leq 0.55$

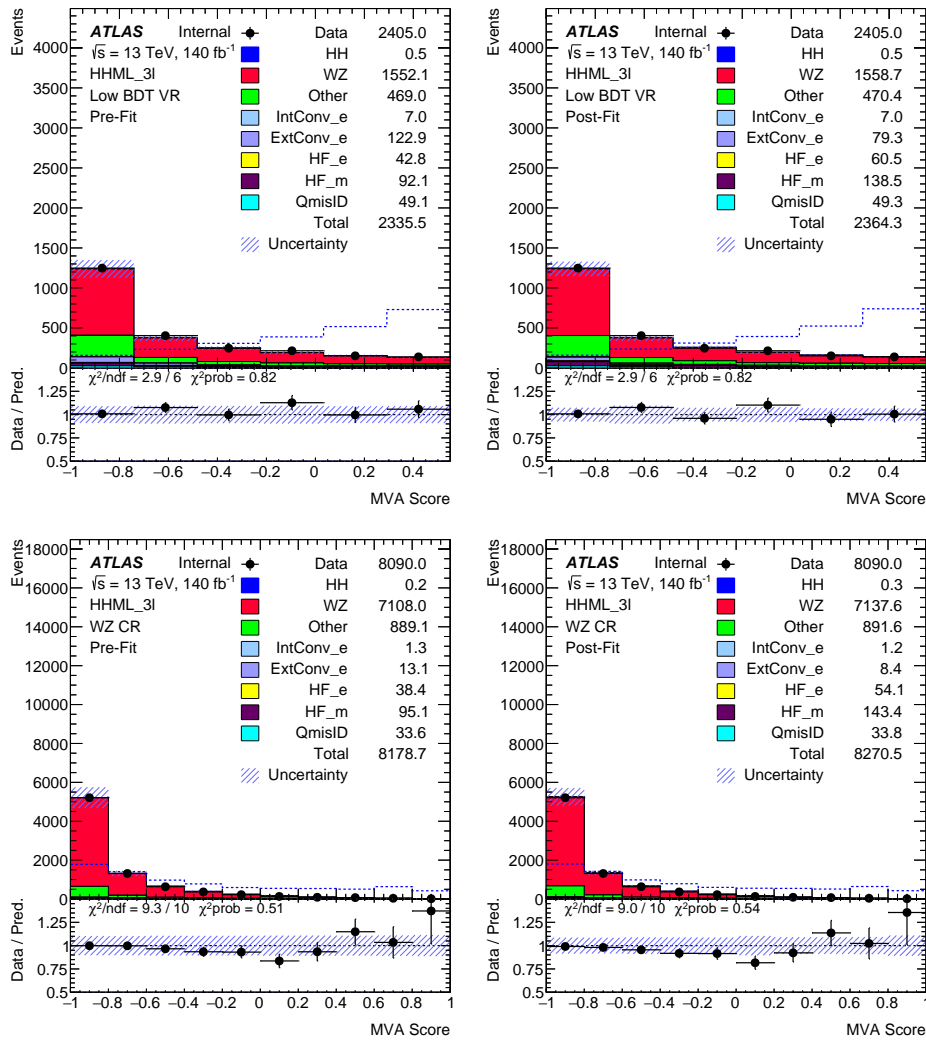


**Figure 5–6** The pre-fit and post-fit distributions of the BDTG score in low BDT VR and WZ-enriched region. Scaling factors for External Conversion, HF(electron), and HF(muon) are applied. Additionally, the WZ background is adjusted using a fitted scaling function. Both statistical uncertainties and systematic errors are accounted for.

2946 The rest of discriminant variables used in BDTG training is presented in figure 5–9.

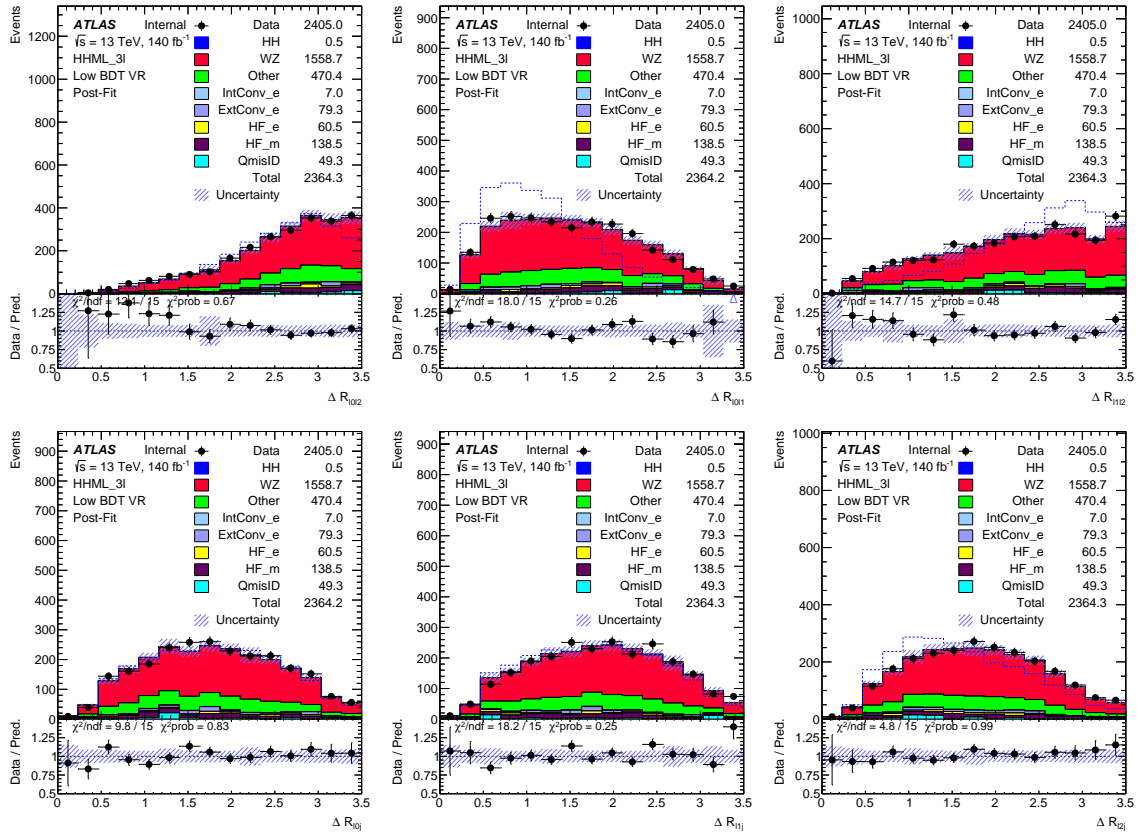


**Figure 5–7** The post-fit distribution of distance of lepton pairs and jets, where all the events are required to pass the pre-selection and BDTG score  $\leq 0.55$ . Scaling factors for External Conversion, HF(electron), and HF(muon) are applied. Additionally, the WZ background is adjusted using a fitted scaling function. Both statistical uncertainties and systematic errors are accounted for.

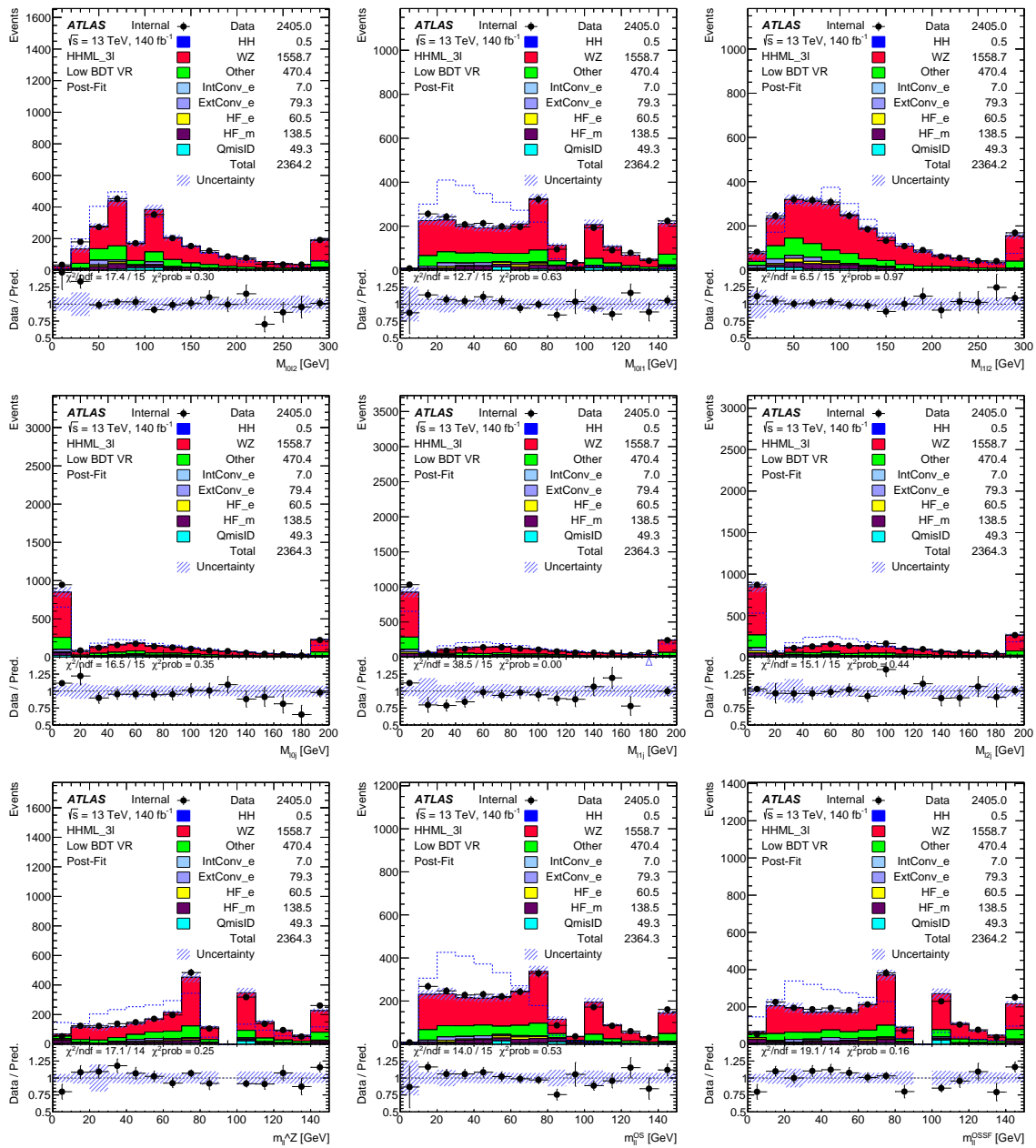
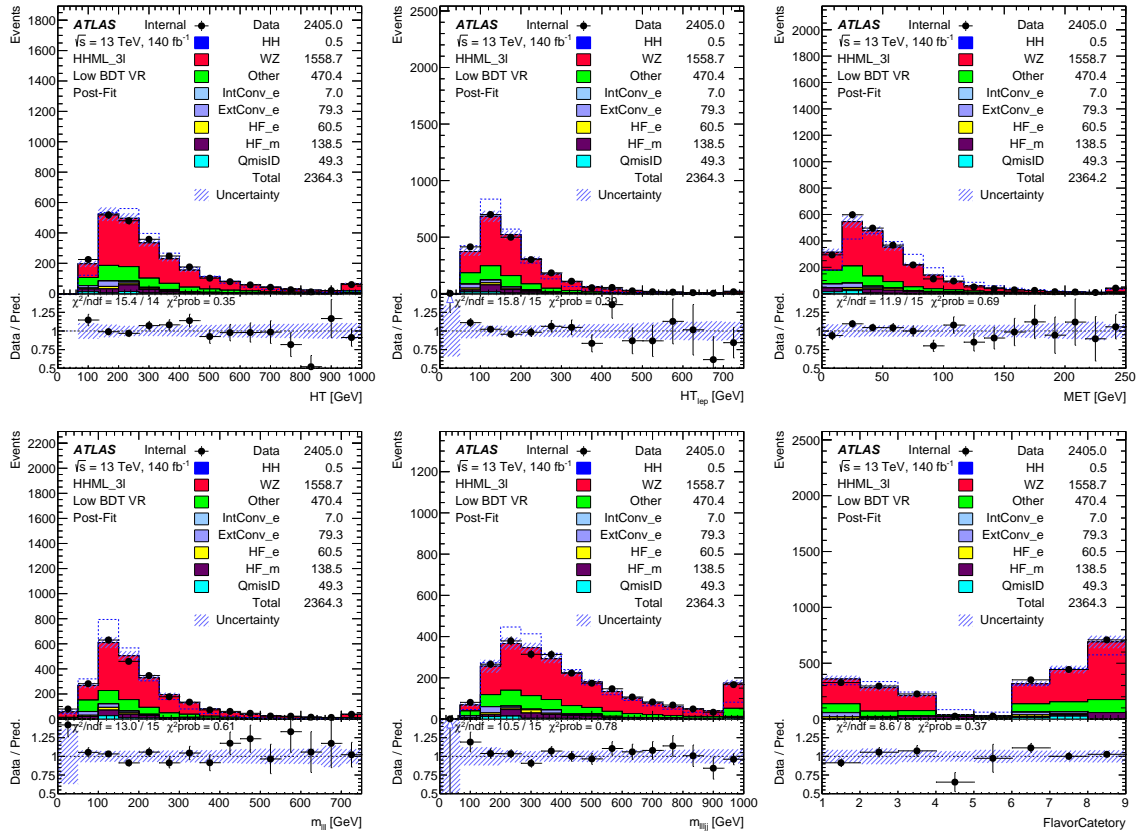


Figure 5–8 The post-fit distribution of invariant mass of lepton pairs and jets, where all the events are required to pass the pre-selection and BDTG score  $\leq 0.55$ . Scaling factors for External Conversion, HF(electron), and HF(muon) are applied. Additionally, the WZ background is adjusted using a fitted scaling function. Both statistical uncertainties and systematic errors are accounted for.



**Figure 5–9** The post-fit distribution of the remaining kinematics, where all the events are required to pass the pre-selection and BDTG score  $\leq 0.55$ . Scaling factors for External Conversion, HF(electron), and HF(muon) are applied. Additionally, the WZ background is adjusted using a fitted scaling function. Both statistical uncertainties and systematic errors are accounted for.

## 2947 5.3.7.3 Control plots in WZ control region

2948 The definition of WZ control region is defined in Sec. 5.3.5.2, where events should pass  
 2949 all preselection but is required to have SFOS lepton pairs whose invariant mass is in the Z  
 2950 mass window. Invariant mass related variables are shown in figure 5–11. Distance related  
 2951 variables and  $HT$  are summarized in figure 5–10. The rest of discriminant variables used in  
 2952 BDTG training is presented in figure 5–12.

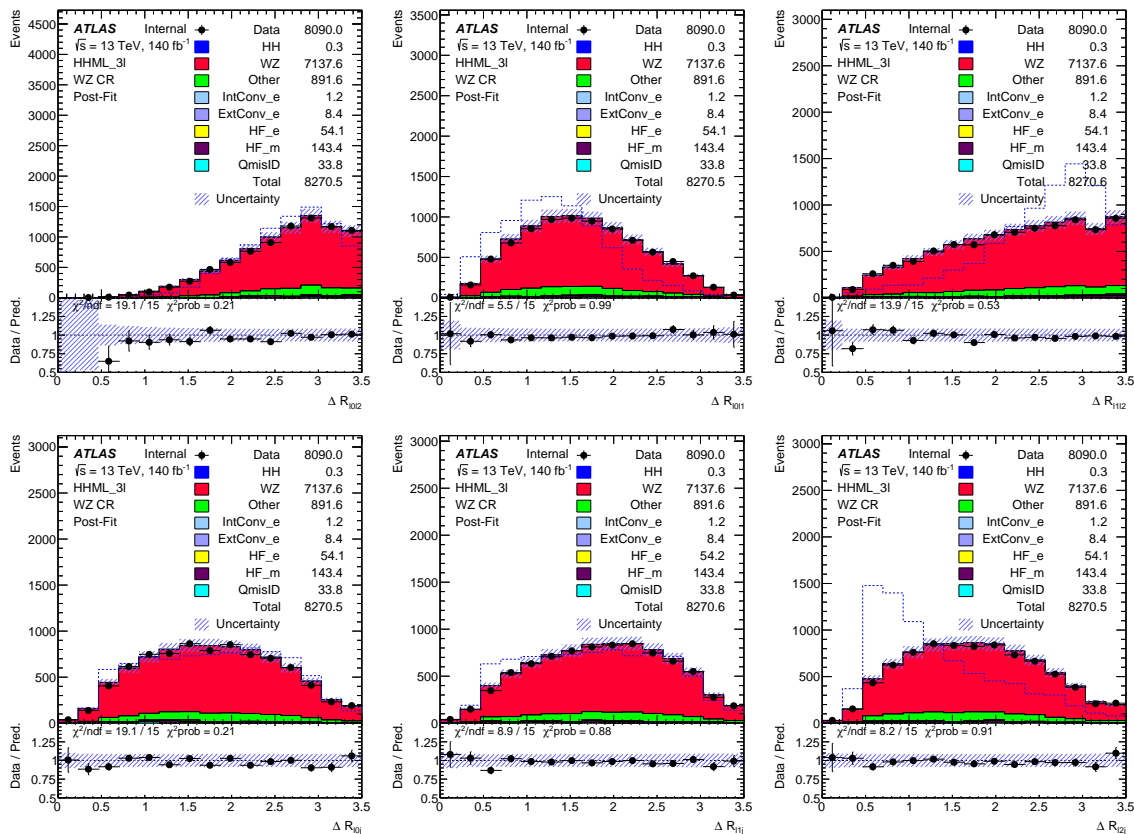


**Figure 5–10** The post-fit distribution of distance of lepton pairs and jets, where all the events are required to pass the pre-selection. Scaling factors for External Conversion, HF(electron), and HF(muon) are applied. Additionally, the WZ background is adjusted using a fitted scaling function. Both statistical uncertainties and systematic errors are accounted for.

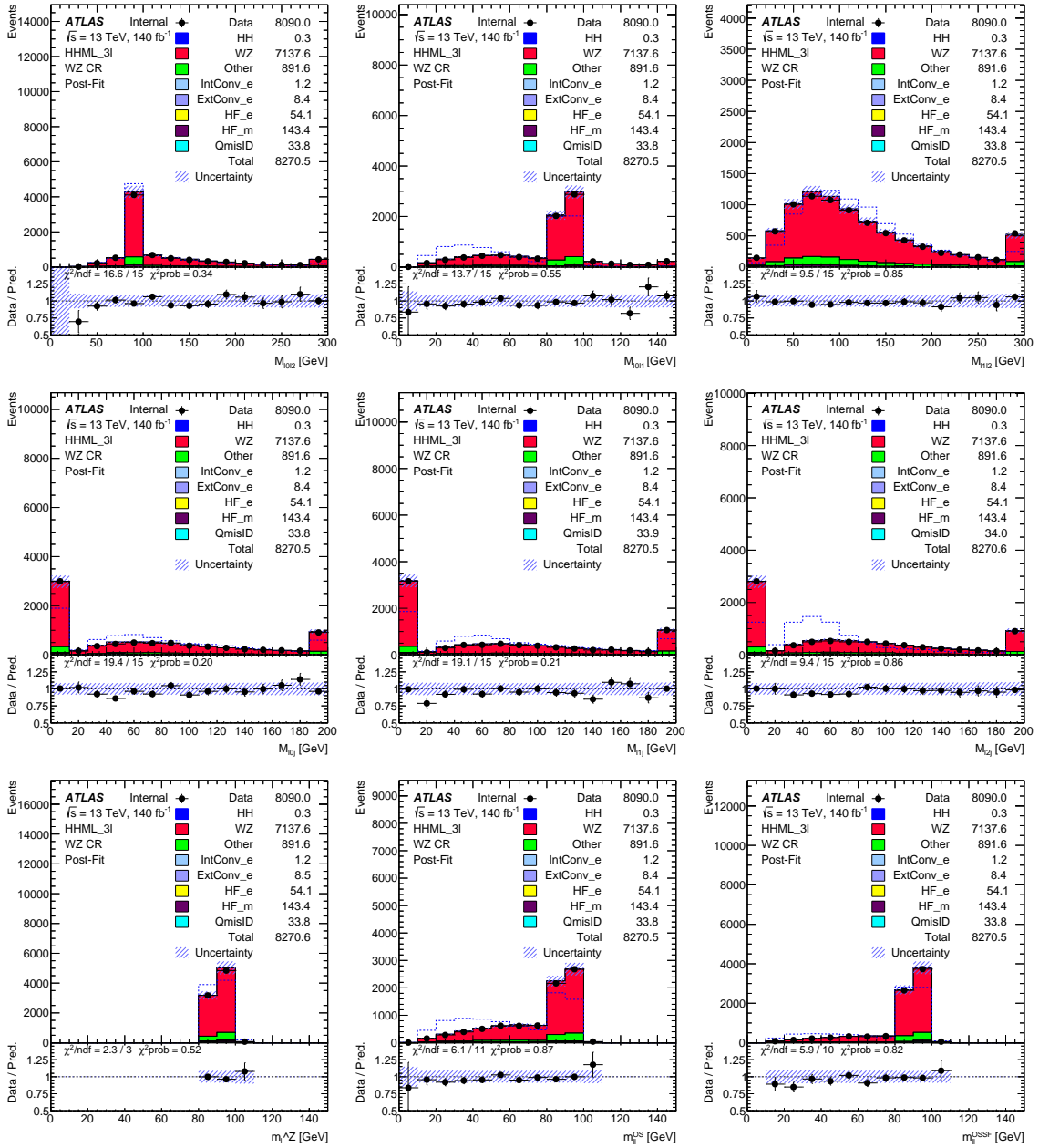


**Figure 5-11** The post-fit distribution of invariant mass of lepton pairs and jets, where all the events are required to pass the pre-selection. Scaling factors for External Conversion, HF(electron), and HF(muon) are applied. Additionally, the WZ background is adjusted using a fitted scaling function. Both statistical uncertainties and systematic errors are accounted for.

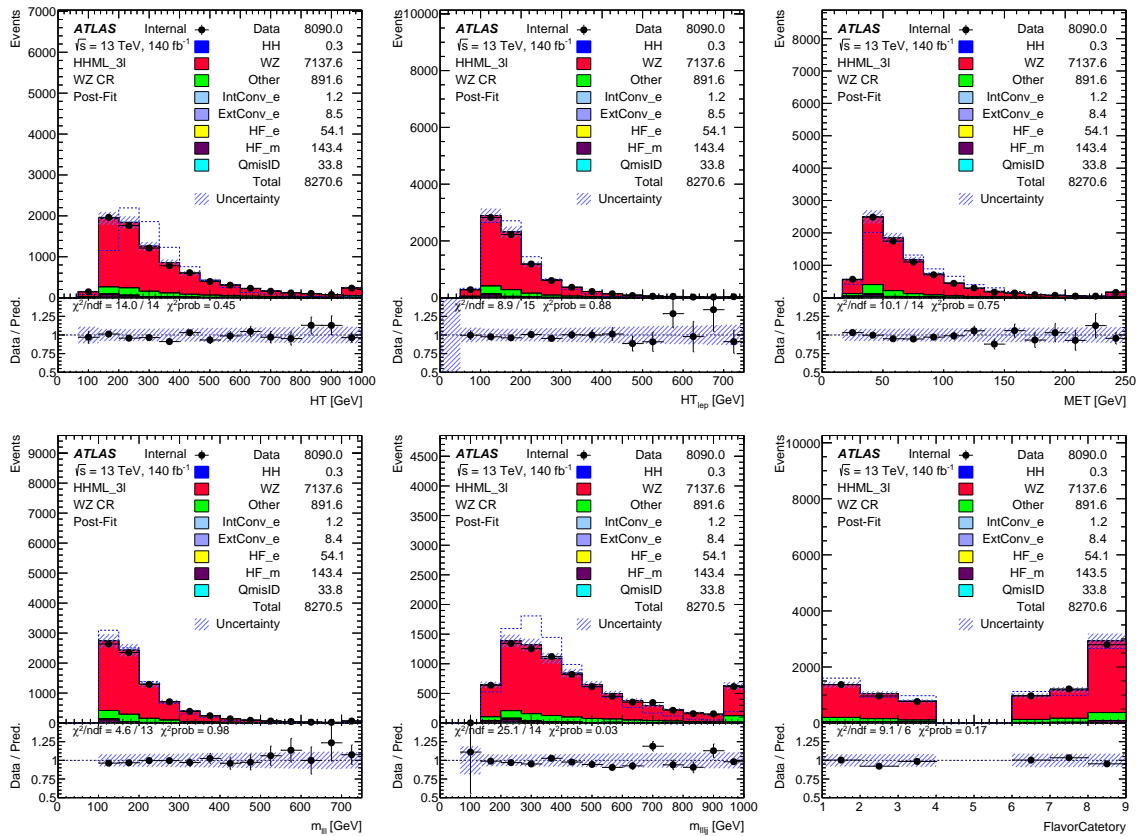


**Figure 5–12** The post-fit distribution of the remaining kinematics, where all the events are required to pass the pre-selection. Scaling factors for External Conversion, HF(electron), and HF(muon) are applied. Additionally, the WZ background is adjusted using a fitted scaling function. Both statistical uncertainties and systematic errors are accounted for.

## 5.4 Systematic Uncertainties

### 5.4.1 Experimental uncertainties

This subsection outlines the systematic uncertainties inherent in the analysis. These uncertainties stem primarily from the reconstruction and identification of physics objects, including light leptons, jets, and Missing Transverse Energy. Additionally, uncertainties in the integrated luminosity of the dataset are taken into account.

- **Luminosity:** Uncertainty in the integrated luminosity of the combined Run-2 dataset is quantified at 1.7%. This value follows the calibration methodology<sup>[141]</sup>, which uses x-y beam-separation scans conducted from 2015 to 2018. This luminosity uncertainty is propagated to all Monte Carlo samples but is exempt for the data and fake continuum background.
- **Pileup:** The procedure for pileup reweighting involves contrasting the mean number of interactions per proton-proton collision ( $\langle \mu \rangle$ ) in the data against that in simulated samples. Uncertainties are assessed through the variation of the scaling factor applied to the data.
- **Trigger:** Uncertainties related to electron and muon trigger efficiency are accounted for through the respective trigger scale factors<sup>[142]</sup>. In leptonic channels, either the Single Lepton Trigger (SLT) or Double Lepton Trigger (DLT) strategy is employed, and the relevant scale factor is applied. Photon trigger uncertainties are also incorporated.
- **Muons:** The Muon Combined Performance group<sup>[143]</sup> provides guidelines for the inclusion of uncertainties concerning muon efficiency, energy scale, resolution, object reconstruction, identification, and isolation. The efficiency uncertainty is disaggregated into both statistical and systematic components, addressing specific conditions such as bad muons, isolation, low transverse momentum muons, and track-to-vertex association (TTVA).
- **Electrons:** Similar to muons, uncertainties for electrons encompass aspects like resolution, scale, and efficiency, as specified by the Egamma Combined Performance group<sup>[144]</sup>.
- **Jets:** Jets are reconstructed using the anti- $k_t$  algorithm with a radius parameter of  $R = 0.4$ , based on energy deposits in topological clusters of calorimeter cells. Uncertainties in the Jet Energy Scale (JES) and Jet Energy Resolution (JER) are considered

and derived through a combination of Monte Carlo-based and in situ calibrations<sup>[145]</sup>. For these uncertainties, both the CategoryReduction and FullJER schemes are implemented.

- **Flavour Tagging:** Excluding the  $b\bar{b} + 4\ell$  channel, a b-jet veto is enforced at a tagging efficiency of 77% to maintain orthogonality with other di-Higgs analyses. Uncertainties originate from the tagging efficiency for jets containing b-hadrons, c-hadrons, light hadrons, or hadronically decaying taus. The associated scale factors are obtained via the BtaggingEfficiencyTool’s getScaleFactor method<sup>[146]</sup>. The Non-Perturbative (NP) reduction scheme used for b-tagging uncertainties is categorized as medium.
- **Missing Transverse Momentum:** Systematic variations are considered with respect to the scale and resolutions (both parallel and perpendicular) of the soft term.

### 5.4.2 Theory uncertainties

The inclusive cross sections for ggF in Higgs boson pair production<sup>[147]</sup> are computed for a Higgs mass  $m_H = 125$  GeV, with a central scale setting of  $\mu_0 = \mu_R = \mu_F = M_{HH}/2$ . Uncertainties to consider include the PDF and  $\alpha_s$  (together termed as "PDF +  $\alpha_s$  unc"), scale, and top-quark mass ( $m_{\text{top}}$ , termed as "Scale +  $m_{\text{top}}$  unc") as recommended by the LHC Higgs Cross Section Working Group<sup>[148]</sup>. Uncertainties in percentage are as follows: QCD Scale:  $^{+2.1}_{-4.9}$ , PDF( $+\alpha_s$ ):  $^{+3}_{-3}$ ,  $m_{\text{top}}$ :  $^{+4}_{-18}$ . Cross section uncertainties for VBF in Higgs pair production are in accordance with the recommendations<sup>[148]</sup>.

The systematic variations stemming from these uncertainties are individually weighted for each event through specialized systematic samples. For background processes, namely  $t\bar{t}V$ , multi-boson processes ( $VV$ ,  $VVV$ ),  $V\gamma$ , as well as rare decay modes ( $tZ$ ,  $WtZ$ ,  $t\bar{t}WW$ ), a comprehensive summary of cross-sections and corresponding treatments for uncertainties, inclusive of those from data, is provided in Table 5–10.

### 5.4.3 WZ reweighting uncertainties

To rigorously quantify the uncertainties introduced by fitting errors in the reweighting of the WZ sample, we establish an eigenspace representation based on the covariance matrix of the fitting parameters A, B, and C, as detailed in Table 5–11. By transforming these parameters and associated uncertainties into this eigenspace (refer to Table 5–12), we obtain the eigenvalues and eigenvectors’ nominal values and uncertainties (denoted as fA, fB, fC). This

Process	Precision order	Cross section central value	Cross section uncertainty	Modelling uncertainty	Normalized to data
MC samples contributing to fake lepton templates					
$t\bar{t}$	NNLO+NNLL	832 pb	-	alternative MC	Yes
$s$ -, $t$ -channel single top	NLO	227 pb	-	-	Yes
$Wt$ single top	NNLO approx	71.7 pb	-	-	Yes
$Z/\gamma^* \rightarrow l^+l^-$	NNLO	0.9751×SHERPA	-	-	
$W \rightarrow \ell\nu$	NNLO	0.9751×SHERPA	-	-	
MC samples of irreducible background processes					
$t\bar{t}W$	NLO	601 fb	-	alternative MC scale variations	Yes
$t\bar{t}\bar{t}$	NLO	12 fb	20%	alternative MC	No
$t\bar{t}(Z/\gamma^* \rightarrow l^+l^-)$	NLO	839 fb	-	alternative MC scale variations	Yes
$t\bar{t}H$	NLO	507 fb	11%	alternative MC scale variations	No
$WH$	NLO	1102 fb	-	scale variations	No
$ZH$	NLO	601 fb	-	scale variations	No
$VV, qqVV$	NLO	SHERPA	-	10% (+LF jets), scale variations	Yes (+HF jets)
$t(Z/\gamma^*)$	LO	240 fb	5%	-	No
$t\bar{t}t$	LO	1.6 fb	50%	-	No
$tW(Z/\gamma^*)$	NLO	16 fb	50%	-	No
$t\bar{t}W^+W^-$	NLO	9.9 fb	50%	-	No
$VVV$	NLO	SHERPA	50%	-	No

**Table 5–10 The background sample normalizations and their uncertainties were used in the analysis. The uncertainties on the inclusive cross sections are taken from the ATLAS Physics Modelling Group Twiki.**

3014 orthogonal transformation of the parameter space provides a more nuanced understanding,  
3015 allowing us to evaluate the impact of each fitting parameter in an independent manner.

3016 Upon obtaining the eigenvalues and eigenvectors (notated as fA, fB, fC) within the es-  
3017 tablished eigenspace, these components are varied by a single standard deviation ( $1\sigma$ ) to  
3018 scrutinize the influence of their respective uncertainties. Given that variations within the  
3019 eigenspace are orthogonal and therefore independent, this ensures that the calculated uncer-  
3020 tainties remain uncorrelated.

3021 Subsequent to this variation, these parameters are transformed back to their original  
3022 space, specifically to the A, B, and C parameters, thereby generating altered fitting functions.

	Correlation Matrix			Covariance Matrix		
	A	B	C	A	B	C
A	1.0000	0.6111	-0.4148	0.0003182	0.0001804	-0.000196
B	0.6111	1.0000	0.4640	0.0001804	0.0002739	0.0002034
C	-0.4148	0.4640	1.0000	-0.000196	0.0002034	0.0007015

Table 5–11 Correlation and Covariance Matrix for Parameters A, B, and C

Eigenvalues		Eigenvectors	
6.1146e-07	0.6217	0.7346	0.2719
4.7741e-04	-0.6885	0.6780	-0.2576
8.1551e-04	0.3736	0.0271	-0.9272

Table 5–12 Eigenvalues and Eigenvectors of the Covariance Matrix for Parameters A, B, and C

3023 Utilizing these modified functions, we proceed to reweight the WZ background and estimate  
 3024 its subsequent contribution to the final state. A comparative analysis between the reweighted  
 3025 WZ background and its nominal counterpart, derived from the initial fitting function, allows  
 3026 us to gauge the uncertainties' repercussions on the reweighting methodology. These findings  
 3027 are graphically represented in Figure 5–13.

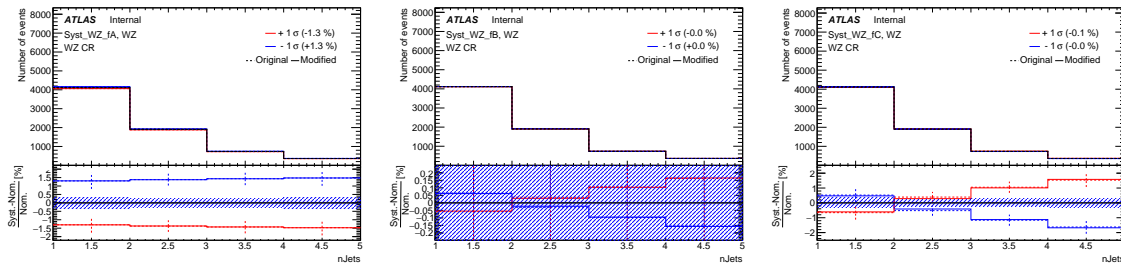


Figure 5–13 The systematics plots for reweighted WZ samples in WZ enriched region.

#### 3028 5.4.4 Uncertainties on data-driven background estimation

3029 The Template Fit method is dependent on Monte Carlo simulations, giving rise to three  
 3030 primary types of systematic uncertainties:

- 3031 •  $t\bar{t}$  modelling uncertainties
- 3032 •  $Z$ +jets modelling uncertainties

- Fakes template uncertainties

For  $t\bar{t}$  and  $Z$ +jets modelling, we employ standard procedures recommended by the top group, involving variations in radiation and scale choices. It is noteworthy that these systematic uncertainties minimally impact the final results.

To address uncertainties in the fakes templates, the comprehensive definition of a "tight lepton" is subdivided into components that target specific origins of fakes: namely, conversions (ambiguity bin) versus heavy flavors (by loosening the criteria for Tight ID Selection on  $\ell_1$  and  $\ell_2$ ). This approach allows us to isolate selections with high proportions of fakes, which are then compared to data after the subtraction of remaining backgrounds. As a result, systematic uncertainties for each heavy flavor template component (either electron or muon) are obtained. These are then used as a correlated nuisance parameter for all bins in the final fit. Importantly, these shape-related systematics are not considered to be among the most impactful uncertainties on the analysis.

Control regions featuring relaxed identification criteria are examined, and the ratio of (Data – Non-Fake BG)/Fake BG is included as an additional systematic uncertainty, specifically for the heavy-flavor (HF) fakes and Conversion fakes in designated control or signal regions as shown in Table 5–8.

## 5.5 Statistical Interpretation

### 5.5.1 Statistical model

The analytical likelihood function is expressed as:

$$\mathcal{L}(\vec{\mu}, \vec{\theta}; \text{data}) = \prod_{c=1}^{N_{\text{cat}}} \mathcal{L}_c(\vec{\mu}, \vec{\theta}; \text{data}) \prod_{k \in \text{NP constraints}} g_k(\theta_k) \quad (5-2)$$

Here,  $\vec{\mu}$  and  $\vec{\theta}$  symbolize the vectors for the parameters of interest (POIs) and nuisance parameters (NPs), respectively.  $N_{\text{cat}}$  represents the total number of categories, and  $\mathcal{L}_c$  signifies the likelihood for each specific category  $c$ . Constraint terms for some of the NPs are represented by  $g_k$ . Further elucidation of the likelihood template can be found in Ref.<sup>[149]</sup>.

POIs can encompass diverse parameters like the signal strength, denoted as  $\mu$ , and coupling variables such as  $\kappa_\lambda$  and  $\kappa_{2V}$ . The NPs are either unconstrained, i.e., determined solely by data, or constrained through auxiliary measurements. In each category  $c$ , the likelihood

3060 is a product of individual Poisson distributions for each bin:

$$\mathcal{L}_c(\vec{\mu}, \vec{\theta}; \text{data}) = \prod_{i=1}^{n_{\text{bin}}} P\left(\sum_s N_{S_s}^c(\vec{\mu}) + \sum_b N_{B_b}^c, n_i\right) \quad (5-3)$$

3061 The Poisson distribution uses  $n_i$  as the observed event count for each bin, and  $\sum_s N_{S_s}^c(\vec{\mu}) +$   
3062  $\sum_b N_{B_b}^c$  as the sum of signal and background yields.

3063 The profile likelihood ratio,  $\Lambda(\mu)$ , for statistical tests is formulated as:

$$\Lambda(\mu) = \frac{\mathcal{L}(\mu, \hat{\hat{\theta}}(\mu))}{\mathcal{L}(\hat{\mu}, \hat{\theta})} \quad (5-4)$$

3064 Here, the terms  $\hat{\hat{\theta}}$  and  $\hat{\theta}$  are the profiled values of the NPs that maximize the likelihood  
3065 conditionally and unconditionally, respectively.

3066 In the regime of large sample sizes, the test statistic  $-2 \ln \Lambda(\mu)$  asymptotically follows  
3067 a  $\chi^2$  distribution. The degrees of freedom (d.o.f) of this distribution correspond to the di-  
3068 dimensionality of the parameter vector  $\vec{\mu}$ . This is predicated on the central limit theorem,  
3069 which states that the sampling distribution of the likelihood will approach a Gaussian distri-  
3070 bution as the sample size increases. This Gaussian approximation allows the transformation  
3071  $-2 \ln \Lambda(\mu)$  to adhere to a  $\chi^2$  distribution, facilitating hypothesis testing for the parameters of  
3072 interest (POIs).

3073 The  $CL_s$  method<sup>[150]</sup> is employed to establish upper limits at a 95% Confidence Level  
3074 (CL) on the  $HH$  signal strength  $\mu_{HH}$  and the associated production cross-section.  $CL_s$  is a  
3075 modified frequentist approach for hypothesis testing that avoids the issue of overly-optimistic  
3076 exclusion limits, a problem encountered in the traditional  $CL$  methodology. It does so by  
3077 normalizing the  $p$ -value of the signal hypothesis by the  $p$ -value of the background-only hy-  
3078 pothesis, thereby incorporating systematic uncertainties in a more conservative manner.

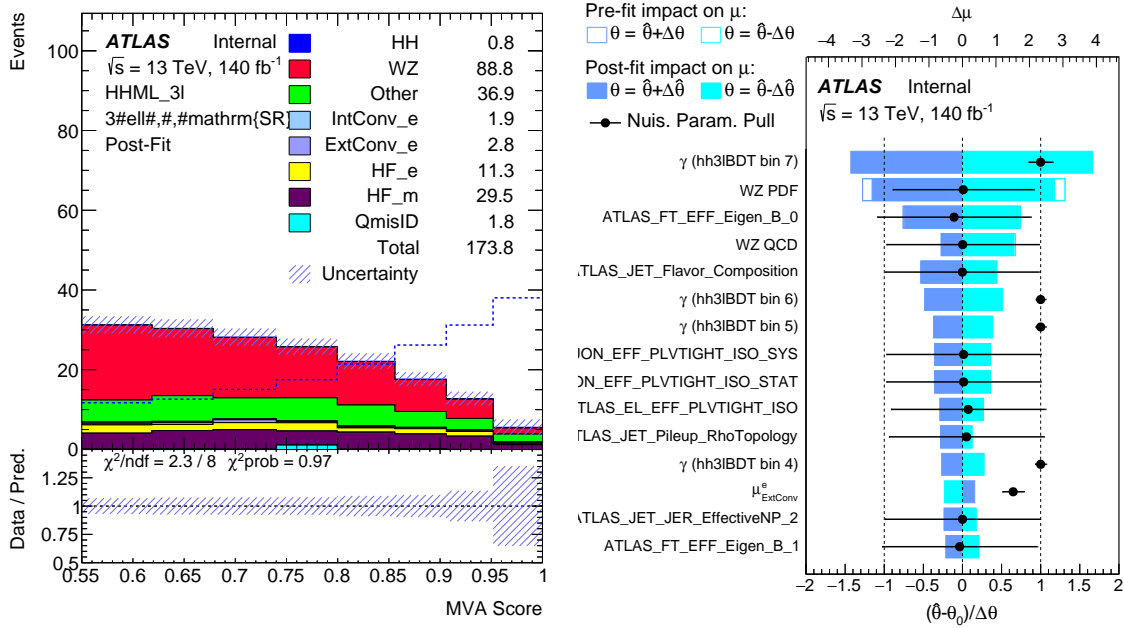
3079 The test statistic  $\tilde{q}_\mu$  utilized in the  $CL_s$  framework is formulated as:

$$\tilde{q}_\mu = \begin{cases} -2 \ln \frac{\mathcal{L}(\mu, \hat{\hat{\theta}}(\mu))}{\mathcal{L}(0, \hat{\hat{\theta}}(0))} & \hat{\mu} < 0, \\ -2 \ln \frac{\mathcal{L}(\mu, \hat{\hat{\theta}}(\mu))}{\mathcal{L}(\hat{\mu}, \hat{\theta})} & 0 \leq \hat{\mu} \leq \mu, \\ 0 & \hat{\mu} > \mu. \end{cases} \quad (5-5)$$

3080 The  $CL_s$  values are computed from the distribution of  $\tilde{q}_\mu$  under the signal-plus-background  
 3081 and background-only hypotheses, which in turn allows one to set data-driven upper limits.

3082 **5.5.2 Statistical analysis and Results**

3083 The statistical analysis for the 3-lepton channel is carried out using the TrexFitter pack-  
 3084 age<sup>[151-152]</sup>. We employ a profile-likelihood fit on the Asimov dataset, which is a theoretical  
 3085 dataset that represents expected outcomes using pure MC dataset, to estimate the expected  
 3086 upper limit on the cross-section for SM HH production. This fit utilizes templates, which are  
 3087 constructed from predicted yields of both the signal and the relevant background processes,  
 3088 divided by bins in the input distribution for the 3-lepton channel specifically. For each bin  
 3089 in the input distribution, Monte Carlo statistical uncertainties are incorporated into the fit  
 3090 through an additional Poisson term ( $\gamma$ ). The BDTG score distribution in the 3-lepton chan-  
 3091 nel is used as the input distribution for the fit (only score  $> 0.55$  is considered as SR). The  
 3092 BDTG score distribution is shown in Figure 5–14a.



(a) BDTG score distribution.

(b) Top 15 nuisance parameters.

**Figure 5–14 Fitting results for 3 $\ell$  channel, including all systematics and data-driven nuisance parameters.**

3093 In the statistical analysis, the discriminant distribution serves as the basis for fitting the

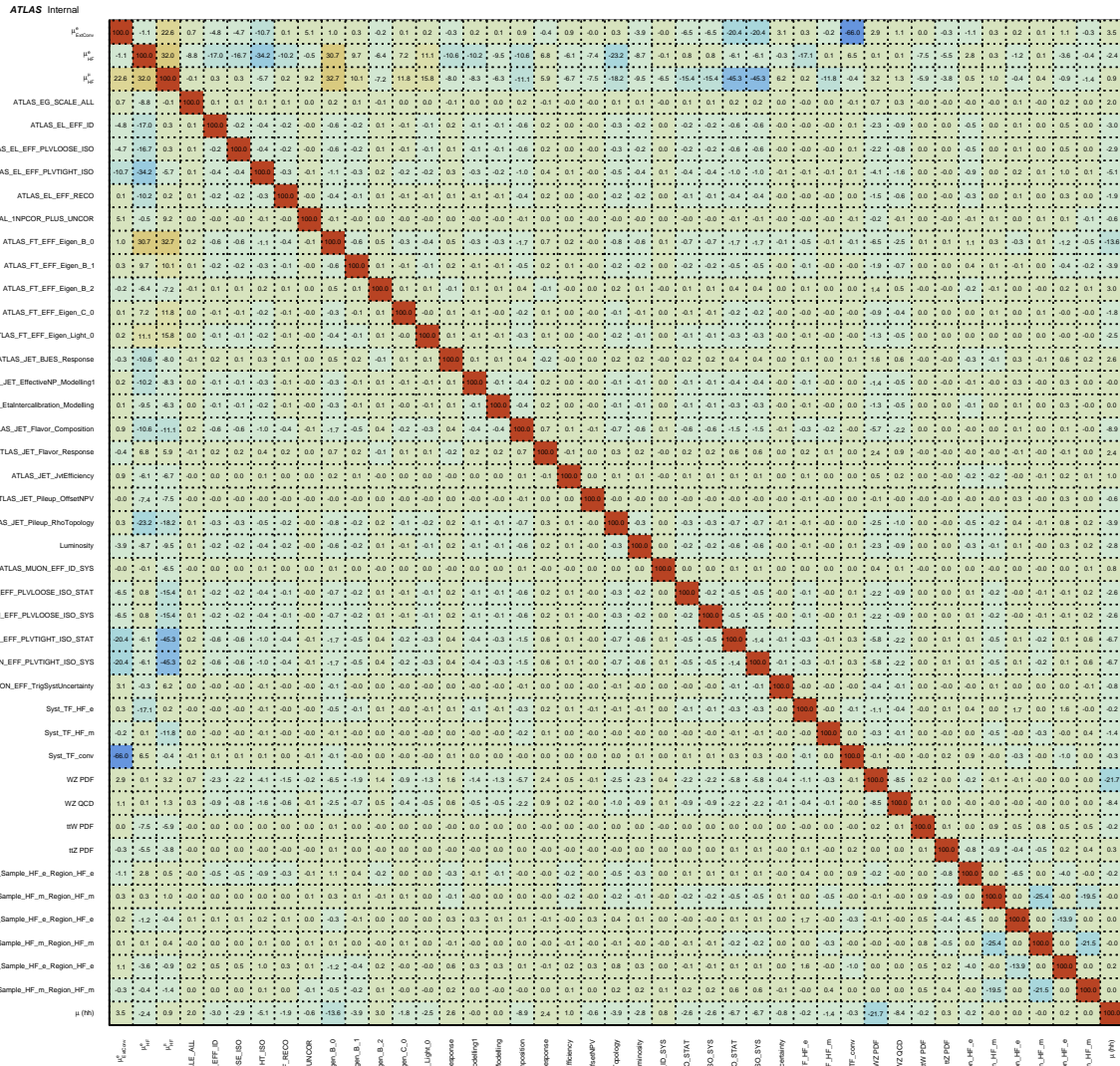


Figure 5–15 The correlation matrix in  $3\ell$  channel. All systematics and data driven nuisance parameters included.

	$-2\sigma$	$-1\sigma$	Expected	$+1\sigma$	$+2\sigma$	Observed
$\sigma_{HH}/\sigma_{HH}^{SM}$ Stats.	12.79	17.16	23.82	34.03	47.68	blinded
$\sigma_{HH}/\sigma_{HH}^{SM}$ Sys.	15.10	20.27	28.13	40.94	58.70	blinded

**Table 5–13 Expected Upper limits in  $3\ell$  channel. First row: Limits with stats only; Second row: Limits with systematics.**

3094 signal and background distributions to the observed data. The primary parameter under  
 3095 scrutiny during the fitting procedure is the ratio of the observed signal cross-section to the  
 3096 Standard Model prediction. Data within the signal region are kept blinded for unbiased re-  
 3097 sults.

3098 Subsequent to the fitting, the maximum signal significance is quantified as 0.073, while  
 3099 the upper limit on the  $HH \rightarrow 3\ell$  cross-section relative to the SM prediction stands at  
 3100  $23.13_{-6.66}^{+10.21}$  (considering only statistical uncertainties) and  $28.09_{-7.86}^{+12.81}$  (inclusive of all un-  
 3101 certainties). A comprehensive summary of these expected upper limits can be found in Ta-  
 3102 ble 5–13.

3103 Figures 5–15 and 5–14b depict the correlation matrix of the nuisance parameters and  
 3104 the ranking of the top 15 nuisance parameters, respectively. Regarding the ranked nuisance  
 3105 parameters, a few observations are noteworthy. The highest-ranking source of uncertainty  
 3106 is the statistical uncertainty of the simulation of the background in the last bin of the Signal  
 3107 Region (SR), an expected outcome owing to low statistics in that region. The second-highest  
 3108 perturbation emanates from the WZ background, which is dominant in this context. Finally,  
 3109 the third-ranking source is the b-jet calibration, which plays a crucial role in the estimation  
 3110 of fake rates in the presence of a  $t\bar{t}$  background.

## 3111 5.6 Combination Results

### 3112 5.6.1 Overview of other channels

Channel	Region	$N_{\text{lep}}^{\Sigma \ell^i}$	$N_{\text{had}}^{\Sigma \ell^i}$	$N_{\text{jet}}$	$N_{b\text{-jet}}$	BDT cut	$m_{\ell\ell\ell}$ [GeV]	$m_{\ell\ell}$ [GeV]	$m_{\ell\ell^*}$ [GeV]	$E_{\text{T}}^{\text{miss}}$ [GeV]	$m_{jj}$ [GeV]
2ℓSS	WZ CR	$3^{+1}$	0	$\geq 2$	0	$BDT_{\text{All}} < -0.4, BDT_{V\text{jets}} > -0.8$	$ m_{\ell\ell\ell} - m_Z  > 10$	$ m_{\ell\ell} - m_Z  < 10$	$ m_{\ell\ell} - m_Z  > 10$	$> 30$	$> 300$
	$W^\pm W^\pm jj$ CR	$2^{+2}$	0	$\geq 2$	0	$BDT_{\text{All}} < -0.4, BDT_{V\text{jets}} > -0.8$	$ m_{\ell\ell\ell} - m_Z  > 10$	$ m_{\ell\ell} - m_Z  < 10$	$ m_{\ell\ell} - m_Z  > 10$	$> 30$	$> 300$
	QmisID	$e^\pm e^\pm / e^\pm e^\mp$	0	$< 2$	0	$BDT_{\text{All}} < -0.4, BDT_{V\text{jets}} > -0.8$	$ m_{\ell\ell\ell} - m_Z  > 10$	$ m_{\ell\ell} - m_Z  < 10$	$ m_{\ell\ell} - m_Z  > 10$	$[76.5, 101.3]$	$> 300$
	Conv CR	$2^{+2}$	0	$\geq 2$	$\geq 1$		$ m_{\ell\ell\ell} - m_Z  > 10$	$ m_{\ell\ell} - m_Z  < 10$	$[78.5, 102.3]$	$[76.5, 101.3]$	$> 300$
	QED CR	$2^{+2}$	0	$\geq 2$	$\geq 1$		$ m_{\ell\ell\ell} - m_Z  > 10$	$ m_{\ell\ell} - m_Z  < 10$			
	HF- $e$ CR	$\ell^\pm e^\pm$	0	2,3	$\geq 1$		$ m_{\ell\ell\ell} - m_Z  > 10$	$ m_{\ell\ell} - m_Z  < 10$			
	HF- $\mu$ CR	$\ell^\pm \mu^\pm$	0	2,3	$\geq 1$		$ m_{\ell\ell\ell} - m_Z  > 10$	$ m_{\ell\ell} - m_Z  < 10$			
	VR	$2^{+2}$	0	$\geq 2$	0	$BDT_{\text{All}} < -0.4$	$ m_{\ell\ell\ell} - m_Z  > 10$	$ m_{\ell\ell} - m_Z  < 10$			$> 30$
	WZ CR	$3^{+1}$	0	$\geq 1$	0		$ m_{\ell\ell\ell} - m_Z  > 10$	$ m_{\ell\ell} - m_Z  < 10$			$> 30$
	VR	$3^{+1}$	0	$\geq 1$	0	$BDT < 0.55$	$ m_{\ell\ell\ell} - m_Z  < 10$	$ m_{\ell\ell} - m_Z  < 10$			$> 30$
$b\bar{b} + 4\ell$	Conv CR	$3^{+1}$	0	$\geq 1$	0		$ m_{\ell\ell\ell} - m_Z  < 10$	$ m_{\ell\ell} - m_Z  < 10$			
	HF- $e$ CR	$\ell^\pm e^\pm e^\mp$	0	$\geq 2$	$\geq 2$		$ m_{\ell\ell\ell} - m_Z  > 10$	$ m_{\ell\ell} - m_Z  < 10$			
	HF- $\mu$ CR	$\ell^\pm \mu^\pm \mu^\mp$	0	$\geq 2$	$\geq 2$		$ m_{\ell\ell\ell} - m_Z  > 10$	$ m_{\ell\ell} - m_Z  < 10$			
	$t\bar{t}$ CR	$\ell^\pm \ell^\mp + e^\pm \mu^\mp$	0	1	$\geq 2$		$ m_{\ell\ell\ell} - m_Z  > 10$	$ m_{\ell\ell} - m_Z  > 10$			
	$t\bar{t}Z$ CR	$\ell^\pm \ell^\mp + e^\pm \mu^\mp$	0	1	$\geq 2$		$ m_{\ell\ell\ell} - m_Z  > 10$	$ m_{\ell\ell} - m_Z  < 10$			
	VV+Higgs CR	$4^0$	0	1	0		$ m_{\ell\ell\ell} - m_Z  > 10$	$ m_{\ell\ell} - m_Z  < 10$			
	Z+jets CR	$4^0$	0	1	$\geq 2$		$ m_{\ell\ell\ell} - m_Z  > 10$	$ m_{\ell\ell} - m_Z  < 10$			
	VR	$4^0$	0	$\geq 2$	$\geq 1, \leq 3$		$ m_{\ell\ell\ell} - m_Z  > 10$	$ m_{\ell\ell\ell} - m_{\text{Higgs}}  \geq 10$			
	VR	$1^{+1}$	$2^{+2}$	$\geq 2$	0		$ m_{\ell\ell\ell} - m_Z  > 10$	$ m_{\ell\ell} - m_Z  < 10$			
	Z+jets CR	$2^0$	$2^{+2}$	$\geq 0$	0		$ m_{\ell\ell\ell} - m_Z  < 10$	$ m_{\ell\ell} - m_Z  < 10$			
$2\ell + 2\tau_{\text{had}}$	$t\bar{t}$ CR	$2^0$	$2^{+2}$	$\geq 0$	1		$ m_{\ell\ell\ell} - m_Z  > 10$	$ m_{\ell\ell} - m_Z  > 10$			
	VR	$2^{+2}$	$2^{+2}$	$\geq 0$	0		$ m_{\ell\ell\ell} - m_Z  > 10$	$ m_{\ell\ell} - m_Z  < 10$			
	Z+jets CR	$2^0$	$2^{+2}$	$\geq 0$	0		$ m_{\ell\ell\ell} - m_Z  < 10$	$ m_{\ell\ell} - m_Z  < 10$			
	$t\bar{t}$ CR	$2^0$	$2^{+2}$	$\geq 0$	1		$ m_{\ell\ell\ell} - m_Z  > 10$	$ m_{\ell\ell} - m_Z  > 10$			
	VV CR	$2^{+2}$	$1^{+1}$	$\leq 1$	0		$ m_{\ell\ell\ell} - m_Z  > 10$	$ m_{\ell\ell} - m_Z  > 10$			
	TF CR	$\ell^\pm \ell^\mp$	$1^{+1}$	$\geq 2$	0		$ m_{\ell\ell\ell} - m_Z  > 10$	$ m_{\ell\ell} - m_Z  > 10$			
	VR	$2^{+2}$	$1^{+1}$	$\geq 2$	0	$BDTG < -0.2$	$ m_{\ell\ell\ell} - m_Z  > 10$	$ m_{\ell\ell} - m_Z  > 10$			
	HF- $e$ CR	$\ell^\pm e^\pm$	$1^{+1}$	$\geq 2$	1		$ m_{\ell\ell\ell} - m_Z  > 10$	$ m_{\ell\ell} - m_Z  > 10$			
	HF- $\mu$ CR	$\ell^\pm \mu^\pm$	$1^{+1}$	$\geq 2$	$\geq 1$		$ m_{\ell\ell\ell} - m_Z  > 10$	$ m_{\ell\ell} - m_Z  > 10$			
	Fit background CR	$\geq 0$	$\geq 0$	$\geq 0$	0	$m_{\gamma\gamma}$ in sideband region in all sub-channels, $ m_{\gamma\gamma} - 125  > 5$	$ m_{\ell\ell\ell} - m_Z  > 10$	$ m_{\ell\ell} - m_Z  > 10$			

**Table 5–14 Selection criteria applied to each of the control and validation regions defined in each channel. The requirements that guarantees orthogonality with respect to the corresponding signal region are highlighted in blue.**

Channels	Selections
$2\ell SS$	Two same-sign tight leptons, $p_T \geq 20$ GeV $N_{\text{jets}} \geq 2$ and $N_{\text{b-jet}} = 0$ $m_{\ell\ell} > 12$ GeV BDT $> -0.4$
$2\ell SS + \tau_{\text{had}}$	Two same-sign tight leptons, $p_T \geq 20$ GeV $m_{\ell\ell} > 12$ GeV $N_{\text{jets}} \geq 2$ and $N_{\text{b-jet}} = 0$ exactly one RNN medium $\tau_{\text{had}}$ with $p_T \geq 25$ GeV tau with opposite charge to leptons BDTG $> -0.2$
$3\ell$	One loose lepton with leading $p_T \geq 10$ GeV and two tight leptons with $p_T > 15$ GeV total electric charge of $\pm 1$ $N_{\text{jets}} \geq 1$ and $N_{\text{b-jet}} = 0$ $m_{\ell\ell} > 12$ GeV and $ m_{\ell\ell} - 91.2  > 10$ GeV for all SFOS lepton pairs $ m_{\ell\ell\ell} - 91.2  > 10$ GeV BDT $> 0.55$
$\ell + 2\tau_{\text{had}}$	exactly one loose lepton exactly two RNN medium $\tau_{\text{had}}$ with opposite-sign $\Delta R_{(\tau_0, \tau_1)} \leq 2$ $N_{\text{jets}} \geq 2$ and $N_{\text{b-jet}} = 0$
$2\ell + 2\tau_{\text{had}}$	exactly two loose leptons with opposite-sign $m_{\ell\ell} > 12$ GeV exactly two RNN medium $\tau_{\text{had}}$ of opposite charge Z-veto for light lepton pairs $\Delta R_{(\tau_0, \tau_1)} \leq 2$ $N_{\text{jets}} \geq 1$ and $N_{\text{b-jet}} = 0$
$b\bar{b} + 4\ell$	Two leading baseline leptons and at least one subleading tight lepton, $p_T^1 \geq 20$ GeV, $p_T^2 \geq 15$ GeV, $p_T^3 \geq 10$ GeV $\Delta R > 0.02$ to any lepton pairs $m_{\ell\ell} > 5$ GeV for OSSF pairs. $50 \text{ GeV} < m_{\text{leading pair}} < 106$ GeV and $m_{\text{sub-leading pair}} < 115$ GeV $N_{\text{jets}} \geq 2$ and $3 \geq N_{\text{b-jet}} \geq 1$ $115 \text{ GeV} < M_{4\ell} < 135$ GeV
$\gamma\gamma + X$	2 tight isolated photons with $E_T > 35$ GeV and $E_T > 25$ GeV $p_T/m_{\gamma\gamma} > 0.35$ (0.25) for the leading (subleading) photon $105 \text{ GeV} < m_{\gamma\gamma} < 160$ GeV b-veto: $N_{\text{b-jet}} = 0$ $p_T^{\gamma\gamma} > 50$ GeV $E_T^{\text{miss}} > 35$ GeV except $\gamma\gamma + 1\mu 0\tau_{\text{had}}$ channel $m_{\ell\ell} > 12$ GeV in $\gamma\gamma + 2\ell$ channel Events are classified in three different categories ( $\gamma\gamma + \ell$ , $\gamma\gamma + \tau_{\text{had}}$ and $\gamma\gamma + 2\ell$ ) by means of the number of light lepton and $\tau_{\text{had}}$ .

**Table 5–15 Selection criteria applied to each channel to form the signal regions.**

3113 The definitions for the Signal Region, Control Regions, and Validation Regions across all  
3114 channels featuring multi-lepton final states have been formulated. These regions are vital for  
3115 both the optimization of the signal sensitivity and the validation of background estimations.  
3116 Detailed tabulations of these region definitions for each channel have been systematically  
3117 organized and can be found in Tables 5–15 and 5–14. These tables serve as comprehensive  
3118 references for the specialized selections employed in each region.

### 3119 5.6.2 Treatment of the Normalization Factors (NFs)

3120 In the overarching framework of this integrated analysis, the workspaces for each indi-  
 3121 vidual channel are aggregated to perform a composite fit, with the parameter  $\mu_{HH}$  designated  
 3122 as the unified Parameter of Interest (POI). To align the theoretical predictions with the em-  
 3123 pirical data, normalization factors are employed. These factors are channel-specific but are  
 3124 harmonized across channels when they address the same background source. Detailed infor-  
 3125 mation regarding these normalization factors, including their fitted values in both individual  
 3126 channels and the composite fit, is provided in Table 5–16. It is noteworthy that specific nor-  
 3127 malization factors such as  $NF\_ExtConv\_e$ ,  $\mu_{HF-e}$ , and  $\mu_{HF-\mu}$  are only fitted in a combined  
 3128 manner as they are common to multiple channels. Channels like  $\ell + 2\tau_{had}$ ,  $2\ell + 2\tau_{had}$ , and  
 3129  $\gamma\gamma + X$  do not utilize any normalization factors. Numbers in brackets in the  $2\ell SS + \tau_{had}$   
 3130 channel denote values obtained from fitting specific Control Regions.

NormFactor	$2\ell SS$	$3\ell$	$2\ell SS + \tau_{had}$	$b\bar{b} + 4\ell$	combined
$NF\_IntConv\_e$	$2.01 \pm 0.28$	-	-	-	-
$NF\_ExtConv\_e$	$0.80 \pm 0.36$	$0.66 \pm 0.13$	-	-	$0.79 \pm 0.16$
$\mu_{HF-e}$	$1.18 \pm 0.27$	$1.50 \pm 0.50$	$1.27 \pm 1.14(0.87)$	-	$1.34 \pm 0.17$
$\mu_{HF-\mu}$	$1.57 \pm 0.17$	$1.51 \pm 0.23$	$0.59 \pm 1.03(0.75)$	-	$1.56 \pm 0.12$
$\mu_{WZ}$	$0.82 \pm 0.06$	-	-	-	-
$\mu_{VVjj}$	$1.62 \pm 0.13$	-	-	-	-
$\mu_{ttW(fake)}$	$1.24 \pm 0.36$	-	-	-	-
$NF\_VV$	-	-	$0.98 \pm 0.42(0.94)$	-	-
$\mu_{i\bar{i}}$	-	-	-	$1.50 \pm 0.28$	-
$\mu_{i\bar{i}Z}$	-	-	-	$1.27 \pm 0.22$	-
$\mu_{VV}$	-	-	-	$1.12 \pm 0.46$	-
$\mu_{Higgs}$	-	-	-	$1.09 \pm 0.42$	-
$\mu_{Z+jets}$	-	-	-	$1.01 \pm 0.36$	-

**Table 5–16 Summary table of employed normalization factors, detailing individual and composite fit values. Specific channels without normalization factors are also indicated.**

#### 3131 5.6.2.1 Systematics Correlation Scheme

3132 A comprehensive outline of the correlation landscape among various uncertainties is pre-  
 3133 sented in Table 5–16. Luminosity and pile-up re-weighting uncertainties are fully correlated  
 3134 across the board. Owing to channel-specific target objects, experimental uncertainties man-

NPs	2lss	2lss1tau	3l	1l2tau	2l2tau	bb4l	yym1	Treatment
Lumi.+PRW	LUMI_Run2 PU_PRW_DATASF							correlated
EGamma	RES_ALL, SCALE_ALL, SCALE_AF2					RES_ALL SCALE_AF2	RES_ALL SCALE_ALL SCALE_AF2	correlated
Photon	-	-	-	-	-	-	EFF_ID EFF_ISO EFF_TRIGGER	-
Lepton	Common ATLAS NPs							correlated
Tau								
Jet+MET								
Flavor								
Theory	HH signal backgrounds					ggHH signal VBF HH signal backgrounds	HH signal Single Higgs	Mostly correlated
Others	QMisID			Fake tau			Background modeling	uncorrelated

Figure 5–16 Correlation scheme of the systematic uncertainties in the analysis.

3135 ifest correlations for common objects between channels. For theoretical uncertainties tied to  
 3136 Di-Higgs signal processes, a full correlation is maintained across all channels, with a notable  
 3137 exception being the  $b\bar{b} + 4\ell$  channel. In this channel, signal uncertainties are partitioned  
 3138 distinctly for ggF and VBF HH processes.

3139 In the  $\gamma\gamma + X$  channel, only uncertainties related to single Higgs processes are factored  
 3140 into the background modeling. The continuum background in this channel is regulated by  
 3141 data from sidebands and encapsulated within the domain of background modeling uncer-  
 3142 tainties. For other theoretical uncertainties, correlation is generally applied where relevant,  
 3143 particularly when the definition of "other background" overlaps between channels.

### 3144 5.6.2.2 Combination Results

3145 The synthesis of 95% Confidence Level upper limits across all multi-lepton sub-channels  
 3146 is enumerated in Table 5–17 and visually represented in Fig. 5–17. These limits are derived  
 3147 using Asimov datasets to separately assess the contributions of statistical uncertainties alone,  
 3148 statistical combined with Monte Carlo uncertainties, and a fully systematic scenario. It is  
 3149 noteworthy that most channels suffer from limited MC statistics, with the  $\gamma\gamma + X$  sub-channels  
 3150 standing as an exception.

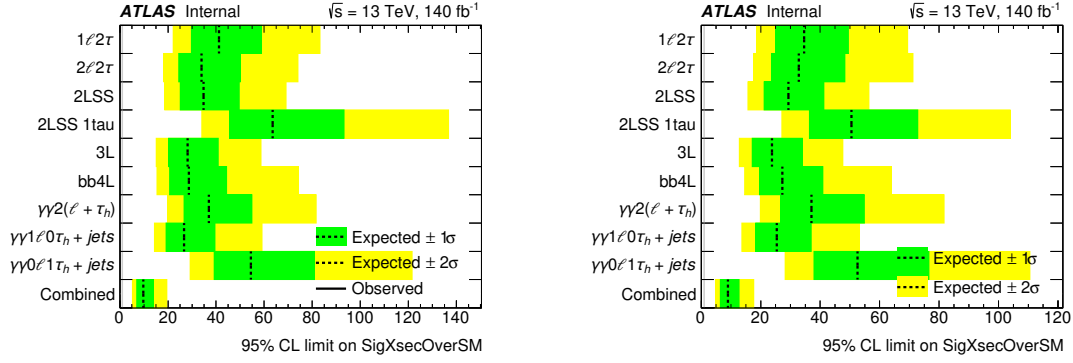


Figure 5–17 Expected individual and combined upper limits in channels, with full systematic uncertainties (left) and statistics only (right).

Channels	Stats. Only	Stats. + MC syst.	Stats.+ full syst.
2lSS	30.70 <sup>43.47</sup> <sub>22.12</sub>	31.62 <sup>44.76</sup> <sub>22.79</sub>	34.81 <sup>49.61</sup> <sub>25.08</sub>
3l	23.82 <sup>34.03</sup> <sub>17.16</sub>	25.58 <sup>37.00</sup> <sub>18.43</sub>	28.13 <sup>40.94</sup> <sub>20.27</sub>
b $\bar{b}$ + 4l	27.24 <sup>40.90</sup> <sub>19.63</sub>	27.62 <sup>41.76</sup> <sub>19.90</sub>	28.71 <sup>44.41</sup> <sub>20.68</sub>
l + 2 $\tau_{had}$	34.64 <sup>49.51</sup> <sub>24.96</sub>	38.31 <sup>54.33</sup> <sub>27.60</sub>	41.21 <sup>58.92</sup> <sub>29.70</sub>
2l + 2 $\tau_{had}$	32.82 <sup>48.34</sup> <sub>23.65</sub>	33.46 <sup>49.12</sup> <sub>24.11</sub>	33.99 <sup>50.09</sup> <sub>24.49</sub>
2LSS + $\tau_{had}$	50.50 <sup>72.83</sup> <sub>36.39</sub>	62.37 <sup>91.18</sup> <sub>44.94</sub>	63.52 <sup>93.27</sup> <sub>45.77</sub>
$\gamma\gamma$ + l	25.43 <sup>36.95</sup> <sub>18.32</sub>	25.43 <sup>36.95</sup> <sub>18.32</sub>	26.68 <sup>39.53</sup> <sub>19.23</sub>
$\gamma\gamma$ + $\tau_{had}$	52.58 <sup>76.54</sup> <sub>37.89</sub>	52.50 <sup>76.57</sup> <sub>37.90</sub>	54.50 <sup>80.98</sup> <sub>39.27</sub>
$\gamma\gamma$ + 2l	37.05 <sup>54.86</sup> <sub>26.70</sub>	37.05 <sup>54.86</sup> <sub>26.70</sub>	38.21 <sup>57.76</sup> <sub>27.53</sub>
Combined	8.93 <sup>12.69</sup> <sub>6.44</sub>	9.29 <sup>13.22</sup> <sub>6.70</sub>	9.74 <sup>13.91</sup> <sub>7.02</sub>

Table 5–17 Table of 95% C.L. upper limits on signal strength for multi-lepton channels. Limits are derived using Asimov datasets under varying scenarios of statistical and systematic uncertainties.

## Chapter 6 SM Di-Higgs Searches in $b\bar{b}\tau^+\tau^-$ Final States

### 6.1 Introduction

The search for SM production of Higgs boson pairs ( $HH$ ) serves as a pivotal probe of the electroweak symmetry breaking mechanism, as mentioned in Section 2.3.2. Among various decay channels, the  $b\bar{b}\tau^+\tau^-$  final state stands unique in terms of both signature and utility. This channel consists of two bottom quarks and two  $\tau$  leptons. It holds the third-highest branching fraction of 7.3%, following  $b\bar{b}b\bar{b}$  (34%) and  $b\bar{b}WW^*$  (25%). Despite its lower branching fraction, the  $b\bar{b}\tau^+\tau^-$  channel offers a cleaner experimental signature compared to the aforementioned channels.

The  $\tau$  leptons can decay in two distinct modes: leptonically ( $\tau_{\text{lep}}$ ) into an electron or a muon, and hadronically ( $\tau_{\text{had}}$ ) into typically one (1-prong) or three (3-prong) charged hadrons accompanied by neutral hadrons. Consequently, this analysis considers two sub-channels:  $b\bar{b}\tau_{\text{lep}}\tau_{\text{had}}$  and  $b\bar{b}\tau_{\text{had}}\tau_{\text{had}}$ , with the  $b\bar{b}\tau_{\text{lep}}\tau_{\text{lep}}$  events being analyzed separately in  $b\bar{b}\ell^+\ell^-$  channel.

The present analysis builds on previous work<sup>[153]</sup> which was primarily optimized for the gluon-gluon fusion Standard Model production mode. The legacy analysis set an upper limit on the  $HH$  cross-section to 130 (110) fb at 95% CL, corresponding to 4.7 (3.9) times the SM prediction. While the legacy analysis provided important constraints on the  $\kappa_\lambda$  modifier, with a 95% confidence interval of  $[-2.4, 9.2]$ , the present analysis aims to improve these results through methodological enhancements and additional categorizations.

This analysis introduces several refinements:

- It is re-optimized specifically for constraining the  $\kappa_\lambda$  modifier by implementing an event categorization based on the invariant mass of the  $HH$  system ( $m_{HH}$ ) in the ggF region.
- The sensitivity to the  $\kappa_{2V}$  parameter has been enhanced by adding a dedicated vector boson fusion (VBF) category.
- Advanced multivariate analysis (MVA) techniques are utilized for optimal signal-background separation, and the MVA outputs serve as the final discriminants in the fitting procedure.

Table 6–1 Summary of MC samples for signal and background processes.

Process	ME generator	ME QCD order	ME PDF	PS and hadronisation	UE model tune	Cross-section order
<b>Signal</b>						
$gg \rightarrow HH$ (ggF with $\kappa_t = 1, 10$ )	POWHEG BOX v2	NLO	PDF4LHC15NLO	PYTHIA 8.244	A14	NNLO FTApprox
$qq \rightarrow qqHH$ (VBF with varied $\kappa_t, \kappa_{2V}, \kappa_V$ )	MADGRAPH5_AMC@NLO 2.7.3	LO	NNPDF3.0NLO	PYTHIA 8.244	A14	N <sup>3</sup> LO(QCD)
<b>Top-quark</b>						
$t\bar{t}$	POWHEG BOX v2	NLO	NNPDF3.0NLO	PYTHIA 8.230	A14	NNLO+NNLL
$t$ -channel	POWHEG BOX v2	NLO	NNPDF3.0NLO	PYTHIA 8.230	A14	NLO
$s$ -channel	POWHEG BOX v2	NLO	NNPDF3.0NLO	PYTHIA 8.230	A14	NLO
$Wt$	POWHEG BOX v2	NLO	NNPDF3.0NLO	PYTHIA 8.230	A14	NLO
$t\bar{t}Z$	SHERPA 2.2.1	NLO	NNPDF3.0NNLO	SHERPA 2.2.1	Default	NLO
$t\bar{t}W$	SHERPA 2.2.8	NLO	NNPDF3.0NNLO	SHERPA 2.2.8	Default	NLO
<b>Vector boson + jets</b>						
$W/Z$ +jets	SHERPA 2.2.11	NLO ( $\leq 2$ jets) LO (3,4,5 jets)	NNPDF3.0NNLO	SHERPA 2.2.11	Default	NNLO
<b>Diboson</b>						
$WW, WZ, ZZ$	SHERPA 2.2.1	NLO ( $\leq 1$ jet) LO (2,3 jets)	NNPDF3.0NNLO	SHERPA 2.2.1	Default	NLO
<b>Single Higgs boson</b>						
ggF	POWHEG BOX v2	NNLO	NNPDF3.0NLO	PYTHIA 8.212	AZNLO	N <sup>3</sup> LO(QCD)+NLO(EW)
VBF	POWHEG BOX v2	NLO	NNPDF3.0NLO	PYTHIA 8.212	AZNLO	NNLO(QCD)+NLO(EW)
$qq \rightarrow WH$	POWHEG BOX v2	NLO	NNPDF3.0NLO	PYTHIA 8.212	AZNLO	NNLO(QCD)+NLO(EW)
$qq \rightarrow ZH$	POWHEG BOX v2	NLO	NNPDF3.0NLO	PYTHIA 8.212	AZNLO	NNLO(QCD)+NLO(EW) <sup>(†)</sup>
$gg \rightarrow ZH$	POWHEG BOX v2	NLO	NNPDF3.0NLO	PYTHIA 8.212	AZNLO	NLO+NNL
$t\bar{t}H$	POWHEG BOX v2	NLO	NNPDF3.0NLO	PYTHIA 8.230	A14	NLO

## 6.2 Data and Monte Carlo samples

The analysis presented in this chapter uses proton-proton collision data, taken at a centre-of-mass energy of  $\sqrt{s} = 13$  TeV by the ATLAS experiment from 2015 to 2018. The data corresponds to an integrated luminosity of  $\mathcal{L} = 140.1 \pm 1.2 \text{ fb}^{-1}$ <sup>[154]</sup>. Event selections were based on the ATLAS Good-Run-List (GRL) to ensure the operational integrity of all relevant detector components.

To simulate the SM backgrounds and both SM and BSM  $HH$  signal, we utilize Monte Carlo event samples. These samples are processed through the ATLAS detector simulation based on Geant4<sup>[129]</sup>. Pile-up effects are incorporated by overlaying minimum-bias events generated via PYTHIA 8.186<sup>[127]</sup> with A3 tune<sup>[128]</sup> and the NNPDF2.3LO<sup>[155]</sup> PDFs. The hadronic decays of  $b$  and  $c$  quarks are modeled by the EVTGEN program<sup>[156]</sup>, except in samples generated with SHERPA<sup>[157]</sup>, where generator-specific models are used.

For all MC samples containing a SM Higgs boson, a mass of 125 GeV is assumed for consistency in both decay branching fractions and cross-section calculations. The cross-sections are calculated with expansions in the strong coupling constant ( $\alpha_s$ ), unless otherwise specified.

3195 The MC samples are summarized in Table 6–1, which details the generators used for  
 3196 simulating the signal and background processes. The nomenclatures ME, PS, and UE refer  
 3197 to matrix element, parton shower, and underlying event, respectively. Note that for samples  
 3198 with ( $\dagger$ ), the  $qq \rightarrow ZH$  process is normalized to the NNLO (QCD) + NLO (EW) cross-  
 3199 section for the  $pp \rightarrow ZH$  process, after the  $gg \rightarrow ZH$  contribution is subtracted.

## 3200 6.2.1 Simulation of Signal Datasets

3201 The  $HH$  signal is modeled considering both gluon-gluon fusion (ggF) and vector-boson  
 3202 fusion (VBF) as contributing processes.

### 3203 6.2.1.1 ggF $HH$ production

3204 Samples<sup>1</sup> for  $\kappa_\lambda$  values of 1.0 and 10.0 were generated using POWHEG BOX v2 at NLO  
 3205 with finite top-quark mass considerations<sup>[158]</sup>. The PDF4LHC15\_NLO\_30\_PDFAS PDF set  
 3206 (code 90400 in LHAPDF<sup>[159]</sup>) was employed<sup>[160]</sup>. Parton showering and hadronisation were  
 3207 performed via PYTHIA 8.244<sup>[127]</sup> using the A14 tune<sup>[161-162]</sup> and NNPDF2.3LO PDF set. Fig-  
 3208 ure 6–1 depicts the invariant mass distribution  $m_{HH}$  for ggF  $HH$  samples in the  $\tau_{\text{had}}\tau_{\text{had}}$  chan-  
 3209 nel, highlighting the potential for analysis categorization as elaborated in Section 6.3.4.

3210 To model ggF  $HH$  events with varied  $\kappa_\lambda$  values in the range  $\kappa_\lambda \in [-20, 20]$ , either of  
 3211 the two base samples can be reweighted using the  $HH$   $\kappa_\lambda$  reweighting tool<sup>2</sup>, which offers  
 3212 event-specific weightings as a function of the desired  $\kappa_\lambda$  value and the true  $m_{HH}$ .

3213 The SM process normalization is defined by the di-Higgs cross-section in the ggF chan-  
 3214 nel,  $\sigma_{\text{ggF}} = 31.05$  fb, as computed at NNLO FTApprox<sup>[163]</sup>, and then multiplied by the  
 3215  $b\bar{b}\tau^+\tau^-$  branching ratio, leading to a value of 2.2683967 fb.

3216 Alternative ggF samples<sup>3</sup> for  $\kappa_\lambda = 1.0, 10.0$  were also generated using the POWHEG BOX v2  
 3217 at NLO and were interfaced with HERWIG 7<sup>[164]</sup> to examine parton showering uncertainties.

### 3218 6.2.1.2 VBF $HH$ production

3219 VBF signal samples were synthesized at leading order (LO) utilizing the MADGRAPH5\_AMC@NLO 2.7.  
 3220 framework, in combination with the NNPDF3.0NLO PDF model<sup>[126]</sup>. The parton showers and  
 3221 subsequent hadronization steps were conducted through PYTHIA 8.244 with the A14 config-

<sup>1</sup> <https://its.cern.ch/jira/browse/ATLMCPROD-8884>

<sup>2</sup> kLambdaReweightTool

<sup>3</sup> <https://its.cern.ch/jira/browse/ATLMCPROD-9170>

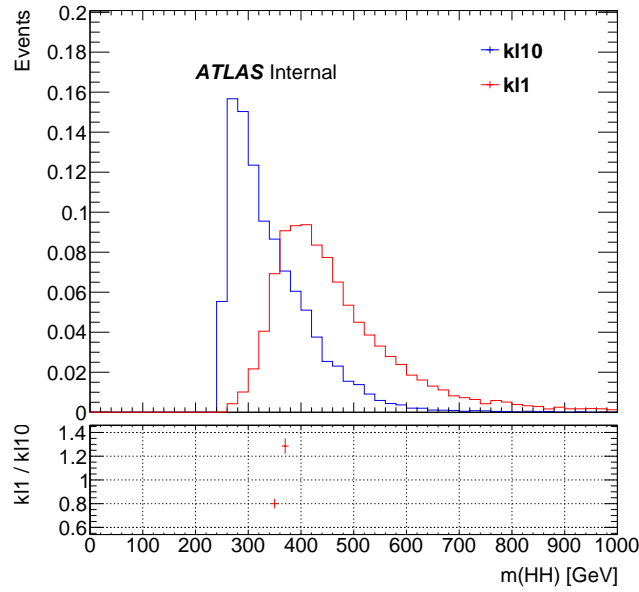


**Figure 6–1** Invariant mass ( $m_{HH}$ ) distribution at the parton level for the ggF  $HH$  signal in the  $T_{had}T_{had}$  channel, with overlaid  $\kappa_\lambda$  values of 1.0 and 10.0.

3222 uration and NNPDF2.3LO PDF set. Various coupling modulators  $\kappa_\lambda$ ,  $\kappa_{2V}$ , and  $\kappa_V$  were em-  
 3223 ployed, as cataloged in Table 6–2. A linear blend of six reference points in the  $(\kappa_\lambda, \kappa_{2V}, \kappa_V)$   
 3224 space allows for more refined granularity in  $\kappa_{2V}$  values.

**Table 6–2** Considered  $\kappa_\lambda$ ,  $\kappa_{2V}$ , and  $\kappa_V$  coupling modifiers for VBF  $HH$  simulations.

$\kappa_\lambda$	$\kappa_{2V}$	$\kappa_V$
1	1	1
1	0	1
1	0.5	1
1	1.5	1
1	2	1
1	3	1
0	1	1
2	1	1
10	1	1
1	1	0.5
1	1	1.5
0	0	1
-5	1	0.5

3225 Figures 6–2 display representative parton-level distributions of these samples, featuring  
 3226 key observables and their relation to the coupling parameters<sup>[166]</sup>.

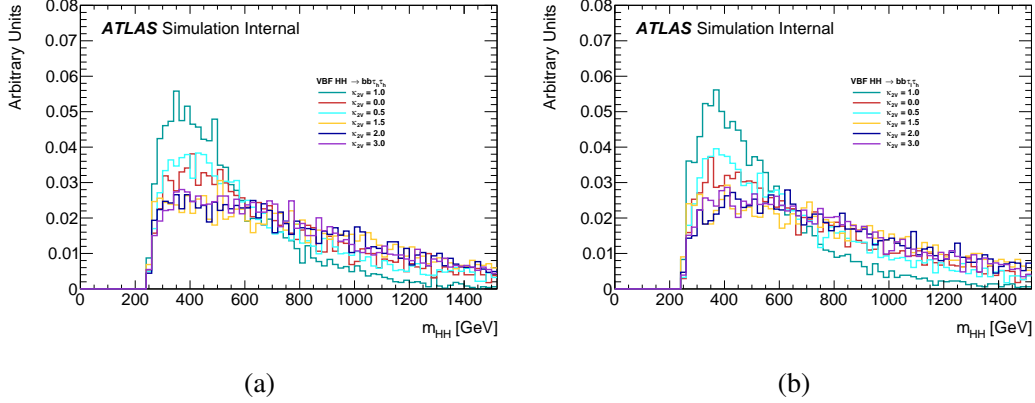


**Figure 6–2 Inclusive distributions of VBF  $HH$  samples for varying  $\kappa_{2V}$  at parton-level, presented for the  $\tau_{\text{had}}\tau_{\text{had}}$  and  $\tau_{\text{lep}}\tau_{\text{had}}$  channels. Couplings are adjusted as outlined in Table 6–2.**

3227 The SM normalization is determined by the VBF  $HH$  cross-section  $\sigma_{\text{VBF}} = 1.726$  fb,  
 3228 calculated at N<sup>3</sup>LO in QCD, and the  $b\bar{b}\tau^+\tau^-$  branching ratio, resulting in a final value of  
 3229  $\sigma_{\text{VBF}} \times \mathcal{B}(b\bar{b}\tau^+\tau^-) = 0.126$  fb. BSM normalization follows a quadratic function of  $\kappa_{2V}$ <sup>[148]</sup>.

3230 For systematic variations in parton shower, alternate VBF  $HH$  samples were produced at  
 3231 specific coupling values, as denoted in Table 6–3, using the MADGRAPH5\_AMC@NLO 2.7.3  
 3232 and NNPDF3.0NLO models, interfaced to HERWIG 7<sup>[164]</sup>.

**Table 6–3 Coupling modifier values for generating alternative VBF  $HH$  samples.**

$\kappa_\lambda$	$\kappa_{2V}$	$\kappa_V$
1	1	1
1	0	1
10	1	1

### 3233 6.2.2 Background Simulation Samples

3234 **Top Quark Processes** The simulation of both top-antitop ( $t\bar{t}$ ) and individual top quark  
 3235 productions in  $Wt$ ,  $s$ , and  $t$ -channels are generated through the POWHEG BOX v2 genera-  
 3236 tor<sup>[167-169]</sup>. The PDF utilized is NNPDF30NLO<sup>[170]</sup>. Post-generation event dynamics, in-  
 3237 cluding parton showers and hadronization, are conducted with PYTHIA 8 version 8.230<sup>[171]</sup>.

3238 The tuning parameter set used is A14<sup>[162,172]</sup>. The decays of bottom and charm hadrons are  
3239 handled via EvtGen v1.6.0<sup>[66]</sup>.

3240 **Vector Boson + Jets ( $V$ +jets)** These events, containing either  $W$  or  $Z$  bosons accompa-  
3241 nied by jets, are generated through the SHERPA 2.2.11<sup>[157]</sup>. A mixed NLO and LO framework  
3242 for matrix elements is used, with NLO matrix elements considering up to two additional  
3243 partons and LO matrix elements accounting for up to five additional partons. These are com-  
3244 puted through Comix<sup>[173]</sup> and OPENLOOPS<sup>[174-176]</sup>.

3245 **Diboson Processes** Diboson events, characterized by one boson decaying hadronically  
3246 and the other leptonically, are modeled using SHERPA version 2.2.1<sup>[157]</sup>. PDFs are based on  
3247 the NNPDF3.0NNLO set<sup>[126]</sup>.

3248 **Top-Quark and Vector Boson Associated Production ( $ttV$ )** Simulations are executed  
3249 using SHERPA v2.2.1 for  $ttZ$  and SHERPA v2.2.8 for  $ttW$ , both employing multileg NLO  
3250 merging techniques. PDFs are based on NNPDF3.0NNLO<sup>[126]</sup>.

3251 **SM Single Higgs Production** This analysis incorporates SM Higgs boson as a part of  
3252 the background and is elaborated below:

- 3253 •  $ttH$ : Produced via POWHEG BOX, it employs NNPDF30NLO for PDFs and PYTHIA 8  
3254 v8.230 for parton showers<sup>[171]</sup>.
- 3255 •  $ZH$ : Utilizes POWHEG BOX v2 and considers both  $qqZH$  and  $ggZH$  channels. PDFs  
3256 are NNPDF3.0NNLO<sup>[126]</sup>.
- 3257 •  $WH$ : Generated using POWHEG BOX v2 with PDFs from NNPDF3.0NNLO<sup>[126]</sup>.
- 3258 •  $ggF H \rightarrow \tau^+\tau^-$ : Simulated through POWHEG BOX v2 with NNPDF3.0NNLO PDFs<sup>[126]</sup>.
- 3259 •  $VBF H \rightarrow \tau^+\tau^-$ : Produced via POWHEG BOX v2, using NNPDF3.0NNLO<sup>[126]</sup> for  
3260 PDFs.

### 3261 6.3 Event selection

3262 The analysis procedure is divided into two sub-channels according to the di- $\tau$  decay  
3263 mode. A schematic representation of this approach is provided in Figure 6–3. The first sub-  
3264 channel, denoted as  $b\bar{b}\tau_{\text{had}}\tau_{\text{had}}$ , focuses on events featuring two oppositely charged  $\tau_{\text{had-vis}}$   
3265 along with two  $b$ -jets. The second, termed  $b\bar{b}\tau_{\text{lep}}\tau_{\text{had}}$ , targets events with one lepton (elec-  
3266 tron or muon), one oppositely charged  $\tau_{\text{had-vis}}$ , and two  $b$ -jets. For both sub-channels, the two  
3267  $b$ -jets are required to pass a working point with 77% efficiency.

3268 The schematic in Figure 6–3 illustrates the sequence of triggers and event selection cri-  
 3269 teria for the two sub-channels. It also depicts the BDT framework that establishes the Signal  
 3270 Regions (SR) orthogonality between ggF and VBF categories. Further, the ggF SR is par-  
 3271 titioned by an invariant mass threshold of 350 GeV to enhance sensitivity to the parameter  
 3272  $K_\lambda$ .

3273 Event classification into ggF and VBF SRs is achieved through specialized BDTs. The  
 3274 ggF SRs are further divided into low- and high-mass regions using an invariant mass cut-off  
 3275 of 350 GeV for the HH system.

3276 A Control Region (CR), designated as Z+HF CR, is established to calibrate the Z+HF  
 3277 background normalization. This CR utilizes  $bbl\ell$  triggers and focuses on the  $m_{\ell\ell}$  shape as  
 3278 the parameter of interest, consistent with the schematic representation.

3279 Both sub-channels are required to pass a common set of object selection criteria as in  
 3280 Section 6.3.1. Detailed trigger configurations for these sub-channels are elaborated in Sec-  
 3281 tion 6.3.2. Subsequent sections will elucidate the updated definition of the Z+HF CR phase  
 3282 space relative to the prior analysis<sup>[177]</sup>.

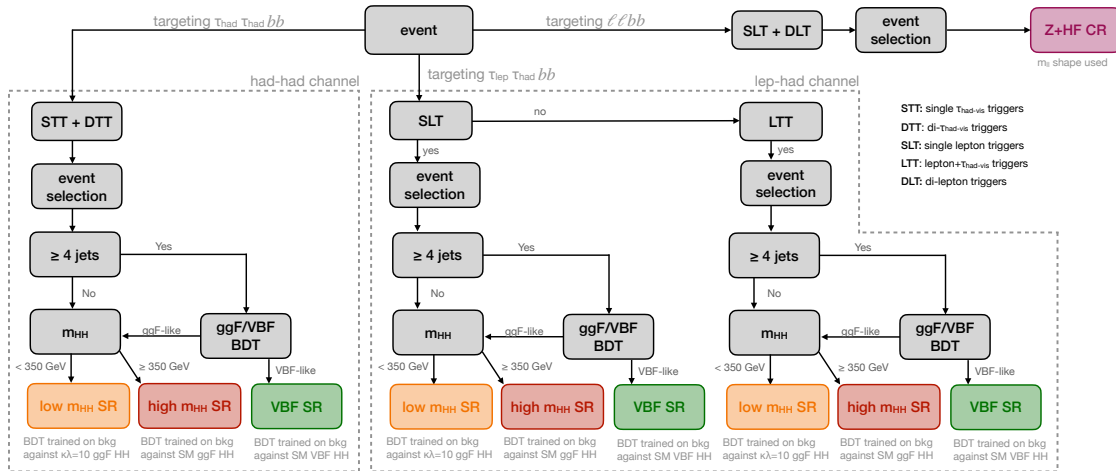


Figure 6–3 Schematic representation of the analysis strategy.

3283 An overview of the event selection procedures is provided in Table 6–4. This table disag-  
 3284 gregates the event criteria according to the different triggers that are employed for selection.  
 3285 For events requiring pairs of reconstructed objects of identical nature, the table specifies dis-  
 3286 tinct  $p_T$  thresholds for both leading and sub-leading objects. These are indicated outside and

$\tau_{\text{had}}\tau_{\text{had}}$ category		$\tau_{\text{lep}}\tau_{\text{had}}$ categories	
STT	DTT	SLT	LTT
<b><math>e/\mu</math> selection</b>			
No loose $e/\mu$		Exactly one loose $e/\mu$	
		$e$ ( $\mu$ ) must be tight (medium and have $ \eta  < 2.5$ )	
		$p_{\text{T}}^e > 25, 27$ GeV	$18$ GeV $< p_{\text{T}}^e <$ SLT cut
		$p_{\text{T}}^\mu > 21, 27$ GeV	$15$ GeV $< p_{\text{T}}^\mu <$ SLT cut
<b><math>\tau_{\text{had-vis}}</math> selection</b>			
Two loose $\tau_{\text{had-vis}}$		One loose $\tau_{\text{had-vis}}$	
		$ \eta  < 2.3$	
$p_{\text{T}} > 100, 140, 180$ (25) GeV	$p_{\text{T}} > 40$ (30) GeV		$p_{\text{T}} > 30$ GeV
<b>Jet selection</b>			
$\geq 2$ jets with $ \eta  < 2.5$			
Leading jet $p_{\text{T}} > 45$ GeV	Trigger dependent	Leading jet $p_{\text{T}} > 45$ GeV	Trigger dependent
<b>Event-level selection</b>			
Trigger requirements passed			
Collision vertex reconstructed			
$m_{\tau\tau}^{\text{MMC}} > 60$ GeV			
Opposite-sign electric charges of $e/\mu/\tau_{\text{had-vis}}$ and $\tau_{\text{had-vis}}$			
Exactly two $b$ -tagged jets			
$m_{bb} < 150$ GeV			

**Table 6–4 Summary of the event selections, shown separately for events that are selected by different triggers.**

3287 inside parentheses, respectively. In cases where the selection constraints are influenced by  
3288 the year of data acquisition, multiple acceptable parameter values are enumerated and sepa-  
3289 rated by commas. Notably, the jet selection criteria under the LTT and DTT triggers are an  
3290 exception and adhere to a more intricate set of guidelines, as detailed in Section 6.3. It is  
3291 essential to note that the listed trigger  $p_{\text{T}}$  thresholds are imposed on offline physics objects  
3292 that have been appropriately matched to their corresponding trigger entities. For the scope  
3293 of this study, the event selection will be exclusively focused on the  $\tau_{\text{had}}\tau_{\text{had}}$  channel.

### 3294 6.3.1 Object Reconstruction

#### 3295 6.3.1.1 Electrons

3296 Electron candidates in the ATLAS experiment undergo a multi-criteria reconstruction  
3297 and identification process, as summarized below<sup>[178]</sup>:

- 3298 • **Identification Criteria:**
- 3299 – Track properties: Imposed requirements on measured track attributes.
- 3300 – Calorimetric clustering: Conditions on energy deposit cluster shape.
- 3301 – Track-to-cluster matching: Quality metrics for association.
- 3302 – Track quality: Additional hit requirements.
- 3303 • **Likelihood Technique:** Utilizes a *loose* working point to achieve 95% electron identification efficiency.
- 3304
- 3305 • **Kinematic Requirements:**
- 3306 –  $p_T > 7 \text{ GeV}$
- 3307 –  $|\eta| < 2.47$  (excluding  $1.37 < |\eta| < 1.52$ )
- 3308 • **Isolation Criteria:**
- 3309 – *fixed cut loose* working point.
- 3310 –  $p_T$ -dependent upper bounds on track momenta and topo-clusters.
- 3311 • **Trigger Specifics:**
- 3312 – LTT involvement necessitates *tight* isolation working point.
- 3313 – Trigger scale factors only available for *tight* isolation electrons.

### 3314 6.3.1.2 Muons

3315 Muon candidates undergo specific reconstruction and identification procedures, as outlined below<sup>[179]</sup>:

3316

- 3317 • **Track Reconstruction:**
- 3318 – Inner Detector (ID): Independent track reconstruction.
- 3319 – Muon Spectrometer (MS): Independent track reconstruction.
- 3320 – Minimum hit requirements: Enforced in both ID and MS.
- 3321 – Combined fit: Utilizes both ID and MS for momentum refinement.
- 3322 • **Kinematic Criteria:**
- 3323 –  $p_T > 7 \text{ GeV}$
- 3324 –  $|\eta| < 2.7$
- 3325 • **Identification:**
- 3326 – Working Point: Required to pass *loose* identification criteria.
- 3327 • **Isolation:**
- 3328 – Criteria: Required to pass PflowLoose\_VarRadIso<sup>[180]</sup>.

3329 – Inversion: Performed for background control region establishment.

### 3330 6.3.1.3 hadronic- $\tau$ Leptons

#### 3331 • **Reconstruction**<sup>[181]</sup>:

3332 – Seeding: Jets formed via anti- $k_t$  algorithm,  $\Delta R = 0.4$ .

3333 – BDT Classification: Sorts tracks into core and isolation tracks within  $\Delta R = 0.4$   
3334 of  $\tau_{\text{had-vis}}$  axis.

3335 – Prongs: Defined by the number of core (charged) tracks.

#### 3336 • **Identification**<sup>[112]</sup>:

3337 – RNN Classifier: Utilized for discrimination against jet-like signatures.

3338 – Algorithms: Specific for 1-prong and 3-prong  $\tau_{\text{had-vis}}$ .

3339 – Working Points: Efficiency = 85% for 1-prong, 75% for 3-prong.

#### 3340 • **Selection Criteria:**

3341 –  $p_T > 20$  GeV

3342 –  $|\eta| < 2.5$  and veto region  $1.37 < |\eta| < 1.52$

3343 – Tracks: One or three.

3344 – Charge: Unit charge.

3345 – Working Point: *loose* with 85% efficiency for 1-prong and 75% for 3-prong.

#### 3346 • **Additional Rejection:** Against electrons.

3347 – BDT: Utilizing track and shower shape information.

3348 – Efficiency: Approximately 95% for true  $\tau_{\text{had-vis}}$ .

#### 3349 • **Anti- $\tau_{\text{had}}$ Definition**<sup>[177,182]</sup>:

3350 – Fail RNN loose  $\tau_{\text{had}}$ -ID with an RNN score  $> 0.01$ .

3351 – Defined by the Fake-Tau-Task-Force, used for background estimation.

3352 – Efficiency: Approximately 99% for true- $\tau_{\text{had}}$  in  $\gamma^* \rightarrow \tau\tau$  events.

#### 3353 • **Anti- $\tau_{\text{had}}$ Selection**<sup>[182]</sup>:

3354 – Selected in events where the number of offline  $\tau_{\text{had}}$  passing the  $\tau_{\text{had-ID}}$  is less than  
3355 the channel-specific requirement (e.g., one for the  $\tau_{\text{lep}}\tau_{\text{had}}$  channel, two for the  
3356  $\tau_{\text{had}}\tau_{\text{had}}$  channel).

3357 – Requirement: Ensures total number of selected  $\tau_{\text{had}}$  (loose and anti- $\tau_{\text{had}}$ ) corre-  
3358 sponds to the required multiplicity.

3359 – Trigger-Level Matching: For channels with  $\tau_{\text{had-ID}}$  at the trigger level, only matched

3360 anti- $\tau_{\text{had}}$  are considered.

- 3361 – Random Selection: Employed when multiple anti- $\tau_{\text{had}}$  satisfy criteria and a  $\tau_{\text{had}}$
- 3362 trigger is not used.

#### 3363 6.3.1.4 Jets

3364 Jets are reconstructed using the anti- $k_r$  algorithm<sup>[183]</sup> with a distance parameter  $R = 0.4$ ,  
 3365 and further refined using the Particle-Flow (PF) algorithm<sup>[184]</sup>. Jet cleaning is performed  
 3366 to mitigate the effects of non-collision backgrounds (NCB) and calorimeter noise, utilizing  
 3367 the jet cleaning algorithm based on certain working points<sup>[185]</sup>. The jet-vertex-tagger (JVT)  
 3368 algorithm is applied for pile-up suppression, specifically with a JVT threshold that varies  
 3369 based on  $p_T$  of the jet<sup>[161]</sup>.

3370 Calibrations for the Jet Energy Scale (JES) and Jet Energy Resolution (JER) are metic-  
 3371 ulously conducted, adhering to the protocols established in the previously cited work<sup>[184]</sup>.  
 3372 Additional corrections for pile-up and underlying event effects are also applied<sup>[186]</sup>.

#### 3373 6.3.1.5 $b$ -jet Identification and Calibration

3374  $b$ -jets are identified using a deep learning-based algorithm, the DL1r tagger<sup>[187-188]</sup>. The  
 3375 tagger utilizes jet kinematics, impact parameters, and the presence of displaced vertices to  
 3376 discriminate between  $b$ -jets and lighter jets. It takes inputs from a recurrent neural network  
 3377 for impact parameter scoring (RNNIP)<sup>[189]</sup>.

3378 The analysis utilizes pseudo-continuous  $b$ -tagging, applying multiple working points cor-  
 3379 responding to 77%, 70%, and 60%  $b$ -tagging efficiencies, following internal documenta-  
 3380 tion<sup>[182]</sup>. These working points are used for multiple discriminant analysis (MDA) optimiza-  
 3381 tions.

3382 Shape comparison plots of the DL1r quantiles of the sub-leading  $b$ -tagged jet are shown  
 3383 in Figure 6–4a for the SM ggF, ggF ( $\kappa_\lambda = 10.0$ ) and SM VBF signals, along with the sum of  
 3384 the backgrounds. Figure 6–4b shows the same variable for each background component.

3385 The  $b$ -jet energy scale (bJES) and  $b$ -jet energy resolution (bJER) are specifically cali-  
 3386 brated based on Ref.<sup>[182]</sup>. Scale factors (SF) for  $b$ -tagging efficiencies are obtained from the  
 3387 CDI file 2020-21-13TeV-MC16-CDI-2021-04-16\_v1.root<sup>[187]</sup>.

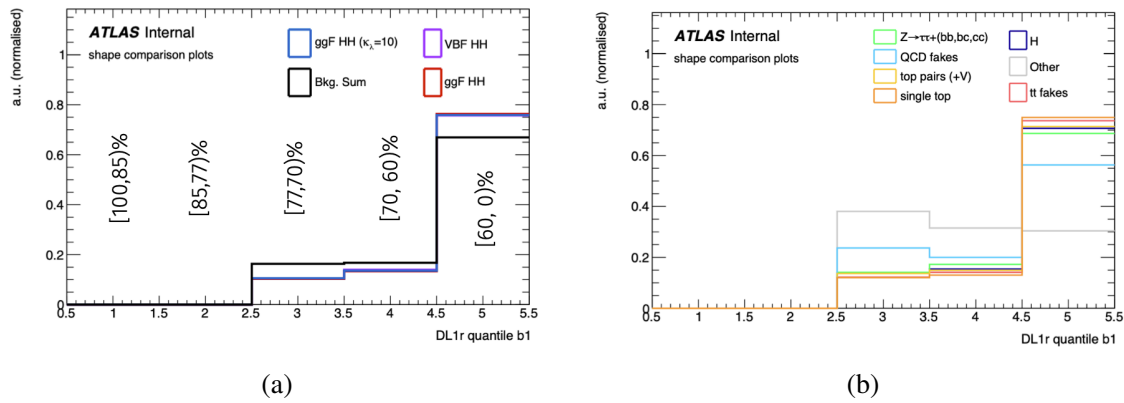


**Figure 6–4** Sub-leading  $b$ -jet DL1r quantiles. **Figure (a)** shows the SM ggF, ggF ( $\kappa_\lambda = 10.0$ ) and SM VBF signals, along with the sum of the backgrounds. **Figure (b)** shows the same variable for each background component.

### 3388 6.3.1.6 Missing Transverse Momentum ( $E_T^{\text{miss}}$ )

3389 The  $E_T^{\text{miss}}$  is determined as the negative of the accumulated transverse momentum vectors  
 3390 of calibrated leptons,  $\tau$ -leptons decaying via hadronic channels, and jets. Additionally, a ‘soft  
 3391 term’ is included, computed as the vector sum of the transverse momenta ( $p_T$ ) of tracks that  
 3392 are linked to the primary vertex but are not connected to any recognized lepton or jet<sup>[190]</sup>.

### 3393 6.3.1.7 Overlap Removal

Pair	Condition	Action	Notes
$e_1 - e_2$	Shared track	Reject $e_1$ if $p_{T1} < p_{T2}$	
$\tau_{\text{had-vis}} - e$	$\Delta R_y < 0.2$	Reject $\tau_{\text{had-vis}}$	$e$ must pass DFCommonElectronsLHLoose
$\tau_{\text{had-vis}} - \mu$	$\Delta R_y < 0.2$	Reject $\tau_{\text{had-vis}}$	Case 1: $p_{T,\tau} > 50$ GeV, $p_{T,\mu} > 2$ GeV and combined $\mu$ Case 2: $p_{T,\tau} \leq 50$ GeV, $p_{T,\mu} > 2$ GeV
$\mu - e$	Calo-muon	Reject $\mu$	Shared ID track
$e - \mu$	–	Reject $e$	Shared ID track
jet - $e$	$\Delta R_y < 0.2$	Reject jet	
$e - \text{jet}$	$\Delta R_y < 0.4$	Reject $e$	
jet - $\mu$	$N_{\text{track}} < 3$ or $\Delta R_y < 0.2$	Reject jet	$p_{T,\text{track}} > 500$ MeV
$\mu - \text{jet}$	$\Delta R_y < 0.4$	Reject $\mu$	
jet - $\tau_{\text{had-vis}}$	$\Delta R_y < 0.2$	Reject jet	Analysis-specific
anti- $\tau_{\text{had-vis}} - \text{jet}$	$\Delta R_y < 0.2$	Reject anti- $\tau$	Only if jet is $b$ -tagged
jet - anti- $\tau_{\text{had-vis}}$	$\Delta R_y < 0.2$	Reject jet	

**Table 6–5** Summary of overlap-removal procedures with the standard working point.

3394 After event reconstruction, an overlap-removal algorithm is utilized to address instances

3395 where a single physical object is identified as multiple particle types in the ATLAS detector.  
 3396 The algorithm measures the angular separation between two reconstructed objects using the  
 3397 metric  $\Delta R_y = \sqrt{\Delta y^2 + \Delta\phi^2}$ .

3398 For most particle combinations, a standard toolkit called AssociationUtils is employed  
 3399 with a default working point<sup>[191]</sup>. However, the overlap between reconstructed  $\tau_{\text{had, vis}}$  and  
 3400 jets follows a unique, analysis-specific procedure. Specialized overlap-removal algorithms  
 3401 are also applied to  $\tau_{\text{had, vis}}$ , anti- $\tau_{\text{had, vis}}$ , and jets, adhering to a predefined priority sequence  
 3402 ( $\tau_{\text{had, vis}} > \text{anti-}\tau_{\text{had, vis}} > \text{jets}$ ). The summary of the overlap removal steps and the standard  
 3403 working point is presented in Table 6–5.

## 3404 6.3.2 Trigger Selection

### 3405 6.3.2.1 $\tau_{\text{had}}\tau_{\text{had}}$

3406 The trigger logic for the  $\tau_{\text{had}}\tau_{\text{had}}$  sub-channel comprises two types: single- $\tau_{\text{had-vis}}$  triggers  
 3407 (STTs) and di- $\tau_{\text{had-vis}}$  triggers (DTTs). STTs require at least one  $\tau_{\text{had-vis}}$  at the High-Level  
 3408 Trigger (HLT) with a  $p_T$  threshold varying between 80 GeV and 160 GeV, dependent on the  
 3409 data collection epoch. DTTs necessitate at least a  $\tau_{\text{had-vis}}$  pair at the HLT with a minimum  $p_T$   
 3410 of 35 GeV and 25 GeV for the leading and sub-leading  $\tau_{\text{had-vis}}$ , respectively.

3411 From 2016 onward, additional criteria were enforced at the Level-1 (L1) trigger to miti-  
 3412 gate DTT rate inflation. For the 2016 dataset, an extra jet with  $E_T > 25$  GeV was required.  
 3413 The 2017 and 2018 periods used additional jet requirements based on offline jet presence,  
 3414 with specific energy and spatial constraints.

3415 To enhance trigger modelling, offline  $\tau_{\text{had-vis}}$  objects are constrained to be spatially near  
 3416 the HLT  $\tau_{\text{had-vis}}$  objects within  $\Delta R = 0.2$  and also meet additional  $p_T$  requirements. Events  
 3417 satisfying both STTs and DTTs are processed using the STT offline constraints.

3418 For a comprehensive list of triggers, refer to Table 6–6. Additional specifications can be  
 3419 found in internal documentation<sup>[182]</sup> and the previous analysis iteration<sup>[177]</sup>.

## 3420 6.3.3 $\tau_{\text{had}}\tau_{\text{had}}$ Event Selection

3421 In addition to the trigger selection delineated in Section 6.3.2, supplementary selection  
 3422 criteria are imposed to isolate the signal region in the  $\tau_{\text{had}}\tau_{\text{had}}$  sub-channel. In this context,

<sup>1</sup> ATL-COM-PHYS-2020-766

Period	Trigger
<b>Single-<math>\tau_{\text{had-vis}}</math> triggers (STT)</b>	
15 – 16 A	HLT_tau80_medium1_tracktwo_L1TAU60
16 B – 16 D3	HLT_tau125_medium1_tracktwo
16 D4 – 17 B4	HLT_tau160_medium1_tracktwo
17 B5 – 17 end	HLT_tau160_medium1_tracktwo_L1TAU100
18 –	HLT_tau160_medium1_tracktwoEF_L1TAU100
18 K –	HLT_tau160_mediumRNN_tracktwoMVA_L1TAU100
<b>Di-<math>\tau_{\text{had-vis}}</math> triggers (DTT)</b>	
15	HLT_tau35_medium1_tracktwo_tau25_medium1_tracktwo_L1TAU20IM_2TAU12IM
16 – 17 B4	HLT_tau35_medium1_tracktwo_tau25_medium1_tracktwo
17	HLT_tau35_medium1_tracktwo_tau25_medium1_tracktwo_L1TAU20IM_2TAU12IM_4J12
17 B5 – 17 end	HLT_tau35_medium1_tracktwo_tau25_medium1_tracktwo_L1DR-TAU20ITAU12I-J25
18 –	HLT_tau35_medium1_tracktwoEF_tau25_medium1_tracktwoEF_L1TAU20IM_2TAU12IM_4J12.0ETA23
18 –	HLT_tau35_medium1_tracktwoEF_tau25_medium1_tracktwoEF_L1DR-TAU20ITAU12I-J25
18 K –	HLT_tau35_mediumRNN_tracktwoMVA_tau25_mediumRNN_tracktwoMVA_L1TAU20IM_2TAU12IM_4J12.0ETA23
18 K –	HLT_tau35_mediumRNN_tracktwoMVA_tau25_mediumRNN_tracktwoMVA_L1DR-TAU20ITAU12I-J25

**Table 6–6 Data-taking triggers for the  $\tau_{\text{had}}\tau_{\text{had}}$  channel.**

each event is mandated to encompass exactly two  $\tau$ -leptons that satisfy the *loose* identification prerequisites. These  $\tau$ -leptons must exhibit opposite-sign charges. Moreover, the event must contain a minimum of two jets, out of which exactly two must be *b*-tagged, adhering to the DL1r 77% working point.

Events presenting any surplus leptons, whether they be electrons or muons, are subjected to vetoing. Furthermore, the leading and sub-leading *b*-tagged jets within the event are compelled to display a transverse momentum ( $p_T$ ) greater than 45 GeV and 20 GeV, respectively.

The invariant mass of the  $\tau$ -lepton pair, denoted as  $m_{\tau\tau}^{\text{MMC}}$ , is ascertained via the Missing Mass Calculator (MMC)<sup>[192]</sup>. This computation employs the four-momenta of the visible hadronic decays of the  $\tau$ -leptons ( $\tau_{\text{had-vis}}$ ) as well as the missing transverse momentum ( $\mathbf{p}_T^{\text{miss}}$ ). The MMC operates under the assumption that the missing transverse momentum originates exclusively from the neutrinos resulting from the  $\tau$ -lepton decays.

For the purpose of mitigating background interference from low-mass Drell-Yan events, a condition is set such that  $m_{\tau\tau}^{\text{MMC}}$  must exceed 60 GeV.

The confluence of these event selection steps culminates in the  $\tau_{\text{had}}\tau_{\text{had}}$  signal region, summarized in Table 6–4. The corresponding cutflow tables for the Standard Model ggF HH and VBF HH signals in the  $\tau_{\text{had}}\tau_{\text{had}}$  sub-channel are provided in Table 6–7 and Table 6–8.

Description	Number of events		Efficiency [%]		Relative Efficiency [%]	
	S TT	D TT	S TT	D TT	S TT	D TT
$HH$	4314.87	x	x	x	x	x
$HH \rightarrow b\bar{b}\tau\tau$	315.23	x	x	x	x	x
$HH \rightarrow b\bar{b}\tau_{\text{had}}\tau_{\text{had}}$	132.32	100.00	100.00	100.00	100.00	100.00
Generator filter	102.78	77.68	77.68	77.68	77.68	77.68
Derivation skimming	88.28	66.72	66.72	66.72	85.89	85.89
Object preselection	40.44	30.56	30.56	30.56	45.81	45.81
Trigger selection (online+offline)	17.30	13.08	13.08	13.08	42.79	42.79
Trigger category	1.95	15.35	1.48	11.60	11.29	88.71
Random $\tau$ selection	1.93	15.31	1.46	11.57	99.03	99.78
Object selection ( $n_\tau = 2$ , further requirements on jets and tau-jet OLR)	1.86	14.12	1.40	10.67	95.92	92.19
Pileup Correction	1.91	14.40	1.44	10.88	x	x
2 Loose $\tau$ s (one Loose $\tau$ already required in derivation)	1.37	11.64	1.04	8.80	71.95	80.84
Subleading $\tau$ $p_T > 25$ GeV	1.21	11.64	0.91	8.80	87.74	x
MMC > 60 GeV	1.15	11.40	0.87	8.62	95.40	97.98
At least one jet with $p_T > 45$ GeV	1.15	11.17	0.87	8.44	99.63	97.95
DTT offline jet cuts	1.15	9.95	0.87	7.52	x	89.05
Scale Factors	1.16	10.48	0.87	7.92	x	x
Opposite charge sign	1.14	10.34	0.86	7.82	98.14	98.71
Both jets are b-tagged	0.57	4.83	0.43	3.65	49.86	46.74
ggF low $m_{HH}$ SR	0.004	0.583	<0.01	0.44	0.71	12.07
ggF high $m_{HH}$ SR	0.504	3.874	0.38	2.93	89.36	80.21
VBF SR	0.056	0.373	0.04	0.28	9.93	7.72

Table 6-7 SM ggF  $HH$  signal cutflow (POWHEG + PYTHIA 8) in the  $\tau_{\text{had}}\tau_{\text{had}}$  sub-channel.

Description	Number of events			Efficiency [%]			Relative Efficiency [%]		
	STT	DTT	S TT	STT	DTT	S TT	STT	DTT	S TT
$HH$	239.85		x	x			x		x
$HH \rightarrow b\bar{b}\tau\tau$	17.52		x	x			x		x
$HH \rightarrow b\bar{b}\tau_{\text{had}}\tau_{\text{had}}$	7.36		100.00	100.00			100.00		100.00
Generator filter	5.00		67.99	67.99			67.99		67.99
Derivation skimming	4.24		57.61	57.61			57.61		57.61
Object preselection	1.89		25.69	25.69			25.69		25.69
Trigger selection (online+offline)	0.74		10.11	10.11			10.11		10.11
Trigger category	0.06	0.69	0.79	0.79	9.32	7.82	0.79	9.32	7.82
Random $\tau$ selection	0.06	0.68	0.78	0.78	9.28	98.64	0.78	9.28	98.64
Object selection ( $n_\tau = 2$ , further requirements on jets and tau-jet OLR)	0.05	0.59	0.72	0.72	7.99	92.33	0.72	7.99	92.33
Pileup Correction	0.05	0.60	0.74	0.74	8.13	x	0.74	8.13	x
2 Loose $\tau$ s (one Loose $\tau$ already required in derivation)	0.04	0.48	0.56	0.56	6.54	74.81	0.56	6.54	74.81
Subleading $\tau$ $p_T > 25$ GeV	0.04	0.48	0.49	0.49	6.54	88.41	0.49	6.54	88.41
MMC > 60 GeV	0.03	0.47	0.47	0.47	6.37	95.60	0.47	6.37	95.60
At least one jet with $p_T > 45$ GeV	0.03	0.45	0.46	0.46	6.07	98.65	0.46	6.07	98.65
DTT offline jet cuts	0.03	0.35	0.46	0.46	4.80	x	0.46	4.80	x
Scale Factors	0.03	0.37	0.47	0.47	5.03	x	0.47	5.03	x
Opposite charge sign	0.03	0.36	0.46	0.46	4.94	97.86	0.46	4.94	97.86
Both jets are b-tagged	0.01	0.15	0.20	0.20	2.07	42.67	0.20	2.07	42.67
ggF low $m_{HH}$ SR	<0.001	0.008	<0.01	<0.01	0.11	0.46	<0.01	0.11	0.46
ggF high $m_{HH}$ SR	0.004	0.041	0.06	0.06	0.57	30.35	0.06	0.57	30.35
VBF SR	0.010	0.102	0.14	0.14	1.38	69.20	0.14	1.38	69.20

Table 6-8 SM VBF  $HH$  signal cutflow (PowHEG + Pythia 8) in the  $\tau_{\text{had}}\tau_{\text{had}}$  sub-channel.

### 3440 6.3.4 Event Categorization

3441 In a substantial improvement from the full Run 2 analysis, the current work introduces  
 3442 a refined categorization scheme for events, visualized in Figure 6–5. This new framework  
 3443 divides each sub-channel into three distinct signal regions, adding an extra layer of granularity  
 3444 to our understanding of these events.

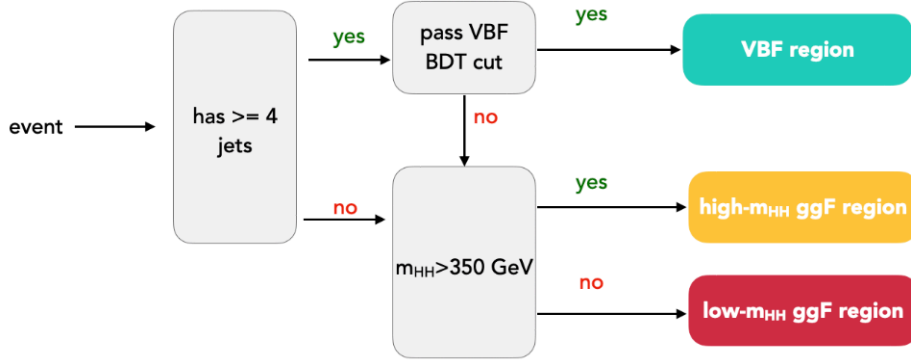


**Figure 6–5 Event categorisation into low- $m_{HH}$  ggF, high- $m_{HH}$  ggF, and VBF signal regions.**

3445 For events with at least four jets, a specialized BDT classifier is deployed to optimally  
 3446 distinguish between ggF and VBF production modes. Events passing a particular working  
 3447 point for this BDT, as specified for example in the  $\tau_{\text{had}}\tau_{\text{had}}$  channel in Section 6.5.2, are tagged  
 3448 as VBF-like and are allocated to a dedicated VBF signal region.

3449 Conversely, events featuring fewer than four jets or failing the BDT threshold are consid-  
 3450 ered ggF-like. Within this category, additional granularity is achieved by classifying these  
 3451 events based on the invariant mass of the di-Higgs system ( $m_{HH}$ ). Specifically, a low-mass  
 3452 ggF signal region is established with an upper  $m_{HH}$  bound of 350 GeV. This low-mass cat-  
 3453 egorization aims to probe BSM scenarios, particularly those characterized by non-standard  
 3454  $\kappa_\lambda$  values.

3455 Events surpassing this 350 GeV limit are designated to a high-mass ggF signal region,  
 3456 thereby focusing on SM-like  $HH$  events. The selection of the 350 GeV threshold aims to  
 3457 maintain a balance between constraining  $\kappa_\lambda$  rigorously and retaining a large enough sample  
 3458 size in the low-mass region.

3459 In a final layer of categorization, separate BDT classifiers are trained for each signal  
 3460 region using different  $HH$  signal hypotheses to achieve optimal separation from background

3461 events. A detailed discussion of these multivariate analytical methods, including the list of  
 3462 input variables and hyperparameter optimization, is presented in Section 6.5. The adoption of  
 3463 this intricate categorization scheme is motivated and supported by a series of MVA training  
 3464 studies and fit analyses, comprehensively discussed in Sections 6.8.4.

### 3465 6.3.5 Z+HF control region

3466 The SHERPA Monte Carlo (MC) simulation is recognized to inadequately model the cross-  
 3467 section of  $Z$  boson production when in concert with heavy flavour ( $b, c$ ) jets. Therefore, data-  
 3468 driven normalization is implemented within a designated control region, in alignment with  
 3469 the protocol established in the prior analytical cycle, as described in the internal note<sup>1[182]</sup> and  
 3470 the preceding analysis round<sup>[177]</sup>. Given that jet production is decoupled from the  $Z$  boson's  
 3471 decay channel, a high-purity sample featuring  $Z \rightarrow \mu\mu/ee$  coupled with heavy flavour jets  
 3472 is chosen. This sample is orthogonal to the selection criteria for signal regions and is used  
 3473 in the simultaneous fit to obtain data-based Z+HF normalization. The criteria delineating  
 3474 the Z+HF control region have been updated for this phase of the analysis, expounded in  
 3475 Section 6.3.5.1.

#### 3476 6.3.5.1 Redefinition of the Z+HF control region phase space

3477 The cross-section for  $Z$ -boson production in conjunction with heavy-flavor jets ( $b, c$ ) is  
 3478 often inaccurately predicted by the SHERPA MC. Therefore, normalization to data is per-  
 3479 formed in a designated control region from the previous analysis cycle<sup>[177]</sup>. Utilizing  $Z \rightarrow$   
 3480  $\mu\mu/ee$  + heavy-flavor jets ensures a high-purity, orthogonal sample to the signal regions,  
 3481 allowing for data-driven Z+HF normalization.

3482 To mitigate phase-space extrapolation uncertainties between the SR and CR, adjustments  
 3483 have been made to the CR criteria. Event selection in the revamped control region is deter-  
 3484 mined as follows:

- 3485 •  $b\bar{b}\ell\ell$  trigger selection using single-lepton and di-lepton triggers.
- 3486 • Exactly two opposite-sign charged muons or electrons.
- 3487 • Two  $b$ -tagged jets with DL1r tagger and 77% working point.
- 3488 •  $75 \text{ GeV} < m_{\ell\ell} < 110 \text{ GeV}$ .
- 3489 •  $m_{bb} < 40 \text{ GeV}$  or  $m_{bb} > 210 \text{ GeV}$ .

---

<sup>1</sup> ATL-COM-PHYS-2020-766

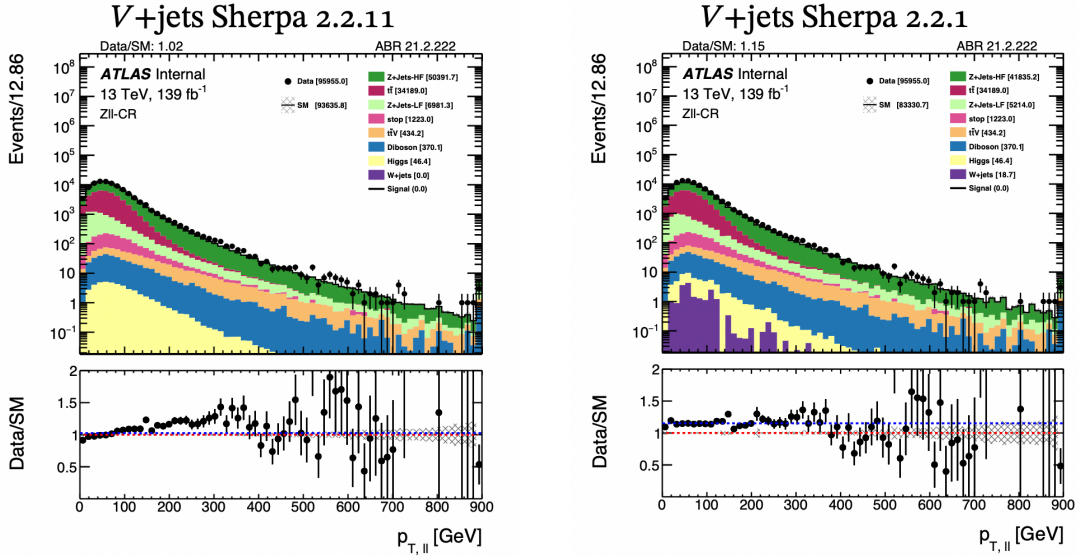


Figure 6–6 Data/MC comparison in the prior  $Z + HF$  control region.

- 3490 • Leading  $b$ -jet  $p_T > 45$  GeV.
- 3491 • Lepton  $p_T > 40$  GeV.

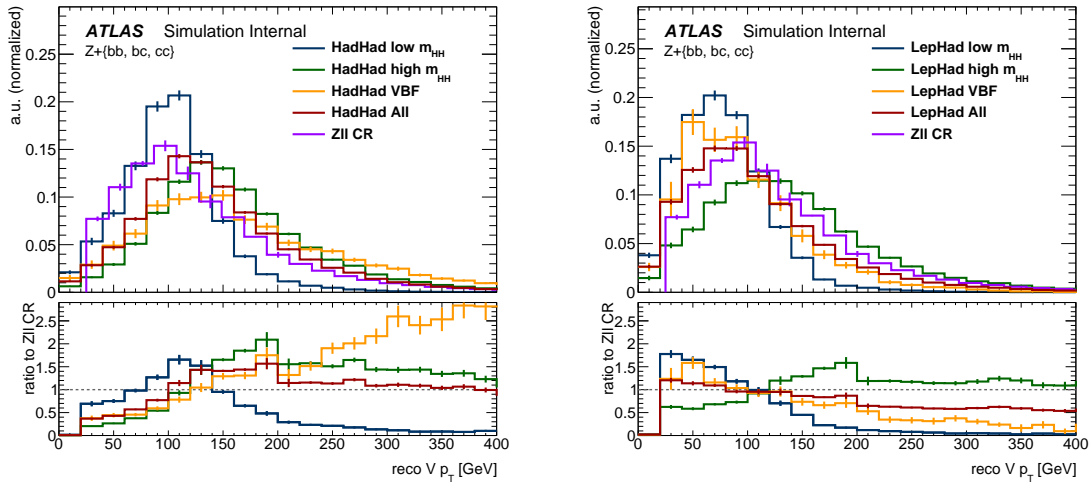


Figure 6–7 Comparison of  $V p_T$  shapes between the SRs and the  $Z$  CR.

3492 These refinements have brought the  $V p_T$  distributions of the SR and CR into closer  
 3493 alignment, as shown in Figure 6–7. Subsequent analysis indicates a normalization factor for  
 3494  $Z+HF$  of  $1.20 \pm 0.05$ , closely aligning with the 1.3 factor from prior analysis rounds. The  
 3495 impact of these changes on the systematic uncertainties and signal strength will be further  
 3496 elaborated.

## 3497 6.3.5.2 Initial Normalization Coefficients

3498 Equations 6–2 and 6–3 present the calculation for the pre-fit normalization constants  
 3499  $\mu_{Z+HF}$ . These constants are obtained for the Z+HF ( $Z + (bb, bc, cc)$ ) terms within the Z+HF  
 3500 control region, computed via the ratio depicted in Equation 6–1<sup>1</sup>.

$$\mu_{Z+HF} = \frac{\text{data} - (\text{sum of backgrounds} + Z(ee, \mu\mu) + \text{HF} + Z(\tau\tau) + \text{HF})}{Z(ee, \mu\mu) + \text{HF} + Z(\tau\tau) + \text{HF}}. \quad (6-1)$$

3501 The normalization constants are extracted using Equation 6–1 and are specifically de-  
 3502 tailed in Equations 6–2 and 6–3 for Sherpa 2.2.1 and Sherpa 2.2.11 configurations, respec-  
 3503 tively.

$$\mu_{Z+HF}^{\text{SHERPA2.2.1}} = \frac{(21458 - 18566.0578 + 9970.59 + 1.210)}{(9970.59 + 1.210)} \approx 1.29 \quad (6-2)$$

$$\mu_{Z+HF}^{\text{SHERPA2.2.11}} = \frac{(21458 - 18596.707 + 10837.434 + 1.309)}{(10837.434 + 1.309)} \approx 1.26 \quad (6-3)$$

3504 For context, the Sherpa 2.2.11 normalization factor derived from the original Z+HF con-  
 3505 trol region, unadjusted for the new cuts, stands at 1.05. The modification in the control region  
 3506 criteria brings the normalization factors of Sherpa 2.2.1 and Sherpa 2.2.11 into closer con-  
 3507 cordance.

## 3508 6.3.5.3 Projection to Signal Regions

3509 To account for the observed discrepancies in the  $V$  transverse momentum ( $V p_T$ ) between  
 3510 the data and MC simulations, a specialized shape uncertainty is formulated. The uncertainty  
 3511 is quantified by the complete difference between the experimental data and the baseline MC  
 3512 estimations in varying bins of the reconstructed  $V p_T$ . This is documented in Figure 6–8.

3513 Subsequently, this shape uncertainty is propagated to the Sherpa 2.2.11 predictions for  
 3514 Z+HF within the three signal regions, in relation to the true-level  $p_T(\tau\tau)$ . This variable is  
 3515 the closest analog to the reconstructed  $V p_T$  assessed in the control region.

---

<sup>1</sup> The equation serves as an approximation attributing to the Z+HF background any data/MC discrepancies. In the full scope of the analysis, the mass distribution fit in the CR will normalize  $t\bar{t}$  to data, encapsulating only excesses that align with the Z process.

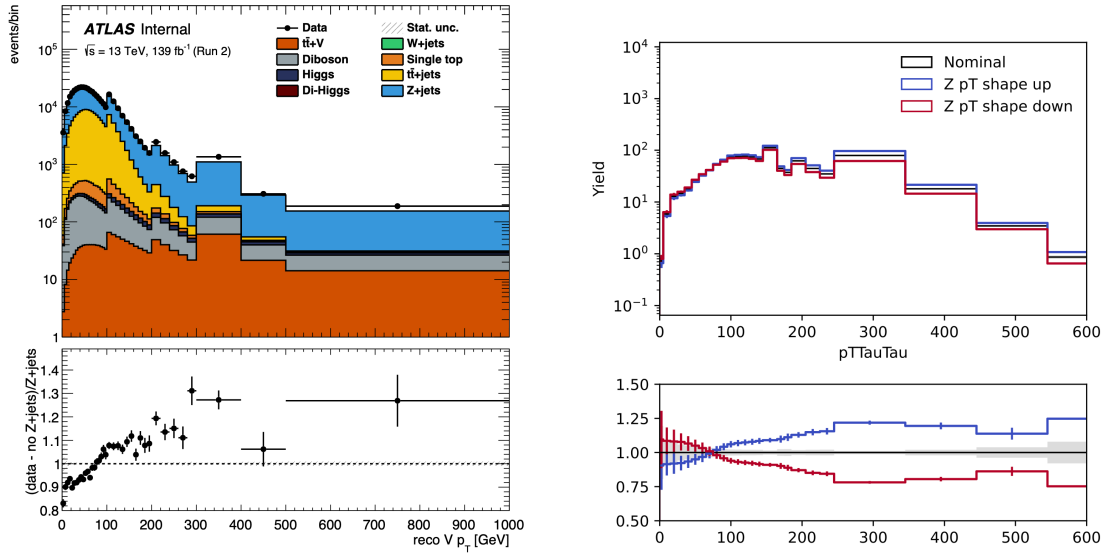


**Figure 6–8 (a) Quantification of the  $V p_T$  shape uncertainty, representing the full discrepancy between data and nominal MC forecast in the Z CR. (b) The subsequent discrete parameterization of the shape uncertainty.**

## 6.4 Background Modelling

Background estimation in our analysis utilizes a combination of simulation and data-driven techniques. Simulated event samples, as outlined in Section 6.2.2, provide the foundation for modeling most background processes. For fake- $\tau_{\text{had}}$  backgrounds, data-driven methods are employed differently across channels.

In the  $\tau_{\text{lep}}\tau_{\text{had}}$  channel, an inclusive fake-factor method handles fake- $\tau_{\text{had}}$  contributions from  $t\bar{t}$  and multi-jet processes. Conversely, in the  $\tau_{\text{had}}\tau_{\text{had}}$  channel, we deploy a two-pronged approach: multi-jet backgrounds rely on a data-driven fake-factor method in Section 6.4.1, while  $t\bar{t}$  backgrounds utilize scale-factors extracted from data to correct MC predictions in Section [sec:6:ttbarfake](#).

The separation of estimation methods for multi-jet and  $t\bar{t}$  in  $\tau_{\text{had}}\tau_{\text{had}}$  is necessitated by distinct fake- $\tau_{\text{had}}$  features and trigger selections in Section 6.3.2. Given the statistical limitations of the Run 2 dataset and the minor impact of fake- $\tau_{\text{had}}$  backgrounds on sensitivity, this segregated approach is justified.

Furthermore, templates for  $t\bar{t}$  with true- $\tau_{\text{had}}$  and Z + HF are MC-based but their normalizations are data-driven and integrated into the final fit model. Minor backgrounds arising from misidentified electrons or muons are treated in simulation and aligned with true- $\tau_{\text{had}}$   $t\bar{t}$

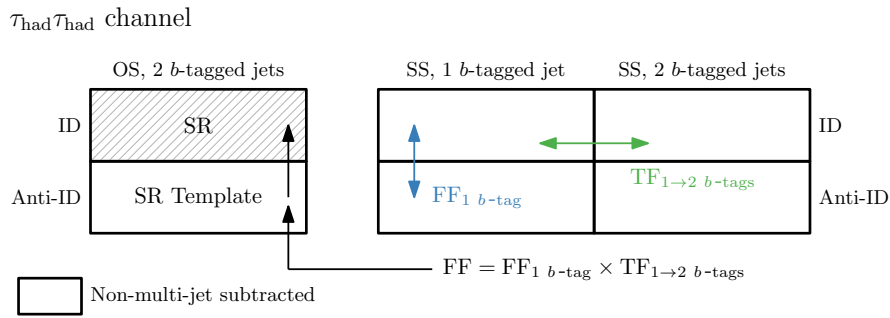


**Figure 6–9 Schematic illustration of the application of the fake-factor method for estimating multi-jet backgrounds featuring fake- $\tau_{\text{had-vis}}$  in the  $\tau_{\text{had}}\tau_{\text{had}}$  channel. In all control regions, non-multi-jet backgrounds are simulated and subsequently deducted from the observed data, as denoted by 'Subtracted Non-Multi-Jet Backgrounds' in the legend.**

3533 events<sup>[177,182]</sup>.

#### 3534 6.4.1 Multijet with fake- $\tau$ backgrounds in the $\tau_{\text{had}}\tau_{\text{had}}$ channel

3535 In the  $\tau_{\text{had}}\tau_{\text{had}}$  channel, the estimation of the multi-jet background employs a data-driven  
 3536 fake-factor approach, consistent with the methodology applied in preceding analyses of the  
 3537  $b\bar{b}\tau_{\text{had}}\tau_{\text{had}}$ <sup>[177,193]</sup>. The fake factors (FFs) used in the prior analysis<sup>[177]</sup> are retained. The  
 3538 Monte Carlo settings' transition from SHERPA 2.2.1 to SHERPA 2.2.11 for the  $V$ +jets samples  
 3539 does not alter the multi-jet background calculations. The leading  $\tau_{\text{had}}$   $p_T$  distributions for each  
 3540 category in the 1-tag SS and 1-tag OS regions show that the new samples do not affect the  
 3541 estimation strategy. The different regions used for the multijet estimation are schematically  
 3542 depicted in Figure 6–9.

3543 FFs are obtained in a control region with two  $\tau_{\text{had-vis}}$  having same-sign charges, as a ratio  
 3544 of events with two loose  $\tau_{\text{had}}$  to those with one loose and one anti- $\tau_{\text{had}}$ . FFs are computed  
 3545 separately for 1- and 3-prong  $\tau_{\text{had}}$ , for STT and DTT trigger categories, and for the 0-, 1-, and  
 3546 2-b-tag regions. Additionally, FFs are year-specific to consider changing  $\tau_{\text{had}}$  identification  
 3547 criteria and trigger selections. Due to low statistics, the 1-b-tag FFs are used in the 2-b-tag  
 3548 region with appropriate transfer factors for corrections.

$$FF_i(p_T \tau_{\text{had}}^i, \eta \tau_{\text{had}}^i, N_{\text{prong}} \tau_{\text{had}}^i, \dots) = \frac{N_{\text{data}}(\text{loose } \tau_{\text{had}}^i) - N_{\text{non-multijet MC}}(\text{loose } \tau_{\text{had}}^i)}{N_{\text{data}}(\text{anti-}\tau_{\text{had}}^i) - N_{\text{non-multijet MC}}(\text{anti-}\tau_{\text{had}}^i)} \quad (6-4)$$

3549 Two types of FFs, labeled as  $FF_0$  and  $FF_1$ , are then averaged. Their statistical compat-

3550 ability has been validated, and they are averaged with respect to their statistical significance  
 3551 in a given  $p_T$  bin.

$$FF_{\text{avg}}(p_T, \tau_{\text{had}}, \eta, \tau_{\text{had}}, N_{\text{prong}}, \tau_{\text{had}}, \dots) = \frac{N_{\text{data}}(\text{loose } \tau_{\text{had}}) - N_{\text{non-multijet MC}}(\text{loose } \tau_{\text{had}})}{N_{\text{data}}(\text{anti-}\tau_{\text{had}}) - N_{\text{non-multijet MC}}(\text{anti-}\tau_{\text{had}})} \quad (6-5)$$

3552 The final fake factors for  $\tau_{\text{had}}\tau_{\text{had}}$  channel are shown in Figure 6–10.

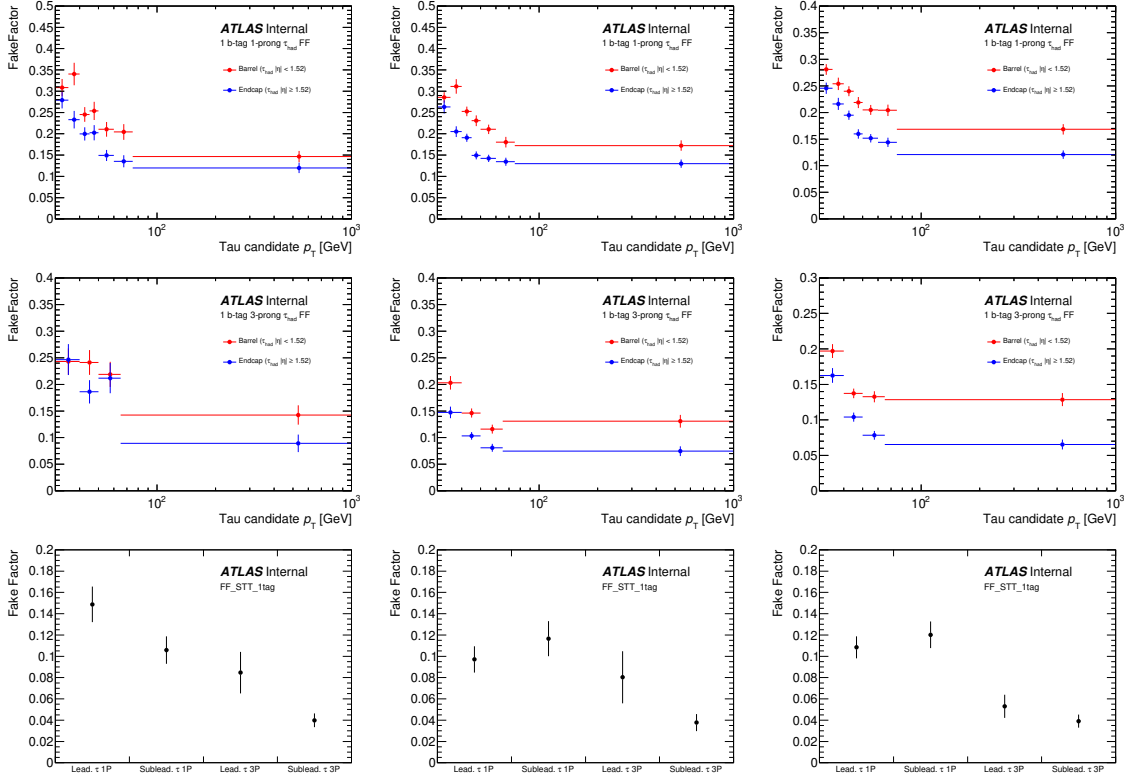
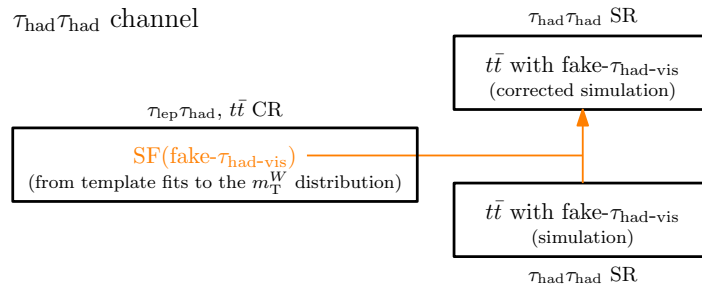


Figure 6–10 Fake factors for 1-prong DTT (top), 3-prong DTT (middle), and STT (bottom) for the data-taking periods 15-16 (left), 17 (centre), and 18 (right) for the di-Higgs  $\tau_{\text{had}}\tau_{\text{had}}$  channel.

#### 3553 6.4.2 $t\bar{t}$ with fake- $\tau_{\text{had}}$ in the $\tau_{\text{had}}\tau_{\text{had}}$ channel with scale-factor method

3554 The background events attributed to  $t\bar{t}$  production that contain fake- $\tau_{\text{had-vis}}$  in the  $\tau_{\text{had}}\tau_{\text{had}}$   
 3555 channel are quantified through simulation. However, for enhanced accuracy, the misidenti-  
 3556 fication efficiencies of fake- $\tau_{\text{had-vis}}$  are modified by data-derived SFs. A graphical overview  
 3557 of this methodology is portrayed in Figure 6–11.

3558 The SFs are a function of the fake- $\tau_{\text{had-vis}}$  transverse momentum ( $p_T$ ), segregated for 1-  
 3559 prong and 3-prong decay modes. A profile-likelihood fit to the transverse mass ( $m_T^W$ ) dis-



**Figure 6–11 Illustrative summary of the data-corrected scale-factor technique employed for evaluating  $t\bar{t}$  background containing fake- $\tau_{\text{had-vis}}$  in the  $\tau_{\text{had}}\tau_{\text{had}}$  channel.**

3560 tribution effectively calibrates the SFs. Separate fitting processes are carried out for distinct  
3561 trigger categories.

3562 The numerical behavior of SFs varies with  $p_T$ : for 1-prong fake- $\tau_{\text{had-vis}}$ , SFs are approxi-  
3563 mately 1 for  $p_T$  below 40 GeV and diminish to around 0.6 for  $p_T$  exceeding 70 GeV. For the  
3564 3-prong mode, the SFs are typically about 20% greater than their 1-prong counterparts.

3565 To evaluate the  $t\bar{t}$  background in the  $\tau_{\text{had}}\tau_{\text{had}}$  SR, the simulation is scaled by the appropriate  
3566 SFs for each fake- $\tau_{\text{had-vis}}$  in the event. Various uncertainties, including detector response and  
3567 theoretical modeling, are accounted for during the likelihood fit for SF extraction.

3568 The resulting covariance matrix, encompassing both statistical and systematic uncertain-  
3569 ties, is diagonalized to produce independent nuisance parameters (NPs), which are subse-  
3570 quently propagated into the final signal extraction fit.

3571 For the estimation of fake- $\tau_{\text{had-vis}}$  background from multi-jet processes, a considerable  
3572 fraction of  $t\bar{t}$  events containing at least one fake- $\tau_{\text{had-vis}}$  must be removed from the data in  
3573 the opposite-sign 2- $b$ -tagged-jet anti-identification (anti-ID) region to accurately gauge the  
3574 multi-jet influence. The modelling of  $t\bar{t}$  events in this region is corrected via data-derived  
3575 SFs, obtained using a methodology similar to the one described.

## 3576 6.5 Multivariate signal extraction

### 3577 6.5.1 General MVA and optimisation strategy

3578 The discriminant employed for isolating the signal is derived from a multivariate algo-  
3579 rithm, as elaborated in Section 5.5.1. Distinct from the complete Run 2 data analysis cycle,  
3580 Boosted Decision Trees (BDTs) are now utilized uniformly for both sub-channels in all cate-

3581 gories, as specified in Section 6.3. An expanded set of predictor variables has been examined,  
 3582 and optimal hyperparameters have been selected to enhance the model’s efficacy. Uniform  
 3583 training protocols are applied to both  $\tau_{\text{had}}\tau_{\text{had}}$  and  $\tau_{\text{lep}}\tau_{\text{had}}$  scenarios, utilizing a standardized  
 3584 training infrastructure<sup>[194]</sup> and based on the TMVA toolkit<sup>[95]</sup>.

3585 The training procedures have been specifically designed for various channels:  $\tau_{\text{had}}\tau_{\text{had}}$ ,  
 3586  $\tau_{\text{lep}}\tau_{\text{had}}$  SLT, and  $\tau_{\text{lep}}\tau_{\text{had}}$  LTT, as detailed in their respective sections. However, the focus of  
 3587 the ensuing discussion will be solely on the  $\tau_{\text{had}}\tau_{\text{had}}$  channel.

### 3588 6.5.1.1 Partitioning Technique for Model Validation

3589 The architectural layout of the MVA approach necessitates a dependable and impartial  
 3590 forecast of the anticipated analytical sensitivity. This constraint dictates that the same events  
 3591 cannot be employed for both the calibration of the BDT (covering its hyperparameters and  
 3592 predictor variables) and the formulation of the histogram schematics for the resultant BDT  
 3593 scores.

3594 A straightforward methodology fulfilling this stipulation is to subdivide the obtainable  
 3595 ensemble of simulated events into three equally-sized subsets. In this specific adaptation, the  
 3596 approach is executed based on the event identification number.

Model	Fold 0 event_number %3 = 0	Fold 1 event_number %3 = 1	Fold 2 event_number %3 = 2
BDT 0	Training	Validation	Testing
BDT 1	Testing	Training	Validation
BDT 2	Validation	Testing	Training

**Table 6–9 Demarcation of the simulated event pools used for the learning, fine-tuning, and scrutiny of the BDT algorithms.**

3597 Consequently, a trio of distinct BDT models are developed, each exploiting an individual  
 3598 subset of the available simulated data (referred to as Training folds) as outlined in Table 6–9.  
 3599 A consistent set of hyperparameters and predictor variables is applied across all trainings.  
 3600 These are ascertained through the maximization of BDT efficacy on the Validation folds,  
 3601 which remain unseen during the training phase.

3602 The synthetic events encapsulated in the Testing folds contribute to the formation of the  
 3603 histogram fit blueprints. Intrinsicly, these events are excluded from the BDT training steps,

3604 thereby safeguarding an impartial forecast of the forthcoming analytical sensitivity.

### 3605 6.5.1.2 Hyperparameter Tuning Strategy

3606 The performance of the BDT is highly sensitive to specific training hyperparameters em-  
3607 ployed within TMVA. Two primary hyperparameters warrant special attention: the number  
3608 of ensemble trees (NTrees) and the maximum depth of each individual tree (MaxDepth).

3609 To optimize these hyperparameters effectively, a comprehensive grid search is under-  
3610 taken. The search is implemented following the partitioning mechanism detailed in Section  
3611 6.5.1.1. Subsequently, the score distribution of the BDT output is analyzed, both for the  
3612 signal and the aggregated backgrounds, utilizing the events within the validation subsets.  
3613 (The bin structure is determined using the same algorithm that defines the binning for the  
3614 likelihood fitting, as discussed in Section 6.7.2.) For performance assessment, the metric of  
3615 binned signal significance is employed, given by

$$Z = \sqrt{\sum_{i \in \text{bins}} 2 \left( (s_i + b_i) \log \left( 1 + \frac{s_i}{b_i} \right) - s_i \right)}, \quad (6-6)$$

3616 where  $s_i$  and  $b_i$  denote the yields of signal and background events in the  $i^{\text{th}}$  bin, respec-  
3617 tively.

3618 A defined hyperparameter space is explored, varying according to the specific analysis  
3619 region and BDT variant. Bayesian optimization techniques are employed to favor hyperpa-  
3620 rameter configurations that yield elevated binned significance metrics.

3621 The optimal hyperparameter set is identified from the ensemble of configurations evalu-  
3622 ated during the tuning process, and utilized in the training, validation, and test phases.

### 3623 6.5.1.3 Optimization of Feature Selection

3624 For the  $b\bar{b}\tau\tau$  system, many variables can help distinguish between different outcomes.  
3625 However, using too many variables can make the model complex and less reliable. So, even  
3626 though it's not a strict requirement, it's simpler and more effective to choose a limited but  
3627 useful set of variables.

3628 The feature selection procedure operates as follows:

- 3629 • A set of "core" variables is invariably included. The specific constituents of this core  
3630 set are BDT-dependent and will be detailed subsequently.

- 3631 • Using a greedy algorithm, further variables are incrementally chosen from the remain-  
3632 ing list based on their ability to enhance the binned signal significance, as quantified  
3633 by Eq. 6–6, evaluated over the validation partitions.
- 3634 • If adding a new variable doesn't improve the performance based on the validation data,  
3635 then the variable that has the smallest negative impact on performance is included  
3636 instead.
- 3637 • The process terminates after  $N_p$  consecutive steps without a significant boost in sig-  
3638 nificance.

3639 Such a heuristic optimization strategy is prone to statistical noise, potentially distorting  
3640 the variable selection. To mitigate this, the binned significance  $Z$  is calculated using a coarser  
3641 binning scheme than that applied in the likelihood fitting procedure, as elaborated upon in a  
3642 later section.

### 3643 6.5.2 $\tau_{\text{had}}\tau_{\text{had}}$ MVAs

3644 In total, four sets of BDTs are utilized in the  $\tau_{\text{had}}\tau_{\text{had}}$  channel, described below.

#### 3645 6.5.2.1 BDT for ggF and VBF Classification

3646 The purpose of the ggF/VBF distinction BDT is to segregate SM ggF HH events from  
3647 SM VBF HH events (see Section 6.3.4 for details). The BDT employs only VBF preselected  
3648 events in both its training and application phases. VBF preselected events are characterized  
3649 as those having a minimum of two jets that are distinct from the  $H \rightarrow b\bar{b}$  jets. Approximately  
3650 50% of ggF HH events and 80% of VBF HH events meet this VBF preselection criterion.  
3651 The BDT is calibrated such that events resembling ggF have scores approaching 1.0, whereas  
3652 events similar to VBF have scores nearing -1.0. A specific score threshold (or working point)  
3653 is chosen to delineate events into the VBF category. The methodology for input variable  
3654 selection and hyperparameter tuning for BDT training is elaborated upon in the following  
3655 sections.

3656 **Input Variable Selection** The performance trajectory of the BDT in ggF/VBF classifica-  
3657 tion is visualized in Figure 6–12. The significance is calculated in accord with the binning  
3658 methodology outlined in Section 6.7.2, albeit without imposing a minimum threshold on the  
3659 number of background events per bin. Here,  $z_s = z_b = 7$ .

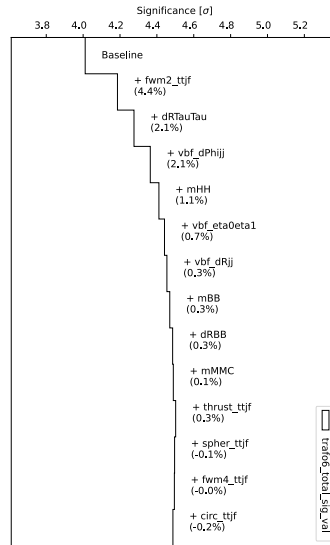


**Figure 6–12 Performance progression of the ggF/VBF classification BDT as supplementary variables are incrementally appended to the baseline variables, which consist of  $m_{jj}$  and  $\Delta\eta_{jj}$ .**

3660 As a foundation, two variables,  $m_{jj}$  and  $\Delta\eta_{jj}$ , are selected. Ultimately, the seven most  
 3661 impactful variables are employed as BDT inputs. These include a Fox-Wolfram moment<sup>[195]</sup>,  
 3662  $m_{HH}$ ,  $\Delta R_{\tau\tau}$ , along with additional VBF-specific variables. A comprehensive listing of these  
 3663 input variables is provided in Table 6–10. Their respective distributions for the ggF and VBF  
 3664 HH signal events are illustrated in Figure 6–13.

Variable	Description
$m_{HH}$	Invariant mass of the HH system, reconstructed from the $\tau$ -lepton pair (using the MMC) and $b$ -tagged jet pair
$\Delta R_{\tau\tau}$	The $\Delta R$ between the two visible $\tau$ decay products
VBF $\eta_0 \times \eta_1$	Product of the pseudorapidities of the leading and sub-leading VBF jets
$\Delta\eta_{jj}^{\text{VBF}}$	The $\Delta\eta$ between the two VBF jets
$\Delta\phi_{jj}^{\text{VBF}}$	The $\Delta\phi$ between the two VBF jets
$m_{jj}^{\text{VBF}}$	Invariant mass of the VBF jet system
$\text{fwm2}(\tau\tau jj)$	$2^{\text{nd}}$ order Fox-Wolfram moment, taking into account the $\tau$ -lepton pair and central and forward jets

**Table 6–10 Input variables used for the ggF/VBF BDT training in the  $\tau_{\text{had}}\tau_{\text{had}}$  channel.**

3665 **Hyperparameter Tuning** In accordance with the method described in Section 6.5.1.2, we  
 3666 focus our optimization efforts on the principal hyperparameters NTrees and MaxDepth. Fig-  
 3667 ure 6–14 illustrates how the binned significance, evaluated on the validation folds, varies with  
 3668 changes in these hyperparameters. Optimal parameter settings are identified by maximizing

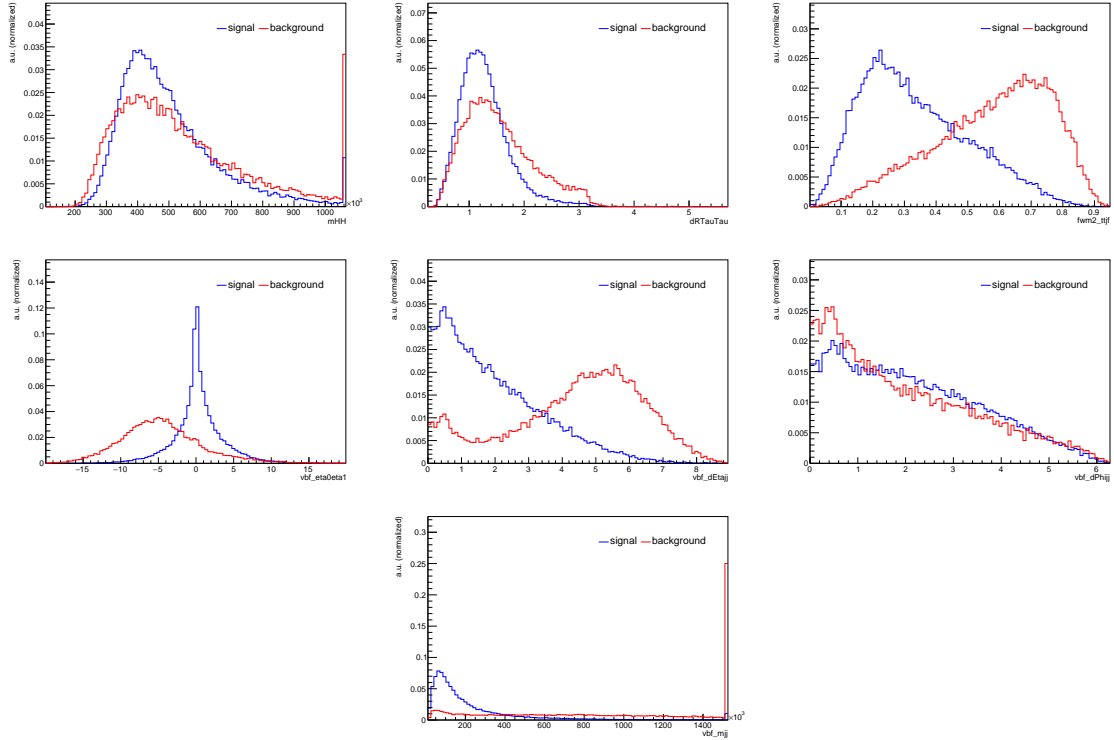


**Figure 6–13** Histograms of input variables for the ggF/VBF BDT in the  $\tau_{\text{had}}\tau_{\text{had}}$  channel, illustrating the distinction between ggF HH events (signal in blue) and VBF HH events (background in red).

3669 this performance metric.

3670 For the other hyperparameters, a marginal impact on the BDT’s performance is observed.

3671 Thus, they are assigned default values. A comprehensive enumeration of these hyperparam-

3672 eter choices is provided in Table 6–11.

Hyperparameter	Selected Value
NTrees	109
MaxDepth	6
MinNodeSize	1%
BoostType	GradBoost
IgnoreNegWeightsInTraining	True

**Table 6–11** Chosen hyperparameters for the ggF/VBF BDT training in the  $\tau_{\text{had}}\tau_{\text{had}}$  channel.

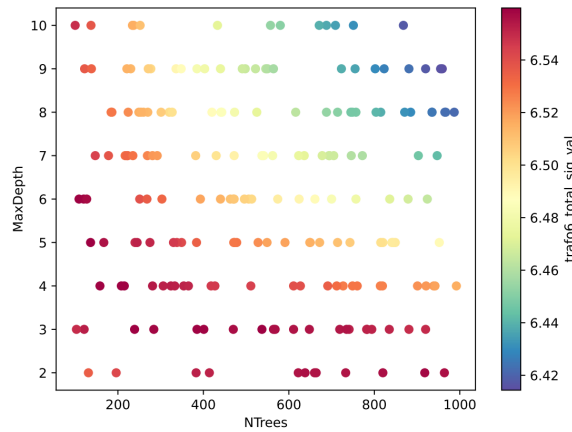


Figure 6–14 Variation of binned significance, as assessed on the validation partitions, with respect to the ensemble’s tree count (NTrees) and each tree’s maximum depth (MaxDepth).

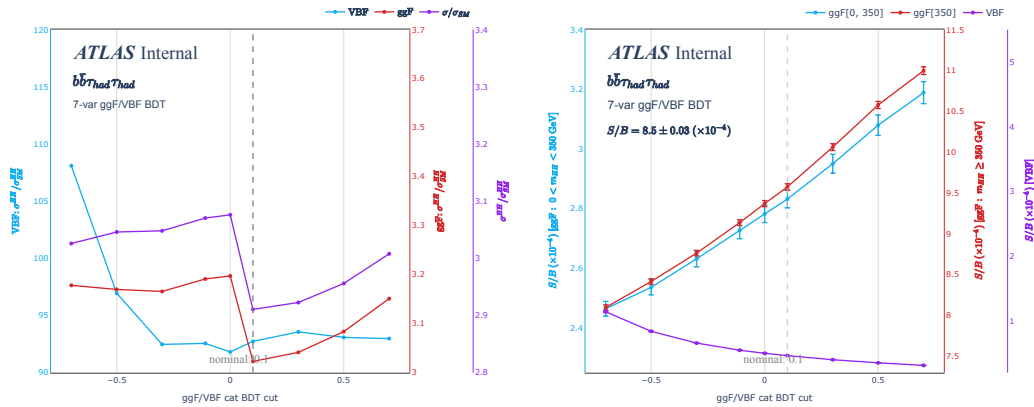


Figure 6–15 Dependence of HH signal strengths on the ggF vs VBF BDT cut value for the refined set of variables (left). The right figure shows the aggregate signal-to-background ratio also as a function of the cut value. A vertical dashed line marks the chosen cut value of 0.1.

3673 **Determination of Optimal Cut Threshold** The SRs for ggF and VBF are demarcated by  
 3674 applying a threshold cut on the ggF/VBF classification BDT output. To identify the opti-  
 3675 mal cut threshold, we evaluate the analysis sensitivity across multiple potential cut values.  
 3676 Figure 6–15 illustrates the influence of the cut value on the ggF, VBF, and inclusive HH  
 3677 signal strengths (left), along with the overall signal-to-background ratio (right). These are  
 3678 computed via a likelihood fit incorporating the three analysis categories as well as the Z CR.

3679 It should be noted that the discriminant scores used for this initial evaluation are derived  
 3680 from a provisional BDT training, prior to the application of the hyperparameter and input

3681 variable optimization procedures outlined in earlier sections. Various tests have confirmed  
 3682 that subsequent retraining does not materially alter the resulting significance.

3683 Based on these evaluations, a cut value of 0.1 is selected for optimal sensitivity to both  
 3684 ggF and VBF HH signals. Additional analyses are conducted to compare the sensitivity of  
 3685 this optimized method with a more basic strategy that employs only the baseline variables  
 3686  $m_{jj}$  and  $\Delta\eta_{jj}$ .

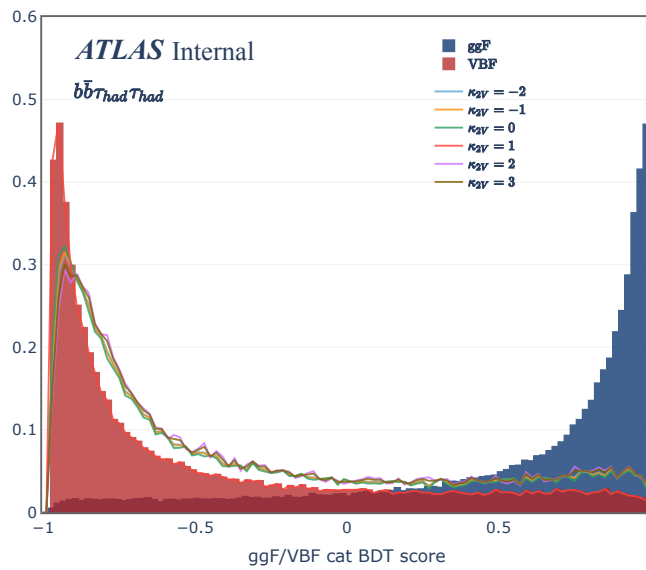


**Figure 6–16 Distribution of ggF/VBF BDT scores for various VBF processes under signal region preselection conditions.**

3687 **Score Distribution Analysis** Figure 6–16 illustrates the score distributions for multiple  
 3688 VBF processes under the preselection criteria in the signal region, utilizing the seven-variable  
 3689 ggF/VBF BDT setup. The histograms filled in blue and red correspond to SM ggF and VBF  
 3690 HH events, respectively. Variations in  $\kappa_{2V}$  are represented by histograms in different colors.  
 3691 The robustness of the seven-variable ggF/VBF BDT in segregating ggF HH events from  $\kappa_{2V}$   
 3692 fluctuations is thereby demonstrated. The absence of a significant systematic trend in the  
 3693 non-SM VBF samples underscores the stable categorization performance of the BDT for  
 3694 VBF events.

## 3695 6.5.2.2 SR-Specific BDTs

3696 Within each of the three SRs, specialized BDTs are constructed to distinguish HH signal  
3697 from the aggregate of all SM backgrounds.

3698 For the low- $m_{\text{HH}}$  region, the BDT is trained utilizing ggF events with  $\kappa_\lambda = 10$ . Conversely,  
3699 the high- $m_{\text{HH}}$  region BDT employs the ggF SM signal sample for training. In both scenarios,  
3700 training sets are restricted to events that meet the full SR criteria, including the previously  
3701 applied ggF/VBF BDT cut.

3702 The BDT aimed at the VBF region employs SM VBF HH signal events for its training.  
3703 Importantly, events from both VBF and ggF SRs contribute to the training dataset to optimize  
3704 statistical power. This approach has been verified to substantially enhance the VBF sensitivity  
3705 when compared to training solely on VBF SR events.

3706 Each BDT's hyperparameters and input variables are individually optimized for their re-  
3707 spective regions. The resulting BDT scores are subsequently employed in a profile likelihood  
3708 fit to derive the ultimate findings, elaborated in Section 6.8.

3709 **Hyperparameter Tuning for Signal Region BDTs** The approach to hyperparameter opti-  
3710 mization is akin to the methodology described in Section 6.5.2.1. The key hyperparameters  
3711 NTrees and MaxDepth are specifically fine-tuned. The target for optimization is the binned  
3712 validation significance, computed in accordance with the binning schema detailed in Sec-  
3713 tion 6.7.2. The constraints for this are a minimum of 1.0 background events per bin, an upper  
3714 limit on the MC background prediction's statistical uncertainty of 20%, and the use of  $z_s = 10$   
3715 and  $z_b = 5$ .

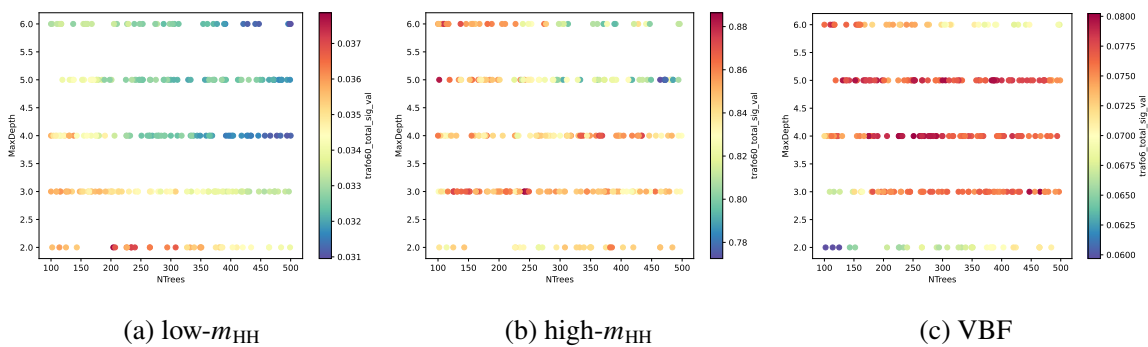


**Figure 6–17 Impact of the NTrees and MaxDepth hyperparameters on the validation significance for the respective BDT training sets in the  $\tau_{\text{had}}\tau_{\text{had}}$  channel.**

Hyperparameter	low- $m_{\text{HH}}$ ggF SR	high- $m_{\text{HH}}$ ggF SR	VBF SR
NTrees	204	241	465
MaxDepth	2	3	3
MinNodeSize	1%	1%	1%
BoostType	Grad	Grad	Grad
Shrinkage	0.2	0.2	0.2
IgnoreNegWeightsInTraining	True	True	True

**Table 6–12 Training hyperparameters chosen for the BDTs used in the three  $\tau_{\text{had}}\tau_{\text{had}}$  analysis categories.**

3716 Figure 6–17 provides a visualization of how NTrees and MaxDepth affect this metric  
 3717 across the three distinct BDT sets. Optimal hyperparameters were chosen based on their  
 3718 ability to maximize the validation significance. The chosen parameters are cataloged in Ta-  
 3719 ble 6–12.

3720 **Optimization of Input Variables** In line with the iterative optimization strategy delineated  
 3721 in Section 6.5.1.3, we begin with a set of five foundational variables:  $m_{jj}$ ,  $m_{bb}$ ,  $m_{\tau\tau}^{\text{MMC}}$ ,  $\Delta R_{bb}$ ,  
 3722 and  $\Delta R_{\tau\tau}$ . Due to statistical constraints imposed by the limited size of the background MC  
 3723 datasets, we utilize a validation significance metric that employs a coarser binning, ensuring  
 3724 a minimum of 5.0 expected background events per bin. This is visualized alongside a finer  
 3725 binning strategy in Figures 6–18.

3726 Especially in the high- $m_{\text{HH}}$  regime, noticeable statistical fluctuations are apparent in the  
 3727 early optimization phases when employing the finer binning. These instabilities stabilize as  
 3728 more variables are incorporated. Ultimately, the top  $N$  predictors are chosen for the final  
 3729 model, where  $N$  is determined by the point at which performance stabilization is achieved in  
 3730 both binnings under investigation.

3731 The finalized input sets for the individual BDTs are cataloged in Table 6–13, Table 6–14  
 3732 and Table 6–15.

3733 The subsequent illustrations present a characteristic ensemble of pre-fit MVA predic-  
 3734 tor variables for each signal region in the  $\tau_{\text{had}}\tau_{\text{had}}$  channel. In these graphical representations,  
 3735 background adjustments are performed using scaling coefficients derived from a comprehen-

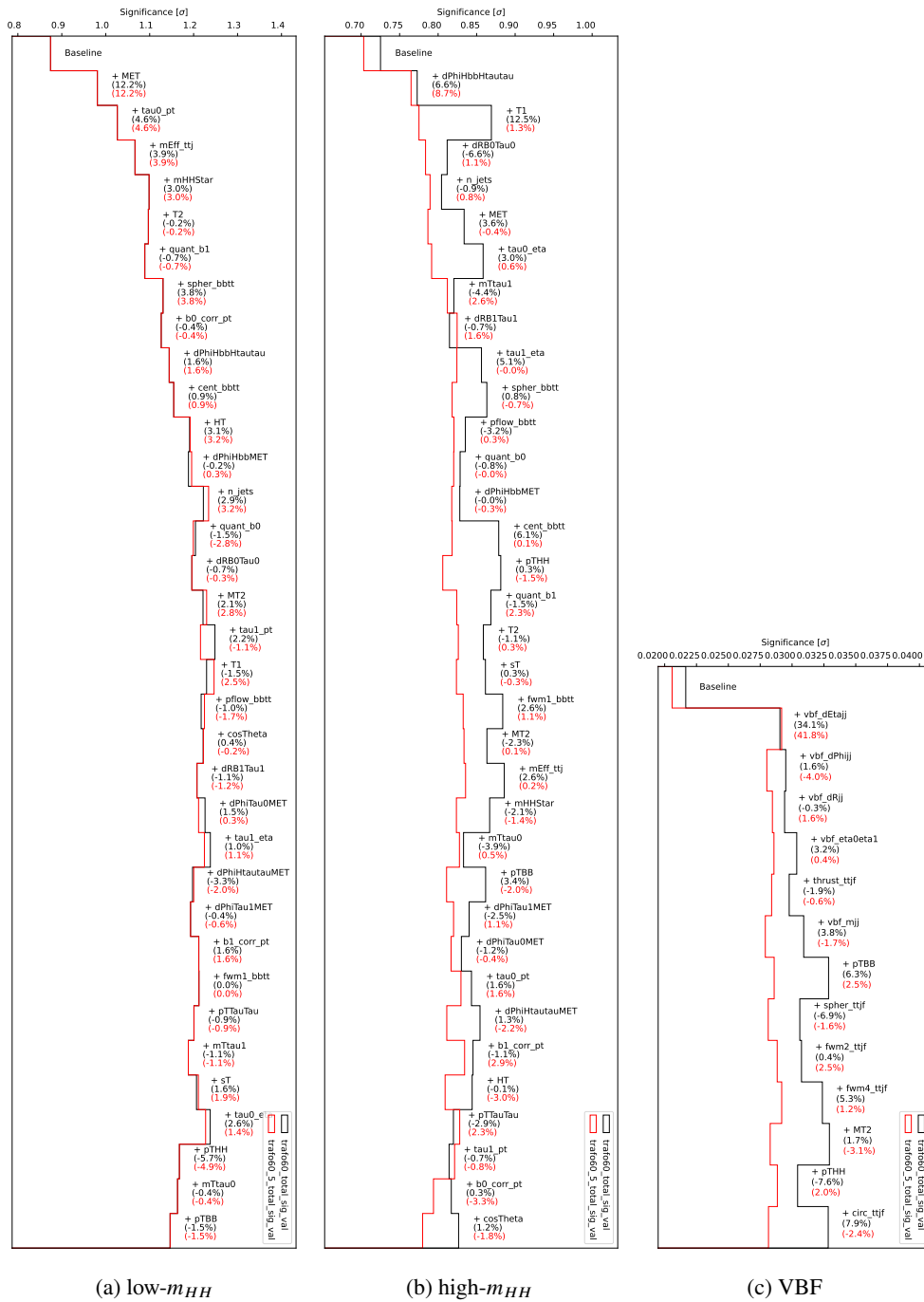


**Figure 6–18 Trajectory of the validation significance as additional predictor variables are incorporated. The baseline set consists of  $m_{jj}$ ,  $m_{bb}$ ,  $m_{\tau\tau}^{MMC}$ ,  $\Delta R_{bb}$ , and  $\Delta R_{\tau\tau}$ . Red curves (trafo60\_5\_total\_sig\_val) represent binned significance with at least 5.0 expected background events per bin, whereas black curves (trafo60\_total\_sig\_val) require only a minimum of 1.0 expected background events per bin.**

Variable	Description
$m_{HH}$	Invariant mass of the $HH$ system, reconstructed from the $\tau$ -lepton pair (using the MMC) and $b$ -tagged jet pair
$m_{bb}$	Invariant mass of the $b$ -tagged jet pair system
$m_{\tau\tau}^{\text{MMC}}$	Invariant mass of the $\tau$ -lepton pair system, calculated using the MMC
$\Delta R_{bb}$	The $\Delta R$ between the two $b$ -tagged jets
$\Delta R_{\tau\tau}$	The $\Delta R$ between the two $\tau_{\text{had-vis}}$
n_jets	Number of jets in the event
$H_T$	Total hadronic transverse energy in the event, perpendicular to the beamline
$T_2$	Topness, as defined in Ref. <sup>Kim:2018exf</sup> assuming $\sigma_t = 15$ GeV and $\sigma_W = 5$ GeV
$E_T^{\text{miss}}$	The missing transverse momentum of the event
$M_{T2}$	Stranverse mass, as defined in Ref. <sup>Lester_1999</sup>
$p_T(\tau_0)$	Transverse momentum of the leading $\tau_{\text{had-vis}}$
$p_T(\tau_1)$	Transverse momentum of the sub-leading $\tau_{\text{had-vis}}$
$p_T(b_0)$	Transverse momentum of the leading $b$ -tagged jet
$\Delta\phi(bb, E_T^{\text{miss}})$	The $\Delta\phi$ between the $b$ -tagged jet pair system and missing transverse energy
$\Delta\phi(bb, \tau\tau)$	The $\Delta\phi$ between the $b$ -tagged jet pair and $\tau$ -lepton pair systems
quant $b_0$	$b$ -tagging quantile of leading $b$ -tagged jet
quant $b_1$	$b$ -tagging quantile of sub-leading $b$ -tagged jet
$m_{HH}^*$	Reduced 4-object invariant mass, defined as $m_{HH}^* = m_{HH} - m_{bb} - m_{\tau\tau}^{\text{MMC}} + 250$ GeV
$\Delta R(b_0, \tau_0)$	The $\Delta R$ between the leading $b$ -tagged jet and $\tau_{\text{had-vis}}$
cent( $bb\tau\tau$ )	Centrality, taking into account only the $HH$ decay products
$m_{\text{eff}}(\tau\tau j)$	Effective mass, taking into account the $\tau$ -lepton pair and central jets
spher( $bb\tau\tau$ )	Sphericity, taking into account only the $HH$ decay products
$\eta(\tau_0)$	Pseudorapidity of the leading $\tau_{\text{had-vis}}$
$\eta(\tau_1)$	Pseudorapidity of the sub-leading $\tau_{\text{had-vis}}$

**Table 6–13 Input variables used for the low- $m_{HH}$  ggF BDT training in the  $\tau_{\text{had}}\tau_{\text{had}}$  channel.**

3736 sive fit to empirical data. Figure 6–19 delineates the distribution of essential variables across  
3737 the triad of signal regions. Concurrently, Figure 6–20 introduces novel variables specifically  
3738 tailored for the discrimination of signal from background through BDT in each designated  
3739 region. Lastly, Figure 6–21 showcases the BDT employed for the stratification between ggF  
3740 and VBF signal domains, restricting the analysis to events featuring a minimum of four jets.

Variable	Description
$m_{HH}$	Invariant mass of the $HH$ system, reconstructed from the $\tau$ -lepton pair (using the MMC) and $b$ -tagged jet pair
$m_{bb}$	Invariant mass of the $b$ -tagged jet pair system
$m_{\tau\tau}^{\text{MMC}}$	Invariant mass of the $\tau$ -lepton pair system, calculated using the MMC
$\Delta R_{bb}$	The $\Delta R$ between the two $b$ -tagged jets
$\Delta R_{\tau\tau}$	The $\Delta R$ between the two $\tau_{\text{had-vis}}$
n_jets	Number of jets in the event
$T_1$	Topness, as defined in Ref. <a href="#">Kim:2018exf</a> assuming $\sigma_t = 5$ GeV and $\sigma_W = 5$ GeV.
$E_T^{\text{miss}}$	The missing transverse momentum of the event
$p_T(HH)$	Transverse momentum of the $HH$ system
$m_T(\tau_1)$	Transverse mass of the sub-leading $\tau_{\text{had-vis}}$
$\Delta\phi(bb, E_T^{\text{miss}})$	The $\Delta\phi$ between the $b$ -tagged jet pair system and missing transverse energy
$\Delta\phi(bb, \tau\tau)$	The $\Delta\phi$ between the $b$ -tagged jet pair and $\tau$ -lepton pair systems
quant $b_0$	$b$ -tagging quantile of leading $b$ -tagged jet
quant $b_1$	$b$ -tagging quantile of sub-leading $b$ -tagged jet
$\Delta R(b_0, \tau_0)$	The $\Delta R$ between the leading $b$ -tagged jet and $\tau_{\text{had-vis}}$
$\Delta R(b_1, \tau_1)$	The $\Delta R$ between the sub-leading $b$ -tagged jet and $\tau_{\text{had-vis}}$
cent( $bb\tau\tau$ )	Centrality, taking into account only the $HH$ decay products
spher( $bb\tau\tau$ )	Sphericity, taking into account only the $HH$ decay products
pflow( $bb\tau\tau$ )	Planar flow, taking into account only the $HH$ decay products
$\eta(\tau_0)$	Pseudorapidity of the leading $\tau_{\text{had-vis}}$
$\eta(\tau_1)$	Pseudorapidity of the sub-leading $\tau_{\text{had-vis}}$

**Table 6–14** Input variables used for the high- $m_{HH}$  ggF BDT training in the  $\tau_{\text{had}}\tau_{\text{had}}$  channel.

Variable	Description
$m_{HH}$	Invariant mass of the $HH$ system, reconstructed from the $\tau$ -lepton pair (using the MMC) and $b$ -tagged jet pair
$m_{bb}$	Invariant mass of the $b$ -tagged jet pair system
$m_{\tau\tau}^{\text{MMC}}$	Invariant mass of the $\tau$ -lepton pair system, calculated using the MMC
$\Delta R_{bb}$	The $\Delta R$ between the two $b$ -tagged jets
$\Delta R_{\tau\tau}$	The $\Delta R$ between the two visible $\tau$ decay products
VBF $\eta_0 \times \eta_1$	Product of the pseudorapidities of the leading and sub-leading VBF jets
$\Delta\eta_{ij}^{\text{VBF}}$	The $\Delta\eta$ between the two VBF jets
$\Delta\phi_{ij}^{\text{VBF}}$	The $\Delta\phi$ between the two VBF jets
$\Delta R_{ij}^{\text{VBF}}$	The $\Delta R$ between the two VBF jets
$m_{ij}^{\text{VBF}}$	Invariant mass of the VBF jet system
thrust( $\tau\tau jf$ )	Thrust, taking into account the $\tau$ -lepton pair and central and forward jets
circ( $\tau\tau jf$ )	Circularity, taking into account the $\tau$ -lepton pair and central and forward jets
$\eta(\tau_0)$	Pseudorapidity of the leading $\tau_{\text{had-vis}}$
$\eta(\tau_1)$	Pseudorapidity of the sub-leading $\tau_{\text{had-vis}}$

**Table 6–15** Input variables used for the VBF BDT training in the  $\tau_{\text{had}}\tau_{\text{had}}$  channel.

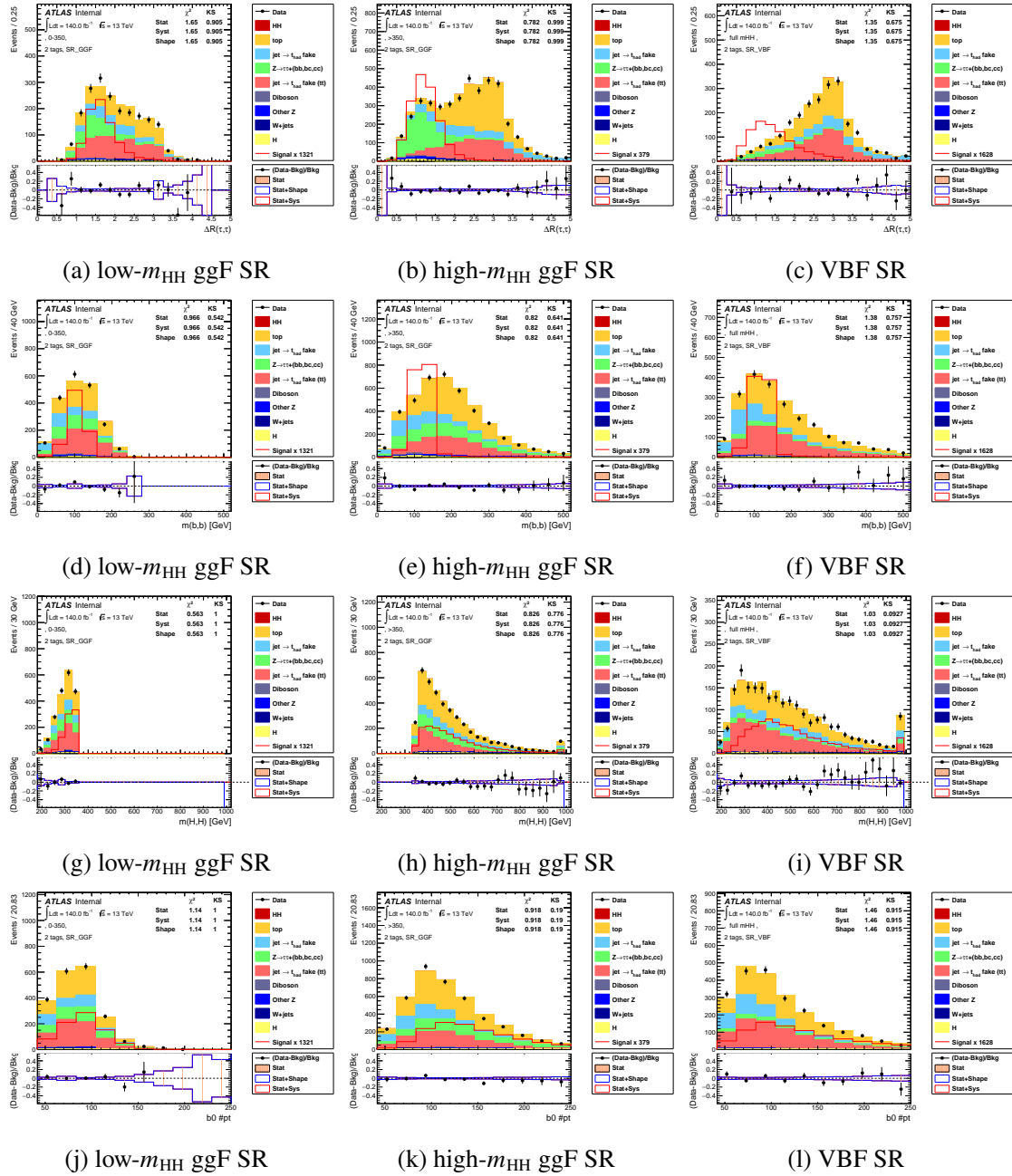


Figure 6-19 Representative set of pre-fit MVA input variable distributions in the  $\tau_{had}\tau_{had}$  SRs.

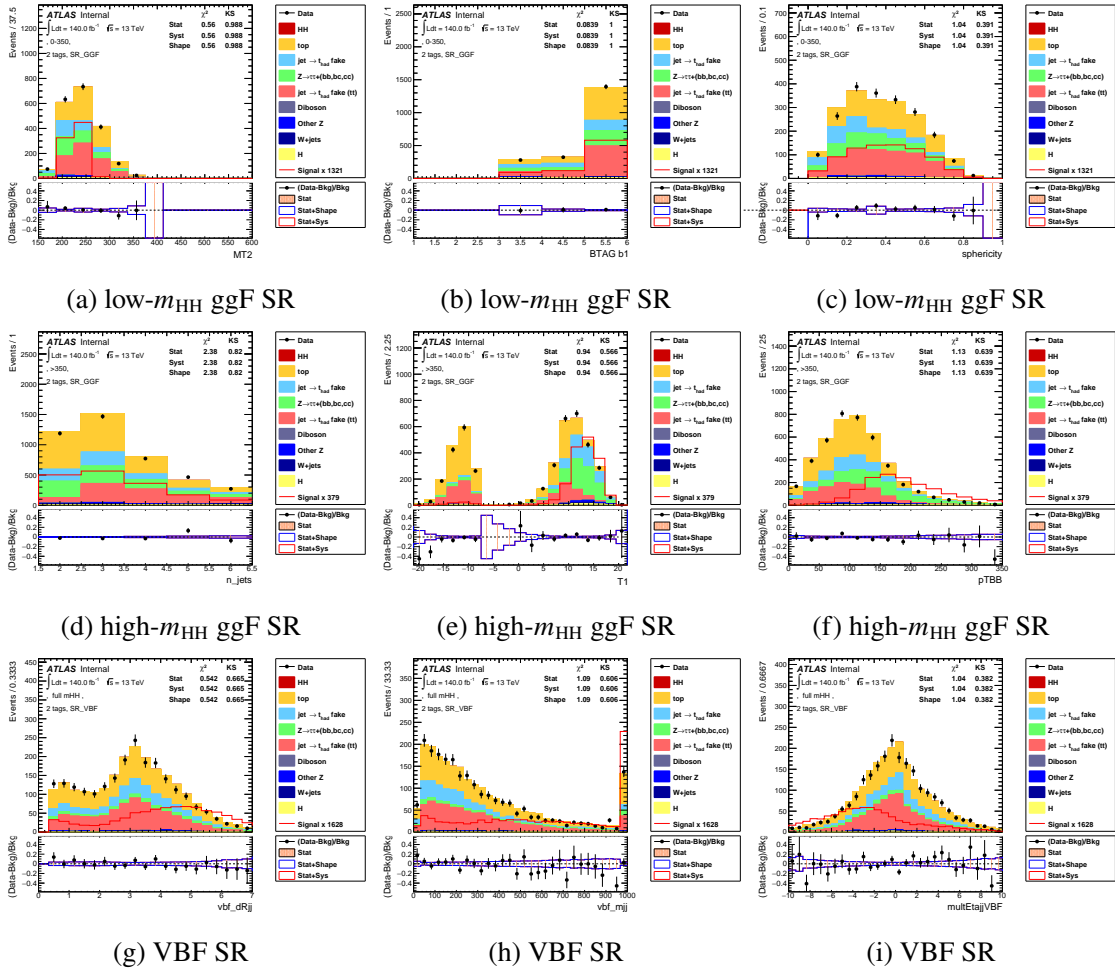


Figure 6–20 Representative set of pre-fit MVA input variable distributions in the  $\tau_{had}\tau_{had}$  SRs.

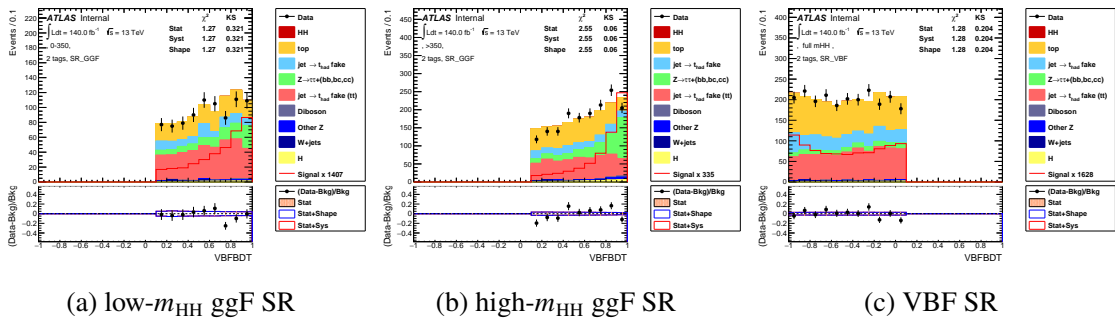


Figure 6–21 Categorisation BDT variable distributions in the  $\tau_{had}\tau_{had}$  SRs.

3741 **BDT Score Distribution Components** Figure 6–23 displays the constituent background  
 3742 yields in the bins most indicative of the signal, based on the binning scheme employed within  
 3743 the likelihood fitting procedure. Comprehensive enumerations of prefit background yields  
 3744 across all three SRs are itemized in Tables 6–16, 6–17 and 6–18.

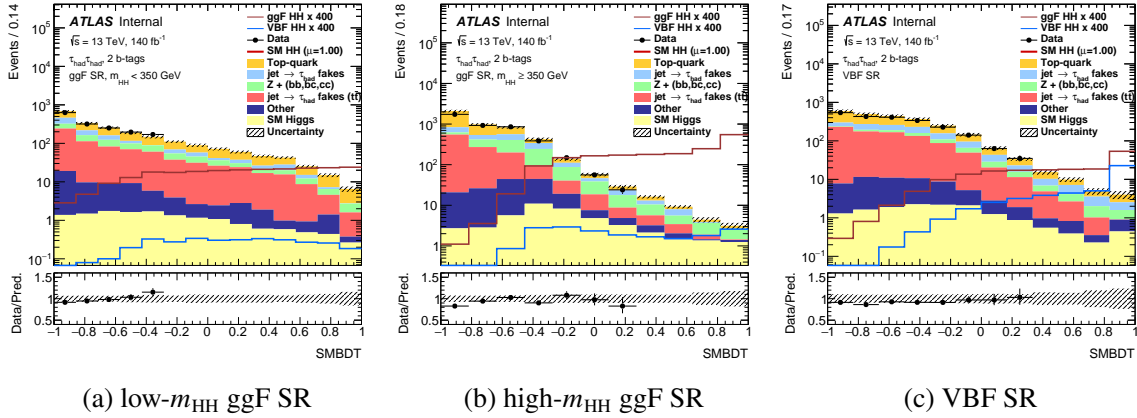


Figure 6–22 Pre-fit BDT score distributions in the  $\tau_{had}\tau_{had}$  signal regions.

3745 In specific scenarios, such as for the QCD fake background in the most signal-like bin  
 3746 within the high- $m_{HH}$  SR, a prefit background projection may yield a negative value accom-  
 3747 panied by significant statistical uncertainty. These negative yields pose no issue; they are  
 3748 adjusted to zero during the generation of the fitting workspace, with the corresponding un-  
 3749 certainties accurately integrated into the constraint term for the Beeston-Barlow nuisance  
 3750 parameter (NP) specific to that bin.

3751 Figure 6–22 illustrates the comparison between the data and model predictions for prefit  
 3752 BDT scores within the  $\tau_{had}\tau_{had}$  SRs. These regions are presently subject to blinding in the

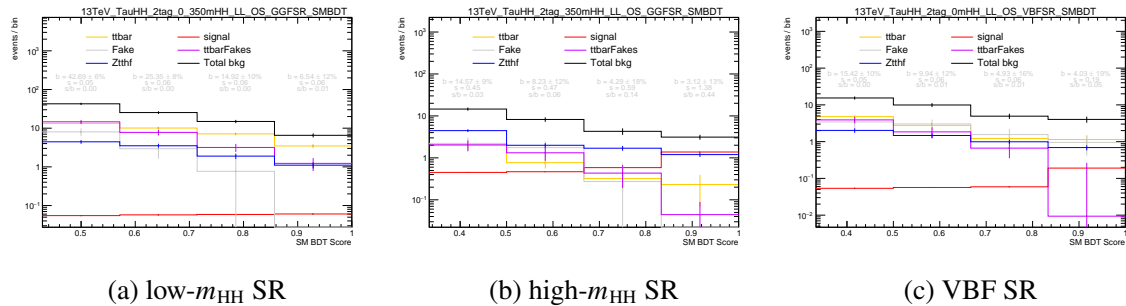


Figure 6–23 Prefit yields of the main background components, the total signal, as well as the total background in the most signal-like BDT bins in the  $\tau_{had}\tau_{had}$  SRs.

Sample	Highest bin	2nd-highest bin	3rd-highest bin	4th-highest bin
Fake	$0.000 \pm 0.268$	$0.272 \pm 0.456$	$1.753 \pm 0.741$	$2.215 \pm 0.838$
ggFHtautau	$0.438 \pm 0.093$	$0.338 \pm 0.090$	$0.324 \pm 0.082$	$0.370 \pm 0.090$
ttbar	$0.231 \pm 0.164$	$0.321 \pm 0.163$	$0.769 \pm 0.209$	$1.987 \pm 0.389$
ttH	$0.246 \pm 0.022$	$0.303 \pm 0.024$	$0.369 \pm 0.027$	$0.457 \pm 0.030$
ttZ	$0.012 \pm 0.010$	$0.059 \pm 0.012$	$0.064 \pm 0.014$	$0.095 \pm 0.020$
ttW	$0.011 \pm 0.007$	$0.002 \pm 0.002$	$0.010 \pm 0.006$	$0.018 \pm 0.008$
VBFHtautau	$0.019 \pm 0.008$	$0.036 \pm 0.009$	$0.031 \pm 0.009$	$0.048 \pm 0.011$
WHtautau	$0.000 \pm 0.000$	$0.000 \pm 0.000$	$0.015 \pm 0.015$	$0.012 \pm 0.012$
qqZHtautau	$0.303 \pm 0.043$	$0.330 \pm 0.043$	$0.305 \pm 0.041$	$0.539 \pm 0.056$
WHbb	$0.002 \pm 0.001$	$0.002 \pm 0.001$	$0.002 \pm 0.001$	$0.001 \pm 0.001$
ggZHbb	$0.031 \pm 0.004$	$0.045 \pm 0.004$	$0.061 \pm 0.005$	$0.129 \pm 0.008$
qqZHbb	$0.079 \pm 0.004$	$0.091 \pm 0.005$	$0.138 \pm 0.006$	$0.242 \pm 0.008$
ggZHtautau	$0.126 \pm 0.023$	$0.120 \pm 0.022$	$0.150 \pm 0.025$	$0.185 \pm 0.028$
W	$0.000 \pm 0.000$	$0.000 \pm 0.000$	$0.000 \pm 0.000$	$0.000 \pm 0.040$
Wtt	$0.000 \pm 0.000$	$0.000 \pm 0.444$	$0.097 \pm 0.097$	$0.295 \pm 0.222$
ttbarFakes	$0.044 \pm 0.044$	$0.433 \pm 0.241$	$1.321 \pm 0.470$	$2.047 \pm 0.585$
Zhf	$0.000 \pm 0.000$	$0.012 \pm 0.012$	$0.000 \pm 0.023$	$0.021 \pm 0.021$
Zlf	$0.000 \pm 0.000$	$0.000 \pm 0.000$	$0.000 \pm 0.000$	$0.000 \pm 0.000$
Ztthf	$1.197 \pm 0.146$	$1.698 \pm 0.223$	$1.995 \pm 0.247$	$4.461 \pm 0.341$
Zttlf	$0.024 \pm 0.016$	$0.009 \pm 0.036$	$0.412 \pm 0.283$	$0.166 \pm 0.058$
stop	$0.267 \pm 0.190$	$0.192 \pm 0.150$	$0.405 \pm 0.238$	$0.914 \pm 0.470$
diboson	$0.092 \pm 0.064$	$0.028 \pm 0.029$	$0.009 \pm 0.065$	$0.367 \pm 0.148$
signal	$1.379 \pm 0.010$	$0.585 \pm 0.006$	$0.467 \pm 0.006$	$0.450 \pm 0.006$
bkg	$3.124 \pm 0.417$	$4.292 \pm 0.759$	$8.233 \pm 1.018$	$14.569 \pm 1.274$

**Table 6–16** Prefit yields of the individual background components and the total ggF+VBF HH signal (labelled signal) in the four most signal-like BDT bins, shown for the  $\tau_{\text{had}}\tau_{\text{had}}$  high- $m_{\text{HH}}$  region.

3753 most sensitive bins, as elaborated in Section 6.7.3.

Sample	Highest bin	2nd-highest bin	3rd-highest bin	4th-highest bin
Fake	$0.000 \pm 0.364$	$0.767 \pm 0.858$	$2.945 \pm 1.319$	$8.037 \pm 1.881$
ggFHtautau	$0.009 \pm 0.007$	$0.117 \pm 0.057$	$0.046 \pm 0.033$	$0.112 \pm 0.052$
ttbar	$3.472 \pm 0.430$	$7.141 \pm 0.568$	$10.091 \pm 0.723$	$13.307 \pm 0.773$
ttH	$0.146 \pm 0.017$	$0.177 \pm 0.018$	$0.196 \pm 0.019$	$0.213 \pm 0.020$
ttZ	$0.004 \pm 0.005$	$0.025 \pm 0.010$	$0.041 \pm 0.024$	$0.052 \pm 0.018$
ttW	$0.000 \pm 0.005$	$0.022 \pm 0.009$	$0.010 \pm 0.007$	$0.032 \pm 0.010$
VBFHtautau	$0.000 \pm 0.000$	$0.006 \pm 0.003$	$0.014 \pm 0.006$	$0.010 \pm 0.005$
WHtautau	$0.000 \pm 0.000$	$0.010 \pm 0.008$	$0.000 \pm 0.000$	$0.000 \pm 0.000$
qqZHtautau	$0.061 \pm 0.019$	$0.052 \pm 0.017$	$0.139 \pm 0.028$	$0.106 \pm 0.025$
WHbb	$0.000 \pm 0.000$	$0.001 \pm 0.001$	$0.000 \pm 0.000$	$0.010 \pm 0.006$
ggZHbb	$0.005 \pm 0.001$	$0.011 \pm 0.002$	$0.011 \pm 0.002$	$0.015 \pm 0.002$
qqZHbb	$0.031 \pm 0.006$	$0.061 \pm 0.009$	$0.068 \pm 0.009$	$0.093 \pm 0.011$
ggZHtautau	$0.012 \pm 0.007$	$0.008 \pm 0.005$	$0.012 \pm 0.007$	$0.027 \pm 0.011$
W	$0.000 \pm 0.000$	$0.000 \pm 0.000$	$0.000 \pm 0.000$	$0.000 \pm 0.000$
Wtt	$0.000 \pm 0.000$	$0.517 \pm 0.517$	$0.104 \pm 0.104$	$0.049 \pm 0.049$
ttbarFakes	$1.230 \pm 0.451$	$3.176 \pm 0.748$	$7.782 \pm 1.284$	$14.618 \pm 1.690$
Zhf	$0.009 \pm 0.009$	$0.000 \pm 0.011$	$0.000 \pm 0.000$	$0.000 \pm 0.000$
Zlf	$0.000 \pm 0.000$	$0.000 \pm 0.000$	$0.000 \pm 0.000$	$0.000 \pm 0.000$
Ztthf	$1.105 \pm 0.195$	$1.896 \pm 0.306$	$3.510 \pm 0.374$	$4.443 \pm 0.487$
Zttlf	$0.028 \pm 0.019$	$0.281 \pm 0.169$	$0.124 \pm 0.065$	$0.152 \pm 0.075$
stop	$0.346 \pm 0.206$	$0.563 \pm 0.282$	$0.101 \pm 0.101$	$1.301 \pm 0.436$
diboson	$0.081 \pm 0.044$	$0.092 \pm 0.081$	$0.157 \pm 0.065$	$0.113 \pm 0.066$
signal	$0.061 \pm 0.002$	$0.059 \pm 0.002$	$0.057 \pm 0.002$	$0.055 \pm 0.002$
bkg	$6.540 \pm 0.777$	$14.922 \pm 1.448$	$25.352 \pm 2.021$	$42.689 \pm 2.727$

**Table 6–17 Prefit yields of the individual background components and the total ggF+VBF HH signal (labelled signal) in the four most signal-like BDT bins, shown for the  $\tau_{\text{had}}\tau_{\text{had}}$  low- $m_{\text{HH}}$  region.**

Sample	Highest bin	2nd-highest bin	3rd-highest bin	4th-highest bin
Fake	$0.952 \pm 0.535$	$1.556 \pm 0.668$	$3.030 \pm 0.935$	$3.430 \pm 1.135$
ggFHtautau	$0.171 \pm 0.064$	$0.064 \pm 0.031$	$0.123 \pm 0.054$	$0.182 \pm 0.060$
ttbar	$1.140 \pm 0.323$	$1.222 \pm 0.220$	$2.773 \pm 0.364$	$4.789 \pm 0.460$
ttH	$0.124 \pm 0.016$	$0.094 \pm 0.014$	$0.154 \pm 0.017$	$0.228 \pm 0.021$
ttZ	$0.014 \pm 0.007$	$0.022 \pm 0.012$	$0.049 \pm 0.016$	$0.103 \pm 0.016$
ttW	$0.002 \pm 0.002$	$0.000 \pm 0.000$	$0.015 \pm 0.016$	$0.038 \pm 0.018$
VBFHtautau	$0.037 \pm 0.009$	$0.016 \pm 0.006$	$0.025 \pm 0.008$	$0.047 \pm 0.011$
WHtautau	$0.014 \pm 0.014$	$0.000 \pm 0.000$	$0.000 \pm 0.000$	$0.000 \pm 0.000$
qqZHtautau	$0.015 \pm 0.009$	$0.000 \pm 0.000$	$0.022 \pm 0.011$	$0.018 \pm 0.010$
ggZHbb	$0.017 \pm 0.003$	$0.016 \pm 0.003$	$0.028 \pm 0.003$	$0.036 \pm 0.004$
qqZHbb	$0.009 \pm 0.002$	$0.010 \pm 0.002$	$0.010 \pm 0.002$	$0.021 \pm 0.003$
ggZHtautau	$0.056 \pm 0.016$	$0.027 \pm 0.010$	$0.026 \pm 0.010$	$0.020 \pm 0.009$
W	$0.000 \pm 0.017$	$0.000 \pm 0.000$	$0.000 \pm 0.000$	$0.000 \pm 0.000$
Wtt	$0.083 \pm 0.071$	$0.000 \pm 0.000$	$0.175 \pm 0.175$	$0.052 \pm 0.160$
WHbb	$0.000 \pm 0.000$	$0.001 \pm 0.001$	$0.000 \pm 0.000$	$0.000 \pm 0.000$
ttbarFakes	$0.009 \pm 0.256$	$0.666 \pm 0.311$	$1.843 \pm 0.614$	$3.902 \pm 0.752$
Zhf	$0.000 \pm 0.000$	$0.000 \pm 0.000$	$0.000 \pm 0.000$	$0.000 \pm 0.000$
Zlf	$0.000 \pm 0.000$	$0.000 \pm 0.000$	$0.000 \pm 0.000$	$0.000 \pm 0.000$
Ztthf	$0.690 \pm 0.110$	$0.992 \pm 0.134$	$1.469 \pm 0.214$	$2.021 \pm 0.285$
Zttlf	$0.161 \pm 0.075$	$0.003 \pm 0.018$	$0.167 \pm 0.079$	$0.150 \pm 0.073$
stop	$0.342 \pm 0.243$	$0.141 \pm 0.141$	$0.000 \pm 0.000$	$0.305 \pm 0.216$
diboson	$0.189 \pm 0.189$	$0.102 \pm 0.075$	$0.024 \pm 0.024$	$0.076 \pm 0.043$
signal	$0.191 \pm 0.003$	$0.059 \pm 0.002$	$0.057 \pm 0.002$	$0.054 \pm 0.002$
bkg	$4.025 \pm 0.761$	$4.931 \pm 0.798$	$9.935 \pm 1.213$	$15.418 \pm 1.494$

**Table 6–18** Prefit yields of the individual background components and the total ggF+VBF HH signal (labelled signal) in the four most signal-like BDT bins, shown for the  $\tau_{\text{had}}\tau_{\text{had}}$  VBF region.

## 3754 6.5.2.3 ggF and VBF Classification: MVA versus Cut-Based

3755 To systematically assess the benefits of utilizing a BDT for differentiating ggF and VBF  
 3756  $HH$  processes in contrast to a basic cut-based methodology, the BDT in question is retrained.  
 3757 This retraining also involves a hyperparameter optimization and is restricted to two param-  
 3758 eters,  $m_{jj}^{\text{VBF}}$  and  $\Delta\eta_{jj}^{\text{VBF}}$ , thereby mimicking the cut-based method. This is juxtaposed with  
 3759 a 7-var BDT and a legacy 15-var BDT, which included variables unsuitable for VBF  $HH$   
 3760 characterization and was consequently supplanted.

3761 Figure 6–24 exhibits a comparative analysis of the 2-var and 7-var ggF/VBF configura-  
 3762 tions, focusing on  $HH$  signal strengths and signal-to-background ratios<sup>1</sup>. The evaluations  
 3763 span across all three signal regions and vary with BDT thresholds. The low- $m_{HH}$  and high-  
 3764  $m_{HH}$  regions are color-coded in blue and red, respectively, and the VBF region is denoted in  
 3765 purple. A nominal BDT threshold of 0.1 is indicated by a dashed grey line. It is observed that  
 3766 the 2-var BDT yields superior signal-to-background ratio in the VBF region at the nominal  
 3767 point, while the 7-var BDT performs more effectively in the ggF regions.

3768 Table 6–19 presents a comparative summary of the 15-var BDT, implemented at the stage  
 3769 of EB request, against the 2-var and 7-var BDTs, discussing the ultimate evaluation metrics  
 3770 (95% CL upper boundaries as well as  $\kappa_\lambda$  and  $\kappa_{2V}$  intervals).

	95% CL Upper Limits on Signal Strength			95% CL Intervals	
	$\mu_{HH}$	$\mu_{\text{ggF}}^{2D}$	$\mu_{\text{VBF}}^{2D}$	$\kappa_\lambda$	$\kappa_{2V}$
15-var BDT	2.92	3.04	90	11.19	2.85
2-var BDT	3.08 (5%)	3.22 (6%)	93.05 (3%)	11.29 (0.9%)	2.91(2%)
7-var BDT	2.90 (-0.7%)	3.01 (-1%)	93.56 (4%)	11.27 (0.7%)	2.92 (2%)

**Table 6–19 Comparison of BDT configurations for ggF/VBF in relation to the ultimate fit outcomes. These limits are derived from a fit that incorporates solely floating normalizations and MC statistical uncertainties. A consistent BDT threshold of 0.1 is employed across all scenarios. The percentage enhancement relative to the 15-var BDT outcome is indicated in parentheses.**

3771 Eliminating variables with low sensitivity to the VBF  $HH$  process yields minimal impact  
 3772 on the BDT’s effectiveness. Notably, a performance enhancement is evident when contrasting  
 3773 the 2-var ggF/VBF BDT with its 7-var counterpart. Consequently, the 7-var BDT is chosen

<sup>1</sup> The ggF  $HH$  process is viewed as the signal in ggF SRs, while the VBF  $HH$  is for the VBF SR.

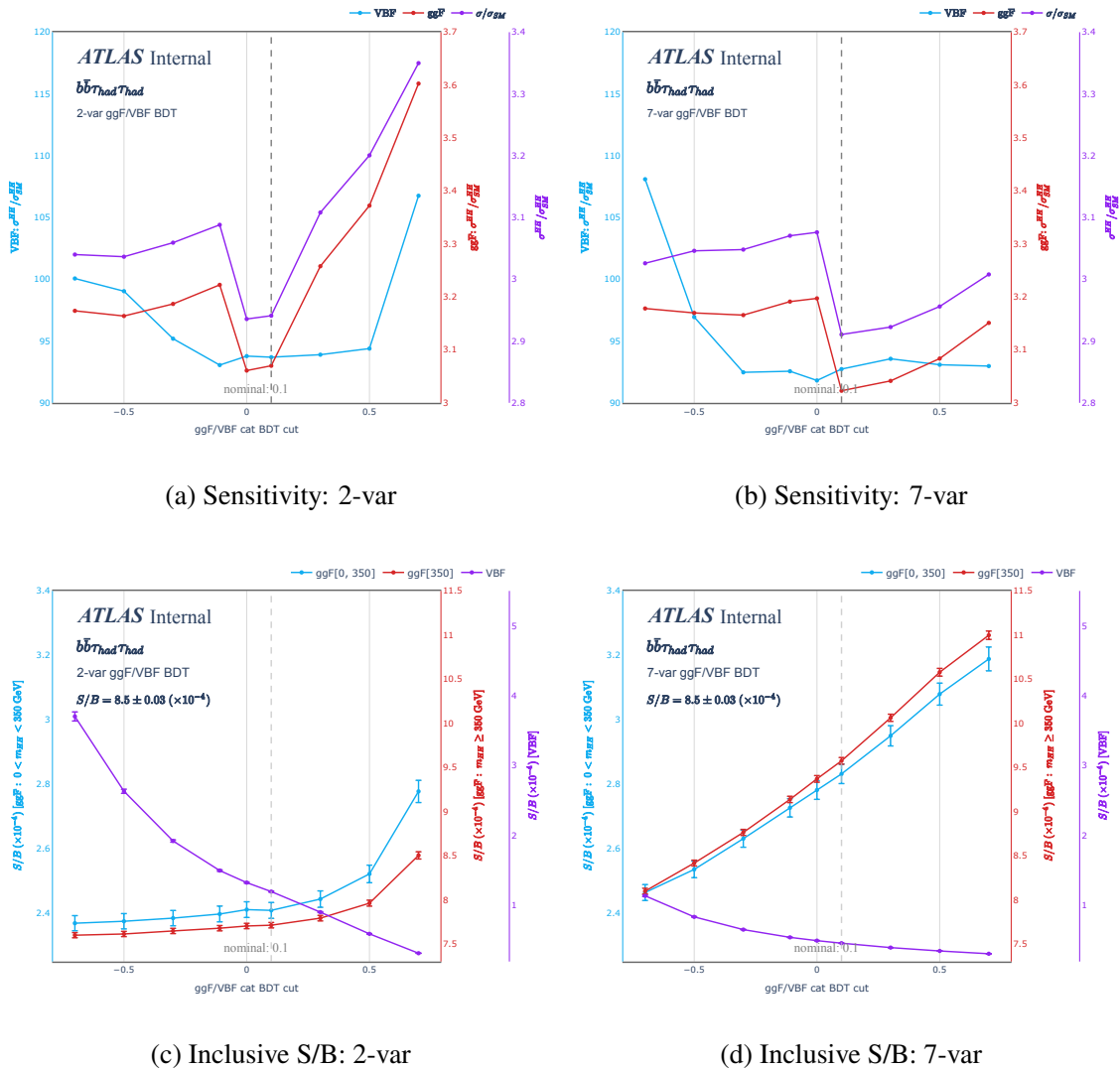


**Figure 6–24 Top row: Sensitivity as a function of the cut on the ggF vs VBF classification BDT for different variable sets. Bottom row: Inclusive S/B as a function of the cut on the ggF vs VBF classification BDT for different variable sets.**

3774 for classification tasks.

## 3775 6.6 Systematic uncertainties

3776 The dominant uncertainty in our analysis arises from the limited dataset. Nonetheless,  
 3777 systematic uncertainties affecting both signal and background estimates cannot be overlooked.  
 3778 For details on detector-response-based uncertainties in object selection and reconstruction,

3779 readers are referred to our previous study<sup>[177]</sup>.

3780 We apply the Beeston-Barlow method in a simplified form to model statistical uncertain-  
3781 ties in background predictions<sup>[196]</sup>. A luminosity uncertainty of 0.8% is applied, derived from  
3782 LUCID-2 measurements<sup>[154,197]</sup>.

3783 For processes reliant on MC simulations, various sources of theoretical uncertainties are  
3784 studied. The BDT shape variations are handled through a specific rebinning algorithm, em-  
3785 phasizing statistically significant variations. Details of these procedures and criteria are elab-  
3786 orated in Section 6.5.

3787 Uncertainties related to  $t\bar{t}$  production involve comparisons between default and alter-  
3788 native MC configurations. For instance, uncertainties originating from hard-scattering and  
3789 parton shower mechanisms are scrutinized through different generator setups. Contributions  
3790 from scales, PDF, and  $\alpha_s$  are also studied. For the  $Wt$  process, uncertainties related to the in-  
3791 terference with  $t\bar{t}$  are evaluated by comparing the diagram removal and subtraction schemes.  
3792 These are parameterized based on the BDT output.

3793 For the  $Z+HF$  process, hard-scatter and parton-shower uncertainties are similarly quan-  
3794 tified using alternative MC setups. Scale and PDF variations are also considered. Effects of  
3795 higher-order corrections are examined and deemed negligible.

3796 For the Standard Model ggF  $HH$  signal, the parton shower-related uncertainties are ex-  
3797 tracted by contrasting the default sample with a HERWIG7-modelled sample. Uncertainties  
3798 related to  $\kappa_\lambda$  reweighting are also assessed. These uncertainties have a direct bearing on the  
3799 categories selected for analysis.

3800 For VBF  $HH$ , the study involves comparisons with HERWIG7 models and variations in  
3801 PDF and QCD scales.

3802 For single-top processes, interference effects are assessed through diagram removal and  
3803 subtraction methods. Uncertainties are parameterized based on BDT output scores.

3804 Cross-section and decay branching ratio uncertainties are implemented according to the  
3805 LHC Higgs Cross Section Working Group<sup>[148]</sup>. Additionally, uncertainties specific to the  
3806 modeling of  $b$  or  $c$  jets in the absence of genuine heavy-flavor quarks are applied to relevant  
3807 single-Higgs processes. The uncertainties from parton-shower models and NLO matching  
3808 are also accounted for. Furthermore, PDF and scale uncertainties are evaluated using standard  
3809 techniques. For the  $t\bar{t}H$  process, additional uncertainties related to the modeling of initial and

3810 final state radiation are also assessed.

3811 Systematic uncertainties for minor backgrounds, such as single-top  $s$ - and  $t$ -channels,  
 3812  $Z$ +light-flavour jets,  $W$ +jets, and di-boson processes, are mainly constrained to acceptance  
 3813 uncertainties affecting only the normalisation. For the  $s$ - and  $t$ -channels of single-top pro-  
 3814 duction, an acceptance uncertainty of 20% is levied based on results from the SM  $VHbb$   
 3815 analysis<sup>ATLAS-CONF-2020-006</sup>. An acceptance uncertainty of 23% is assigned to the  $Z$ +light-  
 3816 flavour jets background, consistent with previous analyses. In the  $W$ +jets background, dif-  
 3817 ferent uncertainties are assigned for the two channels: 37% for the  $\tau_{\text{lep}}\tau_{\text{had}}$  channel and 50%  
 3818 for the  $\tau_{\text{had}}\tau_{\text{had}}$  channel to account for the fake- $\tau$  contribution. Acceptance uncertainties for  
 3819 di-boson processes are delineated as 25% for  $WW$ , 26% for  $WZ$ , and 20% for  $ZZ$ . For the ir-  
 3820 reducible  $ZZ$  background, additional studies reveal that scale uncertainties negligibly impact  
 3821 acceptance and shape within each analysis category. Apart from acceptance uncertainties,  
 3822 cross-section uncertainties are also applied to all minor backgrounds. However, their mag-  
 3823 nitude is comparatively smaller and thus less impactful.

3824 Data-driven estimates for backgrounds involving objects mimicking hadronic  $\tau$  leptons  
 3825 contribute to the analysis selection. These are collectively termed "Fake" in the  $\tau_{\text{lep}}\tau_{\text{had}}$  chan-  
 3826 nel and further subdivided into "Fake" and "ttbarFake" in the  $\tau_{\text{had}}\tau_{\text{had}}$  channel. The estimation  
 3827 techniques closely align with prior work<sup>[182]</sup>. Specifically, the  $\tau$  fake factors are parameter-  
 3828 ized based on variables such as transverse momentum and prong-ness. Since the regions  
 3829 under the current analysis are finer sub-categories of those used previously, we uphold the  
 3830 validity of the existing fake factors. Given this foundation, the systematic uncertainties for  
 3831 Fake- $\tau_{\text{had}}$  backgrounds are modeled consistently with the prior analysis for both the  $\tau_{\text{lep}}\tau_{\text{had}}$   
 3832 and  $\tau_{\text{had}}\tau_{\text{had}}$  channels. The sources and impact of these uncertainties follow the same frame-  
 3833 work as earlier work, with special attention given to instances where the current methodology  
 3834 diverges.

3835 The methodology for evaluating uncertainties on the HH signal, encompassing cross-  
 3836 section, acceptance, and shape, is principally inherited from the previous round of analysis.  
 3837 Alternative MC samples are used to probe the sensitivity to parton shower variations. Internal  
 3838 weights present in the nominal samples facilitate the assessment of PDF and scale variations.  
 3839 Parton Shower uncertainties are evaluated by contrasting nominal samples showered with  
 3840 PYTHIA8 against alternatives with HERWIG7. Internal alternative weights in the nominal

3841 samples are utilized for assessing uncertainties arising from PDF and scale variations. The  
 3842 PDF4LHC recommendations are followed for the combination of PDF and  $\alpha_s$  uncertainties.

## 3843 6.7 Statistical interpretation

3844 The statistical interpretation of the  $HH \rightarrow b\bar{b}\tau^+\tau^-$  analysis is framed within a simulta-  
 3845 neous binned maximum-likelihood fit. This fit targets the MVA output distributions across  
 3846 all considered event categories, both  $\tau_{\text{had}}\tau_{\text{had}}$  and  $\tau_{\text{lep}}\tau_{\text{had}}$ , delineated in Sections 6.3.4 and  
 3847 6.5. Additionally, the fit incorporates the  $m_{ll}$  distribution in the Z+HF CR. The details of  
 3848 mathematical framework for statistical inference can be found in Section 5.5.1.

### 3849 6.7.1 Fit step

3850 The binned profile likelihood fit is conducted across all MVA score categories and addi-  
 3851 tionally incorporates the  $m_{ll}$  distribution in the Z+HF CR.

3852 For the SM fits, the POI is the Higgs boson pair ( $HH$ ) signal strength, denoted by  $\mu_{HH}$ .  
 3853 This POI is normalized to the sum of ggF and VBF cross-sections, i.e.,  $31.05 + 1.726$  fb,  
 3854 multiplied by the branching ratio. Separate fits introducing individual POIs  $\mu_{\text{ggF}}$  and  $\mu_{\text{VBF}}$   
 3855 are also executed, each having an individual normalization constant.

3856 The top quark pair ( $t\bar{t}$ ) and Z+HF jets backgrounds are allowed to freely float during  
 3857 the fit, with their normalization being determined empirically. Normalization uncertainties  
 3858 between the SR and CR are applied as outlined in Section 6.6.

3859 In the scans of likelihood as functions of the couplings  $\kappa_\lambda$  and  $\kappa_{2V}$ , we prepare 3 ggF  
 3860 and 6 VBF templates as elaborated in Section 6.2.1. These scans modify the workspaces  
 3861 to introduce new POIs for  $\kappa_\lambda$  and  $\kappa_{2V}$ . Linear combinations of these templates are used to  
 3862 generate signal distributions for arbitrary  $\kappa_\lambda$  and  $\kappa_{2V}$  values.

3863 All systematic uncertainties discussed in Section 6.6 are incorporated as NPs in the pro-  
 3864 file likelihood fitting procedure. Each NP exerts its influence on either the shape or the nor-  
 3865 malization of the fit templates. While shape uncertainties are encapsulated using alternate  
 3866 histograms, normalization uncertainties are modeled using either flat or Gaussian distribu-  
 3867 tions.

- 3868 • Across all fit regions, experimental, cross-section, and acceptance uncertainties are  
 3869 fully correlated.

- 3870 • Correlations also extend to floating normalisations for  $t\bar{t}$  and Z+HF.
- 3871 • Exceptions include certain uncorrelated shape uncertainties, particularly for Z+HF in
- 3872 control regions.
- 3873 • Data-driven background uncertainties remain uncorrelated.

3874 Preprocessing steps for NPs include symmetrisation, smoothing, and pruning, in that  
3875 order.

- 3876 • Symmetrisation is applied to one-sided and same-sided systematic variations to rectify
- 3877 under-constraint issues.
- 3878 • Smoothing is selectively applied to 4-vector-based CP variations using iterative rebin-
- 3879 ning algorithms, aimed at reducing likelihood minimization instabilities.
- 3880 • Pruning is employed to remove inconsequential systematics, based on specific criteria
- 3881 such as less than 0.5% variation in yield or shape, among others.

3882 Additionally, MC statistical uncertainties are introduced as NPs using Poissonian priors,  
3883 identified by the SR and bin number.

## 3884 6.7.2 Binning

3885 In the analysis, an initial BDT score histogram is constructed with 2090 non-uniform  
3886 bins. The range from -1 to 0.990 uses a  $10^{-3}$  bin width, and the range from 0.990 to 1  
3887 employs a  $10^{-4}$  width. The rebinning algorithm, termed Trafo60, is used uniformly across  
3888 both  $\tau_{\text{lep}}\tau_{\text{had}}$  and  $\tau_{\text{had}}\tau_{\text{had}}$  channels. The algorithm starts with the most signal-like bins and  
3889 iteratively merges them according to criteria described by the function:

$$Z(I[k, l]) = z_s \frac{n_s(I[k, l])}{N_s} + z_b \frac{n_b(I[k, l])}{N_b}, \quad (6-7)$$

3890 Parameters  $(z_s, z_b) = (10, 5)$  are employed in all analysis regions to maintain sensitivity.  
3891 Iterations continue until MC statistical uncertainty on the sum of background events in each  
3892 bin falls below 20% and the number of expected background events in each bin exceeds 3.

## 3893 6.7.3 Blinding strategy

3894 The analysis is conducted under blinded conditions to mitigate the risk of bias. Specif-  
3895 ically, the observed point of interests (POIs) are hidden. For all channels and analysis cat-  
3896 egories, pre-fit MVA score distributions are blinded in the region that includes 85% of the  
3897 total signal. The fitting exercise uses the complete signal region and relies on pre-fit Asimov

3898 data.

## 3899 6.8 Results

3900 The fitting scheme, delineated in Section 5.5.1, is subject to multiple levels of validation.  
 3901 The validation encompasses not only the global fit across all analytical domains but also  
 3902 channel-specific fits for both  $\tau_{\text{had}}\tau_{\text{had}}$  and  $\tau_{\text{lep}}\tau_{\text{had}}$  modes. For the validation exercises, fits are  
 3903 executed on both Asimov datasets as well as actual experimental data. When conducting the  
 3904 fit on the latter, the signal strength corresponding to the signal hypothesis is constrained to  
 3905 zero.

3906 Furthermore, during the data fitting stage, specific NPs, particularly those pertaining to  
 3907 the signal as well as those background NPs exhibiting high correlation with the signal, are  
 3908 omitted from the results display.

### 3909 6.8.1 Fits

#### 3910 6.8.1.1 CR-Only Fit

3911 In the analysis, a crucial step is the validation of the  $Z$ +HF background model in the  
 3912 CR. The default fit configuration includes floating normalisation factors for  $Z$ +HF and  $t\bar{t}$   
 3913 processes. No explicit normalisation uncertainties from modelling are considered.

3914 Figure 6–25 illustrates the variations in the nuisance parameters (NPs) obtained from  
 3915 fitting the CR data. Notably, only a limited set of NPs are either pulled or constrained in  
 3916 the fit. Of particular significance is the constraining effect on the egamma energy resolution,  
 3917 which is a carry-over from the previous iteration of the analysis. Additionally, constraints on  
 3918 the  $Z$ +HF generator NP are imposed, owing to its substantial impact on the  $m_{ll}$  distribution.

3919 The fitted normalisation factors are as follows:

$$\text{NF}_{Z+\text{HF}} = 1.33 \pm 0.09,$$

$$\text{NF}_{t\bar{t}} = 0.96 \pm 0.04.$$

3920 A correlation of +72% between these factors is mainly driven by the FTag systematics. The  
 3921 post-fit distributions in  $m_{ll}$  and  $p_T^{\text{ll}}$  are shown in Figure 6–26.

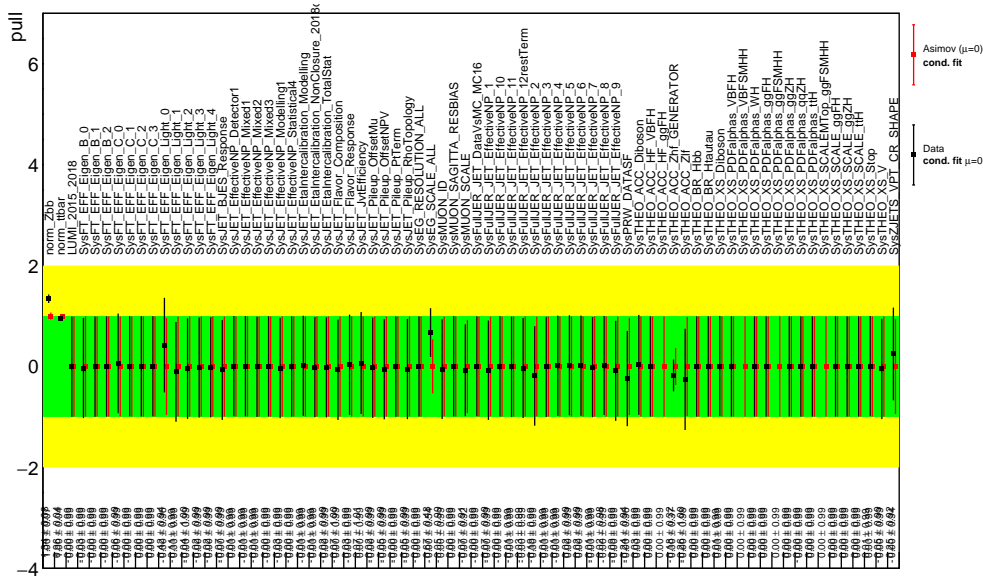


Figure 6–25 Post-fit values of the NPs included in the fit of the di-lepton invariant mass distribution in the CR.

3922 **6.8.2 Data-driven  $t\bar{t}$  Modelling**

3923 As a cross-check to minimize reliance on simulations, a data-driven approach for the  
 3924  $t\bar{t}$  background is performed. A dedicated CR, the  $e\mu$  CR, is defined Section 6.3.5.1. The  
 3925 normalisation factor for Z+HF in this setup is  $1.35 \pm 0.09$ , in agreement with the default  
 3926 setup. The post-fit results are presented in Figure 6–27.

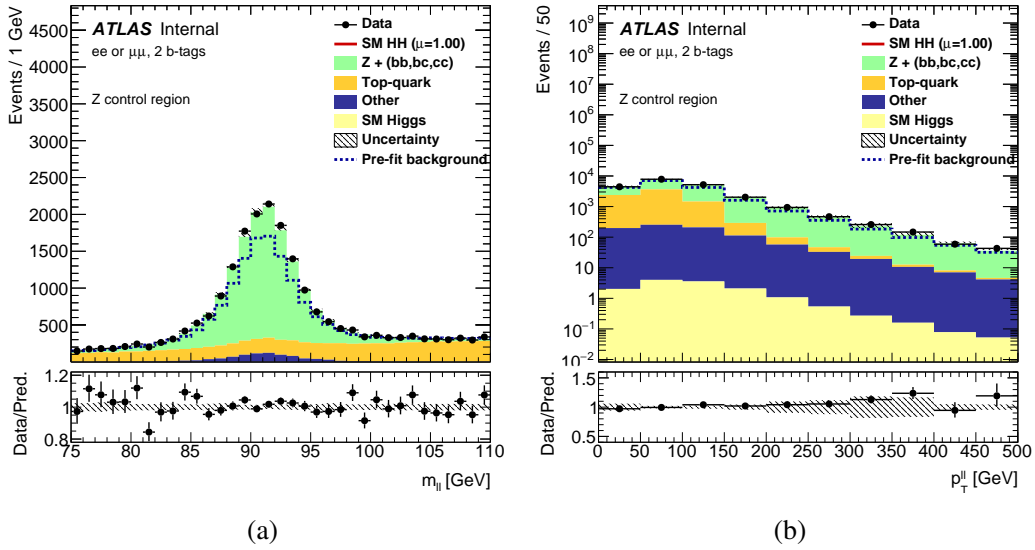


Figure 6–26 Post-fit modelling of the di-lepton invariant mass (left) and  $p_T$  (right) distribution in the CR. In both cases the NP extracted from the fit to  $m_{ll}$  are used.

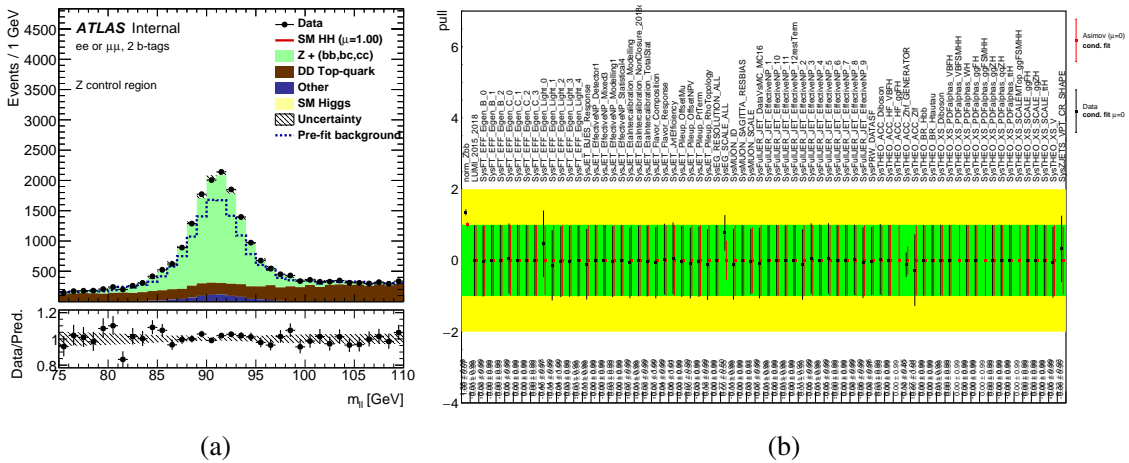


Figure 6–27 a Post-fit modelling of the di-lepton invariant mass distribution in the CR, when the  $t\bar{t}$  contribution is taken from a dedicated  $e\mu$  CR. b Post-fit values of the nuisance parameters included in the fit.

3927 **6.8.3**  $\tau_{had}\tau_{had}$  Fitting Results

3928 There are three distinct signal regions in the  $\tau_{had}\tau_{had}$  fit: low- $m_{HH}$  ggF, high- $m_{HH}$  ggF, and  
 3929 VBF, as well as the Z+ HF control region. In this fitting scheme, the normalisations for both  
 3930  $t\bar{t}$  and Z+HF backgrounds are represented as freely floating NPs. For the purpose of the fit,  
 3931 the signal strength is fixed at zero.

3932

Figure 6–28 depicts the ranking of the NPs based on the fit to the Asimov dataset.

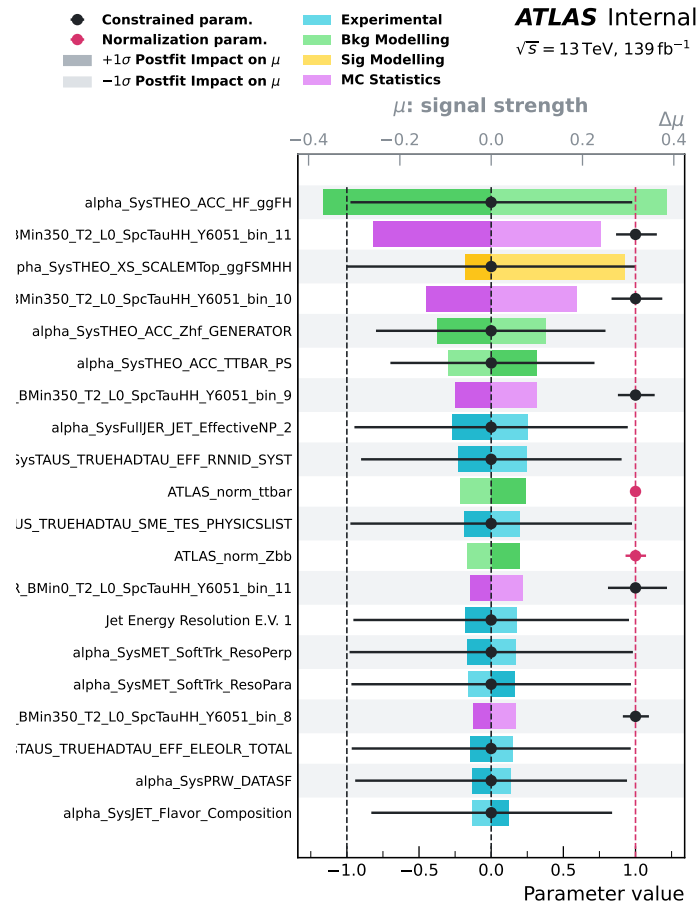


Figure 6–28 Nuisance parameter ranking in the  $\tau_{\text{had}}\tau_{\text{had}}$  fit using the Asimov dataset.

3933

The predominant uncertainties affecting the determination of signal strength are:

3934

1. Uncertainty on the single Higgs plus heavy flavour production.

3935

2. Scale uncertainty on the  $HH$  cross-section.

3936

3. Monte Carlo statistical uncertainties, particularly in the high BDT bins of the high  $m_{HH}$  region.

3937

3938

It is worth mentioning that the expected data statistical uncertainty on the combined signal strength in all 3 SRs is estimated to be 1.15, which is significantly larger than all these contributions.

3940

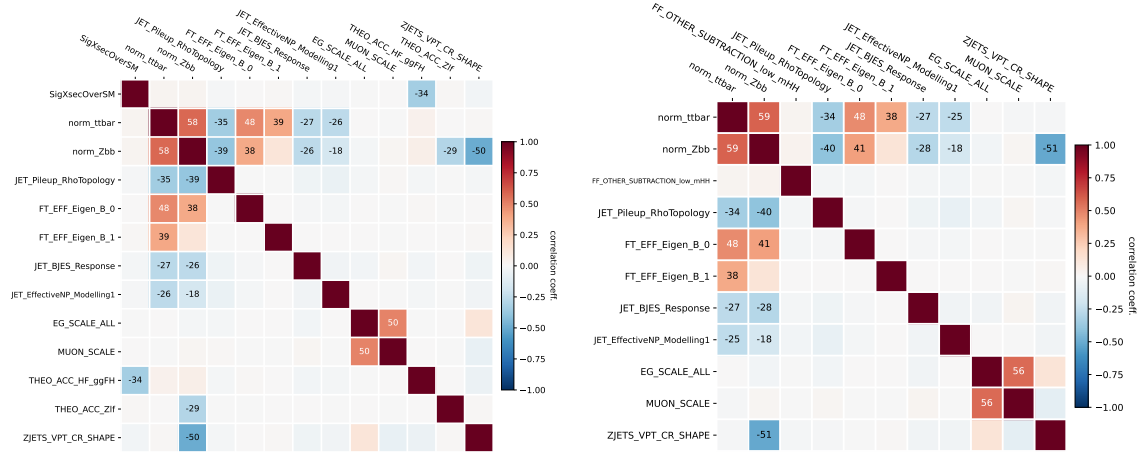
3941

Figure 6–29 portrays the correlations among the highly correlated<sup>1</sup> nuisance parameters as derived from the  $\tau_{\text{had}}\tau_{\text{had}}$  fit to both the Asimov dataset and the actual data. It is important to

3942

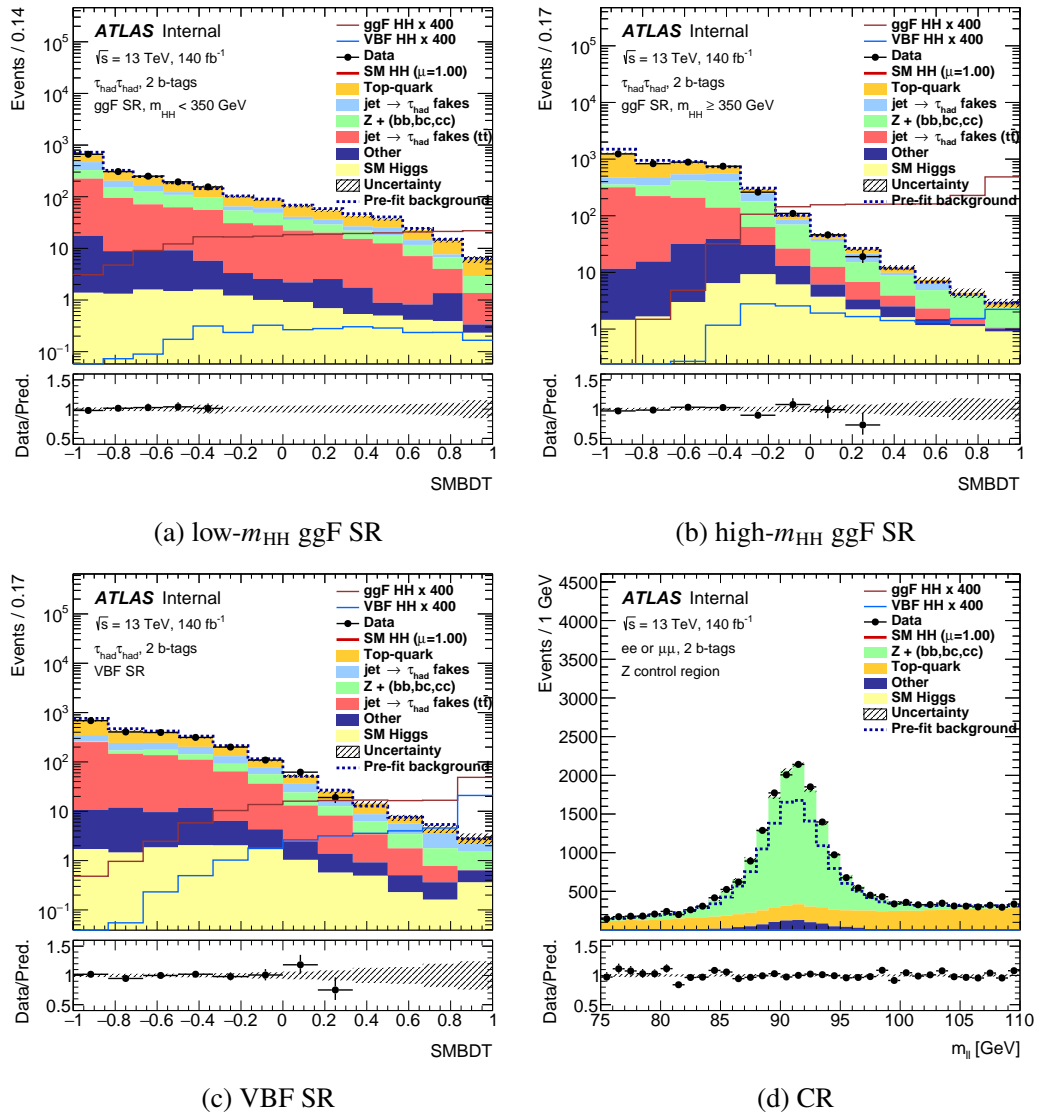
<sup>1</sup> Here, 'highly correlated' refers to NPs having a correlation greater than 25% with at least one other NP.

3943 note that the correlations concerning Monte Carlo (MC) statistical uncertainties are deliberately  
 3944 ately excluded from this representation. An analogous degree of NP correlation is noticeable  
 3945 between the two fit configurations, further solidifying the robustness of the model.



**Figure 6–29** Correlations among NPs in the  $\tau_{\text{had}}\tau_{\text{had}}$  SM fit to the Asimov dataset (left) and real data (right). MC statistical uncertainties are purposefully omitted.

3946 Finally, blinded post-fit distributions of the fitted variables in the 4 regions are shown in  
 3947 Figure 6–30. The choice of the binning is discussed in Section 6.7.2.

Figure 6–30 Post-fit BDT score distributions in the  $\tau_{had}\tau_{had}$  signal regions.3948 **6.8.4 Limits and scans**3949 **6.8.4.1  $\tau_{had}\tau_{had}$** 

3950 Figure 6–20 presents the estimated 95% CL upper limits on the  $HH$  signal strength, fur-  
 3951 ther subdivided into ggF and VBF production modes. These limits are derived from both  
 3952 one-dimensional and two-dimensional fits of  $\mu_{ggF}$  and  $\mu_{VBF}$ , where the other parameter is  
 3953 allowed to float when assessing one<sup>1</sup>. These assessments are conducted within the context

<sup>1</sup> When evaluating the limit on  $\mu_{ggF}$ , the normalisation factor for  $\mu_{VBF}$  is not constrained, and vice versa.

3954 of the  $\tau_{\text{had}}\tau_{\text{had}}$  decay channel, with calculations carried out under a background-only hypoth-  
 3955 esis. Subsequently, the two rightmost columns present the 95% CL expected intervals for  
 3956 the  $\kappa_\lambda$  and  $\kappa_{2V}$  coupling constants. These intervals are extracted based on the negative log-  
 3957 likelihoods (NLLs), computed as functions of  $\kappa_\lambda$  and  $\kappa_{2V}$ . It is pertinent to note that the NLL  
 3958 evaluations are performed under the standard model  $HH$  production assumption.

	95% CL Upper Limits on Signal Strength					95% CL Intervals	
	$\mu_{HH}$	$\mu_{\text{ggF}}^{\text{1D}}$	$\mu_{\text{VBF}}^{\text{1D}}$	$\mu_{\text{ggF}}^{\text{2D}}$	$\mu_{\text{VBF}}^{\text{2D}}$	$\kappa_\lambda$	$\kappa_{2V}$
Baseline w/o syst.	3.46	3.52	219	12.5	778	[-2.79, 9.58]	[-0.58, 2.71]
Baseline w/ syst.	4.2	4.25	260	18.0	1086	[-3.36, 10.3]	[-0.63, 2.76]
Updated w/o syst.	2.95	2.98	90	3.07	93	[-2.35, 8.94]	[-0.37, 2.51]
Updated w/ syst.	3.55	3.60	86	3.66	88	[-2.74, 9.40]	[-0.34, 2.51]

**Table 6–20 Summarized 95% CL expected upper boundaries on  $HH$  signal strength and intervals for  $\kappa_\lambda$  and  $\kappa_{2V}$ , categorized by production mode in the  $\tau_{\text{had}}\tau_{\text{had}}$  channel. All estimations with and without systematic uncertainties are included.**

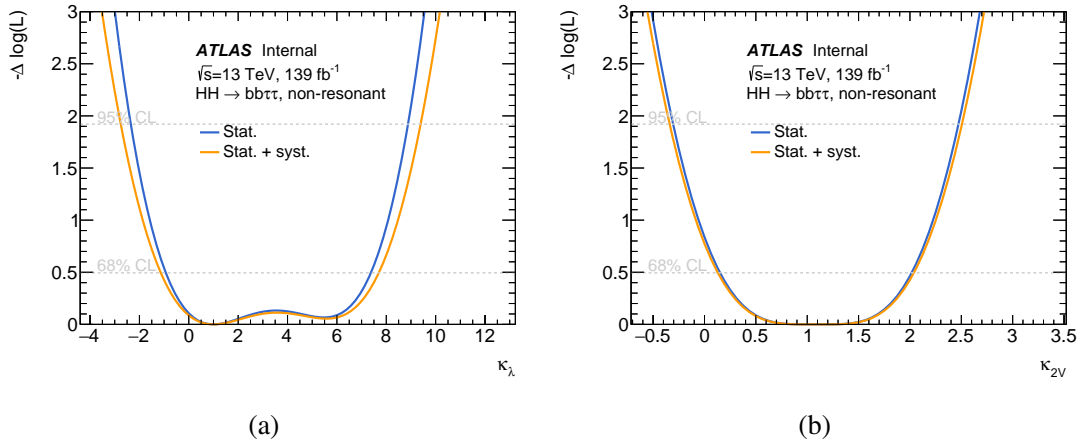


**Figure 6–31 Negative logarithm of the likelihood ratio comparing different  $\kappa_\lambda$  (a) and  $\kappa_{2V}$  (b) hypotheses to an Asimov dataset constructed under the SM hypothesis in the  $\tau_{\text{had}}\tau_{\text{had}}$  channel.**

3959 Pre-fit Asimov dataset-based limits are depicted both with and without the inclusion of  
 3960 systematic uncertainties for all relevant figures of merit. A comparative assessment is per-  
 3961 formed between the limits obtained from the baseline and updated analysis categories.

3962 Likelihood scans are conducted across all three individual analysis categories, as well as  
 3963 for an aggregated case that incorporates all categories. Figure 6–31 displays the likelihood

3964 scans for the coupling constants  $\kappa_\lambda$  and  $\kappa_{2V}$ . When evaluating the likelihood for a specific  
 3965 parameter, either  $\kappa_\lambda$  or  $\kappa_{2V}$ , all other coupling constants that influence both single-Higgs and  
 3966 di-Higgs production are maintained at their Standard Model values.

#### 3967 6.8.4.2 Combined $\tau_{\text{had}}\tau_{\text{had}}$ and $\tau_{\text{lep}}\tau_{\text{had}}$

3968 Tables 6–21 combine the consolidated anticipated upper constraints on signal strength  
 3969 and the confidence intervals for  $\kappa_\lambda$  and  $\kappa_{2V}$  parameters, as obtained from both the updated  
 3970 and baseline analyses. The baseline data are generated using a pre-fit Asimov dataset, serving  
 3971 as a robust benchmark for comparative evaluation. Moreover, the table includes metrics of  
 3972 relative enhancement over the baseline results.

3973 For the  $\tau_{\text{had}}\tau_{\text{had}}$  decay channel specifically, the composite analysis yields a 16% enhance-  
 3974 ment in the upper limit on HH production. Furthermore, the specialized region dedicated to  
 3975 VBF production facilitates the concurrent establishment of upper constraints on both VBF  
 3976 and ggF mechanisms.

	95% CL Upper Limits on Signal Strength					95% CL Intervals	
	$\mu_{HH}$	$\mu_{\text{ggF}}^{\text{1D}}$	$\mu_{\text{VBF}}^{\text{1D}}$	$\mu_{\text{ggF}}^{\text{2D}}$	$\mu_{\text{VBF}}^{\text{2D}}$	$\kappa_\lambda$	$\kappa_{2V}$
Baseline w/o syst.	2.84	2.89	189	9.24	572	[-2.35, 9.19]	[-0.42, 2.55]
Baseline w/ syst.	3.61	3.68	241	13.2	772	[-2.97, 10.1]	[-0.50, 2.63]
Legacy w/o syst.	2.41	2.44	61	2.49	62	[-1.97, 8.58]	[-0.14, 2.32]
Legacy w/ syst.	2.98	3.01	63	3.05	64	[-2.40, 9.11]	[-0.17, 2.34]
Rel. improvement w/o syst.	15%	16%	68%	73%	89%	8.6%	17.2%
Rel. improvement w/ syst.	17%	18%	74%	77%	92%	11.9%	19.8%

**Table 6–21 Expected 95% CL limits on HH signal strength and intervals for  $\kappa_\lambda$  and  $\kappa_{2V}$  from the combined fit. The statistics are reported both with and without systematic uncertainties.**

3977 In Figure 6–32, panels (a) and (b) depict the NLL scans against  $\kappa_\lambda$  and  $\kappa_{2V}$ , respectively.  
 3978 These scans employ a fit to the SM-based Asimov dataset and consider both the aggregated  
 3979 scenario as well as the isolated  $\tau_{\text{had}}\tau_{\text{had}}$  and  $\tau_{\text{lep}}\tau_{\text{had}}$  channels.

3980 The graphical data reinforce the  $\tau_{\text{had}}\tau_{\text{had}}$  channel as the main contributor to the analytic  
 3981 rigor. The inclusion of the  $\tau_{\text{lep}}\tau_{\text{had}}$  channel has a more pronounced impact on the  $\kappa_{2V}$  interval  
 3982 than on the  $\kappa_\lambda$  interval.

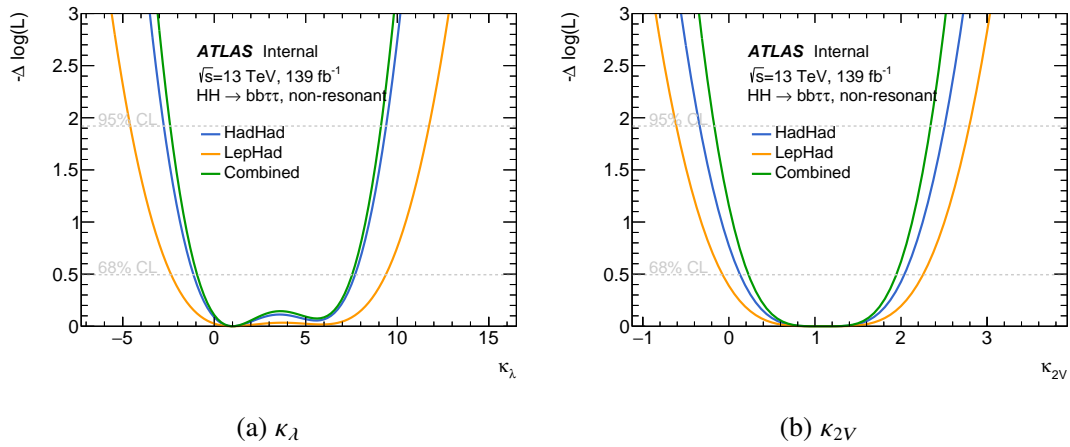


**Figure 6–32** Negative log-likelihood ratios assessing various  $\kappa_\lambda$  and  $\kappa_{2V}$  scenarios, in reference to an Asimov dataset created under the SM framework. Analyses incorporate both individual channels and their amalgamation. Solid lines intersecting dashed horizontal lines indicate 68% and 95% confidence levels.



## Chapter 7 Constraining the Higgs boson self-coupling from single- and double-Higgs production

### 7.1 Introduction

Following the discovery of the Higgs boson by the ATLAS and CMS collaborations<sup>[198-199]</sup>, the Large Hadron Collider (LHC)<sup>[200]</sup> has been tasked with the accurate measurement of its properties. This is done to confirm their alignment with the predictions of the Standard Model (SM)<sup>[201-204]</sup> or to reveal new physics phenomena. In the SM, the Higgs boson plays a crucial role in electroweak symmetry breaking<sup>[205-209]</sup>. This not only furnishes elementary particles with mass but also maintains perturbative unitarity. The trilinear Higgs boson self-coupling,  $\lambda_{\text{HHH}}$ , is dictated by the Higgs boson mass  $m_H$ <sup>[210]</sup> and the Fermi constant  $G_F$ <sup>[211]</sup>.

This work focuses on combining the three most sensitive double-Higgs decay channels:  $b\bar{b}\gamma\gamma$ ,  $b\bar{b}\tau^+\tau^-$ , and  $b\bar{b}b\bar{b}$ <sup>[177,212-213]</sup>. The data used for this analysis was collected by ATLAS from 2015–2018, corresponding to an integrated luminosity of 126–139 fb<sup>-1</sup> at  $\sqrt{s} = 13$  TeV. The coupling modifier  $\kappa_\lambda$  is utilized to report results, where  $\kappa_\lambda = \lambda_{\text{HHH}}/\lambda_{\text{HHH}}^{\text{SM}}$ .

The trilinear self-coupling also affects single-Higgs production via substantial next-to-leading-order (NLO) electroweak corrections<sup>[214-219]</sup>. Further constraints on  $\kappa_\lambda$  are drawn from combining recent ATLAS single-Higgs measurements<sup>[220]</sup> with the aforementioned double-Higgs results. This combination enables  $\kappa_\lambda$  testing without specific assumptions regarding other SM Higgs interactions.

Previous ATLAS combinations on partial Run 2 data have set an upper limit on SM  $HH$  production to be 6.9 (expected 10) times the SM prediction at a 95% CL<sup>[221]</sup>. The permitted range for  $\kappa_\lambda$  was found to be  $-5.0 \leq \kappa_\lambda \leq 12.0$ . The CMS collaboration has also published similar constraints using its complete Run 2 data, up to 138 fb<sup>-1</sup><sup>[222]</sup>.

### 7.2 Theoretical framework

The  $\kappa$  framework offers a methodology for scrutinizing the Standard Model (SM) in the Higgs sector, particularly in relation to single and double-Higgs production<sup>[223-224]</sup>. In this framework, the couplings of the Higgs boson to other SM particles at leading order (LO) are

4010 scaled by factors denoted as  $\kappa_m$ , defined as the ratio of the coupling between the particle  $m$   
4011 and the Higgs boson to its SM value. These scaling factors serve as a simplified yardstick  
4012 for comparing experimental results to SM predictions. The framework principally focuses  
4013 on four coupling modifiers for single-Higgs interactions:  $\kappa_t$ ,  $\kappa_b$ ,  $\kappa_\tau$ , and  $\kappa_V$ . A departure of  
4014  $\kappa$  from unity indicates the presence of Beyond Standard Model (BSM) physics<sup>[223]</sup>.

4015 Double-Higgs production serves as a direct probe into the Higgs boson self-coupling. In  
4016 the SM, the primary mechanism for double-Higgs production is gluon–gluon fusion, con-  
4017 tributing to over 90% of the  $pp \rightarrow HH$  cross-section<sup>[225]</sup>. The process is sensitive to two  
4018 main coupling modifiers:  $\kappa_\lambda$ , and  $\kappa_t$ , which scale different amplitudes in the process, as  
4019 shown in Figure 2–5. Deviations from the SM predictions can be parameterized in terms of  
4020 these coupling modifiers<sup>[224,226–228]</sup>.

4021 The  $pp \rightarrow HH$  process allows for sensitivity to the relative sign of  $\kappa_\lambda$  and the top-quark  
4022 couplings, mainly because of the destructive interference between amplitudes. The second  
4023 most abundant process, VBF, in Figure 2–6, is parameterized using a combination of the  $\kappa_\lambda$ ,  
4024  $\kappa_V$ , and  $\kappa_{2V}$  coupling modifiers<sup>[166]</sup>.

4025 While single-Higgs processes are generally not sensitive to the Higgs boson self-coupling  
4026 at leading order (LO), the complete next-to-leading order (NLO) electroweak (EW) correc-  
4027 tions incorporate  $\lambda_{HHH}$  through Higgs boson self-energy loops and additional diagrams, offer-  
4028 ing indirect constraints on  $\kappa_\lambda$ <sup>[214–215]</sup>. Concurrently, the Simplified Template Cross-Section  
4029 (STXS) framework offers a refined methodology for analyzing single-Higgs processes. It  
4030 employs fiducial phase space regions defined by kinematic variables, enabling the identifica-  
4031 tion of localized deviations from Standard Model predictions<sup>[229]</sup>. This facilitates mapping  
4032 back to constraints on  $\kappa_m$  parameters, enriching the utility of the  $\kappa$  framework. The STXS  
4033 approach categorizes bins by production mode, decay channel, and additional criteria such  
4034 as jet multiplicity and transverse momentum, thereby offering a more detailed understanding  
4035 of Higgs properties<sup>[230–231]</sup>.

4036 Any significant deviation in the measured  $\kappa_m$  from unity, or discrepancies in the cross-  
4037 sections of double-Higgs production processes from SM predictions, would be indicative of  
4038 new physics. Such deviations would warrant further investigation, possibly heralding the  
4039 discovery of particles or interactions not accounted for in the SM.

4040 The  $\kappa$  framework serves as a valuable tool for exploring the Higgs sector. By employ-

4041 ing coupling modifiers, it simplifies the analysis of both single and double-Higgs processes.  
 4042 While the framework has its limitations, such as the absence of considerations for new par-  
 4043 ticles in loop-level diagrams, it remains a robust methodology for initial explorations into  
 4044 BSM physics in the Higgs sector.

### 4045 7.3 Individual channel measurements

4046 This study incorporates both single-Higgs and di-Higgs channels, leveraging the full Run  
 4047 2 dataset acquired by the ATLAS experiment in  $pp$  collisions at 13 TeV during the 2015–  
 4048 2018 data-taking window<sup>[232-234]</sup>. Depending on the trigger selection, the available integrated  
 4049 luminosity spans 126 to 139 fb<sup>-1</sup>. Event selection employs a two-level trigger system<sup>[235]</sup>.

4050 For data reconstruction, analysis, and detector operations, an extensive software frame-  
 4051 work is utilized<sup>[236]</sup>. Although the current focus is on di-Higgs channels, single-Higgs analy-  
 4052 ses also contribute significantly to the study. A concise summary of each input analysis con-  
 4053 tributing to this combination is presented in Table 7–1. These analyses categorize selected  
 4054 events into distinct kinematic and topological regions. For a comprehensive understanding of  
 4055 the individual analyses, readers are referred to the respective references listed in Table 7–1.

**Table 7–1 Summary of datasets for each contributing analysis channel, with their corresponding integrated luminosities in fb<sup>-1</sup>. Detailed descriptions of each channel can be found in the last column’s references.**

Analysis channel	Integrated luminosity [fb <sup>-1</sup> ]	Ref.
$HH \rightarrow b\bar{b}\gamma\gamma$	139	[212]
$HH \rightarrow b\bar{b}\tau^+\tau^-$	139	[177]
$HH \rightarrow b\bar{b}b\bar{b}$	126	[213]
$H \rightarrow \gamma\gamma$	139	[237]
$H \rightarrow ZZ^* \rightarrow 4\ell$	139	[238]
$H \rightarrow \tau^+\tau^-$	139	[239]
$H \rightarrow WW^* \rightarrow e\nu\mu\nu$ (ggF, VBF)	139	[240]
$H \rightarrow b\bar{b}$ (VH)	139	[241]
$H \rightarrow b\bar{b}$ (VBF)	126	[242]
$H \rightarrow b\bar{b}$ ( $t\bar{t}H$ )	139	[243]

## 7.4 Statistical Methodology and Analysis Combination

The statistical methodology adheres to established procedures outlined in the previous works<sup>[244-245]</sup>. We define a global likelihood function,  $L(\vec{\alpha}, \vec{\theta})$ , where  $\vec{\alpha}$  constitutes the model's parameters of interest (POI) and  $\vec{\theta}$  encompasses nuisance parameters, inclusive of systematic uncertainties. These nuisance parameters are constrained by control regions or sidebands in the data.

The global likelihood is a multiplicative aggregation of individual analysis likelihoods, which themselves are products of likelihoods computed across distinct analysis categories. Results are presented through the profile-likelihood-ratio test statistic,  $\Lambda(\vec{\alpha}, \vec{\theta})$ . Confidence intervals at 68% and 95% CL are extracted utilizing asymptotic approximations<sup>[246]</sup>. Upper limits on the cross-section are specifically derived via the  $CL_s$  method<sup>[247]</sup>.

For hypothesis testing, Asimov datasets are generated<sup>[246]</sup>, locking nuisance parameters to data-derived values and fixing POIs to predefined hypothesis values.

Statistical independence is assumed for combining likelihoods. Event overlaps among individual analyses, previously established as negligible<sup>[220]</sup>, are verified to be below 0.1% for newly combined di-Higgs studies.

The origins and correlations of systematic uncertainties are elaborated in the cited references of Table 7–1. Additional cross-correlations among di-Higgs and single-Higgs systematic factors have been scrutinized and integrated as warranted. Data-condition related uncertainties, such as those tied to pile-up and luminosity, are deemed fully correlated. Methodological differences in experimental uncertainties led to the treatment of some as uncorrelated.

A sensitivity study was undertaken to assess the impact of correlation assumptions on the derived exclusion limits. The discrepancy between correlated and uncorrelated treatments is found to be less than 2%.

For di-Higgs analyses, dominant uncertainties arise from data-based background estimations, largely uncorrelated with those in single-Higgs analyses. Altering correlation assumptions yields a marginal influence, with the exception being the  $pp \rightarrow HH$  cross-section theoretical uncertainties, where correlation relaxes signal strength constraints by 7%.

4085 **7.5 Di-Higgs Combined Results**

4086 **7.5.1 Global signal strength**

4087 In this work<sup>[248]</sup>, we combine the analyses focusing on the decay channels  $b\bar{b}b\bar{b}$ ,  $b\bar{b}\tau^+\tau^-$ ,  
 4088 and  $b\bar{b}\gamma\gamma$  as cited in Table 7–1. The aim is to extract constraints on the signal strength param-  
 4089 eter  $\mu_{HH}$ , defined as the observed over expected double-Higgs production cross-section, with  
 4090 particular emphasis on the ggF and VBF mechanisms. The standard model (SM) prediction  
 4091 for this cross-section is 32.7 fb<sup>[225]</sup>.

4092 The aggregate analysis furnishes an observed 95% confidence level (CL) upper bound  
 4093 of  $\mu_{HH} = 2.4$ . In the SM context, the expected 95% CL upper limits are calculated to be  
 4094 2.9 and 4.0, assuming no signal and the presence of an SM-compatible signal, respectively.  
 4095 These results are visually represented in Figure 7–1. A best-fit signal strength value of  $\mu_{HH} =$   
 4096  $-0.7 \pm 1.3$  was attained, commensurate with the SM prediction, yielding a  $p$ -value of 0.2.

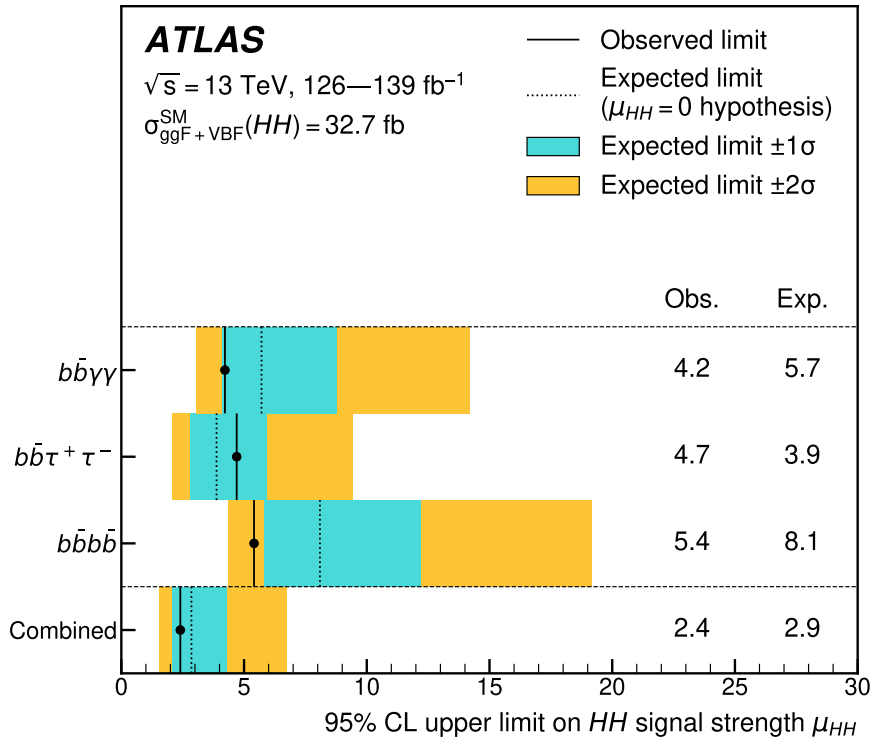


**Figure 7–1 Illustration of the observed and expected 95% CL upper bounds on the signal strength  $\mu_{HH}$  for the considered decay channels and their statistical amalgamation. The SM prediction assumes  $m_H = 125.09 \text{ GeV}$ .**

4097 Further, a stringent 95% CL upper limit on the total double-Higgs production (ggF and

4098 VBF only) cross-section of 73 fb was established, in contrast to an expected limit of 85 fb  
 4099 under the no-signal hypothesis.

## 4100 7.5.2 Constraints on Higgs self-coupling

4101 The analysis that combines different decay channels gives the constraints on the self-  
 4102 coupling  $\kappa_\lambda$  and the quartic coupling  $\kappa_{2V}$  of the Higgs boson.

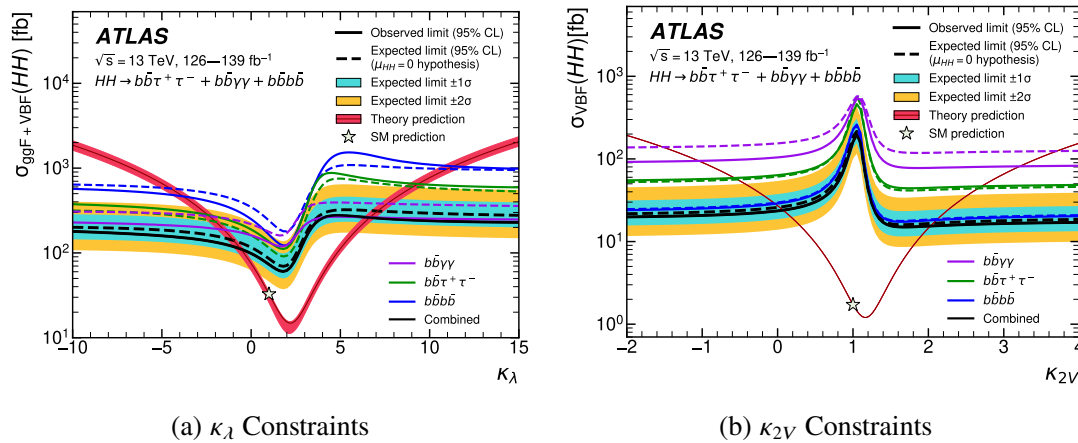


Figure 7–2 95% CL constraints on  $\kappa_\lambda$  and  $\kappa_{2V}$  from the combined analysis. The red lines indicate the theory constraints, while the solid lines represent observed limits.

4103 For the Higgs boson self-coupling  $\kappa_\lambda$ , the 95% confidence level observed constraints are  
 4104  $-0.6 < \kappa_\lambda < 6.6$ . Under the assumption of the Standard Model, the expected constraints are  
 4105  $-2.1 < \kappa_\lambda < 7.8$ . These limits offer significant insights into the non-linear structure of the  
 4106 Higgs potential and serve as a crucial test for the Standard Model.

4107 For the quartic coupling constant  $\kappa_{2V}$ , which relates to the  $HHVV$  interactions, the ob-  
 4108 served limits at a 95% confidence level are  $0.1 < \kappa_{2V} < 2.0$ . The expected limits are  
 4109  $0.0 < \kappa_{2V} < 2.1$  under the Standard Model hypothesis. These constraints are significant  
 4110 for understanding the quartic interactions involving the Higgs boson.

4111 The observed and expected limits are depicted in Figure 7–2, with the subfigures for  $\kappa_\lambda$   
 4112 and  $\kappa_{2V}$  shown in Figure 7–2a and Figure 7–2b, respectively.

## 4113 7.6 Single- and Di-Higgs Combined Results

4114 In this study, the combined single-Higgs and double-Higgs analyses offer enhanced con-  
 4115 straints on the coupling modifier  $\kappa_\lambda$ , as detailed in Table 7–1. Leveraging statistical method-  
 4116 ologies delineated in Section 7.2, multiple fitting procedures are conducted under varying  
 4117 assumptions on the coupling modifiers.

4118 Figure 7–3 presents a thorough investigation into the test statistic  $-2 \ln \Lambda$ , plotted against  
 4119 the Higgs self-coupling modifier  $\kappa_\lambda$ . Two distinct scenarios are examined: observed data and  
 4120 projected or Asimov data. Figure 7–3a depicts the observed  $-2 \ln \Lambda$  values for both single-  
 4121 Higgs and double-Higgs analyses, color-coded in blue and red respectively. Their combined  
 4122 results are shown in black. In addition, a general model allowing for free-floating  $\kappa_t$ ,  $\kappa_b$ ,  
 4123  $\kappa_V$ , and  $\kappa_\tau$  is represented by the green curve. Figure 7–3b mirrors this structure but uses the  
 4124 expected or Asimov data. This figure serves as a cornerstone for the constraint evaluation on  
 4125  $\kappa_\lambda$ , facilitating an intercomparison among various scenarios and assumptions.

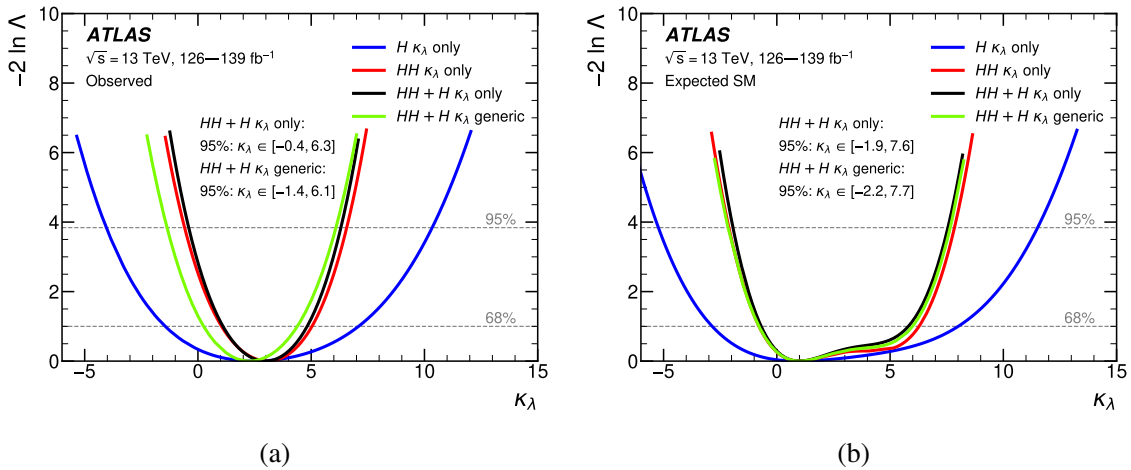
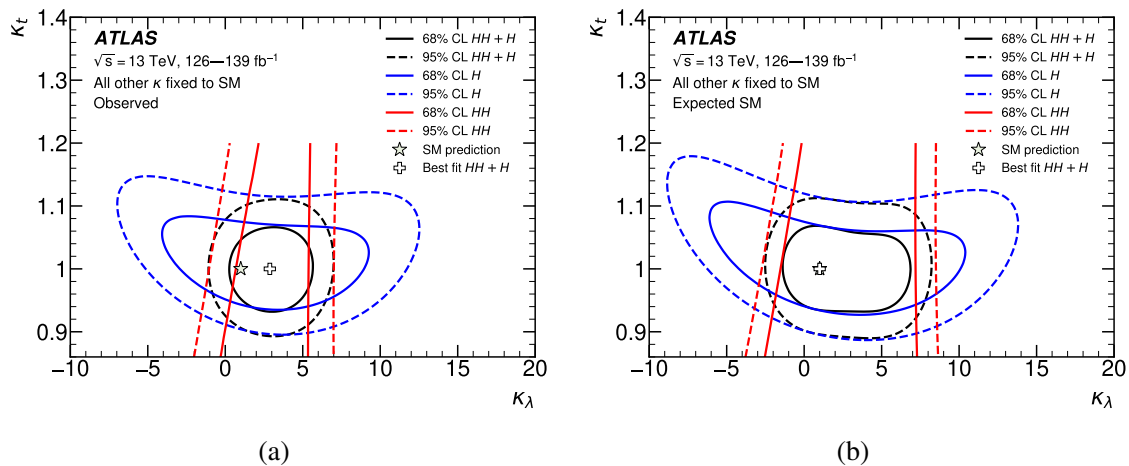


Figure 7–3 Observed (a) and projected (b) test statistics in terms of  $\kappa_\lambda$ .

4126 One of the advantages of integrating the single-Higgs analyses into the overall fit is the  
 4127 additional flexibility it provides in relaxing certain coupling assumptions without substan-  
 4128 tially compromising the robustness of our constraints. Specifically, the assumption on the  
 4129 Higgs boson to top-quark coupling modifier,  $\kappa_t$ , can be considerably relaxed. Thanks to the  
 4130 robust boundaries set by single-Higgs measurements, the constraints on  $\kappa_\lambda$  are hardly affected  
 4131 when the value of  $\kappa_t$  is allowed to float freely, a claim substantiated by the data presented in  
 4132 Table 7–2.

4133 Against this backdrop, Figure 7–4 serves as a critical asset for understanding the rela-  
 4134 tionship between  $\kappa_\lambda$  and  $\kappa_t$ . The figure comprises two sub-figures: Figure 7–4a employs  
 4135 observed data, and Figure 7–4b is constructed using expected, or Asimov, data. Both sub-  
 4136 figures feature 68% and 95% confidence level contours, marked by solid and dashed lines  
 4137 respectively. In Figure 7–4a, constraints solely based on single-Higgs analyses are denoted  
 4138 by blue contours, whereas those emerging from double-Higgs analyses are depicted in red.  
 4139 The black contours represent the synthesized outcome of both these analyses. Importantly,  
 4140 red contours are restricted to  $\kappa_t$  values below 1.2. Figure 7–4b adopts a similar coloring  
 4141 scheme but relies on Asimov data to form its contours.

4142 Overall, the figures demonstrate that when  $\kappa_t$  is allowed to float, the combined single-  
 4143 and double-Higgs analyses still manage to provide nearly as stringent constraints on  $\kappa_\lambda$  as  
 4144 when  $\kappa_t$  is fixed, affirming the efficacy of the integrated analytical approach.



**Figure 7–4 Constraints in the  $\kappa_\lambda$ – $\kappa_t$  parameter space.**

4145 Finally, Table 7–2 provides a rigorous, multi-faceted summary of the constraints on the  
 4146 coupling modifier  $\kappa_\lambda$ . The table covers scenarios ranging from isolated double-Higgs ( $HH$ )  
 4147 and single-Higgs ( $H$ ) combinations to increasingly inclusive fits where additional coupling  
 4148 modifiers are allowed to float. The most generic model is the least restrictive, allowing  $\kappa_\lambda$ ,  
 4149  $\kappa_t$ ,  $\kappa_b$ ,  $\kappa_\tau$ , and  $\kappa_V$  to float, while fixing  $\kappa_{2V}$  to unity due to the absence of a comprehensive  
 4150 parameterization for single-Higgs NLO EW corrections as a function of this modifier. In  
 4151 this most generic fit, we observe an exclusion of  $-1.4 < \kappa_\lambda < 6.1$  at the 95% confidence  
 4152 level, closely aligned with the expected exclusion of  $-2.2 < \kappa_\lambda < 7.7$ . These findings cor-

4153 corroborate that all other coupling modifiers agree with the Standard Model predictions within  
 4154 uncertainties. Notably, the sensitivity of the results to  $\kappa_{2V}$  is minor; a separate check revealed  
 4155 that allowing  $\kappa_{2V}$  to float only weakens the observed constraints on  $\kappa_\lambda$  by less than 5%. This  
 4156 manifests the robustness of our analytical framework even when extended to accommodate  
 4157 more free parameters.

Combination assumption	Obs. 95% CL	Exp. 95% CL	Obs. value $^{+1\sigma}_{-1\sigma}$
<i>HH</i> combination	$-0.6 < \kappa_\lambda < 6.6$	$-2.1 < \kappa_\lambda < 7.8$	$\kappa_\lambda = 3.1^{+1.9}_{-2.0}$
Single- <i>H</i> combination	$-4.0 < \kappa_\lambda < 10.3$	$-5.2 < \kappa_\lambda < 11.5$	$\kappa_\lambda = 2.5^{+4.6}_{-3.9}$
<i>HH+H</i> combination	$-0.4 < \kappa_\lambda < 6.3$	$-1.9 < \kappa_\lambda < 7.6$	$\kappa_\lambda = 3.0^{+1.8}_{-1.9}$
<i>HH+H</i> combination, $\kappa_t$ floating	$-0.4 < \kappa_\lambda < 6.3$	$-1.9 < \kappa_\lambda < 7.6$	$\kappa_\lambda = 3.0^{+1.8}_{-1.9}$
<i>HH+H</i> combination, $\kappa_t$ , $\kappa_b$ , $\kappa_\tau$ , and $\kappa_V$ floating	$-1.4 < \kappa_\lambda < 6.1$	$-2.2 < \kappa_\lambda < 7.7$	$\kappa_\lambda = 2.3^{+2.1}_{-2.0}$

**Table 7–2 Comprehensive summary of  $\kappa_\lambda$  constraints.**



## Chapter 8 Search for Long-Lived Particle with the Future Lepton Collider

### 8.1 Introduction

As introduced in Section 2.4, LLPs can be a potential probe for new physics beyond the Standard Model.

#### 8.1.1 Methods and Subsystems for LLP Detection in Collider Experiments

Collider-based searches for LLPs can be broadly classified into direct and indirect detection methods. In direct detection, the LLP interacts directly with the detector subsystems, whereas indirect detection involves the reconstruction of the LLP's decay into SM particles. A typical collider detector consists of several main subsystems: the inner detector (ID), electromagnetic calorimeter (ECAL), and hadronic calorimeter (HCAL), along with specialized systems for muon tracking (Muon Spectrometer). These subsystems work in tandem to measure various particle properties such as charge, momentum, and energy. It is crucial to note that while these subsystems are optimized for detecting SM particles, they also provide avenues for LLP detection.

#### 8.1.2 Challenges and Considerations in LLP Detection

LLP detection poses unique challenges compared to SM particles. First, the efficiency of LLP detection decreases as the displacement of the LLP from the interaction point increases. Second, traditional tracking algorithms may not adequately capture LLPs, leading to missed or irregular tracks. Nonetheless, the versatility of collider detectors, when adjusted for these specific challenges, makes them powerful tools for LLP searches. In particular, careful consideration must be given to the differences in reconstruction techniques for prompt and displaced particles.

While LLPs may themselves escape detection due to their long lifetimes, they often yield displaced vertices upon decay, creating anomalous tracks in the inner detector or atypical energy deposits in calorimeters. In the case of LLP decays in the muon system, specialized tracks distinct from typical muon signatures may emerge. These atypical features, col-

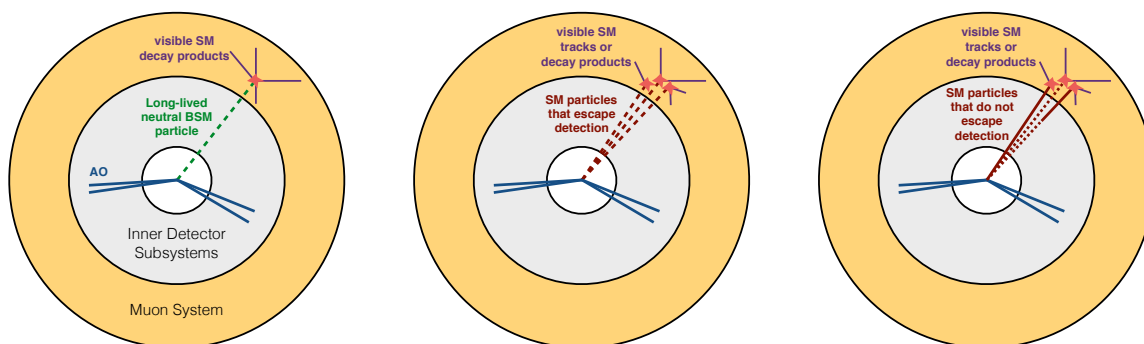


Figure 8–1 The schematic representation of LLPs' decaying process in the detector.

4185 lectively termed as Associated Objects (AOs), serve as key markers for LLP identification.  
 4186 However, LLP searches are complicated by a variety of Standard Model backgrounds. For  
 4187 instance, punch-through jets could mimic the energy deposit pattern of an LLP in calorime-  
 4188 ters. Similarly, bremsstrahlung from high-energy muons can create misleading signatures.  
 4189 Furthermore, some heavy flavor hadrons have lifetimes that could lead to displaced vertices,  
 4190 thus contributing to the background. These backgrounds necessitate rigorous data analysis  
 4191 techniques to discern genuine LLP signatures. A schematic representation of LLPs' decaying  
 4192 process in the detector is shown in Figure 8–1.

### 4193 8.1.3 Signatures of Neutral Long-Lived Particles

4194 The focus of this study is solely on neutral LLPs. Given their neutral charge, these par-  
 4195 ticles do not exhibit some of the signals commonly associated with charged LLPs, such as  
 4196 anomalous tracks in the inner detector or in the muon system. Instead, neutral LLPs are typi-  
 4197 cally identified through their decay products. The following paragraphs describe the various  
 4198 signatures of neutral LLPs in collider experiments.

#### 4199 8.1.3.1 Time-Delayed Detector Responses

4200 A neutral LLP traversing the detector at reduced velocity compared to SM particles ex-  
 4201 hibits time-delayed signals in various subsystems, such as calorimeters and Muon Spectrom-  
 4202 eters (MS). This delayed arrival serves as a unique identifying feature. Precise timing reso-  
 4203 lutions on the order of 1 ns, along with the detector's dimensions, allow for accurate speed  
 4204 measurements. These measurements, in combination with momentum data, facilitate mass  
 4205 determination for the neutral LLP. Unlike SM particles with identical momenta (almost at

4206 the speed of light), heavy, neutral LLPs take an extended period to traverse from the point of  
4207 production to the detection subsystems. The timing disparity<sup>[249]</sup>,  $\Delta t$ , can be quantified as

$$\Delta t = t_{\text{hit}} - \frac{L_{\text{SM}}}{c}, \quad (8-1)$$

4208 where  $t_{\text{hit}}$  is the timestamp of the detector hit,  $L_{\text{SM}}$  represents the distance from the primary  
4209 vertex to the point of detection, and  $c$  is the speed of light. For neutral LLPs,  $\Delta t$  exhibits a  
4210 distribution shifted significantly towards positive values, whereas for SM particles, it clusters  
4211 around zero.

### 4212 8.1.3.2 Non-Prompt Track Signatures

4213 Tracks originating from neutral LLP decays often deviate considerably from the beam  
4214 spot, typically characterized by the transverse impact parameter  $d_0$ . Accounting for detector  
4215 uncertainties, a large  $d_0/\sigma_{d_0}$  ratio is indicative of a displaced track. Due to data and compu-  
4216 tational resource constraints, tracks with large  $d_0$  or  $z_0$  values are not typically reconstructed  
4217 by default algorithms. Specialized reconstruction methods have emerged to address these  
4218 challenges.

### 4219 8.1.3.3 Identifying Displaced Vertices

4220 When multiple tracks from a neutral LLP decay are detected, they often converge at a dis-  
4221 placed vertex (DV). The DV's position and its covariance matrix can be determined through  
4222 vertex-fitting algorithms. This vertex distance is generally more accurate than  $d_0$ , and vari-  
4223 ous kinematic variables can further distinguish it from background. As analysis techniques  
4224 mature, rejection of background vertices near dense material becomes increasingly effective.

### 4225 8.1.3.4 Signatures in Calorimeters

4226 While the Inner Detector (ID) is usually limited to small spatial measurements, calorime-  
4227 ters extend the search to larger distances. Longitudinal shower shapes and energy deposition  
4228 ratios between the Electromagnetic Calorimeter (ECAL) and Hadronic Calorimeter (HCAL)  
4229 can offer insights into neutral LLP decays occurring within the calorimeter volume. These  
4230 features are notably distinct from standard SM jets and thus serve as valuable markers for  
4231 neutral LLPs.

### 4232 8.1.3.5 Composite Detection Methods

4233 While individual signatures are informative, their combined use can enhance the sensi-  
4234 tivity and robustness of neutral LLP searches. Correlations between different subsystems  
4235 provide multiple, uncorrelated handles for background rejection. It's crucial to note that the  
4236 standard reconstruction methods may introduce biases and additional systematic uncertain-  
4237 ties when applied to displaced objects.

### 4238 8.1.3.6 LLP Detection at LHC and Future Lepton Colliders

4239 There are many existing studies on LLPs performed using data from the ATLAS<sup>[250]</sup> and  
4240 CMS<sup>[251]</sup> experiments at the LHC. However, it's crucial to note that the sensitivity of these  
4241 experiments to LLPs is currently suboptimal. A primary limiting factor lies in the high level  
4242 of QCD background, colloquially referred to as *dirty backgrounds*. These pervasive back-  
4243 grounds impose a ceiling on the precision of exclusion limits set by these experiments. More-  
4244 over, the detector designs for ATLAS and CMS were not originally optimized to efficiently  
4245 search for LLP signatures. The constraints are more profound when one considers the in-  
4246 creasing luminosity of the LHC, exacerbating the challenge of identifying relatively weak  
4247 signals from LLPs amid an overwhelming amount of SM background noise.

4248 In contrast, future lepton colliders such as the FCC-ee<sup>[252]</sup> and the CEPC<sup>[253-254]</sup> present  
4249 more promising avenues for LLP detection. These colliders are expected to offer a substan-  
4250 tially cleaner environment with reduced QCD background, thus allowing for more stringent  
4251 exclusion limits for LLPs. The well-defined initial state and fewer sources of systematic  
4252 uncertainty enable these colliders to be highly effective in identifying the subtle signals as-  
4253 sociated with LLPs. Furthermore, the lower center-of-mass energy of these colliders allows  
4254 for the production of LLPs with lower masses, which are challenging to detect at the LHC.

4255 Despite the abundance of theoretical models proposing various LLPs, focusing on final  
4256 states presents a strategic approach to exploring LLPs in future lepton colliders. This fo-  
4257 cus is underpinned by the distinct signature of LLPs, setting them apart from SM particles.  
4258 Typical final states in this context would contain one or two visible LLPs accompanied by  
4259 easily-tagged SM particles, such as the Z-boson. One such production mechanism involves  
4260 a resonance or scalar particle, exemplified by the Higgs boson. Lepton colliders offer a high  
4261 occurrence rate for the  $e^+e^- \rightarrow ZH$  process, serving as a natural avenue for LLP production

4262 via the  $H \rightarrow XX$  decay channel, where  $X$  is the neutral LLP. Therefore, this study will con-  
 4263 centrate on the physics process denoted as  $e^+e^- \rightarrow ZH \rightarrow Z_{\text{products}} + XX$ , where  $X$  could  
 4264 either decay into invisible particles or SM jets/leptons. However, it should be noted that the  
 4265 methodology employed is extensible to any model yielding similar final states.

4266 To this end, this study will be primarily anchored in simulations and data from the CEPC.  
 4267 Leveraging the CEPC's advantageous features, such as its lower systematic uncertainties and  
 4268 cleaner background, we aim to provide a comprehensive analysis of LLP detection mecha-  
 4269 nisms and their underlying implications in a lepton-collider setting.

## 4270 8.2 Event Generation and Simulation at CEPC

### 4271 8.2.1 Overview of CEPC

4272 The CEPC<sup>[253-254]</sup> is engineered to function both as a Higgs boson factory with a center-  
 4273 of-mass energy ( $\sqrt{s}$ ) of 240 GeV and as a Z boson factory at  $\sqrt{s} = 91.2$  GeV. Additionally,  
 4274 it is capable of conducting threshold scans for W boson production around  $\sqrt{s} = 160$  GeV.  
 4275 Table 8–1 outlines the likely operational modes and the projected yields of H, W, and Z  
 4276 bosons.

Operation mode	Z factory	WW threshold	Higgs factory
$\sqrt{s}$ (GeV)	91.2	160	240
Run time (year)	2	1	7
Instantaneous luminosity ( $10^{34} \text{ cm}^{-2} \text{ s}^{-1}$ )	16 – 32	10	3
Integrated luminosity ( $\text{ab}^{-1}$ )	8 – 16	2.6	5.6
Higgs boson yield	-	-	$10^6$
W boson yield	-	$10^7$	$10^8$
Z boson yield	$10^{11} - 10^{12}$	$10^8$	$10^8$

**Table 8–1 Projected Operational Modes of CEPC and Corresponding Yields of Higgs, W, and Z Bosons; calculations Based on Two Interaction Points and Integrated Luminosity**

4277 During its seven-year tenure as a Higgs factory, the CEPC aims to generate roughly 1  
 4278 million Higgs bosons at two interaction points. Concurrently, the collider is expected to  
 4279 yield nearly 100 million W bosons and approximately 1 billion Z bosons. Such large data  
 4280 sets serve dual purposes: detector calibration and precision measurements in electroweak

4281 theory.

4282 When operating around the W boson threshold of  $\sqrt{s} = 160$  GeV, the CEPC is projected to  
 4283 produce about  $10^7$  W bosons within one year. In the Z boson factory mode, estimates suggest  
 4284 a production rate ranging from  $10^{11}$  to  $10^{12}$  Z bosons. These abundant samples facilitate  
 4285 highly precise measurements of a range of electroweak parameters.

#### 4286 8.2.1.1 Preliminary Detector Design

4287 The primary aim of the CEPC experiments is an exhaustive study of Higgs boson proper-  
 4288 ties. Consequently, detectors must exhibit high performance in identifying and reconstructing  
 4289 key physical entities such as charged leptons, photons, jets, and missing variables (energy and  
 4290 momentum). Flavor tagging of jets arising from b, c, or light quarks is particularly essential  
 4291 for isolating hadronic decay channels of the Higgs boson.

Tracking system	
Vertex detector	6 pixel layers
Silicon tracker	3 barrel layers, 6 forward disks on each side
Time projection chamber	220 radial readouts
Calorimetry	
ECAL	W/Si, $24X_0$ , $5 \times 5$ mm <sup>2</sup> cell with 30 layers
HCAL	Fe/RPC, $6\lambda$ , $10 \times 10$ mm <sup>2</sup> cell with 40 layers
Performance	
Track momentum resolution	$\Delta(1/p_T) \sim 2 \times 10^{-5} (1/\text{GeV})$
Impact parameter resolution	$5\mu\text{m} \oplus 10\mu\text{m} / [(p/\text{GeV})(\sin\theta)^{3/2}]$
ECAL energy resolution	$\Delta E/E \sim 16\% / \sqrt{E/\text{GeV}} \oplus 1\%$
HCAL energy resolution	$\Delta E/E \sim 60\% / \sqrt{E/\text{GeV}} \oplus 1\%$

**Table 8–2 Fundamental Specifications and Efficacy Metrics of the CEPC Detector System.**

4292 Inspired by the International Large Detector (ILD)<sup>[255]</sup>, the preliminary detector model  
 4293 for the CEPC is fundamentally aligned with a particle flow paradigm. This strategy is rooted  
 4294 in the principle of optimally employing individual sub-detectors to reconstruct visible final-  
 4295 state particles. The particle flow<sup>[256-258]</sup> approach thus provides a unified interpretation of a  
 4296 complete event and is especially beneficial for tagging complex objects like  $\tau$  leptons and

4297 jets.

4298 To achieve these goals, the CEPC features a low-material tracking system and high-  
4299 granularity calorimetry, encapsulated within a 3.5 Tesla magnetic field. Key components  
4300 include Silicon-based vertex and tracking detectors, a Time Projection Chamber (TPC), and  
4301 advanced calorimeters. The geometric configurations and performance metrics for the CEPC  
4302 detector are summarized in Table 8–2.

### 4303 8.2.2 Event generation and simulation

4304 Event generation and the ensuing simulation processes employ a gamut of specialized  
4305 software tools tailored to accurately model both the SM signal and background events. Specif-  
4306 ically, Whizard<sup>[259]</sup> is utilized for generating a comprehensive dataset comprising Higgs bo-  
4307 son signals alongside SM background events. Post-generation, these events are subjected to  
4308 simulation and reconstruction via MokkaC<sup>[260]</sup>, which serves as the CEPC’s official simula-  
4309 tion software and is constructed upon the framework initially designed for ILC studies<sup>[255]</sup>.

4310 Due to computational limitations, background event samples are occasionally subjected  
4311 to pre-selection based on lax generator-level criteria or are alternatively processed using ac-  
4312 celerated simulation tools. For a more granular simulation and reconstruction, Geant4<sup>[52-53]</sup>  
4313 is applied to all Higgs boson signal samples and a subset of leading background samples.  
4314 The remaining background samples employ a dedicated fast simulation tool where various  
4315 parameters such as detector acceptance, efficiency, and intrinsic resolution are suitably pa-  
4316 rameterized.

4317 Table 8–3 enumerates the expected event yields for various processes at an integrated  
4318 luminosity of  $5.6 \text{ ab}^{-1}$ . It should be noted that interference effects can manifest between  
4319 the same final states originating from different processes subsequent to the decay of W or  
4320 Z bosons (see the main text for details). The cross-section calculations for most processes  
4321 are carried out using the Whizard program<sup>[259]</sup>. For the Bhabha process specifically, cross-  
4322 section values are computed using the BABAYAGA event generator<sup>[261]</sup>, with constraints  
4323 imposed on the final-state particles ( $|\cos \theta| < 0.99$ ) and any resulting photons (if present) to  
4324 have  $E_\gamma > 0.1 \text{ GeV}$  and  $|\cos \theta_{e\pm\gamma}| < 0.99$ .

Process	Cross section	Events in 5.6 ab <sup>-1</sup>
Higgs boson production, cross section in fb		
$e^+e^- \rightarrow ZH$	204.7	$1.15 \times 10^6$
$e^+e^- \rightarrow \nu_e \bar{\nu}_e H$	6.85	$3.84 \times 10^4$
$e^+e^- \rightarrow e^+e^-H$	0.63	$3.53 \times 10^3$
Total	212.1	$1.19 \times 10^6$
Background processes, cross section in pb		
$e^+e^- \rightarrow e^+e^-(\gamma)$ (Bhabha)	850	$4.5 \times 10^9$
$e^+e^- \rightarrow q\bar{q}(\gamma)$	50.2	$2.8 \times 10^8$
$e^+e^- \rightarrow \mu^+\mu^-(\gamma)$ [or $\tau^+\tau^-(\gamma)$ ]	4.40	$2.5 \times 10^7$
$e^+e^- \rightarrow WW$	15.4	$8.6 \times 10^7$
$e^+e^- \rightarrow ZZ$	1.03	$5.8 \times 10^6$
$e^+e^- \rightarrow e^+e^-Z$	4.73	$2.7 \times 10^7$
$e^+e^- \rightarrow e^+\nu W^-/e^-\bar{\nu}W^+$	5.14	$2.9 \times 10^7$

Table 8–3 Cross-Section of Higgs and Background Processes at CEPC

### 4325 8.2.3 LLP Signal Production

4326 The primary mechanism for LLP signal production in this study is the Higgsstrahlung  
4327 process  $e^+e^- \rightarrow ZH$ , where the Z boson is allowed to decay inclusively—that is, into any of  
4328 its possible decay modes. Subsequently, the Higgs boson decays into a pair of LLPs  $H \rightarrow$   
4329  $X_1X_2$ . The specific channel under investigation assumes that  $X_1$  decays into a pair of quarks  
4330 ( $X_1 \rightarrow qq$ ) while  $X_2$  may either decay invisibly or similarly into quarks ( $X_2 \rightarrow qq$ ). Figure 8–  
4331 2 presents Feynman diagrams of two specific final state configurations, viz.,  $X_1 \rightarrow qq, X_2 \rightarrow$   
4332 invisible and  $X_1 \rightarrow qq, X_2 \rightarrow qq$ .

4333 To simulate these processes, we utilize MADGRAPH5\_AMC@NLO3.0<sup>[262]</sup> for event gen-  
4334 eration. Signal samples are generated for three distinct mass points of  $X_1$  and  $X_2$  which are  
4335 1 GeV, 10 GeV, 50 GeV, and for five distinct lifetimes of  $10^{-3}, 10^{-1}, 1, 10, 100$  ns. At each  
4336 point in this parameter space, a total of  $10^6$  events are generated for statistical robustness.

4337 Signal acceptance is dictated in the generator level by the unique characteristics of LLPs,  
4338 which decay according to exponential laws. Given the limitations of the CEPC detector,  
4339 which has a maximum detection range of approximately 6 meters, special attention must  
4340 be paid to the LLPs that decay within this confinement. To model this behavior accurately,  
4341 LLPs are generated with intrinsic lifetimes and then Lorentz-boosted based on their respec-

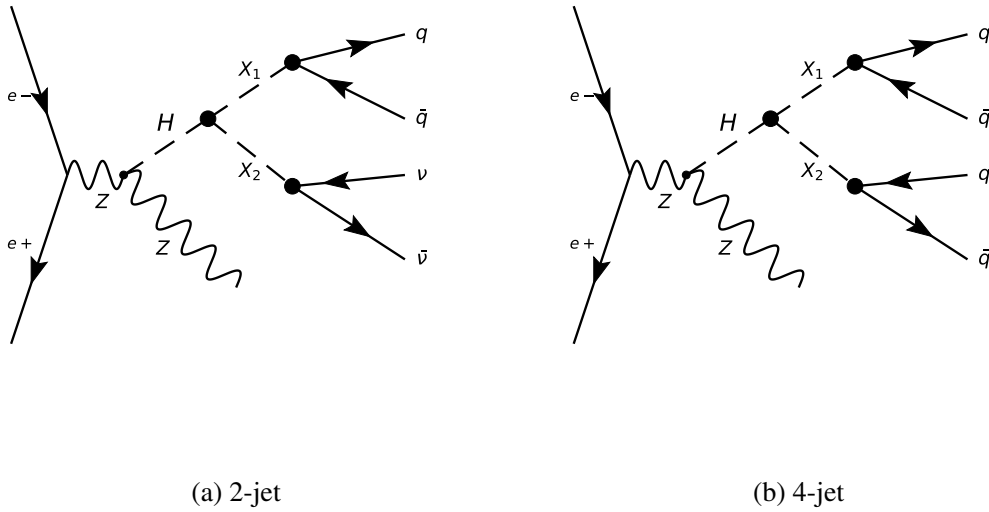


**Figure 8–2 Feynman diagrams illustrating LLP production via the Higgsstrahlung process.**

4342 tive masses and momenta. Subsequently, we apply stringent selection criteria to only include  
 4343 those LLPs whose decay vertices fall within the physical boundaries of the CEPC detector.  
 4344 These selected events are then tabulated for further analysis, as shown in Table 8–4.

Mass (GeV)	Lifetime (ns)				
	0.001	0.1	1	10	100
50	1.0	1.0	1.0	0.993	0.404
10	1.0	1.0	0.998	0.468	0.062
1	1.0	1.0	0.488	0.065	0.007

**Table 8–4 Signal Acceptance for Different Mass and Lifetime Parameters**

### 4345 8.3 Analysis Strategy

4346 The cornerstone of the analysis strategy in this study is the application of machine learn-  
 4347 ing techniques to directly analyze raw detector information. This approach deviates sub-  
 4348 stantially from conventional LLPs studies that primarily focus on analyzing reconstructed  
 4349 object-level data. The motivation behind this unique methodology arises from the complex-  
 4350 ities associated with the LLP signal topology. In different ranges of the LLP decay vertex,

4351 whether it is within the tracking detector, calorimeter, or muon spectrometer, the signal char-  
4352 acteristics and corresponding Standard Model background processes can vary significantly.  
4353 Traditional methods would necessitate categorizing multiple channels based on the LLP de-  
4354 cay length, and potentially developing new reconstruction algorithms for each sub-category,  
4355 thus complicating the analysis pipeline.

4356 In contrast, our approach aims to streamline the analysis by directly using raw detector  
4357 hits as input to classify LLP events from SM background events. This eliminates the need for  
4358 segregating the dataset into multiple sub-channels and simplifies the overall analysis proce-  
4359 dures. We utilize two machine learning algorithms, Convolutional Neural Networks (CNN)  
4360 and Graph Neural Networks (GNN), in parallel for cross-validation. Both algorithms re-  
4361 ceive identical inputs and produce comparable outputs, enabling a more robust assessment  
4362 of performance. Raw detector hits are first transformed into either image-like or graph-like  
4363 structures, which are then fed into the neural networks to generate a five-class score. This  
4364 preliminary classification is further refined using XGBoost<sup>[263]</sup>, which takes the predicted  
4365 score probabilities to categorize the possible event classes. A final discriminant variable is  
4366 computed, serving as the basis for the final statistical fitting of the data.

4367 The analysis strategy is organized as followed. Section 8.3.2 introduces an image-based  
4368 deep learning methodology using CNN. This section focuses on how event data is trans-  
4369 formed into image format and details the configuration of the CNN model. Section 8.3.3  
4370 explores the use of GNN for event classification. In this part, the procedure to construct  
4371 event graphs from raw calorimeter and tracker hits is elaborated, followed by the GNN net-  
4372 work configuration. In Section 8.3.4, we employ XGBoost, to fine-tune the event selection  
4373 process. Lastly, Section 8.3.5 offers an efficiency comparison between the CNN and GNN  
4374 methods. The efficacy of each approach is evaluated post-application of XGBoost, providing  
4375 an integrated perspective on the overall performance.

### 4376 **8.3.1 General Training Configuration**

4377 The training configuration primarily focuses on two aspects: background process deter-  
4378 mination and signal categorization, coupled with an evaluation strategy that ensures minimal  
4379 bias and optimal resource utilization.

## 4380 8.3.1.1 Background Processes:

4381 The distinct decay signature of LLPs allows for minimal interference with Standard Model  
4382 background processes. Nonetheless, some jet configurations could potentially resemble the  
4383 LLP signal, as shown in Figure 8–1. As a result, we identify the  $e^+e^- \rightarrow qq$  process, which  
4384 exhibits the highest branching ratio for jet-related final states, as our primary background.  
4385 This category is labeled the *2-fermion* background, and it now includes the SM  $ZH$  Higgs  
4386 process when it results in 2-fermion final states.

4387 In addition, we also consider other hadronic backgrounds featuring Z bosons in the final  
4388 state as secondary background sources. These include  $e^+e^- \rightarrow WW, ZZ \rightarrow$  jets, known as  
4389 the *4-fermion* backgrounds. The SM  $ZH$  Higgs process is also accounted for in this category  
4390 when it leads to 4-fermion final states.

## 4391 8.3.1.2 Signal Categorization:

4392 Our analysis strategy centers on a refined method of classifying signals, moving away  
4393 from the traditional emphasis on the types of particles in the final state. Rather than catego-  
4394 rizing events based on the number of jets in the final state (i.e., 2-jet or 4-jet), the analysis cen-  
4395 ters on the number of detectable Long-Lived Particles (DLLPs), referred to as 0/1/2–DLLP  
4396 categories. This shift in focus allows us to account for a multitude of scenarios influenced  
4397 by both the geometric constraints of the CEPC detector and the kinematic variables of the  
4398 LLPs.

4399 For example, in scenarios where  $X_1$  decays outside the detection range while  $X_2$  decays  
4400 into an invisible state, the event falls into the 0 – DLLP category, implying zero detectable  
4401 LLPs. Conversely, if  $X_1$  decays within the detection range and  $X_2$  either decays outside or  
4402 into an invisible state, the event belongs to the 1 – DLLP category. Finally, events where both  
4403  $X_1$  and  $X_2$  decay within the detection range and yield visible decay products, specifically into  
4404 jets, are classified under the 2 – DLLP category.

4405 These categories form the basis for subsequent machine learning model training, using  
4406 LLP kinematics and detector geometry. To establish a reliable model, the fraction of de-  
4407 tectable LLPs in 2-jet and 4-jet final states is carefully estimated. This quantification is  
4408 accomplished through truth-level information extracted from MC simulations. This MC-  
4409 derived fraction serves as an essential template during the final statistical fitting procedures,

4410 ensuring that our machine learning models are grounded in physically meaningful catego-  
4411 rizations.

### 4412 8.3.1.3 Training Schema

4413 Given the five designated categories (0/1/2 – DLLP for the signal and 2-fermion and  
4414 4-fermion for the background), the preprocessed data serve as the input to various machine  
4415 learning algorithms. Each algorithm produces a five-score array, where each score corre-  
4416 sponds to a particular category.

4417 Due to computational constraints and the exceedingly large number of background sam-  
4418 ples ( $10^8$ ), we employ a subset of the available data for training. Specifically, only 10%  
4419 of the total background samples are used. These background samples are sourced from the  
4420 official CEPC MC production, while the signal samples are generated in-house.

4421 To mitigate the introduction of biases and to ensure statistical rigor, a k-fold cross-validation  
4422 strategy is adopted. The k-fold distribution is 3-fold for CNN, 5-fold for GNN, and 6-fold  
4423 for XGBoost. This maintains orthogonality between the training, testing, and application  
4424 datasets.

4425 For the final evaluation stage, an unbiased application of the trained models is performed  
4426 on the complete dataset, which includes both the 10% subset used for training and the re-  
4427 maining 90%. This comprehensive evaluation ensures maximum statistical efficiency while  
4428 leveraging the limited computational resources effectively.

## 4429 8.3.2 Image-based Deep Learning Analysis (CNN)

### 4430 8.3.2.1 Event Image Construction

4431 We initially embarked on an investigation that uses CNN to analyze events recorded  
4432 by the CEPC detector. In this methodology, each captured event is converted into a two-  
4433 dimensional, two-channel image with dimensions  $R \times \phi = 200 \times 200$  pixels. Here,  $R$  signifies  
4434 the radial distance from the interaction point to the position of a digital hit (digi), while  $\phi$   
4435 denotes the azimuthal angle of the digi. Each event's raw digital hits are mapped into this  
4436 coordinate system to construct the image.

4437 The two channels serve distinct purposes: the E-channel is responsible for capturing en-  
4438 ergy deposition, and the T-channel records time differences defined in Equation 8–1. Specif-  
4439 ically, the E-channel aggregates the energy of all digital hits contained within each pixel. In

4440 contrast, the T-channel computes the maximum time difference  $\Delta t = t_{\text{digi}} - \frac{R_{\text{digi}}}{c}$  among raw  
 4441 hits with an energy deposition greater than 0.1 GeV, aiming to filter out electronic noise.

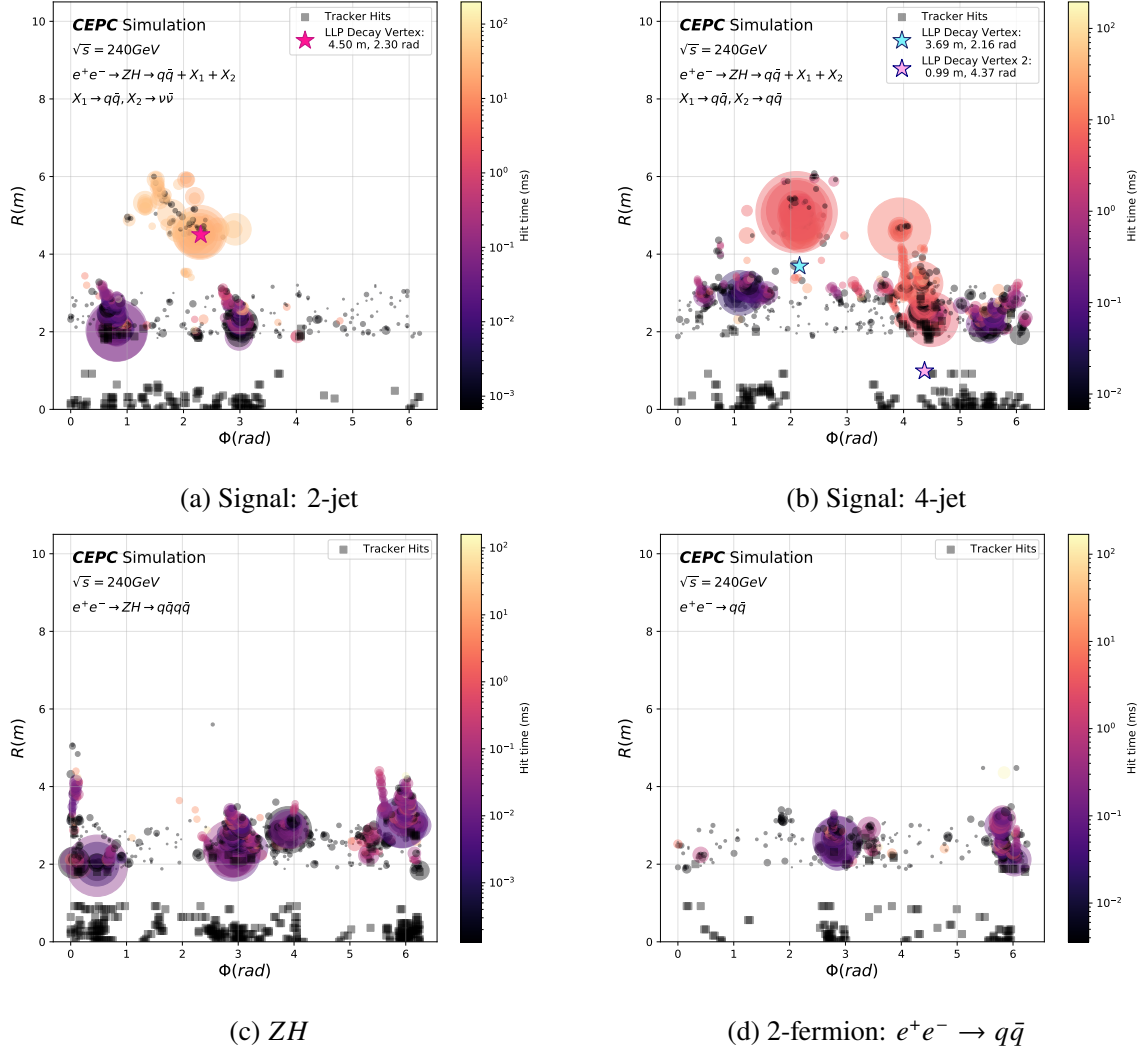
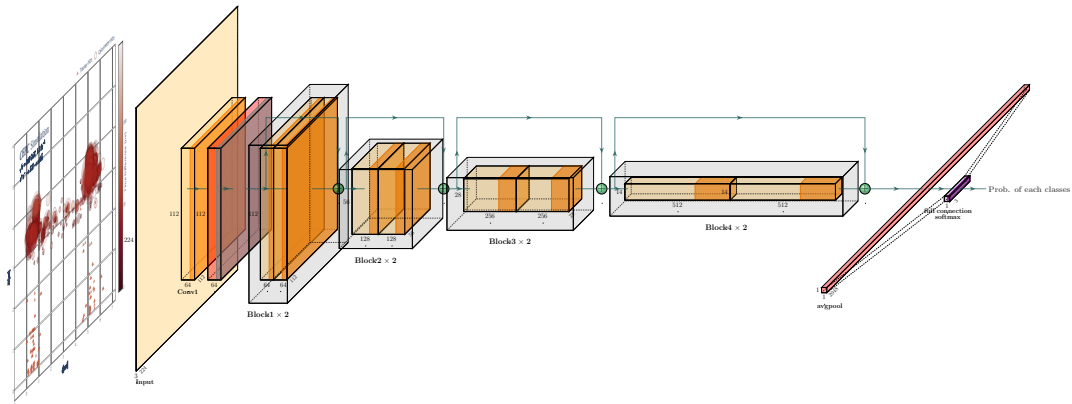


Figure 8-3 Illustration of image built from raw detector hits for four different processes.

4442 In Figure 8-3, four representative images are showcased, illustrating both signal and  
 4443 background events pertinent to two-jet and four-jet final states. In these images, three types  
 4444 of graphical symbols are employed for clarity: a star symbol marks the decay vertex of the  
 4445 LLP, serving as a reference point for the event topology, while circular symbols represent  
 4446 the hits as detected by the calorimeter and the muon spectrometer and square markers are the  
 4447 tracker hits. The size of each circle is proportional to the energy deposition, with a larger cir-  
 4448 cle indicating a greater amount of deposited energy. The color intensity of both the squares



**Figure 8–4 Illustration of the architecture of ResNet-18 based neural network.**

4449 and circles signifies the time of arrival, with darker hues corresponding to earlier times. This  
 4450 pixel-based representation proves effective in discriminating between signal and background  
 4451 events. Specifically, background events generally lack a displaced vertex and tend to show  
 4452 larger energy depositions in the inner detectors, distinguishing them from signal events.

### 4453 8.3.2.2 Network Configuration

4454 The choice of the appropriate CNN model for our analysis is far from trivial, particularly  
 4455 due to the unique LLP signatures and their displaced vertices. To this end, we employ a  
 4456 well-known CNN model, ResNet<sup>[264]</sup>, originally developed for the ImageNet Large Scale  
 4457 Visual Recognition Challenge (ILSVRC) in 2015. The architecture of the ResNet-18 model  
 4458 is detailed in Figure 8–4. ResNet offers the advantage of scalability and efficiency; it can be  
 4459 configured to operate both as a shallow network for simpler tasks and as a deep network for  
 4460 more complex tasks. This flexibility minimizes the need for extensive model modifications  
 4461 tailored to specific tasks.

4462 The learning rate is a crucial hyperparameter that necessitates careful tuning. For our  
 4463 LLP-specific tasks across all mass and lifetime regimes, we have observed rapid model con-  
 4464 vergence with a relatively low number of epochs ( $\approx 15$ ). This suggests that the learning rate  
 4465 can be kept relatively constant, although a task-specific learning rate schedule may further  
 4466 optimize the training process.

4467 The network’s raw output is further processed using the softmax function to generate a

4468 five-class prediction array, mathematically represented as follows:

$$\text{Softmax}(\text{Score}) = \frac{e^{\text{Score}_i}}{\sum_j e^{\text{Score}_j}}$$

4469 For this multi-class classification problem, we employ the cross-entropy loss function,  
4470 defined as:

$$\mathcal{L} = - \sum_i y_i \log(p_i)$$

4471 Where  $y_i$  is the true label and  $p_i$  is the predicted probability for class  $i$ .

### 4472 8.3.3 Graph-based Deep Learning Analysis (GNN)

#### 4473 8.3.3.1 Event Graph Construction

4474 To extend the predictive power and feature representation capabilities of our model, we  
4475 employ Graph Neural Networks (GNNs). These are particularly useful for capturing the  
4476 complex topological structures inherent in high-energy particle collision events.

4477 **Node Types and Edge Construction:** In a single collision event, we represent the raw  
4478 calorimeter and tracker hits as a heterogeneous graph, comprising two types of nodes: one for  
4479 calorimeter hits, referred to as *calorimeter-type nodes*, and the other for tracker hits, referred  
4480 to as *tracker-type nodes*. Within each type, all nodes are fully connected, meaning that every  
4481 node is directly connected to every other node of the same type.

4482 **Calorimeter-Type Node Formation:** For calorimeter-type nodes, a clustering algorithm  
4483 is employed. The most energetic calorimeter hit is identified within the event, and it serves  
4484 as a seed for the clustering process. This seed clusters together all neighboring hits that are  
4485 within a pre-defined radial distance  $R = 50$  mm. To control the quality of clustering, we  
4486 enforce two specific criteria:

- 4487 • Minimum number of neighboring hits in the cluster,  $N_{\text{neighbor}} \geq 3$ .
- 4488 • Minimum number of total hits for forming a valid cluster,  $N_{\text{cluster}} \geq 10$ .

4489 **Momentum Assignment to Calorimeter-Type Nodes:** Following the clustering, each calorimeter-  
4490 type node is assigned a four-momentum  $p^\mu$ . This momentum is defined as being parallel to  
4491 the node's position vector, with a magnitude determined by the energy of the calorimeter hit.

4492 **Tracker-Type Node Formation:** Tracker hits are organized into spatial blocks based on  
 4493 their  $R - \phi$  coordinates. Given computational considerations, the division is designed into  
 4494  $5 \times 6$  blocks. Within each block, tracker hits are aggregated into a tracker-type node, with the  
 4495 node's features being the average spatial position and the summed hit count within the block.

4496 **Feature Translation:** Both calorimeter and tracker features are then transformed into a  
 4497 unified graph-based representation, creating a feature-rich event-level description. The spe-  
 4498 cific definitions of the node and edge features are meticulously cataloged in Table 8–5.

Features	Variable	Definition
calorimeter type node $i$	$ x_i^\mu $	the space-time interval
	$ p_i^\mu $	the invariant mass
	$N_i$	the number of hits
	$\eta_i$	$\frac{1}{2} \ln \frac{1+\frac{p_z}{p}}{1-\frac{p_z}{p}}$
	$\phi_i$	$\arctan \frac{p_y}{p_x}$
	$R_i$	$\sqrt{\eta^2 + \phi^2}$
calorimeter type edge between node $i$ and $j$	$x_i^\mu x_{j\mu}, p_i^\mu p_{j\mu}, x_i^\mu p_{j\mu}, p_i^\mu x_{j\mu}$ $ x_i^\mu - x_j^\mu ,  p_i^\mu - p_j^\mu , \eta_i - \eta_j, \phi_i - \phi_j, R_i - R_j$	
tracker type node $i$	$ r $	euclidean distance
	$N_i$	the number of hits
	$\eta_i$	$\frac{1}{2} \ln \frac{1+\frac{z}{r}}{1-\frac{z}{r}}$
	$\phi_i$	$\arctan \frac{y}{x}$
	$R_i$	$\sqrt{\eta^2 + \phi^2}$
tracker type edge between node $i$ and $j$	$ r_i - r_j , r_i r_j, \eta_i - \eta_j, \phi_i - \phi_j, R_i - R_j$	

**Table 8–5 Node and edge features defined in the heterogenous graph.**

### 4499 8.3.3.2 Network Configuration

4500 To use the topological features of LLP events, we utilize a sophisticated GNN-based  
 4501 heterogeneous architecture, as illustrated in Figure 8–5.

4502 Initial node and edge features are embedded into a high-dimensional latent space. These  
 4503 embeddings serve as inputs to the Heterogeneous Detector Information Block (HDIB), which  
 4504 orchestrates message passing between calorimeter and tracker nodes.

4505 The HDIB comprises two Detector Information Blocks (DIBs) and two Multilayer Per-

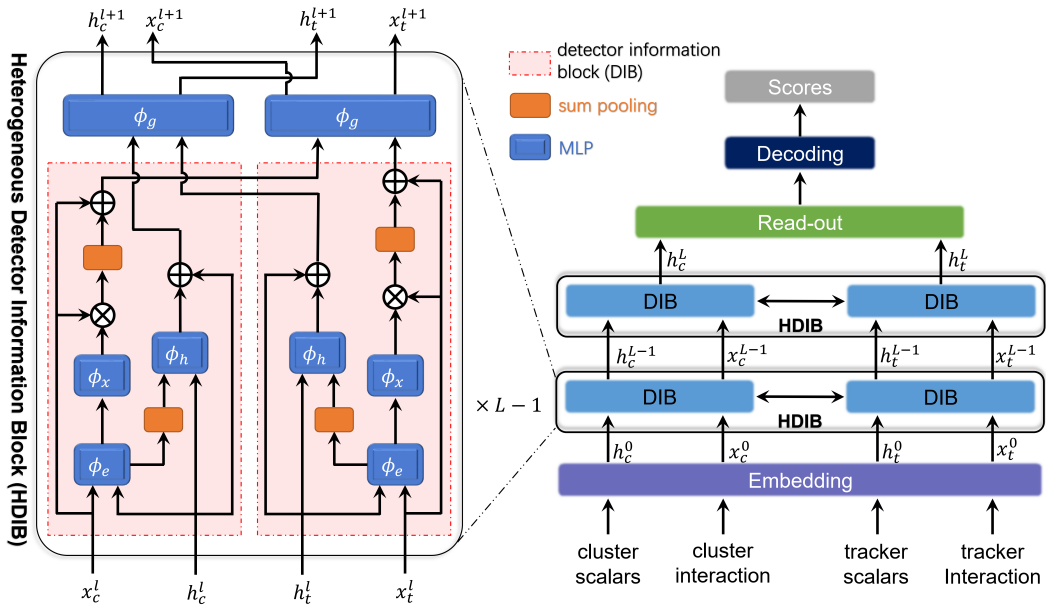


Figure 8-5 Illustration of the architecture of the GNN-based neural network.

4506 ceptrons (MLPs), designated as  $\phi_g$ . Each DIB focuses on processing the node and edge em-  
 4507 beddings of either tracker or calorimeter hits. Inspired by LorentzNet<sup>[265]</sup>, we have extended  
 4508 the DIB architecture to accommodate heterogeneous graphs.

4509 The DIB outputs serve as the latent spaces for the node features  $h^l$  and edge features  $x^l$  at  
 4510 each layer  $l$ . These are computed separately for tracker and calorimeter nodes as  $h_t^l$  and  $h_c^l$ ,  
 4511 respectively.

4512 Since tracker and calorimeter nodes are not directly connected in the heterogeneous  
 4513 graph, their latent spaces are concatenated and processed through a MLP  $\phi_g$ . The outputs of  
 4514  $\phi_g$  are reshaped to obtain the updated latent spaces  $h^{l+1}$  and  $x^{l+1}$ . This scheme facilitates the  
 4515 adaptive exchange of information between tracker and calorimeter nodes.

4516 Following  $L$  layers of HDIBs, the final node embeddings  $h^L$  are aggregated and fed into  
 4517 the decode layer to yield classification scores.

4518 **Training Configuration:**

- 4519 • **Hardware:** The model is trained on a cluster with 8 NVIDIA Tesla V100S PCIE 32  
 4520 GB GPUs.
- 4521 • **Batch Size:** Each GPU processes a batch size of 256 graphs.
- 4522 • **Learning Rate:** An initial learning rate of  $10^{-4}$  is employed.

- 4523 • **Dropout Rate:** A dropout rate of 0.1 is applied to mitigate overfitting.
- 4524 • **Optimizer:** Adam optimizer is used without weight decay.
- 4525 • **Epochs:** The network is trained for a total of 30 epochs, with validation performed at
- 4526 the end of each epoch.
- 4527 • **Model Selection:** The model exhibiting the minimum validation loss is chosen for
- 4528 application to the final test dataset.

### 4529 8.3.4 Event selection with XGBoost

4530 Due to the complexity of the feature space, particularly with five predicted class scores  
 4531 from the neural networks (CNN and GNN), direct rectangular cuts prove to be inefficient for  
 4532 event categorization. Thus, we opt to employ the gradient boosting framework XGBoost to  
 4533 refine the event selection process. The XGBoost model takes the five class-predicted scores  
 4534 as input features and outputs a final discriminant value.

4535 The XGBoost model is trained on three distinct signal categories, namely 0-DLLP, 1-  
 4536 DLLP, and 2-DLLP. The aim is to optimize the discriminant cut for each category such that  
 4537 the background contribution becomes negligible. Subsequently, the cut efficiency within  
 4538 each category essentially represents the signal efficiency in the absence of background con-  
 4539 tamination.

4540 In order to assess the signal efficiency tailored to distinct final states, such as the 2-jet and  
 4541 4-jet scenarios, the output from the XGBoost model is divided into regions. These regions  
 4542 are predicated upon the number of Detectable Long-Lived Particles (DLLPs) present, and  
 4543 are denoted as  $nDLLP_0$ ,  $nDLLP_1$ , and  $nDLLP_2$ .

4544 For systematic representation, we introduce an efficiency matrix,  $\mathbf{E} \in \mathbb{R}^{2 \times 3}$ , where the  
 4545 rows correspond to the 2-jet and 4-jet final states, and the columns correspond to the afore-  
 4546 mentioned  $nDLLP$  regions. Mathematically, the matrix is defined as:

$$\mathbf{E} = \begin{pmatrix} E_{00} & E_{01} & E_{02} \\ E_{10} & E_{11} & E_{12} \end{pmatrix}, \quad (8-2)$$

4547 where  $E_{ij}$  denotes the efficiency for the  $i$ -th final state in the  $j$ -th  $nDLLP$  region.

4548 The elements of  $\mathbf{E}$  are subsequently utilized in the computation of the expected signal  
 4549 yields,  $Y_{ij}$ , defined as:

$$Y_{ij} = E_{ij} \times \text{Acceptance}, \quad (8-3)$$

4550 Where acceptance can be obtained in Table 8–4. These expected yields serve as critical  
4551 parameters in the subsequent stages of statistical fitting.

### 4552 8.3.5 Efficiency comparison between CNN and GNN

4553 To provide an aggregate assessment of the efficiency of CNN and GNN in classifying  
4554 events, the signal efficiencies were weighted across all sub-channels, namely the 2-jet and 4-  
4555 jet categories. The results are compiled in a table that details these efficiencies under various  
4556 scenarios, taking into account both the mass and lifetime parameters of the LLPs.

Approach	Efficiency		Lifetime [ns]			
	Mass [GeV]	0.001	0.1	1	10	100
CNN	1	0.82	0.90	0.79	0.74	0.77
	10	0.80	0.89	0.90	0.89	0.84
	50	0.88	0.96	0.99	0.98	0.93
GNN	1	0.83	0.89	0.80	0.80	0.79
	10	0.77	0.86	0.92	0.86	0.84
	50	0.88	0.92	0.97	0.97	0.93

**Table 8–6 Signal efficiencies for different assumptions of LLPs’ mass and lifetime obtained with CNN-based and GNN-based approaches.**

4557 From Table 8–6, it is evident that both CNN and GNN manifest high signal efficiencies,  
4558 with the majority of the data points exceeding an 80% efficiency threshold. This robust  
4559 performance is consistent across different LLP mass and lifetime considerations. Specifically,  
4560 for low mass (1 GeV) scenarios, both CNN and GNN achieve efficiencies in the approximate  
4561 range of 0.80 – 0.83, and similar behavior is observed for medium (10 GeV) and high (50  
4562 GeV) mass LLPs.

4563 It is noteworthy that the efficiencies obtained from both CNN and GNN methods are  
4564 remarkably consistent, thereby reinforcing the robustness of these deep learning architectures  
4565 in handling complex classification tasks. The product of acceptance and efficiency, which  
4566 serves as both a critical metric for the performance evaluation and the final input for statistical  
4567 interpretation, is further illustrated in Figure 8–6.

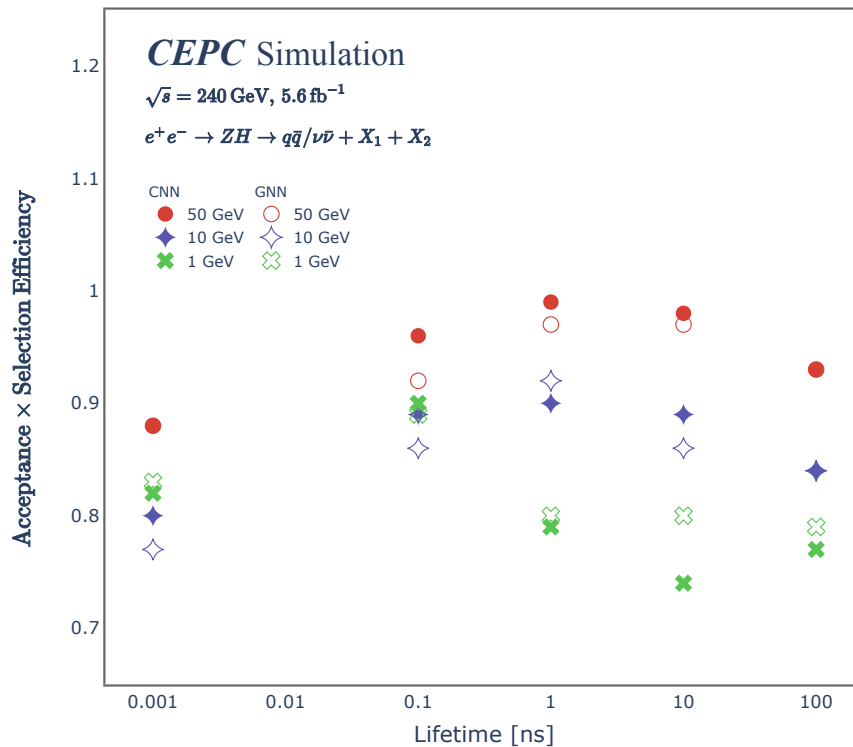


**Figure 8–6** The product of signal efficiencies and acceptance for different assumptions of LLPs' mass and lifetime obtained with CNN-based (solid) and GNN-based (dot) approaches.

## 4568 8.4 Results

4569 Contrary to the  $CL_s$  approach commonly employed in di-Higgs search studies, the present  
 4570 analysis does not permit the use of approximate estimations for exclusion limits. This limi-  
 4571 tation is imposed by the specific condition of having zero background events. To circumvent  
 4572 this, we employ a statistical toy model to compute the upper limits. This model generates  
 4573 pseudo-experiments based on the predicted signal and observed data, allowing for a more  
 4574 robust estimation of the exclusion limits.

4575 Several sources of systematic uncertainties are taken into account. The uncertainty orig-  
 4576 inating from the total number of Higgs bosons is estimated at 1.0%<sup>[266]</sup>. The ML-related un-  
 4577 certainty mainly encompasses network initialization. To assess this uncertainty, we change  
 4578 the random seed during the training and evaluate the corresponding signal efficiency using  
 4579 XGBoost. We obtain 50 different signal efficiencies with different random seeds. The uncer-  
 4580 tainty is then estimated as half of the difference between the maximum and minimum values  
 4581 and is about 1.7%. Overall, the combined systematic uncertainties are quadratically summed

4582 to be 2.0%.

4583 To estimate the sensitivity of the study, we assume a null hypothesis for LLPs signals  
4584 and obtain 95% Confidence Level upper limits on the branching ratio  $\mathcal{B}(H \rightarrow \text{LLPs})$  for the  
4585 process  $e^+e^- \rightarrow ZH(Z \rightarrow \text{inclusive}, H \rightarrow X_1 + X_2)$ . The analyzed samples have a  $5.6 \text{ ab}^{-1}$   
4586 luminosity and about  $10^6$  Higgs bosons.

4587 For the two LLPs signal types, we have considered the following scenarios:

- 4588 • Type I and Type II signal yields have a fixed ratio. We define a parameter  $\epsilon_V :=$   
4589  $\frac{BR(X \rightarrow \nu\bar{\nu})}{BR(X \rightarrow q\bar{q})}$  as the ratio and set it with a fixed value of 0.2. A one-dimensional 95%  
4590 Confidence Level upper limit on  $\mathcal{B}(H \rightarrow \text{LLPs})$  is derived and shown in Figure 8–7a.
- 4591 • Type I and Type II signal yields has a floating ratio and We allow  $\epsilon_V$  to be between  $10^{-6}$   
4592 and 100. A one-dimensional 95% Confidence Level upper limit on  $\mathcal{B}(H \rightarrow \text{LLPs})$  is  
4593 derived and shown in Figure 8–7b.
- 4594 • Type I and Type II signal yields has a floating ratio and two-dimensional 95% Con-  
4595 fidence Level upper limits on  $\mathcal{B}_{2\text{-jet}}$  and  $\mathcal{B}_{4\text{-jet}}$  are derived. A bivariate statistical fit is  
4596 performed to derive the upper limits and results are shown in Figure 8–8. More detailed  
4597 results on 2-D upper limits are shown in Figure 8–9.

4598 Both 1-D and 2-D exclusion limits are summarized in Table 8–7.

Scenario	$\mathcal{B} (\times 10^{-6})$	Lifetime [ns]				
	Mass [GeV]	0.001	0.1	1	10	100
Fixed	1	7	6	19	117	3394
	10	10	7	8	18	99
	50	6	4	5	5	13
Floated	1	11	8	12	74	2395
	10	12	10	5	11	65
	50	8	10	7	8	9

**Table 8–7 The 95% C.L. exclusion limit on  $\text{BR}(h \rightarrow X_1 X_2)$  for all signal channels: fixed and floated  $\epsilon_V$ , based on CNN’s efficiency.**

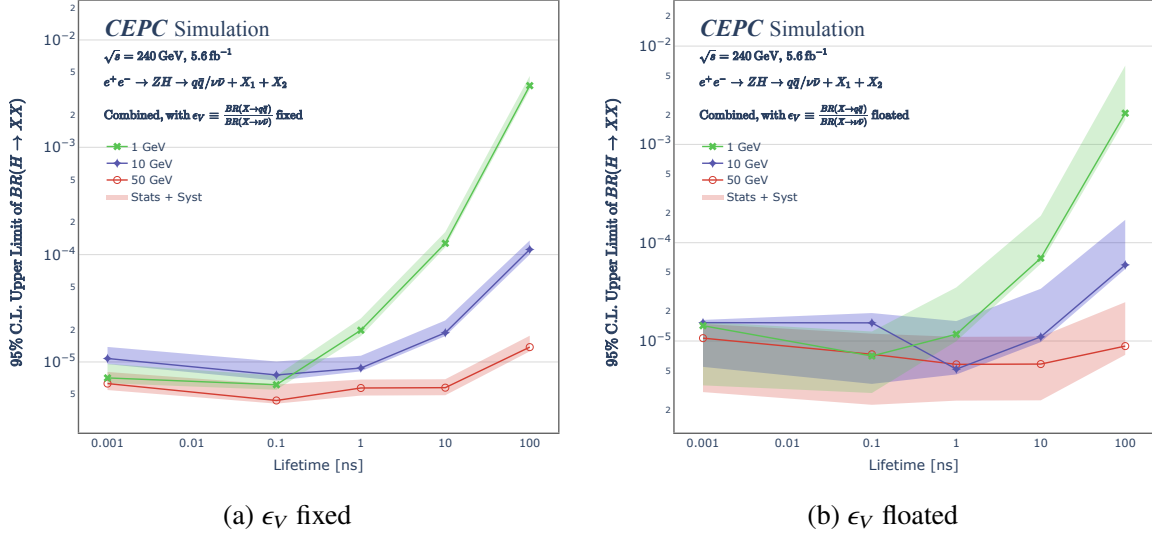


Figure 8–7 The 95% C.L. upper limit on  $BR(h \rightarrow X_1 X_2)$  for the process  $e^+e^- \rightarrow Zh$  with the condition of  $\epsilon_V$  fixed (left) and  $\epsilon_V$  floated (right), where  $\epsilon_V := \frac{BR(X \rightarrow \nu \bar{\nu})}{BR(X \rightarrow q \bar{q})}$ . Different colored lines indicate different LLPs masses. Shaded area indicate statistical and systematic uncertainties combined.

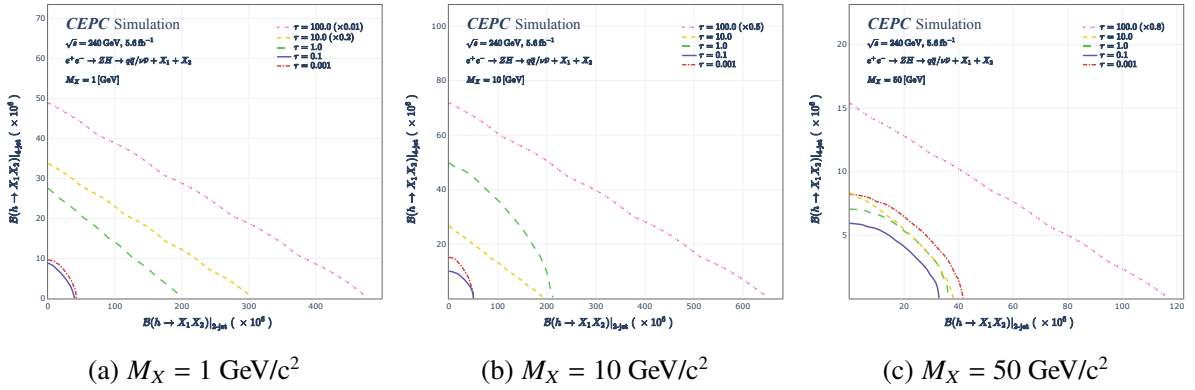
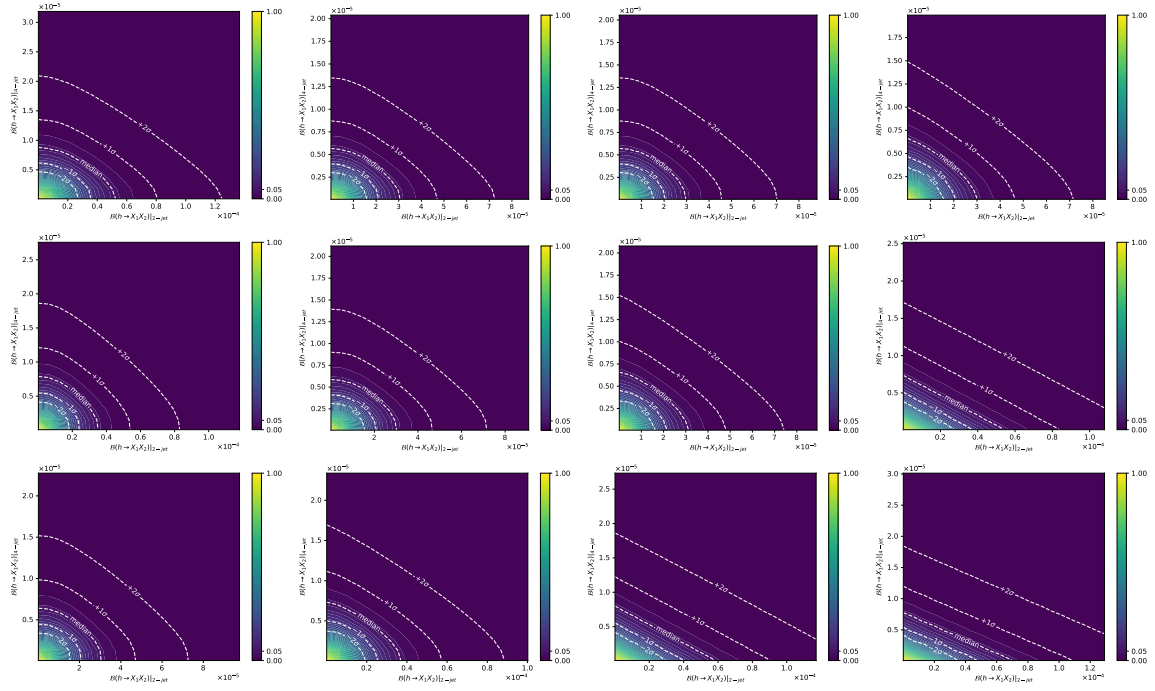


Figure 8–8 The 95% C.L. 2-D upper limit on  $(\mathcal{B}_{2\text{-jet}}, \mathcal{B}_{4\text{-jet}})$  for the process  $e^+e^- \rightarrow Zh$  for three LLPs masses 50 GeV (left), 10 GeV (middle), 1 GeV (right). Different colored lines indicate different LLPs lifetimes. The uncertainties on the limits are omitted and a few limits are scaled by a factor for better visibility.



**Figure 8-9** The 2D fitting for  $(\mathcal{B}_{2\text{-jet}}, \mathcal{B}_{4\text{-jet}})$ . From top to bottom, the mass is 50, 10, 1  $GeV/c^2$ ;  
From left to right, the lifetime is 0.0001, 0.1, 1.0, 10 ns.

## 4599 8.5 Discussion and Summary

### 4600 8.5.1 Comparison with Hadron Colliders: ATLAS and CMS

4601 We evaluate the effectiveness of our ML-based approach for LLPs detection at future  
4602 lepton colliders by comparing our results with results at hadron colliders with the ATLAS  
4603 experiment<sup>[250]</sup> and CMS experiment<sup>[251]</sup> as well as future HL-LHC experiments<sup>[267]</sup>. The  
4604 comparison is based on four primary metrics: signal acceptance, selection efficiency, analysis  
4605 strategy and signal yields:

- 4606 • **Signal Acceptance:** Both ATLAS and CMS results have limited signal acceptance,  
4607 typically a few percent, as they focus on LLPs decaying in the muon detector. In  
4608 contrast, our ML-based approach covers the entire detector, resulting in 100% signal  
4609 acceptance except for LLPs with long lifetime ( $> 1$  ns) and low mass ( $< 1$  GeV).
- 4610 • **Selection Efficiency:** For hadron colliders, LLPs events typically trigger on displaced  
4611 decays and/or large missing transverse energy. The LLPs trigger efficiency at the AT-  
4612 LAS experiment is estimated to be between  $10^{-3}$  and 0.3<sup>[250]</sup>. Besides trigger effi-  
4613 ciency, there are additional efficiencies involved such as displaced vertex/object re-

4614 construction efficiencies which are typically in the order of a few percent. In contrast,  
4615 LLPs event selection at lepton colliders can adapt to a triggerless approach owing to  
4616 the clean environment. ML-based approach can be applied directly with low-level de-  
4617 tector information without any event-level reconstruction. As a result, our ML-based  
4618 approach with lepton colliders can achieve an overall selection efficiency as high as  
4619 99%, an improvement of several orders in magnitude when comparing with LHC or  
4620 HL-LHC efficiencies.

4621 • **Analysis Strategy:** Traditionally, analyses of LLPs conducted elsewhere have em-  
4622 ployed a selection-based method, which involves categorizing events into multiple  
4623 subsets with different decay modes and orthogonal signal types. These analyses neces-  
4624 sitate manual re-tuning and re-optimization for each subset and different LLPs mass  
4625 and lifetime configurations. In contrast, our ML-based approach eliminates the need  
4626 for manual categorization and optimization. Deep neural networks can be retrained au-  
4627 tomatically for each LLPs mass and lifetime, resulting in higher efficiencies compared  
4628 to the selection-based method.

4629 • **Signal Yields and Upper Limits Comparison:** LHC and HL-LHC can produce a  
4630 significantly larger number of Higgs bosons compared to lepton colliders. Despite  
4631 this, higher signal acceptance and selection efficiencies in our ML-based approach  
4632 compensate for the relatively low number of Higgs bosons. We achieve upper limits  
4633 as low as  $4 \times 10^{-6}$  on  $\mathcal{B}(H \rightarrow \text{LLPs})$  with  $1 \times 10^6$  Higgs bosons. This upper limit is  
4634 approximately three orders of magnitude better than the  $10^{-3}$  limit observed at the  
4635 ATLAS and CMS experiments with  $10^7$  Higgs bosons and it is comparable to the  
4636 projected HL-LHC limit with about  $10^8$  expected Higgs bosons.

4637 Besides comparing with hadron colliders, we have also compared our result with a pre-  
4638 liminary study<sup>[268]</sup> on the ILC sensitivity<sup>[269]</sup> with a traditional selection-based method. The  
4639 ILC sensitivity study searches for long-lived dark photons produced in Higgstrahlung events  
4640 via the Higgs portal. We have compared our result with the hadronic decay dark photo re-  
4641 sult since the event signature is similar. We have seen that the signal acceptance factors are  
4642 similar between ILC and CEPC detectors but the signal efficiencies differ significantly. The  
4643 signal efficiencies in the ILC study range from 0.1% to 10%, which is at least an order of  
4644 magnitude lower than ours. The upper limits on  $\mathcal{B}(H \rightarrow \text{LLPs})$  in the ILC study are derived

4645 under the assumption of 100% truth-level signal efficiency. Only after making this assump-  
4646 tion, two results show similar sensitivities in the low lifetime region ( $< 1$  ns) of LLPs. In  
4647 the long lifetime region, for example, for a 1 GeV LLP with a lifetime of a few nanoseconds,  
4648 our result yields an upper limit of about  $10^{-5}$  which is an order of magnitude better than the  
4649 ILC's upper limit of  $10^{-4}$ .

4650 In summary, we have developed a ML-based approach for LLP searches that outperforms  
4651 traditional selection-based methods on almost all fronts. Moreover, our ML-based approach  
4652 can be easily applied to other future lepton collider experiments, including the ILC, FCC<sup>[270]</sup>,  
4653 and CLIC<sup>[271]</sup>.



## Chapter 9 Summary and Future prospects

As we reach the concluding chapter of this dissertation, it is both timely and essential to circle back to the fundamental questions and theoretical frameworks that have informed these diverse yet interconnected endeavors. The Standard Model (SM) of particle physics provides the backbone for understanding the elemental building blocks and interactions that shape our universe. While this framework has been corroborated by a multitude of experimental findings, it nonetheless presents outstanding questions that beckon further scrutiny. Notably, the Higgs sector remains a significant arena for exploration, both to corroborate the SM and to potentially unearth phenomena that lie Beyond the Standard Model.

A parameter of particular interest within this sector is the Higgs boson's self-coupling which holds far-reaching implications for the stability of our universe. The observation and measurement of this unique interaction is a central goal of elementary particle physics research. Understanding it requires not just the identification and study of individual Higgs bosons but also the complex interactions in di-Higgs events. Moreover, this serves as a possible gateway to explore yet unidentified particles and interactions, opening up new horizons for physics beyond our current understanding.

In this dissertation, the first analysis is based on a luminosity of  $140 \text{ fb}^{-1}$  of proton-proton collision data at  $\sqrt{s} = 13 \text{ TeV}$ , collected by the ATLAS detector during Run 2 of the LHC. The focus of this work is on the SM Higgs pair ( $HH$ ) production in 3-lepton final states, predominantly produced via gluon-gluon fusion (ggF) with Vector Boson Fusion (VBF) as an additional signal yield. The primary background,  $WZ$ , known for mismodelling in high jet multiplicities, is reweighted using a fitting function. The secondary background arises from fake leptons, estimated via the Template Fit method. Three normalization factors were extracted from multiple control regions to quantify the fake lepton backgrounds. A multivariate analysis strategy employing Gradient Boosted Decision Trees was utilized to optimize the signal and background discrimination. To make full use of the available Monte Carlo statistics, a 3-fold training method was implemented to improve the smoothness of the Receiver Operating Characteristic (ROC) curve. Detailed hyperparameter tuning was performed for model optimization. Our 3-lepton channel has attained a maximum signal significance of 0.073, with an upper limit of  $23.13_{-6.66}^{+10.21}$  on the  $HH \rightarrow 3\ell$  cross-section relative to the SM.

4684 When including all uncertainties, the limit stands at  $28.09^{+12.81}_{-7.86}$ . This represents a 9.4-fold im-  
 4685 provement in the upper limit compared to the prior analysis in the  $HH \rightarrow WW^*WW^* \rightarrow 3\ell$   
 4686 channel. In the combined multilepton results, the expected upper limit is  $8.93^{+12.69}_{-6.44}$  statis-  
 4687 tically and  $9.74^{+13.91}_{-7.02}$  including all systematic uncertainties. Notably, this 3-lepton channel  
 4688 offers the most robust results among pure leptonic channels and is very close to the lead-  
 4689 ing  $\gamma\gamma + 1\ell$  channel. I have been responsible for the entire 3-lepton analysis strategy, acted  
 4690 as the internal note editor, and represented our multilepton group in several editorial board  
 4691 meetings and unblinding request approval talks. Upon the completion of the ATLAS internal  
 4692 review, this analysis is poised to make a significant contribution to  $HH$  searches.

4693 The second analysis of the dissertation is the  $HH \rightarrow b\bar{b}\tau^+\tau^-$  analysis, which builds upon  
 4694 previous work with  $140 \text{ fb}^{-1}$  of Full Run 2 data and aims to refine methodological approaches,  
 4695 primarily in the context of the  $\kappa_\lambda$  and  $\kappa_{2V}$  modifiers. Contrary to the legacy analysis, which  
 4696 was primarily optimized for the gluon-gluon fusion SM production mode, the present study  
 4697 employs advanced Multivariate Analysis techniques for optimal signal-background separa-  
 4698 tion. These techniques are focused on an event categorization based on the invariant mass  
 4699 of the HH system ( $m_{HH}$ ) in the ggF region and also incorporate a dedicated VBF category to  
 4700 improve sensitivity to the  $\kappa_{2V}$  parameter. The utilization of MVA outputs as final discrimi-  
 4701 nants in the fit has led to notable improvements over the legacy data. Specifically, we have  
 4702 achieved a 17% improvement in the baseline with systematics for  $\mu_{HH}$  and an 11.9% (19.8%)  
 4703 improvement in the 95% confidence interval for  $\kappa_\lambda$  ( $\kappa_{2V}$ ). Within the  $HH \rightarrow b\bar{b}\tau^+\tau^-$  work-  
 4704 ing group, my research has been centered around the application and optimization of BDTs  
 4705 for the separation of ggF and VBF regions and signal-background separation in each signal  
 4706 region. This involved detailed study and optimization of BDT hyperparameters and input  
 4707 variables, exerting a direct influence on the final analysis results.

4708 The HH+H combination analysis serves as a study that amalgamates the primary double-  
 4709 Higgs analyses ( $HH \rightarrow b\bar{b}b\bar{b}$ ,  $HH \rightarrow b\bar{b}\gamma\gamma$ ,  $HH \rightarrow b\bar{b}\tau^+\tau^-$ ) with the single-Higgs  
 4710 workspace. This integrated approach is specifically designed to furnish rigorous constraints  
 4711 on the coupling modifiers, chiefly  $\kappa_\lambda$  and  $\kappa_{2V}$ . In the most generalized fit that allows multi-  
 4712 ple coupling modifiers,  $\kappa_t$ ,  $\kappa_b$ ,  $\kappa_\tau$ , and  $\kappa_V$ , to vary freely, we report a 95% confidence level  
 4713 interval of  $-1.4 < \kappa_\lambda < 6.1$ , closely mirroring the expected bounds of  $-2.2 < \kappa_\lambda < 7.7$ . The  
 4714 robustness of these constraints is underscored by a negligible sensitivity to variations in  $\kappa_{2V}$ ,

4715 which affect the observed  $\kappa_\lambda$  bounds by less than 5%. This serves to affirm the agreement of  
4716 all other coupling modifiers with the SM within the associated uncertainties. My specific role  
4717 in this undertaking involved the consolidation of the double-Higgs workspaces, facilitating  
4718 their subsequent integration into the single-Higgs analysis.

4719 Within the scope of ATLAS experiments, the research began with an exploration into the  
4720  $HH \rightarrow$  multilepton channel. This served as an entry point for engaging with a full-chain  
4721 analysis, encompassing every phase from production to final results. Subsequently, the re-  
4722 search focus shifted to the  $HH \rightarrow b\bar{b}\tau^+\tau^-$  channel, which offered an extensive environment  
4723 for delving into the nuances of BDTs. Detailed investigations into BDT behaviors were con-  
4724 ducted, leading to a comprehensive understanding of their effects on the analysis. Lastly,  
4725 the research culminated in a combined HH+H study. This phase provided a broader frame-  
4726 work for understanding di-Higgs phenomena, particularly illuminating the interplay between  
4727 single-Higgs and double-Higgs processes as well as the roles of various  $\kappa$  modifiers. This  
4728 structured research trajectory has thus facilitated not only specific channel-based insights but  
4729 also a more integrative view of di-Higgs physics.

4730 In a natural progression from exploring the complex landscape of di-Higgs interactions,  
4731 the research embarks on an expedition into realms beyond the SM, specifically addressing  
4732 the Higgs decays into Long-Lived Particles (LLPs). Utilizing a novel analytical framework,  
4733 designed for the forthcoming future Lepton Colliders, the study uses the power of convolu-  
4734 tional neural networks (CNNs) and graph neural networks (GNNs) directly on raw detector  
4735 data. These machine-learning models have not only yielded consistent results but have also  
4736 simplified the analytical landscape. Remarkably, this approach has achieved an expected up-  
4737 per limit of approximately  $4 \times 10^{-6}$ , significantly outperforming the  $1 \times 10^{-3}$  limits set by  
4738 hadron colliders such as ATLAS and CMS. Furthermore, when compared with lepton col-  
4739 liders like the International Linear Collider (ILC), this methodology outperforms by nearly  
4740 an order of magnitude in expected exclusion limits for LLPs with lifetimes larger than 1 ns.

4741 Both the  $HH \rightarrow$  multilepton and  $HH \rightarrow b\bar{b}\tau^+\tau^-$  analyses currently face statistical lim-  
4742 itations as their primary constraint. The anticipated doubling of data statistics in ATLAS  
4743 Run 3 will improve the sensitivity to these channels. Concurrent advancements in algo-  
4744 rithms and detector technologies, such as the recently introduced PromptLeptonVeto (PLV)  
4745 reducing fake lepton backgrounds, signify promising avenues for further refinement. While

4746 the  $HH \rightarrow$  multilepton benefits from reduced fake lepton backgrounds, the  $HH \rightarrow b\bar{b}\tau^+\tau^-$   
 4747 stands to gain from enhanced b-jet and tau-lepton tagging technologies. These developments  
 4748 collectively herald a more robust and precise di-Higgs measurement in future ATLAS runs.

4749 The principal bottleneck in expanding the LLP study to a more general-purpose collider  
 4750 analysis is computational power. The application of advanced machine learning algorithms  
 4751 like CNNs and GNNs directly on raw collider data requires significant computational re-  
 4752 sources. Specifically, the memory requirements for handling large datasets present a lim-  
 4753 iting factor. Future work will focus on acquiring more computational power and exploring  
 4754 algorithmic modifications to accommodate large-scale data without sacrificing the integrity  
 4755 of the analysis. This expansion in computational capacity will not only benefit LLP studies  
 4756 but also potentially revolutionize broader applications within Beyond the Standard Model  
 4757 physics.

4758 Through simulation-based analysis in the DarkSHINE experiments, the study effectively  
 4759 suppresses background noise, resulting in an expected background yield of 0.015 for  $3 \times$   
 4760  $10^{14}$  electrons on target (EOT). Upper limits on the kinetic mixing parameter  $\epsilon^2$  have been  
 4761 established over varying EOT scenarios, offering competitive constraints relative to existing  
 4762 experiments. As future steps, the project aims to validate the extrapolation method further  
 4763 and improve the statistical power (up to  $10^{16}$  EOT), potentially refining the exclusion limits  
 4764 for various dark photon models.

4765 In summary, this dissertation describes the di-Higgs searches at the LHC in multiple  
 4766 channels, especially in multi-lepton and  $b\bar{b}\tau^+\tau^-$  channels. With the combination of three  
 4767 major di-Higgs channels ( $b\bar{b}b\bar{b}$ ,  $b\bar{b}\gamma\gamma$ , and  $b\bar{b}\tau^+\tau^-$ ) and all single Higgs channels, con-  
 4768 straints on the Higgs self-coupling parameter  $\kappa_\lambda$  at 95% confidence level interval give  $-1.4 <$   
 4769  $\kappa_\lambda < 6.1$  with the most generalized assumption. The dissertation also searches for new phe-  
 4770 nomena during Higgs rare decay, where a Higgs particle decays to a pair of LLPs resulting  
 4771 in multiple jets in the final state. This study gives the expected upper limit of  $4 \times 10^{-6}$  for  
 4772 the branching ratio of  $H \rightarrow$  LLPs with a LLP mass of 50 GeV and 1 ns lifetime, which  
 4773 is one of the best exclusion limits with an estimated statistics of  $10^6$  Higgs. Furthermore,  
 4774 the dissertation sets expected exclusion limits parameterized in dark photon mass and kinetic  
 4775 mixing coefficient ( $\epsilon$ ) via the proposed DarkSHINE fixed-target experiment. The expected  
 4776  $\epsilon^2$  exclusion upper limit can reach  $1.3 \times 10^{-14}$  for a dark photon mass of 1 MeV, exceeding all

4777 known experimental results by several orders of magnitude. Together, these detailed studies  
4778 search for new physics on various fronts in experimental particle physics and enhance our  
4779 understanding of the SM.



## Bibliography

4780

- [1] FEYNMAN R P. Space-Time Approach to Quantum Electrodynamics[J/OL]. Phys. Rev., 1949, 76: 769-789. <https://link.aps.org/doi/10.1103/PhysRev.76.769>. DOI: 10.1103/PhysRev.76.769.
- [2] SCHWINGER J. Quantum Electrodynamics. I. A Covariant Formulation[J/OL]. Phys. Rev., 1948, 74: 1439-1461. <https://link.aps.org/doi/10.1103/PhysRev.74.1439>. DOI: 10.1103/PhysRev.74.1439.
- [3] GELL-MANN M. THE EIGHTFOLD WAY: A THEORY OF STRONG INTERACTION SYMMETRY[J/OL]. 1961. <https://www.osti.gov/biblio/4008239>. DOI: 10.2172/4008239.
- [4] GELL-MANN M. A schematic model of baryons and mesons[J/OL]. Physics Letters, 1964, 8(3): 214-215. <https://www.sciencedirect.com/science/article/pii/S00316364920013>. DOI: [https://doi.org/10.1016/S0031-9163\(64\)92001-3](https://doi.org/10.1016/S0031-9163(64)92001-3).
- [5] FRITZSCH H, GELL-MANN M, LEUTWYLER H. Advantages of the color octet gluon picture[J/OL]. Physics Letters B, 1973, 47(4): 365-368. <https://www.sciencedirect.com/science/article/pii/0370269373906254>. DOI: [https://doi.org/10.1016/0370-2693\(73\)90625-4](https://doi.org/10.1016/0370-2693(73)90625-4).
- [6] GLASHOW S L. Partial-symmetries of weak interactions[J/OL]. Nuclear Physics, 1961, 22(4): 579-588. <https://www.sciencedirect.com/science/article/pii/0029558261904692>. DOI: [https://doi.org/10.1016/0029-5582\(61\)90469-2](https://doi.org/10.1016/0029-5582(61)90469-2).
- [7] SALAM A. Weak and electromagnetic interactions[M/OL]//Selected Papers of Abdus Salam: 244-254. eprint: [https://www.worldscientific.com/doi/pdf/10.1142/9789812795915\\_0034](https://www.worldscientific.com/doi/pdf/10.1142/9789812795915_0034). [https://www.worldscientific.com/doi/abs/10.1142/9789812795915\\_0034](https://www.worldscientific.com/doi/abs/10.1142/9789812795915_0034). DOI: 10.1142/9789812795915\_0034.
- [8] WEINBERG S. A Model of Leptons[J]. prl, 1967, 19(21): 1264-1266. DOI: 10.1103/PhysRevLett.19.1264.
- [9] COLLABORATION T A. Observation of a new particle in the search for the Standard Model Higgs boson with the ATLAS detector at the LHC[J/OL]. Physics Letters B, 2012, 716(1): 1-29. <https://doi.org/10.1016%2Fj.physletb.2012.08.020>. DOI: 10.1016/j.physletb.2012.08.020.

4809

- 4810 [10] YUKAWA H. On the Interaction of Elementary Particles I[J]. Proc. Phys. Math. Soc.  
4811 Jap., 1935, 17: 48-57. DOI: 10.1143/PTPS.1.1.
- 4812 [11] PESKIN M, SCHROEDER D. An Introduction to Quantum Field Theory[M/OL].  
4813 Avalon Publishing, 1995. <https://books.google.fr/books?id=i35LALN0GosC>.
- 4814 [12] WOITHE J, WIENER G J, der VEKEN F F V. Let's have a coffee with the Standard  
4815 Model of particle physics![J/OL]. Physics Education, 2017, 52(3): 034001. [https://dx](https://dx.doi.org/10.1088/1361-6552/aa5b25)  
4816 [.doi.org/10.1088/1361-6552/aa5b25](https://dx.doi.org/10.1088/1361-6552/aa5b25). DOI: 10.1088/1361-6552/aa5b25.
- 4817 [13] DI LELLA L, RUBBIA C. The Discovery of the W and Z Particles[J]. Adv. Ser.  
4818 Direct. High Energy Phys., 2015, 23: 137-163. DOI: 10.1142/9789814644150\_000  
4819 6.
- 4820 [14] KLEIN M, YOSHIDA R. Collider Physics at HERA[J]. Prog. Part. Nucl. Phys., 2008,  
4821 61: 343-393. arXiv: 0805.3334 [hep-ex]. DOI: 10.1016/j.pnpnp.2008.05.002.
- 4822 [15] MYERS S. The LEP collider, from design to approval and commissioning[J]. 1991.  
4823 DOI: 10.5170/CERN-1991-008.
- 4824 [16] HOLMES S, MOORE R S, SHILTSEV V. Overview of the Tevatron collider com-  
4825 plex: goals, operations and performance[J/OL]. Journal of Instrumentation, 2011,  
4826 6(08): T08001. <https://dx.doi.org/10.1088/1748-0221/6/08/T08001>. DOI: 10.1088  
4827 /1748-0221/6/08/T08001.
- 4828 [17] ABRAMOWICZ H, ABT I, ADAMCZYK L, et al. Combination of measurements  
4829 of inclusive deep inelastic  $e^\pm p$  scattering cross sections and QCD analysis of HERA  
4830 data[J/OL]. The European Physical Journal C, 2015, 75(12): 580. [https://doi.org/10](https://doi.org/10.1140/epjc/s10052-015-3710-4)  
4831 [.1140/epjc/s10052-015-3710-4](https://doi.org/10.1140/epjc/s10052-015-3710-4). DOI: 10.1140/epjc/s10052-015-3710-4.
- 4832 [18] ENGLERT F, BROUT R. Broken Symmetry and the Mass of Gauge Vector Mesons  
4833 [J/OL]. Phys. Rev. Lett., 1964, 13: 321-323. [https://link.aps.org/doi/10.1103/PhysR](https://link.aps.org/doi/10.1103/PhysRevLett.13.321)  
4834 [evLett.13.321](https://link.aps.org/doi/10.1103/PhysRevLett.13.321). DOI: 10.1103/PhysRevLett.13.321.
- 4835 [19] HIGGS P W. Broken Symmetries and the Masses of Gauge Bosons[J/OL]. Phys.  
4836 Rev. Lett., 1964, 13: 508-509. <https://link.aps.org/doi/10.1103/PhysRevLett.13.508>.  
4837 DOI: 10.1103/PhysRevLett.13.508.
- 4838 [20] CERN. CERN Yellow Reports: Monographs, Vol 2 (2017): Handbook of LHC Higgs  
4839 cross sections: 4. Deciphering the nature of the Higgs sector[EB/OL]. CERN. 2017.  
4840 <https://e-publishing.cern.ch/index.php/CYRM/issue/view/32>.

- 4841 [21] GROUP T L H W. The LHC Higgs Working Group[EB/OL]. 2023 [2023-06-16].  
4842 <https://twiki.cern.ch/twiki/bin/view/LHCPhysics/LHCHWG?redirectedfrom=LHC>  
4843 [Physics.LHCHXSWG](https://twiki.cern.ch/twiki/bin/view/LHCPhysics/LHCHXSWG).
- 4844 [22] DAWSON S, DITTMAIER S, SPIRA M. Neutral Higgs-boson pair production at  
4845 hadron colliders: QCD corrections[J/OL]. Phys. Rev. D, 1998, 58: 115012. <https://link.aps.org/doi/10.1103/PhysRevD.58.115012>. DOI: 10.1103/PhysRevD.58.11501  
4846 2.
- 4847 [23] De FLORIAN D, MAZZITELLI J. Higgs Boson Pair Production at Next-to-Next-to-  
4848 Leading Order in QCD[J/OL]. Phys. Rev. Lett., 2013, 111: 201801. [https://link.aps.o](https://link.aps.org/doi/10.1103/PhysRevLett.111.201801)  
4849 [rg/doi/10.1103/PhysRevLett.111.201801](https://link.aps.org/doi/10.1103/PhysRevLett.111.201801). DOI: 10.1103/PhysRevLett.111.201801.
- 4850 [24] BAGLIO J, CAMPANARIO F, GLAUS S, et al. Gluon fusion into Higgs pairs at  
4851 NLO QCD and the top mass scheme[J/OL]. The European Physical Journal C, 2019,  
4852 79(6). <https://doi.org/10.1140/epjc/s10052-019-6973-3>. DOI: 10.1140/epjc  
4853 /s10052-019-6973-3.
- 4854 [25] CEPEDA M, GORI S, ILTEN P, et al. Higgs Physics at the HL-LHC and HE-LHC  
4855 [Z]. 2019. arXiv: 1902.00134 [hep-ph].
- 4856 [26] COLLABORATION D. A search for heavy stable and long-lived squarks and slep-  
4857 tons in  $e^+e^-$  collisions at energies from 130 to 183 GeV[J]. Physics Letters B, 1998,  
4858 444(3): 491-502.
- 4859 [27] COLLABORATION C. Search for heavy, long-lived neutralinos that decay to pho-  
4860 tons at CDF II using photon timing[J/OL]. Phys. Rev. D, 2008, 78: 032015. [https://l](https://link.aps.org/doi/10.1103/PhysRevD.78.032015)  
4861 [ink.aps.org/doi/10.1103/PhysRevD.78.032015](https://link.aps.org/doi/10.1103/PhysRevD.78.032015). DOI: 10.1103/PhysRevD.78.03201  
4862 5.
- 4863 [28] STRASSLER M J, ZUREK K M. Echoes of a hidden valley at hadron colliders  
4864 [J/OL]. Physics Letters B, 2007, 651(5-6): 374-379. [https://doi.org/10.1016/2](https://doi.org/10.1016/j.physletb.2007.06.055)  
4865 [Fj.physletb.2007.06.055](https://doi.org/10.1016/j.physletb.2007.06.055). DOI: 10.1016/j.physletb.2007.06.055.
- 4866 [29] ARKANI-HAMED N, DIMOPOULOS S. Supersymmetric unification without low  
4867 energy supersymmetry and signatures for fine-tuning at the LHC[J/OL]. Journal of  
4868 High Energy Physics, 2005, 2005(06): 073-073. [https://doi.org/10.1088/1126-6](https://doi.org/10.1088/1126-6708/2005/06/073)  
4869 [708/2005/06/073](https://doi.org/10.1088/1126-6708/2005/06/073). DOI: 10.1088/1126-6708/2005/06/073.
- 4870 [30] ABDULLAHI A M, ALZÁ S P B, BATELL B, et al. The present and future status  
4871

- 4872 of heavy neutral leptons[J/OL]. Journal of Physics G: Nuclear and Particle Physics,  
4873 2023, 50(2): 020501. <https://doi.org/10.1088/1361-6471/ac98f9>. DOI:  
4874 10.1088/1361-6471/ac98f9.
- 4875 [31] EVANS L R. The Large Hadron Collider Project[J/OL]. 1997. <https://cds.cern.ch/record/313675>.
- 4876
- 4877 [32] BRÜNING O, BURKHARDT H, MYERS S. The Large Hadron Collider[J/OL].  
4878 Prog. Part. Nucl. Phys., 2012, 67: 705-734. <https://cds.cern.ch/record/1443022>.  
4879 DOI: 10.1016/j.ppnp.2012.03.001.
- 4880 [33] COLLABORATION A. ATLAS Experiment at CERN[EB/OL]. 2023. <https://atlas.cern/>.
- 4881
- 4882 [34] CERN. CERN[EB/OL]. 2023. <https://home.cern/>.
- 4883 [35] LOPIENSKA E. The CERN accelerator complex, layout in 2022. Complexe des ac-  
4884 célérateurs du CERN en janvier 2022[J/OL]. 2022. <https://cds.cern.ch/record/2800984>.
- 4885
- 4886 [36] COLLABORATION A. Public ATLAS Luminosity Results for Run-2 of the LHC  
4887 [EB/OL]. 2023. <https://twiki.cern.ch/twiki/bin/view/AtlasPublic/LuminosityPublicResultsRun2>.
- 4888
- 4889 [37] COLLABORATION A. Luminosity determination in  $pp$  collisions at  $\sqrt{s} = 13$  TeV  
4890 using the ATLAS detector at the LHC[Z]. 2022. arXiv: 2212.09379 [hep-ex].
- 4891 [38] ATLAS: technical proposal for a general-purpose pp experiment at the Large Hadron  
4892 Collider at CERN[M/OL]. Geneva: CERN, 1994. <https://cds.cern.ch/record/290968>. DOI: 10.17181/CERN.NR4P.BG9K.
- 4893
- 4894 [39] ATLAS detector and physics performance: Technical Design Report, 1[M/OL].  
4895 Geneva: CERN, 1999. <https://cds.cern.ch/record/391176>.
- 4896 [40] PEQUENAO J. Computer generated image of the whole ATLAS detector[Z/OL].  
4897 2008. <https://cds.cern.ch/record/1095924>.
- 4898 [41] ATLAS inner detector: Technical Design Report, 1[M/OL]. Geneva: CERN, 1997.  
4899 <https://cds.cern.ch/record/331063>.
- 4900 [42] PEQUENAO J. Computer generated image of the ATLAS inner detector[Z/OL].  
4901 2008. <https://cds.cern.ch/record/1095926>.
- 4902 [43] ATLAS calorimeter performance: Technical Design Report[M/OL]. Geneva:

- 4903 CERN, 1996. <https://cds.cern.ch/record/331059>.
- 4904 [44] PEQUENAO J. Computer Generated image of the ATLAS calorimeter[Z/OL].  
4905 2008. <https://cds.cern.ch/record/1095927>.
- 4906 [45] ATLAS muon spectrometer: Technical Design Report[M/OL]. Geneva: CERN,  
4907 1997. <https://cds.cern.ch/record/331068>.
- 4908 [46] PEQUENAO J. Computer generated image of the ATLAS Muons subsystem[Z/OL].  
4909 2008. <https://cds.cern.ch/record/1095929>.
- 4910 [47] COLLABORATION T A. The ATLAS Experiment at the CERN Large Hadron Col-  
4911 lider[J/OL]. Journal of Instrumentation, 2008, 3(08): S08003. [https://dx.doi.org/10](https://dx.doi.org/10.1088/1748-0221/3/08/S08003)  
4912 [.1088/1748-0221/3/08/S08003](https://dx.doi.org/10.1088/1748-0221/3/08/S08003). DOI: 10.1088/1748-0221/3/08/S08003.
- 4913 [48] RODRIGUEZ VERA A M, ANTUNES PEQUENAO J. ATLAS Detector Magnet  
4914 System[Z/OL]. 2021. <https://cds.cern.ch/record/2770604>.
- 4915 [49] ELSING M, SCHOERNER-SADENIUS T. Configuration of the ATLAS Trigger  
4916 System[Z]. 2003. arXiv: physics/0306046 [physics.ins-det].
- 4917 [50] COLLABORATION T A. The ATLAS Data Acquisition and High Level Trigger  
4918 system[J/OL]. JINST, 2016, 11(06): P06008. <https://cds.cern.ch/record/2255808>.  
4919 DOI: 10.1088/1748-0221/11/06/P06008.
- 4920 [51] CERN. AthenaCore Package Documentation[EB/OL]. [http://atlas-computing.web](http://atlas-computing.web.cern.ch/atlas-computing/packages/athenaCore/athenaCore.php)  
4921 [.cern.ch/atlas-computing/packages/athenaCore/athenaCore.php](http://atlas-computing.web.cern.ch/atlas-computing/packages/athenaCore/athenaCore.php).
- 4922 [52] AGOSTINELLI S, ALLISON J, AMAKO K, et al. Geant4—a simulation toolkit  
4923 [J/OL]. Nuclear Instruments and Methods in Physics Research Section A: Acceler-  
4924 ators, Spectrometers, Detectors and Associated Equipment, 2003, 506(3): 250-303.  
4925 <https://www.sciencedirect.com/science/article/pii/S0168900203013688>. DOI:  
4926 [https://doi.org/10.1016/S0168-9002\(03\)01368-8](https://doi.org/10.1016/S0168-9002(03)01368-8).
- 4927 [53] ALLISON J, AMAKO K, APOSTOLAKIS J, et al. Geant4 developments and appli-  
4928 cations[J]. IEEE Transactions on Nuclear Science, 2006, 53(1): 270-278. DOI: 10.1  
4929 109/TNS.2006.869826.
- 4930 [54] The ATLAS Collaboration. The ATLAS Simulation Infrastructure[J/OL]. The Eu-  
4931 ropean Physical Journal C, 2010, 70(3): 823-874. <https://doi.org/10.1140/epjc>  
4932 [%2Fs10052-010-1429-9](https://doi.org/10.1140/epjc). DOI: 10.1140/epjc/s10052-010-1429-9.
- 4933 [55] BUCKLEY A, ILTEN P, KONSTANTINOV D, et al. The HepMC3 event record li-

- 4934           brary for Monte Carlo event generators[J/OL]. *Computer Physics Communications*,  
4935           2021, 260: 107310. <https://doi.org/10.1016/j.cpc.2020.107310>. DOI: 10.1016/j  
4936           .cpc.2020.107310.
- 4937 [56] BOS K, BROOK N, DUELLMANN D, et al. LHC computing Grid: Technical Design  
4938           Report. Version 1.06 (20 Jun 2005)[M/OL]. Geneva: CERN, 2005. [https://cds.cern  
4939           .ch/record/840543](https://cds.cern.ch/record/840543).
- 4940 [57] BRANCO M, CAMERON D, GAIDIOZ B, et al. Managing ATLAS data on a  
4941           petabyte-scale with DQ2[J/OL]. *J. Phys.: Conf. Ser.*, 2008, 119: 062017. [https://cd  
4942           s.cern.ch/record/1177372](https://cds.cern.ch/record/1177372). DOI: 10.1088/1742-6596/119/6/062017.
- 4943 [58] CORCELLA G, KNOWLES I G, MARCHESINI G, et al. HERWIG 6: an event  
4944           generator for hadron emission reactions with interfering gluons (including supersym-  
4945           metric processes)[J/OL]. *Journal of High Energy Physics*, 2001, 2001(01): 010-010.  
4946           <https://doi.org/10.1088/1126-6708/2001/01/010>. DOI: 10.1088/112  
4947           6-6708/2001/01/010.
- 4948 [59] BÄHR M, GIESEKE S, GIGG M A, et al. HERWIG physics and manual[J/OL]. *The  
4949           European Physical Journal C*, 2008, 58(4): 639-707. [https://doi.org/10.1140/epj  
4950           c/s10052-008-0798-9](https://doi.org/10.1140/epjc/s10052-008-0798-9). DOI: 10.1140/epjc/s10052-008-0798-9.
- 4951 [60] SJÖSTRAND T, MRENN A S, SKANDS P. PYTHIA 6.4 physics and manual  
4952           [J/OL]. *Journal of High Energy Physics*, 2006, 2006(05): 026-026. [https://doi.or  
4953           g/10.1088/1126-6708/2006/05/026](https://doi.org/10.1088/1126-6708/2006/05/026). DOI: 10.1088/1126-6708/2006  
4954           /05/026.
- 4955 [61] SJÖSTRAND T, ASK S, CHRISTIANSEN J R, et al. An introduction to PYTHIA  
4956           8.2[J/OL]. *Computer Physics Communications*, 2015, 191: 159-177. [https://doi.org  
4957           /10.1016/j.cpc.2015.01.024](https://doi.org/10.1016/j.cpc.2015.01.024). DOI: 10.1016/j.cpc.2015.01.024.
- 4958 [62] GLEISBERG T, HÖCHE S, KRAUSS F, et al. Event generation with SHERPA 1.1  
4959           [J/OL]. *Journal of High Energy Physics*, 2009, 2009(02): 007-007. [https://doi.org/1  
4960           0.1088/1126-6708/2009/02/007](https://doi.org/10.1088/1126-6708/2009/02/007). DOI: 10.1088/1126-6708/2009/02  
4961           /007.
- 4962 [63] GROUP P D. Quantum Chromodynamics[R/OL]. Lawrence Berkeley National Lab-  
4963           oratory. 2021. <https://pdg.lbl.gov/2021/reviews/rpp2021-rev-qcd.pdf>.
- 4964 [64] BIERLICH C, CHAKRABORTY S, DESAI N, et al. A comprehensive guide to the

- 4965 physics and usage of PYTHIA 8.3[Z]. 2022. arXiv: 2203.11601 [hep-ph].
- 4966 [65] DOBBS M A, FRIXIONE S, LAENEN E, et al. Les Houches Guidebook to Monte  
4967 Carlo Generators for Hadron Collider Physics[Z]. 2004. arXiv: hep-ph/0403045  
4968 [hep-ph].
- 4969 [66] LANGE D J. The EvtGen particle decay simulation package[J/OL]. Nuclear Instru-  
4970 ments and Methods in Physics Research Section A: Accelerators, Spectrometers, De-  
4971 tectors and Associated Equipment, 2001, 462(1): 152-155. <https://www.sciencedirect.com/science/article/pii/S0168900201000894>. DOI: [https://doi.org/10.1016/S0168-9002\(01\)00089-4](https://doi.org/10.1016/S0168-9002(01)00089-4).
- 4974 [67] FRIXIONE S, NASON P, WEBBER B R. Matching NLO QCD and parton showers  
4975 in heavy flavour production[J/OL]. Journal of High Energy Physics, 2003, 2003(08):  
4976 007. <https://dx.doi.org/10.1088/1126-6708/2003/08/007>. DOI: 10.1088/1126-6708/2003/08/007.
- 4978 [68] BOURILKOV D, GROUP R C, WHALLEY M R. LHAPDF: PDF Use from the  
4979 Tevatron to the LHC[Z]. 2006. arXiv: hep-ph/0605240 [hep-ph].
- 4980 [69] PLOTHOW-BESCH H. PDFLIB: a library of all available parton density functions of  
4981 the nucleon, the pion and the photon and the corresponding  $\alpha_s$  calculations[J/OL].  
4982 Comput. Phys. Commun., 1993, 75: 396-416. <https://cds.cern.ch/record/239783>.  
4983 DOI: 10.1016/0010-4655(93)90051-D.
- 4984 [70] TUNG W K, LAI H L, PUMPLIN J, et al. Global QCD Analysis and Collider  
4985 Phenomenology-CTEQ[Z]. 2007. arXiv: 0707.0275 [hep-ph].
- 4986 [71] An NLO QCD analysis of inclusive cross-section and jet-production data from the  
4987 ZEUS experiment[J/OL]. The European Physical Journal C, 2005, 42(1): 1-16. <https://doi.org/10.1140/epjc/s2005-02293-x>. DOI: 10.1140/epjc/s2005-02293-x.
- 4989 [72] GROUP T Q W, ALBROW M, BEGEL M, et al. Tevatron-for-LHC Report of the  
4990 QCD Working Group[Z]. 2006. arXiv: hep-ph/0610012 [hep-ph].
- 4991 [73] ATLAS PIXEL C. Pixel Offline Analysis for EndcapA Cosmic Data[R/OL]. for The  
4992 ATLAS Pixel Collaboration. Geneva: CERN, 2007. <https://cds.cern.ch/record/1074907>.
- 4994 [74] KITTELMANN T H. Slepton spin determination and simulation of the transition  
4995 radiation tracker at the ATLAS experiment[D/OL]. 2007. <https://cds.cern.ch/record/1074907>.

- d/2224292.
- [75] GADOMSKI S. Model of the SCT detectors and electronics for the ATLAS simulation using Geant4[R/OL]. revised version number 1 submitted on 2001-06-18 18:53:11. Geneva: CERN, 2001. <https://cds.cern.ch/record/684197>.
- [76] LAMPL W, LAPLACE S, LECHOWSKI M, et al. Digitization of LAr calorimeter for CSC simulations[R/OL]. This is the calo CSC note calo-5. Geneva: CERN, 2007. <https://cds.cern.ch/record/1057879>.
- [77] REBUZZI D, ASSAMAGAN K A, DI SIMONE A, et al. Geant4 Muon Digitization in the ATHENA Framework[R/OL]. Geneva: CERN, 2007. <https://cds.cern.ch/record/1010495>.
- [78] BARBERIO E, BOUDREAU J, BUTLER B, et al. The Geant4-Based ATLAS Fast Electromagnetic Shower Simulation[R/OL]. Geneva: CERN, 2008. <https://cds.cern.ch/record/1064665>. DOI: 10.1142/9789812819093\_0133.
- [79] BARBERIO E, BOUDREAU J, BUTLER B, et al. Fast shower simulation in the ATLAS calorimeter[J/OL]. *J. Phys.: Conf. Ser.*, 2008, 119: 032008. <https://cds.cern.ch/record/1176890>. DOI: 10.1088/1742-6596/119/3/032008.
- [80] GROUP U H. ATLFAST[EB/OL]. <http://www.hep.ucl.ac.uk/atlas/atlfast/>.
- [81] RICHTER-WAS E, FROIDEVAUX D, POGGIOLI L. ATLFAST 2.0 a fast simulation package for ATLAS[R/OL]. Geneva: CERN, 1998. <https://cds.cern.ch/record/683751>.
- [82] MECHNICH J. FATRAS - the ATLAS Fast Track Simulation project[R/OL]. Geneva: CERN, 2011. <https://cds.cern.ch/record/1321871>.
- [83] AABOUD M, AAD G, ABBOTT B, et al. Performance of the ATLAS track reconstruction algorithms in dense environments in LHC Run 2[J]. *The European Physical Journal C*, 2017, 77(10): 673.
- [84] CORNELISSEN T, ELSING M, GAVRILENKO I, et al. The new ATLAS track reconstruction (NEWT)[J/OL]. *Journal of Physics: Conference Series*, 2008, 119(3): 032014. <https://dx.doi.org/10.1088/1742-6596/119/3/032014>. DOI: 10.1088/1742-6596/119/3/032014.
- [85] PEI Y, BISWAS S, FUSSELL D S, et al. An Elementary Introduction to Kalman Filtering[Z]. 2019. arXiv: 1710.04055 [eess.SY].

- 5027 [86] FRUEHWIRTH R. Application of Kalman filtering to track and vertex fitting[Z].  
5028 1987. DOI: 10.1016/0168-9002(87)90887-4.
- 5029 [87] COLLABORATION T A. A neural network clustering algorithm for the ATLAS sil-  
5030 icon pixel detector[J/OL]. Journal of Instrumentation, 2014, 9(09): P09009-P09009.  
5031 <https://doi.org/10.1088/1748-0221/9/09/p09009>. DOI: 10.1088/174  
5032 8-0221/9/09/p09009.
- 5033 [88] Electron and photon reconstruction and performance in ATLAS using a dynamical,  
5034 topological cell clustering-based approach[R/OL]. Geneva: CERN, 2017. [https://cd  
5035 s.cern.ch/record/2298955](https://cds.cern.ch/record/2298955).
- 5036 [89] COLLABORATION T A. Electron efficiency measurements with the ATLAS de-  
5037 tector using 2012 LHC proton–proton collision data[J/OL]. The European Physical  
5038 Journal C, 2017, 77(3). <https://doi.org/10.1140/epjc/s10052-017-4756-2>.  
5039 DOI: 10.1140/epjc/s10052-017-4756-2.
- 5040 [90] COLLABORATION T A. Measurement of the photon identification efficiencies with  
5041 the ATLAS detector using LHC Run-1 data[J/OL]. The European Physical Journal  
5042 C, 2016, 76(12). <https://doi.org/10.1140/epjc/s10052-016-4507-9>. DOI:  
5043 10.1140/epjc/s10052-016-4507-9.
- 5044 [91] COLLABORATION T A. Electron reconstruction and identification in the ATLAS  
5045 experiment using the 2015 and 2016 LHC proton–proton collision data at  $\sqrt{s} = 13$   
5046 TeV[J/OL]. The European Physical Journal C, 2019, 79(8): 639. [https://doi.org/10  
5047 .1140/epjc/s10052-019-7140-6](https://doi.org/10.1140/epjc/s10052-019-7140-6). DOI: 10.1140/epjc/s10052-019-7140-6.
- 5048 [92] COLLABORATION T A. Topological cell clustering in the ATLAS calorimeters  
5049 and its performance in LHC Run 1[J/OL]. The European Physical Journal C, 2017,  
5050 77(7). <https://doi.org/10.1140/epjc/s10052-017-5004-5>. DOI: 10.1140/epjc  
5051 /s10052-017-5004-5.
- 5052 [93] HE F. High Precision Electron and Muon Reconstruction Performance with ATLAS  
5053 at LHC Run-2[R/OL]. Geneva: CERN, 2022. <https://cds.cern.ch/record/2841383>.  
5054 DOI: 10.22323/1.414.0675.
- 5055 [94] COLLABORATION T A. Electron reconstruction and identification in the ATLAS  
5056 experiment using the 2015 and 2016 LHC data[J/OL]. The European Physical Jour-  
5057 nal C, 2019, 79(8). <https://doi.org/10.1140/epjc/s10052-019-7140-6>. DOI:

- 10.1140/epjc/s10052-019-7140-6.
- [95] HOECKER A, SPECKMAYER P, STELZER J, et al. TMVA - Toolkit for Multivariate Data Analysis[Z]. 2009. arXiv: physics/0703039 [physics.data-an].
- [96] COLLABORATION A. EGAM-2022-02[EB/OL]. CERN. 2022. <https://atlas.web.cern.ch/Atlas/GROUPS/PHYSICS/PLOTS/EGAM-2022-02/>.
- [97] COLLABORATION T A. Electron and photon performance measurements with the ATLAS detector using the 2015 – 2017 LHC proton-proton collision data[J/OL]. Journal of Instrumentation, 2019, 14(12): P12006-P12006. <https://doi.org/10.1088/1748-0221/14/12/p12006>. DOI: 10.1088/1748-0221/14/12/p12006.
- [98] COLLABORATION A. EGAM-2021-01[EB/OL]. CERN. 2021. <http://atlas.web.cern.ch/Atlas/GROUPS/PHYSICS/PAPERS/EGAM-2021-01/>.
- [99] ZHANG Y, LI L, BERNARDI G. Improvement of photon ID against electron fakes of the ATLAS experiment[R/OL]. Geneva: CERN, 2022. <https://cds.cern.ch/record/2808007>.
- [100] GUO F, FANG Y, LOU X. Topo-cluster variable performance study with Radiative Z events in 13TeV ATLAS data[R/OL]. Geneva: CERN, 2021. <https://cds.cern.ch/record/2774734>.
- [101] SJÖSTRAND T, MRENNA S, SKANDS P. A brief introduction to PYTHIA 8.1 [J/OL]. Computer Physics Communications, 2008, 178(11): 852-867. <https://doi.org/10.1016/j.cpc.2008.01.036>. DOI: 10.1016/j.cpc.2008.01.036.
- [102] ALIOLI S, NASON P, OLEARI C, et al. A general framework for implementing NLO calculations in shower Monte Carlo programs: the POWHEG BOX[J/OL]. Journal of High Energy Physics, 2010, 2010(6). [https://doi.org/10.1007/jhep06\(2010\)043](https://doi.org/10.1007/jhep06(2010)043). DOI: 10.1007/jhep06(2010)043.
- [103] CORNELISSEN T, ELSING M, FLEISCHMANN S, et al. Concepts, Design and Implementation of the ATLAS New Tracking (NEWT)[R/OL]. Geneva: CERN, 2007. <https://cds.cern.ch/record/1020106>.
- [104] Performance of the ATLAS Silicon Pattern Recognition Algorithm in Data and Simulation at  $\sqrt{s} = 7$  TeV[R/OL]. Geneva: CERN, 2010. <https://cds.cern.ch/record/1281363>.

- 5089 [105] ILLINGWORTH J, KITTLER J. A survey of the hough transform[J/OL]. Computer  
5090 Vision, Graphics, and Image Processing, 1988, 44(1): 87-116. <https://www.sciencedirect.com/science/article/pii/S0734189X88800331>. DOI: [https://doi.org/10.1016/S0734-189X\(88\)80033-1](https://doi.org/10.1016/S0734-189X(88)80033-1).
- 5093 [106] COLLABORATION T A. Muon reconstruction performance of the ATLAS detector  
5094 in proton–proton collision data at  $\sqrt{s} = 13$  TeV[J/OL]. The European Physical  
5095 Journal C, 2016, 76(5). <https://doi.org/10.1140/epjc/s10052-016-4120-y>. DOI:  
5096 10.1140/epjc/s10052-016-4120-y.
- 5097 [107] COLLABORATION T A. MUON-2018-03[EB/OL]. 2018. <https://atlas.web.cern.ch/Atlas/GROUPS/PHYSICS/PAPERS/MUON-2018-03/>.
- 5099 [108] CACCIARI M, SALAM G P, SOYEZ G. The anti- $k_T$  jet clustering algorithm[J/OL].  
5100 Journal of High Energy Physics, 2008, 2008(04): 063-063. <https://doi.org/10.1088/1126-6708/2008/04/063>. DOI: 10.1088/1126-6708/2008/04/063.
- 5102 [109] COLLABORATION T A. Identification and energy calibration of hadronically decaying  
5103 tau leptons with the ATLAS experiment in pp collisions at  $\sqrt{s} = 8$  TeV[J/OL].  
5104 The European Physical Journal C, 2015, 75(7). <https://doi.org/10.1140/epjc/s10052-015-3500-z>. DOI: 10.1140/epjc/s10052-015-3500-z.
- 5106 [110] Measurement of the tau lepton reconstruction and identification performance in the  
5107 ATLAS experiment using  $pp$  collisions at  $\sqrt{s} = 13$  TeV[R/OL]. Geneva: CERN,  
5108 2017. <https://cds.cern.ch/record/2261772>.
- 5109 [111] Reconstruction, Energy Calibration, and Identification of Hadronically Decaying Tau  
5110 Leptons in the ATLAS Experiment for Run-2 of the LHC[R/OL]. Geneva: CERN,  
5111 2015. <https://cds.cern.ch/record/2064383>.
- 5112 [112] COLLABORATION T A. Identification of hadronic tau lepton decays using neural  
5113 networks in the ATLAS experiment[EB/OL]. CERN. 2019. <https://atlas.web.cern.ch/Atlas/GROUPS/PHYSICS/PUBNOTES/ATL-PHYS-PUB-2019-033/>.
- 5115 [113] Jet global sequential corrections with the ATLAS detector in proton-proton collisions  
5116 at  $\sqrt{s} = 8$  TeV[R/OL]. Geneva: CERN, 2015. <https://cds.cern.ch/record/2001682>.
- 5117 [114] Data-driven determination of the energy scale and resolution of jets reconstructed  
5118 in the ATLAS calorimeters using dijet and multijet events at  $\sqrt{s} = 8$  TeV[R/OL].  
5119 Geneva: CERN, 2015. <https://cds.cern.ch/record/2008678>.

- 5120 [115] COLLABORATION T A. Jet reconstruction and performance using particle flow  
5121 with the ATLAS Detector. Jet reconstruction and performance using particle flow  
5122 with the ATLAS Detector[J/OL]. Eur. Phys. J. C, 2017, 77(7): 466. arXiv: 1703.10  
5123 485. <https://cds.cern.ch/record/2257597>. DOI: 10.1140/epjc/s10052-017-5031-2.
- 5124 [116] CACCIARI M, SALAM G P, SOYEZ G. The catchment area of jets[J/OL]. Journal  
5125 of High Energy Physics, 2008, 2008(04): 005-005. <https://doi.org/10.1088/1126-6708/2008/04/005>.  
5126 DOI: 10.1088/1126-6708/2008/04/005.
- 5127 [117] CACCIARI M, SALAM G P. Pileup subtraction using jet areas[J/OL]. Physics Let-  
5128 ters B, 2008, 659(1-2): 119-126. <https://doi.org/10.1016/j.physletb.2007.09.077>.  
5129 DOI: 10.1016/j.physletb.2007.09.077.
- 5130 [118] Monte Carlo Calibration and Combination of In-situ Measurements of Jet Energy  
5131 Scale, Jet Energy Resolution and Jet Mass in ATLAS[R/OL]. Geneva: CERN, 2015.  
5132 <https://cds.cern.ch/record/2044941>.
- 5133 [119] Optimisation of the ATLAS *b*-tagging performance for the 2016 LHC Run[R/OL].  
5134 Geneva: CERN, 2016. <https://cds.cern.ch/record/2160731>.
- 5135 [120] COLLABORATION A. Performance of *b*-jet identification in the ATLAS experi-  
5136 ment[J/OL]. Journal of Instrumentation, 2016, 11(04): P04008. <https://dx.doi.org/10.1088/1748-0221/11/04/P04008>.  
5137 DOI: 10.1088/1748-0221/11/04/P04008.
- 5138 [121] GRAVES A. Supervised Sequence Labelling with Recurrent Neural Networks:  
5139 vol. 385[M]. 2012. DOI: 10.1007/978-3-642-24797-2.
- 5140 [122] COLLABORATION T A. Identification of Jets Containing *b*-Hadrons with Recur-  
5141 rent Neural Networks at the ATLAS Experiment[R/OL]. CERN. 2017. [https://atlas  
5142 .web.cern.ch/Atlas/GROUPS/PHYSICS/PUBNOTES/ATL-PHYS-PUB-2017-003  
5143 /](https://atlas.web.cern.ch/Atlas/GROUPS/PHYSICS/PUBNOTES/ATL-PHYS-PUB-2017-003/).
- 5144 [123] COLLABORATION T A. Performance of missing transverse momentum reconstruc-  
5145 tion with the ATLAS detector using proton–proton collisions at  $\sqrt{s} = 13$  TeV[J/OL].  
5146 The European Physical Journal C, 2018, 78(11): 903. [https://doi.org/10.1140/epjc/s  
5147 10052-018-6288-9](https://doi.org/10.1140/epjc/s10052-018-6288-9). DOI: 10.1140/epjc/s10052-018-6288-9.
- 5148 [124] ATLAS Collaboration. ATLAS data quality operations and performance for  
5149 2015–2018 data-taking[J]. JINST, 2020, 15: P04003. arXiv: 1911 . 04632  
5150 [physics.ins-det]. DOI: 10.1088/1748-0221/15/04/P04003.

- 5151 [125] PileupReweighting. <https://twiki.cern.ch/twiki/bin/viewauth/AtlasProtected/ExtendedPileupReweighting>.  
5152
- 5153 [126] BALL R D, et al. Parton distributions for the LHC run II[J]. JHEP, 2015, 04: 040.  
5154 arXiv: 1410.8849 [hep-ph]. DOI: 10.1007/JHEP04(2015)040.
- 5155 [127] SJÖSTRAND T, MRENNA S, SKANDS P. A brief introduction to PYTHIA 8.1[J].  
5156 Comput. Phys. Commun., 2008, 178: 852-867. arXiv: 0710.3820 [hep-ph]. DOI:  
5157 10.1016/j.cpc.2008.01.036.
- 5158 [128] ATLAS Collaboration. The Pythia 8 A3 tune description of ATLAS minimum  
5159 bias and inelastic measurements incorporating the Donnachie–Landshoff diffractive  
5160 model. ATL-PHYS-PUB-2016-017. 2016. <https://cds.cern.ch/record/2206965>.
- 5161 [129] GEANT4 Collaboration, AGOSTINELLI S, et al. GEANT4 – a simulation toolkit[J].  
5162 Nucl. Instrum. Meth. A, 2003, 506: 250. DOI: 10.1016/S0168-9002(03)01368-8.
- 5163 [130] LAI S, LI X, LI L, et al. Search for Higgs pair production decaying to WWWW  
5164 with the final state of three leptons, missing energy and at least two jets in  $36.1 \text{ fb}^{-1}$   
5165 proton-proton data at  $\sqrt{s} = 13 \text{ TeV}$ [R/OL]. Geneva: CERN, 2016. <https://cds.cern.ch/record/2229725>.  
5166
- 5167 [131] ATLAS Collaboration. Vertex Reconstruction Performance of the ATLAS Detector  
5168 at  $\sqrt{s} = 13 \text{ TeV}$ . ATL-PHYS-PUB-2015-026. 2015. <https://cds.cern.ch/record/2037717>.  
5169
- 5170 [132] VAZQUEZ SCHROEDER T, POLIFKA R, POVEDA TORRES X, et al. Search for  
5171 the Associated Production of a Higgs Boson and a Top Quark Pair in multilepton final  
5172 states in  $80 \text{ fb}^{-1} pp$  Collisions at  $\sqrt{s} = 13 \text{ TeV}$  with the ATLAS Detector[R/OL].  
5173 Geneva: CERN, 2018. <https://cds.cern.ch/record/2314122>.
- 5174 [133] TriggerEfficiency. <https://twiki.cern.ch/twiki/bin/viewauth/Atlas/TrigGlobalEfficiencyCorrectionTool>.  
5175
- 5176 [134] OSPANOV R, ROBERTS R T, WYATT T R. Tagging non-prompt electrons and  
5177 muons[R/OL]. Geneva: CERN, 2016. <https://cds.cern.ch/record/2220954>.
- 5178 [135] COLLABORATION A. ATLAS flavour-tagging algorithms for the LHC Run 2 pp  
5179 collision dataset[J]. The European Physical Journal C, 2023, 83(7): 681.
- 5180 [136] COLLABORATION A. ATLAS Flavor-Tagging Calibration Results with  $139 \text{ fb}$   
5181 [EB/OL]. 2019. <http://atlas.web.cern.ch/Atlas/GROUPS/PHYSICS/PLOTS/F>

- 5182 TAG-2019-004/.
- 5183 [137] COLLABORATION A. Expected performance of the 2019 ATLAS b-taggers  
5184 [EB/OL]. 2019. <http://atlas.web.cern.ch/Atlas/GROUPS/PHYSICS/PLOTS/F>  
5185 TAG-2019-005/.
- 5186 [138] Overlap Removal. <https://twiki.cern.ch/twiki/bin/view/AtlasProtected/TopRecoObj>  
5187 TwikiModel#Overlap\_Removal.
- 5188 [139] AGARAS M N. Search for vector-like leptons coupling to first and second generation  
5189 Standard Model leptons in multilepton final states[R/OL]. Geneva: CERN, 2022. h  
5190 [ttps://cds.cern.ch/record/2845251](https://cds.cern.ch/record/2845251).
- 5191 [140] BRUN R, RADEMAKERS F. ROOT: An object oriented data analysis framework[J].  
5192 Nucl. Instrum. Meth. A, 1997, 389: 81-86. DOI: 10.1016/S0168-9002(97)00048-X.
- 5193 [141] ATLAS Collaboration. Luminosity determination in  $pp$  collisions at  $\sqrt{s} = 13$  TeV  
5194 using the ATLAS detector at the LHC. ATLAS-CONF-2019-021. 2019. <https://cds>  
5195 [.cern.ch/record/2677054](https://cds.cern.ch/record/2677054).
- 5196 [142] trigger recommendations. [https://twiki.cern.ch/twiki/bin/view/Atlas/TriggerRecom](https://twiki.cern.ch/twiki/bin/view/Atlas/TriggerRecommendationsForAnalysisGroupsFullRun2)  
5197 [mendationsForAnalysisGroupsFullRun2](https://twiki.cern.ch/twiki/bin/view/Atlas/TriggerRecommendationsForAnalysisGroupsFullRun2).
- 5198 [143] Muon CP group. <https://twiki.cern.ch/twiki/bin/view/AtlasProtected/MCPAnalysis>  
5199 [WinterMC16](https://twiki.cern.ch/twiki/bin/view/AtlasProtected/MCPAnalysis).
- 5200 [144] Egamma-CP. [https://twiki.cern.ch/twiki/bin/view/AtlasProtected/LatestRecommen](https://twiki.cern.ch/twiki/bin/view/AtlasProtected/LatestRecommendationsElectronIDRun2)  
5201 [dationsElectronIDRun2](https://twiki.cern.ch/twiki/bin/view/AtlasProtected/LatestRecommendationsElectronIDRun2).
- 5202 [145] ATLAS Collaboration. Jet energy scale measurements and their systematic uncer-  
5203 tainties in proton–proton collisions at  $\sqrt{s} = 13$  TeV with the ATLAS detector[J].  
5204 Phys. Rev. D, 2017, 96: 072002. arXiv: 1703.09665 [hep-ex]. DOI: 10.1103/Ph  
5205 ysRevD.96.072002.
- 5206 [146] Btagging Calibration. <https://twiki.cern.ch/twiki/bin/view/AtlasProtected/BTagging>  
5207 [\\_Calibration\\_December2020CDI](https://twiki.cern.ch/twiki/bin/view/AtlasProtected/BTagging).
- 5208 [147] GRAZZINI M, HEINRICH G, JONES S, et al. Higgs boson pair production at NNLO  
5209 with top quark mass effects[J/OL]. Journal of High Energy Physics, 2018, 2018(5):  
5210 59. [https://doi.org/10.1007/JHEP05\(2018\)059](https://doi.org/10.1007/JHEP05(2018)059). DOI: 10.1007/JHEP05(2018)059.
- 5211 [148] LHC Higgs Cross Section HH Sub-group[EB/OL]. <https://twiki.cern.ch/twiki/bin>  
5212 [/view/LHCPhysics/LHCHWGHH?redirectedfrom=LHCPhysics.LHCHXSWGHH](https://twiki.cern.ch/twiki/bin/view/LHCPhysics/LHCHWGHH?redirectedfrom=LHCPhysics.LHCHXSWGHH).

- 5213 [149] CRANMER K, LEWIS G, MONETA L, et al. HistFactory: A tool for creating sta-  
5214 tistical models for use with RooFit and RooStats. New York, 2012. [https://cds.cern.c](https://cds.cern.ch/record/1456844)  
5215 [h/record/1456844](https://cds.cern.ch/record/1456844).
- 5216 [150] READ A L. Presentation of search results: the CLs technique[J]. Journal of Physics  
5217 G: Nuclear and Particle Physics, 2002, 28(10): 2693.
- 5218 [151] TRexFitter framework documentatio. [https://trexfitter-d](https://trexfitter-docs.web.cern.ch/trexfitter-d)  
5219 [ocs/](https://trexfitter-docs.web.cern.ch/trexfitter-d).
- 5220 [152] TRexFitter framework gitlab project.
- 5221 [153] COLLABORATION T A. Search for resonant and non-resonant Higgs boson pair  
5222 production in the  $b\bar{b}\tau^+\tau^-$  decay channel using 13 TeV  $pp$  collision data from the  
5223 ATLAS detector[J]. Journal of High Energy Physics, 2023, 2023(7): 40.
- 5224 [154] ATLAS Collaboration. Luminosity determination in  $pp$  collisions at  $\sqrt{s} = 13$  TeV  
5225 using the ATLAS detector at the LHC[J]. 2022. arXiv: 2212.09379 [hep-ex].
- 5226 [155] BALL R D, et al. Parton distributions with LHC data[J]. Nucl. Phys. B, 2013, 867:  
5227 244. arXiv: 1207.1303 [hep-ph]. DOI: 10.1016/j.nuclphysb.2012.10.003.
- 5228 [156] LANGE D J. The EvtGen particle decay simulation package[J]. Nucl. Instrum. Meth.  
5229 A, 2001, 462: 152. DOI: 10.1016/S0168-9002(01)00089-4.
- 5230 [157] BOTHMANN E, et al. Event generation with Sherpa 2.2[J]. SciPost Phys., 2019,  
5231 7(3): 034. arXiv: 1905.09127 [hep-ph]. DOI: 10.21468/SciPostPhys.7.3.034.
- 5232 [158] ALIOLI S, NASON P, OLEARI C, et al. A general framework for implementing  
5233 NLO calculations in shower Monte Carlo programs: the POWHEG BOX[J]. JHEP,  
5234 2010, 06: 043. arXiv: 1002.2581 [hep-ph]. DOI: 10.1007/JHEP06(2010)043.
- 5235 [159] BUCKLEY A, FERRANDO J, LLOYD S, et al. LHAPDF6: parton density ac-  
5236 cess in the LHC precision era[J]. Eur. Phys. J. C, 2015, 75: 132. arXiv: 1412.7420  
5237 [hep-ph]. DOI: 10.1140/epjc/s10052-015-3318-8.
- 5238 [160] BUTTERWORTH J, et al. PDF4LHC recommendations for LHC Run II[J]. J. Phys.  
5239 G, 2016, 43: 023001. arXiv: 1510.03865 [hep-ph]. DOI: 10.1088/0954-3899/43  
5240 /2/023001.
- 5241 [161] ATLAS Collaboration. ATLAS Pythia 8 tunes to 7 TeV data. ATL-PHYS-PUB-2014-  
5242 021. 2014. <https://cds.cern.ch/record/1966419>.
- 5243 [162] ATLAS Collaboration. Summary of ATLAS Pythia 8 tunes. ATL-PHYS-PUB-2012-

- 5244 003. 2012. <https://cds.cern.ch/record/1474107>.
- 5245 [163] GRAZZINI M, HEINRICH G, JONES S, et al. Higgs boson pair production at NNLO  
5246 with top quark mass effects[J]. JHEP, 2018, 05: 059. arXiv: 1803.02463 [hep-ph].  
5247 DOI: 10.1007/JHEP05(2018)059.
- 5248 [164] BÄHR M, et al. Herwig++ physics and manual[J]. Eur. Phys. J. C, 2008, 58: 639.  
5249 arXiv: 0803.0883 [hep-ph]. DOI: 10.1140/epjc/s10052-008-0798-9.
- 5250 [165] ALWALL J, FREDERIX R, FRIXIONE S, et al. The automated computation of tree-  
5251 level and next-to-leading order differential cross sections, and their matching to par-  
5252 ton shower simulations[J]. JHEP, 2014, 07: 079. arXiv: 1405.0301 [hep-ph]. DOI:  
5253 10.1007/JHEP07(2014)079.
- 5254 [166] BISHARA F, CONTINO R, ROJO J. Higgs pair production in vector-boson fusion  
5255 at the LHC and beyond[J]. Eur. Phys. J. C, 2017, 77(7): 481. arXiv: 1611.03860  
5256 [hep-ph]. DOI: 10.1140/epjc/s10052-017-5037-9.
- 5257 [167] P. Nason. A New method for combining NLO QCD with shower Monte Carlo algo-  
5258 rithms[J]. JHEP, 2004, 11: 040. arXiv: hep-ph/0409146 [hep-ph]. DOI: 10.1088  
5259 /1126-6708/2004/11/040.
- 5260 [168] S. Frixione, P. Nason and C. Oleari. Matching NLO QCD computations with parton  
5261 shower simulations: the POWHEG method[J]. JHEP, 2007, 11: 070. arXiv: 0709.20  
5262 92 [hep-ph]. DOI: 10.1088/1126-6708/2007/11/070.
- 5263 [169] ALIOLI S, NASON P, OLEARI C, et al. A general framework for implementing  
5264 NLO calculations in shower Monte Carlo programs: the POWHEG BOX[J]. JHEP,  
5265 2010, 06: 043. arXiv: 1002.2581 [hep-ph]. DOI: 10.1007/JHEP06(2010)043.
- 5266 [170] NNPDF Collaboration. Parton distributions for the LHC Run II[J]. 2014. arXiv: 141  
5267 0.8849 [hep-ph].
- 5268 [171] SJOSTRAND T, et al. An Introduction to PYTHIA 8.2[J]. Comput.Phys.Commun.,  
5269 2015, 191: 159-177. arXiv: 1410.3012 [hep-ph].
- 5270 [172] ATLAS Collaboration. ATLAS Pythia 8 tunes to 7 TeV data. ATL-PHYS-PUB-2014-  
5271 021. 2014. <https://cds.cern.ch/record/1966419>.
- 5272 [173] GLEISBERG T, HÖCHE S. Comix, a new matrix element generator[J]. JHEP, 2008,  
5273 12: 039. arXiv: 0808.3674 [hep-ph]. DOI: 10.1088/1126-6708/2008/12/039.
- 5274 [174] BUCCIONI F, LANG J N, LINDERT J M, et al. OpenLoops 2[J]. Eur. Phys. J. C,

- 5275 2019, 79(10): 866. arXiv: 1907.13071 [hep-ph]. DOI: 10.1140/epjc/s10052-019  
5276 -7306-2.
- 5277 [175] CASCIOLI F, MAIERHÖFER P, POZZORINI S. Scattering Amplitudes with Open  
5278 Loops[J]. Phys. Rev. Lett., 2012, 108: 111601. arXiv: 1111.5206 [hep-ph]. DOI:  
5279 10.1103/PhysRevLett.108.111601.
- 5280 [176] DENNER A, DITTMAIER S, HOFER L. COLLIER: A fortran-based complex one-  
5281 loop library in extended regularizations[J]. Comput. Phys. Commun., 2017, 212: 220-  
5282 238. arXiv: 1604.06792 [hep-ph]. DOI: 10.1016/j.cpc.2016.10.013.
- 5283 [177] ATLAS Collaboration. Search for resonant and non-resonant Higgs boson pair pro-  
5284 duction in the  $b\bar{b}\tau^+\tau^-$  decay channel using 13 TeV  $pp$  collision data from the ATLAS  
5285 detector[J]. 2022. arXiv: 2209.10910 [hep-ex].
- 5286 [178] ATLAS Collaboration. Electron reconstruction and identification efficiency mea-  
5287 surements with the ATLAS detector using the 2011 LHC proton-proton collision  
5288 data[J]. Eur. Phys. J. C, 2014, 74: 2941. arXiv: 1404.2240 [hep-ex]. DOI: 10.11  
5289 40/epjc/s10052-014-2941-0.
- 5290 [179] ATLAS Collaboration. Muon reconstruction performance of the ATLAS detector in  
5291 proton-proton collision data at  $\sqrt{s} = 13$  TeV[J]. Eur. Phys. J. C, 2016, 76: 292. arXiv:  
5292 1603.05598 [hep-ex]. DOI: 10.1140/epjc/s10052-016-4120-y.
- 5293 [180] ATLAS Collaboration. Recommended Isolation Working Points[J/OL]. [https://twiki.cern.ch/twiki/bin/viewauth/AtlasProtected/RecommendedIsolationWPs#Muon\\_working\\_points](https://twiki.cern.ch/twiki/bin/viewauth/AtlasProtected/RecommendedIsolationWPs#Muon_working_points).  
5294  
5295
- 5296 [181] AAD G, et al. Identification and energy calibration of hadronically decaying tau lep-  
5297 tons with the ATLAS experiment in  $pp$  collisions at  $\sqrt{s}=8$  TeV[J]. Eur. Phys. J., 2015,  
5298 C75(7): 303. arXiv: 1412.7086 [hep-ex]. DOI: 10.1140/epjc/s10052-015-3500-  
5299 Z.
- 5300 [182] BETTI A, BEVAN A J, BOKAN P, et al. Searches for Higgs boson pair production  
5301 in the  $b\bar{b}\tau^+\tau^-$  final state with 139 fb<sup>-1</sup> of  $pp$  collision data with the ATLAS detector  
5302 [R/OL]. Geneva: CERN, 2020. <https://cds.cern.ch/record/2743097>.
- 5303 [183] CACCIARI M, SALAM G P, SOYEZ G. The anti- $k_t$  jet clustering algorithm[J].  
5304 JHEP, 2008, 04: 063. arXiv: 0802.1189 [hep-ph]. DOI: 10.1088/1126-6708/200  
5305 8/04/063.

- 5306 [184] AABOUD M, et al. Jet reconstruction and performance using particle flow with  
5307 the ATLAS Detector[J]. Eur. Phys. J., 2017, C77(7):466. arXiv: 1703 . 10485  
5308 [hep-ex]. DOI: 10.1140/epjc/s10052-017-5031-2.
- 5309 [185] ATLAS Collaboration. 2015 start-up trigger menu and initial performance assess-  
5310 ment of the ATLAS trigger using Run-2 data. ATL-DAQ-PUB-2016-001. 2016. ht  
5311 tps://cds.cern.ch/record/2136007.
- 5312 [186] ATLAS Collaboration. Jet Calibration and Systematic Uncertainties for Jets Recon-  
5313 structed in the ATLAS Detector at  $\sqrt{s} = 13$  TeV. ATL-PHYS-PUB-2015-015. 2015.  
5314 https://cds.cern.ch/record/2037613.
- 5315 [187] ATLAS Collaboration. ATLAS  $b$ -jet identification performance and efficiency mea-  
5316 surement with  $t\bar{t}$  events in  $pp$  collisions at  $\sqrt{s} = 13$  TeV[J]. Eur. Phys. J. C, 2019, 79:  
5317 970. arXiv: 1907.05120 [hep-ex]. DOI: 10.1140/epjc/s10052-019-7450-8.
- 5318 [188] ATLAS Collaboration. Optimisation and performance studies of the ATLAS  $b$ -  
5319 tagging algorithms for the 2017-18 LHC run. ATL-PHYS-PUB-2017-013. 2017. ht  
5320 tps://cds.cern.ch/record/2273281.
- 5321 [189] ATLAS Collaboration. Identification of Jets Containing  $b$ -Hadrons with Recurrent  
5322 Neural Networks at the ATLAS Experiment. ATL-PHYS-PUB-2017-003. 2017. ht  
5323 tps://cds.cern.ch/record/2255226.
- 5324 [190] AABOUD M, et al. Performance of missing transverse momentum reconstruction  
5325 with the ATLAS detector using proton-proton collisions at  $\sqrt{s} = 13$  TeV[J]. Eur. Phys.  
5326 J., 2018, C78(11):903. arXiv: 1802.08168 [hep-ex]. DOI: 10.1140/epjc/s10052  
5327 -018-6288-9.
- 5328 [191] ATLAS Collaboration. Recommended Overlap Removal Working Points[J/OL]. ht  
5329 tps://indico.cern.ch/event/631313/contributions/2683959/attachments/1518878/237  
5330 3377/Farrell\_ORTools\_ftaghbb.pdf.
- 5331 [192] ELAGIN A, MURAT P, PRANKO A, et al. A New Mass Reconstruction Technique  
5332 for Resonances Decaying to di-tau[J]. Nucl. Instrum. Meth. A, 2011, 654:481-489.  
5333 arXiv: 1012.4686 [hep-ex]. DOI: 10.1016/j.nima.2011.07.009.
- 5334 [193] ATLAS Collaboration. A search for resonant and non-resonant Higgs boson pair  
5335 production in the  $b\bar{b}\tau^+\tau^-$  decay channel in  $pp$  collisions at  $\sqrt{s} = 13$  TeV with  
5336 the ATLAS detector[J]. Phys. Rev. Lett., 2018, 121:191801. arXiv: 1808.00336

- 5337 [hep-ex]. DOI: 10.1103/PhysRevLett.121.191801.
- 5338 [194] Bbtautau ML Toolkit. HBBHtautau ML Toolkit[Z]. <https://gitlab.cern.ch/bmoser/hbbhatautau/mltoolkit>. CERN GitLab repository. 2023.
- 5339
- 5340 [195] BERNACIAK C, BUSCHMANN M S A, BUTTER A, et al. Fox-Wolfram moments
- 5341 in Higgs physics[J/OL]. Physical Review D, 2013, 87(7). [https://doi.org/10.1103/](https://doi.org/10.1103/PhysRevD.87.073014)
- 5342 [%2Fphysrevd.87.073014](https://doi.org/10.1103/PhysRevD.87.073014). DOI: 10.1103/physrevd.87.073014.
- 5343 [196] BARLOW R, BEESTON C. Fitting using finite Monte Carlo samples[J]. Computer
- 5344 Physics Communications, 1993, 77(2): 219-228.
- 5345 [197] G. Avoni et al. The new LUCID-2 detector for luminosity measurement and moni-
- 5346 toring in ATLAS[J]. JINST, 2018, 13(07): P07017. DOI: 10.1088/1748-0221/13/07
- 5347 /P07017.
- 5348 [198] ATLAS Collaboration. Observation of a new particle in the search for the Standard
- 5349 Model Higgs boson with the ATLAS detector at the LHC[J]. Phys. Lett. B, 2012,
- 5350 716: 1. arXiv: 1207.7214 [hep-ex]. DOI: 10.1016/j.physletb.2012.08.020.
- 5351 [199] CMS Collaboration. Observation of a new boson at a mass of 125 GeV with the
- 5352 CMS experiment at the LHC[J]. Phys. Lett. B, 2012, 716: 30. arXiv: 1207.7235
- 5353 [hep-ex]. DOI: 10.1016/j.physletb.2012.08.021.
- 5354 [200] L. Evans and P. Bryant. LHC Machine[J]. JINST, 2008, 3: S08001. DOI: 10.1088/1
- 5355 748-0221/3/08/S08001.
- 5356 [201] GLASHOW S L. Partial-symmetries of weak interactions[J]. Nucl. Phys., 1961, 22:
- 5357 579-588. DOI: 10.1016/0029-5582(61)90469-2.
- 5358 [202] SALAM A. Weak and Electromagnetic Interactions[J]. Conf. Proc. C, 1968, 680519:
- 5359 Proceedings of the eighth Nobel symposium. DOI: 10.1142/9789812795915\_0034.
- 5360 [203] WEINBERG S. A Model of Leptons[J]. Phys. Rev. Lett., 1967, 19: 1264-1266. DOI:
- 5361 10.1103/PhysRevLett.19.1264.
- 5362 [204] 'T HOOFT G, VELTMAN M J G. Regularization and Renormalization of Gauge
- 5363 Fields[J]. Nucl. Phys. B, 1972, 44: 189-213. DOI: 10.1016/0550-3213(72)90279-9.
- 5364 [205] ENGLERT F, BROUT R. Broken Symmetry and the Mass of Gauge Vector Mesons
- 5365 [J]. Phys. Rev. Lett., 1964, 13: 321-323. DOI: 10.1103/PhysRevLett.13.321.
- 5366 [206] HIGGS P W. Broken symmetries, massless particles and gauge fields[J]. Phys. Lett.,
- 5367 1964, 12: 132-133. DOI: 10.1016/0031-9163(64)91136-9.

- 5368 [207] HIGGS P W. Broken Symmetries and the Masses of Gauge Bosons[J]. Phys. Rev.  
5369 Lett., 1964, 13: 508-509. DOI: 10.1103/PhysRevLett.13.508.
- 5370 [208] HIGGS P W. Spontaneous Symmetry Breakdown without Massless Bosons[J]. Phys.  
5371 Rev., 1966, 145: 1156-1163. DOI: 10.1103/PhysRev.145.1156.
- 5372 [209] GURALNIK G S, HAGEN C R, KIBBLE T W B. Global Conservation Laws and  
5373 Massless Particles[J]. Phys. Rev. Lett., 1964, 13: 585. DOI: 10.1103/PhysRevLett.1  
5374 3.585.
- 5375 [210] ATLAS and CMS Collaborations. Combined Measurement of the Higgs Boson Mass  
5376 in  $pp$  Collisions at  $\sqrt{s} = 7$  and 8 TeV with the ATLAS and CMS Experiments[J].  
5377 Phys. Rev. Lett., 2015, 114: 191803. arXiv: 1503.07589 [hep-ex]. DOI: 10.1103  
5378 /PhysRevLett.114.191803.
- 5379 [211] Particle Data Group, WORKMAN R L, et al. Review of Particle Physics[J]. PTEP,  
5380 2022, 2022: 083C01. DOI: 10.1093/ptep/ptac097.
- 5381 [212] ATLAS Collaboration. Search for Higgs boson pair production in the two bottom  
5382 quarks plus two photons final state in  $pp$  collisions at  $\sqrt{s} = 13$  TeV with the ATLAS  
5383 detector[J]. Phys. Rev. D, 2021, 106: 052001. arXiv: 2112.11876 [hep-ex]. DOI:  
5384 10.1103/PhysRevD.106.052001.
- 5385 [213] ATLAS Collaboration. Search for non-resonant pair production of Higgs bosons in  
5386 the  $b\bar{b}b\bar{b}$  final state in  $pp$  collisions at  $\sqrt{s} = 13$  TeV with the ATLAS detector. 2023.  
5387 arXiv: 2301.03212 [hep-ex].
- 5388 [214] DEGRASSI G, GIARDINO P P, MALTONI F, et al. Probing the Higgs self coupling  
5389 via single Higgs production at the LHC[J]. JHEP, 2016, 12: 080. arXiv: 1607.04251  
5390 [hep-ph]. DOI: 10.1007/JHEP12(2016)080.
- 5391 [215] MALTONI F, PAGANI D, SHIVAJI A, et al. Trilinear Higgs coupling determina-  
5392 tion via single-Higgs differential measurements at the LHC[J]. Eur. Phys. J. C, 2017,  
5393 77(12): 887. arXiv: 1709.08649 [hep-ph]. DOI: 10.1140/epjc/s10052-017-5410-  
5394 8.
- 5395 [216] DI VITA S, GROJEAN C, PANICO G, et al. A global view on the Higgs self-coupling  
5396 [J]. JHEP, 2017, 09: 069. arXiv: 1704.01953 [hep-ph]. DOI: 10.1007/JHEP09(2  
5397 017)069.
- 5398 [217] GORBAHN M, HAISCH U. Indirect probes of the trilinear Higgs coupling:  $gg \rightarrow h$

- 5399 and  $h \rightarrow \gamma\gamma$ [J]. JHEP, 2016, 10: 094. arXiv: 1607.03773 [hep-ph]. DOI: 10.100  
5400 7/JHEP10(2016)094.
- 5401 [218] BIZON W, GORBAHN M, HAISCH U, et al. Constraints on the trilinear Higgs  
5402 coupling from vector boson fusion and associated Higgs production at the LHC[J].  
5403 JHEP, 2017, 07: 083. arXiv: 1610.05771 [hep-ph]. DOI: 10.1007/JHEP07(2017  
5404 )083.
- 5405 [219] MCCULLOUGH M. An Indirect Model-Dependent Probe of the Higgs Self-  
5406 Coupling[J]. Phys. Rev. D, 2014, 90(1): 015001. arXiv: 1312.3322 [hep-ph].  
5407 DOI: 10.1103/PhysRevD.90.015001.
- 5408 [220] ATLAS Collaboration. A detailed map of Higgs boson interactions by the ATLAS  
5409 experiment ten years after the discovery[J]. Nature, 2022, 607: 52. arXiv: 2207.00092  
5410 [hep-ex]. DOI: 10.1038/s41586-022-04893-w.
- 5411 [221] ATLAS Collaboration. Combination of searches for Higgs boson pairs in  $pp$  colli-  
5412 sions at  $\sqrt{s} = 13$  TeV with the ATLAS detector[J]. Phys. Lett. B, 2020, 800: 135103.  
5413 arXiv: 1906.02025 [hep-ex]. DOI: 10.1016/j.physletb.2019.135103.
- 5414 [222] CMS Collaboration. A portrait of the Higgs boson by the CMS experiment ten years  
5415 after the discovery[J]. Nature, 2022, 607: 60. arXiv: 2207.00043 [hep-ex]. DOI:  
5416 10.1038/s41586-022-04892-x.
- 5417 [223] LHC Higgs Cross Section Working Group, HEINEMEYER S, et al. Handbook  
5418 of LHC Higgs Cross Sections: 3. Higgs Properties[J]. CERN-2013-004, CERN,  
5419 Geneva, 2013. arXiv: 1307.1347 [hep-ph]. DOI: 10.5170/CERN-2013-004.
- 5420 [224] LHC Higgs Cross Section Working Group, de FLORIAN D, et al. Handbook of LHC  
5421 Higgs Cross Sections: 4. Deciphering the Nature of the Higgs Sector[J]. CERN-2017-  
5422 002-M, 2017. arXiv: 1610.07922 [hep-ph]. DOI: 10.23731/CYRM-2017-002.
- 5423 [225] DI MICCO B, et al. Higgs boson potential at colliders: Status and perspectives[J].  
5424 Reviews in Physics, 2020, 5: 100045. arXiv: 1910.00012. DOI: [https://doi.org/10.1  
5425 016/j.revip.2020.100045](https://doi.org/10.1016/j.revip.2020.100045).
- 5426 [226] DAWSON S, DITTMAYER S, SPIRA M. Neutral Higgs boson pair production at  
5427 hadron colliders: QCD corrections[J]. Phys. Rev. D, 1998, 58: 115012. arXiv: hep-p  
5428 h/9805244 [hep-ph]. DOI: 10.1103/PhysRevD.58.115012.
- 5429 [227] BOROWKA S, GREINER N, HEINRICH G, et al. Higgs Boson Pair Production

- 5430 in Gluon Fusion at Next-to-Leading Order with Full Top-Quark Mass Dependence  
5431 [J]. Phys. Rev. Lett., 2016, 117(1): 012001. arXiv: 1604.06447 [hep-ph]. DOI:  
5432 10.1103/PhysRevLett.117.012001.
- 5433 [228] BAGLIO J, CAMPANARIO F, GLAUS S, et al. Gluon fusion into Higgs pairs at  
5434 NLO QCD and the top mass scheme[J]. Eur. Phys. J. C, 2019, 79(6): 459. arXiv:  
5435 1811.05692 [hep-ph]. DOI: 10.1140/epjc/s10052-019-6973-3.
- 5436 [229] ANDERSEN J R, et al. Les Houches 2015: Physics at TeV Colliders Standard Model  
5437 Working Group Report[C]//9th Les Houches Workshop on Physics at TeV Colliders  
5438 (PhysTeV 2015) Les Houches, France, June 1-19, 2015. 2016. arXiv: 1605.04692  
5439 [hep-ph].
- 5440 [230] ATLAS Collaboration. Constraint of the Higgs boson self-coupling from Higgs  
5441 boson differential production and decay measurements[R/OL]. ATL-PHYS-PUB-  
5442 2019-009. Geneva: CERN, 2019. <https://cds.cern.ch/record/2667570>.
- 5443 [231] LHC Higgs Cross Section Working Group. Modelling of the single-Higgs simplified  
5444 template cross-sections (STXS 1.2) for the determination of the Higgs boson trilinear  
5445 self-coupling[R/OL]. LHCHWG-2022-002. Geneva: CERN, 2022. [https://cds.cern](https://cds.cern.ch/record/2803606)  
5446 [.ch/record/2803606](https://cds.cern.ch/record/2803606).
- 5447 [232] ATLAS Collaboration. The ATLAS Experiment at the CERN Large Hadron Collider  
5448 [J]. JINST, 2008, 3: S08003. DOI: 10.1088/1748-0221/3/08/S08003.
- 5449 [233] ATLAS Collaboration. ATLAS Insertable B-Layer Technical Design Report. 2010.  
5450 <https://cds.cern.ch/record/1291633>.
- 5451 [234] ABBOTT B, et al. Production and integration of the ATLAS Insertable B-Layer[J].  
5452 JINST, 2018, 13(05): T05008. arXiv: 1803.00844 [physics.ins-det]. DOI:  
5453 10.1088/1748-0221/13/05/t05008.
- 5454 [235] ATLAS Collaboration. Performance of the ATLAS trigger system in 2015[J]. Eur.  
5455 Phys. J. C, 2017, 77: 317. arXiv: 1611.09661 [hep-ex]. DOI: 10.1140/epjc/s100  
5456 52-017-4852-3.
- 5457 [236] ATLAS Collaboration. The ATLAS Collaboration Software and Firmware. ATL-  
5458 SOFT-PUB-2021-001. 2021. <https://cds.cern.ch/record/2767187>.
- 5459 [237] ATLAS Collaboration. Measurement of the properties of Higgs boson production at  
5460  $\sqrt{s} = 13$  TeV in the  $H \rightarrow \gamma\gamma$  channel using  $139 \text{ fb}^{-1}$  of  $pp$  collision data with the

- 5461 ATLAS experiment[J]. 2022. arXiv: 2207.00348 [hep-ex].
- 5462 [238] ATLAS Collaboration. Higgs boson production cross-section measurements and  
5463 their EFT interpretation in the  $4\ell$  decay channel at  $\sqrt{s} = 13$  TeV with the ATLAS  
5464 detector[J]. Eur. Phys. J. C, 2020, 80:957. arXiv: 2004.03447 [hep-ex]. DOI:  
5465 10.1140/epjc/s10052-020-8227-9.
- 5466 Erratum: Eur. Phys. J. C, 2021, 81:29. DOI: 10.1140/epjc/s10052-020-08644-x.
- 5467 [239] ATLAS Collaboration. Measurements of Higgs boson production cross-sections in  
5468 the  $H \rightarrow \tau^+\tau^-$  decay channel in  $pp$  collisions at  $\sqrt{s} = 13$  TeV with the ATLAS  
5469 detector[J]. JHEP, 2022, 08: 175. arXiv: 2201.08269 [hep-ex]. DOI: 10.1007/JH  
5470 EP08(2022)175.
- 5471 [240] ATLAS Collaboration. Measurements of Higgs boson production by gluon–gluon  
5472 fusion and vector-boson fusion using  $H \rightarrow WW^* \rightarrow e\nu\mu\nu$  decays in  $pp$  collisions at  
5473  $\sqrt{s} = 13$  TeV with the ATLAS detector[J]. 2022. arXiv: 2207.00338 [hep-ex].
- 5474 [241] ATLAS Collaboration. Measurements of  $WH$  and  $ZH$  production in the  $H \rightarrow b\bar{b}$   
5475 decay channel in  $pp$  collisions at 13 TeV with the ATLAS detector[J]. Eur. Phys. J.  
5476 C, 2021, 81: 178. arXiv: 2007.02873 [hep-ex]. DOI: 10.1140/epjc/s10052-020-  
5477 08677-2.
- 5478 [242] ATLAS Collaboration. Measurements of Higgs Bosons Decaying to Bottom Quarks  
5479 from Vector Boson Fusion Production with the ATLAS Experiment at  $\sqrt{s} = 13$  TeV  
5480 [J]. Eur. Phys. J. C, 2020, 81: 537. arXiv: 2011.08280 [hep-ex]. DOI: 10.1140/e  
5481 pjc/s10052-021-09192-8.
- 5482 [243] ATLAS Collaboration. Measurement of Higgs boson decay into  $b$ -quarks in asso-  
5483 ciated production with a top-quark pair in  $pp$  collisions at  $\sqrt{s} = 13$  TeV with the  
5484 ATLAS detector[J]. JHEP, 2021, 06: 097. arXiv: 2111.06712 [hep-ex]. DOI: 10  
5485 .1007/JHEP06(2022)097.
- 5486 [244] ATLAS and CMS Collaborations. Measurements of the Higgs boson production and  
5487 decay rates and constraints on its couplings from a combined ATLAS and CMS anal-  
5488 ysis of the LHC  $pp$  collision data at  $\sqrt{s} = 7$  and 8 TeV[J]. JHEP, 2016, 08: 045. arXiv:  
5489 1606.02266 [hep-ex]. DOI: 10.1007/JHEP08(2016)045.
- 5490 [245] ATLAS Collaboration. Combined measurements of Higgs boson production and de-  
5491 cay using up to  $80 \text{ fb}^{-1}$  of proton–proton collision data at  $\sqrt{s} = 13$  TeV collected

- 5492 with the ATLAS experiment[J]. Phys. Rev. D, 2020, 101: 012002. arXiv: 1909.0284  
5493 5 [hep-ex]. DOI: 10.1103/PhysRevD.101.012002.
- 5494 [246] COWAN G, CRANMER K, GROSS E, et al. Asymptotic formulae for likelihood-  
5495 based tests of new physics[J]. Eur. Phys. J. C, 2011, 71: 1554. arXiv: 1007.1727  
5496 [physics.data-an]. DOI: 10.1140/epjc/s10052-011-1554-0.
- 5497 [247] READ A L. Presentation of search results: the  $CL_s$  technique[J]. J. Phys. G, 2002,  
5498 28: 2693-2704. DOI: 10.1088/0954-3899/28/10/313.
- 5499 [248] AAD G, et al. Constraints on the Higgs boson self-coupling from single- and double-  
5500 Higgs production with the ATLAS detector using pp collisions at  $s=13$  TeV[J]. Phys.  
5501 Lett. B, 2023, 843: 137745. arXiv: 2211.01216 [hep-ex]. DOI: 10.1016/j.physle  
5502 tb.2023.137745.
- 5503 [249] LIU J, LIU Z, WANG L T. Enhancing Long-Lived Particles Searches at the LHC  
5504 with Precision Timing Information[J/OL]. Physical Review Letters, 2019, 122(13).  
5505 <https://doi.org/10.1103/PhysRevLett.122.131801>. DOI: 10.1103/physrevlett.122  
5506 .131801.
- 5507 [250] Search for events with a pair of displaced vertices from long-lived neutral particles  
5508 decaying into hadronic jets in the ATLAS muon spectrometer in  $pp$  collisions at  
5509  $\sqrt{s} = 13$  TeV[J/OL]. Phys. Rev. D, 2022, 106: 032005. [https://link.aps.org/doi/10.1](https://link.aps.org/doi/10.1103/PhysRevD.106.032005)  
5510 [1103/PhysRevD.106.032005](https://link.aps.org/doi/10.1103/PhysRevD.106.032005). DOI: 10.1103/PhysRevD.106.032005.
- 5511 [251] Search for long-lived particles decaying in the CMS muon detectors in proton-proton  
5512 collisions at  $\sqrt{s} = 13$  TeV[R/OL]. Geneva: CERN, 2023. [https://cds.cern.ch/record](https://cds.cern.ch/record/2864874)  
5513 [/2864874](https://cds.cern.ch/record/2864874).
- 5514 [252] AGAPOV I, BENEDIKT M, BLONDEL A, et al. Future Circular Lepton Collider  
5515 FCC-ee: Overview and Status[Z]. 2022. arXiv: 2203.08310 [physics.acc-ph].
- 5516 [253] GROUP T C S. CEPC Conceptual Design Report: Volume 1 - Accelerator[Z]. 2018.  
5517 arXiv: 1809.00285 [physics.acc-ph].
- 5518 [254] GROUP T C S. CEPC Conceptual Design Report: Volume 2 - Physics & Detector  
5519 [Z]. 2018. arXiv: 1811.10545 [hep-ex].
- 5520 [255] GROUP T I C. The International Large Detector: Letter of Intent[Z]. 2010. arXiv:  
5521 1006.3396 [hep-ex].
- 5522 [256] THOMSON M. Particle flow calorimetry and the PandoraPFA algorithm[J/OL]. Nu-

- 5523 clear Instruments and Methods in Physics Research Section A: Accelerators, Spec-  
5524 trometers, Detectors and Associated Equipment, 2009, 611(1): 25-40. <https://doi.org/10.1016%2Fj.nima.2009.09.009>. DOI: 10.1016/j.nima.2009.09.009.
- 5525
- 5526 [257] RUAN M. Arbor, a new approach of the Particle Flow Algorithm[Z]. 2014. arXiv:  
5527 1403.4784 [physics.ins-det].
- 5528 [258] Particle-Flow Event Reconstruction in CMS and Performance for Jets, Taus, and  
5529 MET[R/OL]. Geneva: CERN, 2009. <http://cds.cern.ch/record/1194487>.
- 5530 [259] KILIAN W, OHL T, REUTER J. WHIZARD—simulating multi-particle processes  
5531 at LHC and ILC[J/OL]. The European Physical Journal C, 2011, 71(9). <https://doi.org/10.1140%2Fepjc%2Fs10052-011-1742-y>. DOI: 10.1140/epjc/s10052-011-17  
5532 42-y.
- 5533
- 5534 [260] MORA DE FREITAS P, VIDEAU H. Detector simulation with MOKKA / GEANT4:  
5535 Present and future[C] // International Workshop on Linear Colliders (LCWS 2002).  
5536 2002: 623-627.
- 5537 [261] CARLONI CALAME C, MONTAGNA G, NICROSINI O, et al. The BABAYAGA  
5538 event generator[J]. Nuclear Physics B - Proceedings Supplements, 2004, 131: 48-55.
- 5539 [262] ALWALL J, HERQUET M, MALTONI F, et al. MadGraph 5: going beyond[J/OL].  
5540 Journal of High Energy Physics, 2011, 2011(6). <https://doi.org/10.1007%2Fjhep06%282011%29128>. DOI: 10.1007/jhep06(2011)128.
- 5541
- 5542 [263] CHEN T, GUESTRIN C. XGBoost[C/OL] // Proceedings of the 22nd ACM  
5543 SIGKDD International Conference on Knowledge Discovery and Data Mining.  
5544 ACM, 2016. <https://doi.org/10.1145%2F2939672.2939785>. DOI: 10.1145/293  
5545 9672.2939785.
- 5546 [264] HE K, ZHANG X, REN S, et al. Deep Residual Learning for Image Recognition[Z].  
5547 2015. arXiv: 1512.03385 [cs.CV].
- 5548 [265] GONG S, MENG Q, ZHANG J, et al. An efficient Lorentz equivariant graph neural  
5549 network for jet tagging[J/OL]. Journal of High Energy Physics, 2022, 2022(7). <https://doi.org/10.1007%5C%2Fjhep07%5C%282022%5C%29030>. DOI: 10.1007/jhep  
5550 07(2022)030.
- 5551
- 5552 [266] SMILJANIC I, JELISAVCIC I B, KACAREVIC G, et al. Systematic uncertain-  
5553 ties in integrated luminosity measurement at CEPC[J]. 2020. arXiv: 2010.15061

- 5554 [physics.ins-det].
- 5555 [267] LIU J, LIU Z, WANG L T. Enhancing Long-Lived Particles Searches at the LHC  
5556 with Precision Timing Information[J/OL]. Phys. Rev. Lett., 2019, 122: 131801. <https://link.aps.org/doi/10.1103/PhysRevLett.122.131801>. DOI: 10.1103/PhysRevLett  
5557 .122.131801.
- 5558
- 5559 [268] JEANTY L, NOSLER L, POTTER C. Sensitivity to decays of long-lived dark  
5560 photons at the ILC (A Snowmass White Paper)[Z]. 2022. arXiv: 2203 . 08347  
5561 [hep-ph].
- 5562 [269] AIHARA H, et al. The International Linear Collider. A Global Project[J]. 2019.  
5563 arXiv: 1901.09829 [hep-ex].
- 5564 [270] ABADA A, et al. FCC Physics Opportunities: Future Circular Collider Conceptual  
5565 Design Report Volume 1[J]. 2019, 79(6): 474. DOI: 10.1140/epjc/s10052-019-6904  
5566 -3.
- 5567 [271] De BLAS J, et al. The CLIC Potential for New Physics[J]. 2018, 3/2018. arXiv: 181  
5568 2.02093 [hep-ph]. DOI: 10.23731/CYRM-2018-003.
- 5569 [272] HOOPER D, FINKBEINER D P, DOBLER G. Possible evidence for dark matter  
5570 annihilations from the excess microwave emission around the center of the Galaxy  
5571 seen by the Wilkinson Microwave Anisotropy Probe[J/OL]. Phys. Rev. D, 2007, 76:  
5572 083012. <https://link.aps.org/doi/10.1103/PhysRevD.76.083012>. DOI: 10.1103/Phys  
5573 RevD.76.083012.
- 5574 [273] COLLABORATION P. Planck 2013 results. XXII. Constraints on inflation[J]. A&A,  
5575 2014, 571: A22.
- 5576 [274] GRIEST K, KAMIONKOWSKI M. Unitarity limits on the mass and radius of dark-  
5577 matter particles[J/OL]. Phys. Rev. Lett., 1990, 64: 615-618. [https://link.aps.org/doi](https://link.aps.org/doi/10.1103/PhysRevLett.64.615)  
5578 /10.1103/PhysRevLett.64.615. DOI: 10.1103/PhysRevLett.64.615.
- 5579 [275] HO C M, SCHERRER R J. Limits on MeV dark matter from the effective number of  
5580 neutrinos[J/OL]. Phys. Rev. D, 2013, 87: 023505. [https://link.aps.org/doi/10.1103](https://link.aps.org/doi/10.1103/PhysRevD.87.023505)  
5581 /PhysRevD.87.023505. DOI: 10.1103/PhysRevD.87.023505.
- 5582 [276] NOLLETT K M, STEIGMAN G. BBN and the CMB constrain light, electromagnet-  
5583 ically coupled WIMPs[J/OL]. Phys. Rev. D, 2014, 89: 083508. [https://link.aps.org](https://link.aps.org/doi/10.1103/PhysRevD.89.083508)  
5584 /doi/10.1103/PhysRevD.89.083508. DOI: 10.1103/PhysRevD.89.083508.

- 5585 [277] NOLLETT K M, STEIGMAN G. BBN and the CMB constrain neutrino coupled  
5586 light WIMPs[J/OL]. *Phys. Rev. D*, 2015, 91: 083505. [https://link.aps.org/doi/10.11](https://link.aps.org/doi/10.1103/PhysRevD.91.083505)  
5587 03/PhysRevD.91.083505. DOI: 10.1103/PhysRevD.91.083505.
- 5588 [278] GREEN D, RAJENDRAN S. The cosmology of sub-MeV dark matter[J]. *Journal of*  
5589 *High Energy Physics*, 2017, 2017(10): 13.
- 5590 [279] STEIGMAN G. Equivalent neutrinos, light WIMPs, and the chimera of dark radi-  
5591 ation[J/OL]. *Phys. Rev. D*, 2013, 87: 103517. [https://link.aps.org/doi/10.1103/Phys](https://link.aps.org/doi/10.1103/PhysRevD.87.103517)  
5592 [RevD.87.103517](https://link.aps.org/doi/10.1103/PhysRevD.87.103517). DOI: 10.1103/PhysRevD.87.103517.
- 5593 [280] BØEHM C, DOLAN M J, MCCABE C. A lower bound on the mass of cold thermal  
5594 dark matter from Planck[J]. *Journal of Cosmology and Astroparticle Physics*, 2013,  
5595 2013(08): 041.
- 5596 [281] CLOWE D, BRADAČ M, GONZALEZ A H, et al. A Direct Empirical Proof of the  
5597 Existence of Dark Matter\*[J]. *The Astrophysical Journal*, 2006, 648(2): L109.
- 5598 [282] ALEMANNIO F. Latest results from the DAMPE space mission[Z]. 2022. arXiv:  
5599 2209.06014 [astro-ph.HE].
- 5600 [283] GIOVACCHINI F, CASAUS J, OLIVA A. The AMS-02 RICH detector: Status and  
5601 physics results[J]. *Nuclear Instruments and Methods in Physics Research Section*  
5602 *A: Accelerators, Spectrometers, Detectors and Associated Equipment*, 2020, 952:  
5603 161797.
- 5604 [284] BEHR J K. Searches for Dark Matter with the ATLAS and CMS Experiments using  
5605 LHC Run 2 (2015–2018) Data[R/OL]. Geneva: CERN, 2021. [https://cds.cern.ch/re](https://cds.cern.ch/record/2790201)  
5606 [cord/2790201](https://cds.cern.ch/record/2790201).
- 5607 [285] MENG Y, WANG Z, TAO Y, et al. Dark Matter Search Results from the PandaX-4T  
5608 Commissioning Run[J/OL]. *Phys. Rev. Lett.*, 2021, 127: 261802. [https://link.aps.or](https://link.aps.org/doi/10.1103/PhysRevLett.127.261802)  
5609 [g/doi/10.1103/PhysRevLett.127.261802](https://link.aps.org/doi/10.1103/PhysRevLett.127.261802). DOI: 10.1103/PhysRevLett.127.261802.
- 5610 [286] BILLARD J, BOULAY M, CEBRIÁN S, et al. Direct detection of dark matter—  
5611 APPEC committee report\*[J]. *Reports on Progress in Physics*, 2022, 85(5): 056201.
- 5612 [287] HOLDOM B. Two U(1)'s and  $\epsilon$  charge shifts[J]. *Physics Letters B*, 1986, 166(2):  
5613 196-198.
- 5614 [288] FOOT R, HE X G. Comment on ZZ' mixing in extended gauge theories[J]. *Physics*  
5615 *Letters B*, 1991, 267(4): 509-512.

- 5616 [289] FUYUTO K, HE X G, LI G, et al. *CP*-violating dark photon interaction[J/OL]. Phys.  
5617 Rev. D, 2020, 101: 075016. <https://link.aps.org/doi/10.1103/PhysRevD.101.075016>.  
5618 DOI: 10.1103/PhysRevD.101.075016.
- 5619 [290] CHOI G J, YANAGIDA T T, YOKOZAKI N. Dark photon dark matter in the minimal  
5620 B-L model[J]. Journal of High Energy Physics, 2021, 2021(1): 57.
- 5621 [291] IZAGUIRRE E, KRNJAIC G, SCHUSTER P, et al. Testing GeV-scale dark matter  
5622 with fixed-target missing momentum experiments[J/OL]. Phys. Rev. D, 2015, 91:  
5623 094026. <https://link.aps.org/doi/10.1103/PhysRevD.91.094026>. DOI: 10.1103/Phys  
5624 RevD.91.094026.
- 5625 [292] GRAHAM M, HEARTY C, WILLIAMS M. Searches for Dark Photons at Acceler-  
5626 ators[J]. Annual Review of Nuclear and Particle Science, 2021, 71(1): 37-58.
- 5627 [293] ANDREAS S, NIEBUHR C, RINGWALD A. New limits on hidden photons from  
5628 past electron beam dumps[J/OL]. Phys. Rev. D, 2012, 86: 095019. [https://link.aps.o](https://link.aps.org/doi/10.1103/PhysRevD.86.095019)  
5629 [rg/doi/10.1103/PhysRevD.86.095019](https://link.aps.org/doi/10.1103/PhysRevD.86.095019). DOI: 10.1103/PhysRevD.86.095019.
- 5630 [294] BJORKEN J D, ESSIG R, SCHUSTER P, et al. New fixed-target experiments to  
5631 search for dark gauge forces[J/OL]. Phys. Rev. D, 2009, 80: 075018. [https://link.ap](https://link.aps.org/doi/10.1103/PhysRevD.80.075018)  
5632 [s.org/doi/10.1103/PhysRevD.80.075018](https://link.aps.org/doi/10.1103/PhysRevD.80.075018). DOI: 10.1103/PhysRevD.80.075018.
- 5633 [295] FABBRICHESI M, GABRIELLI E, LANFRANCHI G. The Physics of the Dark Pho-  
5634 ton[M/OL]. Springer International Publishing, 2021. <https://doi.org/10.1007/978-3-030-62519-1>.  
5635 DOI: 10.1007/978-3-030-62519-1.
- 5636 [296] WAN J, LENG Y, GAO B, et al. Simulation of wire scanner for high repetition free  
5637 electron laser facilities[J]. Nuclear Instruments and Methods in Physics Research  
5638 Section A: Accelerators, Spectrometers, Detectors and Associated Equipment, 2022,  
5639 1026: 166200.
- 5640 [297] ZHAO Z T, FENG C, ZHANG K Q. Two-stage EEHG for coherent hard X-ray gen-  
5641 eration based on a superconducting linac[J]. Nuclear Science and Techniques, 2017,  
5642 28(8): 117.
- 5643 [298] ZHAO Z, FENG C, CHEN J, et al. Two-beam based two-stage EEHG-FEL for co-  
5644 herent hard X-ray generation[J]. Science Bulletin, 2016, 61(9): 720-727.
- 5645 [299] BELYAEV A, CHRISTENSEN N D, PUKHOV A. CalcHEP 3.4 for collider physics  
5646 within and beyond the Standard Model[J]. Computer Physics Communications, 2013,

- 5647 184(7): 1729-1769.
- 5648 [300] COLLABORATION T N. Search for vector mediator of dark matter production in  
5649 invisible decay mode[J/OL]. Phys. Rev. D, 2018, 97: 072002. <https://link.aps.org/doi/10.1103/PhysRevD.97.072002>. DOI: 10.1103/PhysRevD.97.072002.
- 5650
- 5651 [301] DENIVERVILLE P, POSPELOV M, RITZ A. Observing a light dark matter beam  
5652 with neutrino experiments[J/OL]. Phys. Rev. D, 2011, 84: 075020. <https://link.aps.org/doi/10.1103/PhysRevD.84.075020>. DOI: 10.1103/PhysRevD.84.075020.
- 5653
- 5654 [302] BATELL B, POSPELOV M, RITZ A. Exploring portals to a hidden sector through  
5655 fixed targets[J/OL]. Phys. Rev. D, 2009, 80: 095024. <https://link.aps.org/doi/10.1103/PhysRevD.80.095024>. DOI: 10.1103/PhysRevD.80.095024.
- 5656
- 5657 [303] BATELL B, ESSIG R, SURUJON Z. Strong Constraints on Sub-GeV Dark Sectors  
5658 from SLAC Beam Dump E137[J/OL]. Phys. Rev. Lett., 2014, 113: 171802. <https://link.aps.org/doi/10.1103/PhysRevLett.113.171802>. DOI: 10.1103/PhysRevLett.113  
5659 .171802.
- 5660
- 5661 [304] COLLABORATION B. Search for Invisible Decays of a Dark Photon Produced in  
5662  $e^+e^-$  Collisions at BaBar[J/OL]. Phys. Rev. Lett., 2017, 119: 131804. <https://link.aps.org/doi/10.1103/PhysRevLett.119.131804>. DOI: 10.1103/PhysRevLett.119.131  
5663 804.
- 5664
- 5665 [305] AGUILAR-AREVALO A A, BACKFISH M, BASHYAL A, et al. Dark Matter  
5666 Search in a Proton Beam Dump with MiniBooNE[J/OL]. Phys. Rev. Lett., 2017,  
5667 118: 221803. <https://link.aps.org/doi/10.1103/PhysRevLett.118.221803>. DOI:  
5668 10.1103/PhysRevLett.118.221803.
- 5669 [306] ESSIG R, MANALAYSAY A, MARDON J, et al. First Direct Detection Limits on  
5670 Sub-GeV Dark Matter from XENON10[J/OL]. Phys. Rev. Lett., 2012, 109: 021301.  
5671 <https://link.aps.org/doi/10.1103/PhysRevLett.109.021301>. DOI: 10.1103/PhysRev  
5672 Lett.109.021301.
- 5673 [307] ÅKESSON T, BLINOV N, BRYNGEMARK L, et al. A high efficiency photon veto  
5674 for the Light Dark Matter eXperiment[J]. Journal of High Energy Physics, 2020,  
5675 2020(4): 3.



## Appendix A DarkSHINE Experiment

Over the last few decades, the Standard Model (SM) has been extraordinarily successful in corroborating a multitude of experimental outcomes in particle colliders. Nevertheless, certain phenomena point to the SM being a low-energy effective theory, implying the necessity of new physics beyond the SM. Strong astronomical and cosmological evidence attests to the existence of dark matter (DM), which constitutes approximately five times the mass of ordinary baryonic matter<sup>[272-273]</sup>. This necessitates the exploration of DM to uncover physics beyond the SM.

One prevalent hypothesis postulates DM's origin in the early universe via thermal equilibrium, eventually leading to a stable density due to universal expansion and consequent temperature reduction; this is termed the *freeze-out* mechanism<sup>[274-278]</sup>. The DM mass in this scenario ranges from MeV to tens of TeV to match the observed DM density<sup>[279-280]</sup>.

DM is primarily studied through its gravitational interactions in astronomical observations<sup>[281]</sup>. However, questions about its mass and interaction mechanisms with both gravitational and SM forces remain open. Complementary approaches include space experiments such as DAMPE<sup>[282]</sup> and AMS<sup>[283]</sup>, collider setups like the LHC<sup>[284]</sup>, and underground detectors like PandaX<sup>[285]</sup>. Most of these focus on weakly interacting massive particles (WIMPs), which have so far yielded no evidence, constraining a significant portion of DM parameter space in the GeV–TeV mass range<sup>[286]</sup>.

The domain of sub-GeV DM particles remains relatively unexplored. One intriguing hypothesis posits that DM might engage in interactions through a novel *dark force*, analogous to electromagnetism in ordinary matter, mediated by a dark photon ( $A'$ )<sup>[287-288]</sup>. This mediator can couple to photons via a kinetic mixing parameter  $\epsilon$ , enabling interactions between DM and SM particles<sup>[289-290]</sup>.

In the study at hand, dark photons are produced via electron-nucleon interactions in an electron-on-fixed-target experiment. These dark photons subsequently decay into DM candidates that elude detection, manifesting as missing momentum. For dark photons in the MeV–GeV mass range, this methodology enhances the constraints on the kinetic mixing parameter  $\epsilon$ <sup>[291]</sup>. Given the low production rates of dark photons, this work employs GEANT4 simulations<sup>[52-53]</sup> of 2.5 billion inclusive electron-on-target events and specialized background

5706 samples. Discriminative variables include the count of reconstructed tracks and the energy  
5707 deposition in both electromagnetic and hadronic calorimeters.

## 5708 A.1 Theory Assumption

5709 Although the dark photon does not engage in direct coupling with particles in the Standard  
5710 Model (SM), it can manifest a minimal coupling to the electromagnetic current owing to  
5711 the kinetic mixing of the SM hypercharge and the  $A'$  field strength tensor. The Lagrangian  
5712 corresponding to this scenario is articulated as

$$L = L_{\text{SM}} + \varepsilon F^{\mu\nu} F'_{\mu\nu} + \frac{1}{4} F'^{\mu\nu} F'_{\mu\nu} + m_{A'}^2 A'^{\mu} A'_{\mu},$$

5713 where  $m_{A'}$  denotes the dark photon mass,  $A'_{\mu}$  signifies the dark photon field, and  $F'_{\mu\nu}$  is its  
5714 associated field strength tensor. The kinetic mixing parameter  $\varepsilon$  varies from  $10^{-8}$  to  $10^{-2}$   
5715 depending on the mass point<sup>[292]</sup>.

5716 Dark photons can be produced in laboratory conditions and can either decay into de-  
5717 tectable SM end states or elusive dark sector final states, contingent on whether  $m_{A'} > 2m_{\chi}$ .  
5718 The minimal dark photon model incorporates merely three undetermined parameters:  $\varepsilon$ ,  $m_{A'}$ ,  
5719 and the decay branching ratio to the dark sector, which is conventionally taken as either zero  
5720 or unity. This investigation narrows its focus to the parameter space defined by  $[m_{A'}, \varepsilon]$ ,  
5721 presuming a 100% decay branching ratio of dark photons to dark matter.

5722 Four primary mechanisms of dark photon production are highlighted, with three possible  
5723 decay modes, as illustrated in figure A-1 (left): bremsstrahlung in fixed-target experiments  
5724 ( $eZ \rightarrow eZA'$  and  $pZ \rightarrow pZA'$ ), annihilation in  $e^+e^-$  colliders ( $e^+e^- \rightarrow A'\gamma$ ), decays of  
5725 mesons ( $\pi^0 \rightarrow A'\gamma$  or  $\eta \rightarrow A'\gamma$ ), and the Drell-Yan process ( $q\bar{q} \rightarrow A'$ )<sup>[293]</sup>.

5726 The cross-section for bremsstrahlung production is governed by

$$\frac{d\sigma}{dx_e} = 4\alpha^3 \varepsilon^2 \xi \sqrt{1 - \frac{m_{A'}^2}{E_e^2} \frac{1 - x_e + \frac{x_e^2}{3}}{m_{A'}^2 \frac{1-x_e}{x_e} + m_e^2 x_e}},$$

5727 where  $x_e = \frac{E_{A'}}{E_e}$  represents the energy fraction of the incoming electron carried by the dark  
5728 photon. The effective photon flux  $\xi$  is

$$\xi(E_e, m_{A'}, Z, A) = \int_{t_{\min}}^{t_{\max}} dt \frac{t - t_{\min}}{t^2} G_2(t),$$

5729 where  $t_{\min}$  and  $t_{\max}$  are defined in the text<sup>[294]</sup>.

5730 If the dark photon decays into dark matter ( $A' \rightarrow \chi\bar{\chi}$ ) are kinematically permissible, i.e.,  
5731  $m_{A'} > 2m_\chi$ , the partial widths for these decays are given by

$$\Gamma(A' \rightarrow \chi\bar{\chi}) = \frac{1}{3}\alpha_D m_{A'} \sqrt{1 - \frac{4m_\chi^2}{m_{A'}^2}} \left(1 + \frac{2m_\chi^2}{m_{A'}^2}\right).$$

5732 For an incident electron with 8 GeV energy and assuming  $\varepsilon = 1$ , Figure A–2 delineates the  
5733 cross-section as a function of  $m_{A'}$ .

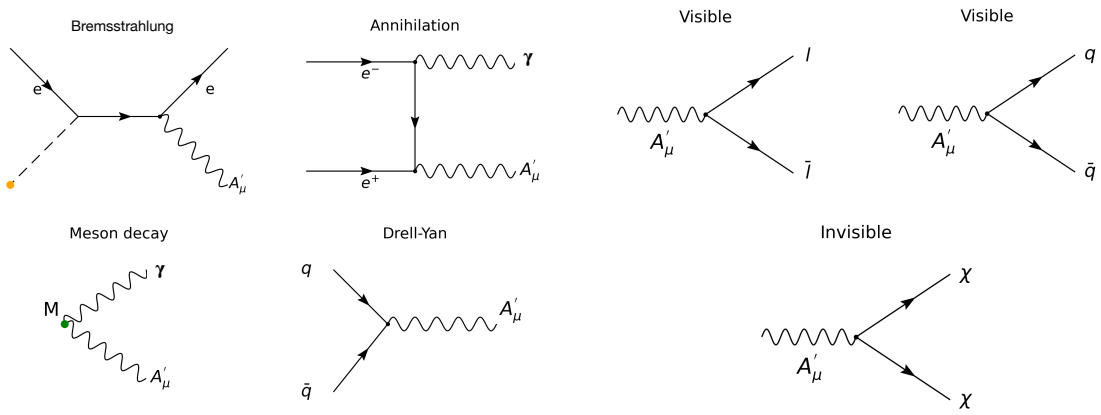


**Figure A–1** *Left: Production of dark photons: bremsstrahlung, annihilation, meson decay, and Drell–Yan.*<sup>[295]</sup> *Right: Decay of the massive dark photon into visible (SM leptons or hadrons) and invisible (DM) modes.*<sup>[295]</sup>

## 5734 A.2 Experimental Setup

### 5735 A.2.1 SHINE Facility

5736 In this investigation, a high-frequency electron beam is utilized, which is furnished by  
5737 the under-construction Shanghai High Repetition-Rate XFEL and Extreme Light Facility  
5738 (SHINE)<sup>[296-298]</sup>. The SHINE facility is designed to generate a beam with an energy level of  
5739 8 GeV and a frequency of 1 MHz. Figure A–3 illustrates the configuration of the SHINE  
5740 linac and the various kicker systems, including those designated for the Free Electron Lasers  
5741 (FEL-I, FEL-II, FEL-III) and for the present experiment. Specifically, SHINE’s microwave  
5742 system, operating at 1.3 GHz, supplies 1.3 billion buckets per second. For every set of 1300  
5743 buckets, a 100 pC charge of electrons is loaded into a single bucket, which corresponds to a

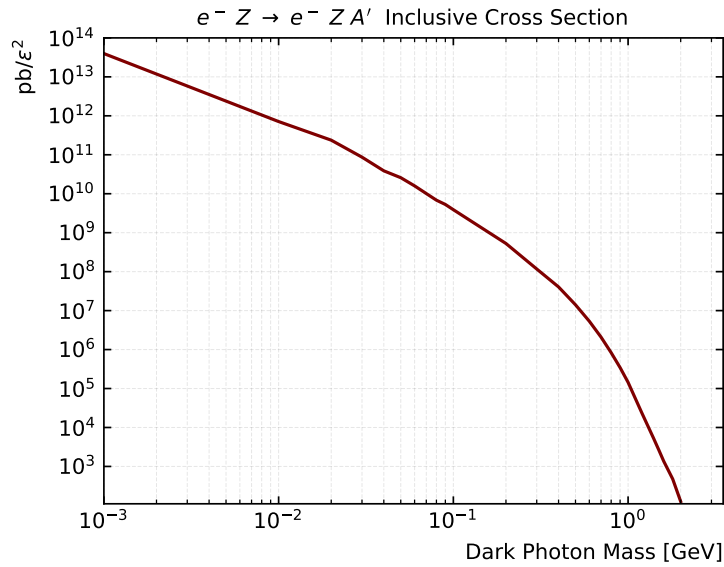


**Figure A–2 Inclusive cross section of dark photon bremsstrahlung from electron interacting with tungsten target, which is produced by Calchep and is normalized to  $\varepsilon = 1$ , with 8 GeV beam energy.**

5744 frequency of 1 MHz. This produces a bunch population of  $6.25 \times 10^8$  electrons, which is too  
5745 high for efficient dark photon detection.

5746 To remedy this, a specialized single-electron beamline is proposed to be incorporated into  
5747 the existing SHINE linac. This additional beamline aims to make use of the empty buckets  
5748 by injecting a single electron into each. Post-acceleration, these electrons are distributed by a  
5749 dedicated kicker system. When considering the response time of the kicker and the detection  
5750 systems, an effective rate of 10 MHz is achieved. This configuration is projected to yield  
5751 around  $3 \times 10^{14}$  electron-on-target (EOT) events during a single year of commissioning for  
5752 the DarkSHINE experiment.

### 5753 A.2.2 Detector Design

5754 The detector for the DarkSHINE experiment is composed of three primary sub-detector  
5755 systems: a silicon tracker, an electromagnetic calorimeter (denoted as ECAL), and a hadronic  
5756 calorimeter (referred to as HCAL). Figure A–4 provides a schematic representation of these  
5757 systems in spatial relation to each other. Along the direction of the incident electron from  
5758 left to right, one first encounters a dipole magnet, depicted in red with a blue brace in the  
5759 figure. The magnet operates at a field strength of 1.5 T. Situated at the center of this magnet

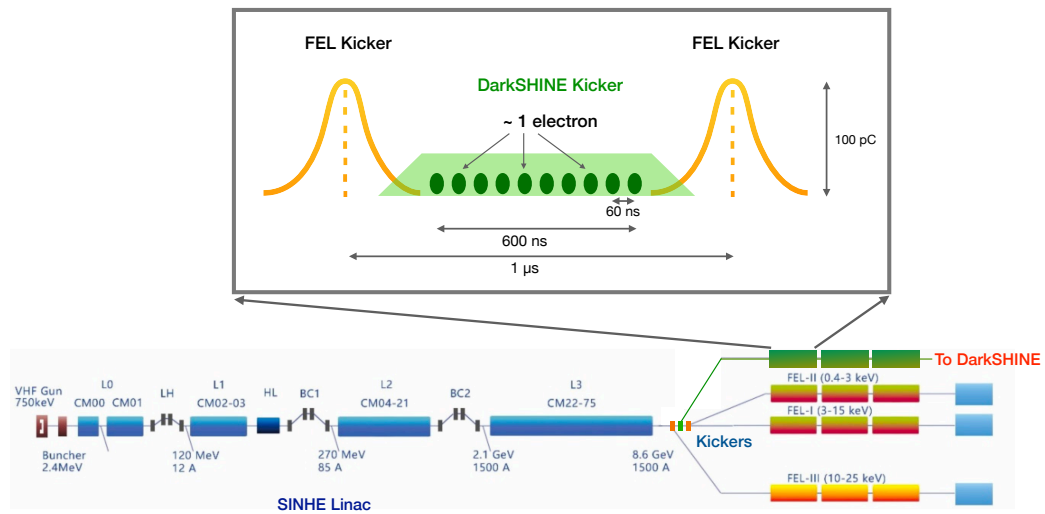


**Figure A-3 Schematic representation of the beamline and kicker systems.**

5760 is the tagging tracker, which is designed to identify and tag particles. Adjacent to the edge  
 5761 of the magnet lies the recoil tracker. The experimental target is strategically positioned in  
 5762 the middle of these tracking systems. Following the recoil tracker, the ECAL is placed, and  
 5763 it is subsequently succeeded by the HCAL. The parameters based on the geometry of these  
 5764 sub-detectors are summarized in Table A-1, which serves as the baseline setup for this study.

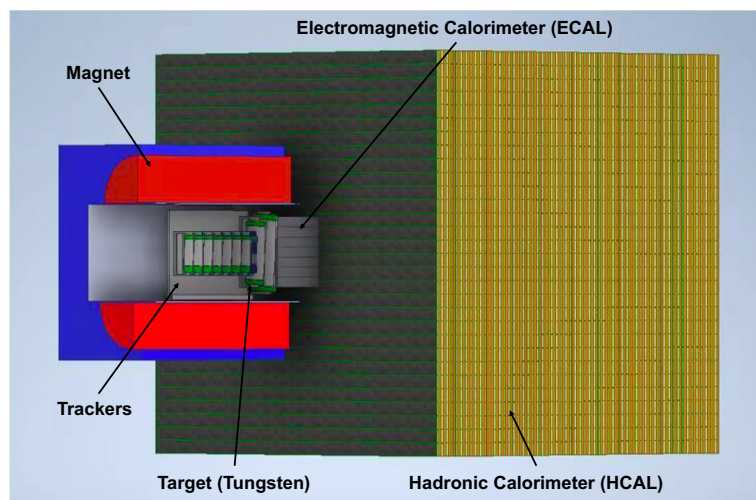


**Figure A-4 Schematic layout of the detector and its components.**

5765 The DarkSHINE experiment incorporates a sophisticated tracking system embedded within

Node	Centre (mm)		Size (mm)		Arrangement	Comments
	z	x	y	z		
Tagging tracker	-307.783	200	400	600.216	7 layers	Second layer rotation: 0.1 rad
Target	0	100	200	0.35	-	
Recoil tracker	94.032	500	800	172.714	6 layers	Second layer rotation: 0.1 rad
ECAL	408.539	506	506	454.3	20 × 20 × 11 cells	-
HCAL	2660.69	4029.51	4029.51	4048.01	4 × 4 × 1 modules	-

**Table A-1 The detector geometry overview.**

5766 a dipole magnet generating a magnetic field of 1.5 T. A silicon-based tracker is employed for  
 5767 the purpose of reconstructing both incident and recoil electron trajectories, thereby enabling  
 5768 the calculation of their respective momenta. Illustrated in Figure A-5, the tagging tracker  
 5769 comprises seven layers of silicon strip detectors, while the recoil tracker is designed with six  
 5770 such layers. Situated between these two tracking modules is a tungsten (W) target with a de-  
 5771 cay length of  $0.1X_0$ . To enhance the spatial resolution, each layer of both tracking modules  
 5772 accommodates two silicon strip sensors, which are oriented at a small angle of 100 mrad  
 5773 relative to one another. This configuration facilitates the precise measurement of particle  
 5774 positions in the x-y plane. The system achieves an impressive horizontal resolution of ap-  
 5775 proximately  $6 \mu\text{m}$  and a vertical resolution of around  $60 \mu\text{m}$ .

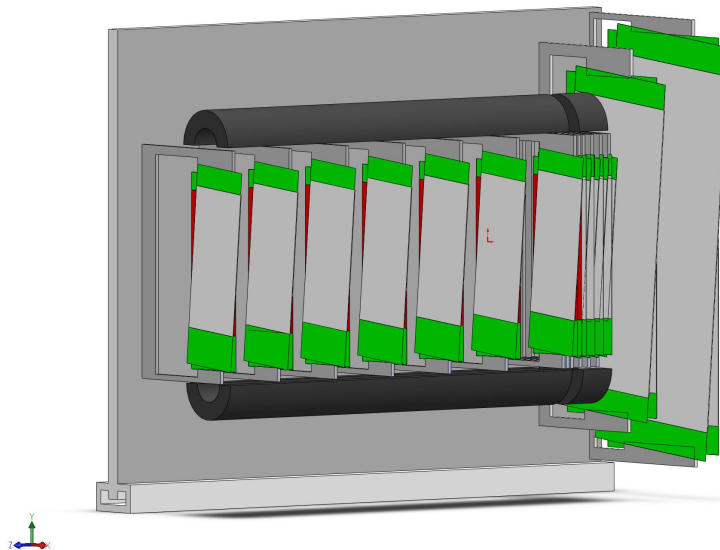


**Figure A-5 Illustration of tracking system components.**

5776 The DarkSHINE experiment features a high-resolution electromagnetic calorimeter (ECAL)  
5777 situated immediately downstream of the recoil tracker. This ECAL is designed to capture and  
5778 reconstruct the energy deposition of incident particles. The scintillation material chosen for  
5779 this application is LYSO(Ce) crystal, selected for its advantageous properties, such as high  
5780 light yield, rapid decay time, and minimal electronic noise. The ECAL is comprised of a  
5781  $20 \times 20 \times 11$  array of these LYSO crystals. Each individual crystal has a cross-sectional  
5782 area measuring  $2.5 \times 2.5 \text{ cm}^2$  and a length of 4 cm. The total decay length facilitated by  
5783 this LYSO array amounts to  $44 X_0$ , ensuring that final state electrons and photons are fully  
5784 absorbed, thereby allowing for a complete energy reconstruction. The energy resolution of  
5785 the LYSO crystal array has been experimentally determined to be approximately 10% when  
5786 calibrated using a  $^{22}\text{Na}$  radioactive source.

5787 Subsequent to the ECAL a hadronic calorimeter (HCAL) is installed to capture and veto  
5788 hadronic background, with a particular emphasis on muon elimination. The HCAL is engi-  
5789 neered as a scintillator-based sampling calorimeter featuring steel absorbers. It has dimen-  
5790 sions of  $100 \text{ cm} \times 100 \text{ cm}$  in the  $x$ - $y$  plane. Each of the scintillators in HCAL is encapsulated  
5791 in a carbon envelope and contains a centrally located wavelength-shifting fiber, enhancing  
5792 its detection capabilities.

### 5793 **A.3 Simulation**

5794 This study employs simulations based on the baseline detector geometry delineated in  
5795 Sec. A.2. The incident electron energy is fixed at 8 GeV. Signal samples are generated  
5796 parametrically as functions of the dark photon mass. Both inclusive backgrounds and key  
5797 rare processes, such as photon–nuclear interactions, electron–nuclear interactions, and pho-  
5798 ton decays to muon pairs, are simulated to enhance the understanding and quantification of  
5799 background events. Additional background contributions deemed negligible are explored in  
5800 Sec. A.5.3.

5801 The DarkSHINE Software framework consolidates multiple functionalities, including  
5802 detector simulation, digitization, event display, event reconstruction, and data analysis. It  
5803 employs a proprietary data structure model for seamless data flow across various computa-  
5804 tional stages. GEANT4 v10.6.0<sup>[52-53]</sup> serves as the simulation engine, specifically tailored  
5805 for the DarkSHINE detector.

5806 **A.3.1 Signal Sample Production**

5807 Dark photon signal events are generated using CalcHEP v3.4<sup>[299]</sup>, while GEANT4 v10.6.0  
 5808 is utilized for detector simulation. A total of 25 signal samples are produced, each comprising  
 5809  $1 \times 10^5$  events, across a range of dark photon masses denoted as  $m_{A'}$ , varying from 1 MeV to  
 5810 2000 MeV.

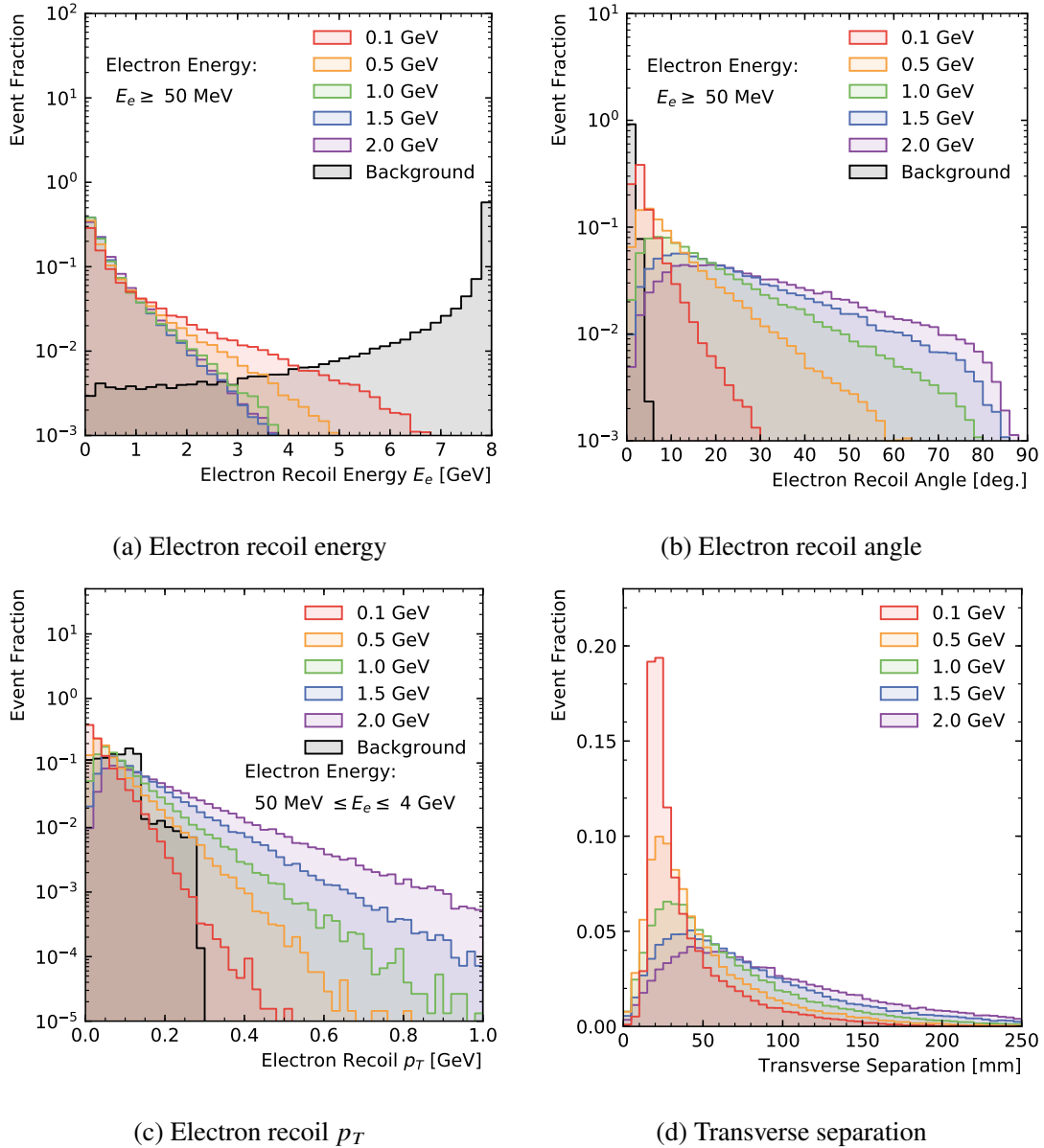


**Figure A-6 Kinematic distributions of recoil electron variables, juxtaposing signal samples with an inclusive background sample.**

5811 Figure A–6 exhibits the kinematic distributions of the signal and inclusive background.  
5812 Signal events primarily transfer their momentum to the dark photon, leading to a recoil elec-  
5813 tron with typically less than a quarter of the initial momentum. Conversely, in background  
5814 events, the recoil electron retains most of the incident momentum. Hence, imposing a cut  
5815 on the recoil electron momentum proves pivotal for signal region delineation. For increas-  
5816 ing dark photon masses in signal events, the recoil electron angle and transverse momentum,  
5817 on average, manifest higher values, in contrast to their smaller magnitudes in background  
5818 events. The transverse momentum in the background concentrates around 100 MeV due to  
5819 the magnetic field’s 1.5 T strength. Upon inspection of the transverse separation in the signal  
5820 events, higher dark photon mass tends to yield greater average distances.

### 5821 A.3.2 Background Sample Production

5822 Figure A–7 illustrates the hierarchy of major background processes, along with their  
5823 corresponding relative rates. Predominantly, incident electrons traverse the target without  
5824 undergoing any interaction. However, approximately 6.7% of these electrons emit hard  
5825 bremsstrahlung photons, leading to a final state comprising a recoil electron and a pho-  
5826 ton. Subsequently, these bremsstrahlung photons can engage in photon–nuclear interactions  
5827 with the materials of ECAL and the target, occurring with relative rates of  $2.31 \times 10^{-4}$  and  
5828  $1.37 \times 10^{-6}$  with respect to the inclusive rate, respectively. Furthermore, the bremsstrahlung  
5829 photons can undergo conversions, resulting in muon pairs at ECAL and the target, with rel-  
5830 ative rates of  $1.63 \times 10^{-6}$  and  $1.50 \times 10^{-8}$ , respectively. Although bremsstrahlung photons  
5831 can also yield electron pairs at a substantially high rate, these electrons are readily identifi-  
5832 able and reconstructable by the tracking system and ECAL. Apart from the aforementioned  
5833 processes instigated by hard bremsstrahlung photons, electron–nuclear interactions involving  
5834 the materials of ECAL and the target also contribute significantly to the background, with  
5835 relative rates of  $3.25 \times 10^{-6}$  and  $5.10 \times 10^{-7}$ .

5836 An inclusive background sample comprising  $2.5 \times 10^9$  events was generated for this study.  
5837 In addition, six rare processes were also simulated, the statistics of which, along with the  
5838 corresponding EOTs, are detailed in Table A–2.

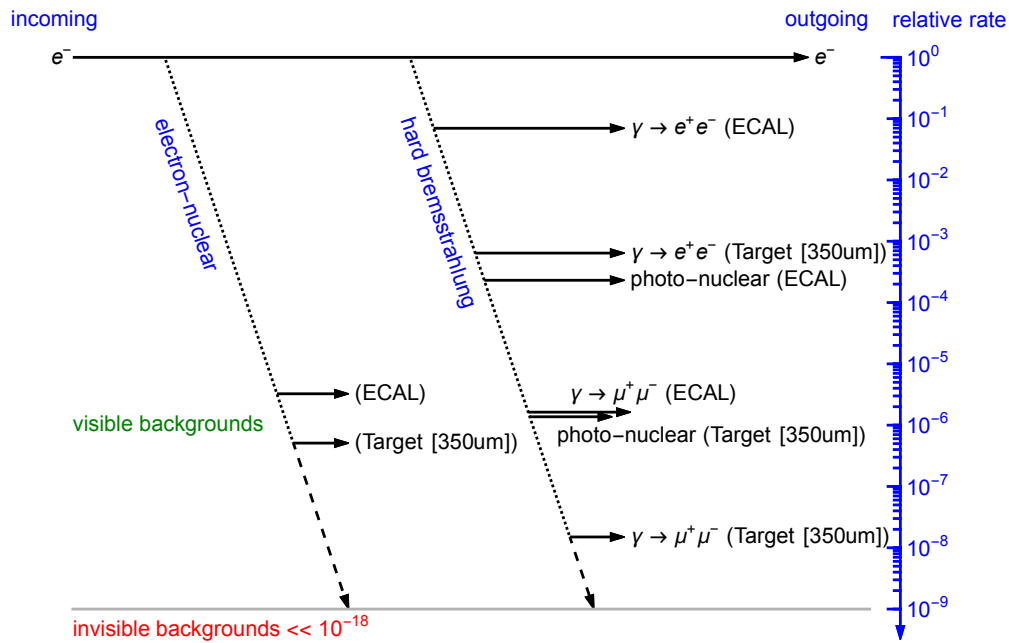


**Figure A-7 Schematic depiction of the principal background processes and their associated relative rates. These rates serve as branching ratios and are tabulated in Table A-2.**

Process	Generate Events	Branching Ratio	EOTs
Inclusive	$2.5 \times 10^9$	1.0	$2.5 \times 10^9$
Bremsstrahlung	$1 \times 10^7$	$6.70 \times 10^{-2}$	$1.5 \times 10^8$
GMM_target	$1 \times 10^7$	$1.5(\pm 0.5) \times 10^{-8}$	$4.3 \times 10^{14}$
GMM_ECAL	$1 \times 10^7$	$1.63(\pm 0.06) \times 10^{-6}$	$6.0 \times 10^{12}$
PN_target	$1 \times 10^7$	$1.37(\pm 0.05) \times 10^{-6}$	$4.0 \times 10^{12}$
PN_ECAL	$1 \times 10^8$	$2.31(\pm 0.01) \times 10^{-4}$	$4.4 \times 10^{11}$
EN_target	$1 \times 10^8$	$5.1(\pm 0.3) \times 10^{-7}$	$1.6 \times 10^{12}$
EN_ECAL	$1 \times 10^7$	$3.25(\pm 0.08) \times 10^{-6}$	$1.8 \times 10^{12}$

**Table A-2 Summary of background sample production, specifying branching ratios and corresponding EOTs for each rare process. The branching ratios are derived from the inclusive sample, conditioned on the energy of the electron being greater than 4 GeV.**

## 5839 A.4 Signal Region Definition

5840 Informed by the distribution of background processes as illustrated in figure A–7, we  
5841 construct a set of event selection criteria, leveraging the following detector variables:

- 5842 • Count of reconstructed tracks in the tagging tracker, denoted as  $N_{\text{trk}}^{\text{tag,rec}} = 1$ ;
- 5843 • Disparity in electron momentum, represented as  $p_{\text{tag}} - p_{\text{rec}} > 4 \text{ GeV}$ ;
- 5844 • Cumulative energy measured in ECAL, quantified by  $E_{\text{ECAL}}^{\text{total}} < 2.5 \text{ GeV}$ ;
- 5845 • Aggregate energy observed in HCAL, not exceeding  $E_{\text{HCAL}}^{\text{total}} < 0.1 \text{ GeV}$ ;
- 5846 • Peak energy registered in an individual HCALcell, confined to  $E_{\text{HCAL}}^{\text{MaxCell}} < 2 \text{ MeV}$ .

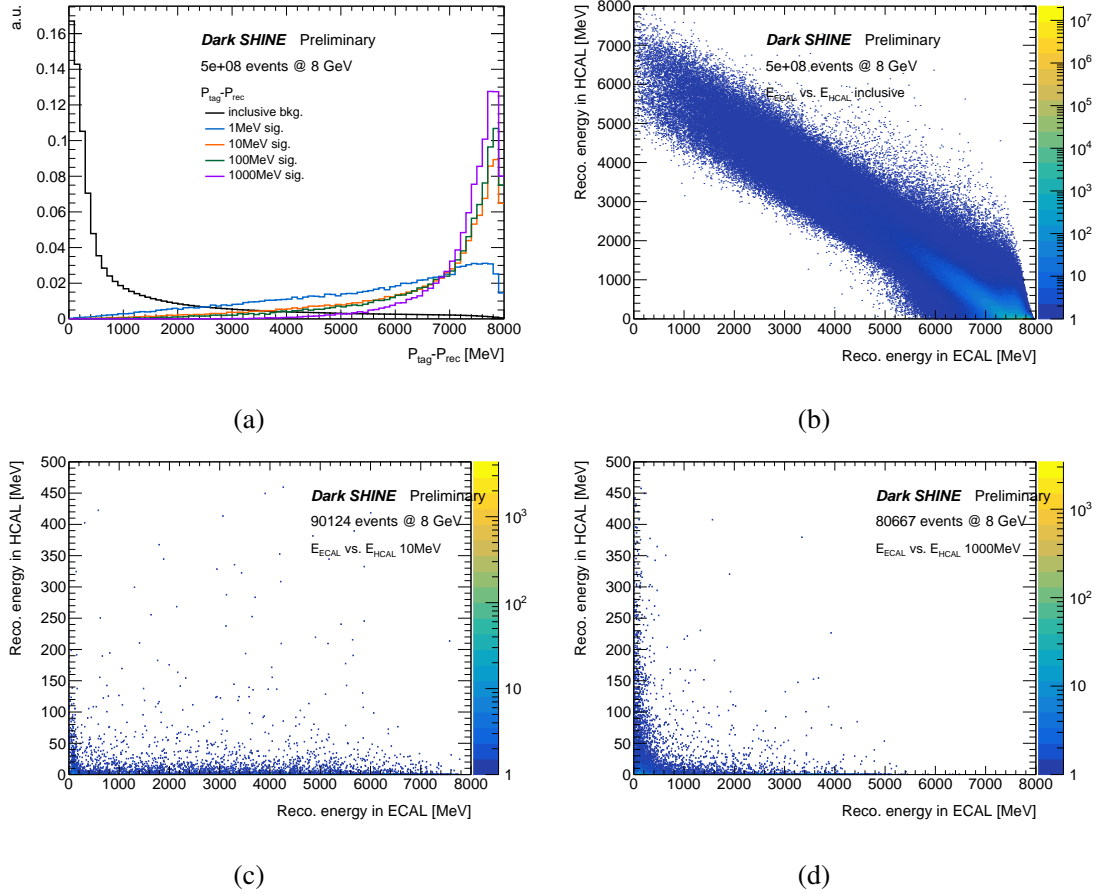
5847 Subsequent analysis confirms that these thresholds are optimized to effectively mitigate  
5848 background events while retaining high signal sensitivity.

5849 Focusing on tracking data, it is observed that dark photon signal events typically mani-  
5850 fest as a solitary reconstructed track in both the tagging and recoil trackers. The momentum  
5851 difference between these two tracks, depicted in the top-left quadrant of figure A–8, clearly  
5852 segregates signal from background. Specifically, in the signal case, the ‘missing momentum’  
5853 —attributed to the dark photon—tends to be higher, whereas it decays rapidly in background  
5854 scenarios dominated by hard bremsstrahlung events. To exclude such background contam-  
5855 ination effectively, a preselection criterion on missing momentum,  $p_{\text{tag}} - p_{\text{rec}} > 4 \text{ GeV}$ , is  
5856 instituted.

5857 Pivoting to the calorimeter system, Figure A–8 contains several significant plots. Sub-  
5858 figure (a) shows the difference in momentum between the tagging and recoil electrons ( $P_{\text{tag}} -$   
5859  $P_{\text{rec}}$ ) for the inclusive background, as well as for signal samples of 1 MeV, 10 MeV, 100 MeV,  
5860 and 1000 MeV. Subfigures (b, c, d) display the two-dimensional distribution of total energy  
5861 in ECAL and HCAL for the inclusive background and the 10 MeV and 1000 MeV signal  
5862 samples, respectively.

5863 In the case where a dark photon decays into a Dark Matter (DM) pair, the decay prod-  
5864 ucts would evade detection, leaving no energy trace in ECAL and HCAL. Conversely, back-  
5865 ground processes generally register substantial energy deposits in these calorimeters, espe-  
5866 cially hadronic backgrounds which are predominantly absorbed in HCAL. Hence, judicious  
5867 selection criteria based on the total and maximum cell energy in HCAL can effectively filter  
5868 out such backgrounds while maintaining high signal fidelity.

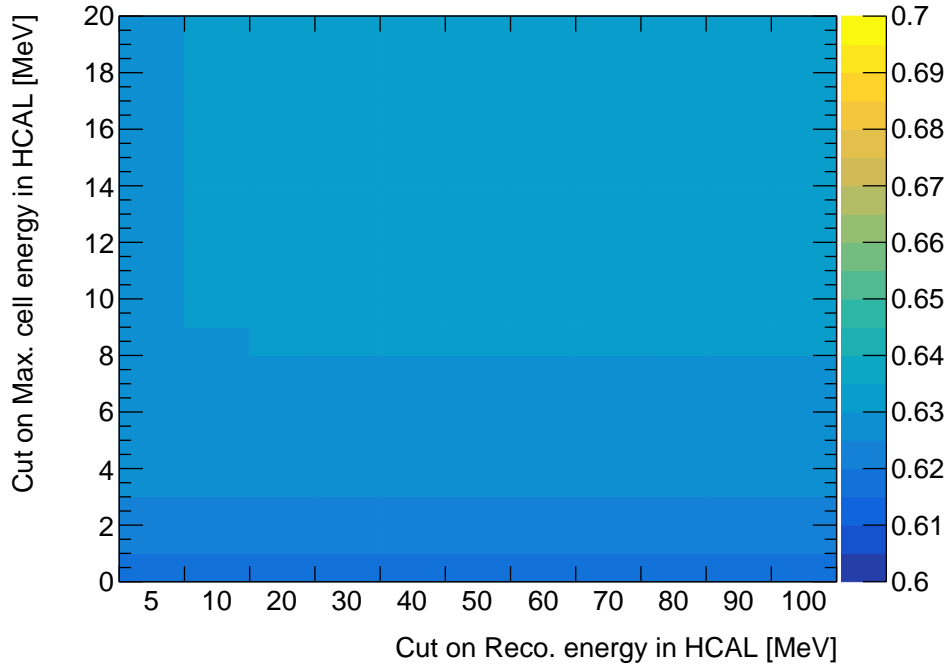
5869 To enhance the analytical sensitivity, cuts on HCAL energy are rigorously optimized. In



**Figure A–8 Distributions of key variables for different signal and background samples.**

5870 typical dark photon signal scenarios, no energy deposition in HCAL is expected, thereby  
 5871 necessitating stringent HCAL veto criteria to suppress specific backgrounds, including  $\gamma \rightarrow$   
 5872  $\mu\mu$  events and hadronic final states. The acceptance efficiency, as a function of HCAL energy,  
 5873 is depicted in Figure A–9 for a simulated 10 MeV signal sample. Here, the total HCAL energy  
 5874 cut varies from 5 MeV to 100 MeV, and the maximum cell energy in HCAL varies from 1 MeV  
 5875 to 20 MeV. Within this energy range, the efficiency remains relatively invariant. Specifically,  
 5876 the 10 MeV signal sample experiences a signal efficiency increase from 61% to 63% when  
 5877 the cut combination of  $(E_{HCAL}^{total}, E_{HCAL}^{MaxCell})$  is relaxed from (5 MeV, 1 MeV) to (100 MeV,  
 5878 10 MeV). Approximately a 1–2% efficiency improvement is also observed for other signal  
 5879 samples. Consequently, the final cut values chosen for optimal background suppression are  
 5880  $E_{HCAL}^{total} < 100$  MeV and  $E_{HCAL}^{MaxCell} < 2$  MeV.

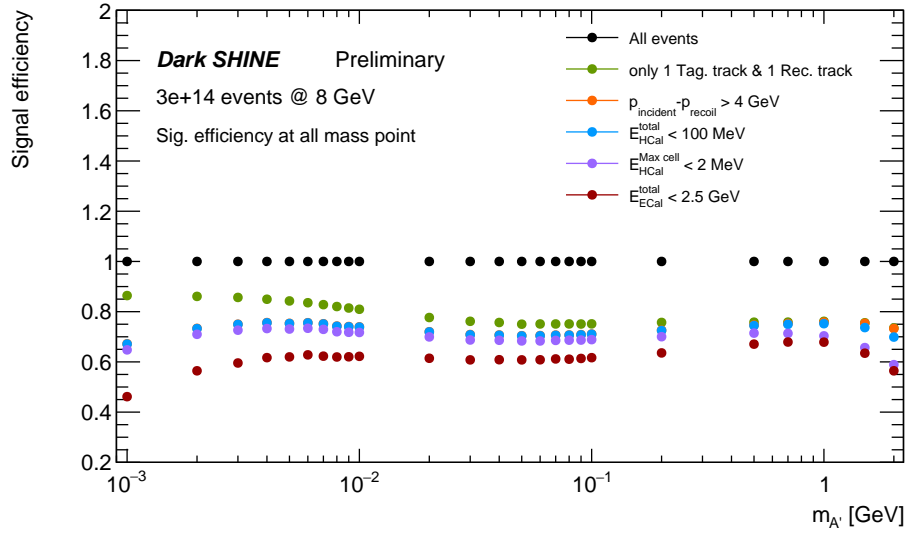
5881 As depicted in Figure A–10, the acceptance efficiencies for various simulated signal sam-



**Figure A-9 Efficiency vs. HCAL energy for the 10 MeV signal.**

5882 ples are plotted as a function of the dark photon mass,  $m_{A'}$ . Overall, high signal efficiencies  
 5883 surpassing 60% are sustained across most of the  $m_{A'}$  range subsequent to the application of  
 5884 all selection criteria. However, the efficiencies witness a decline to approximately 50% when  
 5885  $m_{A'}$  is in the range of a few MeV or above 1 GeV. For the lower  $m_{A'}$  values, the prevailing  
 5886 ECAL and HCAL energy cuts might be excessively stringent, thereby suggesting the need  
 5887 for tailored optimization. Additionally, events with large incident or recoil angles are likely  
 5888 to bypass the ECAL and directly impact the HCAL due to specific geometric configurations  
 5889 at the simulation level. This phenomenon becomes increasingly prevalent for larger  $m_{A'}$  val-  
 5890 ues and results in their rejection by the HCAL energy cuts, thereby leading to diminished  
 5891 selection efficiencies.

5892 To summarize, a comprehensive overview of the background cut flow and corresponding  
 5893 selection efficiencies are documented in Tables A-3 and A-4, respectively.

Figure A-10 Dark photon signal efficiencies across  $m_{A'}$ .

	EN_ECAL	PN_ECAL	GMM_ECAL	EN_target	PN_target	GMM_target	hard_brem	inclusive
total events	$2.48 \times 10^7$	$1.66 \times 10^8$	$1.74 \times 10^7$	$1.09 \times 10^8$	$1.05 \times 10^7$	$1.05 \times 10^7$	$1.02 \times 10^7$	$2.50 \times 10^9$
only 1 track	$1.46 \times 10^7$	$1.17 \times 10^8$	$1.52 \times 10^7$	$6.38 \times 10^6$	$6.17 \times 10^5$	77	$8.03 \times 10^6$	$2.11 \times 10^9$
$p_{tag} - p_{rec} > 4 \text{ GeV}$	1091	5531	707	$6.08 \times 10^6$	$5.73 \times 10^5$	1	$7.19 \times 10^6$	$1.20 \times 10^8$
$E_{HCAL}^{total} < 100 \text{ MeV}$	135	1348	0	322135	75501	0	$1.19 \times 10^8$	$2.89 \times 10^7$
$E_{HCAL}^{MaxCell} < 10 \text{ MeV}$	56	676	0	141808	27949	0	$1.12 \times 10^8$	$2.72 \times 10^7$
$E_{HCAL}^{MaxCell} < 2 \text{ MeV}$	30	363	0	63644	9999	0	$1.01 \times 10^8$	$2.46 \times 10^7$
$E_{ECAL}^{total} < 2.5 \text{ GeV}$	0	0	0	0	0	0	0	0

Table A-3 Event cut flow for each background sample in Table A-2. The number of events remaining after each cut is listed in the table.

## 5894 A.5 Background Estimation

5895 As evidenced by the background cut flow tables (Tables A-3 and A-4), none of the  
 5896  $2.5 \times 10^9$  simulated inclusive background events survive the selection criteria, mirroring  
 5897 the outcome for each of the rare background processes. To project the background yields  
 5898 for a one-year operation of the DarkSHINE experiment, corresponding to  $3 \times 10^{14}$  EOTs,  
 5899 an initial investigation into the background rejection efficiency within side-band regions is  
 5900 mandated, subsequently facilitating extrapolations into the signal region.

5901 To this end, rare background samples of substantial statistical heft, ranging from  $10^{11}$

	EN_ECAL	PN_ECAL	GMM_ECAL	EN_target	PN_target	GMM_target	hard_brem	inclusive
total events	100%	100%	100%	100%	100%	100%	100%	100%
only 1 track	58.87%	70.48%	87.36%	5.85%	5.88%	$< 10^{-3}\%$	78.73%	84.40%
$p_{tag} - p_{rec} > 4 \text{ GeV}$	0.0044%	0.0033%	0.0041%	5.58%	5.46%	$< 10^{-5}\%$	70.49%	4.80%
$E_{HCAL}^{total} < 100 \text{ MeV}$	$< 10^{-3}\%$	$< 10^{-3}\%$	0%	0.30%	0.72%	0%	69.61%	4.76%
$E_{HCAL}^{MaxCell} < 10 \text{ MeV}$	$< 10^{-3}\%$	$< 10^{-3}\%$	0%	0.13%	0.27%	0%	65.00%	4.48%
$E_{HCAL}^{MaxCell} < 2 \text{ MeV}$	$< 10^{-3}\%$	$< 10^{-3}\%$	0%	0.058%	0.095%	0%	58.14%	4.04%
$E_{ECAL}^{total} < 2.5 \text{ GeV}$	0%	0%	0%	0%	0%	0%	0%	0%

**Table A–4 Event cut flow for each background sample in Table A–2. The selection efficiencies of each cut are listed in the table.**

5902 to  $10^{12}$  EOTs as per Table A–2, are deployed for the extraction of anticipated background  
 5903 yields via the fitting of event ratios at prespecified ECAL energy thresholds. For verification  
 5904 purposes, this extrapolation strategy is reciprocally applied to both the inclusive background  
 5905 sample and a series of low-beam energy samples.

5906 Section A.5.1 elaborates on the extrapolation methodology specific to rare background  
 5907 processes. Section A.5.2 furnishes details concerning the validation via inclusive background  
 5908 simulation. Further, Sec. A.5.3 deliberates on rare backgrounds featuring neutrinos in their  
 5909 final states. A summarial discourse on background estimation is presented in Sec. A.5.4.

### 5910 A.5.1 Extrapolation from rare processes simulation

5911 Figure A–11 depicts the event ratios as a function of energy cut values on ECAL for cases  
 5912 with only one tagged track and one recoil track. The data points for six rare background  
 5913 processes (EN\_ECAL, EN\_target, PN\_ECAL, PN\_target, GMM\_ECAL, and GMM\_target)  
 5914 are exhibited, each scaled in accordance with its corresponding branching ratio. In terms  
 5915 of event ratios, the individually generated samples for each of these rare processes align  
 5916 well with their inclusive background counterparts. The composite of these six processes,  
 5917 represented by gray circles, is derived from the rare background samples, whereas the gray  
 5918 dots are obtained from the inclusive background samples. Notably, concordance between  
 5919 these summed fractions is observed, particularly in regions of high energy where statistical  
 5920 robustness is sufficient. A nominal ECAL energy cut at 2.5 GeV is denoted by a blue dashed  
 5921 line.

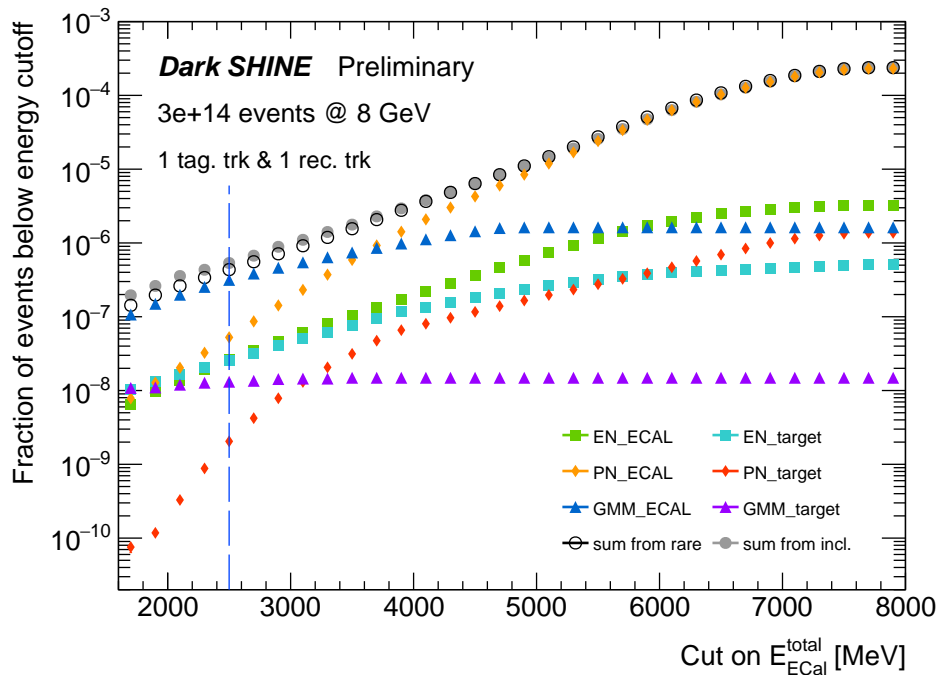


Figure A–11 Event ratio as a function of ECAL energy cut.

5922 The expected background yield at a given ECAL energy cut is computed from the cor-  
 5923 responding event ratio. For instance, with an event ratio below  $10^{-14}$  at an energy cut  $x$ , it  
 5924 can be inferred that fewer than one background event will remain in a sample of  $10^{14}$  events  
 5925 when imposing the condition  $E_{ECAL}^{total} < x$  MeV. To derive the comprehensive background  
 5926 yield within the signal region, the full set of selections delineated in Sec. A.4 must be ap-  
 5927 plied. However, the limited statistics preclude a straightforward extrapolation. The efficacy  
 5928 of HCAL energy cuts results in the depletion of statistics for most processes displayed in  
 5929 Figure A–11, particularly below the nominal ECAL energy cut of 2.5 GeV. Therefore, both  
 5930 high-statistics rare background samples and an extrapolation methodology are employed to  
 5931 extend event ratio trends into low-energy regimes. This approach facilitates the evaluation  
 5932 of background yields for each of the six rare processes, the sum of which serves as the final  
 5933 background yield after validation.

5934 GMM processes are comparatively easier to eliminate. Given the present statistical breadth,  
 5935 no events from GMM\_ECAl ( $6 \times 10^{12}$  EOTs) or GMM\_target ( $4.3 \times 10^{14}$  EOTs) survive the  
 5936 signal region selection per Table A–3. As shown in Figure A–11, the event ratio for the GMM  
 5937 channel is largely unaffected by ECAL energy cuts. Most of the energy is deposited in the

5938 HCAL due to the muon pair. Application of HCAL energy cuts results in a residual GMM  
 5939 event fraction less than  $10^{-6}$ , validating its exclusion from this analysis.

5940 Figure A–12 illustrates background extrapolation plots, showing the fraction of events  
 5941 below certain energy cutoffs for four key processes: EN\_ECAL, EN\_target, PN\_ECAL, and  
 5942 PN\_target. These fractions are scaled according to their respective branching ratios. The  
 5943 function  $e^{a \log(x)+b}$  is fitted to these fractions, where  $x$  is the ECAL energy cut value, and  $a$   
 5944 and  $b$  are free parameters.

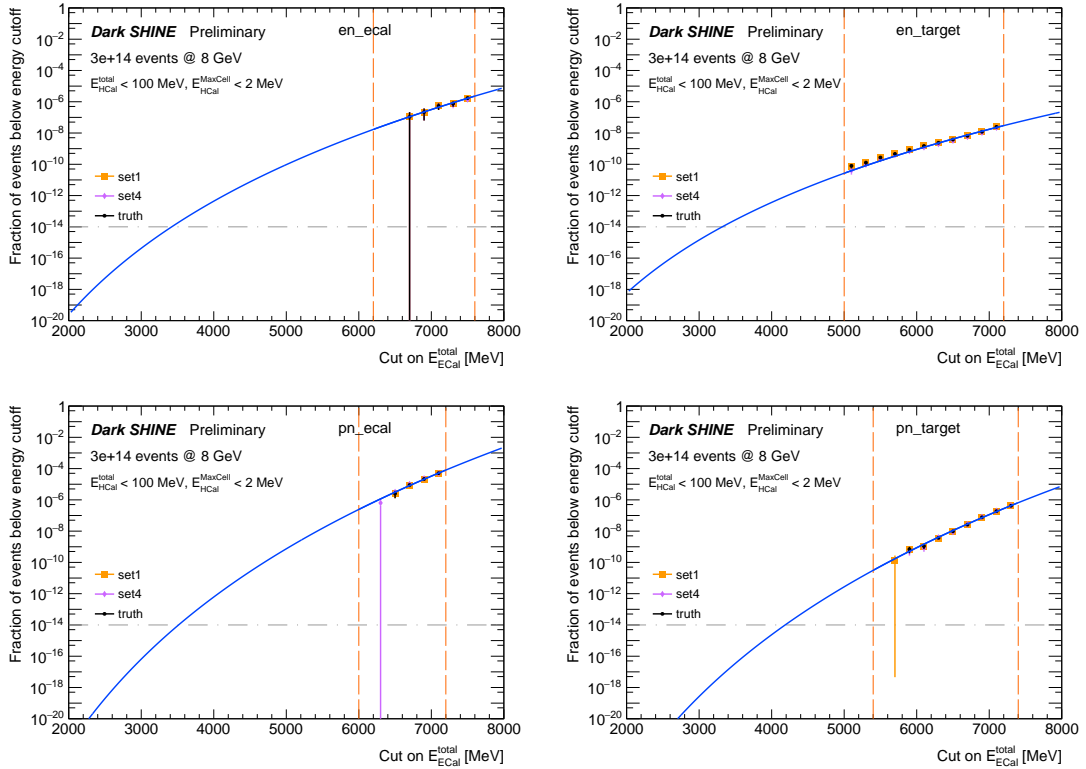


Figure A–12 Background extrapolation plots for four key processes.

Rare process	EN_ECAL	EN_target	PN_ECAL	PN_target	GMM
Estimated yield	0.0016	0.013	$5.93 \times 10^{-5}$	$2.53 \times 10^{-7}$	0

Table A–5 Expected number of each background process, estimated from the extrapolation method. The background yields listed in the table correspond to  $3 \times 10^{14}$  EOTs.

5945 To obtain the background yield at  $E_{ECAL}^{total} = 2.5$  GeV for the remaining four processes,  
 5946 an exponential-logarithmic function is employed to fit the event ratio while maintaining all

5947 other signal region cuts. It should be highlighted that each background channel exhibits  
 5948 distinct cut efficiencies, necessitating individualized functional forms and parameter tuning.  
 5949 Figure A–12 displays the fit extrapolations for the EN\_ECAL, EN\_target, PN\_ECAL, and  
 5950 PN\_target channels. All the criteria defining the signal region, with the exception of the  
 5951 ECAL energy cut, are applied. The fractions for each channel are scaled in accordance with  
 5952 their respective branching ratios. The blue solid line in the plots represents the fitted function,  
 5953 which satisfactorily captures the form of the event ratio within the fit range delineated by the  
 5954 orange dashed lines. The estimated background yields for these channels are summarized  
 5955 in Table A–5. The aggregated background yield for these rare processes is calculated to be  
 5956 approximately 0.015 upon summing their extrapolated yields.

### 5957 **A.5.2 Validation from inclusive background simulation**

5958 The baseline background yield is primarily derived from the rare processes; however, for  
 5959 cross-validation, an inclusive background sample is also analyzed, as depicted in Figure A–  
 5960 13. Here, the event ratio curve is fitted using an exponential-quadratic function of the form  
 5961  $e^{ax^2+bx+c}$ , resulting in an expected background yield of  $2.53 \times 10^{-3}$  when all signal region  
 5962 criteria are applied. The low statistics in the low-energy region prompt further validation  
 5963 efforts.

5964 Additional inclusive background samples, each with  $1 \times 10^7$  events, are generated at  
 5965 discrete electron beam energies ranging from 3 to 7.5 GeV. The event selection criteria are  
 5966 adapted to suit these lower-energy beams, with the missing momentum requirement now set  
 5967 to exceed half of the beam energy. The energy cuts in the HCAL detector are temporarily  
 5968 relaxed to  $E_{HCAL}^{total} < 100$  MeV and  $E_{HCAL}^{MaxCell} < 20$  MeV to preserve adequate statistics. The  
 5969 event fractions from these samples are scaled and aligned to corroborate with the 8 GeV  
 5970 sample, forming the basis for a direct extrapolation method shown in Figure A–14.

5971 To obtain background yields conforming to the signal region conditions, a scale factor  
 5972 is established between the fit outcomes for different HCAL maximum cell energy cuts. Fig-  
 5973 ure A–15 illustrates the fitting procedure for the more relaxed HCAL cut of  $E_{HCAL}^{MaxCell} <$   
 5974 20 MeV. The scaling process yields an extrapolated background estimate of  $9.23 \times 10^{-3}$  for  
 5975  $3 \times 10^{14}$  EOTs, corroborating the results of the original fit extrapolation method.

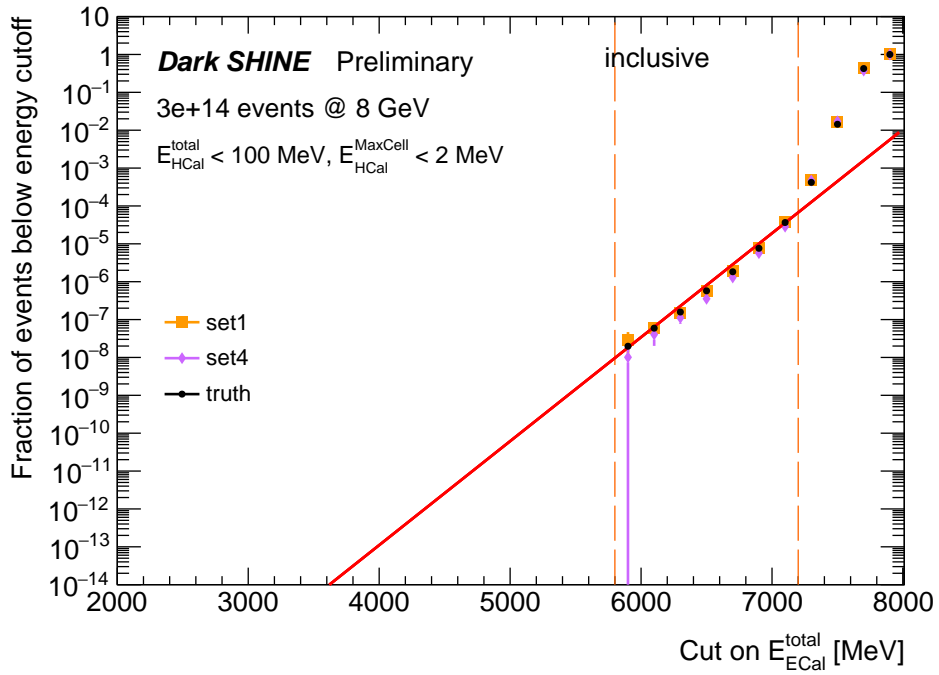


Figure A-13 Background Extrapolation from Inclusive Sample

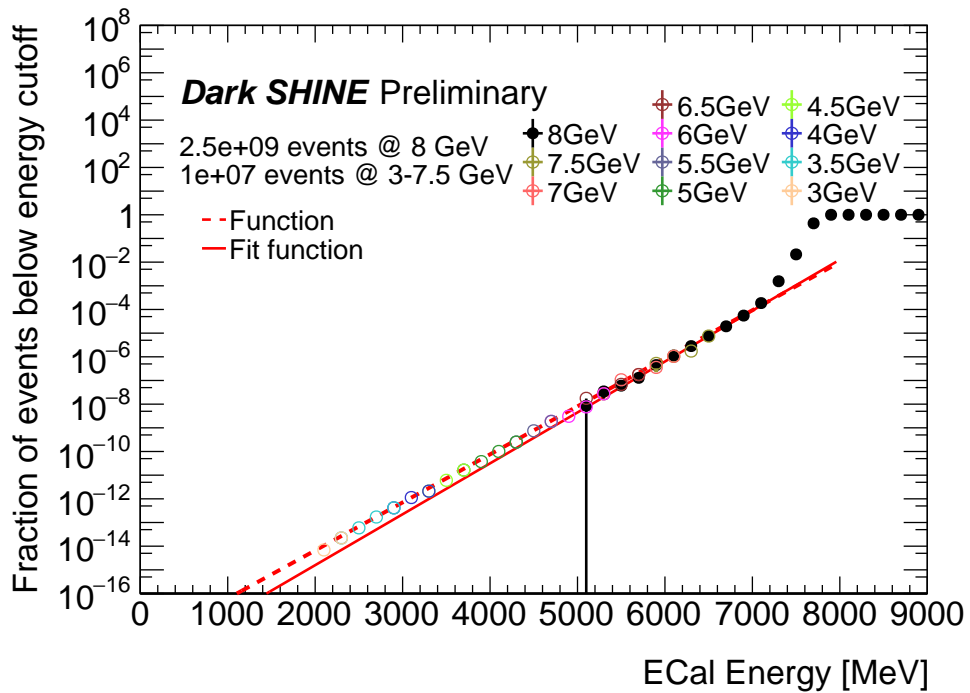


Figure A-14 Background Extrapolation Validation

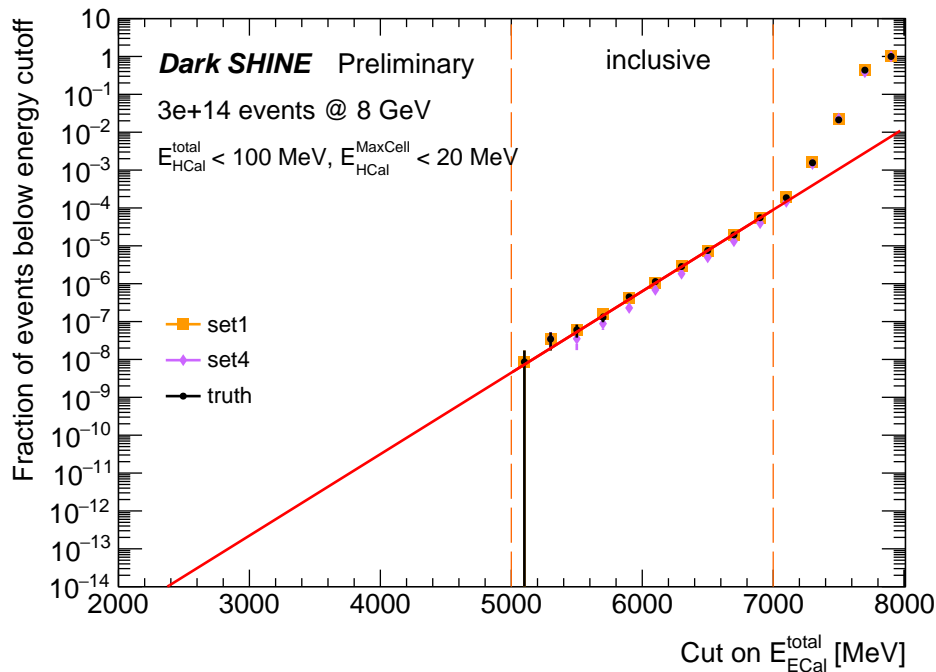


Figure A-15 Background Extrapolation with Relaxed HCAL Cut

### 5976 A.5.3 Invisible background estimation

5977 Neutrino backgrounds originating from specific production reactions constitute a critical  
 5978 source of irreducible backgrounds, indistinguishable from the signal processes. According  
 5979 to Section IV of<sup>[291]</sup>, there are primarily two leading reactions to consider. The first en-  
 5980 compasses Moller scattering followed by charged-current quasi-elastic (CCQE) reactions,  
 5981 mathematically denoted as  $e^-e^- \rightarrow e^-e^-$  and  $e^-p \rightarrow \nu_e n$ . For an incident electron energy  
 5982 of 10 GeV with a W target, the Moller cross-section  $\sigma_{\text{Moller}}$  is roughly 0.4 b and  $\sigma_{\text{CCQE}}$  is 8  
 5983 fb per nucleon. Given that DarkSHINE employs a 0.035-cm W target, this results in an es-  
 5984 timated  $10^{-4}$  events per  $10^{14}$  EOTs. The second category involves neutrino pair production,  
 5985  $e^-N \rightarrow e^-N\nu\bar{\nu}$ , with a cross-section of 0.03 fb, yielding  $6 \times 10^{-6}$  events per  $10^{14}$  EOTs. No-  
 5986 tably, DarkSHINE utilizes an 8 GeV incident electron energy, which implies that the above  
 5987 ratios serve as upper limits for this experiment.

5988 In addition to these irreducible reactions, two other background scenarios are outlined  
 5989 in<sup>[291]</sup>: bremsstrahlung  $\oplus$  CCQE and charge current exchange with exclusive  $e^-p \rightarrow \nu n \pi_0$ .  
 5990 Both yield approximately 0.1 event per  $10^{14}$  EOTs in DarkSHINE but can be effectively dis-

The irreducible reaction	Moller scattering	neutrino pair production
estimated yield	$3 \times 10^{-4}$	$< 1.8 \times 10^{-5}$
The irreducible reaction	Bremsstrahlung $\oplus$ CCQE	charge current exchange
estimated yield	0.3	0.3

**Table A–6 Summary of Invisible Backgrounds**

5991 regarded due to their inability to pass the one-track criterion, which forms part of the signal  
5992 region selection.

5993 Furthermore, during the analysis, a small number of events were observed that left no  
5994 energy deposition in ECAL. Specifically, 2 out of  $1 \times 10^7$  hard bremsstrahlung samples and 6  
5995 out of  $5 \times 10^8$  inclusive samples exhibited this characteristic. These events were traced back  
5996 to photons produced via hard bremsstrahlung, which managed to traverse the gaps between  
5997 ECAL cells to deposit energy exclusively in HCAL. The minimum energy deposition noted  
5998 in HCAL was 527.7 MeV. Such events are effortlessly discarded through the application of  
5999 HCAL energy cuts.

#### 6000 A.5.4 Background Estimation Summary

6001 To consolidate our understanding of the background processes, we summarize the ex-  
6002 pected numbers of background events in the sensitivity study. These numbers are derived  
6003 from multiple avenues: event cut flow, background extrapolation methods, and the invis-  
6004 ible background estimation. Table A–7 displays the yield for each method, corresponding  
6005 to a total exposure of  $3 \times 10^{14}$  EOTs. It should be noted that the cumulative yield from  
6006 the rare background processes is conservatively high but is in agreement with the validation  
6007 conducted on the inclusive sample.

Method	Cut Flow	Rare Extrapolation	Inclusive Extrapolation	Inclusive Validation	Invisible Background
Yield	0	$1.5 \times 10^{-2}$	$2.53 \times 10^{-3}$	$9.23 \times 10^{-3}$	Negligible

**Table A–7 Summary of Background Yields**

## 6008 A.6 Sensitivity study

6009 The relationship between the kinetic mixing parameter  $\varepsilon$  and the expected signal yield  
6010  $N_{\text{sig}}$  is governed by the formula:

$$N_{\text{sig}} = \sigma_{A'} \times 0.1X_0 \times L \times N_A/M_W \times 10^{-36} \times \varepsilon^2,$$

6011 where  $\sigma_{A'}$  is the production cross section for a dark photon of mass  $m_{A'}$  (see Figure A–2),  
6012  $0.1X_0 = 0.676 \text{ g/cm}^2$  denotes the thickness of the tungsten target,  $L = 3 \times 10^{14} \text{ EOTs}$   
6013 signifies the number of events,  $N_A$  is the Avogadro constant, and  $M_W = 184$  represents the  
6014 atomic mass of tungsten.

6015 Given the low estimated background yield elaborated in Section A.5, it is reasonable to  
6016 model all observed events as background following a Poisson distribution. Therefore, the  
6017 upper limit on signal times acceptance efficiency at 90%-CL is

$$s_{\text{up}} \times \varepsilon_{\text{sig}} = \frac{1}{2} F_{\chi^2}^{-1}(1 - \alpha; 2(n_{\text{obs}} + 1)) - b,$$

6018 where  $\varepsilon_{\text{sig}}$  is the acceptance efficiency, dependent on  $m_{A'}$  (see Figure A–10), and  $n_{\text{obs}} = b =$   
6019  $0.015$  is the constant background yield. This leads to upper limits on  $\varepsilon^2$ :

$$\varepsilon^2 = s_{\text{up}}/\varepsilon_{\text{sig}} \times \sigma_{A'} \times 0.1X_0 \times L \times N_A/M_W \times 10^{-36}.$$

6020 The current constraints and sensitivity estimates on  $\varepsilon^2$  as a function of  $m_{A'}$  are displayed  
6021 in Figure A–16. This figure visualizes the expected upper limits on  $\varepsilon^2$  for different data  
6022 collection periods:  $3 \times 10^{14} \text{ EOTs}$  (1 year),  $9 \times 10^{14} \text{ EOTs}$  (3 years), and  $1.5 \times 10^{15} \text{ EOTs}$   
6023 (5 years). Results from other experiments are also integrated for comparison.

6024 In our investigation, we focus on the projected sensitivity in the dimensionless interaction  
6025 strength  $y = \varepsilon^2 \alpha_D (m_\chi/m_{A'})^4$  as a function of Dark Matter (DM) mass  $m_\chi$ . We adopt the  
6026 conventional assumptions that  $m_{A'} = 3m_\chi$  and  $\alpha_D = 0.5$ . Figure A–17 illustrates this sen-  
6027 sitivity, with the calculated projections for the data collected by the DarkSHINE experiment  
6028 under various conditions of event numbers:  $3 \times 10^{14}$ ,  $9 \times 10^{14}$ ,  $1.5 \times 10^{15}$ , and  $10^{16}$  EOTs.

6029 The results indicate promising prospects for the DarkSHINE experiment. For example,  
6030 with a data-taking duration of at least one year, the DarkSHINE experiment will likely com-  
6031 mence probing the existence of thermal relic DM in the MeV mass range. Existing and  
6032 anticipated constraints are also plotted for comparison<sup>[300-306]</sup>.

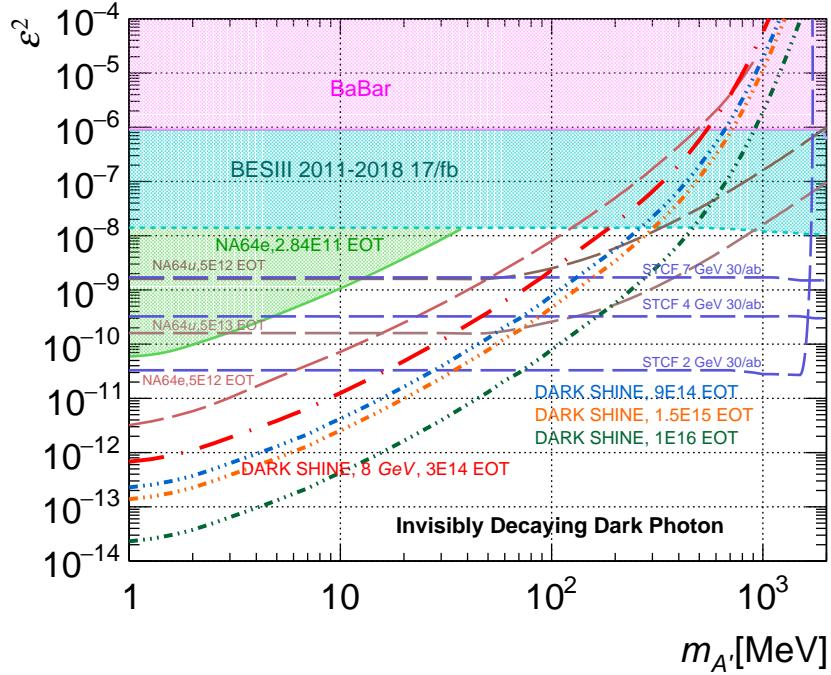


Figure A-16 Constraints on  $\varepsilon^2$  vs  $m_{A'}$

6033 Additionally, our results allow for direct comparison with the Linac to End-Station A  
 6034 (LESA) at the LDMX R&D experiment<sup>[307]</sup>. LESA at LCLS-II will provide a 4 GeV elec-  
 6035 tron beam during its Phase 1, commencing in 2025, and will upgrade to an 8 GeV electron  
 6036 beam for Phase 2 in 2027. Our study indicates that the DarkSHINE experiment offers com-  
 6037 petitive or superior sensitivity, particularly at higher mass ranges owing to the higher incident  
 6038 electron energy and the utilization of LYSO crystal with superior energy resolution. By con-  
 6039 trast, LDMX, with its Si-W sampling calorimeter, excels in spatial resolution and thus shows  
 6040 greater sensitivity in the high-mass region. Given the similar aims of these two experiments,  
 6041 they can serve as immediate cross-checks in the discovery phase space.

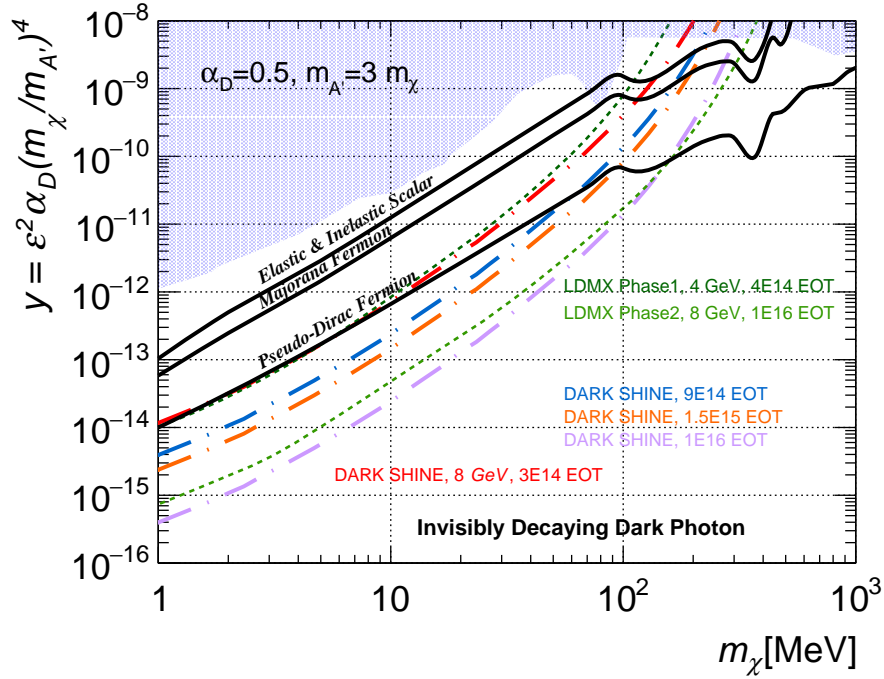


Figure A-17 Projected 90% CL exclusion limits on  $y$  at different event numbers (DarkSHINE experiment).

## 6042 A.7 Summary

6043 This paper investigates the search for the invisible decay of dark photons in fixed-target  
 6044 DarkSHINE experiments utilizing electron beams. Through rigorous simulation methods,  
 6045 we have scrutinized both signal and background signatures. The optimized signal region  
 6046 was identified to minimize background contributions while maximizing signal acceptance  
 6047 efficiency.

6048 For the background estimation, simulated samples were employed to study the contribu-  
 6049 tion from various processes. Due to statistical limitations, an extrapolation method is invoked  
 6050 for a more accurate estimation, and its validity is confirmed through inclusive samples. Un-  
 6051 der these considerations, the expected background yield in the optimized signal region is  
 6052 computed to be 0.015 for  $3 \times 10^{14}$  electrons on target (EOTs).

6053 Subsequently, upper limits at the 90% confidence level were derived for the kinetic mixing  
 6054 parameter  $\varepsilon^2$ , as a function of the dark photon mass  $m_{A'}$ . These limits were calculated for

6055 varying electron-on-target scenarios:  $3 \times 10^{14}$  EOTs,  $9 \times 10^{14}$  EOTs,  $1.5 \times 10^{15}$  EOTs, and  
6056  $10^{16}$  EOTs, corresponding respectively to 1 year, 3 years, and 5 years of data collection,  
6057 including the Phase II upgrade.

6058 Finally, a comparative analysis with operational and prospective experiments yields highly  
6059 competitive results. Specifically, the sensitivity of the DarkSHINE experiment is sufficient  
6060 to probe, and potentially exclude, parameter spaces for models involving elastic and inelastic  
6061 scalars, Majorana fermions, and pseudo-Dirac fermions.



6062

## Acknowledgements

6063

Will be added later.



## List of Research Achievements

6064

### Scholarly paper

6065

- 6066 [1] Chen, J., Chen, JY., Chen, JF. et al. Prospective study of light dark matter search with  
6067 a newly proposed DarkSHINE experiment. *Sci. China Phys. Mech. Astron.* 66, 211062  
6068 (2023).
- 6069 [2] The ATLAS Collaboration. Constraints on the Higgs boson self-coupling from single-  
6070 and double-Higgs production with the ATLAS detector using  $pp$  collisions at  $\sqrt{s} =$   
6071 13 TeV. *Physics Letters B*, 843, 137745 (2023).
- 6072 [3] The ATLAS Collaboration. Search for non-resonant Higgs boson pair production in  
6073 final states with leptons and photons in proton-proton collisions at  $\sqrt{s} = 13$  TeV with  
6074 the ATLAS detector. ANA-HDBS-2019-04 (to be submitted to XXXX).
- 6075 [4] The ATLAS Collaboration. Search for the non-resonant production of Higgs boson  
6076 pairs via gluon fusion and vector-boson fusion in the  $b\bar{b}\tau^+\tau^-$  final state in proton-proton  
6077 collisions at  $\sqrt{s} = 13$  TeV with the ATLAS detector. ANA-HDBS-2019-27 (to be sub-  
6078 mitted to XXXX).
- 6079 [5] Zhang, Y., et al. Search for Long-lived Particles at Future Lepton Colliders Using Deep  
6080 Learning Techniques. (to be submitted to XXXX).